transactions of the ASME
Published Quarterly by
The American Society of
Mechanical Engineers
Volume 93 • Series C • Number 4
NOVEMBER 1971

journal of heat transfer

EDITED and PUBLISHED quarterly at the offices of The American Society of Mechanical Engineers, United Engineering Center, 345 E. 47th St., New York, N. Y. 10017. Cable address, "Mechaneer," New York. Second-class postage paid at New York, N. Y., and at additional mailing offices.

CHANGES OF ADDRESS must be received at Society headquarters seven weeks before they are to be effective. Please send old label and new address.

PRICES: To members, $15.00, annually; to nonmembers, $30.00. Single copies, $10.00 each. Add $1.50 for postage to countries outside the United States and Canada.

INDEXED by the Engineering Index, Inc.

(Contents continued on page 480)

CONTENTS (CONTINUED)

J. KESTIN
Professor.
Mem. ASME

R. T. WOOD
Division of Engineering,
Brown University,
Providence, R. I.

The Influence of Turbulence on Mass Transfer From Cylinders

This paper describes new local mass-transfer measurements from two cylinders, coated with a layer of paradichlorobenzene (p-$C_6H_4Cl_2$), to air. The cylinders were placed in cross flow, and measurements were performed at three nominal values of the Reynolds number (75, 100, 125 $\times$ 10^3) as well as at varying levels of turbulence intensity. In the range where the boundary layer is laminar, the effect of turbulence intensity is always to increase the transfer rate, approximately by a constant factor ϕ which depends on the turbulence intensity as well as the Reynolds number. Across the turbulent boundary layer and wake the influence is not systematic, as both increases and decreases are observed. The data for the stagnation line are compared with other measurements. They can all be correlated against the single parameter $Tu\mathrm{Re}^{1/2}$, as suggested by a semi-empirical theory due to Smith and Kuethe. However, the global correlation equation (a second-degree polynomial) differs from the originally proposed linear relationship, and the uncertainty is one of ± 8 percent.

Introduction

THE WORK of Brun, Diep, and Kestin [1][1] established the existence of a spanwise variation in the rate of mass transfer from the front of a cylinder in cross flow. Kestin and Wood [2, 3] investigated the flow field in the laminar boundary layer formed at the front of a cylinder and demonstrated both analytically and experimentally that it, too, is three-dimensional in character. This flow pattern has turned out to be sensitive to the turbulence intensity of the free stream through the latter's influence on the pitch, λ, and the amplitude, A, of the spanwise system of vortices which is formed as a result of the instability of the external flow.

From a practical point of view, these investigations confirmed that the rate of mass transfer across the laminar boundary layer on a cylinder in cross flow is slightly higher than would be the case for Hiemenz flow for zero intensity of turbulence, increasing quite dramatically for relatively small increases in turbulence intensity.

Since the same flow pattern is formed on a cylinder whose surface temperature differs from that of the free stream, analogous effects must be expected in heat transfer. Such increases were measured by Kestin, Maeder, and Sogin [4], among others.

The objective of this paper is to extend the mass-transfer measurements of reference [1] in order to provide additional experimental data for the theory of references [2, 3]. Local measurements were performed over the whole cylinder surface, even though the effect of free-stream turbulence on the transfers across the turbulent boundary layer and wake have not been studied analytically or experimentally in a systematic way.

Experimental Procedure

The mass-transfer experiments were conducted with the aid of two cylinders (3 and 4 in. nominal diameter). Each cylinder was constructed from a 10-in. length of plexiglass tubing coated with paradichlorobenzene to a thickness of about $^3/_{32}$ in. The ends of the cylinders were closed by circular brass caps mounted on a steel shaft common with the axis of the plexiglass tube. Two plexiglass gage rings were mounted on the caps for indexing. The plexiglass tubes were coated by rotating them partially immersed in a bath of molten paradichlorobenzene kept at 60 deg C. After cooling, the coating was machined in a lathe and sanded down carefully to be flush with the gage rings.

The cylinder was quickly assembled in the wind tunnel and exposed to a steady stream for about 1 hour. The mass lost by the cylinder during a wind-tunnel test was determined by measuring the change in coating thickness with respect to the gage rings. This was done with the aid of a dial gage which read to 0.0001 in. and whose stem was fitted with a delrin pad to avoid scoring the surface. During the measuring operations, the cylinder was mounted between centers in a lathe. Local thickness profiles around the cylinder were taken at three spanwise stations (at center and $^1/_2$ in. to each side).

Each step in the procedure was carefully timed, and corrections for free-convection losses were applied. On the average, the surface lost thickness at the rate of 0.25×10^{-4} in/min in still air. Additional corrections were applied to allow for the starting and stopping of the tunnel. They proved to be small.

[1] Numbers in brackets designate References at end of paper.

Contributed by the Heat Transfer Division and presented at the Winter Annual Meeting, New York, N. Y., November 29–December 3, 1970, of THE AMERICAN SOCIETY OF MECHANICAL ENGINEERS. Manuscript received by the Heat Transfer Division January 19, 1970; revised manuscript received May 19, 1970. Paper No. 70-WA/HT-3.

Free-Stream Turbulence

Two square-mesh grids of different geometries and a plane framework of evenly spaced horizontal rods were used to generate turbulence in the free stream. For each case, the plane of the generator was placed normal to the flow, and the intensity of turbulence approaching the model was varied by altering the upstream location of the generator relative to the model.

The behavior of the clear-tunnel turbulence intensity downstream from each generator for one wind speed (16 m/sec) has been plotted in Fig. 1, which shows that the present decay data, correlated by the dashed lines, display excellent agreement with the earlier measurements (solid line) of Dryden, et al. [5] under comparable conditions. Fig. 2 illustrates the variation of turbulence intensity with air speed at selected distances downstream from the turbulence generators; in all cases, it was possible to achieve a turbulence level that was within 15 percent of a nominal value over a satisfactory range of air speeds.

In this work the values reported for the turbulence intensity of the free stream were determined at a location corresponding to 1.5 cylinder diameters upstream from the stagnation line of the cylinder. As shown in Fig. 3 for a set of representative conditions, the turbulence level at this location has just begun to be affected by the presence of the cylinder. For practical purposes, the turbulence intensity here is independent of whether the cylinder is in the flow or removed from it.

No measurements of the scale of the turbulence were undertaken. However, by analogy with heat-transfer measurements (e.g., reference [6]), where the effect of scale amounts to only a few percent, the influence of the turbulence scale on the stagnation-line mass transfer is expected to be small. Indeed, the resolution of the present data is inadequate to disclose the effect.

The secondary importance of the scale of the turbulence on the forward stagnation boundary layer is also implied by our theory, which was described briefly in the Introduction. In the more detailed accounts of references [2, 3], it has been indicated that the principal length scale of the problem is the wavelength, λ, of the spanwise system of vortices formed from an instability of the external flow. This wavelength is governed primarily by the *average* flow conditions (Reynolds number), although it has been shown both experimentally and analytically that the turbulence *intensity* does have an effect on it. Finally, in reference [3], evidence has been presented which demonstrates that the vortex system can lead to high rates of heat or mass transfer across the stagnation boundary layer. This suggests the physical picture that the slightest amount of free-stream turbulence triggers the flow instability, and that increased intensities affect both the wavelength and the amplitude of the vortex motion ensuing from the instability, thereby causing dramatic increases in the transfers of mass, momentum, and energy across the boundary layer. In this process, the actual structure of the free-stream turbulence assumes a subordinate role.

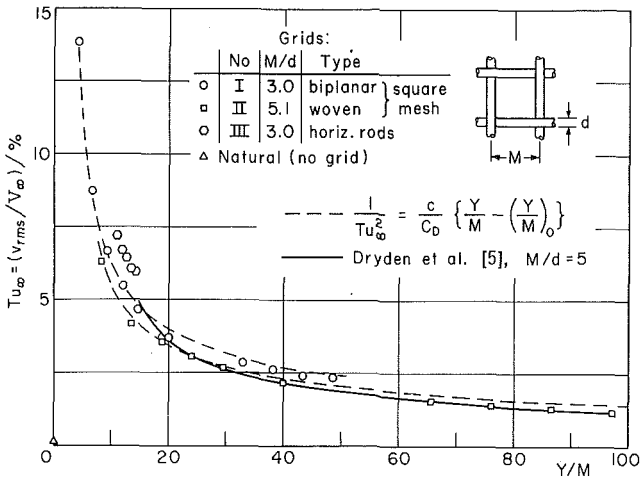

Fig. 1 Variation of turbulence intensity Tu_∞ with distance Y/M downstream from grids

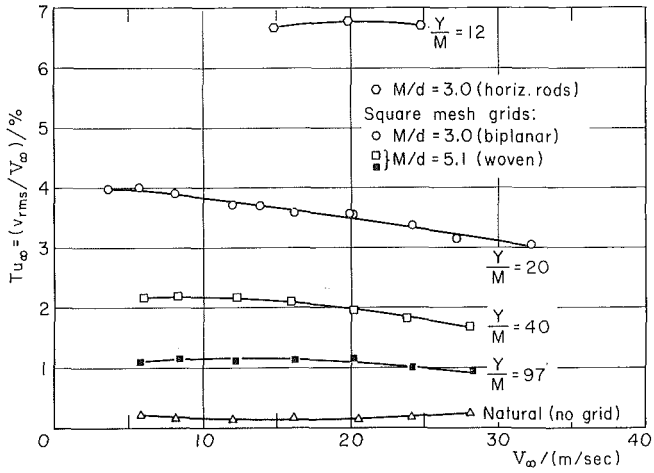

Fig. 2 Variation of turbulence intensity Tu_∞ with velocity V_∞ at selected distances Y/M from grids

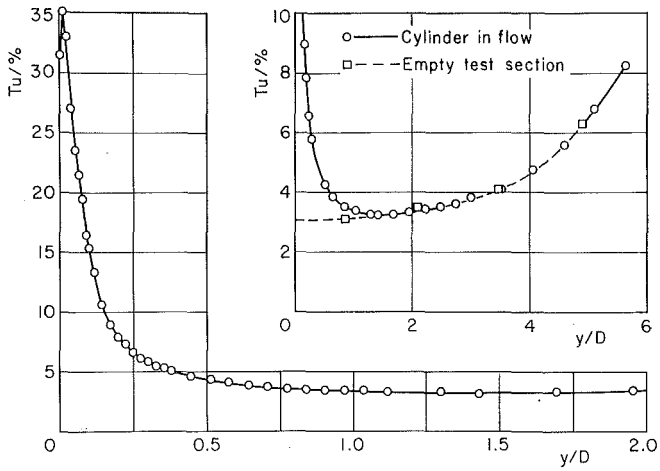

Fig. 3 Variation of turbulence intensity along the stagnation streamline for grid II

Data Reduction

The mass-transfer rate is measured by the Sherwood number

$$\mathrm{Sh} = \frac{b\mathrm{D}}{D}, \tag{1}$$

where D is the diameter of the cylinder, D is the coefficient of binary diffusion of paradichlorobenzene into air, and b is the mass-transfer coefficient. The latter is given by

$$b = \frac{\dot{m}''}{\rho_{v,w} - \rho_{v,\infty}}. \tag{2}$$

The symbols $\rho_{v,w}$ and $\rho_{v,\infty}$ denote the density of the vapor at the wall and outer stream, respectively, whereas $\dot{m}''$ is the loss of mass per unit area and time. In turn

$$\dot{m}'' = \frac{\Delta r}{\Delta t}\rho_s, \tag{3}$$

where Δr is the loss of thickness in time Δt, and ρ_s is the density of solid paradichlorobenzene.

Evidently $\rho_{v,\infty} = 0$, and for the concentration of the vapor at the wall we may write

$$\rho_{v,w} = \frac{P_{v,w}}{k_v T_w}, \tag{4}$$

assuming perfect-gas properties. The partial pressure $P_{v,w}$ at saturation was evaluated from a semiempirical correlation of the form [7]

$$\log (P_{r,w}/P_1) = A - (B/T_w). \tag{5}$$

Thus the working equation could be written

$$\mathrm{Sh} = \frac{\Delta r}{\Delta t}\frac{\mathrm{D}}{D}\frac{\rho_s}{\rho_{v,w}} = \frac{\Delta r}{\Delta t}\frac{\mathrm{D}}{\nu}\frac{\rho_s(T_w)}{\rho_{v,w}(T_w)}\,\mathrm{Sc}. \tag{6}$$

Here, $\mathrm{Sc} = \nu/D$ is the Schmidt number, and ν is the kinematic viscosity of the vapor.

Given values for the thermodynamic and transport properties of paradichlorobenzene, the remaining unknown in equation (6) is the wall temperature T_w. Since the latent heat of sublimation l_{su} must be supplied from the air by convection (radiation and conduction neglected), the recovery temperature T_r which the surface would reach in the absence of sublimation is depressed. The amount of this depression can be computed from the steady-state energy balance

$$h(T_r - T_w) = \dot{m}'' l_{su}. \tag{7}$$

If the analogy between heat and mass transfer is applied to eliminate the heat-transfer coefficient h from equation (7), then the wall temperature can be computed from

$$T_w = T_r - K\frac{P_{v,w}}{P_0}, \tag{8a}$$

as shown by Sogin [8]. The constant K is

$$K = \left(\frac{\mathrm{Pr}}{\mathrm{Sc}}\right)^{2/3}\frac{M_v}{M}\frac{l_{su}}{c_P}, \tag{8b}$$

where Pr, M, and c_P are the Prandtl number, the molecular mass, and the specific heat of air; M_v is the molecular mass of paradichlorobenzene; and P_0 is the total pressure of the air-vapor mixture.

The wall temperature required for the evaluation of the Sherwood number, equation (6), was computed iteratively by combining equations (5) and (8a). The total pressure P_0 was taken to be atmospheric; the temperature indicated by a bare thermocouple in the stream was assumed to be the recovery temperature T_r.

The mass-transfer coefficients of the three spanwise profiles measured for a given run always differed, but not in any apparent systematic fashion. Rather than destroy the consistency of the individual profiles by averaging, the profile of median values was chosen to represent the mass-transfer data for a test. The extremes fell within ±5 percent of the median in most cases.

The values recorded for the turbulence intensity of the stream were determined at a location corresponding to 1.5 cylinder diameters upstream from the stagnation line of the cylinder. As already mentioned in the section Free-Stream Turbulence, it was ascertained that the turbulence level at this location has just begun to be affected by the presence of the cylinder.

Properties of Paradichlorobenzene (p-$C_6H_4Cl_2$)

Following is a list of the properties of the paradichlorobenzene which were used in reducing the data:

Molecular mass [7]: $M_v = 147.01$ lbm/lbmol

Specific gas constant ($= R/M_v$): $\mathrm{R}_v = 10.512\ \dfrac{\text{ft-lbf}}{\text{lbm R}}$

Density of solid (pycnometer determination): $\rho_s = 90.84$ lbm/ft³

Vapor-pressure curve [7]:

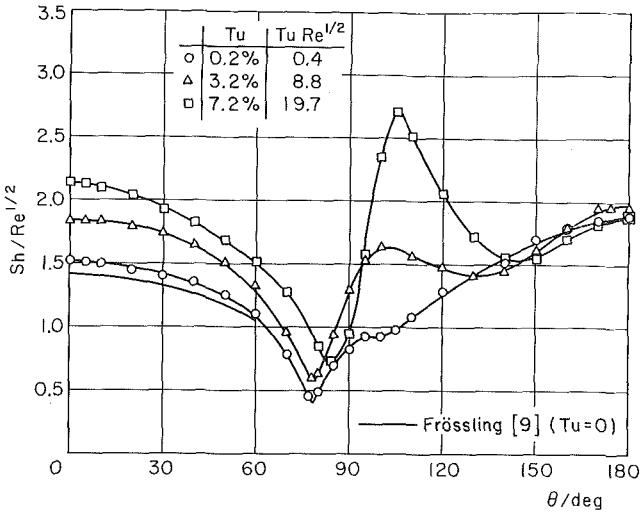

Fig. 4 Effect of turbulence on mass-transfer rate around a cylinder at Reynolds number: Re = 75,000 (nominal)

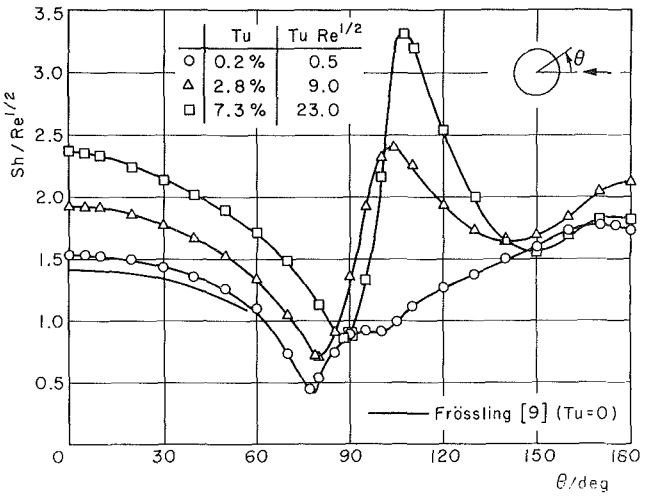

Fig. 5 Effect of turbulence on mass-transfer rate around a cylinder at Reynolds number: Re = 100,000 (nominal)

$$\log\left[\frac{P_{v,w}}{\text{lbf/ft}^2}\right] = 12.430 - \frac{6426}{(T_w/\mathrm{R})} \qquad (510\ \mathrm{R} \le T_w \le 580\ \mathrm{R})$$

Constant K defined by equation (8b) [8]: $K = 1700$ R

Schmidt number ($= \nu/D$): $\mathrm{Sc} = 2.40$.

The value Sc = 2.40 is a compromise for the results discussed by Sogin [8] and may be in error by as much as 15 percent.

Experimental Results

The present measurements were performed at three nominal Reynolds numbers and at several values of turbulence intensity. They have been listed in Table 1 and plotted in Figs. 4, 5, and 6.

The Nusselt number Nu has been evaluated by the application of the heat–mass-transfer analogy. The analogy reads

$$\frac{\mathrm{Nu}}{\mathrm{Re}^{1/2}} = \frac{\mathrm{Sh}}{\mathrm{Re}^{1/2}}\left(\frac{\mathrm{Pr}}{\mathrm{Sc}}\right)^{1/3}, \tag{9a}$$

and becomes

$$\frac{\mathrm{Nu}}{\mathrm{Re}^{1/2}} = 0.669\,\frac{\mathrm{Sh}}{\mathrm{Re}^{1/2}} \tag{9b}$$

for Sc = 2.40 and Pr = 0.72. An uncertainty of 15 percent in the Schmidt number reflects as approximately a 5 percent uncertainty in the Nusselt number.

Table 1 Local coefficient of mass (heat) transfer around a cylinder

A. Re = 75,000

Tu = 0.15% D = 3.00 in.			Tu = 3.20% D = 3.00 in.			Tu = 3.67% D = 4.05 in.			Tu = 7.20% D = 3.00 in.		
θ/deg	$Sh/Re^{1/2}$	$Nu/Re^{1/2}$	θ/deg	$Sh/Re^{1/2}$	$Nu/Re^{1/2}$	θ/deg	$Sh/Re^{1/2}$	$Nu/Re^{1/2}$	θ/deg	$Sh/Re^{1/2}$	$Nu/Re^{1/2}$
0	1.52	1.02	0	1.84	1.23	0	1.84	1.23	0	2.15	1.44
5	1.51	1.01	5	1.84	1.23	5	1.83	1.22	5	2.13	1.43
10	1.50	1.00	10	1.84	1.23	10	1.81	1.21	10	2.10	1.40
20	1.46	0.98	20	1.80	1.20	20	1.75	1.17	20	2.04	1.36
30	1.42	0.95	30	1.75	1.17	30	1.66	1.11	30	1.93	1.29
40	1.36	0.91	40	1.65	1.10	40	1.57	1.05	40	1.83	1.22
50	1.26	0.84	50	1.51	1.01	50	1.46	0.98	50	1.69	1.13
60	1.11	0.74	60	1.33	0.89	60	1.26	0.84	60	1.52	1.02
70	0.79	0.53	70	0.96	0.64	70	0.91	0.61	70	1.28	0.86
77	0.46	0.31	78	0.60	0.40	80	0.42	0.28	80	0.85	0.57
80	0.50	0.33	80	0.63	0.42	85	0.62	0.41	84	0.73	0.49
85	0.71	0.47	85	0.94	0.63	90	1.02	0.68	90	0.95	0.64
90	0.83	0.56	90	1.29	0.86	95	1.40	0.94	95	1.58	1.06
95	0.93	0.62	95	1.53	1.02	100	1.57	1.05	100	2.35	1.57
100	0.92	0.62	100	1.63	1.09	104	1.57	1.05	105	2.71	1.81
105	0.98	0.66	110	1.56	1.04	110	1.50	1.00	110	2.52	1.68
110	1.09	0.73	120	1.47	0.98	120	1.35	0.90	120	2.06	1.38
120	1.28	0.86	130	1.42	0.95	130	1.26	0.84	130	1.71	1.14
130	1.40	0.94	140	1.46	0.98	140	1.27	0.85	140	1.53	1.02
140	1.52	1.02	150	1.61	1.08	150	1.40	0.94	150	1.56	1.04
150	1.70	1.14	160	1.79	1.20	160	1.59	1.06	160	1.71	1.14
160	1.79	1.20	170	1.95	1.30	170	1.78	1.19	170	1.83	1.22
170	1.86	1.24	174	1.96	1.31	180	1.86	1.24	178	1.88	1.26
180	1.87	1.25	180	1.95	1.30				180	1.87	1.25

Table 1 (continued)

B. Re = 100,000

Tu = 0.15% D = 3.00 in.			Tu = 2.84% D = 3.00 in.			Tu = 3.50% D = 4.05 in.			Tu = 7.28% D = 3.00 in.		
θ/deg	$Sh/Re^{1/2}$	$Nu/Re^{1/2}$	θ/deg	$Sh/Re^{1/2}$	$Nu/Re^{1/2}$	θ/deg	$Sh/Re^{1/2}$	$Nu/Re^{1/2}$	θ/deg	$Sh/Re^{1/2}$	$Nu/Re^{1/2}$
0	1.54	1.03	0	1.91	1.28	0	1.93	1.29	0	2.37	1.58
5	1.53	1.02	5	1.91	1.28	5	1.92	1.28	5	2.35	1.57
10	1.52	1.02	10	1.91	1.28	10	1.90	1.27	10	2.33	1.56
20	1.49	1.00	20	1.86	1.24	20	1.84	1.23	20	2.24	1.50
30	1.43	0.96	30	1.77	1.18	30	1.76	1.18	30	2.14	1.43
40	1.36	0.91	40	1.66	1.11	40	1.68	1.12	40	2.02	1.35
50	1.26	0.84	50	1.52	1.02	50	1.54	1.03	50	1.88	1.26
60	1.11	0.74	60	1.33	0.89	60	1.39	0.93	60	1.71	1.14
70	0.73	0.49	70	1.04	0.70	70	1.12	0.75	70	1.49	1.00
77	0.44	0.29	79	0.72	0.48	80	0.72	0.48	80	1.13	0.76
80	0.54	0.36	80	0.72	0.48	85	0.92	0.62	88	0.87	0.58
85	0.74	0.49	85	0.91	0.61	90	1.51	1.01	90	0.91	0.61
90	0.90	0.60	90	1.36	0.91	95	2.25	1.50	95	1.33	0.89
95	0.92	0.61	95	1.92	1.28	100	2.64	1.77	100	2.17	1.45
100	0.91	0.61	100	2.32	1.55	102	2.67	1.79	107	3.31	2.22
105	0.99	0.66	104	2.40	1.60	110	2.36	1.58	110	3.19	2.14
110	1.12	0.75	110	2.25	1.50	120	1.94	1.30	120	2.54	1.70
120	1.27	0.85	120	1.93	1.29	130	1.67	1.12	130	2.00	1.34
130	1.37	0.92	130	1.73	1.16	140	1.52	1.02	140	1.65	1.10
140	1.50	1.00	140	1.64	1.10	150	1.58	1.06	150	1.56	1.04
150	1.60	1.07	150	1.69	1.13	160	1.77	1.18	160	1.69	1.13
160	1.73	1.16	160	1.84	1.23	170	1.92	1.28	170	1.83	1.22
170	1.79	1.20	170	2.04	1.36	180	1.97	1.32	180	1.82	1.22
175	1.76	1.18	180	2.12	1.42						
180	1.71	1.14									

The solid line in Figs. 4–6 corresponds to Frössling's theoretical (zero-turbulence) calculation for laminar transfer [9], Table 2. It is seen that up to about $\theta = 60$ deg, that is at the base of the laminar boundary layer, the effect of increasing the intensity of turbulence is to multiply the theoretical value by a nearly constant factor, ϕ. Average values of this factor have been plotted against turbulence intensity in Fig. 7 for three values of the Reynolds number. For $\theta > 60$ deg, an increase in the intensity of turbulence at a constant Reynolds number does not seem to affect the Nusselt number in a particular direction, both increases and decreases being observed.

Comparison With Other Heat- and Mass-Transfer Measurements

In order to compare the present results with those of other experimenters, it is necessary to restrict oneself to the stagnation point, and it is convenient to use the single correlation parameter $Tu\mathrm{Re}^{1/2}$. The latter has been suggested by Smith and Kuethe [10] on the basis of a semiempirical theory. The present data have been listed in Table 3, and all measurements have been graphed in Fig. 8. The broken line in the diagram corresponds to the theory of reference [10].

It is seen that the theory describes the measurements of its authors reasonably well, but that it fails to conform to the general trend of the remaining body of data. In particular, it would appear that the analysis should be based on Frössling's [9] theoretical (zero-turbulence) calculation $\mathrm{Nu}/\mathrm{Re}^{1/2} = 0.945$ rather than on Squire's [11] approximate value $\mathrm{Nu}/\mathrm{Re}^{1/2} = 1.00$.

A better representation can be obtained by interpolating a faired curve by the method of least squares and by forcing it to pass through $\mathrm{Nu}/\mathrm{Re}^{1/2} = 0.945$ at $Tu\mathrm{Re}^{1/2} = 0$, as is shown by the full line in Fig. 8. This correlation can be represented by the equation

$$\frac{\mathrm{Nu}}{\mathrm{Re}^{1/2}} = 0.945 + 3.48\left(\frac{Tu\mathrm{Re}^{1/2}}{100}\right) - 3.99\left(\frac{Tu\mathrm{Re}^{1/2}}{100}\right)^2 \quad (10)$$

in the range $0 < (Tu\mathrm{Re}^{1/2}) < 40$. Here Tu is expressed as an absolute (as opposed to a percentage) fraction.

The mass-transfer results of the present investigation lie

Table 1 (continued)

C. Re = 125,000

Tu = 0.20% D = 3.00 in.			Tu = 2.59% D = 3.00 in.			Tu = 3.42% D = 4.05 in.			Tu = 6.98% D = 3.00 in.		
θ/deg	$Sh/Re^{1/2}$	$Nu/Re^{1/2}$	θ/deg	$Sh/Re^{1/2}$	$Nu/Re^{1/2}$	θ/deg	$Sh/Re^{1/2}$	$Nu/Re^{1/2}$	θ/deg	$Sh/Re^{1/2}$	$Nu/Re^{1/2}$
0	1.49	1.00	0	1.99	1.33	0	2.04	1.36	0	2.26	1.51
5	1.49	1.00	5	1.98	1.33	5	2.02	1.35	5	2.23	1.49
10	1.48	0.99	10	1.97	1.32	10	2.00	1.34	10	2.20	1.47
20	1.44	0.96	20	1.89	1.26	20	1.94	1.30	20	2.12	1.42
30	1.39	0.93	30	1.82	1.22	30	1.84	1.23	30	2.02	1.35
40	1.32	0.88	40	1.68	1.12	40	1.74	1.16	40	1.90	1.27
50	1.21	0.81	50	1.46	0.98	50	1.60	1.07	50	1.76	1.18
60	1.04	0.70	60	1.38	0.92	60	1.43	0.96	60	1.59	1.06
65	0.91	0.61	70	1.09	0.73	70	1.20	0.80	70	1.38	0.92
70	0.65	0.43	80	0.76	0.51	80	0.79	0.53	80	1.08	0.72
77	0.33	0.22	85	0.88	0.59	84	0.67	0.45	88	0.83	0.55
80	0.53	0.35	90	1.29	0.86	90	1.05	0.70	90	0.84	0.56
85	0.68	0.45	95	1.89	1.26	95	2.03	1.36	95	1.16	0.78
90	0.86	0.58	100	2.54	1.70	100	3.14	2.10	100	1.87	1.25
95	0.80	0.53	104	2.84	1.90	103	3.44	2.30	109	3.40	2.27
100	0.79	0.53	110	2.62	1.75	110	2.96	1.98	110	3.35	2.24
110	1.01	0.67	120	2.21	1.48	120	2.26	1.51	120	2.65	1.77
120	1.13	0.76	130	1.90	1.27	130	1.80	1.20	130	2.03	1.36
130	1.19	0.80	140	1.72	1.15	140	1.57	1.05	140	1.60	1.07
140	1.30	0.87	150	1.72	1.15	150	1.62	1.08	150	1.43	0.96
150	1.44	0.96	160	1.89	1.26	160	1.82	1.22	160	1.54	1.03
160	1.52	1.02	170	2.07	1.38	170	2.03	1.36	170	1.75	1.17
165	1.54	1.03	176	2.12	1.42	180	2.09	1.40	174	1.79	1.20
170	1.55	1.04	180	2.11	1.41				180	1.74	1.17
175	1.55	1.04									
180	1.54	1.03									

Table 2 Local coefficient of mass (heat) transfer around a cylinder; Frössling's [9] theoretical calculation for laminar range

	Tu = 0%	
θ/deg	$Sh/Re^{1/2}$	$Nu/Re^{1/2}$
0	1.41	0.945
5	1.41	0.945
10	1.40	0.937
20	1.38	0.923
30	1.33	0.890
40	1.27	0.853
50	1.18	0.790
60	1.06	0.710

Table 3 Local coefficient of mass (heat) transfer at stagnation line of circular cylinders

Re × 10^{-3}	Tu %	$Tu Re^{1/2}$	$Sh/Re^{1/2}$	$Nu/Re^{1/2}$
	D = 3.00 in.			
75.0	0.15	0.41	1.52	1.01
75.3	3.20	8.75	1.84	1.22
75.3	7.20	19.7	2.15	1.44
100.4	0.15	0.48	1.54	1.03
100.7	2.84	9.00	1.91	1.28
99.4	7.28	23.0	2.37	1.58
124.9	0.20	0.71	1.49	0.99
125.6	2.59	9.15	1.99	1.33
125.3	6.98	24.7	2.26	1.51
	D = 4.05 in.			
74.8	3.67	10.0	1.84	1.23
100.1	3.50	11.1	1.93	1.29
125.6	3.42	12.1	2.04	1.36

within 8 percent of the line fitted through the center of the data. Much of this tolerance can be attributed to errors in the paradichlorobenzene property values and to direct errors of measurement. Similarly, the data given in Fig. 8 do not appear to be internally consistent owing to the absence of a uniform experimental technique among the various investigators. Thus the empirical correlation (10) of the existing data must be burdened with the rather large tolerance of ±8 percent.

Acknowledgment

The work presented in this paper was supported jointly by the National Science Foundation and the Aerospace Research Laboratories of the U. S. Air Force. The latter contract remained under the technical supervision of Dr. M. Scherberg.

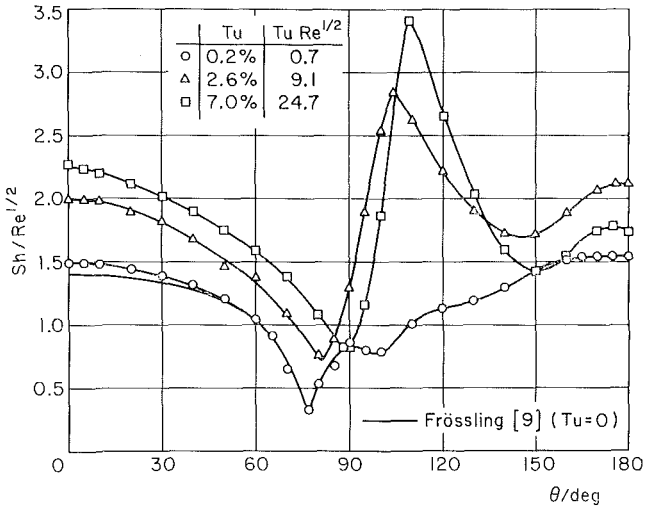

Fig. 6 Effect of turbulence on mass-transfer rate around a cylinder at Reynolds number: Re = 125,000 (nominal)

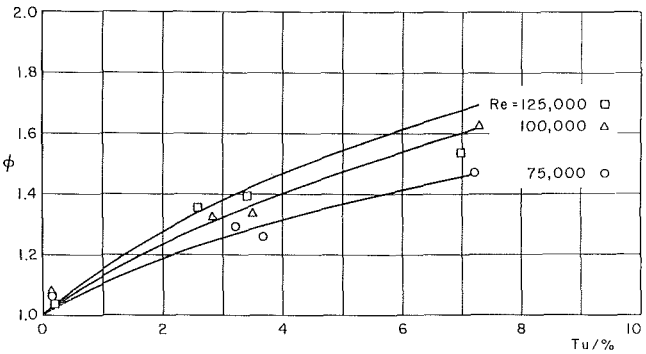

Fig 7. The augmentation factor ϕ in terms of turbulence intensity Tu for three values of the Reynolds number

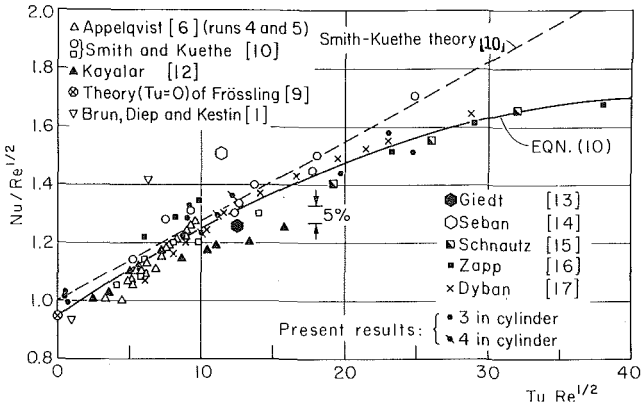

Fig. 8 Measurements for the local rate of heat (mass) transfer at the stagnation line of cylinders in cross flow

References

1 Brun, E. A., Diep, G. B., and Kestin, J., "Sur un nouveau type des tourbillons longitudinaux dan l'écoulement autour d'un cylindre. Influence de l'angle d'attaque et de la turbulence du courant libre," *C. R. Acad. Sci.*, Vol. 263, 1966, p. 742.

2 Kestin, J., and Wood, R. T., "On the Stability of Two-Dimensional Stagnation Flow" (to be published).

3 Kestin, J., and Wood, R. T., "The Mechanism which Causes Free-Stream Turbulence to Enhance Stagnation-Line Heat and Mass Transfer" (to be published).

4 Kestin, J., Maeder, P. F., and Sogin, H. H., "The Influence of Turbulence on the Transfer of Heat to Cylinders Near the Stagnation Point," *Journal of Applied Mathematics and Physics*, Vol. 7, 1961, p. 115.

5 Dryden, H. L., Schubauer, G. B., Mock, W. C., Jr., and Skramstad, H. K., "Measurements of Intensity and Scale of Wind-Tunnel Turbulence and Their Relation to the Critical Reynolds Number of Spheres," NACA Report No. 581, 1937.

6 Appelqvist, B., "The Influence of Turbulence on the Local Heat Transfer from a Cylinder Normal to an Air Stream, Including Further Development of a Method for Local Heat Transfer Measurements," Doctoral dissertation, Institute of Applied Thermo and Fluid Dynamics, Chalmers University of Technology, Gothenburg, 1965.

7 Weast, R. C., and Selby, S. M., editors, *Handbook of Chemistry and Physics*, The Chemical Rubber Co., Cleveland, 1967.

8 Sogin, H. H., "Sublimation From Disks to Air Streams Flowing Normal to Their Surfaces," TRANS. ASME, Vol. 80, 1958, p. 61.

9 Frössling, N., "Verdungstung, Wärmeübertragung und Geschwindigkeitsverteilung bei zweidimensionaler und rotationssymmetrischer Grenzschichtströmung," Lunds Univ. Arsskrift. N. F., Vol. 2, 1940, p. 36.

10 Smith, M. C., and Kuethe, A. M., "Effects of Turbulence on Laminar Skin Friction and Heat Transfer," *Physics of Fluids*, Vol. 9, 1966, p. 2337.

11 Squire, H. B., *Modern Developments in Fluid Dynamics*, Sect. 270, ed. S. Goldstein, Dover Publications, New York, 1965.

12 Kayalar, L., "Experimentelle und theoretische Untersuchungen über den Einfluss des Turbulenzgrades auf den Wärmeübergang in der Umgebung des Staupunktes eines Kreiszlinders" (to be published in *Forschung a.d.G. des Ing.-Wesens*).

13 Giedt, W. H., "Investigation of Variation of Point Unit Heat Transfer Coefficient Around a Cylinder Normal to an Air Stream," TRANS. ASME, Vol. 71, 1949, p. 375.

14 Seban, R. A., "The Influence of Free Stream Turbulence on the Local Heat Transfer From Cylinders," JOURNAL OF HEAT TRANSFER, TRANS. ASME, Series C, Vol. 82, 1960, p. 101.

15 Schnautz, J. A., "Effect of Turbulence Intensity on Mass Transfer From Plates, Cylinders and Spheres in Air Streams," Doctoral dissertation, Oregon State University, 1958.

16 Zapp, G. M., "The Effect of Turbulence on Local Heat Transfer Coefficients Around a Cylinder Normal to an Air Stream," Master's thesis, Oregon State University, 1950.

17 Dyban, E. P., and Epick, E. Ya., "Some Heat Transfer Features in the Air Flow of Intensified Turbulence," Proceedings of the Fourth International Heat Transfer Conference, Paris, 1970.

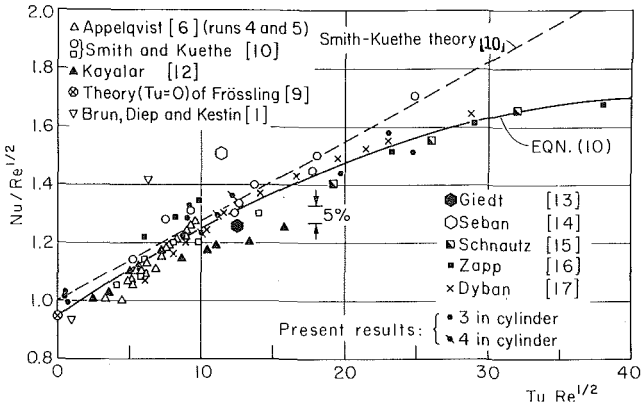

Fig. 8 Measurements for the local rate of heat (mass) transfer at the stagnation line of cylinders in cross flow

References

1 Brun, E. A., Diep, G. B., and Kestin, J., "Sur un nouveau type des tourbillons longitudinaux dan l'écoulement autour d'un cylindre. Influence de l'angle d'attaque et de la turbulence du courant libre," *C. R. Acad. Sci.*, Vol. 263, 1966, p. 742.

2 Kestin, J., and Wood, R. T., "On the Stability of Two-Dimensional Stagnation Flow" (to be published).

3 Kestin, J., and Wood, R. T., "The Mechanism which Causes Free-Stream Turbulence to Enhance Stagnation-Line Heat and Mass Transfer" (to be published).

4 Kestin, J., Maeder, P. F., and Sogin, H. H., "The Influence of Turbulence on the Transfer of Heat to Cylinders Near the Stagnation Point," *Journal of Applied Mathematics and Physics*, Vol. 7, 1961, p. 115.

5 Dryden, H. L., Schubauer, G. B., Mock, W. C., Jr., and Skramstad, H. K., "Measurements of Intensity and Scale of Wind-Tunnel Turbulence and Their Relation to the Critical Reynolds Number of Spheres," NACA Report No. 581, 1937.

6 Appelqvist, B., "The Influence of Turbulence on the Local Heat Transfer from a Cylinder Normal to an Air Stream, Including Further Development of a Method for Local Heat Transfer Measurements," Doctoral dissertation, Institute of Applied Thermo and Fluid Dynamics, Chalmers University of Technology, Gothenburg, 1965.

7 Weast, R. C., and Selby, S. M., editors, *Handbook of Chemistry and Physics*, The Chemical Rubber Co., Cleveland, 1967.

8 Sogin, H. H., "Sublimation From Disks to Air Streams Flowing Normal to Their Surfaces," TRANS. ASME, Vol. 80, 1958, p. 61.

9 Frössling, N., "Verdungstung, Wärmeübertragung und Geschwindigkeitsverteilung bei zweidimensionaler und rotationssymmetrischer Grenzschichtströmung," Lunds Univ. Arsskrift. N. F., Vol. 2, 1940, p. 36.

10 Smith, M. C., and Kuethe, A. M., "Effects of Turbulence on Laminar Skin Friction and Heat Transfer," *Physics of Fluids*, Vol. 9, 1966, p. 2337.

11 Squire, H. B., *Modern Developments in Fluid Dynamics*, Sect. 270, ed. S. Goldstein, Dover Publications, New York, 1965.

12 Kayalar, L., "Experimentelle und theoretische Untersuchungen über den Einfluss des Turbulenzgrades auf den Wärmeübergang in der Umgebung des Staupunktes eines Kreiszlinders" (to be published in *Forschung a.d.G. des Ing.-Wesens*).

13 Giedt, W. H., "Investigation of Variation of Point Unit Heat Transfer Coefficient Around a Cylinder Normal to an Air Stream," TRANS. ASME, Vol. 71, 1949, p. 375.

14 Seban, R. A., "The Influence of Free Stream Turbulence on the Local Heat Transfer From Cylinders," JOURNAL OF HEAT TRANSFER, TRANS. ASME, Series C, Vol. 82, 1960, p. 101.

15 Schnautz, J. A., "Effect of Turbulence Intensity on Mass Transfer From Plates, Cylinders and Spheres in Air Streams," Doctoral dissertation, Oregon State University, 1958.

16 Zapp, G. M., "The Effect of Turbulence on Local Heat Transfer Coefficients Around a Cylinder Normal to an Air Stream," Master's thesis, Oregon State University, 1950.

17 Dyban, E. P., and Epick, E. Ya., "Some Heat Transfer Features in the Air Flow of Intensified Turbulence," Proceedings of the Fourth International Heat Transfer Conference, Paris, 1970.

DISCUSSION

A. M. Kuethe[2]

In their discussion of the theory and experiments given by Smith and Kuethe in reference [10], the authors state "... the theory describes the measurements of its authors reasonably well, but ... it fails to conform to the general trend of the remaining body of data." The theory referred to, as Messrs. Kestin and Wood are aware, is the only one extant; it contains only one empirical constant and it fits satisfactorily *most* of the experimental data of Fig. 8. The theory may require modification for $Tu\ Re^{1/2} > 20$, though the data of Fig. 8 needs checking for high $Tu\ Re^{1/2}$ since the points in this range were taken (see Fig. 1 and Table 1) in the region where the distance from the grid is less than 10 mesh lengths; hence the turbulence would not be homogeneous and its magnitude would vary greatly over the diameter of the cylinder.

Arun S. Mujumdar[3] and W. J. M. Douglas[4]

The purpose of this discussion is to make a few observations based on the data of Kestin and Wood and our own results which are reported elsewhere [18]. Specifically, we observed during our study of the effects of free-stream turbulence on the stagnation point and overall heat transfer from cylinders that the Frössling number could be correlated better in terms of a turbulence Reynolds number, Re_T ($= I\ Re$, where I is the fractional intensity of turbulence and Re is the nominal Reynolds number), rather than with the Smith and Kuethe parameter, $I\ Re^{1/2}$, which is based on a phenomenological hypothesis. This observation is, of course, difficult to justify physically.

In view of our favorable experience with the use of the turbulence Reynolds number, we made a comparative analysis of the data under discussion. Specifically, a least-squares analysis of the data of Kestin and Wood for 3-in. cylinders (their Table 3), made without forcing the curve to pass through the Frössling value of $Nu/Re^{1/2} = 0.945$ for $I = 0$, yields the following correlations:

1 With the Smith and Kuethe parameter ($I\ Re^{1/2}$)

$$\frac{Nu}{Re^{1/2}} = 0.9762 + 0.0138\, I(Re \times 10^{-3})^{1/2} - 1.32 \times 10^{-6}(I\sqrt{Re})^2$$

(standard error = 0.0477)

2 With Re_T ($= I\ Re$)

$$\frac{Nu}{Re^{1/2}} = 0.981 + 1.017 \times 10^{-4}\, Re_T + 2.74 \times 10^{-9}\, Re_T^2$$

(standard error = 0.0329)

The standard error increases if the curves are forced through $Nu/\sqrt{Re} = 0.945$ for $I = 0$.

It is apparent that, for the case of the Kestin and Wood data, the comparison between the Smith and Kuethe parameter and the turbulence Reynolds number does not indicate a clear choice between the two.

The use of Re_T as a correlation parameter appears to date from its use by Lavender and Pei [19] in the correlation of their data for spheres. However, very recently Gostowski and Costello [20] had only rather limited success when they used Re_T in correlating their data for stagnation-point heat transfer data for spheres. This may be due in part to the extremely high turbulence levels (up to 40 percent) employed to generate data for high values of Re_T. Under these conditions the free stream would be highly anisotropic and would contain discrete frequency fluctuations depending on the grid geometry and the mean flow. Such streams may not be classified as truly turbulent. By contrast, our own heat transfer results showed that Re_T is a good correlation parameter for both the average and the stagnation-point heat transfer. Even including the above comparison based on the data of Kestin and Wood, the case for the use of the turbulence Reynolds number therefore remains unresolved.

Also, we wish to point out that mass-transfer data may be influenced by the rather small span-to-diameter ratio test models

[2] Aerospace Engineering Department, University of Michigan, Ann Arbor, Mich.

[3] Mechanical Engineer, Research Div., Carrier Corp., Syracuse, N. Y.

[4] Professor of Chemical Engineering, McGill University, Montreal, Canada.

used by Kestin and Wood. Morsbach [21] has shown that, in the subcritical region, there is no appreciable influence of the span-to-diameter ratio on the flow at the middle section of the cylinder. However, it has been shown by Achenbach [22] that for small values of span-to-diameter ratio (<3.0) in the critical region, the flow at the middle section is affected by the walls. Referring to Bearman's correlation [23] between the critical Reynolds number for cylinder and turbulence parameters, it would appear that any possible effect of the finite length of the cylinder would be limited to the large-diameter test model (4 in.) and the highest turbulence intensity (7.2 percent). It is impossible to assess the magnitude of this effect quantitatively without experimentation. It may not exceed the level of experimental uncertainty.

Further comments by Professor Kestin or his co-workers on the points raised in this discussion would be appreciated by all investigators of these phenomena, particularly because his group is identified with so much of the present-day knowledge in this field.

Additional References

18 Mujumdar, A. S., and Douglas, W. J. M., "Some Effects of Turbulence and Wake-Induced Periodicity on Heat Transfer from Cylinders," paper presented at the 20th Canadian Chemical Engineering Conference, Sarnia, Ont., Canada, Oct. ,1970.

19 Lavender, W. J., and Pei, D. C. T., "The Effect of Fluid Turbulence on the Rate of Heat Transfer from Spheres," *International Journal of Heat and Mass Transfer*, Vol. 10, 1967, pp. 529–539.

20 Gostowski, V. J., and Costello, F. A., "The Effect of Free Stream Turbulence on the Heat Transfer from the Stagnation Point of a Sphere," *International Journal of Heat and Mass Transfer*, Vol. 13, 1970, pp. 1382–1386.

21 Morsbach, M., "Über die Bedingungen für eine Wirbelstrassenbildung hinter Kreiszylindern," dissertation, T. H. Aachen, Germany, 1967.

22 Achenbach, E., "Distribution of Local Pressure and Skin Friction around a Circular Cylinder," *Journal of Fluid Mechanics*, Vol. 34, 1968, p. 625.

23 Bearman, P. W., NPL Aero Rept. 1296, National Physical Laboratory, Teddington, England, 1969.

Authors' Closure

We wish to thank our discussers for their comments, and we shall attempt to answer their observations in turn.

First, it was not our intention to disparage the theory of Smith and Kuethe; indeed, as Professor Kuethe notes, this is the only semiempirical theory that fits satisfactorily most of the experimental data. (By comparison, the results of semiempirical theory proposed by Kayalar [12] are inferior.) However, we did see the need to provide an empirical correlation of the data in order to estimate their consistency.

The behavior of our experimental results for $Tu\mathrm{Re}^{1/2} > 20$ has clear support from the other heat- and mass-transfer measurements shown in Fig. 8. Thus, there is little reason to suspect that our grid III placement, which was slightly more than 10 mesh lengths (15 in.) from the stagnation line, biased the spanwise uniformity of our results. Furthermore, the grid in question consisted of horizontal rods whose axes were parallel with the axis of the cylinder, so that the free-stream turbulence was probably homogeneous in the spanwise direction. In this connection, we should remark that almost all grid-generated turbulence is quite anisotropic, being at best homogeneous in planes parallel with the grid before the influence of the model takes hold. Fortunately, the turbulence energy (intensity), and not the scale, is the dominant variable.

Still on the subject of our data, we neglected to mentioned that the 10-in. coated cylinder was fitted with tubular end adapters to form a composite cylinder equal in length to the shorter dimension of our 22-in. × 32-in. test section. Hence, we observed some end effects near the edges of the coating, but they did not appear to influence the center-span mass transfer. One might also question the influence of blockage, except that the maximum blockage ratio was a tolerable 12 percent, and the agreement between the results for the 3-in. and 4-in. cylinders is within our experimental precision.

We must agree with the conclusion of Mujumdar and Douglas that empirically it is not possible to define a clear choice between the Smith–Kuethe parameter and the turbulence Reynolds number. (Apparently the latter was first utilized as a correlating parameter by Van Der Hegge Zijnen [24].) Moreover, an adequate theory to describe the interaction of free-stream turbulence with the three-dimensional flow pattern might not substantiate the choice of either parameter. For example, our stability analysis [2] has revealed that the wavelength of the three-dimensional motion is dependent on the $\frac{1}{3}$-power of the wall shear-stress rate, which, in turn, is influenced by the free-stream turbulence in a currently unknown manner. The amplitude of the motion also depends on the turbulence, and both the amplitude and the wavelength govern the transfer processes nonlinearly.

In view of the unstable nature of two-dimensional stagnation flow, it is doubtful that the theoretical Frössling limit, $\mathrm{Nu}/\mathrm{Re}^{1/2} = 0.945$, can ever be realized in the laboratory. Therefore, following the above work of Mujumdar and Douglas, we would suggest that future empirical correlations allow the data and the fit criterion to determine the zero-turbulence heat-transfer coefficient.

Additional References

24 Van Der Hegge Zijnen, B. G., *Appl. Sci. Res.*, Vol. A7, 1957, p. 205.

E. M. SPARROW
Professor.
Mem. ASME

H. S. YU

Department of Mechanical Engineering,
University of Minnesota,
Minneapolis, Minn.

Local Non-Similarity Thermal Boundary-Layer Solutions

A solution method is described and applied for treating non-similar thermal boundary layers. The solutions are locally autonomous (that is, independent of information from other streamwise locations) and are found by solving quasi-ordinary differential equations of the similarity type. All non-similar terms appearing in the conservation equations are retained without approximation, and only in derived subsidiary equations are terms selectively neglected. The accuracy of the results can be appraised from comparisons internal to the method itself. Thermal boundary-layer non-similarity arising both from velocity-field non-similarity and from streamwise variations of surface temperature are analyzed. Numerical results for the surface heat transfer and for the boundary-layer temperature distribution are presented for various physical situations.

Introduction

THIS PAPER is concerned with thermal boundary-layer problems which do not admit similarity solutions. Among the presently available approaches for treating such problems, the method of local similarity is perhaps the one most frequently employed, owing to its conceptual and computational simplicity. One of the especially attractive features of the local-similarity method is that the solution at a particular streamwise location can be found without having to perform calculations at upstream locations, that is, each solution is locally autonomous. A second advantage of this method is that the governing equations encountered in the course of its application can be treated as ordinary differential equations and resemble those for similarity boundary layers. They can, therefore, be solved by employing well-established techniques.

On the other hand, the local-similarity method has a serious drawback in that the results which it provides are of uncertain accuracy. This is because, in the application of the method, certain streamwise derivatives are discarded, and there is no positive way to establish the effect of these deletions on the final results.

In the present paper, a method for obtaining locally non-similar solutions for the thermal boundary layer is described and illustrated. The method preserves the attractive features of the local-similarity approach (locally autonomous solutions, quasi-ordinary differential equations), while retaining all of the non-similarity terms of the energy equation. Furthermore, comparisons internal to the method itself serve as a means for estimating the accuracy of the results.

Contributed by the Heat Transfer Division for publication (without presentation) in the JOURNAL OF HEAT TRANSFER. Manuscript received by the Heat Transfer Division November 19, 1970. Paper No. 71-HT-L.

Thermal boundary-layer non-similarity may result from a variety of causes. Perhaps the most common cause is the non-similarity of the velocity boundary layer. In turn, there are various factors which may give rise to velocity boundary-layer non-similarity, among which are: (*a*) streamwise variations in the free-stream velocity, (*b*) surface mass transfer, and (*c*) transverse curvature. Also, the thermal boundary layer can be non-similar even when the velocity boundary layer is similar, as will occur when streamwise variations in surface temperature, surface heat flux, or volume heat generation are not restricted to certain simple forms. Thus, there are many classes of thermal boundary-layer non-similarity.

The different classes of thermal boundary-layer non-similarity are governed by mathematical systems which differ in various details one from the other. However, the solutions for the different classes of problems by the present method all follow a common line of attack. In the presentation that follows, consideration is successively given to thermal boundary non-similarity caused by various forms of velocity non-similarity and by streamwise variations in surface temperature. Specifically, the succeeding sections of the paper deal with the solution of non-similar thermal boundary layers in the presence of surface mass transfer, transverse curvature, streamwise variations of the free-stream velocity, and streamwise variations of the surface temperature. The first section, which contains the exposition of the local-non-similarity solution method, will be more detailed than the subsequent sections.

Surface Mass Transfer

Description of the Problem. Consider now a flat plate aligned parallel to a uniform free-stream flow (velocity U_∞), with x denoting the streamwise coordinate and y the transverse coordinate. It is known that if there is surface mass transfer characterized by a transverse velocity $v_w \sim x^{-1/2}$, then similarity solutions are

possible. Otherwise, the velocity boundary layer is non-similar. In particular, the case of uniform surface mass transfer gives rise to a non-similarity boundary layer. Furthermore, the errors incurred by employing the local-similarity method are markedly greater for uniform injection (blowing) than for uniform suction. Therefore, consideration is given here to the flat plate with uniform surface blowing.

The starting point of the analysis is the conservation equations for constant-property, forced-convection boundary-layer flow over a flat plate

$$\partial u/\partial x + \partial v/\partial y = 0, \qquad u\partial u/\partial x + v\partial u/\partial y = \nu\partial^2 u/\partial y^2 \quad (1)$$

$$u\partial T/\partial x + v\partial T/\partial y = \alpha\partial^2 T/\partial y^2 \quad (2)$$

with boundary conditions

$$\begin{aligned} y = 0: \quad & u = 0, \qquad v = v_w, \qquad T = T_w \\ y \to \infty: \quad & u = U_\infty, \qquad T = T_\infty \end{aligned} \quad (3)$$

where v_w is a constant. Since we are concerned here with thermal boundary-layer non-similarities which are caused by velocity non-similarities, the surface temperature will be restricted to the form

$$T_w - T_\infty = Ax^\lambda \quad (4)$$

such that $\lambda = 0$ corresponds to uniform surface temperature. However, by making use of the principle of superposition, solutions for different λ values can be employed to construct solutions corresponding to the distribution

$$T_w - T_\infty = \sum_i A_i x^{\lambda_i} \quad (5)$$

Surface temperature variations other than those expressed by (4) and (5) give rise to thermal boundary-layer non-similarities. Such cases will be treated in a later section.

Transformation of the Governing Equations. The first step in the development of the solution method is to transform the problem from the x, y coordinate system to the ξ, η system. The coordinate η, which involves both x and y, may be termed a pseudo-similarity variable; it is chosen so as to reduce to a true similarity variable for boundary layers which are similar. On the other hand, ξ is related to x alone and is so chosen that x does not appear explicitly in the transformed conservation equations or boundary conditions.

The purpose of the aforementioned transformation is to lessen the dependence of the solution on the streamwise coordinate. The transformation tends to remove the streamwise dependence associated with the natural growth of the boundary layer, such as occurs for similarity boundary layers.[1] Therefore, the remaining streamwise dependence is that due to the non-similarity.

In accordance with the foregoing, η and ξ for the problem of uniform-surface mass transfer are chosen as

$$\eta = y\sqrt{U_\infty/2\nu x}, \qquad \xi = (v_w/U_\infty)\sqrt{2U_\infty x/\nu} \quad (6)$$

[1] Indeed, after transformation, similarity boundary layers do not depend on the streamwise coordinate.

The reduced stream function f corresponds to the thus-chosen η, and θ is a dimensionless temperature, that is

$$f(\xi, \eta) = \psi/\sqrt{2\nu x U_\infty}, \qquad \theta(\xi, \eta) = (T - T_\infty)/(T_w - T_\infty) \quad (7)$$

With these, the conservation equations (1) and (2), with their boundary conditions, transform to

$$f''' + ff'' = \xi[f'(\partial f'/\partial\xi) - f''(\partial f/\partial\xi)] \quad (8)$$

$$f + \xi = -\xi[\partial f/\partial\xi] \quad \text{at} \quad \eta = 0, \quad f'(\xi, 0) = 0, \quad f'(\xi, \infty) = 1 \quad (9)$$

$$(1/\mathrm{Pr})\theta'' + f\theta' - 2\lambda f'\theta = \xi[f'(\partial\theta/\partial\xi) - \theta'(\partial f/\partial\xi)] \quad (10)$$

$$\theta(\xi, 0) = 1, \quad \theta(\xi, \infty) = 0 \quad (11)$$

where $' = \partial/\partial\eta$ and λ is the exponent appearing in equation (4). The first of the boundary conditions (9) is responsible for the non-similarity of the velocity problem which, in turn, causes thermal boundary-layer non-similarity.

Local Similarity. Before proceeding to the local-non-similarity solution method, it is useful to examine equations (8) through (11) from the standpoint of local similarity. According to this approach, the right-hand sides of equation (8), of the first of equations (9), and of equation (10) are postulated to be sufficiently small so that they may be approximated by zero. This gives

$$f''' + ff'' = 0; \quad f(\xi, 0) = -\xi, \qquad f'(\xi, 0) = 0, \quad f'(\xi, \infty) = 1 \quad (12)$$

$$(1/\mathrm{Pr})\theta'' + f\theta' - 2\lambda f'\theta = 0; \quad \theta(\xi, 0) = 1, \quad \theta(\xi, \infty) = 0 \quad (13)$$

The quantity ξ may be regarded as a constant parameter at any streamwise location. Thus, although the f''' and θ'' equations are partial differential equations, they may be treated as ordinary differential equations and solved by well-established techniques appropriate to similarity boundary layers. The solution corresponding to any given ξ value is independent of the solution at any other ξ. By assigning a succession of ξ values, the streamwise dependence of the velocity and temperature fields can be determined.

In order to justify the reduction of equations (8)–(11) to equations (12) and (13) without requiring that ξ be small, it must be assumed that the bracketed quantities appearing on the right-hand sides of the former are negligible. The uncertainty as to the validity of this assumption is a weakness of the local-similarity method.

Local Non-Similarity. In approaching the local-non-similarity solution of equations (8)–(11), it is first convenient to eliminate the explicit presence of the ξ derivatives of f and θ by defining

$$g(\xi, \eta) = \partial f/\partial\xi, \qquad \phi(\xi, \eta) = \partial\theta/\partial\xi \quad (14)$$

After the substitution of these quantities, equations (8)–(11) become

$$f''' + ff'' = \xi[f'g' - f''g] \quad (8a)$$

Nomenclature

f = reduced stream function
g = ξ-derivative of f
h = ξ-derivative of g
h = local heat-transfer coefficient, $q/(T_w - T_\infty)$
k = thermal conductivity
Nu_x = local Nusselt number, hx/k
Pr = Prandtl number, ν/α
q = local heat-transfer rate per unit area
R = cylinder radius
r = radial coordinate
Re_x = Reynolds number, $U_\infty x/\nu$
T = temperature
U = velocity at edge of boundary layer
u = streamwise velocity component
v = transverse velocity component
x = streamwise coordinate
y = transverse coordinate
α = thermal diffusivity
η = pseudo-similarity variable
θ = dimensionless temperature
λ = exponent in wall-temperature variation
ν = kinematic viscosity
ξ = transformed streamwise coordinate
ϕ = ξ-derivative of θ
χ = ξ-derivative of ϕ
ψ = stream function
Ω = wall-temperature grouping, equation (45)

$$f + \xi = -\xi g \quad \text{at} \quad \eta = 0, \quad f'(\xi, 0) = 0, \quad f'(\xi, \infty) = 1 \tag{9a}$$

$$(1/\mathrm{Pr})\theta'' + f\theta' - 2\lambda f'\theta = \xi[f'\phi - \theta' g] \tag{10a}$$

$$\theta(\xi, 0) = 1, \quad \theta(\xi, \infty) = 0 \tag{11a}$$

Then, equations (8a)–(11a) are differentiated with respect to ξ, giving

$$g''' + fg'' - f'g' + 2f''g = \xi[\partial/\partial\xi(f'g' - f''g)] \tag{15}$$

$$2g + 1 = -\xi[\partial g/\partial\xi] \quad \text{at} \quad \eta = 0,$$

$$g'(\xi, 0) = 0, \quad g'(\xi, \infty) = 0 \tag{16}$$

$$(1/\mathrm{Pr})\phi'' + f\phi' - (1 + 2\lambda)f'\phi + 2g\theta' - 2\lambda g'\theta = \xi[\partial/\partial\xi(f'\phi - \theta' g)] \tag{17}$$

$$\phi(\xi, 0) = 0, \quad \phi(\xi, \infty) = 0 \tag{18}$$

where terms explicitly involving ξ derivatives are grouped on the right-hand sides.

Equations (15)–(18) serve as auxiliaries to the conservation equations and their boundary conditions, equations (8a)–(11a). The f and g functions appear in both equations (8a) and (15), so that they must be treated simultaneously. By the same token, the θ and ϕ functions are present in both (10a) and (17), necessitating simultaneous solution.

To proceed, all terms in the conservation equations and their boundary conditions, equations (8a)–(11a), are retained without approximation. In the auxiliary equations, it is postulated that the right-hand sides of equation (15), of the first of equations (16), and of equation (17) are sufficiently small so that they may be dropped. With this, the governing equations (8a), (9a), (15), and (16) for the velocity problem may be brought together as

$$f''' + ff'' = \xi[f'g' - f''g] \tag{19}$$

$$g''' + fg'' - f'g' + 2f''g = 0 \tag{20}$$

$$f(\xi, 0) = -\tfrac{1}{2}\xi, \quad g(\xi, 0) = -\tfrac{1}{2},$$

$$f'(\xi, 0) = g'(\xi, 0) = g'(\xi, \infty) = 0, \quad f'(\xi, \infty) = 1 \tag{21}$$

When ξ is regarded as a constant prescribable parameter at any streamwise location, then equations (19)–(21) may be treated as a system of ordinary differential equations and may be solved by the usual techniques for similarity boundary layers.

In like manner, the governing equations (10a), (11a), (17), and (18) for the thermal boundary layer reduce to

$$(1/\mathrm{Pr})\theta'' + f\theta' - 2\lambda f'\theta = \xi[f'\phi - \theta' g] \tag{22}$$

$$(1/\mathrm{Pr})\phi'' + f\phi' - (1 + 2\lambda)f'\phi + 2g\theta' - 2\lambda g'\theta = 0 \tag{23}$$

$$\theta(\xi, 0) = 1, \quad \theta(\xi, \infty) = \phi(\xi, 0) = \phi(\xi, \infty) = 0 \tag{24}$$

For a fixed ξ, equations (22)–(24) may be treated as a set of ordinary differential equations, with the velocity functions f and g as input. The θ, ϕ system is readily solved by the same methods used for similarity boundary layers.

The just-outlined non-similarity solution method preserves the two most attractive features of the local-similarity method, that is, (a) the solution at any given ξ is independent of that at any other ξ and (b) the resulting equations can be solved as if they were ordinary differential equations of the similarity type. Furthermore, the local–non-similarity approach retains all terms in the momentum and energy equations, as is evidenced in equations (19) and (22). Terms are deleted only from subsidiary equations (that is, from the g and ϕ equations). This is in contrast to the local-similarity method, where terms are deleted from the momentum and energy equations themselves. On this basis, it is expected that the local–non-similarity method should yield more accurate results than those from local-similarity solutions.

It may be noted that although the solution for the velocity problem provides information for both the f and g functions, it is only f and its derivatives that are physically relevant (for instance, $u/U_\infty = f'$). In like manner, from the thermal boundary-layer solutions for θ and ϕ, only the former is of interest.

The form of the local–non-similarity method that has been described thus far will be referred to as the two-equation model. This terminology derives from the fact that the velocity and thermal boundary-layer problems each involve the solution of two simultaneous equations. The two-equation model is the first stage in a succession of locally applicable multi-equation systems which are expected to provide increasingly more accurate results. The three-equation model will now be briefly developed. For conciseness and because the thermal boundary layer is of primary interest here, only the governing equations for the temperature field will be derived. As was already demonstrated in the case of the two-equation model, the derivations of the governing equations for the velocity and temperature boundary layers follow the same pattern.

To proceed, one differentiates equation (17) with respect to ξ, introducing the new functions

$$h = \partial g/\partial\xi = \partial^2 f/\partial\xi^2, \qquad \chi = \partial\phi/\partial\xi = \partial^2\theta/\partial\xi^2 \tag{25}$$

The terms which explicitly involve ξ derivatives are grouped on the right-hand side and are found to be $\xi[\partial^2/\partial\xi^2(f'\phi - \theta' g)]$. It is now postulated that this quantity is small enough to be approximated by zero. On the other hand, all terms in the energy equation (10a) and in the ϕ'' equation (17) are retained without approximation. This yields the following set of three differential equations and boundary conditions

$$(1/\mathrm{Pr})\theta'' + f\theta' - 2\lambda f'\theta = \xi[f'\phi - \theta' g] \tag{26}$$

$$(1/\mathrm{Pr})\phi'' + f\phi' - (1 + 2\lambda)f'\phi + 2g\theta' - 2\lambda g'\theta = \xi[g'\phi + f'\chi - \phi' g - \theta' h] \tag{27}$$

$$(1/\mathrm{Pr})\chi'' + f\chi' - (2 + 2\lambda)f'\chi - (2 + 4\lambda)g'\phi + 4g\phi' + 3h\theta' - 2\lambda h'\theta = 0 \tag{28}$$

$$\theta(\xi, 0) = 1, \quad \theta(\xi, \infty) = \phi(\xi, 0) = \phi(\xi, \infty) = \chi(\xi, 0) = \chi(\xi, \infty) = 0 \tag{29}$$

Once again, at a fixed ξ, equations (26)–(29) can be treated as a coupled set of ordinary differential equations of the similarity type. In deriving this system, terms were deleted in an equation which is secondarily subsidiary to the energy equation, but the energy equation itself and the first subsidiary equation are both intact. Since the truncation of the system of equations is now twice removed from the energy equation, it is expected that results from the three-equation model should be more accurate than those from the two-equation model.

An indication of the accuracy of the results can be obtained by comparing the findings from the successive equation systems (i.e., local similarity, two-equation model, etc.). For instance, if the results obtained from the two-equation model are essentially identical to those from the three-equation model, then high accuracy can be assumed to exist.

Numerical Solutions and Results. The governing equations for local similarity and for the two- and three-equation local–non-similarity models have been solved for the case of an isothermal surface, $\lambda = 0$ in equation (4), and for $\mathrm{Pr} = 0.7$. The solutions cover the range of $(v_w/U_\infty)\sqrt{U_\infty x/\nu}$ $(= \xi/\sqrt{2})$ from 0 to 0.5. The heat-transfer results from these solutions may be represented in terms of a local heat-transfer coefficient h, local Nusselt number Nu_x, and local Reynolds number Re_x.

$$h = q/(T_w - T_\infty), \qquad \mathrm{Nu}_x = hx/k, \qquad \mathrm{Re}_x = U_\infty x/\nu \tag{30}$$

From Fourier's law, $q = -(k\partial T/\partial y)_0$, in conjunction with equations (6) and (7), it follows that $\mathrm{Nu}_x/\sqrt{\mathrm{Re}_x} = -\theta'(\xi, 0)/\sqrt{2}$.

The heat-transfer results are plotted in Fig. 1. It is seen from the figure that the curves representing the two- and three-equation models are virtually coincident, except for small deviations

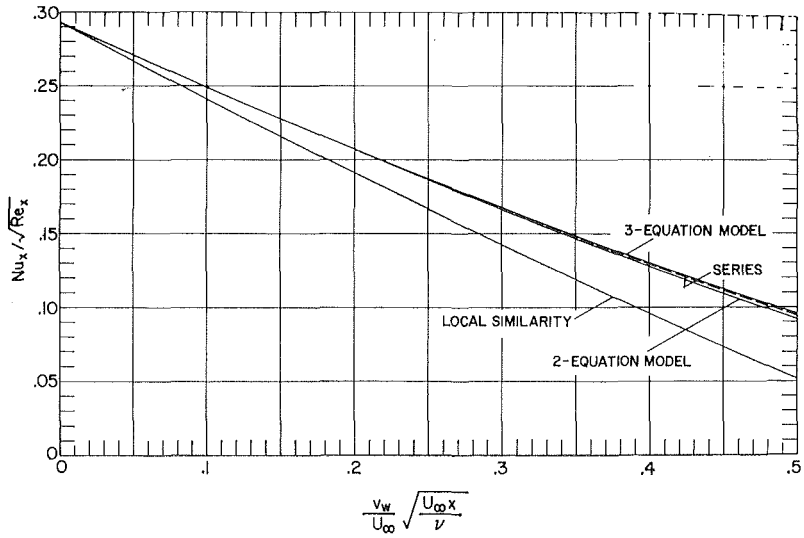

Fig. 1 Heat-transfer results, flat plate with uniform surface mass transfer

at the larger abscissa values (i.e., at higher blowing rates). This near-congruence suggests that the results are highly accurate. Indeed, prior experience with velocity boundary-layer problems has affirmed, on the basis of comparisons with available numerically exact solutions, that close agreement between the two- and three-equation models is a certain indication of high accuracy [1].[2] In contrast to the results from the local–non-similarity method, those based on local similarity are low and are seriously in error at the larger blowing rates.

It does not appear that there are either finite-difference or difference-differential solutions available for comparison with those found here. A series solution, expanded in powers of $x^{1/2}$, has been performed by Wanous [2]. The heat-transfer results from that solution, shown as a dashed line in Fig. 1, are in excellent agreement with those from the three-equation model. This level of agreement is somewhat unexpected, since such series solutions often diverge rapidly, away from the immediate neighborhood of $x = 0$.

Although numerically exact heat-transfer results do not appear to be available in the literature for the problem under consideration, finite-difference solutions for the corresponding velocity problem have been published. A comparison given in reference [1] shows that the friction-factor results from the three-equation model are essentially coincident with those from the finite-difference solutions over the range of $(v_w/U_\infty)\sqrt{U_\infty x/\nu}$ considered. This outcome lends confidence to the local–non-similarity solution method.

Temperature profiles for the flat plate with uniform blowing are apparently unreported in the literature. Such profiles, given directly by the present solutions as $\theta = (T - T_\infty)/(T_w - T_\infty)$, are plotted in Fig. 2. These profiles are from the three-equation model. The successive profiles are increasingly S-shaped, a trend which also occurs for similarity blowing (i.e., $v_w \sim x^{-1/2}$).

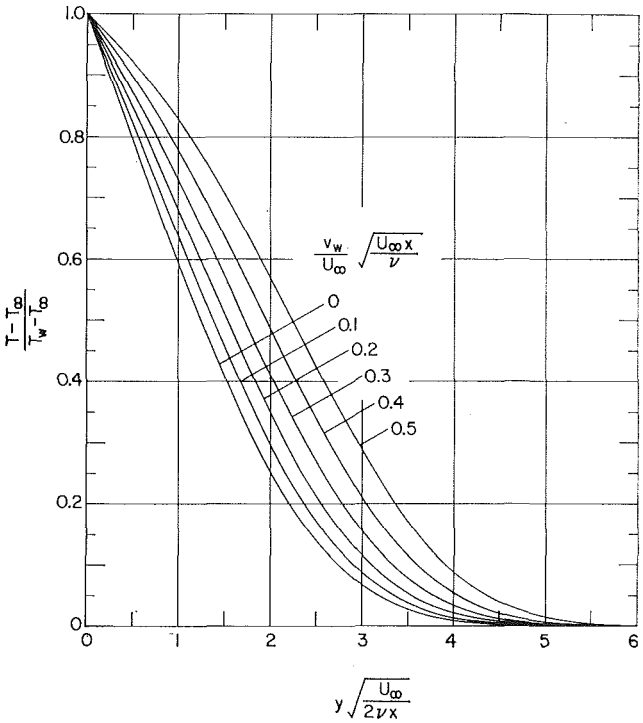

Fig. 2 Boundary-layer temperature profiles, flat plate with uniform surface mass transfer

Transverse Curvature

The boundary-layer flow longitudinal to the surface of a circular cylinder (radius R) situated in a uniform free stream is affected by transverse curvature[3] and is, therefore, non-similar. In terms of x, r cylindrical coordinates, the relevant boundary-layer equations are

$$\partial/\partial x(ru) + \partial/\partial r(rv) = 0,$$

$$u\partial u/\partial x + v\partial u/\partial r = (\nu/r)[\partial/\partial r(r\partial u/\partial r)] \quad (31)$$

$$u\partial T/\partial x + v\partial T/\partial r = (\alpha/r)[\partial/\partial r(r\partial T/\partial r)] \quad (32)$$

The presence of the various factors of r is, mathematically speaking, responsible for the non-similar nature of the problem.

The first step in the local–non-similarity analysis is the transformation from x, r to ξ, η. For this purpose, it is convenient to use the ξ, η variables first suggested by Seban and Bond [3] in connection with a series solution.

$$\eta = [(r^2 - R^2)/4R]\sqrt{U_\infty/\nu x}, \quad \xi = (4/R)\sqrt{\nu x/U_\infty} \quad (33)$$

$$f(\xi, \eta) = \psi/R\sqrt{\nu U_\infty x}, \quad \theta(\xi, \eta) = (T - T_\infty)/(T_w - T_\infty) \quad (34)$$

For small x, where the boundary layer is very thin, $(r^2 - R^2)/4R$

[2] Numbers in brackets designate References at end of paper; reference [1] deals with non-similar velocity boundary layers without heat transfer.

[3] That is, curvature of the surface in a plane transverse to the streamwise direction.

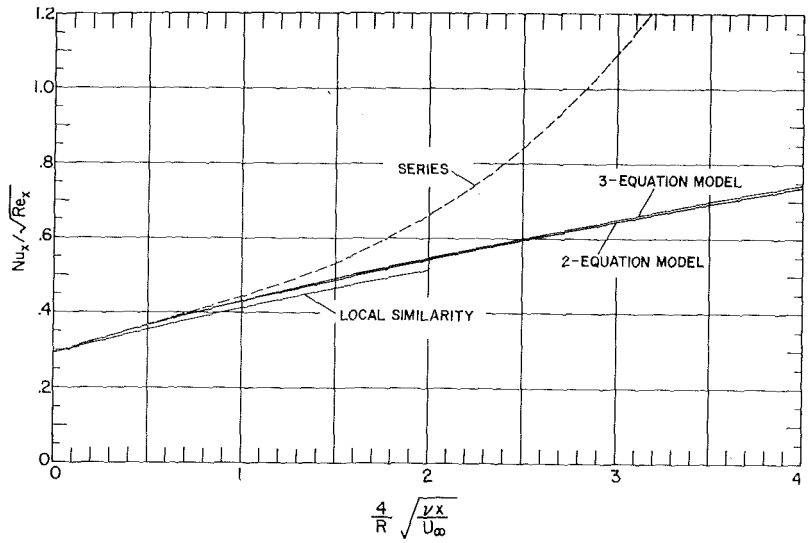

Fig. 3 Heat-transfer results, cylinder in longitudinal flow

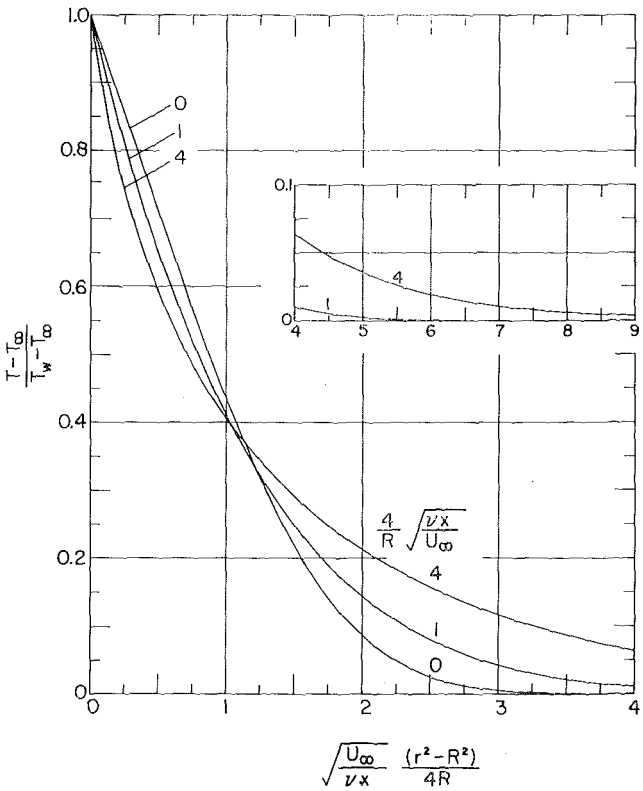

Fig. 4 Boundary-layer temperature profiles, cylinder in longitudinal flow

$\rightarrow y/2$, with $y = (r - R)$, so that η reduces to a true similarity variable.

The subsequent development is focussed on the energy equation, the transformation of which yields

$$(1/\mathrm{Pr})[(1 + \eta\xi)\theta']' + f\theta' = \xi[f'\phi - \theta' g] \qquad (35)$$

with boundary conditions $\theta(\xi, 0) = 1$ and $\theta(\xi, \infty) = 0$. The g and ϕ variables, respectively, represent $\partial f/\partial\xi$ and $\partial\theta/\partial\xi$, as before. Equation (35) pertains specifically to uniform wall temperature, but is readily generalized to accommodate the power-law variation (4).

The governing equation for local similarity is arrived at by dropping the right-hand side of (35), giving

$$(1 + \eta\xi)\theta'' + (\xi + \mathrm{Pr}\, f)\theta' = 0, \quad \theta(\xi, 0) = 1, \quad \theta(\xi, \infty) = 0 \qquad (36)$$

To derive the two-equation model, equation (35) is differentiated with respect to ξ and the term $\xi[\partial/\partial\xi(f'\phi - \theta' g)]$ is deleted. Then, taking the complete energy equation (35) together with the thus-derived ϕ'' equation, one has

$$(1 + \eta\xi)\theta'' + (\xi + \mathrm{Pr}\, f)\theta' = \mathrm{Pr}\ \xi[f'\phi - \theta' g] \qquad (37)$$

$$(1 + \eta\xi)\phi'' + (\xi + \mathrm{Pr}\, f)\phi' - \mathrm{Pr}\, f'\phi + \eta\theta'' + (1 + 2\ \mathrm{Pr}\, g)\theta' = 0 \qquad (38)$$

$$\theta(\xi, 0) = 1, \quad \theta(\xi, \infty) = \phi(\xi, 0) = \phi(\xi, \infty) = 0 \qquad (39)$$

The three-equation model consists of equation (35), or, equivalently, equation (37), the complete ϕ'' equation obtained by differentiating equation (35) with respect to ξ, the χ'' equation obtained by two successive ξ differentiations of (35) and deleting $\xi[\partial^2/\partial\xi^2(f'\phi - \theta' g)]$, and boundary conditions which include those of equation (39) plus $\chi(\xi, 0) = \chi(\xi, \infty) = 0$. As before, $\chi = \partial^2\theta/\partial\xi^2$. The statement of the governing equations for the three-equation model will be omitted to conserve space.

Numerical solutions for the local similarity model and for the two- and three-equation local-non-similarity models have been carried out for $\mathrm{Pr} = 0.7$ and for a number of discrete ξ values between 0 and 4. The local heat-transfer results, represented in terms of the parameters defined in equation (30), are evaluated from the solutions through the relation $\mathrm{Nu}_x/\sqrt{\mathrm{Re}_x} = -\theta'(\xi, 0)/2$. The results thus obtained are plotted in Fig. 3. Inspection of the figure shows that the two- and three-equation models are in excellent accord, the greatest deviation between the curves being less than 1 percent. As was previously discussed, this near-coincidence is an indication of high accuracy. The local-similarity solutions were terminated at $\xi = 2$, at which point the $\mathrm{Nu}_x/\sqrt{\mathrm{Re}_x}$ value was about 6 percent less than that of the three-equation model.

Within the knowledge of the authors, neither finite-difference nor difference-differential results are available for comparison with those of Fig. 3. A series solution, originally derived by Seban and Bond [3], has been extended to four terms and refined by Wanous [2]. A three-term series solution in terms of a somewhat different expansion parameter has also been reported by Eshghy and Hornbeck [4]. Heat-transfer results from Wanous' series solution are shown as a dashed line in Fig. 3, where they appear to be of satisfactory accuracy in the range from $\xi = 0$ to $\xi = 1$, but diverge rapidly thereafter. It may also be

noted that an interpolation formula provided by Eshghy and Hornbeck falls between the curves representing the two- and three-equation models for the entire abscissa range of Fig. 3.

Representative temperature profiles at selected streamwise locations are presented in Fig. 4. The most evident trends with increasing downstream distance are the substantial growth in the thermal boundary-layer thickness and the increase in $\partial\theta/\partial\eta$ at the surface.

Streamwise Variations of Free-Stream Velocity

It is known that variations of the free-stream velocity that are proportional to x^ω admit similarity velocity boundary layers, whereas other streamwise variations give rise to velocity boundary-layer non-similarity and, correspondingly, to thermal boundary-layer non-similarity. The analysis of such thermal boundary layers will now be outlined. In the analysis, surface temperature distributions will be restricted to the power-law form, equations (4) and (5).

The conservation equations appropriate to the class of problems under consideration are expressed by (1) and (2), modified by the addition of the term $U(dU/dx)$ to the right-hand side of the momentum equation. The corresponding boundary conditions are

$$y = 0: \quad u = v = 0, \quad T = T_w; \qquad y \to \infty: \quad u = U, \quad T = T_\infty \tag{40}$$

There are a number of candidate transformations $(x, y \to \xi, \eta)$ which are available for initiating the local–non-similarity solution for the velocity boundary layer. In reference [1], it was found that the Görtler-Meksyn transformation was highly effective for this purpose. It is expected that this same transformation would be equally effective for non-similar thermal boundary layers in the presence of isothermal bounding surfaces. However, this transformation is cumbersome to use for non-isothermal surfaces. Rather, in such cases, it is expeditious to employ

$$\eta = y\sqrt{U/2\nu x}, \quad \xi = x/L, \quad f(\xi, \eta) = \psi/\sqrt{2\nu x U}, \quad \theta(\xi, \eta) = (T - T_\infty)/(T_w - T_\infty) \tag{41}$$

where L is any convenient reference length.

The application of (41) to the energy equation yields

$$(1/\mathrm{Pr})\theta'' + (\beta + 1)f\theta' - 2\lambda f'\theta = 2\xi[f'\phi - \theta' g] \tag{42}$$

with boundary conditions $\theta(\xi, 0) = 1$ and $\theta(\xi, \infty) = 0$. The velocity functions f and g depend parametrically on the quantity $\beta(\xi) = (x/U)(dU/dx)$.

The derivation of the governing equations for the local-similarity and local–non-similarity methods proceeds as before. For local similarity, equation (42), with the right-hand side replaced by zero, is to be solved subject to the given boundary conditions. The two-equation model consists of the complete equation (42) plus a ϕ'' equation derived by differentiating equation (42) and deleting $\xi[\partial/\partial\xi(f'\phi - \theta' g)]$, with boundary conditions expressed by (24). And so forth and so on. These equations are similar in form to those displayed earlier in the paper and are, therefore, omitted in the interest of a more concise presentation. Inasmuch as ξ and β appear as parameters, each specific $U(x)$ distribution requires specific numerical treatment.

Streamwise Variations of Surface Temperature

In the classes of problems examined in the earlier portions of the paper, the thermal boundary-layer non-similarity was caused by non-similarities in the velocity field. Now, attention is turned to thermal boundary-layer non-similarity which results from streamwise variations of surface temperature. As was already noted, only power-law surface temperature variations, equations (4) and (5), admit similarity.

In the treatment that follows, the velocity boundary layer will be taken to be similar, with the free-stream velocity being expressed as $U \sim x^\omega$. Suitable velocity similarity variables are

$$\eta = y\sqrt{U/2\nu x}, \qquad f(\eta) = \psi/\sqrt{2\nu x U} \tag{43}$$

in which it is emphasized that f is now a function of η alone.

The transformation of the energy equation (2) and its boundary conditions may now be carried out, with the result that

$$(1/\mathrm{Pr})\theta'' + (\omega + 1)f\theta' - 2\Omega f'\theta = 2\xi[f'\partial\theta/\partial\xi], \qquad \theta(\xi, 0) = 1, \quad \theta(\xi, \infty) = 0 \tag{44}$$

where

$$\xi = x/L, \quad \theta(\xi, \eta) = (T - T_\infty)/(T_w - T_\infty), \qquad \Omega(\xi) = x(dT_w/dx)/(T_w - T_\infty) \tag{45}$$

The streamwise variation of the surface temperature is contained in Ω. For the power-law temperature variation expressed by equation (4), $\Omega = \lambda =$ constant, so that $\theta = \theta(\eta)$ and the right-hand side of the θ'' equation is identically zero. It is apparent that the power law is the only distribution for which Ω is a constant.

The local-similarity form of the problem is arrived at by deleting the right-hand side of the θ'' equation. For the two-equation model, a derivation paralleling those of earlier problems (but now noting that f is independent of ξ) yields

$$(1/\mathrm{Pr})\theta'' + (\omega + 1)f\theta' - 2\Omega f'\theta = 2\xi f'\phi \tag{46}$$

$$(1/\mathrm{Pr})\phi'' + (\omega+1)f\phi' - (2 + 2\Omega)f'\phi - 2(d\Omega/d\xi)f'\theta = 0 \tag{47}$$

with $\phi = \partial\theta/\partial\xi$ and boundary conditions expressed by (24). And so on and so forth for the three-equation model.

The velocity functions f and f' correspond to a specific numerical value of the quantity ω (recall that $U \sim x^\omega$). For the local-similarity solution of the thermal boundary layer, Ω enters as a ξ-dependent parameter. In the case of the multi-equation models, e.g., equations (46) and (47), numerical values of Ω and its derivatives, as well as of ξ itself, must be introduced as input data. Therefore, each specific surface temperature variation requires specific numerical treatment.

Concluding Remarks

It has been the objective of this paper to describe and apply a method for obtaining locally non-similar thermal boundary-layer solutions. A basic feature of the method is that the non-similar terms in the conservation equations are retained without approximation, while only in auxiliary equations are terms selectively deleted. The thus-derived governing differential equations can be applied at any streamwise location without recourse to information from other streamwise locations. Solutions can be carried out by treating the governing equations as ordinary differential equations.

In the paper, the method was applied to several different types of thermal boundary-layer non-similarity in order to establish the general line of attack. The heat-transfer information presented herein suggests that the solution method is capable of providing accurate results. Comparison of the present heat-transfer results with those from finite-difference or difference-differential solutions would have afforded a more definitive appraisal of accuracy; however, such solutions were not found to be available in the published literature. In this connection, mention might be made of various comparisons presented in reference [1], where velocity-field solutions were obtained by the local–non-similarity method. There, friction-factor comparisons with finite-difference and/or difference-differential solutions indicated that the local–non-similarity method provides results of high accuracy at all streamwise locations except those near a point of separation.

References

1 Sparrow, E. M., Quack, H., and Boerner, C. J., "Local Non-Similarity Boundary Layer Solutions," *AIAA Journal*, Vol. 8, 1970, pp. 1936–1942.

2 Wanous, D. J., and Sparrow, E. M., "Heat Transfer for Flow Longitudinal to a Cylinder With Surface Mass Transfer," JOURNAL OF HEAT TRANSFER, TRANS. ASME, Series C, Vol. 87, No. 2, May 1965, pp. 317–319.

3 Seban, R. A., and Bond, R., "Skin Friction and Heat Transfer Characteristics of a Laminar Boundary Layer on a Cylinder in Axial Incompressible Flow," *Journal of the Aeronautical Sciences*, Vol. 18, 1954, pp. 671–675.

4 Eshghy, S., and Hornbeck, R. W., "Flow and Heat Transfer in the Axisymmetric Boundary Layer over a Circular Cylinder," *International Journal of Heat and Mass Transfer*, Vol. 10, 1967, pp. 1757–1766.

M. AKIYAMA
G. J. HWANG
K. C. CHENG
Assoc. Mem. ASME

Department of Mechanical Engineering,
The University of Alberta,
Edmonton, Alberta, Canada

Experiments on the Onset of Longitudinal Vortices in Laminar Forced Convection Between Horizontal Plates

An experimental investigation is carried out to determine the onset of longitudinal columnar vortices due to buoyant forces for fully developed laminar forced convection between two infinite horizontal plates, each wall subjected to identical uniform axial temperature gradient but maintained at temperatures T_1 and T_2 ($T_1 > T_2$, $T_1 < T_2$, and $T_1 = T_2$) at lower and upper surfaces, respectively. The limiting case with vanishing axial temperature gradient and heating from below ($T_1 > T_2$) is known to have a critical Rayleigh number of 1708 and is used to check the accuracy of the testing apparatus. The onset of secondary flow is determined by a direct flow-visualization technique using cigarette smoke, and confirmed by a transverse temperature-profile measurement using a single thermocouple traverse. Experimental results for the critical Rayleigh number are compared with theory and the agreement is found to be good.

Introduction

THE EFFECT of buoyancy forces on fully developed laminar forced convection in horizontal rectangular channels under the thermal boundary conditions of axially uniform wall heat flux and peripherally uniform wall temperature was studied by Cheng and Hwang [1][1] for various aspect ratios. It was found that as the aspect ratio (horizontal width divided by vertical height) increases, the eyes of a pair of vortices move toward the shorter vertical side walls. Consequently, the effect of secondary flow is negligible as the aspect ratio approaches infinity, but in reality a thermal instability problem [2] concerned with the onset of longitudinal vortex rolls arises.

For horizontal fluid layer subjected to an adverse temperature gradient with the lower surface temperature T_1 higher than the upper surface temperature T_2, the system is potentially unstable because of its top-heavy situation, and the onset of convection is marked by the critical value of the Rayleigh number. For horizontal fluid layer, the system is theoretically stable if the upper surface is maintained at higher temperature than that at the lower surface, namely, $T_2 > T_1$. However, with the main flow between two infinite horizontal plates subjected to uniform axial temperature gradient, and the fluid temperature lower than both T_1 and T_2, the region near the lower surface will be subjected to an adverse temperature gradient regardless of either $T_1 > T_2$ or $T_1 < T_2$, and the system is potentially unstable.

A theoretical investigation [2] was carried out recently to determine the conditions marking the onset of longitudinal columnar vortices or rolls due to buoyant forces in a fully developed laminar forced convection between two infinite horizontal parallel plates, see Fig. 1. The thermal boundary condition of uniform axial temperature gradient was considered for the cases $T_1 > T_2$, $T_1 = T_2$, and $T_1 < T_2$. The analysis [2] based on Boussinesq approximation shows that the onset of longitudinal vortices or rolls (critical Rayleigh number) in laminar forced convection between two horizontal infinite parallel plates depends on the dimensionless parameter μ and Prandtl number. The Rayleigh number and the characteristic parameter μ are defined, respectively, as [2]

$$\begin{aligned} \mathrm{Ra} &= g\beta\Delta T h^3/\nu\kappa \\ \mu &= \mathrm{Re}_\tau h/\Delta T \end{aligned} \tag{1}$$

For the limiting case with $T_1 = T_2$ (or $\Delta T = 0$, $|\mu| = \infty$), the Rayleigh number is defined as

$$\mathrm{Ra}_\tau = g\beta\tau h^4/\nu\kappa \tag{2}$$

Recently, Mori and Uchida [3] carried out a theoretical and experimental study on the effect of longitudinal vortex rolls on forced-convection heat transfer between horizontal plates where the lower plate is heated isothermally and the upper plate is cooled isothermally. More recently Sparrow and Husar [4] re-

[1] Numbers in brackets designate References at end of paper.

Contributed by the Heat Transfer Division and presented at the ASME-AIChE Heat Transfer Conference, Tulsa, Okla., August 15–18, 1971. Manuscript received by the Heat Transfer Division January 21, 1971. Paper No. 71-HT-1.

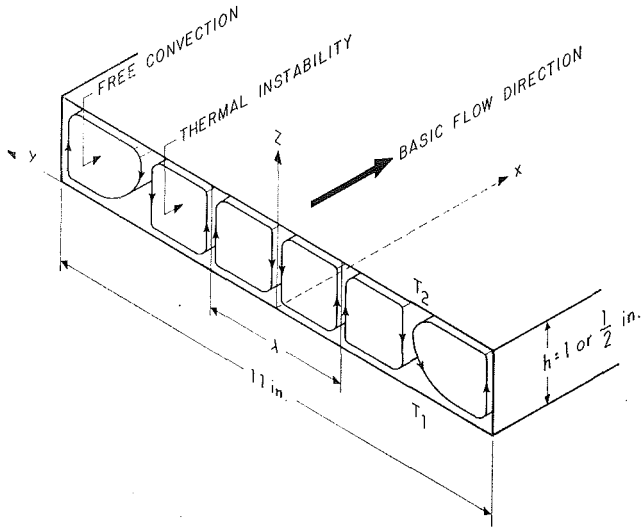

Fig. 1 Configuration and coordinate system

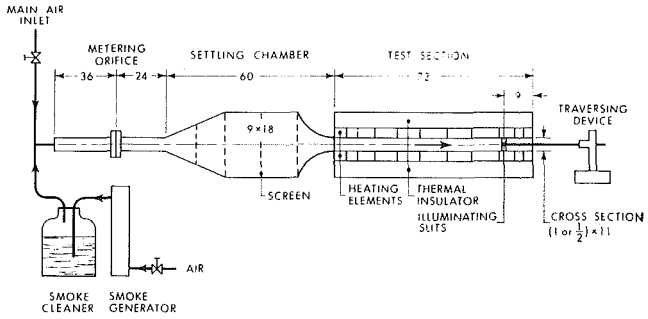

Fig. 2 Schematic diagram of experimental apparatus (unit: in.)

ported an experimental investigation on the occurrence and the characteristics of longitudinal vortices superposed upon the natural-convection main flow on an inclined plate. Experimentally, the longitudinal vortices were observed by Terada and Tamano [5], Mori and Uchida [3] in Poiseuille flow, and by Chandra [6] and others in plane Couette flow, all heated from below. Theoretically, the longitudinal vortex rolls (Taylor-Goertler vortices) were observed in forced-convection boundary-layer flows on concave walls by Görtler [7] where the vortices arise from the destabilizing effect of the centrifugal forces due to the concavity of the wall, and by Görtler [8] and Kirchgässner [9] where a buoyancy-force component normal to a wall was shown to have a similar effect on a forced-convection main flow.

In the present experimental investigation, the onset of longitudinal vortex rolls for the fully developed laminar forced convection between two horizontal flat plates subjected to uniform axial wall temperature gradient is studied for air in order to verify the theoretical results reported in [2].

Experimental Apparatus and Procedure

The schematic diagram of the testing apparatus is shown in Fig. 2. Air from a centrifugal blower (or air tap) passes through a settling chamber and enters a horizontal rectangular channel with a cross section of 11 × 1 in. in one series of tests and 11 × $^1/_2$ in. in another series of tests. The test section is constructed of two mirror-like brass plates (6 × 1 × $^1/_8$ in.) with side walls made of marinite insulator. In order to insure uniform surface heating, the heating elements and the brass plates are separated by a $^3/_{16}$-in-thick aluminum plate. The heating elements consist of 0.008 × $^1/_8$-in. Nikrothal tape wound around $^1/_{16}$-in-thick mica sheet with a pitch of $^3/_8$ in. and the electrical insulation is provided by $^1/_{16}$-in-thick mica sheets. The heaters for each plate are subdivided into 13 segments in the direction of the main flow with each segment consisting of one main heater and two guard heaters, one on each side. Two large-capacity voltage controllers are used to regulate the temperature difference between the upper and lower plates, with each heater being controlled individually by the voltage controller. The surface temperature of the flat plates is measured by iron–constantan thermocouples (0.01 in. diameter) embedded in the brass plates and electrically insulated to minimize the electrical noise on the temperature-recording system.

The flow rate of air is measured by providing a metering orifice as shown in Fig. 2 and pressure difference is measured by a Chattock-type manometer. The metering system is calibrated by a rotary-type gas meter with an error of approximately 0.5 percent. Throughout the experiment the Reynolds number was generally kept below 100 in order to eliminate the growth of any undesirable disturbances which might be caused by possible irregularity of the flow passage.

Initially an attempt was made to inject cigarette smoke through a $^1/_{32}$-in. slit placed underneath and along the channel width at the inlet of the test section and determine the onset of secondary flow by direct flow visualization at the exit of the channel. It was found that the smoke injection has no effect on the fully developed velocity distribution. This observation is similar to that reported in reference [3] where heavier paraffin smoke was used. Although the ratio of smoke flow rate to the main air flow rate was estimated to be less than the order of 0.01, the smoke particles tended to creep along the lower test plate and developed a smoke layer which might increase the density of the air near the lower plate. The increase of density near the lower plate has a stabilizing effect on the main flow and this is considered to be undesirable for the experiment.

It was then decided to place the slit of the smoke chamber at the upper plate right opposite the one tried earlier. This time the thin smoke layer developed near the upper plate tended to come down as it moved along the main flow. The heavier smoke particles moving downward toward the lower plate seem to have the undesirable effect of destabilizing the main flow and as a consequence tend to decrease the critical value of the Rayleigh number. For the purpose of observing the secondary flow pattern and its intensity for the post-critical Rayleigh number regime, the procedures described above are quite satisfactory. In order to eliminate the undesirable effect of stabilizing or destabilizing the main flow by injecting the cigarette smoke at the inlet of the test section, the smoke generator was finally located at some distance ahead of the metering orifice as shown in Fig. 2. This arrangement yields uniform smoke distribution at the inlet

Nomenclature

a = wave number, $2\pi h/\lambda$
g = gravitational acceleration
h = height of horizontal rectangular channel
Pr = Prandtl number, ν/κ
Ra = Rayleigh number, $g\beta\Delta T h^3/\nu\kappa$
Ra_τ = Rayleigh number, $g\beta\tau h^4/\nu\kappa$
Re = Reynolds number, $U_0 h/2\nu$
T = temperature
T_m = average temperature at $z = h/4$
T_w = wall temperature
U = velocity in the x direction
U_0 = maximum velocity in the unperturbed flow
x, y, z = rectangular coordinates
β = coefficient of thermal expansion
ΔT = temperature difference between two plates, $T_1 - T_2$
κ = thermal diffusivity
λ = wavelength of vortex rolls
μ = characteristic parameter, $\mathrm{Re}\tau h/\Delta T$
ν = kinematic viscosity
τ = uniform axial temperature gradient for two plates

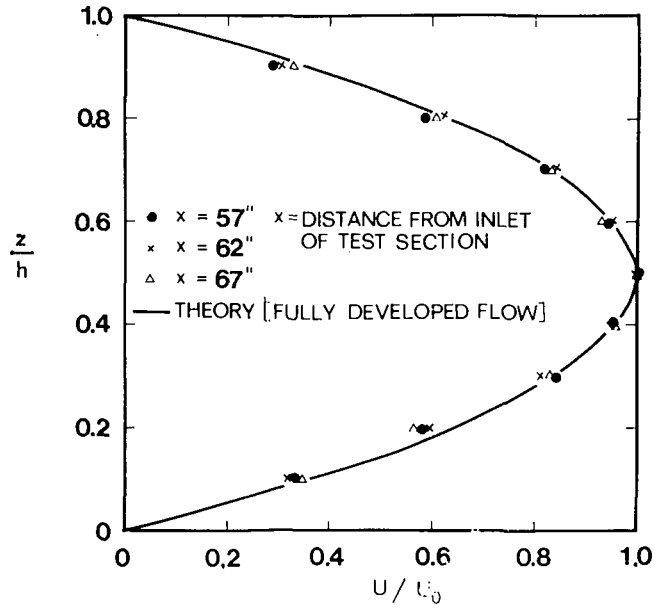

Fig. 3 Comparison of experimental data with theoretical velocity distribution at $y = 0$ with $h = 1$ in. and Re = 160

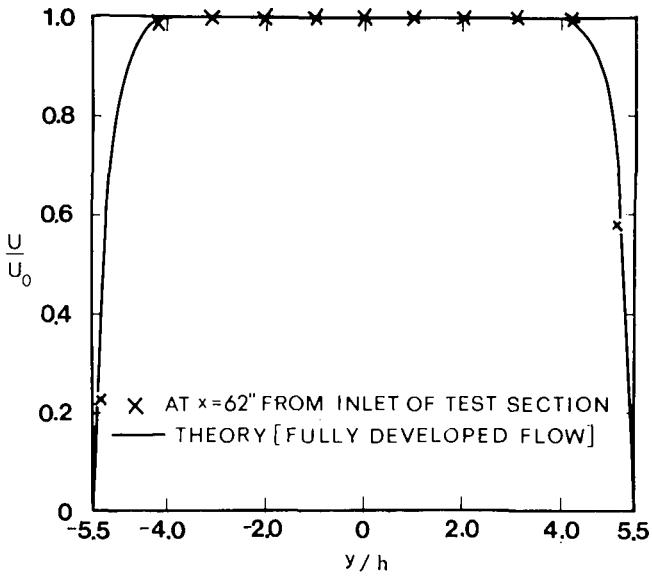

Fig. 4 Comparison of experimental data with theoretical velocity distribution along transverse direction y at $z/h = 0.5$ with $h = 1$ in. and Re = 160

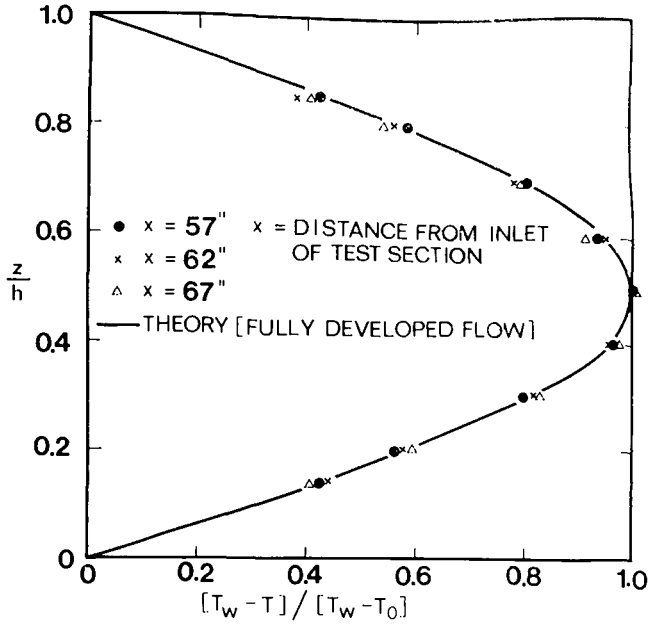

Fig. 5 Comparison of experimental data with theoretical temperature distribution at $y = 0$ with Re = 140, $h = 1$ in., $\tau = 1.85$ deg F/in.; $T_w = 85.6$ deg F at $x = 62$ in.

of the test section and it is believed that the undesirable effect of smoke supply in determining the critical value of the Rayleigh number by flow visualization is successfully eliminated. This observation is confirmed by the experimental verification of the well-known critical Rayleigh number of 1708 for the limiting case of $\mu = 0$ and the determination of the critical ReRa_τ by transverse temperature measurement for the case of $|\mu| = \infty$ which will be described later. It can now be said that the smoke system developed in this investigation is quite satisfactory for the present rather intricate experiment. It may also be of interest to note that the cigarette smoke was chosen for this experiment because of its smallest particle size among the many smoke sources available.

In one series of tests with the channel height $h = 1/2$ in., the upper plate has either heating element or water cooling system. The latter consists of nine independently controlled segments arranged in the direction of main flow. For a given value of the Reynolds number and a channel height h, an examination of the characteristic parameter $\mu = \mathrm{Re}\tau h/\Delta T$ shows that the value of the parameter μ can be increased by adjusting either the axial temperature gradient τ or the temperature difference ΔT between the upper and lower plates. However, there is an upper limit to the value of the axial temperature gradient τ to be imposed since in the theoretical analysis [2] the property values are all considered to be constant except for the density in the buoyancy term (Boussinesq approximation). One also notes that for a given channel height h and a fluid such as air, the only way one can raise the value of the Rayleigh number is by increasing the temperature difference ΔT between two plates. Consequently, with the channel height $h = 1/2$ in. it was found that the value of the characteristic parameter μ cannot exceed around 10. However, this channel was found to be quite satisfactory for the experiments with $\mu = 0$ and positive Rayleigh number for $\mu < 10$.

In another series of tests, the channel height was raised to $h = 1$ in. with the upper plate having heating elements only. This modification enables one to carry out the experiment at higher values of the characteristic parameter μ and is found to be very satisfactory for the case $\mu = 0$ and the case of negative Rayleigh number.

Experimental Results and Discussion

In order to confirm fully developed laminar flow at the test section, measurements using hot-wire anemometer (diameter of platinum wire = 5μ) for the velocity profile in the central vertical direction were made at distances 57, 62, and 67 in. from the entrance of the channel without heating at either upper or lower plate. The data are shown in Fig. 3 along with the theoretical plane Poiseuille profile. Since a flow between two infinite horizontal parallel plates is simulated by a horizontal rectangular channel with finite aspect ratio, the extent of the influence of the two side walls must be ascertained. For this purpose the transverse velocity profile through the center of the channel was also measured and a typical result is compared against the theoretical curve for the rectangular channel in Fig. 4. Both Figs. 3 and 4 show clearly that the velocity distribution is fully developed at the measuring stations even at a relatively high Reynolds number of 160. Consequently, with lower Reynolds number one is further assured of the fully developed laminar flow regime. It is also seen

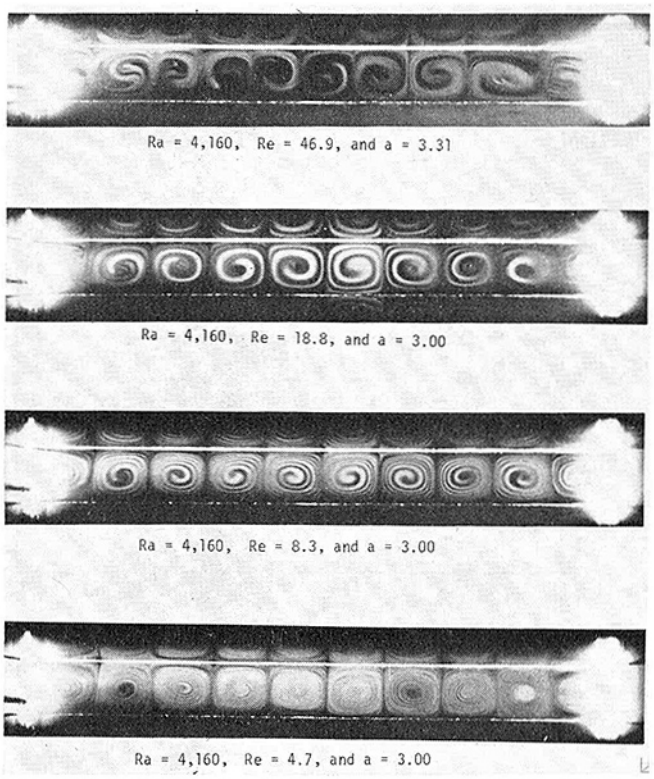

Fig. 6 Secondary flow patterns for the case $\mu = 0$ and $h = 1$ in.

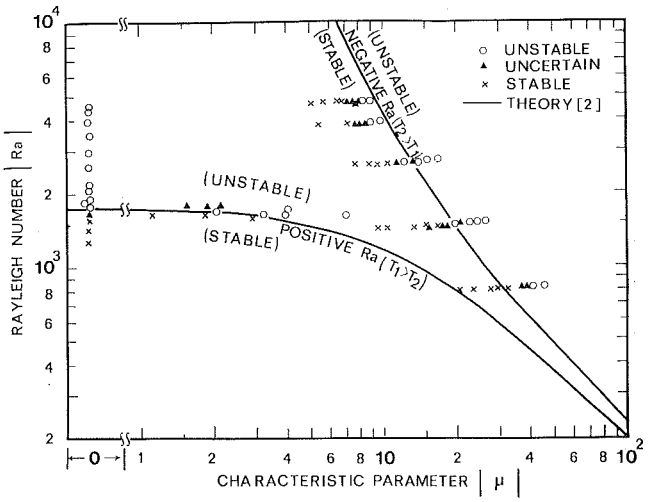

Fig. 7 Comparison of experimental data with theoretical stability curves for longitudinal vortex rolls

that a fairly wide central part of around $7h$ with $h = 1$ in. may be considered as fully developed Poiseuille profile for the parallel-plate channel. One can conclude that hydrodynamically the aspect ratios of the rectangular channel used are sufficiently large to simulate plane Poiseuille flow in the central region of the channel.

In addition to confirming hydrodynamically fully developed laminar flow, the thermally fully developed temperature field was also ascertained by temperature measurements at several axial stations, and typical results of the temperature measurements in the central vertical direction are shown in Fig. 5 for the thermal boundary conditions of $T_1 = T_2$ and uniform axial temperature gradient of 1.85 deg F/in. The curve in Fig. 5 represents the theoretical result for plane Poiseuille flow, and it is seen that the agreement with experimental data is good. It is further noted that the linear temperature distributions in the axial direction for both upper and lower plates were quite satisfactory.

Based on the theoretical result for isothermals of perturbation temperature shown in Fig. 6 of reference [2], it is estimated that the maximum temperature fluctuation would occur approximately at $z = h/4$ from the bottom plate surface. Consequently, transverse temperature measurements were made at $z = h/4$ in the central region of the channel. For the purpose of flow visualization and photographing the flow pattern from the exit of the channel, the test section was illuminated by light sources provided by two conventional slide projectors placed 1 ft distant from the two transparent mica side slits of $^1/_8$-in. width located 9 in. from the exit. The photographs of the flow patterns were taken on plus-x film using an aperture f = 5.6 and shutter speed of $^1/_{15}$ sec. at a distance of about 3 ft from the exit of the test section. Prints were made on F3 contrast grade paper. Temperature measurement was made using two-dimensional traversing mechanism for a thermocouple with diameter of 0.01 in. under smoke-free conditions.

In this investigation the experiment was done for the following four cases:

1 The characteristic parameter $\mu = 0$ or $\tau = 0$ and $T_1 > T_2$ with Re $\neq 0$. This case was specifically designed to check the accuracy of the testing apparatus by utilizing the well-known critical Rayleigh number of 1708 regardless of the presence of forced flow. One notes that the variation of Reynolds number has no effect on the onset of secondary flow. However, at extremely low Reynolds number, the longitudinal vortices may disappear.

2 The case $\mu > 0$, Ra > 0 ($T_1 > T_2$), and $\tau =$ constant. The data for this case were obtained from the channel with height $h = {}^1/_2$ in. and the magnitude of the parameter μ was limited to less than around 7 because of the limitation imposed by the height of the channel as explained earlier.

3 The Rayleigh number is negative ($T_2 > T_1$) and $\tau =$ constant. The range of the characteristic parameter used was $-6 > \mu > -60$. This case of negative Rayleigh number allows one to traverse the stable, neutral, and unstable regions by simply varying the Reynolds number. The data for this case were obtained from the channel with $h = 1$ in. only.

4 The limiting case of $|\mu| \to \infty$ with the top and bottom plates being kept at the same temperature and $\tau =$ constant.

The experimental results on the determination of the critical Rayleigh number for the foregoing four cases will be explained next. For case 1 with vanishing axial temperature gradient, the eigenvalue problem concerned with the onset of the vortex rolls is independent of the fully developed velocity profile and the problem is identical to that solved by Pellew and Southwell [10]. Four different flow patterns of the vortex rolls for the channel with $h = 1$ in. and Ra $= 4160$ are shown in Fig. 6 in the order of increasing Reynolds number. For the cases with Ra > 1708, the flow pattern is very regular and the pitch of the vortex rolls does not seem to change appreciably. It is also noted that the sidewall effect may be negligible for the case $\mu = 0$. For a given Rayleigh number, the number of closed streamlines increases as the Reynolds number decreases. This is clearly seen in Fig. 6. Excellent photographs of the secondary flow patterns for the case of $\mu = 0$ and $h = {}^1/_2$ in. were also obtained in the neighborhood of Ra $= 1708$ but will not be presented here, for brevity. The results of flow visualization for the case with $\mu = 0$ are plotted in Fig. 7 where a cross means "no detectable secondary flow," a triangle means "an uncertain situation," and a circle means "a definitely observable secondary motion." Since the experimental data confirm the known critical Rayleigh number of 1708, one may conclude that the testing apparatus yields sufficiently accurate data.

For the reason explained earlier, the channel with height $h = {}^1/_2$ in. is not suitable for the experiments involving the cases when $|\mu| > 8$. Case 2 of the experiment was conducted using this channel. For this case the instability is caused by the presence of

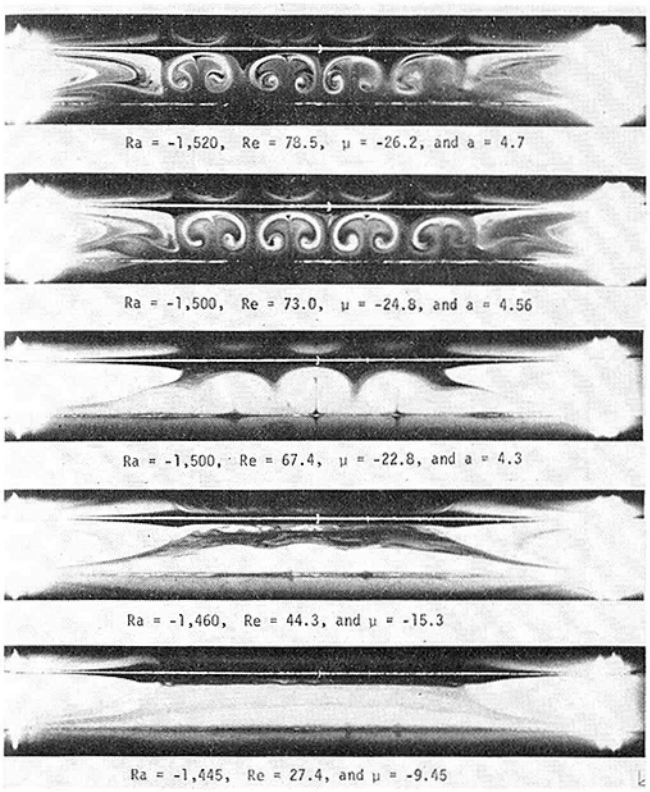

Fig. 8 Formation of secondary flow patterns with free-convection effect for the case of negative μ and $h = 1$ in.

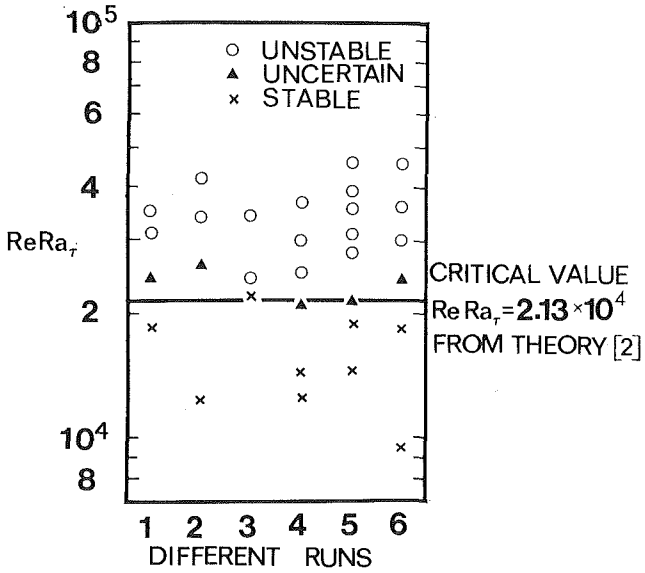

Fig. 9 Comparison of experimental data with critical $ReRa_\tau$ for the case $|\mu| \to \infty$

both the vertical adverse temperature gradient and the product of axial temperature gradient τ and the main flow disturbance velocity u' [2]. The experimental data from flow visualization are plotted in Fig. 7. An examination of the neutral stability curve for the case of positive Rayleigh number ($T_1 > T_2$), see Fig. 7, shows that the slope of the curve is rather small for the value of the characteristic parameter μ ranging from 1 to 10. Consequently, in order to obtain a series of data crossing the theoretical stability curve for a given value of μ, one must adjust the value of the Rayleigh number by changing the temperature difference ΔT between the upper and lower plates and this requires quite a long time. It was found that due to the variable-property effect for air the constancy of μ from the entrance to the test section could not be maintained by simply holding axial temperature gradient τ constant for the cases μ greater than say 2. In other words, to keep μ constant throughout the channel, one must maintain certain curvilinear axial temperature profiles for the upper and lower plates. Furthermore, it became more difficult to control ΔT. Consequently separate calibration curve was required for each value of μ ranging from around 3 to 7 as shown by data points in Fig. 7. For this series of experiment the temperature difference ΔT ranged from 20 to 35 deg F and the axial temperature gradient τ ranged from 1.5 to 4.0 deg F per inch. It was found that with the channel height of $^1/_2$ in. the experimental process becomes progressively tedious as the value of the parameter μ increases and definite difficulty is encountered at around $\mu = 10$. As the value of μ increases, the axial temperature difference between the entrance and the test section of the channel also increases and eventually the Boussinesq approximation will not be valid. At this point it is noted that all the property values were evaluated at local mean temperature of the test section which is located 9 in. from the exit. In this connection, error analysis shows that the errors for the computation of Re, Ra, Ra_τ, and μ are ± 2.1, ± 6.0, ± 6.3, and ± 9.1 percent respectively. The difficulty with the variable-property effect can be overcome readily by increasing the channel height to $h = 1$ in.

The experimental data for the case of negative Rayleigh number ($T_2 > T_1$) using channel height $h = 1$ in. will be discussed next. From the foregoing discussion it is evident that a channel with 1-in. height is quite suitable for the experiment with positive Rayleigh number ($T_1 > T_2$) and the characteristic parameter μ greater than 10. An examination of the theoretical stability curve, see Fig. 7, for the negative-Rayleigh-number case shows that it is convenient to cross the stability curve by varying the value of the parameter μ. For this series of tests the temperature difference ΔT between two plates was kept generally from a few degrees to less than 10 deg F and the axial temperature gradient τ was kept constant in each case with the value ranging from 0.81 to 0.96 deg F per inch. The variation of the value of the parameter μ can be accomplished solely by adjusting the Reynolds number for the present case of $T_2 > T_1$.

The experimental data from flow visualization for the case of negative Rayleigh number are compared against the theoretical stability curve in Fig. 7. The deviation from the theoretical stability curve for the two sets of experimental data at higher values of Rayleigh number can be attributed to the free-convection effect due to side walls, variable property, and the thinner unstable fluid layer near the lower plate at higher Rayleigh number. As the unstable fluid layer becomes thinner, the experimental uncertainty increases correspondingly. The remaining three sets of experimental data at lower values of Rayleigh number are considered to be quite satisfactory and in particular at $Ra = -800$ the agreement with theory is excellent.

Fig. 8 demonstrates clearly the gradual formation of the longitudinal vortex rolls. At $\mu = -9.45$ and $Ra = -1445$, the central region of the channel is still stable but free-convection motion appears near the side walls. This situation is marked as a cross in Fig. 7. At $\mu = 15.3$ and $Ra = -1460$, one can barely detect slight movement of smoke particles and this situation is marked as a triangle. At $\mu = -22.8$ and $Ra = -1500$, one can see the initial formation of three pairs of longitudinal vortex rolls and this situation is marked as a circle in Fig. 7 indicating definite instability. At $\mu = -24.8$ and $Ra = -1500$, the intensity of the secondary motion becomes stronger. Fig. 8 clearly shows that one has boundary-value problem near the side walls and eigenvalue problem in the central region of the channel simultaneously. The practical implication of this phenomenon will be discussed later.

The experimental data from flow visualization and transverse temperature measurement for the limiting case of $|\mu| \to \infty$ are

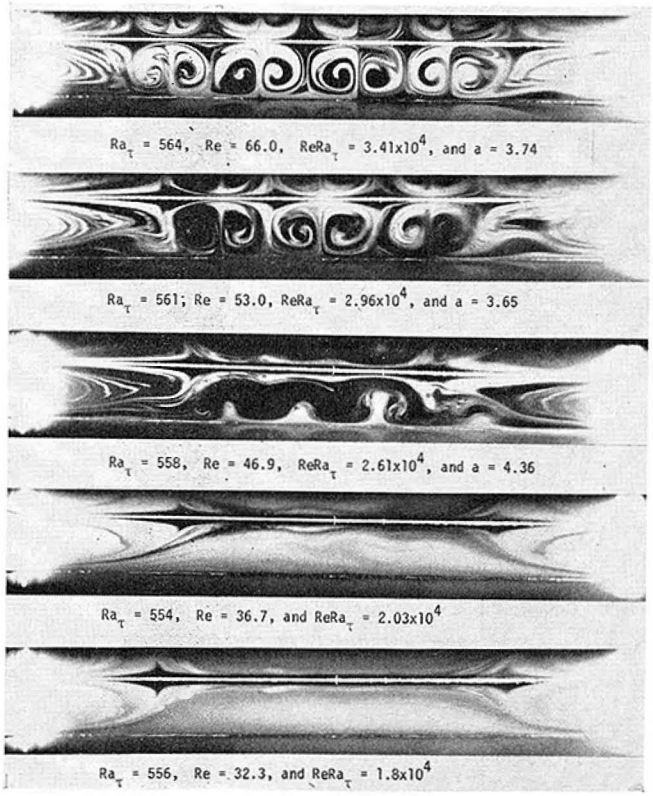

Fig. 10 Formation of secondary flow patterns with free-convection effect for the case $|\mu| \to \infty$ and $h = 1$ in.

compared against the theoretical critical value of $ReRa_\tau = 2.13 \times 10^4$ in Fig. 9. One set of flow patterns illustrating a sequence for the gradual development of secondary flow starting from completely stable state to the post-critical state is shown in Fig. 10. The general situation is similar to the ones discussed earlier.

In particular one notes the development of buoyant plumes at $ReRa_\tau = 2.61 \times 10^4$. In addition to photographic results, one set of experimental data from the transverse-temperature-profile measurement made at a distance $z = h/4$ from the bottom plate surface is presented in Fig. 11. It is noted that the test run number 2 in Fig. 9 corresponds to Fig. 11. Referring to Fig. 11, at $ReRa_\tau = 1.23 \times 10^4$, one can detect slight variation of transverse temperature distribution but this result is marked as a cross in Fig. 9 indicating stability because of its rather uniform distribution and uncertain nature of disturbances which could easily be caused by experimental error. At $ReRa_\tau = 2.65 \times 10^4$ one can see definite periodic fluctuation of transverse temperature profile around mean temperature but this result is considered to be uncertain in Fig. 9 since the pitch is not clearly defined yet. At $ReRa_\tau = 3.37 \times 10^4$, one can clearly see the periodic distribution indicating the definite establishment of the secondary flow. With further increase of $ReRa_\tau$, the amplitude of the periodic temperature fluctuation increases further and the secondary-flow intensity becomes stronger. One notes that for a given value of $ReRa_\tau$ in the post-critical regime, the amplitude of temperature fluctuation increases as the Rayleigh number increases. For the limiting case of $|\mu| \to \infty$, the experimental data from flow visualization check with those from transverse temperature measurement, and the agreement serves to demonstrate the adequacy of the flow-visualization technique.

The present experimental study, see Fig. 10, reveals that with the aspect ratio of 11, another type of secondary flow in the form of longitudinal vortices due to thermal instability appears at a certain critical $ReRa_\tau$ depending on Prandtl number in addition to the known secondary motion due to free convection near the side walls. The practical implication of Fig. 10, for example, is significant since it reveals that with the aspect ratio of around 10

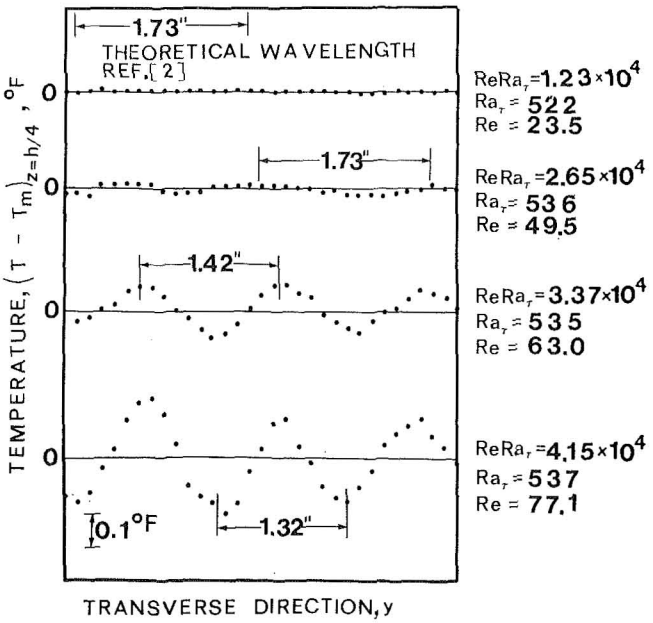

Fig. 11 Transverse-temperature-measurement data for $|\mu| \to \infty$ and $Ra_\tau = 522] - 537$

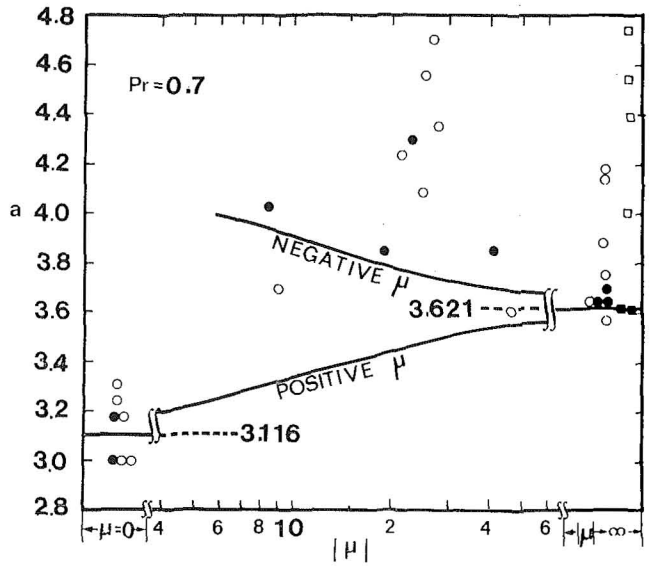

Fig. 12 Comparison of critical wave number versus μ from theory [2] with experimental data from post-critical regime

or even as small as 5 for the horizontal rectangular channel, the flow and heat transfer characteristics cannot be predicted with the existing theory considering the free-convection effect alone after reaching a certain critical $ReRa_\tau$. This also means that the known Nusselt number of 8.23 for fully developed laminar flow between two parallel plates with uniform wall heat flux cannot be applied after the $ReRa_\tau$ reaches a critical value.

Based on the photographic results and thermocouple data for the post-critical regime, it is also possible to compare critical wave number, a, versus the characteristic parameter μ from linearized theory [2] with the experimental data from post-critical regime as shown in Fig. 12. The results from thermocouple data are shown as a square, and the solid circle or square represents the nearest datum point to the theoretical curve for a given series of tests. Referring to Fig. 12, one may speculate the behavior of the wave number, a, in the post-critical regime; at $\mu = 0$, the wave number seems to remain constant or increase very slightly with the variation of the Rayleigh number. For the

cases when $|\mu| \neq 0$, the wave number seems to increase with the variation of the Rayleigh number for $|\mu|$ = finite or ReRa_τ for $|\mu| = \infty$. All the data for $|\mu|$ = finite shown in Fig. 12 are obtained from the cases with μ = negative. Because of the free-convection effect from the side walls, experimental error, and other uncertainties, the above remark must be considered as tentative.

Concluding Remarks

1 Experimental data on the onset of longitudinal vortices for the fully developed laminar forced convection between two horizontal plates are compared with theory and the agreement is found to be good. The accuracy of the testing apparatus is ascertained by considering the limiting case of vanishing axial temperature gradient and heating from below with a critical Rayleigh number of 1708. The adequacy of the direct flow-visualization technique used is confirmed by the transverse temperature measurement at a distance of $h/4$ from the bottom surface for another limiting case of $|\mu| \to \infty$.

2 For the negative Rayleigh number case, the free-convection effect due to side walls is appreciable. The exact reasons for the deviation of experimental data from theory at high Rayleigh numbers are difficult to assess. However, free-convection effect due to side walls, variable property, and the thinner unstable fluid layer near the lower plate are believed to be the contributing factors.

3 The flow-visualization technique developed is satisfactory for the present investigation and reasonably good flow patterns are obtained for the secondary flow. The flow-visualization technique is expected to be effective also for the experimental study concerning post-critical regime. For example, the measurement of the pitch of vortex rolls can be made readily.

4 The practical implication of the photographic results is believed to be significant since it reveals that for a horizontal rectangular channel with a large aspect ratio, say near the order of 10, the effect of longitudinal vortices due to thermal instability must be considered in addition to free-convection effect near the side walls for the evaluation of flow and heat transfer results after critical value of the characteristic parameter is reached. It is seen that one has a boundary-value problem near the side walls and a thermal-instability problem in the central region of the channel. At present theoretical study along this line does not appear to be available in the literature. Because of the free-convection effect from side walls, care must be exercised in applying the theoretical results presented in reference [2] to the problem in practice.

5 The experimental work would be easier if a larger channel height h were employed, but the channel width must be increased correspondingly to avoid side-wall effect. The advantage of increasing the height might be offset by the decrease of the temperature difference ΔT required for onset of secondary flow to the extent that measurement error may no longer be considered to be small as compared with ΔT. A practical lower limit for ΔT in this experiment is estimated to be 2–4 deg F.

Acknowledgment

This work was supported by the National Research Council of Canada through grant NRC A-1655. The first author (M.A.) wishes to thank the University of Alberta for a Province of Alberta Graduate Fellowship (1969–70). The second author (G.J.H.) is grateful to the National Research Council of Canada for a postgraduate scholarship. The authors also wish to thank Mrs. E. S. Buchanan for typing the manuscript.

References

1 Cheng, K. C., and Hwang, G. J., "Numerical Solution for Combined Free and Forced Laminar Convection in Horizontal Rectangular Channels," JOURNAL OF HEAT TRANSFER, TRANS. ASME, Series C, Vol. 91, No. 1, Feb. 1969, pp. 59–66.

2 Nakayama, W., Hwang, G. J., and Cheng, K. C., "Thermal Instability in Plane Poiseuille Flow," JOURNAL OF HEAT TRANSFER, TRANS. ASME, Series C, Vol. 92, No. 1, Feb. 1970, pp. 61–68.

3 Mori, Y., and Uchida, Y., "Forced Convective Heat Transfer Between Horizontal Flat Plates," *International Journal of Heat and Mass Transfer*, Vol. 9,1966, pp. 803–817.

4 Sparrow, E. M., and Husar, R. B., "Longitudinal Vortices in Natural Convection Flow on Inclined Plates," *Journal of Fluid Mechanics*, Vol. 37, 1969, pp. 251–255.

5 Terada, T., and Tamano, M., "Further Researches on Periodic Columnar Vortices Produced by Convection," Report of the Aeronautical Research Institute, Tokyo University, Vol. 4, 12, No. 53, Dec. 1929.

6 Chandra, K., "Instability of Fluids Heated from Below," *Proceedings of the Royal Society*, Series A, London, Vol. 164, 1938, pp. 231–242.

7 Görtler, H., "On the Three-Dimensional Instability of Laminar Boundary Layers on Concave Walls," NACA Technical Memorandum 1375, June 1954.

8 Görtler, H., "Über eine Analogie zwischen den Instabilitäten laminarer Grenzschichtströmungen an konkaven Wänden und an erwärmten Wänden," *Ingenieur-Archiv*, Band 28, 1959, pp. 71–78.

9 Kirchgässner, K., "Einige Beispiele zur Stabilitätstheorie von Strömungen an konkaven und erwärmten Wänden," *Ingenieur-Archiv*, Band 31, 1962, pp. 115–124.

10 Pellew, A., and Southwell, R. V., "On Maintained Convective Motion in a Fluid Heated from Below," *Proceedings of the Royal Society*, Series A, London, Vol. 176, 1940, pp. 312–343.

JOHN W. MITCHELL
Associate Professor,
Department of Mechanical Engineering,
University of Wisconsin,
Madison, Wisc.

Base Heat Transfer in Two-Dimensional Subsonic Fully Separated Flows

An experimental investigation of the heat transfer from the base of a two-dimensional wedge-shaped body to the separated-flow region was conducted in a low-speed wind tunnel. The Stanton number has been determined as a function of Reynolds number for two geometries that are representative of heat-exchanger surfaces. The heat transfer is found to be comparable in magnitude to that for attached flows. An analysis based on the mechanisms of vortex shedding and boundary-layer behavior is developed. The analysis agrees fairly well with the data and indicates the parameters governing base heat transfer.

Introduction

Fully separated subsonic flows occur in the flow of fluids over bluff shapes such as heat-exchanger fins and surfaces. These separated regions are characterized by an unsteady, sometimes periodic, flow. The heat transfer from the surface to the separated flow is relatively high. In spite of the common occurrence and importance of such flows, little has been done to evaluate the heat transfer. It is the objective of this paper to:

1 Present experimental results for heat transfer in subsonic separated non-reattaching flows.

2 Develop a mechanistic model for predicting the heat transfer in such flows.

The fluid behavior at the rear of a bluff body has been reviewed by Nash [1],[1] Hanson and Richardson [2], and Morkovin [3]. Extensive experiments on a variety of bluff shapes have been conducted by Roshko [4]. For Reynolds numbers greater than 50, a vortex street is formed in which the vortices are alternately shed from either side of the body. Bluff shapes, such as a flat plate normal to the flow, have larger wakes than streamlined shapes such as circular cylinders.

In Fig. 1 is shown a typical wake for a bluff body. The frequency of the vortex shedding is n, the vortex street is of width d_s, and the free-stream velocity at the edge of the street is U_s. Roshko [4] combined analysis with experiment to develop a semiempirical model that relates these wake parameters. For

Contributed by the Heat Transfer Division for publication (without presentation) in the Journal of Heat Transfer. Manuscript received by the Heat Transfer Division February 12, 1970; revised manuscript received June 4, 1970. Paper No 71-HT-D.

[1] Numbers in brackets designate References at end of paper.

Nomenclature

A = heat-transfer area, ft²
A_m = frontal area of model, ft²
A_{wt} = cross-sectional area of wind tunnel, ft²
c_p = specific heat, Btu/lbm-deg F
C = thermal capacitance of model, Btu/deg F
d = base height, ft
d_s = wake width, Fig. 1, ft
h = heat-transfer coefficient, Btu/hr-ft²-deg F
n = vortex shedding frequency, 1/sec
t = temperature, deg F
t_w = temperature of heat-transfer surface, deg F
$t_{w,i}$ = initial temperature of heat-transfer surface, deg F
t_∞ = free-stream temperature, deg F
U_m = free-stream velocity in the presence of the model, equation (6), ft/sec
U_s = free-stream velocity at edge of wake, Fig. 1, ft/sec
U_∞ = free-stream velocity, ft/sec
x = coordinate, Fig. 10, ft
y = coordinate, Fig. 10, ft
α = thermal diffusivity, ft²/hr
ν = kinematic viscosity, ft²/hr
ρ = air density, lbm/ft³
τ = time, sec
τ_0 = period of vortex street, equation (15), sec
τ_s = time for boundary layer to establish, equation (14), sec

Nondimensional Parameters

Pr = ν/α = Prandtl number
Re = $U_\infty d/\nu$ = Reynolds number
Re* = $U_s d_s/\nu$ = Reynolds number based on wake parameters
S = nd/U_∞ = Strouhal number
S* = nd_s/U_s = Strouhal number based on wake prameters
St = $h/\rho c_p U_\infty$ = Stanton number

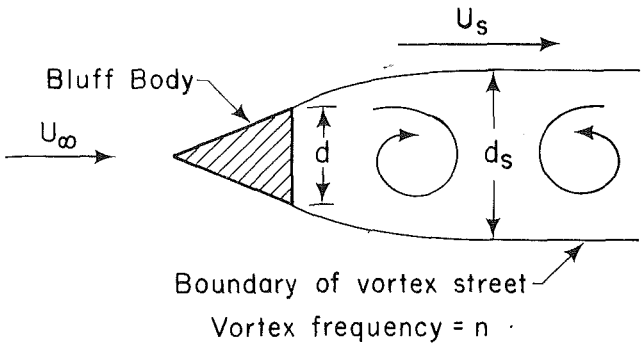

Fig. 1 Schematic of the flow over a two-dimensional bluff body

normal flat plates, circular cylinders, 90-deg wedges, and plates and cylinders with interference elements in the wake, he showed that the wake Strouhal number S* was a function of the wake Reynolds number Re* only. For the range Re* = 8×10^3 to 4.4×10^4, the value of S* was found to be 0.16 for all shapes. Using potential-flow techniques, a method for computing the normalized wake width d_s/d and the velocity ratio U_s/U_∞ for a given shape was developed. For several shapes, d_s/d and U_s/U_∞ have been determined. These results provide the basis for the heat-transfer model developed later.

Abernathy [5] conducted an experimental and analytical investigation of the flow over a flat plate inclined 35 to 90 deg with respect to the main stream. S* was established as 0.147 to 0.153 over the Reynolds-number range 3×10^4 to 1.3×10^5; these values are in good agreement with those of Roshko. Nash, Quincey, and Callahan [6] studied the flow over a two-dimensional wedge at Reynolds numbers of 1 to 2×10^6. S* was estimated at 0.25; it might be expected that S* would be different at the higher Reynolds numbers.

These studies establish the general flow picture for a subsonic wake. The information available on the details of the flow near the surface shows the velocity field to be unsteady and to fluctuate at the Strouhal-number frequency. Additional knowledge of the details of the flow are needed in order to develop adequate models for the heat transfer.

Heat-transfer results for fully separated flows are quite limited. The existing experimental results for air and the theories are summarized in Fig. 2. The laminar and turbulent flat-plate relations are also shown in order to indicate the relatively high heat transfer in the separated region.

The extensive data on cylinders has been analyzed by Richardson [7, 8] in an attempt to determine the heat-transfer contribution of the separated region. The data on heat-transfer coefficient from different investigators varies by a factor of two. For the Reynolds-number range of 10^2 to 10^5, Richardson estimated the best relationship for the heat transfer in the separated region of circular cylinders to be

$$\mathrm{St} = 0.19\ \mathrm{Re}^{-1/5} \tag{1}$$

Sogin [9] has experimentally determined the local heat-transfer coefficient in the separated region behind normal and inclined flat plates and a half-round cylinder over the Reynolds-number range of 1 to 4×10^5. For the two geometries that are closest to the present work, the mean heat-transfer results are:

Normal flat plate

$$\mathrm{St} = 0.28\ \mathrm{Re}^{-1/3} \tag{2}$$

Half-round cylinder with flat rear surface

$$\mathrm{St} = 0.22\ \mathrm{Re}^{-1/3} \tag{3}$$

The larger wake of the normal flat plate, compared to that of the cylinder, accounts for the 25-percent-higher heat transfer. The results are higher than the estimates of Richardson for the circular cylinder by 15 to 45 percent, and indicate the importance of geometry on the base heat transfer.

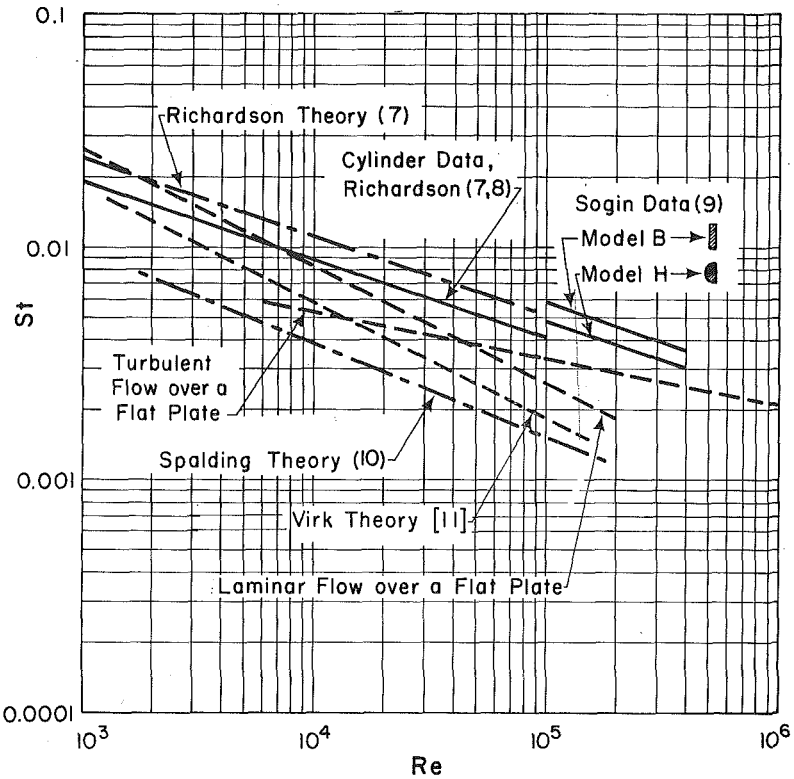

Fig. 2 Summary of existing data and analyses for heat transfer in fully separated flows

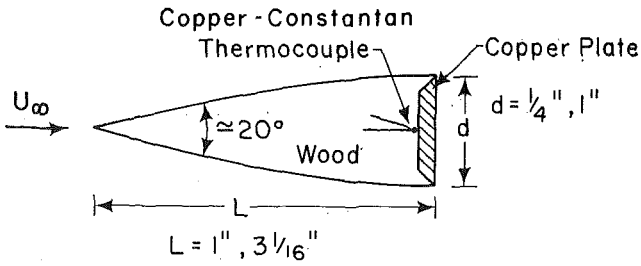

Fig. 3 Cross section of experimental model

Richardson [7] has developed an analysis to predict the heat transfer based on the idea that flow transists from attached to separated at some very low Reynolds number. If the value of the heat-transfer coefficient is known at this transition point, then the heat-transfer coefficient for the separated flow can be estimated by extrapolation. The results of this approach are some 25 percent higher than the experimental results, equation (1), but show the same Reynolds-number dependency.

A phenomenological theory has been developed by Spalding [10]. In separated flow, the maximum shear occurs in the fluid away from the surface in contrast to boundary-layer flows in which the maximum shear is at the surface. The turbulence generated in this region is the mechanism by which heat is conveyed from the surface. The solution of the diffusion equation for turbulence yields an expression for heat transfer. Using estimated values for the parameters for flow over cylinders, the heat transfer is predicted to be

$$\mathrm{St} = 0.15\ \mathrm{Re}^{-0.4} \tag{4}$$

These results are lower than the cylinder data by a factor of two to three over the Reynolds-number range 10^2 to 10^5.

The analysis by Virk [11], which became available while the present paper was under review, is based on the assumption that the flow in the wake region is stagnant. Heat transfer from the surface is assumed to occur only by molecular conduction. The total heat transfer is then the same as that for a semi-infinite slab over a time period equal to the period of the vortex street. Using a value for Strouhal number of 0.2, the predicted heat-transfer relationship for air is:

$$\mathrm{St} = 0.59\ \mathrm{Re}^{-1/2} \tag{5}$$

This result is lower than the cylinder data by a factor of two.

In summary, there are some data available for heat transfer in the wake region behind circular cylinders, half-round cylinders, and normal and inclined flat plates. These data show a definite effect of geometry, and indicate that larger wakes produce higher heat transfer. The theory of Richardson agrees quite well with the data for circular cylinders, but the prediction does not account for geometrical differences. Spalding's theory is considerably lower than the existing data; presumably, either other mechanisms are present or reevaluation of the values of the constants are needed. The relationship proposed by Virk is also lower than the data and does not account for convection in the wake region. None of the geometries studied are truly representative of many heat-exchanger surfaces and the Reynolds-number range for all but the circular-cylinder results is considerably higher than that found in heat exchangers.

Test Procedure

The test facility consists of a 6-in-dia free-discharge wind tunnel. The air velocity may be varied from 35 to 160 fps and is measured using a pitot-static tube. The velocity profile at the discharge nozzle is flat to within 1 percent over the center 5 in.

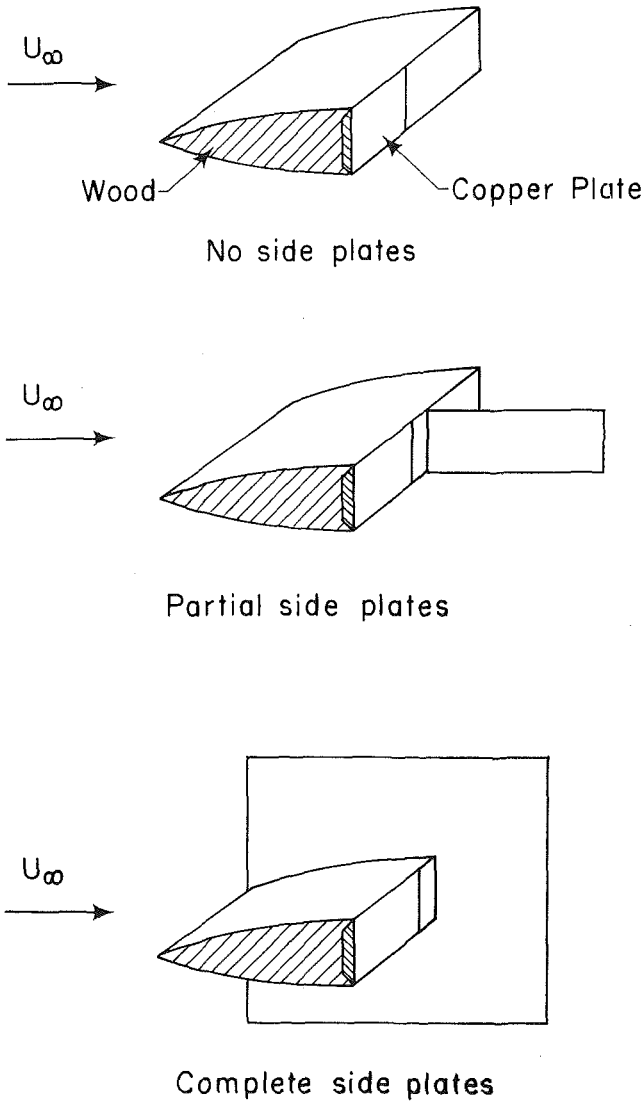

Fig. 4 Schematic of experimental tests using side plates

The turbulence intensity has been estimated using a hot-wire anemometer to be about 2.5 percent. All temperatures were measured using copper–constantan thermocouples.

The heat-transfer models were of a streamlined wedge shape with a flat base normal to the free stream, Fig. 3. The shape was chosen so that the flow at the end of the model was parallel to the main stream, similar to that for heat-exchanger surfaces. The models were constructed of wood with a 4-in-long copper plate inset into the rear of the model. The height of the copper plate was the same as that of the wedge and the two base heights employed were ¼ and 1 in. with wedge lengths of 1 and 3 1/16 in. respectively. Tests were conducted with and without two sets of side plates as indicated in Fig. 4.

The heat-transfer coefficient for the base was obtained using the transient lumped-parameter approach [12]. The base was heated to a temperature about 30 deg F higher than that of the air using a hot-air gun. The model was then inserted into the wind tunnel, and the temperature difference between the base and air flow was measured as a function of time.

In the lumped-parameter approach, the assumption is made that all the thermal capacitance is in the copper plate and all of the thermal resistance is in the boundary layer. The mean heat-transfer coefficient is then computed from

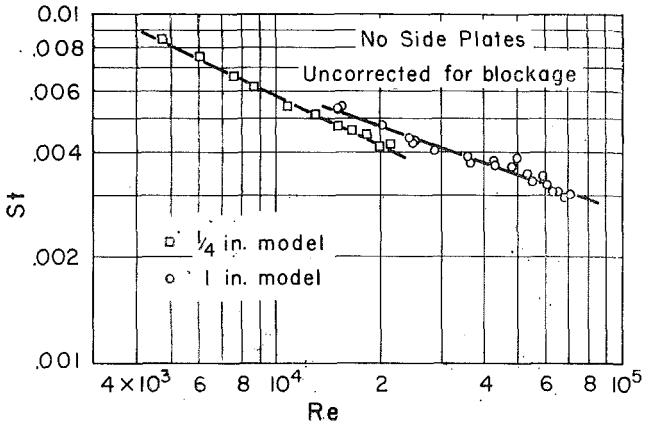

Fig. 5 Heat-transfer results for no side plates, uncorrected for blockage effect

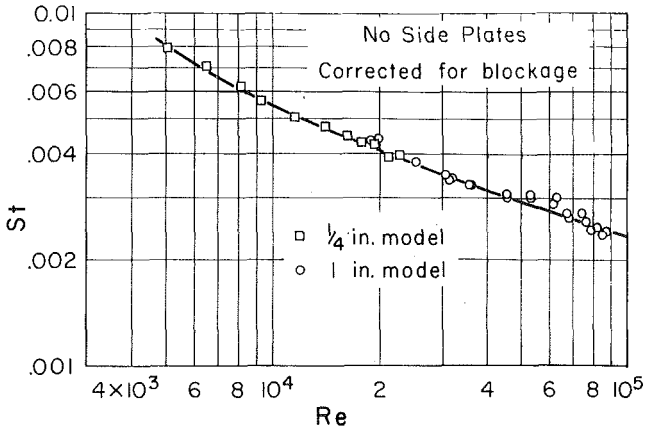

Fig. 7 Heat-transfer results for no side plates, corrected for blockage effect

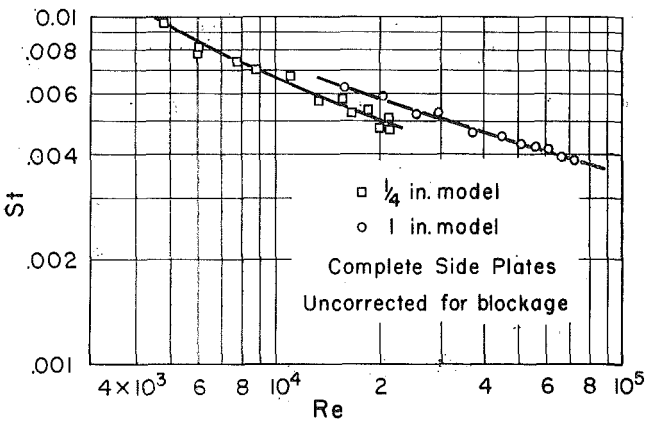

Fig. 6 Heat-transfer results for complete side plates, uncorrected for blockage effect

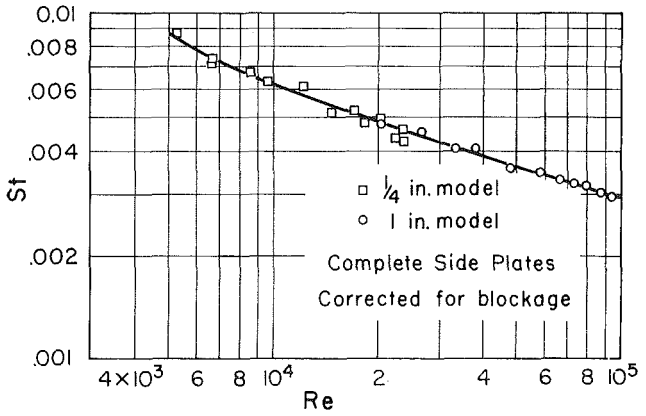

Fig. 8 Heat-transfer results for complete side plates, corrected for blockage effect

$$h = \left(\frac{C}{A}\right)\frac{1}{\tau}\ln\left(\frac{t_{w,i} - t_\infty}{t_w - t_\infty}\right) \tag{6}$$

The heat-transfer coefficient determined in this manner is an average coefficient over both time and position on the base.

A least-mean-squares fit of equation (6) using the temperatures at several times was employed to determine the best value of the heat-transfer coefficient. It is estimated that the heat-transfer coefficient is accurate to within ±5 percent.

The Biot number for the copper plate is less than 0.002 for all tests, and thus the lumped-parameter approach is valid. Transient conduction to the wood was estimated and found to be negligible. Radiant heat transfer was less than 1 percent of the total for all tests.

Blockage effects due to the relatively large frontal area of the models compared to the wind-tunnel area were found to be important. The results are presented both uncorrected and corrected for the free-stream flow acceleration around the model. The velocity in the presence of the model is calculated from the velocity measured in the absence of the model using the one-dimensional flow relation

$$U_m = U_\infty \Big/ \left[1 - \frac{A_m}{A_{wt}}\right] \tag{7}$$

This correction to the velocity is about 20 percent for the 1-in. model and 8 percent for the ¼-in. model. The validity of this correction is discussed in the next section.

Test Results

The test results for no side plates and for complete side plates are presented in Figs. 5 and 6. The results corrected for the blockage effect are presented in Figs. 7 and 8. Since the corrected data for the ¼-in. and 1-in. models are correlated using Stanton number and Reynolds number as would be expected, it is felt that the blockage correction is a valid one. The literature is not clear on this correction for free-discharge wind tunnels. It is recommended that Figs. 7 and 8 be employed for determining the heat-transfer coefficient for a given situation.

The base heat-transfer coefficient for the wedge model is about 60 percent as high as that for flow over cylinders. This is expected as the wake is considerably smaller. The slope is approximately $-1/3$ at the higher Reynolds numbers, but, at the lower Reynolds numbers, the relationship deviates from a simple power relationship. The data for no side plates is about 10 to 25 percent lower than that for complete side plates.

Over the range $\mathrm{Re} = 6 \times 10^3$ to 10^5, the data of Figs. 7 and 8 can be represented within ±5 percent by the following power relationships:

No side plates

$$\mathrm{St} = 0.23\ \mathrm{Re}^{-0.4} \tag{8}$$

Complete side plates

$$\mathrm{St} = 0.135\ \mathrm{Re}^{-1/3} \tag{9}$$

In Fig. 9, the results of an investigation of the effect of side

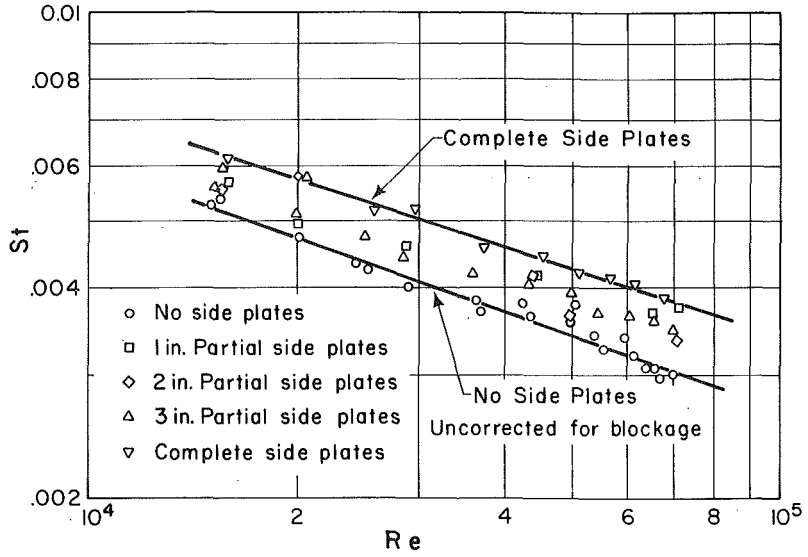

Fig. 9 Effect of side plates on the heat transfer

plates on the heat transfer for the 1-in. model are presented. The partial side plates were 1, 2, and 3 in. long in the downstream direction, Fig. 4. It is seen that the heat transfer for complete side plates is consistently 20 to 25 percent higher than that for no side plates. This is probably due to a containment of the wake by the side plates. Since the potential core of the wind tunnel persists to about 6 diameters or 36 in., the difference is probably not due to containment of the free stream by the side plates.

The results for the three partial plates do not differ significantly from each other, and are midway between the complete and no-side-plate results. The effect of these plates is to prevent significant flow between the wake and the surrounding atmosphere; apparently this is not a large effect. These side-plate tests indicate that the wake may behave two-dimensionally.

The effect of the boundary layer on the wedge on the heat transfer from the base appears to be small. The transition Reynolds number for the boundary layer on the wedge surface for the test wind tunnel turbulence intensity corresponds to a Reynolds number based on base height of about 4×10^4. In Fig. 9, there is a slight increase in Stanton number for Reynolds numbers greater than 4×10^4. This is presumably due to a turbulent boundary layer at the edge of the separation region which provides more agitation in the wake than does a laminar boundary layer. The small effect of this difference in boundary-layer character is probably due to the thinness of the boundary layer; the boundary-layer thickness is only about 15 percent of the base height. Larger ratios of boundary-layer thickness to base height would significantly affect both the flow and heat transfer [1].

Analytical Model

The analytical model combines the vortex-shedding results with conventional boundary-layer theory. It is assumed that a new boundary layer forms on the base surface each time a vortex forms, it builds up until the vortex is shed, and then it sheds with the vortex. The free-stream velocity for the boundary layer on the base surface is assumed to be the velocity at the edge of the wake U_s. This situation is depicted schematically in Fig. 10. Water-table studies have been carried out which support the general framework for this model, but detailed flow measurements have not been made.

The analysis is developed in two parts. First, there is an initial buildup of the boundary layer which is modeled as the problem of a surface initially accelerated to U_s. This boundary layer eventually becomes fully established, and then is treated as a conventional laminar boundary layer.

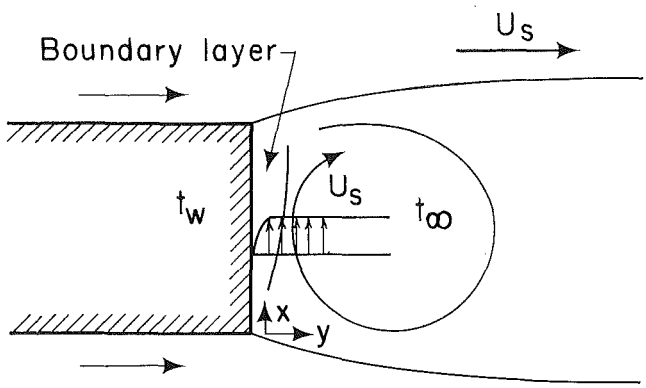

Fig. 10 Schematic of the flow behavior assumed for the analytical model formulation

Rosenhead [13] discusses the situation of a plate initially at rest and suddenly accelerated to a fixed velocity U_s. For short times ($\tau U_s/d < 1$), the convective terms may be neglected in the momentum equation. Under these conditions, the boundary-layer equation simplifies to

$$\frac{\partial t}{\partial \tau} = \alpha \frac{\partial^2 t}{\partial y^2} \tag{10}$$

The boundary conditions for the energy equation are

$$\left.\begin{aligned} t(y, 0) &= t_\infty \\ t(\infty, \tau) &= t_\infty \\ t(0, \tau) &= t_w \end{aligned}\right\} \tag{11}$$

The energy equation is not coupled to the momentum equation, and the solution is readily obtained in terms of the error function

$$\frac{t - t_w}{t_\infty - t_w} = \operatorname{erf}\left(\frac{y}{2\sqrt{\alpha\tau}}\right) \tag{12}$$

The surface heat flux can be obtained from equation (12) using the conduction-mechanism equation. In order to combine this result with the boundary-layer relations, a heat-transfer coefficient is defined as a ratio of heat flux to the temperature difference between the wall and the free stream. This relation is put in terms of a Stanton and Reynolds number with d and U_∞ as character-

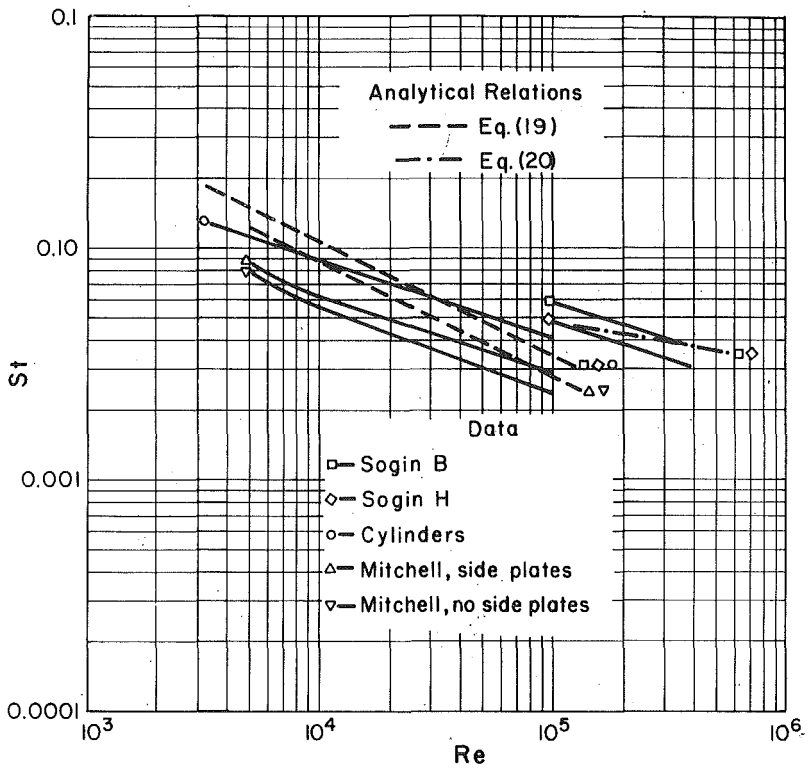

Fig. 11 Comparison of present analysis and experimental heat-transfer results

istic dimensions. The heat transfer during the initial phase is then

$$\mathrm{St} = \left(\frac{d^2}{\pi\nu\tau}\right)^{1/2} \mathrm{Pr}^{-1/2}\,\mathrm{Re}^{-1} \tag{13}$$

During this initial vortex-buildup phase, the heat transfer is a function only of time and not of position.

For long times, $\tau U_s/d > 1$, the conventional steady-state laminar-boundary-layer results apply. The mean heat transfer is given by

$$\mathrm{St} = 0.664(U_s/U_\infty)^{1/2}\,\mathrm{Pr}^{-2/3}\,\mathrm{Re}^{-1/2} \tag{14}$$

The ratio $(U_s/U_\infty)^{1/2}$ appears since the vortex velocity is U_s, but the nondimensional parameters are based on U_∞.

The total heat transfer for each cycle of vortex formation and shedding is obtained by adding up short-term and long-term contributions. In adding these two, the criterion of Rosenhead that the short-term solution persists until $\tau U_s/d = 1$ is modified. The short-term solution is employed only until the value of heat-transfer coefficient equals that for the long time. This appears more realistic in that it gives a value for the heat-transfer coefficient that starts high and decreases to the steady-state value.

The length of time that the short-term solution applies is obtained by equating equations (13) and (14).

$$\tau_s = 0.723\left(\frac{d^2}{\nu}\right)\left(\frac{U_s}{U_\infty}\right)^{-1} \mathrm{Pr}^{1/3}\,\mathrm{Re}^{-1} \tag{15}$$

The time for the complete cycle from vortex formation to shedding for $\mathrm{S}^* = 0.16$ is

$$\tau_0 = 1/n = 6.25d_s/U_s \tag{16}$$

The ratio of the time for the boundary layer to become established to the vortex cycle time is

$$\tau_s/\tau_0 = 0.116(d/d_s)\quad \mathrm{Pr}^{1/3} \tag{17}$$

The short-term solution is seen to apply only for about 10 percent of the total period; the boundary layer establishes very quickly.

The mean heat transfer for each cycle, which is that measured experimentally, is given by

$$\mathrm{St} = \frac{1}{\tau_0}\left[\int_0^{\tau_s}\left(\frac{d^2}{\pi\nu\tau}\right)^{1/2}\mathrm{Pr}^{-1/2}\,\mathrm{Re}^{-1}d\tau + \int_{\tau_s}^{\tau_0} 0.664\left(\frac{U_s}{U_\infty}\right)^{1/2}\mathrm{Pr}^{-2/3}\,\mathrm{Re}^{-1/2}d\tau\right] \tag{18}$$

The integration yields the following general expression for the heat transfer:

$$\mathrm{St} = [0.664 + 0.076(d/d_s)\,\mathrm{Pr}^{1/3}](U_s/U_\infty)^{1/2}\,\mathrm{Pr}^{-2/3}\,\mathrm{Re}^{-1/2} \tag{19}$$

The analysis predicts that the ratio of wake width to base height does not, directly, have a significant effect on the heat transfer. However, the velocity along the edge of the wake, which is greater than the free-stream value due to, in part, the wake width, does have a strong influence. The effect of the frequency of vortex shedding is quite small since the boundary layer establishes quickly in the cycle. The heat transfer behaves essentially as conventional laminar flat-plate heat transfer.

The heat-transfer predictions for the various geometries are given as:

Geometry	d_s/d	U_s/U	$\mathrm{St}\,\mathrm{Re}^{1/2}$
Mitchell	1.0*	1.0*	0.91
Sogin, B	1.7†	1.38†	1.03
Sogin, H	1.2†	1.35†	1.04
Circular cylinder	1.2†	1.38†	1.04

* Water-table results.
† Roshko, $\mathrm{Re} = 8 \times 10^3$ to 5×10^4.

The analytical predictions and corresponding data are plotted in Fig. 11. There is fair agreement between the present data and the analysis at high Reynolds numbers, but the analysis is

high by about 30 percent at low Reynolds numbers. It appears that a $-1/3$ exponent of Reynolds number would produce a better fit than the predicted $-1/2$ exponent.

The agreement between the analysis and the cylinder data is quite good. The large spread in the cylinder data is probably enough to accommodate the difference in exponents over the Reynolds-number range of the data.

The data of Sogin are considerably higher than the model relation. For these tests, the Reynolds number based on U_s and d is close to the transition Reynolds number, and it is possible that the boundary layer on the base is turbulent. If the transient boundary-layer development is neglected, and if it is assumed that an established flat-plate turbulent-boundary-layer flow exists on the base region, the heat-transfer relationship for models B and H is the standard flat-plate relationship for turbulent flow based on U_s and d. In terms of the present parameters, the heat transfer is

$$\mathrm{St} = 0.048\ \mathrm{Re}^{-0.2} \tag{20}$$

This relation is also plotted in Fig. 11, and yields surprisingly good agreement with the data of Sogin.

The conclusion to be drawn from these comparisons is that the present model formulation, while incorporating known mechanisms, is only a preliminary one for predicting base heat transfer. Considerably more experimental information is needed in order to construct accurate analytical relationships.

Conclusions

The following conclusions can be drawn from the results presented in this paper:

1 The heat transfer in the separated region behind a two-dimensional bluff body has been determined experimentally. These results are presented in Figs. 7 and 8, and cover the Reynolds-number range of interest in heat-exchanger applications.

2 A preliminary analysis based on the mechanisms of vortex shedding and boundary-layer behavior has been developed. The analytical relations compare reasonably well with the existing data. The comparisons indicate that considerably more information is needed in order to develop an accurate model for subsonic base heat transfer.

References

1 Nash, J. F., "A Review of Research on Two-Dimensional Base Flow," ARC R and M No. 3323, March 1962.

2 Hanson, F. B. and Richardson, P. D., "Mechanics of Turbulent Separated Flows as Indicated by Heat Transfer: A Review," *Symposium on Fully Separated Flows*, ASME, 1964, pp. 27–32.

3 Morkovin, M. C., "Flow Around a Circular Cylinder—A Kaleidoscope of Challenging Fluid Phenomena," *Symposium on Fully Separated Flows*, ASME, 1964, pp. 102–118.

4 Roshko, A., "On the Drag and Shedding Frequency of Two-Dimensional Bluff Bodies," NACA TN 3169, July 1954.

5 Abernathy, F. H., "Flow Over an Inclined Plate," *Journal of Basic Engineering*, TRANS. ASME, Series D, Vol. 84, No. 3, Sept. 1962, pp. 380–388.

6 Nash, J. F., Quincey, V. G., and Callahan, J., "Experiments on Two-Dimensional Base Flows at Subsonic and Transonic Speeds," ARC R and M No. 3427, Jan. 1963.

7 Richardson, P. D., "Estimation of the Heat Transfer From the Rear of an Immersed Body to the Region of Separated Flows," ARL Rept. 62-423, Sept. 1962.

8 Richardson, P. D., "Heat and Mass Transfer in Turbulent Separated Flows," *Chemical Engineering Science*, Vol. 18, 1963, pp. 149–155.

9 Sogin, H. H., "A Summary of Experiments on Local Heat Transfer From the Rear of Bluff Obstacles to a Low Speed Airstream," JOURNAL OF HEAT TRANSFER, TRANS. ASME, Series C, Vol. 86, No. 2, May 1964, pp. 200–202.

10 Spalding, D. B., "Heat Transfer From Turbulent Separated Flows," *Journal of Fluid Mechanics*, Vol. 27, No. 1, 1967, pp. 97–109.

11 Virk, P. S., "Heat Transfer From the Rear of a Cylinder in Transverse Flow," JOURNAL OF HEAT TRANSFER, TRANS. ASME, Series C, Vol. 92, No. 1, Feb. 1970, pp. 206–207.

12 London, A. L., Nottage, H. B., and Boelter, L. M. K., "Determination of Unit Conductances in Heat and Mass Transfer by the Transient Method," *Industrial and Engineering Chemistry*, Vol. 33, 1941, p. 467.

13 Rosenhead, L., *Laminar Boundary Layers*, Oxford, Clarendon Press, 1963.

MATTHEW KELLEHER
Assistant Professor,
Department of Mechanical Engineering,
Naval Postgraduate School,
Monterey, Calif.
Assoc. Mem. ASME

Free Convection From a Vertical Plate With Discontinuous Wall Temperature

Free convection from a vertical plate with a step discontinuity in wall temperature is analyzed by using asymptotic series. Expansions for the velocity and temperature profiles are obtained in the region immediately above the discontinuity. By series truncation, the wall heat flux is obtained in terms of a simple polynomial. Calculations are made for Pr = *0.72 and 10.0 and for various wall-temperature ratios. Comparison of the results with experimental data and previous numerical solutions is good.*

Introduction

THE STUDY of non-similar free-convection flows has not received a great deal of attention until recently. Schetz and Eichhorn [1][1] conducted an experimental study of the free-convection boundary layer on a vertical plate which has a step discontinuity in surface temperature. Subsequently, Hayday et al. [2] presented a numerical study of the same situation. The results obtained compared favorably with the experimental results of Schetz and Eichhorn. It is the aim of this paper to provide an alternative analysis for the problem of free convection with discontinuous wall temperatures. The technique used holds great promise in the study of boundary layers with discontinuous boundary conditions. The method is essentially the classical asymptotic expansion developed by Goldstein [3] to study the laminar wake behind a flat plate in a uniform stream. This procedure has subsequently been extended by Yang [4] to study the free-convection wake above a vertical heated plate. In the present analysis, the technique is used to obtain velocity and temperature profiles in the region immediately above a discontinuity in surface temperature. As distance up the plate increases, these profiles are seen to approach the similar solution that would be expected at distances far from the discontinuity.

Formulation

The physical situation is shown in Fig. 1. A semi-infinite vertical plate is maintained at temperature $\bar{T}_{w1}$ above ambient for a distance L from the leading edge. At $\bar{x} = L$, the plate temperature is changed to $\bar{T}_{w2}$ also above ambient. The effect of this temperature discontinuity is much the same as the leading edge in the usual boundary layer. This effect is greatest when the lower portion of the plate is at ambient temperature. In this case the discontinuity becomes the leading edge. For increased values of the lower-plate temperature the effect of the discontinuity becomes less until it completely disappears when the lower and upper temperatures are the same The governing equations then are taken to be the usual free-convection boundary-layer equations, expressing conservation of mass, momentum, and energy. Using dimensionless coordinates, these are:

$$\frac{\partial u}{\partial x} + \frac{\partial v}{\partial y} = 0 \tag{1}$$

$$u\frac{\partial u}{\partial x} + v\frac{\partial u}{\partial y} = \mathrm{Gr}_2\,\theta + \frac{\partial^2 u}{\partial y^2} \tag{2}$$

$$u\frac{\partial \theta}{\partial x} + v\frac{\partial \theta}{\partial y} = \frac{1}{\mathrm{Pr}}\frac{\partial^2 \theta}{\partial y^2} \tag{3}$$

It should be noted that the origin of the x, y coordinate system is taken to be located at the temperature discontinuity. The boundary conditions associated with these equations are:

$$\begin{aligned} y = 0 \quad & u = v = 0 \quad \theta = 1 \\ y \to \infty \quad & u \to 0 \quad \theta \to 0 \end{aligned} \tag{4}$$

Also associated with these equations are the initial conditions:

$$\begin{aligned} x = 0 \quad & u = u_i(y) \\ & \theta = \theta_i(y) \end{aligned} \tag{5}$$

The initial conditions can be evaluated as follows: For a vertical plate at a temperature $\bar{T}_{w1}$, the velocity and temperature profiles can be determined from the following ordinary differential equations:

$$\begin{aligned} F''' + 3FF'' - 2F'^2 + H = 0 \\ \frac{1}{\mathrm{Pr}}H'' + 3FH' = 0 \end{aligned} \tag{6}$$

[1] Numbers in brackets designate References at end of paper.

Contributed by the Heat Transfer Division for publication (without presentation) in the JOURNAL OF HEAT TRANSFER. Manuscript received by the Heat Transfer Division April 27, 1970; revised manuscript received August 17, 1970. Paper No. 71-HT-B.

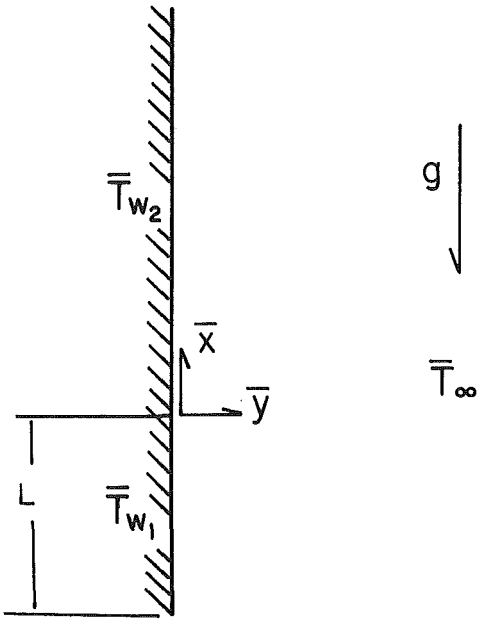

Fig. 1 Physical model

where primes refer to derivatives with respect to the similarity variable which when evaluated at a distance L from the leading edge becomes:

$$y_1^* = y\left(\frac{\mathrm{Gr}_1}{4}\right)^{1/4}$$

and Gr_1 is the Grashof number based on the lower-wall temperature difference $(\bar{T}_{w_1} - \bar{T}_\infty)$. The relation between the initial profiles and the similar solution is then:

$$\begin{aligned} u_i &= (4\mathrm{Gr}_1)^{1/2}F'(y_1^*) \\ \theta_i &= \epsilon H(y_1^*) \end{aligned} \tag{7}$$

where the parameter ϵ is the wall-temperature difference ratio:

$$\epsilon = \frac{\bar{T}_{w_1} - \bar{T}_\infty}{\bar{T}_{w_2} - \bar{T}_\infty} = \frac{\mathrm{Gr}_1}{\mathrm{Gr}_2} \tag{8}$$

This parameter will be used extensively throughout the analysis.

The governing equations can be further simplified by introducing a stream function to satisfy continuity and by stretching the y coordinate:

$$\begin{aligned} y^* &= y\left(\frac{\mathrm{Gr}_2}{4}\right)^{1/4} \\ u^* &= (4\mathrm{Gr}_2)^{-1/2}u = \frac{\partial\Psi}{\partial y^*} \\ v^* &= (64\mathrm{Gr}_2)^{-1/4}v = -\frac{\partial\Psi}{\partial x} \end{aligned} \tag{9}$$

This gives:

$$4\frac{\partial\Psi}{\partial y^*}\frac{\partial^2\Psi}{\partial x\partial y^*} - 4\frac{\partial\Psi}{\partial x}\frac{\partial^2\Psi}{\partial y^{*2}} = \theta + \frac{\partial\Psi}{\partial y^{*3}} \tag{10}$$

$$4\frac{\partial\Psi}{\partial y^*}\frac{\partial\theta}{\partial x} - 4\frac{\partial\Psi}{\partial x}\frac{\partial\theta}{\partial y^*} = \frac{1}{\mathrm{Pr}}\frac{\partial^2\theta}{\partial y^{*2}} \tag{11}$$

In the manner of Goldstein [3] and Yang [4], solutions to equations (10) and (11) will be sought in the form of asymptotic expansions in x.

Solutions for Small y^*

For small values of y^*, we will seek expansions for Ψ and θ in the following forms:

Nomenclature

A_1, B_1, D_1
A_1^*, B_1^*
A_2, B_2, C_2, E_2
A_2^*, B_2^*, C_2^* = constants defined in equation (33)

a_n, b_n = constant coefficients in initial profiles

F = stream function in similar solution

f_0, f_1, f_2 = coefficient functions in inner expansion of stream function

g = gravitational acceleration

g_0, g_1, g_2 = coefficient functions in inner expansion of temperature

H = temperature variable in similar solution

k = thermal conductivity

L = length of plate at $\bar{T}_{w_1}$

Gr = Grashof number $\equiv \dfrac{g\beta L^3(T_w - T_\infty)}{\nu^2}$

Pr = Prandtl number $= \dfrac{\nu}{\alpha}$

q_w = heat flux at the wall

$\bar{T}$ = temperature

$u = \dfrac{\bar{u}L}{\nu}$

$\bar{u}$ = velocity component in $\bar{x}$ direction

$u^* = (4\mathrm{Gr}_2)^{-1/2}u$

$v = \dfrac{\bar{v}L}{\nu}$

$\bar{v}$ = velocity component in $\bar{y}$ direction

$x = \bar{x}/L$

$\bar{x}$ = streamwise coordinate measured from temperature discontinuity

$Y_{10}, Y_{11}, Y_{20}, Y_{21}, Y_{22}$ = universal functions defined in equations (28) and (29)

$y = \bar{y}/L$

$\bar{y}$ = coordinate normal to plate measured from plate surface

$y^* = (\mathrm{Gr}_2/4)^{1/4}y$

$y_1^* = \epsilon^{1/4}y^*$

Z_{00}, Z_{01} = universal functions defined in equation (27)

Z_{10}, Z_{11}, Z_{12}
$Z_{20}, Z_{21}, Z_{22}, Z_{23}$ = universal functions defined in equations (28) and (29)

α = thermal diffusivity

β = coefficient of volumetric expansion

$\epsilon = \dfrac{\mathrm{Gr}_1}{\mathrm{Gr}_2} = \dfrac{\bar{T}_{w_1} - \bar{T}_\infty}{\bar{T}_{w_2} - \bar{T}_\infty}$

$\eta = \frac{1}{3}\epsilon^{1/4}y^*x^{-1/3}$

$\theta = \dfrac{\bar{T} - \bar{T}_\infty}{\bar{T}_{w_2} - \bar{T}_\infty}$

$\theta_0, \theta_1, \theta_2$ = coefficient functions in outer expansion for temperature

ν = kinematic viscosity

$\xi = x^{1/3}$

Ψ = dimensionless stream function

Ψ_0, Ψ_1, Ψ_2 = coefficient functions for Ψ in outer expansion

Subscripts

i = initial conditions

w = plate surface conditions

∞ = ambient conditions

w_1, w_2 = surface conditions pertaining to wall temperature $\bar{T}_{w_1}$ or $\bar{T}_{w_2}$, respectively

$$\Psi(x, y^*) = \Psi(\xi, \eta) = \epsilon^{1/4} \frac{\xi^2}{4} [f_0(\eta) + \xi f_1(\eta) + \xi^2 f_2(\eta) + \ldots] \quad (12)$$

$$\theta(x, y^*) = \theta(\xi, \eta) = 1 + \epsilon[g_0(\eta) + \xi g_1(\eta) + \xi^2 g_2(\eta) + \ldots] \quad (13)$$

where

$$\xi = x^{1/3} \quad \eta = \epsilon^{1/4} \frac{y^*}{3} x^{-1/3} \quad (14)$$

Substituting equations (12) and (13) into equations (10) and (11) and equating terms in like powers of ξ, the following ordinary differential equations for the coefficient functions are obtained:

$$f_0''' + 2f_0 f_0'' - f_0'^2 = 0$$
$$\frac{1}{\mathrm{Pr}} g_0'' + 2f_0 g_0' = 0 \quad (15)$$

$$f_1''' + 2f_0 f_1'' - 3f_0' f_1' + 3f_0'' f_1 = -\frac{108}{\epsilon} - 108 g_0$$
$$\frac{1}{\mathrm{Pr}} g_1'' + 2f_0 g_1' - f_0' g_1 + 3g_0' f_1 = 0 \quad (16)$$

$$f_2''' + 2f_0 f_2'' - 4f_0' f_2' - 4f_0'' f_2 = 2f_1'^2 - 3f_1 f_1'' - 108 g_1$$
$$\frac{1}{\mathrm{Pr}} g_2'' + 2f_0 g_2' - 2f_0' g_2 + 4f_2 g_0 = f_1' g_1 - 3f_1 g_1' \quad (17)$$

Since these solutions are valid for small y^*, they must satisfy the boundary conditions at $y^* = 0$ or $\eta = 0$. Therefore, according to equation (4), we have:

$$f_k(0) = f_k'(0) = g_k(0) = 0 \qquad k = 0, 1, 2, \ldots \quad (18)$$

Two additional boundary conditions for each set of the functions f_k and g_k can be derived from the initial conditions. For any small but fixed y^*, $x \to 0$ implies $\eta \to \infty$. Considering the relation between the velocity components and the stream function given in equation (9) and the definitions of η and ϵ given in equation (14), we can use equation (13) to obtain:

$$u = \frac{1}{12} (4\mathrm{Gr}_2)^{1/2} \epsilon^{1/2} \left(\epsilon^{1/4} \frac{y^*}{3\eta}\right) \left[f_0' + \left(\epsilon^{1/4} \frac{y^*}{3\eta}\right) f_1' + \left(\epsilon^{1/4} \frac{y^*}{3\eta}\right)^2 f_2' + \ldots\right] \quad (19)$$

$$\theta = 1 + \epsilon \left[g_0 + \left(\epsilon^{1/4} \frac{y^*}{3\eta}\right) g_1 + \left(\epsilon^{1/4} \frac{y^*}{3\eta}\right)^2 g_2 + \ldots\right]$$

For small y^*, the initial profiles in (7) may be expressed as a power series in y_1^*:

$$u_i = (4\mathrm{Gr}_1)^{1/2} F'(y_1^*) = (4\mathrm{Gr}_1)^{1/2} \sum_{n=2}^{m} n a_n y_1^{*n-1}$$
$$\theta_i = \epsilon H(y_1^*) = \epsilon \left[1 + \sum_{n=1}^{m} b_n y_1^{*n}\right] \quad (20)$$

where m is the number of terms to be considered. Since y_1^* and y^* are related by:

$$y_1^* = \epsilon^{1/4} y^* \quad (21)$$

equations (20) can be rewritten as:

$$u_i = (4\mathrm{Gr}_1)^{1/2} \sum_{n=2}^{m} n a_n (\epsilon^{1/4} y^*)^{n-1} \quad (22)$$

$$\theta_i = \epsilon \left[1 + \sum_{n=1}^{m} b_n (\epsilon^{1/4} y^*)^n\right] \quad (22)\ (Cont.)$$

If the coefficients of like powers of y^* in equations (19) and (22) are equated, the following behavior for f_k' and g_k as $\eta \to \infty$ $(x \to 0)$ is obtained:

$$\frac{f_0'}{\eta} \to 72 a_2$$
$$g_0 \to 1 - \frac{1}{\epsilon}$$
$$\frac{f_1'}{\eta^2} \to 324 a_3$$
$$\frac{g_1}{\eta} \to 3 b_1 \quad (23)$$
$$\frac{f_2'}{\eta^3} \to 1296 a_4$$
$$\frac{g_2}{\eta^2} \to 9 b_2$$

The coefficients in equations (20) can be derived quite easily from the similarity solution and are:

$$a_2 = \frac{1}{2} F'''(0) \qquad b_1 = H'(0)$$
$$a_3 = -\frac{1}{6} \qquad b_2 = 0 \quad (24)$$
$$a_4 = -\frac{H'(0)}{24} \qquad b_3 = 0$$

With these coefficients, the boundary conditions in (23) are fully determined. The equation (15) for f_0 and g_0 can be integrated directly and with boundary conditions (18) and (23) we have:

$$f_0 = 36 a_2 \eta^2$$
$$g_0 = \frac{1 - \frac{1}{\epsilon}}{\frac{1}{3}\Gamma\left(\frac{1}{3}\right)} (24 a_2 \mathrm{Pr})^{1/3} \int_0^\eta e^{-(24 a_2 \mathrm{Pr}) \eta^3} d\eta \quad (25)$$

Tabulations of the integral in equation (25) are readily available [5]. Because of the form of equations (16) and (17) and of the function g_0, it can be seen that the higher-order functions depend on ϵ and are therefore not universal functions. This difficulty can be overcome by expressing the functions as combinations of suitably chosen universal functions. By examining equation (25), we can express g_0 as:

$$g_0 = Z_{00} + \frac{1}{\epsilon} Z_{01} \quad (26)$$

where Z_{00} and Z_{01} are universal functions depending only on Prandtl number and are given by:

$$Z_{00}(\eta) = -Z_{01}(\eta) = \frac{(24 a_2 \mathrm{Pr})^{1/3}}{\frac{1}{3}\Gamma\left(\frac{1}{3}\right)} \int_0^\eta e^{-(24 a_2 \mathrm{Pr}) \eta^3} d\eta \quad (27)$$

In a similar manner, we can express the remaining functions as:

$$f_1 = Y_{10} + \frac{1}{\epsilon} Y_{11} \quad (28)$$

$$g_1 = Z_{10} + \frac{1}{\epsilon} Z_{11} + \frac{1}{\epsilon^2} Z_{12} \quad (28)\ (Cont.)$$

$$f_2 = Y_{20} + \frac{1}{\epsilon} Y_{21} + \frac{1}{\epsilon^2} Y_{22}$$

$$g_2 = Z_{20} + \frac{1}{\epsilon} Z_{21} + \frac{1}{\epsilon^2} Z_{22} + \frac{1}{\epsilon^3} Z_{23} \quad (29)$$

where Y_{10}, Z_{10}, etc., are universal functions of η and depend only on Prandtl number. Since the equations (16) and (17) are linear, we can substitute (28) and (29) and separate like powers of ϵ to obtain the governing equations for the universal functions.

$$Y_{10}''' + 2f_0Y_{10}'' - 3f_0'Y_{10}' + 3f_0''Y_{10} = -108Z_{00}$$

$$\frac{1}{\mathrm{Pr}} Z_{10}'' + 2f_0Z_{10}' - f_0'Z_{10} = -3Y_{10}Z_{00}'$$

$$Y_{11}''' + 2f_0Y_{11}'' - 3f_0'Y_{11}' + 3f_0''Y_{11} = -108(1 + Z_{01})$$

$$\frac{1}{\mathrm{Pr}} Z_{11}'' + 2f_0Z_{11}' - f_0'Z_{11} = -3Y_{10}Z_{01}' - 3Y_{11}Z_{00}'$$

$$\frac{1}{\mathrm{Pr}} Z_{12}'' + 2f_0Z_{12}' - f_0'Z_{12} = -3Y_{11}Z_{01}'$$

$$Y_{20}''' + 2f_0Y_{20}'' - 4f_0'Y_{20}' + 4f_0''Y_{20} = 2Y_{10}'^2 - 3Y_{10}Y_{10}'' - 108Z_{10}$$

$$\frac{1}{\mathrm{Pr}} Z_{20}'' + 2f_0Z_{20}' - 2f_0'Z_{20} = Y_{10}'Z_{10} - 3Y_{10}Z_{10}' - 4Y_{20}Z_{00}' \quad (30)$$

$$Y_{21}''' + 2f_0Y_{21}'' - 4f_0'Y_{21}' + 4f_0''Y_{21} = 4Y_{10}'Y_{11}' - 3Y_{10}Y_{11}'' - 3Y_{10}''Y_{11} - 108Z_{11}$$

$$\frac{1}{\mathrm{Pr}} Z_{21}'' + 2f_0Z_{21}' - 2f_0'Z_{21} = Y_{10}'Z_{11} + Y_{11}'Z_{10} - 3Y_{10}Z_{11}' - 3Y_{11}Z_{10}' - 4Y_{20}Z_{01}' - 4Y_{21}Z_{00}'$$

$$Y_{22}''' + 2f_0Y_{22}'' - 4f_0'Y_{22}' + 4f_0''Y_{22} = 2Y_{11}'^2 - 3Y_{11}Y_{11}'' - 108Z_{12}$$

$$\frac{1}{\mathrm{Pr}} Z_{22}'' + 2f_0Z_{22}' - 2f_0'Z_{22} = Y_{10}'Z_{12} + Y_{11}'Z_{11} - 3Y_{10}Z_{12}' - 3Y_{11}Z_{11}' - 4Y_{21}Z_{01}' - 4Y_{22}Z_{00}'$$

$$\frac{1}{\mathrm{Pr}} Z_{23}'' + 2f_0Z_{23}' - 2f_0'Z_{23} = Y_{11}'Z_{12} - 3Y_{11}Z_{12}' - 4Y_{22}Z_{01}'$$

From (18) and (23), the associated boundary conditions are:

$$\eta = 0 \quad Y_{10} = Y_{11} = Y_{20} = Y_{21} = Y_{22} = 0$$

$$Y_{10}' = Y_{11}' = Y_{20}' = Y_{21}' = Y_{22}' = 0$$

$$Z_{10} = Z_{11} = Z_{12} = 0$$

$$Z_{20} = Z_{21} = Z_{22} = Z_{23} = 0$$

$$\eta \to \infty \quad \frac{Y_{10}'}{\eta^2} \to 324a_3; \quad Y_{11}' \to 0$$

$$\frac{Y_{20}'}{\eta^3} \to 1296a_4; \quad Y_{21}' \to 0; \quad Y_{22}' \to 0 \quad (31)$$

$$\frac{Z_{10}}{\eta} \to 3b_1; \quad Z_{11} \to 0; \quad Z_{12} \to 0$$

$$\frac{Z_{20}}{\eta^2} \to 9b_2; \quad Z_{21} \to 0; \quad Z_{22} \to 0; \quad Z_{23} \to 0$$

Equations (30) with the boundary conditions (31) have been solved numerically for Prandtl numbers of 0.72 and 10.0, using an IBM 360/67 digital computer. The procedure of Nachtsheim and Swigert [6] was used to find the starting values for the fourth-order Runge-Kutta numerical integration scheme. These starting values are given in Table 1.

To facilitate further calculations, it will be useful to investigate the asymptotic behavior of the functions f_k and g_k as η becomes large. By examining the ordinary differential equations and the form of the boundary conditions (23), it can be seen that as η becomes large, the asymptotic forms for f_k and g_k are:

$$f_0 = 36a_2\eta^2 = A_0\eta^2 + B_0$$

$$g_0 = 1 - \frac{1}{\epsilon}$$

$$f_1 = A_1\eta^3 + B_1\eta^2 + C_1\eta + D_1 \quad (32)$$

$$g_1 = A_1^*\eta + B_1^*$$

$$f_2 = A_2\eta^4 + B_2\eta^3 + C_2\eta^2 + D_2\eta + E_2$$

$$g_2 = A_2^*\eta^2 + B_2^*\eta + C_2^*$$

where

$$A_0 = 36a_2; \quad B_0 = 0$$

$$A_1 = 108a_3; \quad B_1 = 0; \quad D_1 = 0$$

$$A_1^* = 3b_1; \quad B_1^* = 0$$

$$A_2 = 324a_4; \quad B_2 = 0 \quad (33)$$

$$C_2 = \frac{3A_1C_1}{2A_0}; \quad E_2 = \frac{C_1^2}{4A_0}$$

$$A_2^* = 0; \quad B_2^* = 0; \quad C_2^* = \frac{C_1A_1^*}{2A_0}$$

Constants C_1 and D_2 are evaluated from the numerical solutions and are functions of Prandtl number and ϵ. By noting the form of f_1 and f_2 in terms of the universal functions in equations (28) and (29), we can write C_1 and D_2 as:

$$C_1 = C_{10} + \frac{1}{\epsilon} C_{11}$$

$$D_2 = D_{20} + \frac{1}{\epsilon} D_{21} + \frac{1}{\epsilon^2} D_{22} \quad (34)$$

where C_{10}, C_{11}, D_{20}, D_{21}, and D_{22} are functions of Prandtl number only and can be determined from the numerical solutions for the universal functions. Table 2 contains values of these constants for the two Prandtl numbers considered.

Table 1

Pr	0.72	10.0
$F''(0)$	0.676016	0.419196
$H'(0)$	−0.504632	−1.169334
$f_0''(0)$	24.336576	15.091068
$Z_{00}'(0)$	2.016735	4.133882
$Y_{10}''(0)$	−21.051796	−13.200141
$Y_{11}''(0)$	21.051787	13.200142
$Z_{10}'(0)$	−2.288044	−5.031231
$Z_{11}'(0)$	1.104520	2.330807
$Z_{12}'(0)$	−0.330372	−0.807575
$Y_{20}''(0)$	−0.303394	0.059112
$Y_{21}''(0)$	4.217213	2.424556
$Y_{22}''(0)$	−0.391170	−2.483664
$Z_{20}'(0)$	0.030580	0.361962
$Z_{21}'(0)$	0.228901	0.281664
$Z_{22}'(0)$	−0.394513	−0.975558
$Z_{23}'(0)$	0.135033	0.331930

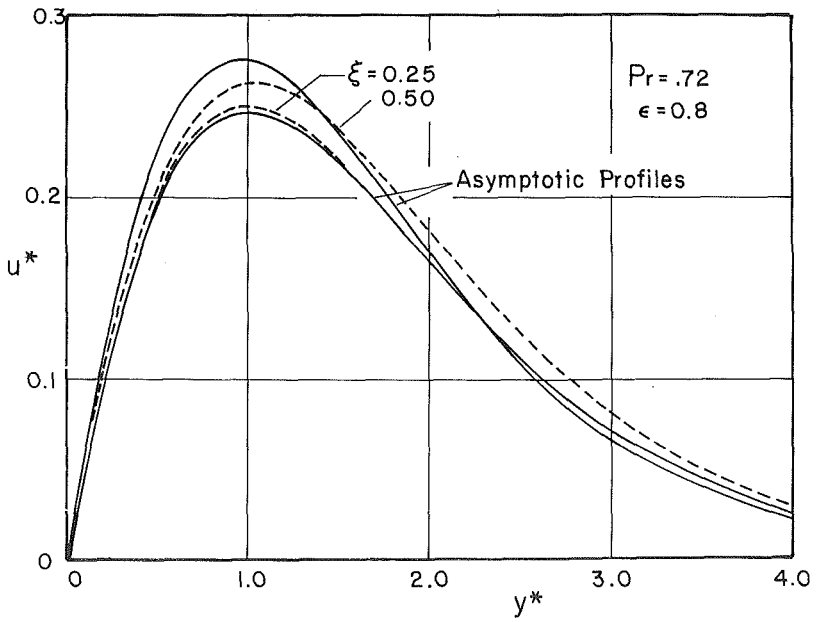

Fig. 2 Velocity profiles: Pr = 0.72; ϵ = 0.8

Table 2

	0.72	10.0
C_{10}	−1.597517	−0.795421
C_{11}	1.597464	0.795422
D_{20}	−3.708835	−1.693134
D_{21}	4.588268	−17.936374
D_{22}	−0.832428	−0.380798

Solution for Large y^*

As y^* becomes large, the asymptotic forms given in (32) can be expected to be valid. Therefore, using the definition of η and rearranging terms, we can rewrite Ψ and θ as:

$$\Psi = \frac{\epsilon^{1/4}}{4}\left\{\left[A_0\left(\frac{y^*}{3}\epsilon^{1/4}\right)^2 + A_1\left(\frac{y^*}{3}\epsilon^{1/4}\right)^3 + A_2\left(\frac{y^*}{3}\epsilon^{1/4}\right)^4 + \ldots\right] + \xi\left[B_0\left(\frac{y^*}{3}\epsilon^{1/4}\right) + B_1\left(\frac{y^*}{3}\epsilon^{1/4}\right)^2 + B_2\left(\frac{y^*}{3}\epsilon^{1/3}\right)^3 + \ldots\right] + \xi^2\left[C_0 + C_1\left(\frac{y^*}{3}\epsilon^{1/4}\right) + C_2\left(\frac{y^*}{3}\epsilon^{1/4}\right)^2 + \ldots\right] + \xi^3\left[D_1 + D_2\left(\frac{y^*}{3}\epsilon^{1/4}\right) + \ldots\right] + \ldots\right\}$$

$$\theta = \epsilon\left\{\left[1 + A_1^*\left(\frac{y^*}{3}\epsilon^{1/4}\right) + \ldots\right] + \xi\left[B_1^* + B_2^*\left(\frac{y^*}{3}\epsilon^{1/4}\right) + B_3^*\left(\frac{y^*}{3}\epsilon^{1/4}\right)^2 + \ldots\right] + \xi^2\left[C_2^* + C_3^*\left(\frac{y^*}{3}\epsilon^{1/4}\right) + \ldots\right] + \xi^3[D_3^* + \ldots] + \ldots\right\} \tag{35}$$

The expansions for Ψ and θ given by (12) and (13) are inner expansions and therefore they are useful only for small values of y^*. For large values of y^*, we must obtain different expansions. Consequently, following Goldstein, examination of equations (35) leads us to assume the following forms for Ψ and θ valid for large y^*:

$$\Psi = \Psi_0(y^*) + \xi\Psi_1(y^*) + \frac{1}{2!}\xi^2\Psi_2(y^*) + \frac{1}{3!}\xi^3\Psi_3(y^*)$$
$$\theta = \theta_0(y^*) + \xi\theta_1(y^*) + \frac{1}{2!}\xi^2\theta_2(y^*) + \frac{1}{3!}\xi^3\theta_3(y^*) \tag{36}$$

Since as $\xi \to 0$ we must obtain the initial profiles, we can say that:

$$\Psi_0(y^*) = \epsilon^{1/4}F(y_1^*) = \epsilon^{1/4}F(\epsilon^{1/4}y^*)$$
$$\theta_0(y^*) = \epsilon H(y_1^*) = \epsilon H(\epsilon^{1/4}y^*)$$

The asymptotic forms (36) can be substituted into the governing equations (10) and (11) and terms in like powers of ξ equated to give the following equations for Ψ_k and θ_k:

$$\Psi_0'\Psi_1' - \Psi_0''\Psi_1 = 0$$
$$\Psi_0'\Psi_2' - \Psi_0''\Psi_2 = \Psi_1\Psi_1'' - \Psi_1'^2$$
$$\Psi_0'\Psi_3' - \Psi_0''\Psi_3 = -3\Psi_1'\Psi_2' + \Psi_1\Psi_2'' + 2\Psi_2\Psi_1'' + \frac{3}{2}\theta_0 + \frac{3}{2}\Psi_0'''$$
$$\Psi_0'\theta_1 - \Psi_1\theta_0' = 0$$
$$\Psi_0'\theta_2 + \Psi_1'\theta_1 - \Psi_1\theta_1' - \Psi_2\theta_0' = 0$$
$$\Psi_0'\theta_3 + 2\Psi_1'\theta_2 + \Psi_2'\theta_1 - \Psi_1\theta_2' - 2\Psi_2\theta_1' - \Psi_3\theta_0' - \frac{3}{2}\frac{1}{\mathrm{Pr}}\theta_0'' = 0 \tag{37}$$

All of the equations for the Ψ_k are first-order linear and may be integrated in closed form. The equations for θ_k are algebraic and may be solved quite easily.

By noting that the coefficients of ξ^k in the first of equations (35) are simply expansions of Ψ_k in powers of y^*, we can obtain the constants of integration for the Ψ_k. We then obtain:

$$\Psi_1 = 0$$
$$\Psi_2 = \frac{3C_1}{2A_0}\epsilon^{1/4}\Psi_0'$$
$$\Psi_3 = \frac{9}{2}\Psi_0 - \frac{3}{2}y^*\Psi_0' + \frac{3D_2}{2A_0}\epsilon^{-1/4}\Psi_0' \tag{38}$$

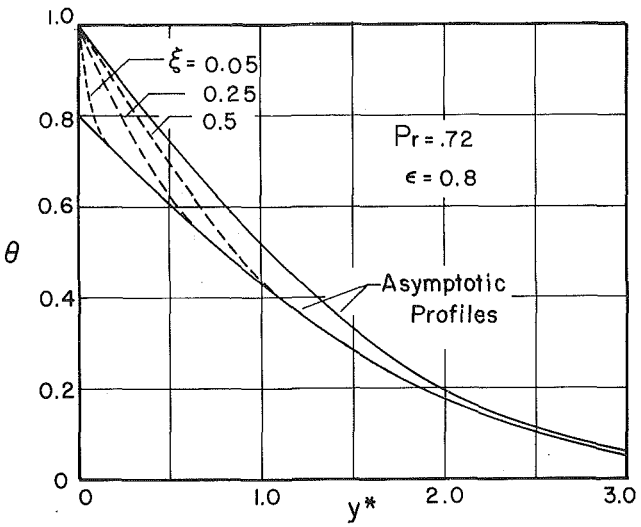

Fig. 3 Temperature profiles: Pr = 0.72; ϵ = 0.8

$$\theta_1 = 0 \tag{38}$$

(*Cont.*)

$$\theta_2 = \frac{3C_1}{2A_0}\,\epsilon^{1/4}\theta_0'$$

$$\theta_3 = \frac{3D_2}{2A_0}\,\epsilon^{-1/4}\theta_0' - \frac{3}{2}\,y^*\theta_0'$$

The expansions for large y^* can now be considered complete.

Having both the inner and outer expansions, the velocity and temperature profiles in the neighborhood above the discontinuity can be written as:

$$u^* = \frac{\epsilon^{1/2}}{12}\,\xi[f_0' + \xi f_1' + \xi^2 f_2' + \ldots]$$
$$\theta = 1 + \epsilon[g_0 + \xi g_1 + \xi^2 g_2 + \ldots] \tag{39}$$

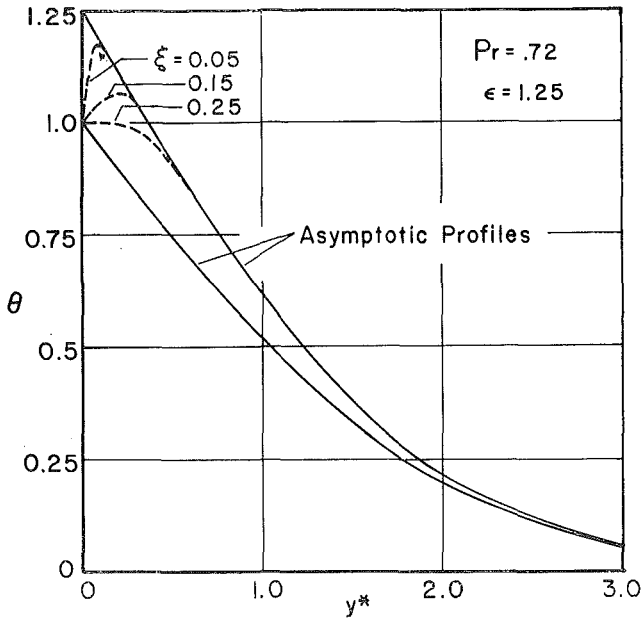

Fig. 5 Temperature profiles: Pr = 0.72; ϵ = 1.25

for small y^* and

$$u^* = \Psi_0' + \frac{1}{2!}\,\xi^2\Psi_2' + \frac{1}{3!}\,\xi^3\Psi_3' + \ldots$$
$$\theta = \theta_0 + \frac{1}{2!}\,\xi^2\theta_2 + \frac{1}{3!}\,\xi^3\theta_3 + \ldots \tag{40}$$

for large y^*. Detailed calculations have been made for a broad range of values of ϵ for both Prandtl numbers of 0.72 and 10.0. Figs. 2–5 show the profiles for representative values of ϵ of 0.8 and 1.25 for Prandtl number of 0.72.

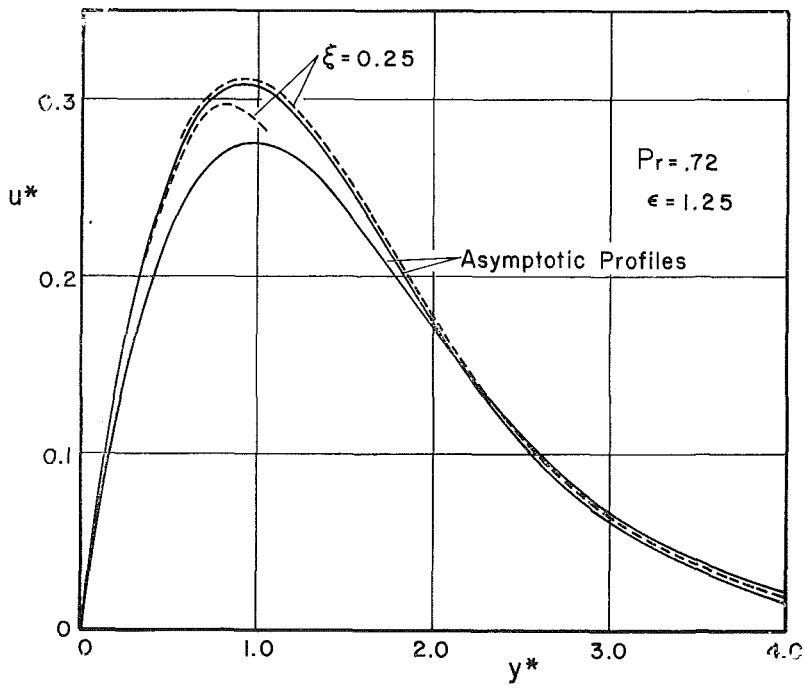

Fig. 4 Velocity profiles: Pr = 0.72; ϵ = 1.25

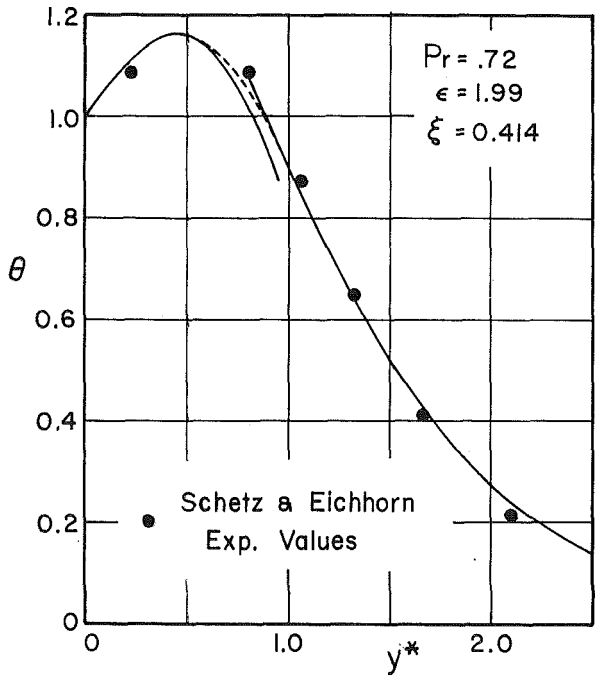

Fig. 6 Comparison of calculated and experimental temperature profiles: Pr = 0.72; $\epsilon = 1.99$

Heat Transfer

From equation (39) for θ the local wall heat flux may be evaluated by using Fourier's heat-conduction law at $y = 0$, thus:

$$\frac{q_{w_2}}{q_{w_1}} = \frac{1}{3H'(0)}\left\{\frac{1}{\xi}\,g_0'(0) + g_1'(0) + \xi g_2'(0)\right\}$$

$$= \frac{1}{3H'(0)}\left\{\frac{1-\frac{1}{\epsilon}}{\xi}\,Z_{00}'(0) + Z_{10}'(0) + \frac{1}{\epsilon}\,Z_{11}'(0) + \frac{1}{\epsilon^2}\,Z_{12}'(0) + \xi\left[Z_{20}'(0) + \frac{1}{\epsilon}\,Z_{21}'(0) + \frac{1}{\epsilon^2}\,Z_{22}'(0) + \frac{1}{\epsilon^3}\,Z_{23}'(0)\right]\right\} \tag{41}$$

where q_{w_1} is the heat flux with the wall maintained at temperature T_{w_1} and

$$q_{w_1} = -\frac{k(\bar{T}_{w_1} - \bar{T}_\infty)}{L}\left(\frac{\mathrm{Gr}_1}{4}\right)^{1/4} H'(0)$$

Since the functions Z_k are universal functions of η, dependent only on Prandtl number, the terms $Z_k'(0)$ in equation (41) are constants for any given Prandtl number (see Table 1). Therefore, for a given Prandtl number and ϵ, equation (41) for the heat-flux ratio is a simple polynomial function of ξ.

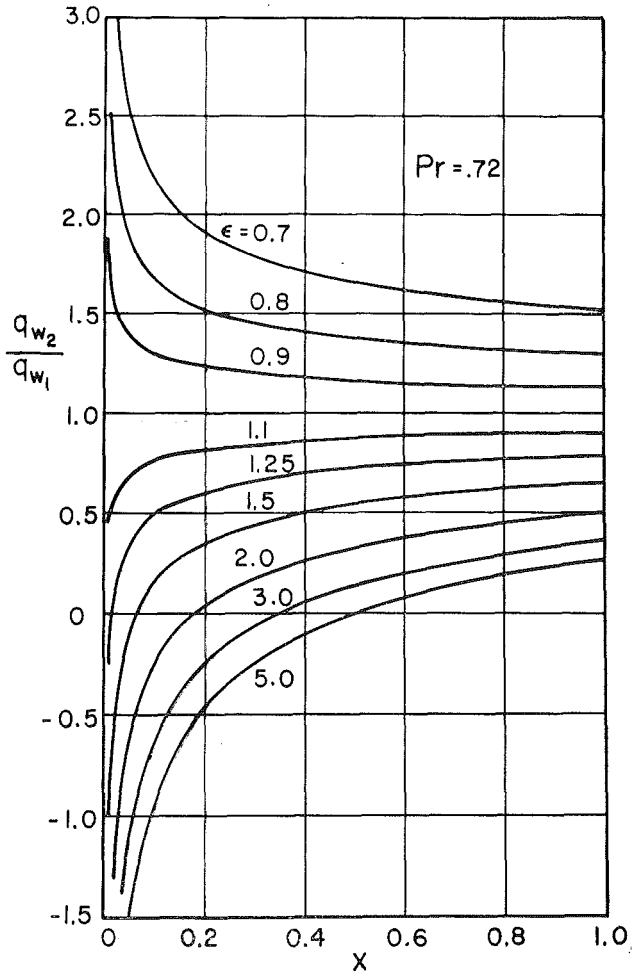

Fig. 7 Wall-heat-flux variation: Pr = 0.72

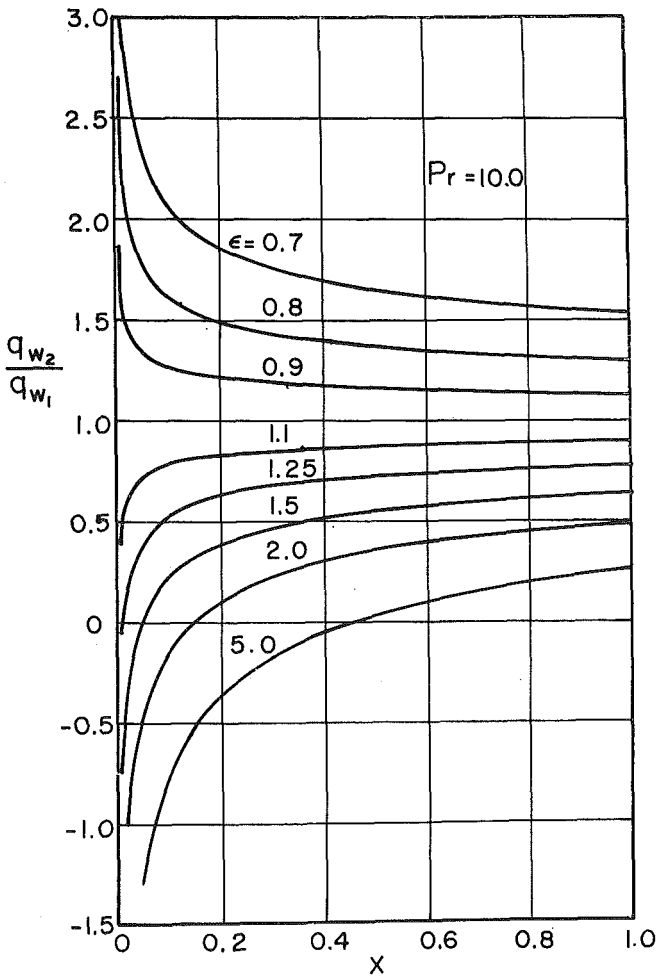

Fig. 8 Wall-heat-flux variation: Pr = 10.0

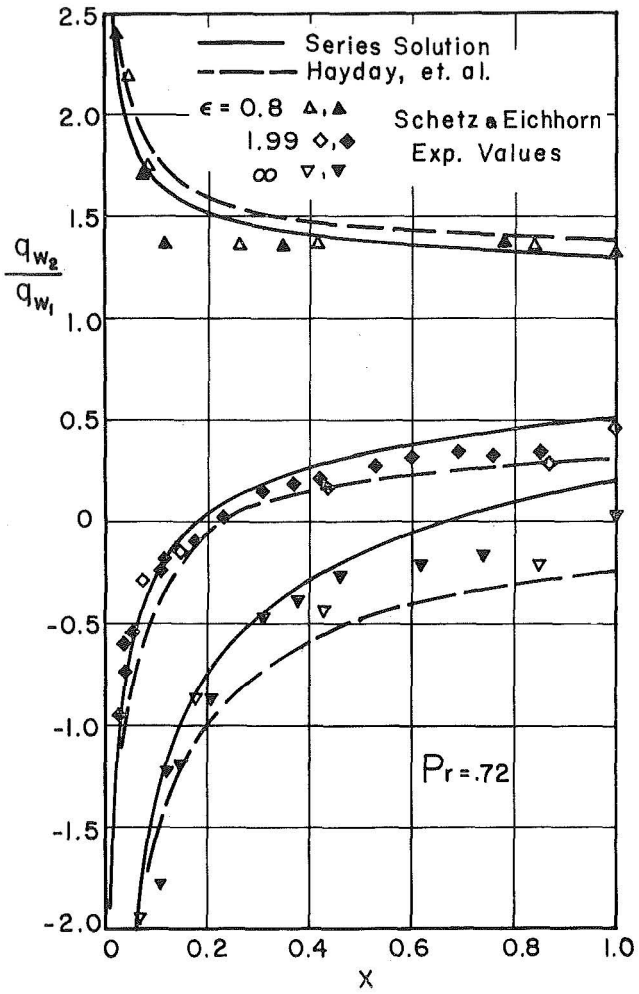

Fig. 9 Comparison of calculated wall-heat-flux variation with experimental and numerical results

Results and Discussion

Velocity and temperature profiles for Prandtl number 0.72 and for ϵ values of 0.8 and 1.25 are shown in Figs. 2–5. Each of these figures includes the asymptotic similar profiles which prevail immediately below the discontinuity and at large distances above the discontinuity. The velocity profiles show a tendency to be too high. This is especially true for the case of $\epsilon = 1.25$. Fig. 4 shows the tendency of the inner expansion to underestimate the velocity maximum while the outer expansion overestimates. It is felt that the validity of the expansion for the velocity profiles for $\epsilon = 0.8$ and both Prandtl numbers is restricted to values of ξ less than about 0.25 while for $\epsilon = 1.25$ the validity seems to be restricted to ξ less than 0.1.

The temperature profiles all show the severe gradients characteristic of this type of discontinuity. Fig. 5 for $\epsilon = 1.25$ shows the reversal in temperature gradient which would be expected from lowering the temperature of the upper portion of the plate below that of the lower portion. This indicates the fact that the fluid in a small region above the temperature discontinuity must transfer heat to the plate in order to adjust to the discontinuity.

Fig. 6 is a comparison of the temperature profile obtained by the present asymptotic expansions with the experimental work of Schetz and Eichhorn [1]. The agreement with the experiment is quite good. The dotted line is a faired curve joining the inner and outer expansions. It should be noted that the relatively large values of $\epsilon = 1.99$ and $\xi = 0.414$ are a severe test of the convergence of the asymptotic expansions. The comparison with the experiment indicates that the temperature profiles are valid over a much larger range of ϵ than are the velocity profiles. This seems reasonable in view of the fact that the discontinuity is a disturbance in temperature and therefore the temperature profile is directly affected while the velocity profile is affected indirectly through the temperature profile.

Figs. 7 and 8 give the heat-transfer results in the form of q_{w_2}/q_{w_1}, as a function of x, for both Prandtl numbers. Here q_{w_2} is the local heat-transfer rate and q_{w_1} is the local heat-transfer rate that would obtain if the plate were maintained at T_{w_1}. Both sets of curves are for a broad range of values of ϵ. The effect of Prandtl number is clearly seen by comparing Figs. 7 and 8. From these figures it can be seen that the region of reversed heat flux is smaller for Prandtl number 10.0 than for Prandtl number 0.72. This indicates that the higher-Prandtl-number fluid responds to the temperature change in a shorter distance. This appears reasonable in view of the thinner thermal boundary layer in the higher-Prandtl-number fluid. Fig. 9 is a comparison of the present heat-transfer results with the experimental results of Schetz and Eichhorn [1] and with the numerical work of Hayday et al. [2]. The agreement is, in general, quite good. It should be noted again that for a given Prandtl number and ϵ the heat-transfer rate as a function of x is in the form of a very simple polynomial, the coefficients of which are obtained from the universal functions. With the universal functions obtained in the present work and the wall values provided in Table 1, the heat-transfer results for Prandtl numbers of 0.72 or 10.0 can be obtained very easily for any value of ϵ and ξ.

Acknowledgment

The author wishes to thank Dr. K. T. Yang for his thoughtful discussions.

References

1 Schetz, J. A., and Eichhorn, R., "Natural Convection with Discontinuous Wall-Temperature Variations," *Journal of Fluid Mechanics*, Vol. 18, Part 2, 1964, pp. 167–176.

2 Hayday, A. A., Bowlus, D. A., and McGraw, R. A., "Free Convection From a Vertical Flat Plate With Step Discontinuities in Surface Temperature," JOURNAL OF HEAT TRANSFER, TRANS. ASME, Series C, Vol. 89, No. 3, Aug. 1967, pp. 244–250.

3 Goldstein, S., "Concerning Some Solutions of the Boundary Layer Equations in Hydrodynamics," *Proceedings of the Cambridge Philosophical Society*, Vol. 26, 1929–1930, pp. 1–30.

4 Yang, K. T., "Laminar Free-Convection Wake Above a Heated Vertical Plate," *Journal of Applied Mechanics*, Vol. 31, TRANS. ASME, Series E, Vol. 86, No. 1, Mar. 1964, pp. 131–138.

5 Abromowitz, M., and Stegun, I., *Handbook of Mathematical Functions*, Dover Publications, New York, 1965.

6 Nachtsheim, P. R., and Swigert, P., "Satisfaction of Asymptotic Boundary Conditions in the Numerical Solution of Systems of Nonlinear Equations of Boundary Layer Type," NASA-TN-D-3004, 1965.

L. A. HALE
Assistant Professor.
Assoc. Mem. ASME

S. A. ANDERSON
Instructor.
Assoc. Mem. ASME

Department of Mechanical Engineering,
Texas A & M University,
College Station, Texas

Surface Temperatures and Heat Fluxes Associated With the Evaporation of a Liquid Film on a Semi-Infinite Solid

The boundary-value problem associated with the evaporation of a thin liquid film from a thick surface is presented in terms of several dimensionless parameters. A numerical solution is presented for a particular limiting case and the result is used to suggest criteria for determining the significance of thin-film evaporation in saturated pool boiling.

Introduction

After many years of investigation, two basic models of the surface-to-liquid heat-transfer mechanism in nucleate pool boiling have evolved. In the older model the development, growth, and departure of a bubble from the solid-liquid interface disturbs the thermal boundary layer and the resulting intimate contact between the cold liquid and the hot surface produces large heat-transfer coefficients. The bubble growth is thought to occur primarily by evaporation from the surrounding mass of superheated liquid in the boundary layer. The primary heat flow is from solid surface to cool liquid to vapor bubble in a repeated cycle as bubbles are generated on the surface. The total heat-transfer rate in this model is governed by the solid-to-liquid transfer and the liquid-to-vapor transfer. The bubble growth rate controls the frequency of bubble formation and therefore limits the overall process. A discussion of a model of this type is given by Mikic and Rohsenow [1].[1]

The second model, the evaporating-film model, attributes a significant portion of the total heat transfer during each bubble cycle to the rapid evaporation of a thin liquid film formed between the vapor bubble and the solid surface as the bubble grows. The heat-flow path is from solid surface through the evaporating film to the vapor bubble. Evidence of the formation of such a film has been presented by several investigators, including Sharp [2], Cooper [3], Cooper and Lloyd [4, 5], and Jawurek [6], but the significance of such a process in the determination of the overall heat flux has not been established. In either model bubble growth is a significant process since it controls the number of heat-transfer cycles per unit time and thereby controls the overall

Contributed by the Heat Transfer Division for publication (without presentation) in the Journal of Heat Transfer. Manuscript received by the Heat Transfer Division October 13, 1969; revised manuscript received August 17, 1970. Paper No. 71-HT-C.

[1] Numbers in brackets designate References at end of paper.

Nomenclature

c = specific heat (Btu/lb$_m$ deg R)
H = heat-transfer coefficient (Btu/hr ft^2 deg R)
h_{fg} = latent heat (Btu/lb$_m$)
k = thermal conductivity (Btu/hr ft deg R)
Q = heat flux (Btu/hr ft^2)
R = specific gas constant (ft^2/hr^2 deg R)
T = temperature (deg R)
t = time (hr)
x = coordinate (ft)
α = thermal diffusivity (ft^2/hr)
ϵ = a constant
δ = liquid-film thickness (ft), equations (6), (7)
ρ = density (lb$_m$/ft^3)

Subscripts

AV = average
s = solid
L = liquid
P = peak or maximum
v = vapor
0 = at time zero
T = total elapsed time
M = time for complete evaporation

Dimensionless Groups

B = parameter $[(\rho_v\delta_0/4\alpha_s\rho_L)\sqrt{8R(T_0 - T_v)/\pi}]$
C = thermal-capacity ratio $[\rho_s c_s(T_0 - T_v)/\rho_L h_{fg}]$
K = thermal-conductivity ratio (k_L/k_s)
X = dimensionless space coordinate (x/δ_0)
θ = dimensionless time $(\alpha_s t/\delta_0^2)$
δ = dimensionless film thickness (δ/δ_0), except equations (6), (7)
ϕ = dimensionless temperature difference $[(T - T_v)/(T_0 - T_v)]$
ψ = parameter $[T_v/(T_0 - T_v)]$

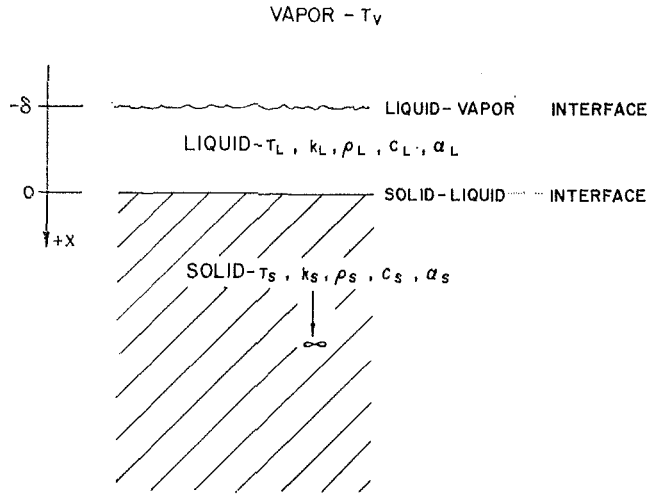

Fig. 1 Microlayer evaporation model

heat flux. If the first model is correct, the heat transferred per cycle is governed by the transient conduction process which is initiated when the cooler fluid comes into contact with the surface as each bubble departs from the surface. If the second model is correct, the heat transferred per cycle is governed by the evaporation of a thin liquid film formed beneath the bubble as it grows. In view of the successful correlations based on the first model and the experimental evidence supporting the thin-film model, it is natural to question the significance of thin-film evaporation even if it does, in fact, occur.

Model of Thin-Film Evaporation

With reference to Fig. 1, the evaporation of a one-dimensional superheated film of liquid from a thick solid surface into a saturated-vapor region can be formulated as

$$\frac{\partial^2 T_s(x,t)}{\partial x^2} = \frac{1}{\alpha_s}\frac{\partial T_s(x,t)}{\partial t}, \tag{1}$$

$$\frac{\partial^2 T_L(x,t)}{\partial x^2} = \frac{1}{\alpha_L}\frac{\partial T_L(x,t)}{\partial t}, \tag{2}$$

$$T_L(0,t) = T_s(0,t), \tag{3}$$

$$k_L\frac{\partial T_L(0,t)}{\partial x} = k_s\frac{\partial T_s(0,t)}{\partial x}, \tag{4}$$

$$\lim_{x\to\infty} T_s(x,t) = T_s(x,0), \tag{5}$$

$$k_L\frac{\partial T'_L(-\delta,t)}{\partial x} = H(T_L(-\delta,t) - T'_v) + \rho_L h_{fg}\frac{\partial \delta}{\partial t}, \tag{6}$$

$$\frac{\partial \delta(t)}{\partial t} = \frac{\rho_v}{4\rho_L}\sqrt{\frac{8R}{\pi}}\left(\sqrt{T_L(-\delta,t)} - \sqrt{T'_v}\right), \tag{7}$$

$$T_s(x,0) = T_{s0}(x), \tag{8}$$

$$T_L(x,0) = T_{L0}(x). \tag{9}$$

If the thermal capacity of the liquid film is neglected, if the initial temperature distribution in the solid and liquid is assumed to be constant, and if the first term on the right in equation (6) is assumed to be small, the problem can be reformulated in dimensionless form as

$$\frac{\partial^2 \phi_s(X,\theta)}{\partial X^2} = \frac{\partial \phi_s(X,\theta)}{\partial \theta}, \tag{10}$$

$$\lim_{X\to\infty} \phi_s(X,\theta) = 1, \tag{11}$$

$$\phi_s(X,0) = 1, \tag{12}$$

$$\frac{\partial \phi_s(0,\theta)}{\partial X} = K\frac{\phi_s(0,\theta) - \phi_L(-\delta,\theta)}{\delta(\theta)}, \tag{13}$$

$$\frac{\partial \phi_s(0,\theta)}{\partial X} = \frac{1}{C}\frac{\partial \delta(\theta)}{\partial \theta}, \tag{14}$$

$$\frac{\partial \delta(\theta)}{\partial \theta} = B\left(\sqrt{\phi_L(-\delta,\theta) + \psi} - \sqrt{\psi}\right). \tag{15}$$

Two special cases of this problem have been presented in the literature. Dzakowic and Frost [7] presented a solution in which the temperature at the interface between the liquid and vapor was assumed to be equal to the temperature at the interface between the solid and liquid, i.e., they neglected the thermal resistance of the liquid film. This corresponds to the formulation given above if $B \to 0$ or $\psi \to \infty$.

The other special case assumes the interface temperature between the liquid and vapor is equal to the vapor temperature, i.e., the temperature drop at the liquid–vapor interface is neglected. This corresponds to the formulation above if $B \to \infty$

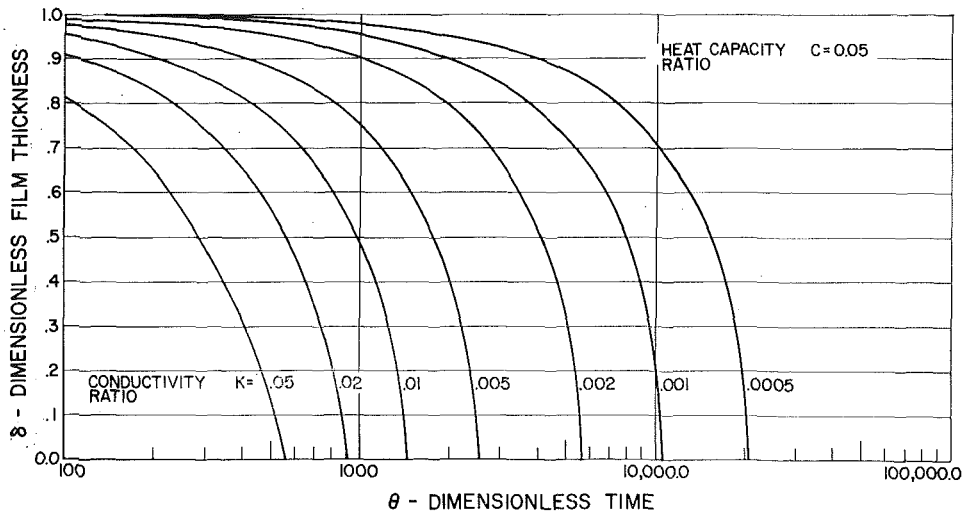

Fig. 2 Dimensionless film thickness vs. dimensionless time, C = 0.05

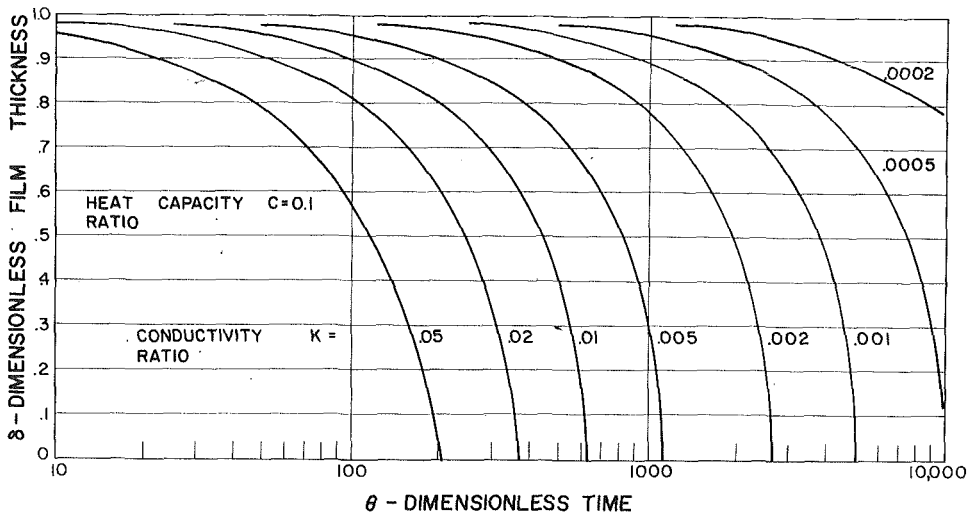

Fig. 3 Dimensionless film thickness vs. dimensionless time, $C = 0.1$

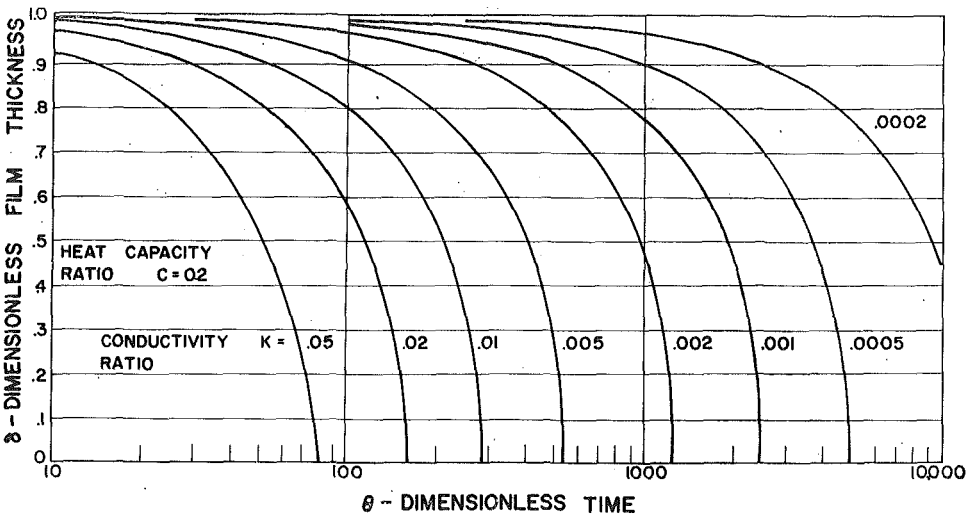

Fig. 4 Dimensionless film thickness vs. dimensionless time, $C = 0.2$

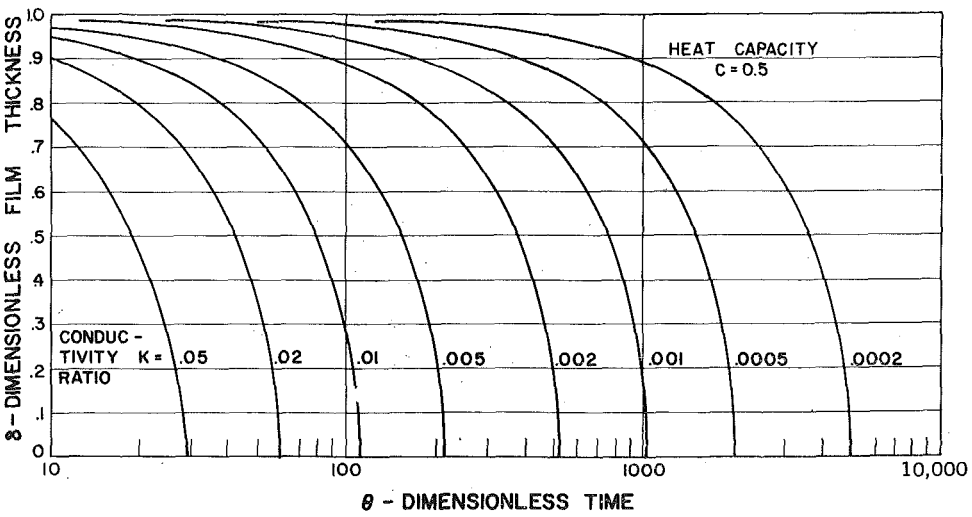

Fig. 5 Dimensionless film thickness vs. dimensionless time, $C = 0.5$

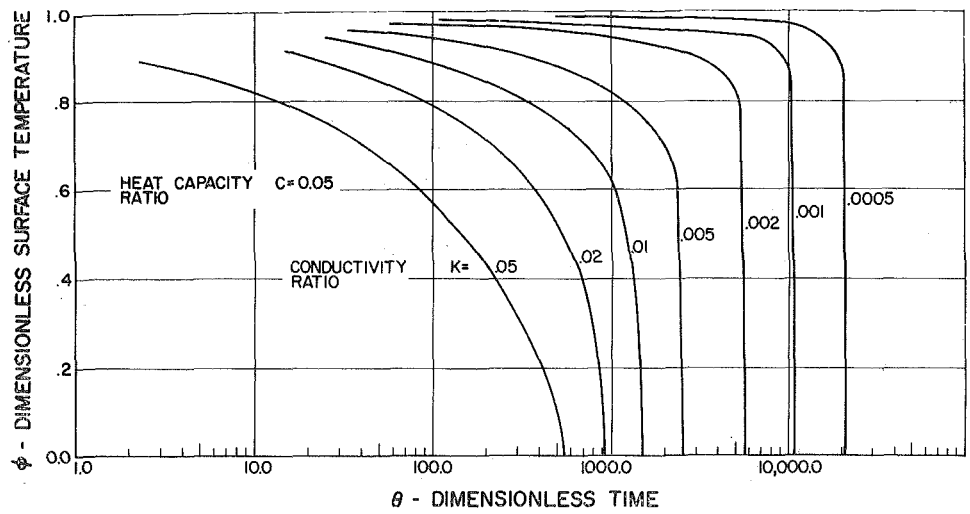

Fig. 6 Dimensionless surface temperature vs. dimensionless time, $C = 0.05$

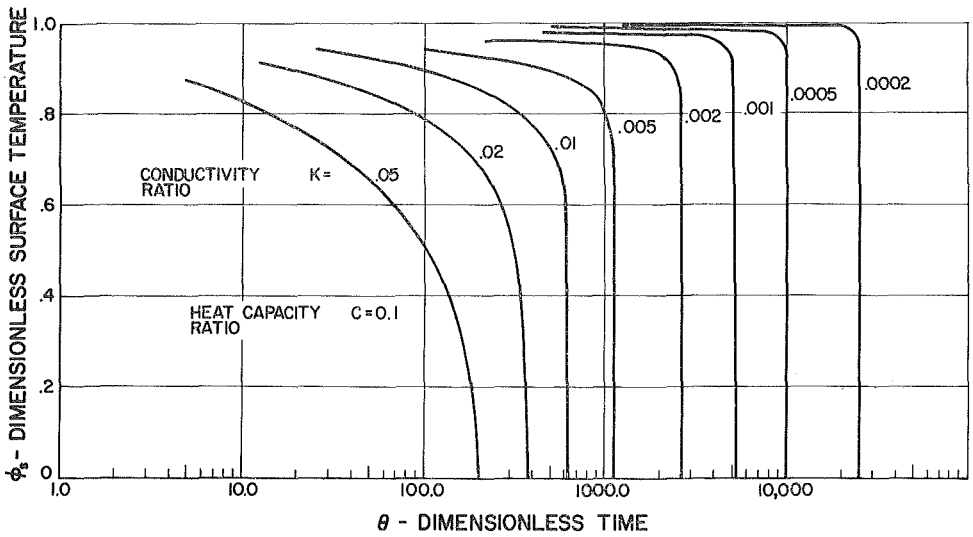

Fig. 7 Dimensionless surface temperature vs. dimensionless time, $C = 0.1$

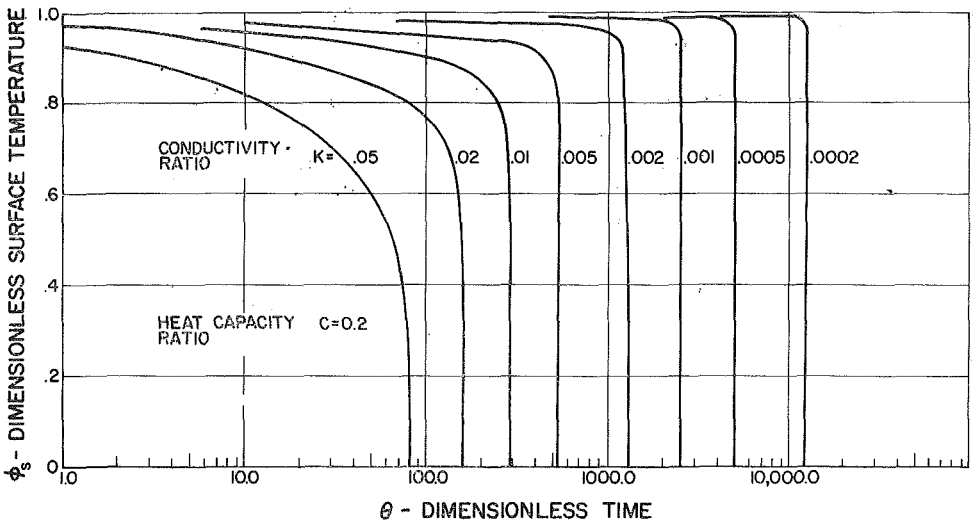

Fig. 8 Dimensionless surface temperature vs. dimensionless time, $C = 0.2$

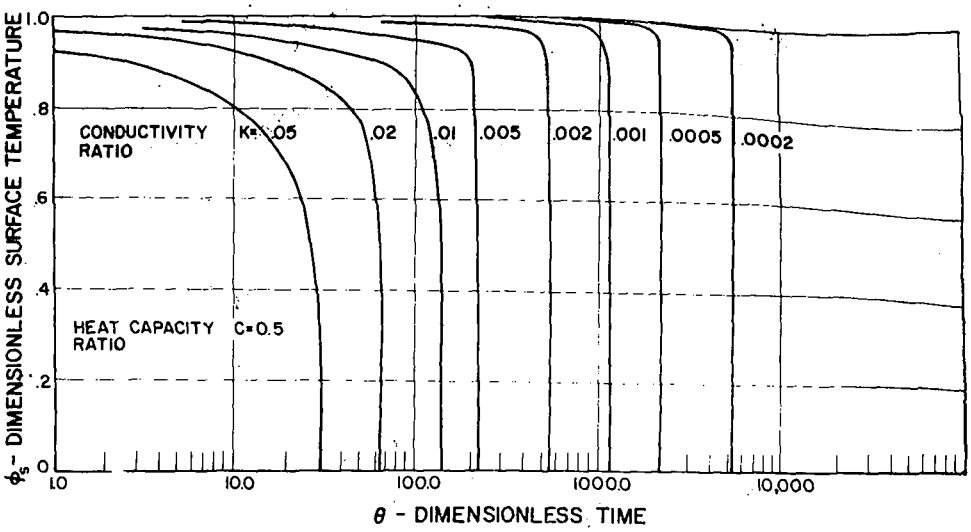

Fig. 9 Dimensionless surface temperature vs. dimensionless time, $C = 0.5$

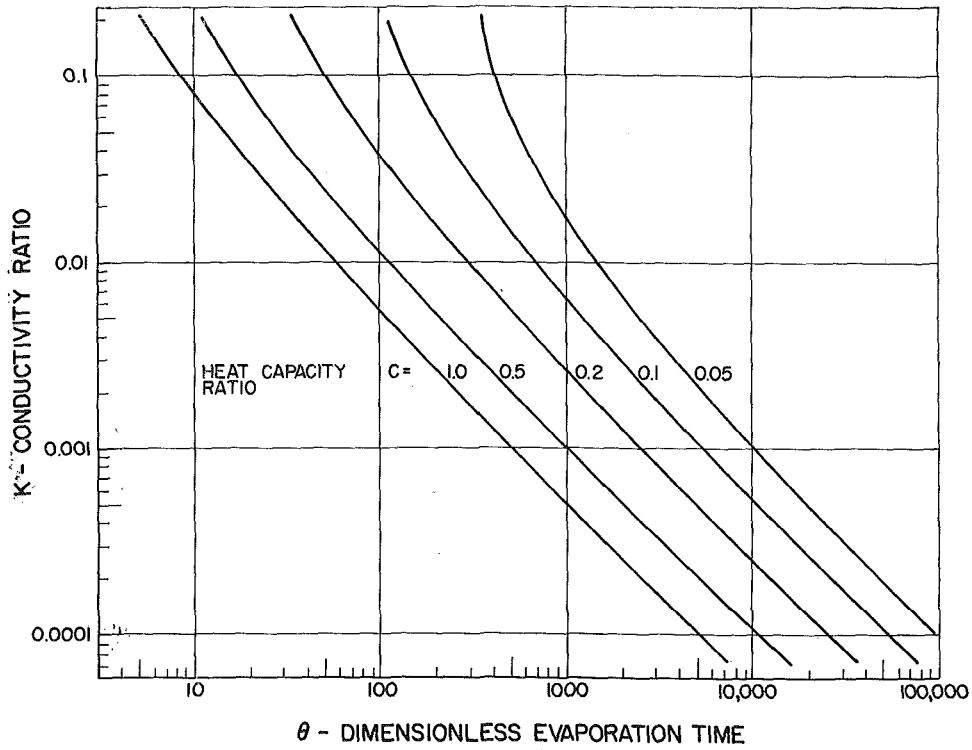

Fig. 10 Conductivity ratio vs. dimensionless total evaporation time

and $\psi \to 0$. The latter approximation was used by Cooper and Lloyd to determine the initial film thickness from measurements of the surface-temperature fluctuations. Either approximation may introduce significant error into the complete solution since each one underestimates the total thermal resistance between the solid surface and the vapor. In general, the first approximation will introduce significant errors for thick films and the second will be in error for thin films.

A complete parametric study of the problem as defined by equations (10)–(15) is not feasible because of the large number of variables involved. A solution for the surface temperature as a function of time would involve ϕ_s, θ, K, C, B, and ψ. If the second approximation is adopted the solutions will involve only ϕ_s, θ, K, and C and the influence of K and C on the evaporation process can be determined. The resulting equations,

$$\frac{\partial^2 \phi_s(X, \theta)}{\partial X^2} = \frac{\partial \phi_s(X, \theta)}{\partial \theta}, \tag{16}$$

$$\lim_{X \to \infty} \phi_s(X, \theta) = 1, \tag{17}$$

$$\phi_s(X, 0) = 1, \tag{18}$$

$$\frac{\partial \phi_s(0, \theta)}{\partial X} = K \frac{\phi_s(0, \theta)}{\delta(\theta)}, \tag{19}$$

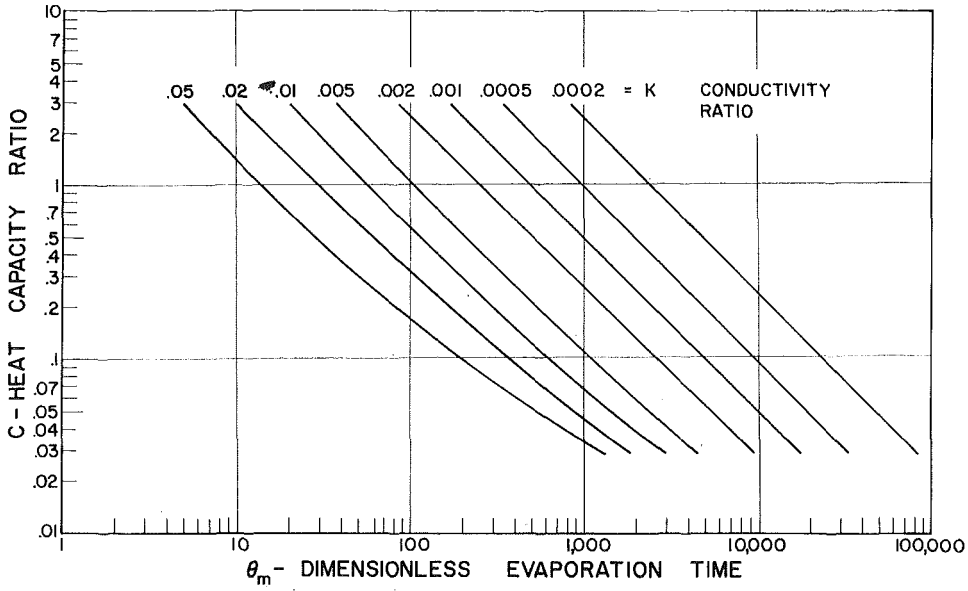

Fig. 11 Heat-capacity ratio vs. dimensionless total evaporation time

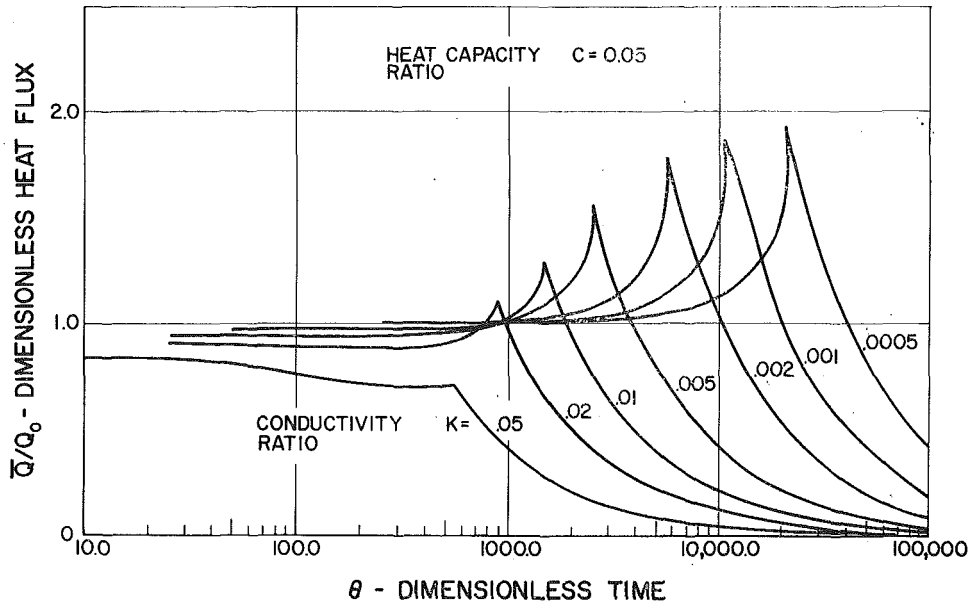

Fig. 12 Dimensionless heat flux vs. dimensionless time, $C = 0.05$

$$\frac{\partial \phi_s(0, \theta)}{\partial X} = \frac{1}{C} \frac{\partial \delta(\theta)}{\partial \theta}, \tag{20}$$

have been solved by a simple explicit numerical technique for values of $0.05 \leq K \leq 0.0002$ and $0.05 \leq C \leq 0.5$. The results are shown in Figs. 2–9 with ϕ_s and δ shown as functions of θ. In the numerical solution the boundary condition specified by equation (17) was replaced by

$$\frac{\partial \phi_s(X', \theta)}{\partial X} = 0, \tag{21}$$

where

$$X' = 10 \quad \text{if} \quad 2/C < 10,$$

or

$$X' = 2/C \quad \text{if} \quad 2/C > 10.$$

Figs. 10 and 11 show the time required for complete evaporation, θ_M, as a function of K and C.

In determining the significance of the evaporation process to boiling, the quantity of interest is the average heat flux during the complete evaporation cycle. This quantity, $\bar{Q}$, can be determined from the amount of liquid evaporated from the film. A simple dimensionless heat-flux ratio can be formed as

$$\frac{\bar{Q}}{Q_0} = \frac{(1 - \delta)}{\theta_T \cdot K \cdot C} \quad \text{if} \quad \theta_T < \theta_M, \tag{22a}$$

$$\frac{\bar{Q}}{Q_0} = \frac{1}{\theta_T \cdot K \cdot C} \quad \text{if} \quad \theta_T \geq \theta_M, \tag{22b}$$

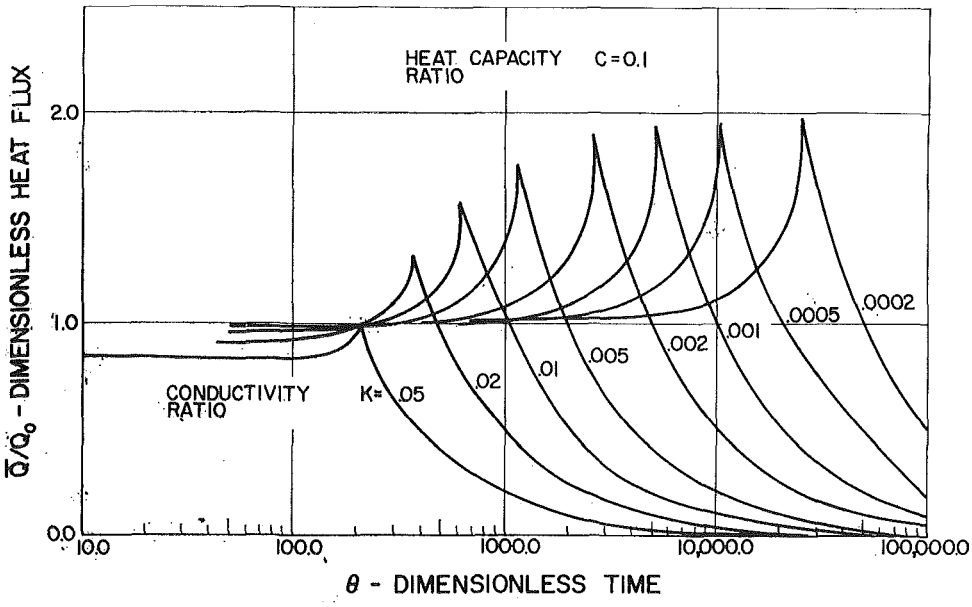

Fig. 13 Dimensionless heat flux vs. dimensionless time, $C = 0.1$

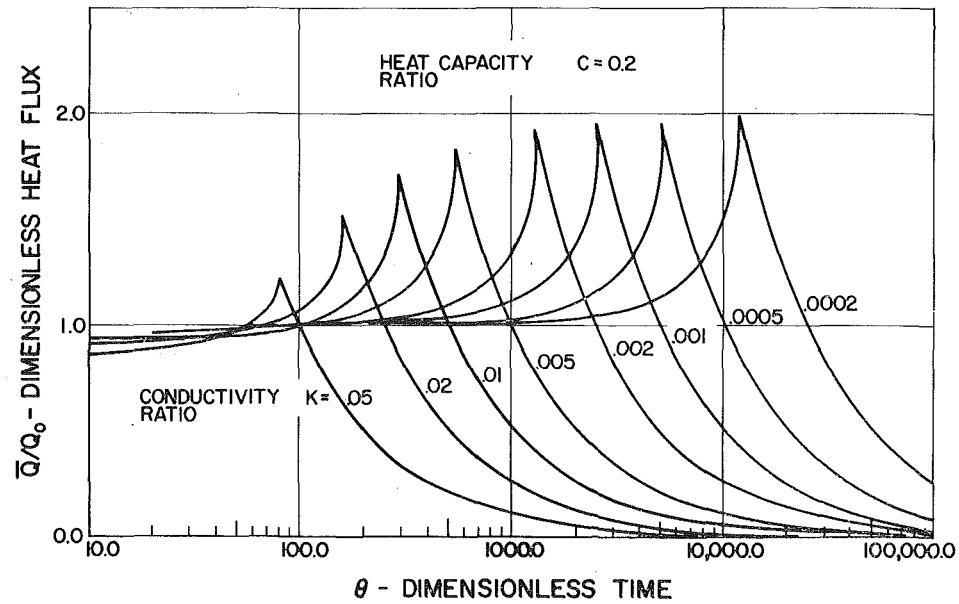

Fig. 14 Dimensionless heat flux vs. dimensionless time, $C = 0.2$

where

$$Q_0 \equiv \frac{k_L(T_s(0, 0) - T_v)}{\delta_0}. \tag{22c}$$

The dimensionless average heat flux, $(\bar{Q}/Q_0)$ is shown as a function of θ_T, K, and C in Figs. 12–15.

Discussion of Results

For a limited range of values of C and K the time required for total evaporation of the film can be determined by

$$\theta_M = \frac{0.5}{K \cdot C}; \quad 0.0001 < K < 0.01; \quad 0.05 < C < 3. \tag{23}$$

Examination of Figs. 6–9 shows that the surface-temperature drop associated with the evaporation of a particular film may be expected to increase with increasing values of K and with decreasing values of C. The relation between expected surface-temperature drop, C, and K cannot be obtained directly from the numerical results because the formulation of the problem requires that $\phi_s \to 0$ as $\theta \to \theta_M$. This is obviously not true in a real situation.

Application to Saturated Pool Boiling

If thin-film evaporation is to be considered the dominant process in nucleate boiling the initial film thickness must be such that the average heat flux during a complete bubble growth cycle is equal to or greater than the peak heat flux. Thus, for film evaporation to be the dominant heat-transfer mechanism,

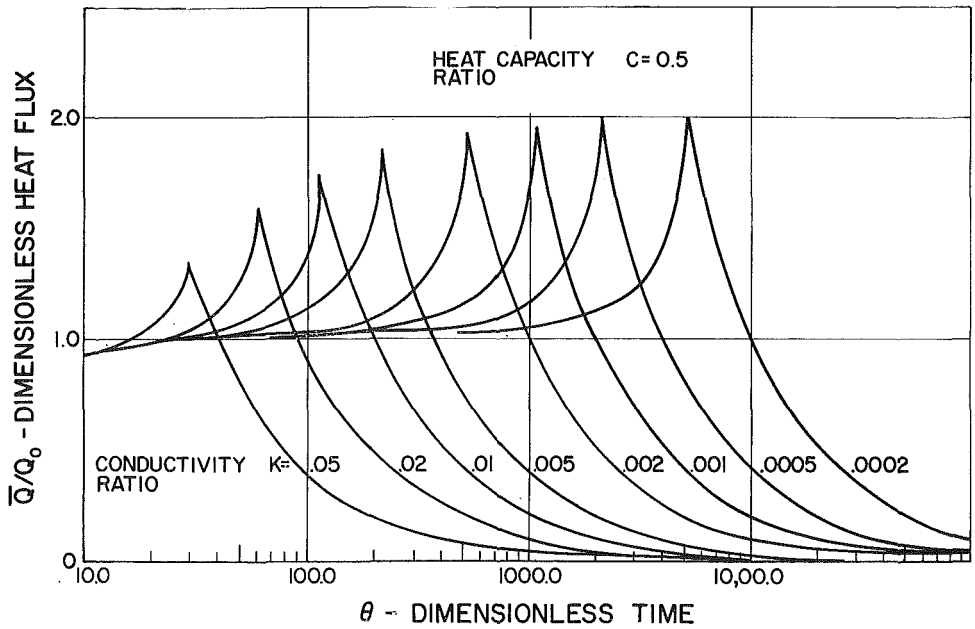

Fig. 15 Dimensionless heat flux vs. dimensionless time, $C = 0.5$

$$\frac{\bar{Q}}{Q_0} \geq \frac{Q_P}{Q_0}, \tag{24}$$

where $\bar{Q}/Q_0$ is based on the temperature difference, initial film thickness, and bubble period near the peak heat flux. This criterion is arbitrary but seems reasonable in view of the limited experimental data available at the present time.

The application of equation (24) to a particular saturated-pool-boiling situation requires a simultaneous independent measurement of film thickness, bubble period, and surface temperature near the peak heat flux. Unfortunately, this type of data is not readily available in the literature.

A test for significance might be somewhat less rigid. For example,

$$\frac{\bar{Q}}{Q_0} \geq \epsilon \frac{Q_{AV}}{Q_0} \tag{25}$$

might be used as a criterion of significance with $1 \geq \epsilon > 0$ and with $\bar{Q}/Q_0$ to be evaluated at any point of interest on the boiling curve. The value chosen for ϵ is arbitrary and would depend on the experimental procedure employed in the determination of the film thickness and bubble period. Considering the great variability of data and correlations for bubble periods and the other boiling parameters, it seems that any determinations of significance must be based on complete data from a single system.

Conclusions

1 The dimensionless time (θ_M) required for the complete evaporation of a thin liquid film decreases with increasing values of the conductivity ratio K and the thermal capacity ratio C.

2 The surface-temperature drop associated with the evaporation of a thin liquid film increases with increasing K and with decreasing value of C.

3 Additional data relating film thickness, bubble growth period, and other system parameters are required to determine the general significance of the thin-film evaporation process in pool boiling.

References

1 Mikic, B. B. and Rohsenow, W. M., "A New Correlation of Pool-Boiling Data Including the Effect of Heating Surface Characteristics," JOURNAL OF HEAT TRANSFER, TRANS. ASME, Series C, Vol. 91, No. 2, May 1969, pp. 245–250.

2 Sharp, R. R., "The Nature of Liquid Film Evaporation During Nucleate Boiling," NASA TND-1997, 1964.

3 Cooper, M. G., "The Microlayer and Bubble Growth in Nucleate Pool Boiling," *International Journal of Heat and Mass Transfer*, Vol. 12, 1969.

4 Cooper, M. G. and Lloyd, A. B., "Transient Local Heat Flux in Nucleate Boiling," *Proceedings of the Third International Heat Transfer Conference*, Chicago, Aug. 1966.

5 Cooper, M. G. and Lloyd, A. J. P., "The Microlayer in Nucleate Pool Boiling," *International Journal of Heat and Mass Transfer*, Vol. 12, 1969.

6 Jawurek, H. H., "Simultaneous Determination of Microlayer Geometry and Bubble Growth in Nucleate Boiling," *International Journal of Heat and Mass Transfer*, Vol. 12, 1969.

7 Dzakowic, G. S. and Frost, W., "An Analytical Solution for the Transient Temperature of a Heated Surface During Microlayer Evaporation," ASME Paper No. 67-WA/HT-21.

J. W. RAMSEY[1]
Assoc. Mem. ASME

R. J. GOLDSTEIN
Professor.
Mem. ASME

Department of Mechanical Engineering,
University of Minnesota,
Minneapolis, Minn.

Interaction of a Heated Jet With a Deflecting Stream

An experimental investigation of the interaction of a heated jet with a deflecting flow has been performed in a wind tunnel. The secondary (jet) flow is introduced at angles of 90 and 35 deg to the mainstream flow direction. Visualization studies using tufts of yarn and a carbon dioxide–water fog are reported. Temperature profiles in the interaction region are presented for blowing rates (ratio of mass flux of injected gas to mass flux of free stream) from 0.1 to 2.0 for normal injection and at blowing rates of 1.0 and 2.0 for 35 deg injection. Velocity and turbulence-intensity profiles are reported for normal injection at blowing rates of 1.0 and 2.0.

Introduction

THE INTERACTION of a subsonic circular jet with a subsonic deflecting stream has recently been the subject of renewed interest. This type of flow configuration exhibits many features such as production of large-scale eddies and high levels of turbulence including flow reversal which are of interest in basic fluid dynamics. In addition, there are a number of applications of this type of flow, such as film cooling, mixing of two fluid streams, and impingement cooling. It is of interest to note that these different applications have different desideratums in terms of the path of the jet. Thus, in film cooling it is of interest that the jet remains as close as possible to the wall from which it issues. In mixing of two streams it is usually desirable that the jet mixes fully and uniformly with the main flow. With impingement cooling the jet should penetrate across the flow and spread itself out on the surface opposite that from which it is injected.

The present paper reports on the experimental results of an investigation which is concerned with film cooling utilizing injection of air through circular holes into an air mainstream. The overall aim is to obtain a better understanding of film cooling.

In order to accomplish this it is necessary to study the more fundamental process by which fluid jets interact with mainstreams in the neighborhood of solid surfaces. With further understanding of the basic processes the ability to predict film cooling as well as the other applications mentioned above should be greatly enhanced.

The study reported herein concerns primarily the interaction of a jet with the flow stream. Results are reported of flow-visualization studies, temperature measurements in the flow field for heated injection, and velocity measurements in the flow field for an unheated jet. A turbulent boundary layer exists on the wall through which the jet exits, and this wall is designed to be adiabatic. Temperature profiles are reported for blowing-rate parameters from 0.1 to 2.0 for normal injection, and blowing rate parameters of 1.0 and 2.0 for 35 deg injection. Velocity and turbulence-intensity profiles are obtained at blowing-rate parameters of 1.0 and 2.0 for injection of an unheated jet perpendicular to the mainstream.

Review of Previous Studies

The flow field following injection from a single hole into a mainstream has received considerable attention. Lee [1][2] presents a brief review of the literature. A qualitative description of the interactions which occur and the shape of the flow field is presented by Keffer and Baines [2] and Abramovich [3]. A flow diagram for a secondary flow entering through a circular tube normal to the free stream is presented in Fig. 1, based on the discussions in [2] and [3] and on flow-visualization results of the present study. As the jet of fluid leaves the surface it retards the main flow along the upstream side of the jet causing an increased pressure. At the downstream side of the jet a rarefaction occurs. This pressure difference provides the force necessary to deform the jet. Jordinson [4] has compared this flow to that around a porous cylinder with suction. The jet takes on a "horseshoe" or "kidney" shape. Abramovich [3] explains this deformation of the jet's cross section by the character of its interaction with the deflecting flow. Because of the intensive intermixing of the jet with the deflecting flow, a turbulent layer quickly develops around the periphery of the jet. The slower peripheral particles of the jet are more forcefully bent away from the initial direction than the higher-velocity particles of the core and are moved along more-curved trajectories by the deflecting flow leading to the horseshoe shape. The deflecting flow and circulatory zones cause the particles of the jet to branch out more and more from

[1] Presently with Honeywell Inc., St. Paul, Minn.

Contributed by the Heat Transfer Division and presented at the ASME-AIChE Heat Transfer Conference, Tulsa, Okla., August 15–18, 1971. Manuscript received by the Heat Transfer Division January 11, 1971. Paper No. 71-HT-2.

[2] Numbers in brackets designate References at end of paper.

the plane of symmetry. Consequently, the legs of the "horseshoe" move apart. This gives rise to additional circulatory or vortex motion in the jet. The action of the vortices augments the entrainment of fluid, causing internal circulation and large-scale mixing within the jet.

The deformation and turning of the jet is strongly affected by the mass-velocity ratio or blowing rate, M. In general, the larger the blowing rate the farther the injected fluid penetrates into the main flow. With normal injection at blowing rates up to approximately 4 the potential core of the jet (the region where the velocity is equal to the initial jet velocity) is deflected by the pressure field [2]. At still larger blowing rates the potential core is conical with the apex almost directly above the center of the jet orifice.

Experimental studies to determine the flow conditions with isothermal mixing of a jet and mainstream of the same fluid are described by a number of investigators [1–5]. In these investigations the fluid jet is injected normal to the mainstream and at blowing rates greater than or equal to two. Gordier [5] used water while in the other investigations air was used. The general shape of the deflected jet axis is essentially the same in the various investigations [6]. The measured height of the jet axis using air as the working fluid agrees with an empirical equation within approximately 10 percent in air tests [2, 4], while the jet is about 20 percent higher in a study in which water was used [5]. The greater penetration in the water experiments may be due to the relatively thick mainstream boundary layer which was present.

One semi-empirical analysis [3] for the position of the jet axis in a deflecting flow consists of a force balance on the jet using measured jet cross sections and expansion rates and an empirical aerodynamic force constant. Proper selection of empirical constants yields reasonable agreement with experimental data for a distance of approximately three or four diameters from the point of injection. The distortion and deflection of a normal jet due to dynamic pressure forces acting on it during the first diameter of travel have also been calculated [7]. Potential flow is assumed and the pressure distribution about the jet at the plane of egress is assumed identical to that about an infinite cylinder of the same diameter in an air stream at the same Reynolds number. The path of the jet axis is then determined by extrapolating the deflection curve. Fair agreement is indicated [7] with experiment for approximately three diameters downstream of the injection location.

Extensive studies of the penetration of heated air jets into deflecting air streams have been conducted by NACA. The jets are introduced at considerably higher temperatures than the main flow (160 to 185 deg C), and the depth of penetration is sensed with a temperature probe. The first investigation [8] reports the penetration of a circular air jet directed perpendicular to the deflecting flow. The penetrating depth of the upper edge of the jet, defined as the height above the wall at which the temperature of the jet exceeds the temperature of the mainstream by about $^1/_2$ deg C, is empirically correlated as a function of density and velocity ratios of the jet and mainstream flows. The correlation is improved by the inclusion of the orifice coefficient [9] in defining an effective orifice diameter [10]. Studies of depth penetration from circular, square, and elliptical orifices [10] indicate the penetration depth is greatest for square orifices and lowest for circular orifices. Gordier [5] compares his results for the location of the upper edge of the jet, as determined from visualization studies, with the results of [10] and finds good agreement. Temperature profiles are measured for perpendicular injection [11] and for angles of 90, 60, 45, and 30 deg to the main flow [12]. The tunnel used for the NACA experiments is quite narrow and most of the data are taken at downstream positions where the jet has expanded to the side walls. This confinement of the jet by the side walls may strongly affect the shape of the measured profiles and the penetration depth.

A question arises as to the scaling parameter that best correlates the phenomena associated with a heated jet deflected by a cross flow. The present paper presents the results of the experimental study as a function of the blowing parameter, $M = \rho_2 U_2/\rho_\infty U_\infty$, which has often been found useful in correlating film-cooling results. This parameter would be expected to be significant as it is proportional to the relative enthalpy flux of the entering jet. Abramovich, on the other hand, uses the momentum-flux ratio, $\rho_2 U_2^2/\rho_\infty U_\infty^2$ to characterize the trajectory of a jet in a cross flow. In the present study, only small density differences exist between the jet and mainstream flows and consequently the relative importance of the blowing parameter, M, and the momentum-flux parameter cannot easily be differentiated.

In reference [6] a "heat-sink" model is used to predict the temperature distribution downstream of the injection location for low blowing rates. Application of the model to experimental results indicates that at low blowing rates the temperature distribution is well characterized by the use of M, which, along with the temperature of the injected gas, defines the enthalpy flux of the jet. At higher blowing rates the model breaks down primarily due to the added jet penetration. Thus, one expects that as the blowing rate increases, the momentum flux is also a significant parameter, although the relative enthalpy deficit, proportional to M times a specific heat ratio, should be included as well.

An experimental investigation has been carried out at the University of Minnesota to determine adiabatic wall-temperature distributions with injection of air through a discrete circular hole into a turbulent boundary layer of air on a flat plate [13, 14]. These experiments are conducted for a range of blowing-rate parameters from 0.1 to 2.0 with an air jet entering at an angle of either 35 or 90 deg to the main flow. Basic trends for the two injection angles are found to be similar with differences occurring only at large injection rates. The dimensionless adiabatic wall temperature or effectiveness (θ_{aw}/θ_2) reaches a maximum for a blowing-rate parameter of approximately one-half. Injection at an angle of 35 deg yields considerably higher film-cooling effectiveness, especially at larger blowing rates.

Nomenclature

D = diameter of injection tube
M = blowing rate parameter, $M = \rho_2 U_2/\rho_\infty U_\infty$
T = temperature
T_2 = temperature of secondary injected air
T_∞ = mainstream temperature
U = velocity
U_2 = average air velocity in injection tube
U_∞ = mainstream velocity
$\bar{U}$ = time-average velocity
u_1 = fluctuating component of velocity in the direction of $\bar{U}$
$\overline{u_1^2}$ = time-average value of the square of the velocity u_1
X = distance downstream of injection hole, see Fig. 1
Y_J = vertical position of maximum velocity at $Z = 0$
Y = distance normal to tunnel floor, referenced to injection hole, see Fig. 1
Z = lateral distance from injection hole, see Fig. 1
β = angle between the direction of injection and the direction of the mainstream in the X-Y plane
θ = temperature difference; $\theta = T - T_\infty$
θ_2 = temperature difference; $\theta_2 = T_2 - T_\infty$
θ_{aw} = adiabatic wall temperature minus mainstream temperature
θ_{max} = maximum θ for a given temperature profile
θ_w = the value of θ at the wall
ρ = density
ρ_2 = density of secondary air
ρ_∞ = density of mainstream

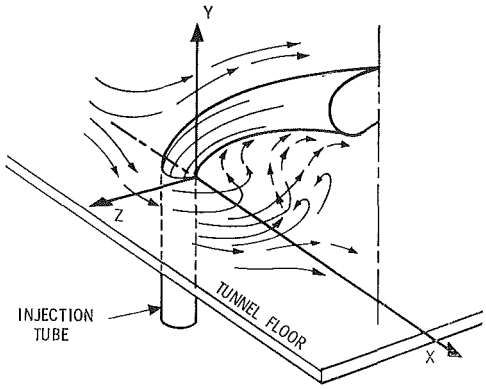

Fig. 1 Sketch of half-jet based on tuft observations

Apparatus and Operating Conditions

Wind Tunnel. The present investigation is carried out in a subsonic wind tunnel capable of air velocities of up to 70 mps (meters per second) in the test section. The main flow of air, drawn from the room, passes through an entrance section, test section, and diffuser. It then flows to the blower, from which it is discharged through a silencer to the outside. The tunnel is described in detail in references [6, 13, 14].

The test section of the wind tunnel is 20.3 cm × 20.3 cm in cross section. The mainstream turbulence intensity in the absence of secondary flow is approximately 0.5 percent at a mainstream velocity of 30 mps. A 0.064-cm-dia boundary layer trip wire is located on the bottom wall of this segment approximately 3.8 cm downstream from the end of the contraction section. The downstream end of the injection tube is about 20 cm from this trip with the normal injection tube, and about 45 cm for the 35 deg tube. The injection of the secondary air is through a 2.35-cm-ID stainless steel tube approximately 1 m long. Fully developed turbulent flow is present at the tube exit. The secondary air temperature, T_2, is taken as that measured by thermocouples attached to the injection tube at positions $4^1/_2$ and 6 diameters upstream of its end (both of which indicate the same temperature).

The test section downstream of the injection location contains thermocouples for measuring wall-temperature distribution downstream of the injection. The bottom wall is an adiabatic test plate designed according to the following considerations: It should have a rapid thermal response and it should be adiabatic including low conduction in all directions parallel to the plate surface. It consists of a 0.32-cm Textolite plate thinned to 0.16 cm at the thermocouple locations, backed by approximately 5 cm of Styrofoam insulation.

Probes. The temperature probe to survey the air stream consists of a thermocouple stretched across two supports. The junction is made large (0.13-cm diameter or approximately 10 wire diameters) in order to minimize conduction effects in the three-dimensional temperature field investigated. The reference junction for the probe is located on the wall of the tunnel test section at a point upstream of the injection which is at mainstream temperature and not affected by the secondary flow, so that the probe indicates the temperature difference between the large junction and the mainstream. A traversing assembly for the probe provides movement in the axial direction and in the direction normal to the adiabatic test plate. The lateral position of the probe, relative to the injection location, is varied by moving the injection section of the tunnel.

A hot-film probe with a 0.025-mm-dia × 0.51-mm-long sensor is used for velocity measurements. The probe is operated by a constant-temperature hot-wire anemometer system which, in addition to maintaining the sensor at constant temperature, provides a signal-monitoring voltmeter. The probe is calibrated in the tunnel in the absence of secondary flow by measuring the free-stream velocity using a total-pressure probe as reference. The turbulence intensity in the flow field is also measured using the hot-film probe anemometer.

Tunnel Operating Conditions. The tunnel operating conditions are basically the same as those used earlier [13]. These are: (*a*) a fully developed turbulent boundary layer on the test surface in the absence of secondary flow, (*b*) mainstream velocity of either 30 or 61 mps, (*c*) boundary layer displacement thickness at the 90 deg injection location of 0.09 cm and 0.07 cm for 30 and 61 mps respectively and at the 35 deg injection location of 0.14 cm and 0.12 cm for 30 and 61 mps respectively, (*d*) fully developed turbulent pipe flow at the end of the injection tube in the absence of primary flow, (*e*) a uniform temperature distribution at the end of the injection tube in the absence of primary flow, (*f*) injection air temperature approximately 55 deg C higher than that of the mainstream for temperature studies, (*g*) injection temperature approximately equal to that of the mainstream for velocity studies, and (*h*) steady-state conditions during the tests.

The probe is positioned along the tunnel center line and the various lateral positions are obtained by translating the injection tube laterally relative to the tunnel center line. The distributions are laterally symmetric, and usually the tube is only moved in one direction from the tunnel center line.

Experimental Results

Visualization Studies

Tuft Study. A small tuft of yarn attached to the end of a thin rod was used to examine the flow field in and around the jet. A sketch of the observed field is shown in Fig. 1. As the jet enters it leaves a void (low-pressure condition) downstream of it which is filled by mainstream air moving around the jet. In the region near the wall and for a distance almost halfway around the jet the flow patterns look similar to what is found around a cylinder in cross flow. The flow continues around the jet and into the apparent low-pressure region on its downstream side.

At a blowing rate of two, immediately downstream of the injection location the incoming mainstream air moves parallel to the floor of the tunnel and laterally with almost no component of velocity in the downstream direction. As the mainstream air moves toward the zero lateral position ($Z/D = 0$) it begins to move upward away from the wall, apparently being entrained by the jet. This region where the air enters in from the side and then moves vertically extends approximately two diameters downstream and is a region of extreme fluctuations.

Approximately one diameter downstream, as the air moves vertically away from the wall it reaches a height where it turns upstream and reverse flow exists. At greater distances from the wall the flow changes from reverse to forward flow. The inclination of the jet relative to the mainstream direction reaches zero between $2^1/_2$ and 3 diameters from the wall.

Farther downstream the flow, after rising from the wall, turns downstream rather than upstream and lateral components away from the center line are also observed, indicating the possible formation of vortices as suggested by previous investigators [2, 3]. It is not possible to follow this circulation pattern away from the center line with the tuft since the outer portion of the vortex flow becomes overwhelmed by the main flow and the lateral velocities appear to diminish rapidly. At distances greater than two diameters downstream the lateral velocity components diminish with axial distance until at approximately 10 diameters no lateral velocity is observable.

Tufts were also used at a second blowing rate, $M = 1$. The trends observed were the same as those for the higher injection rate, the mainstream flow being drawn in to fill the void on the downstream side of the jet, this flow moving inward and then upward. Finally, depending on the axial position, the flow moves either upstream (reverse flow) or downstream and is then entrained by the jet. The principal difference between the flow

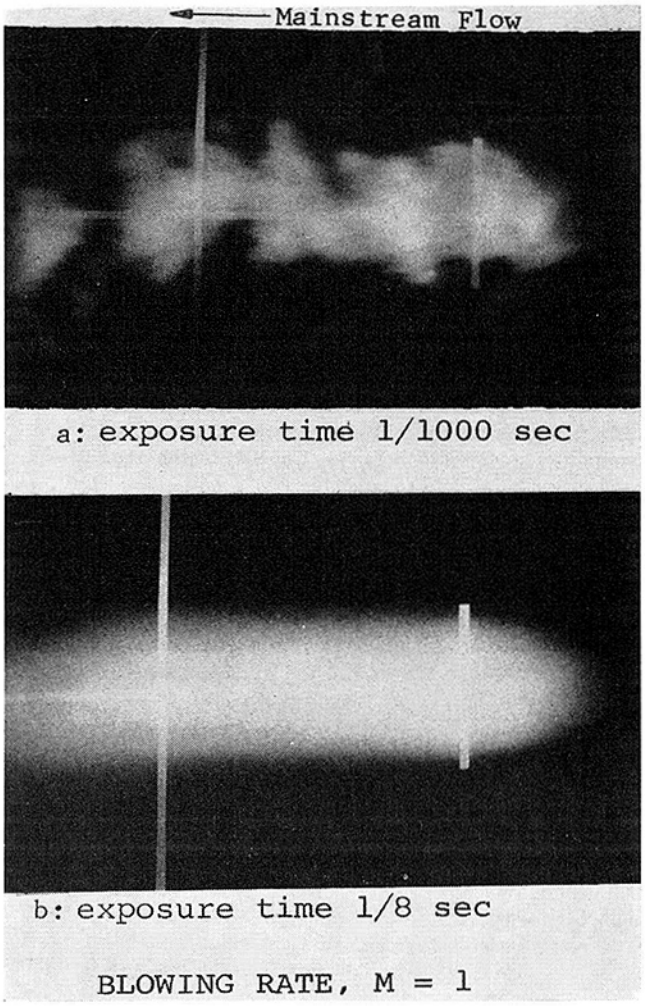

Fig. 2 Flow visualization of jet entering free stream

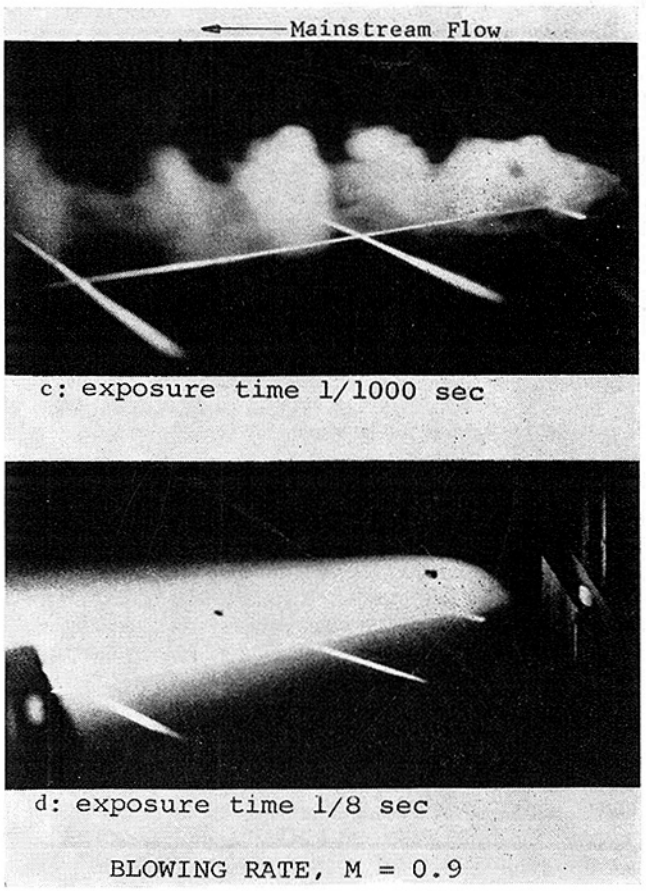

Fig. 2 Flow visualization of jet entering free stream

patterns of the two blowing rates is that at the lower injection rate the vertical components of velocity in all regions are smaller.

Table 1 shows the inclination of the flow in the X-Y plane as determined from the tufts.

Photographic Study. In order to observe the jet as it interacts with the mainstream, a carbon dioxide–water fog is injected through the injection tube. The fog is produced by putting solid carbon dioxide and hot water in a container fitted with a tube to allow passage of the resulting fog to the injection tube and into the tunnel. The mass flow rate is determined from the change in weight of the dry ice–water container. A blowing rate of unity was achieved by operating the tunnel with a mainstream velocity of 15 mps. White marking tapes, see Fig. 2, are placed axially down the center line (i.e., at $Z/D = 0$), partway across the span at $X/D = 1$, and spanning the full width of the tunnel at $X/D = 5$ and $X/D = 10$.

Figs. 2(a) and 2(b), taken from above the jet, show the lateral spreading of the jet to be quite limited. Figs. 2(c) and 2(d), taken from the side and downstream of the incoming jet, show the penetration and turning of the jet. Note that at shorter exposure time, $^1/_{1000}$ sec, the jet is irregularly shaped and intermittent, indicating large-scale eddies. To insure that the intermittency pictured is due to the interaction between the jet and mainstream and is not introduced by irregularities in the secondary flow system, the top of the tunnel was removed and pictures taken at $^1/_{1000}$ sec of the jet in still air. These pictures indicate no irregularities in the jet flow.

Temperature Distribution. Temperature profiles are presented in terms of the dimensionless temperature ratio θ/θ_2 for injection normal to the mainstream at blowing rates of $M = 0.1$, 0.5, 1.0, and 2.0. A mainstream velocity of 61 mps is used for $M = 0.1$ and 30 mps for the other blowing rates. Check runs made for $M = 0.5$ at a mainstream velocity of 61 mps were found to have temperature profiles similar to those obtained at 30 mps. Temperature profiles are also obtained for two blowing rates (1.0 and 2.0) with injection at an angle of 35 deg to the main flow

Table 1 Angle of inclination to the mainstream in the X-Y plane (deg) measured with tuft, $Z/D = 0$

	$M = 2$			$M = 1$		
Y/D	$X/D = 3$	$X/D = 5$	$X/D = 10$	$X/D = 3$	$X/D = 5$	$X/D = 10$
$^1/_4$	0	0	0	0	0	4
$^1/_2$	5	0	0	7	0	3
$^3/_4$	20	5	0	4	2	0
1	30	15	5	0	0	
$1^1/_4$	45	15	5			
$1^1/_2$	30	20	5			
$1^3/_4$	25	10	5			
2	20	10	5			
$2^1/_4$	15	10	5			
$2^1/_2$	10	10	5			
$2^3/_4$	5	5	5			
3	0	0	0			

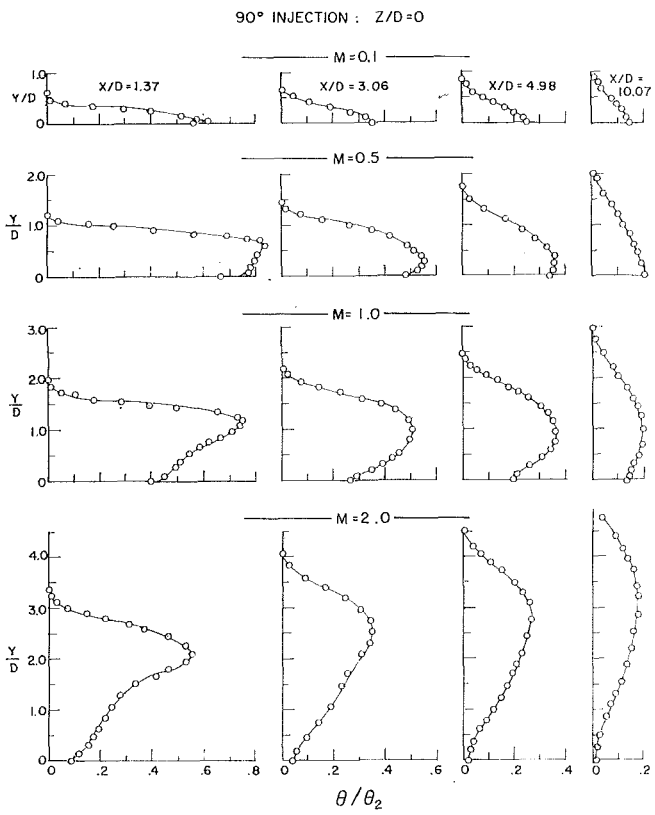

Fig. 3 Temperature profiles for 90 deg injection angle, $Z/D = 0$

direction. The mainstream velocity for these tests is 30 mps.

The temperature profiles at $Z/D = 0$ for normal injection are presented in Fig. 3. At $M = 0.1$, the lowest blowing rate investigated, little or no penetration of the secondary air into the mainstream occurs. The maximum temperature occurs near or at the wall. As the jet moves downstream it spreads and the maximum temperature decreases.

At a blowing rate of 0.5 the jet penetrates significantly into the main flow. At $X/D = 1.37$ the maximum temperature occurs at a position 0.6 diameter above the wall. In addition to the increased penetration, the wall and maximum temperatures also increase in going from $M = 0.1$ to $M = 0.5$. As the jet travels downstream it spreads in such a way that the location of maximum temperature moves closer to the wall.

The profiles for the higher blowing rates, $M = 1.0$ and 2.0, indicate larger penetrations with increasing blowing rate. Note that for $M = 1.0$ the position of maximum temperature remains nearly constant in going from $X/D = 1.37$ to $X/D = 3.06$. Beyond $X/D = 3.06$ the location of the maximum temperature decreases somewhat with increasing axial distance as before. This is consistent with the previously described visualization study in which the use of tufts indicated that the jet is still moving slightly away from the wall at $X/D = 3$ and is essentially turned in the direction of the mainstream at $X/D = 5$. At the largest blowing rate investigated, $M = 2.0$, the jet penetrates sufficiently far into the main flow that the wall temperature is nearly unaffected by its presence. The position above the wall of the maximum temperature is found to increase with increasing axial distance for the entire range considered, consistent with the tuft measurements.

The temperature profiles measured at a lateral position one diameter from the jet axis are presented in Fig. 4. Notice that for $M = 0.1$, the maximum temperature increases with axial distance, due to the increasing lateral width of the jet as it move downstream. Comparing the profiles for the various blowing rates at $Z/D = 1.0$ shows that the lateral spreading of the jet increases with blowing rate.

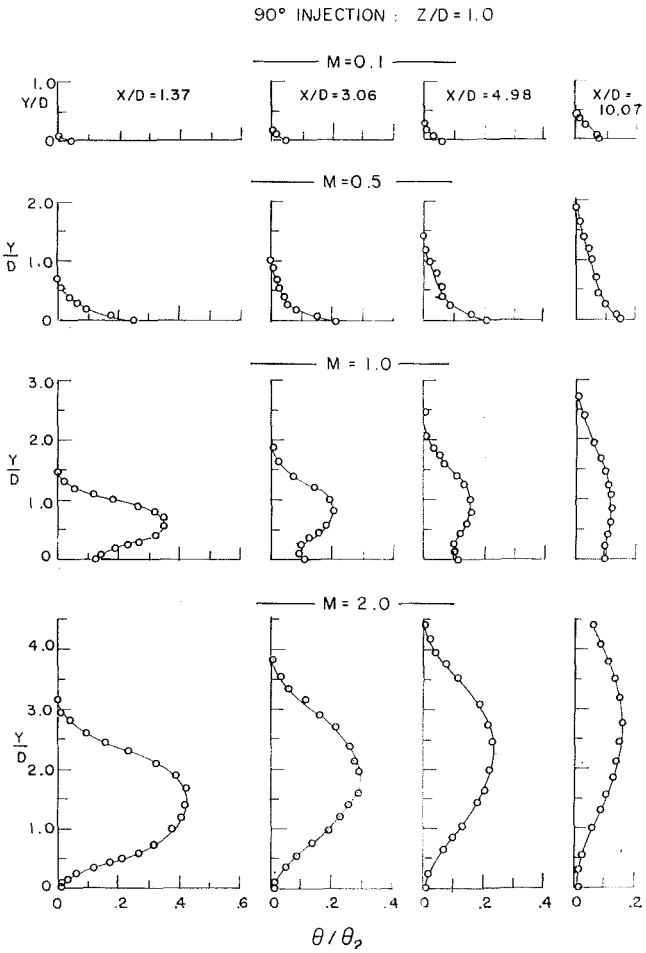

Fig. 4 Temperature profiles for 90 deg injection angle, $Z/D = 1$

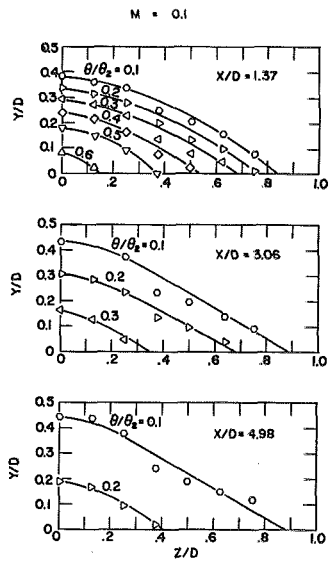

Fig. 5 Constant-temperature contours for 90 deg injection angle, $M = 0.1$

The spreading effects can be better observed by presenting the data in the form of lines of constant dimensionless temperature, θ/θ_2, at a given axial plane normal to the tunnel floor. A number of these constant-temperature contours are presented in Figs. 5–8.

At a blowing rate of $M = 0.1$, Fig. 5, the constant-temperature

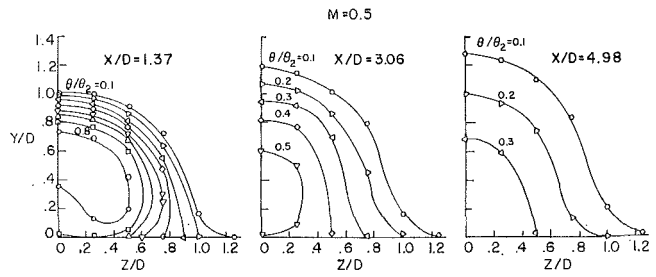

Fig. 6 Constant-temperature contours for 90 deg injection angle, $M = 0.5$

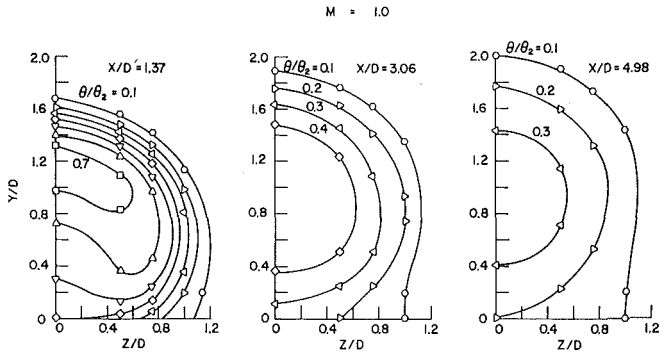

Fig. 7 Constant-temperature contours for 90 deg injection angle, $M = 1.0$

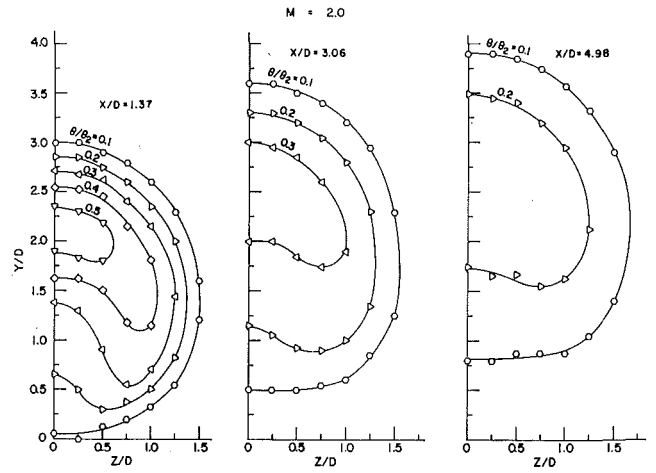

Fig. 8 Constant-temperature contours for 90 deg injection angle, $M = 2.0$

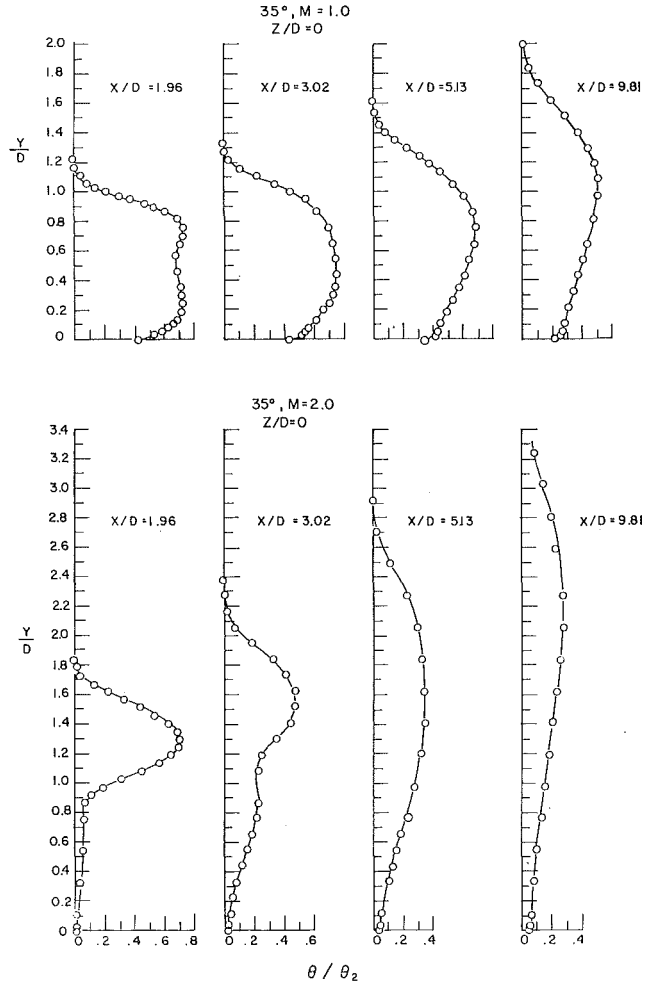

Fig. 9 Temperature profiles for 35 deg injection angle, $Z/D = 0$

contours indicate smooth or regular spreading in both the vertical and lateral directions. Fig. 6 shows the effect of penetration of the jet for $M = 0.5$. At axial distances of 1.37 and 3.06 diameters downstream the highest temperature regions are seen to be in the air stream above the wall. At the position $X/D = 1.37$ the jet appears to be starting to develop the characteristic kidney shape observed in previous velocity studies at higher blowing rates [2–5]. Fig. 7 shows a more pronounced kidney shape at $X/D = 1.37$ for $M = 1.0$. As the jet moves downstream it spreads in such a way that the constant-temperature lines become nearly circular. Increasing the blowing rate to $M = 2.0$, Fig. 8, results in the jet penetrating sufficiently that it is almost totally above the wall. The contours indicate that the temperature of the air flowing next to the wall is only slightly affected by the jet. This air is very likely mainstream air which has moved around and under the jet.

The constant-temperature contours also depict the effect of secondary injection on the adiabatic wall-temperature distribution. At low injection rates the maximum temperature occurs on the wall and along the center line. The limited amount of heated mass injected results in this maximum temperature being relatively low and causes it to decrease rapidly with increasing axial distance. Increasing the amount of injected air raises the wall temperature until a point is reached (approximately $M = 0.5$) where the increased penetration causes the jet to move away from the wall. The wall temperature then decreases with increasing injection rate. An injection rate is reached where the jet is totally above the wall and the wall temperature is close to the mainstream temperature. For injection normal to the mainstream this occurs at approximately $M = 2$.

Some temperature profiles for a round jet directed normal to the mainstream have been measured previously [11, 12]. One of the profiles in each of the reports is for a blowing rate and axial position similar to one considered in the present study. A comparison [6] indicates reasonable agreement which is somewhat surprising since in the earlier investigation the jet is confined by the tunnel walls.

A limited number of temperature profiles for injection at an angle of 35 deg to the mainstream direction are presented in Fig. 9. At a blowing rate of $M = 1$ the jet penetrates well into the mainstream. At the zero lateral position the penetration depth, as characterized by the position of maximum temperature, is seen to increase with increasing axial distance. For normal injection at $M = 1.0$, recall that the vertical height of maximum temperature decreased with increasing axial distance for X/D greater than approximately three. The depth of penetration is less for 35 deg injection. For perpendicular injection the maximum temperature at $X/D = 1.37$ and $Z/D = 0$ occurs at $Y/D = 1.2$ while for 35 deg injection the maximum jet tempera-

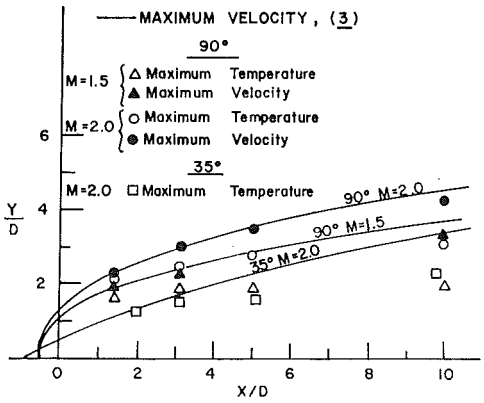

Fig. 10 Positions of maximum temperature and velocity as a function of axial position for 90 and 35 deg injection angles, $Z/D = 0$, $M = 1.5$ and 2.0

ture has not penetrated to that depth as far downstream as $X/D = 9.8$.

Away from the axis the temperature level decreases rapidly when going from $Z/D = 0.5$ to $Z/D = 0.75$. The jet does not spread to $Z/D = 1$ until approximately $X/D = 9.8$. This spreading is considerably less than that observed for normal injection, cf. Fig. 8.

A significant effect of reduced penetration as compared to normal injection is a much slower decline of the maximum temperature with axial distance for injection at 35 deg. Approximately 10 diameters downstream and at $Z/D = 0$ the maximum dimensionless temperature, θ/θ_2, is 0.5 for 35 deg injection and 0.2 for perpendicular injection, both for $M = 1.0$.

The same comparisons between the results for the two injection angles that are made for $M = 1.0$ can be made for $M = 2.0$. Specifically, for 35 deg injection the penetration depth is less, and the temperature drops less rapidly in the axial direction, but more rapidly in the lateral direction.

The jet penetration as a function of axial position is shown in Fig. 10 for blowing rates of $M = 2.0$ and 1.5 with normal injection and a blowing rate of $M = 2.0$ with 35 deg injection. The measured positions of maximum velocity (to be discussed later) are also included. An empirical relation for determining the axis from the position of maximum velocity of a circular jet deflected by an external flow is presented by Abramovich [3]. The relation is:

$$\frac{X}{D} + 0.5 = \frac{\rho_\infty U_\infty^2}{\rho_2 U_2^2}\left(\frac{Y_J}{D}\right)^{2.55} + \frac{Y_J}{D}\left[1 + \frac{\rho_\infty U_\infty^2}{\rho_2 U_2^2}\right]\cot\beta \quad (1)$$

The experiments from which this equation was derived were carried out for 45 deg $\leq \beta \leq$ 90 deg and $2 \leq \dfrac{\rho_2 U_2^2}{\rho_\infty U_\infty^2} \leq 22$ or assuming $\rho_2 = \rho_\infty$, $1.4 \leq M \leq 4.5$. The jet penetration predicted by equation (1) is included in Fig. 10. The figure shows that the velocity data of the present investigation for $M > 1.5$ is in good agreement with Abramovich's empirical prediction. The largest difference, at $X/D = 10$, is less than 10 percent. The position of maximum temperature is below the position of maximum velocity.

Velocity Distributions. Velocity distributions are measured for an unheated jet at two blowing rates, $M = 1.0$ and 2.0, for a mainstream velocity of 30 mps. The cylindrical probe sensor is aligned with its axis parallel to the Z axis so that the velocity measured is in the X-Y plane. The direction of the velocity in this plane is not described by the probe measurements. Therefore what are actually measured with the probe are velocity magnitudes in the X-Y plane. These values along with the tuft studies give a picture of the velocity field.

In addition to the mean velocity, the velocity fluctuations u_1 in the X-Y plane are also measured in terms of the turbulence intensity, $(\overline{u_1^2})^{1/2}/\bar{U}$. In converting voltage-output readings of the

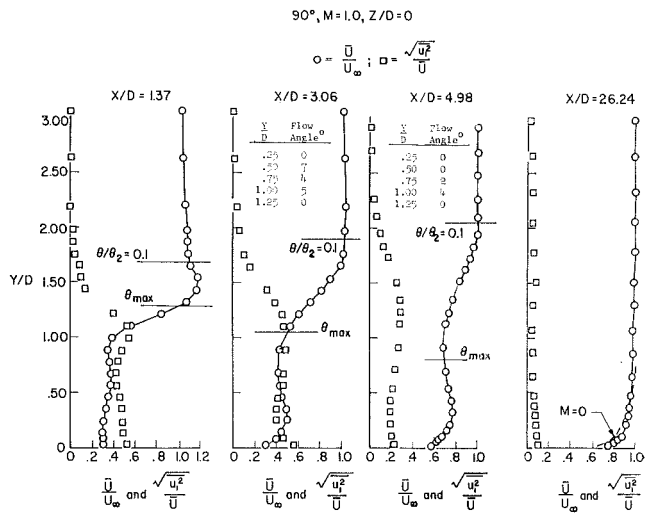

Fig. 11 Velocity and turbulence-intensity profiles for 90 deg injection angle, $Z/D = 0$, $M = 1.0$

constant-temperature anemometer to mean-velocity and turbulence-intensity values the assumption is made that the fluctuating components of velocity are small relative to the mean velocity. At a turbulence intensity of 0.5 approximately 10 percent error (in intensity) can be introduced by the assumption of low turbulence, while this error drops to 2.5 percent for a turbulence intensity of 0.25 [6]. The error in velocity introduced by the assumption of low turbulence is approximately 6 percent for a turbulence intensity of 0.5 dropping to 1.5 percent for a turbulence intensity of 0.25 [6]. The maximum turbulence intensity observed in this investigation is approximately 0.6. In addition to errors introduced by turbulence, reading errors of 10 and 2 percent are estimated to exist in the turbulence and velocity measurements respectively.

The velocity and turbulence distributions for the blowing rate of $M = 1.0$ and the lateral position $Z/D = 0$ are presented in Fig. 11. Also included in the figure are lines indicating the positions of maximum temperature as measured in the temperature study. To further indicate how the temperature distribution compares with the velocity, the position at which $\theta/\theta_2 = 0.1$ is indicated. At axial positions where the flow angle of inclination to the mainstream in the X-Y plane is available from the tuft study this information is tabulated in the figures. For $X/D = 1.37$ there is a region of nearly constant low velocity from the wall to an elevation of approximately $Y/D = 1$. In this region, while the magnitude of the velocity is nearly uniform, the visualization study using tufts indicates the flow direction is very nonuniform. Included in this region is some reverse flow. It is into this region, particularly near the wall, that the tuft studies indicate a sizable mass flow from the mainstream. As might be expected from the nature of the flow, the turbulence level in this region is very large. Above this region the velocity increases until a maximum is reached at approximately 1.5 diameters above the wall. At this point the velocity is in the direction of the main flow. The position of maximum velocity is seen to be above that of the temperature as indicated earlier in Fig. 10. Farther from the wall the velocity decreases until it equals that of the mainstream.

As the jet moves farther downstream it is turned and accelerated in the direction of mainstream flow. This acceleration appears to take place both along the upper and lower edge of the jet, as indicated by the velocity peak near the wall. As the velocity increases, the turbulence level drops. The results of the tuft study, tabulated in the figure, indicate that the jet flow is nearly in the direction of the mainstream for axial distances greater than three diameters. A slight distortion of the velocity field still exists far downstream. This is apparent in Fig. 11 at an axial position of $X/D = 26.24$ where the profile for $M = 0$,

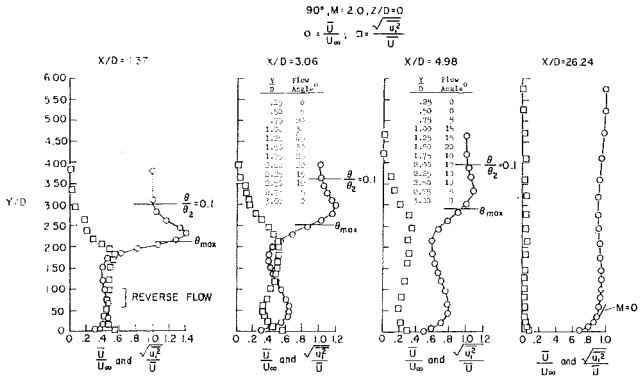

Fig. 12 Velocity and turbulence-intensity profiles for 90 deg injection angle, $Z/D = 0$, $M = 2.0$

also measured with the hot-film probe, is compared with that for $M = 1.0$.

Velocity and turbulence profiles are presented for a blowing rate of $M = 2.0$ in Fig. 12. These profiles are similar in shape to those for $M = 1.0$. As expected, increasing the blowing rate increases the height above the wall at which the maximum velocity occurs. Note also the region of reverse flow at $X/D = 1.37$.

Coupled with the increased penetration at the higher blowing rates is the slower turning of the jet into the direction of the main flow as indicated by the flow directions measured with the tuft. These results are tabulated in Fig. 12 for easy reference.

Summary

The interaction of a heated subsonic circular air jet issuing into a subsonic main flow of air has been investigated experimentally. The jet is introduced into the test section through a circular tube, whose exit is flush with a well-insulated wall of the test tunnel. In the absence of a secondary flow, a fully developed flat-plate turbulent boundary layer is present and the free-stream turbulence intensity is approximately 0.5 percent.

Visualization studies present information on the general shape and path of the incoming jet and indicate that upon entry to a deflecting flow the jet boundary is very irregular with large-scale eddies.

As the jet enters, mainstream air is drawn in from the sides to fill the low-pressure region immediately downstream of the jet. At large blowing rates a reverse-flow region exists on the downstream side of the entering jet.

Temperature profiles for injection perpendicular to the mainstream show the jet penetration increases with increasing blowing-rate parameter. The maximum temperature occurs at or near the wall for $M = 0.1$ while for $M = 2.0$ the maximum is at a height greater than two diameters above the wall even quite close to the jet entrance.

Increasing the blowing-rate parameter influences the wall temperature in two counteracting ways. The increased secondary mass flow and resulting increased enthalpy addition to the stream tend to increase the temperature while the increased penetration moves the path of the jet's maximum temperature farther from the wall and tends to lower the wall temperature. The first effect predominates at the lower blowing rates ($M \leq 0.5$). At larger blowing rates the effect of increased penetration causes the wall temperature to decline with increasing blowing rate. At $M = 2.0$ the jet penetration is such that the jet has very little effect on the wall temperature.

Injection at an angle of 35 deg to the direction of main flow exhibits less penetration and less spreading in both the vertical and lateral directions than perpendicular injection. The reduced spreading in the vertical direction occurs at both the top and bottom of the jet. The reduced spreading along the bottom of the jet results in less effect of the jet on the off-axis wall temperature.

In an unheated jet entering perpendicular to the mainstream, low velocities are measured directly downstream of the incoming jet. Above this region the velocity increases, reaching a maximum greater than the free-stream velocity, and then declines to the free-stream value. The turbulence intensity is found to be very large in the low-velocity region. As the jet moves farther downstream the low-velocity region is accelerated by the mainstream and the turbulence level drops. Some distortion of the velocity profile, as compared to the no-blowing condition, exists as far as 26 diameters downstream of the injection position.

A comparison of the velocity and temperature studies shows the position of maximum velocity to be somewhat farther from the wall than the position of maximum temperature for the same blowing-rate parameter. This, coupled with the tuft study, suggests the air in the region of maximum velocity is in the outer region of the jet which is accelerated more than the region near the wall.

References

1 Lee, C. C., "A Review of Research on the Interaction of a Jet with an External Stream," Brown Engineering Co , Inc., Huntsville, Ala. Research Labs., Rep. No. TN-R-184, March 1966; Defense Documentation Center acquisition number AD 630 294.

2 Keffer, J. F., and Baines, W. D., "The Round Turbulent Jet in a Cross Wind," *Journal of Fluid Mechanics*, Vol. 15, No. 4, 1963, pp. 481–497.

3 Abramovich, G. N., *The Theory of Turbulent Jets*, M.I.T. Press, Cambridge, Mass., 1963, pp. 541–556.

4 Jordinson, R., "Flow in a Jet Directed Normal to the Wind," Aero. Res. Council, R & M, No. 3074, 1956.

5 Gordier, R. L., "Studies on Fluid Jets Discharging Normally into Moving Liquid," St. Anthony Falls Hyd. Lab., University of Minnesota, Tech. Paper No. 28, Series B, 1959.

6 Ramsey, J. W., "The Interaction of a Heated Air Jet with a Deflecting Flow," PhD thesis, University of Minnesota, 1969.

7 Fraser, J. P., "Three-Dimensional Study of a Jet Penetrating a Stream at Right Angles," *Journal of the Aeronautical Sciences*, Vol. 21, No. 1, 1954, pp. 59–61.

8 Callaghan, E. E., and Ruggeri, R. S., "Investigation of the Penetration of an Air Jet Directed Perpendicularly to an Air Stream," NACA TN 1615, 1948.

9 Callaghan, E. E., and Bowden, D. T., "Investigation of Flow Coefficients of Circular, Square, and Elliptical Orifices at High Pressure Ratios," NACA TN 1947, 1949.

10 Ruggeri, R. S., Callaghan, E. E., and Bowden, D. T., "Penetration of Air Jet Issuing from Circular, Square and Elliptical Orifices Directed Perpendicularly to an Air Stream," NACA TN 2019, 1950.

11 Callaghan, E. E., and Ruggeri, R. S., "A General Correlation of Temperature Profiles Downstream of a Heated-Air Jet Directed Perpendicularly to an Air Stream," NACA TN 2466, 1951.

12 Ruggeri, R. S., "General Correlation of Temperature Profiles Downstream of a Heated Air Jet Directed at Various Angles to Air Stream," NACA TN 2855, 1952.

13 Goldstein, R. J., Eckert, E. R. G., and Ramsey, J. W., "Film Cooling With Injection Through Holes: Adiabatic Wall Temperatures Downstream of a Circular Hole," *Journal of Engineering for Power*, TRANS. ASME, Series A, Vol. 90, No. 4, Oct. 1968, pp. 384–395.

14 Goldstein, R. J., Eckert, E. R. G., and Ramsey, J. W., "Film Cooling with Injection Through a Circular Hole," NASA CR-54604, May 1968; also HTL TR No. 82

H. L. JULIEN
General Motors Research Laboratories, Warren, Mich.

W. M. KAYS
Professor.
Mem. ASME

R. J. MOFFAT
Associate Professor.
Assoc. Mem. ASME

Department of Mechanical Engineering, Stanford University, Stanford, Calif.

Experimental Hydrodynamics of the Accelerated Turbulent Boundary Layer With and Without Mass Injection

Mean velocity-profile data are reported for blown, unblown, and sucked accelerated turbulent boundary layers. The pressure gradients investigated are those corresponding to constant values of the pressure-gradient parameter

$$K = \frac{\nu}{U_\infty^2}\frac{dU_\infty}{dx}$$

The two values of K considered in detail are 0.57×10^{-6} and 1.45×10^{-6}. For each pressure gradient, the surface boundary conditions cover a range of constant blowing and sucking fractions from $F = -0.002$ to $+0.004$. Velocity profiles corresponding to these accelerated flows are shown to differ substantially from those characteristic of zero-pressure-gradient flows. For each case of a constant K acceleration, sequential values of the momentum-thickness Reynolds number approach a specific constant, and the velocity distributions near the wall are similar in both wall coordinates and outer coordinates. Results obtained here can be reproduced by a numerical integration of the boundary-layer equations using a modification of the van Driest damping factor, A^+, derived from the data presented here. The A^+ correlation is presented.

Introduction

THE TURBULENT boundary layer with non-zero normal velocity at the surface, v_w, is of considerable practical interest. Injection of fluid at a surface is frequently used for thermal protection, and suction is used for boundary-layer control. In many applications the mainstream fluid is accelerating or decelerating and the combined effects of transpiration at the surface and acceleration of the main flow must be considered. A survey of the existing data on the turbulent boundary layers where transpiration and mainstream acceleration are present indicates a need for further work. Existing turbulent boundary-layer "theory" presently relies heavily on experimental results; accurate and well-documented velocity measurements are necessary as a test for any theoretical developments.

The present paper is restricted to boundary-layer flows characterized by constant values of the acceleration parameter K $\left(K = \frac{\nu}{U_\infty^2}\frac{dU_\infty}{dx}\right)$ and blowing fraction F $\left(F = \frac{(\rho v)_w}{(\rho U)_\infty}\right)$. The flows considered are two-dimensional, constant-property flows over an aerodynamically smooth surface, as nearly as the apparatus permits.

Review of Previous Experimental Work. Although in recent years a number of experimental hydrodynamic investigations have been concerned with transpired or accelerated boundary layers, only two are known to consider the combined effects. Each dealt only with blown layers, and neither presented enough experimental data to adequately represent the boundary-layer characteristics.

Romanenko and Kharchenko [1][1] recorded friction-factor and Stanton-number data for some combined cases, but did not present profiles of velocity or temperature. McQuaid [2] reports two combined blowing and accelerated runs. Using friction factors corresponding to Stevenson's inner law [3], McQuaid was able to predict momentum-thickness distributions which agreed well with the experimentally determined distributions, but there is a question as to whether this is a sensitive test of friction factor when blown boundary layers are considered. Accelerations were relatively small compared to those considered here.

Experimental investigations have shown that significant changes in boundary-layer characteristics result from acceleration

Contributed by the Heat Transfer Division for publication (without presentation) in the JOURNAL OF HEAT TRANSFER. Manuscript received by the Heat Transfer Division December 29, 1970. Paper No. 71-HT-F.

[1] Numbers in brackets designate References at end of paper.

even on an impermeable surface. Launder and Stinchcombe [4] studied flows with accelerations at constant K in which the local momentum-thickness Reynolds number, Re_M, approached an asymptotic limit. The velocity profiles exhibited similarity. Tests were run at $K = 0.7 \times 10^{-6}$, 1.25×10^{-6}, and 3×10^{-6} and, as K was increased, a continuous shift from a typical non-accelerated turbulent profile was shown. This shift was characterized by a thickening of the viscous region resulting in an upward displacement of the velocity profile in the logarithmic region on u^+, y^+ coordinates, and a simultaneous decrease in the extent and strength of the wake region. Later experiments of Launder and Jones [5] do not corroborate the quantitative results of Launder and Stinchcombe, but the same qualitative conclusions were found to apply. This behavior in the inner regions of the boundary layer is consistent with the findings of the structure studies of Kline, Reynolds, Schraub, and Runstadler [6]. They found that a decrease in the bursting rate of turbulent disturbances originating at the wall is associated with an increase in K.

The experiments of Badri Narayanan and Ramjee [7] were concerned with both constant and variable K flows, and demonstrated the same profile behavior. The experiments of Patel and Head [8] were concerned with boundary-layer flows for which K was strongly varying, but showed some of these same effects.

The case of transpiration with constant free-stream velocity has been fairly completely studied (see for example McQuaid [2] and Simpson [9]). It is evident that the case of acceleration with no transpiration has been only incompletely studied, and the combined case of transpiration with acceleration has been virtually untouched. In view of the substantial structural changes observed for either of these effects alone, it is extremely difficult to anticipate the influence of the combination of transpiration and acceleration.

Description of an Asymptotic Boundary Layer. The two-dimensional momentum integral equation can be presented in the form

$$\frac{d\mathrm{Re}_M}{d\mathrm{R}_x} = \frac{c_f}{2} - \mathrm{Re}_M(H + 1)K + F \tag{1}$$

where

$$d\mathrm{R}_x = \frac{U_\infty}{\nu} dx. \tag{2}$$

For constant values of K and F, the possibility exists that the boundary layer will develop such that the terms on the right side of equation (1) will balance, forcing the derivative $d\mathrm{Re}_M/d\mathrm{R}_x$ to zero. Such a boundary layer will be termed asymptotic in the region where Re_M is constant. There is no question that such boundary layers exist for laminar flows; in fact, they form a family of similarity solutions. Turbulent boundary layers also behave in this manner. Such boundary layers exhibit both inner and outer similarity, with $c_f/2$ and H being constant, as well as Re_M.

The experiments reported here were restricted to asymptotic and near-asymptotic boundary layers for purposes of convenience. For these flows, equation (1) yields one method of estimating friction factor since the derivative, $d\mathrm{Re}_M/d\mathrm{R}_x$, represents a correction to the asymptotic form of equation (1). This is a desirable characteristic since direct measurement of friction factor was not possible on the apparatus used. These flows are also characterized by constant values of the blowing parameters B and $v_w{}^+$, as well as P^+, which are desirable characteristics in the formulation of data correlations.

Objectives of the Present Work. The overall intent of the work presented here was to investigate the fluid dynamic behavior of the turbulent boundary layer where the combined effects of transpiration and acceleration are present. The range of blowing, suction, and acceleration considered covers many practical applications where turbulent boundary-layer theory is appropriate. The particular objectives of this paper are:

1 To present mean velocity-profile data taken on the Stanford heat- and mass-transfer apparatus;

2 To present skin-friction results obtained from the mean velocity profiles;

3 To represent the combined effects of transpiration and acceleration in the form of a mixing-length model based on the van Driest damping function.

Experimental Apparatus

The Stanford heat- and mass-transfer apparatus was used in these experiments. Since this is described in detail by Moffat and Kays [10, 11], only a brief description will be presented here.

The apparatus consists of a 24-segment porous plate, 8 ft long and 18 in. wide. The plate forms the lower surface of a test duct of rectangular cross section, 20 in. wide and 6 in. high at the inlet

Nomenclature

A^+ = function in modified van Driest mixing-length hypothesis

B = blowing parameter; $\dfrac{(\rho v)_w}{(\rho U)_\infty (c_f/2)}$

$c_f/2$ = friction factor; $c_f/2 = g_c \tau_w / (\rho_\infty U_\infty{}^2)$

exp = base of natural logarithms

F = blowing fraction; $F = (\rho v)_w / (\rho U)_\infty$

H = profile shape parameter; $H = \dfrac{\delta_1}{\delta_2}$

k = von Karman constant

K = local pressure-gradient parameter; $K = \dfrac{\nu}{U_\infty{}^2}\left[\dfrac{dU_\infty}{dx}\right]$

l = Prandtl mixing length defined by $\tau = \rho l^2 \left|\dfrac{\partial u}{\partial y}\right| \dfrac{\partial u}{\partial y}$

P = pressure

P^+ = pressure-gradient parameter; $P^+ = \dfrac{g_c \mu_w}{\rho_w{}^2 u_\tau{}^3}\left(\dfrac{dP}{dx}\right) = \dfrac{-K}{(c_f/2)^{3/2}}$

Re_x = Reynolds number based on position along the plate; $\dfrac{U_\infty x}{\nu}$

Re_M = $U_\infty \delta_2 / \nu$

R_x = integrated x-Reynolds number; $\mathrm{R}_x = \displaystyle\int_0^x \frac{U_\infty}{\nu} dx$

U_∞ = mainstream velocity, fps

u = velocity, fps

u^+ = dimensionless velocity; $u^+ = u/u_\tau$

u_τ = shear velocity; $u_\tau = \sqrt{\tau_w g_c/\rho}$, fps

v = velocity perpendicular to the wall, fps

$v_w{}^+$ = dimensionless blowing velocity; $v_w{}^+ = v_w/u_\tau$

x = distance along the plate in the flow direction, in.

y = distance along a line perpendicular to the plate, in.; $y = 0$ at plate surface

y^+ = dimensionless distance; $y^+ = y u_\tau / \nu$

δ = boundary-layer thickness; y at $\dfrac{u}{U_\infty} = 0.99$

δ_1 = displacement thickness; $\delta_1 = \displaystyle\int_0^\infty \left(1 - \frac{\rho u}{\rho_\infty U_\infty}\right) dy$

δ_2 = momentum thickness of the boundary layer; $\delta_2 = \displaystyle\int_0^\infty \frac{\rho u}{\rho_\infty U_\infty}\left(1 - \frac{u}{U_\infty}\right) dy$

λ = outer-region mixing-length constant

μ = dynamic viscosity, $\mathrm{lb}_m/(\mathrm{sec}\cdot\mathrm{ft})$

ν = kinematic viscosity, $\mathrm{ft}^2/\mathrm{sec}$

ρ = density, $\mathrm{lb}_m/\mathrm{ft}^3$

τ = shear stress, $\mathrm{lb}_f/\mathrm{ft}^2$

τ^+ = dimensionless shear stress; $\tau^+ = \tau/\tau_w$

Subscripts

t = denotes turbulent contribution

w = wall condition

∞ = free-stream condition

end of the duct. The upper surface is adjustable to achieve any desired free-stream velocity distribution along the duct. The plates are 1/4 in. thick, smooth to the touch and uniform in porosity within ±6 percent in the 6-in. span along the test duct centerline where velocity profiles are taken. Separate mainstream and transpiration blowers provide the system with air, while heat exchangers are used to control air temperature. Conventional temperature and flow-rate instruments were used to monitor the operation of the apparatus.

Mean velocity profiles were taken with stagnation pressure probes similar to those used by Simpson [9] and using the same manual traversing equipment. The probes had flattened mouths, 0.012 in. by 0.035 in. They were attached to micrometer-driven traversing instruments fastened to a rigid support frame. Dynamic pressures were measured with calibrated inclined manometers.

Static pressure taps were located at 2-in. intervals along one side-wall of the test section. Free-stream static pressure was shown to be equal to that sensed by the side-wall taps by using static pressure probes in each accelerated flow. All recorded data were taken using the side-wall taps.

Qualification of the Apparatus

It has already been reported by Simpson, Moffat, and Kays [12] that the apparatus meets the requirements of the idealized flow model for constant free-stream velocity: i.e., steady, two-dimensional, constant-property flow over a smooth uniformly permeable flat plate. Acceleration emphasizes other requirements, beyond those of the flat plate. Those effects given additional consideration [13] in the present experiments are summarized below.

Free-stream turbulence intensities were found to be between 0.8 and 1.2 percent at the inlet conditions although velocity profiles for impermeable flat-plate flows satisfy Coles' criterion for "normal" boundary layers [14].

Surface-roughness effects were investigated by a series of tests at 42, 86, and 126 fps. In the data for 42 and 86 fps, mean velocity profiles exhibited u^+ vs. y^+ similarity near the wall ($y^+ < 150$) when wall shear was determined from sequential velocity profiles by means of the momentum integral equation. In the data for 126 fps a slight drop in u^+ was observed for the velocity profiles, so tests were restricted to velocities less than 86 fps. Plate-roughness elements, considered as half the particle diameter, were calculated to remain inside the viscous region of the boundary layer as best as this can be determined.

Accelerating flows are necessarily accompanied by streamwise variations in static pressure. Variations in the transpiration mass flux through each plate due to these variations were found to be negligible. For each static-pressure distribution in the experiments reported no temperature gradients were found in the plates when they were heated, with either blowing or suction applied. The pressure drop through each plate was found to be not less than 10 times the drop across the span of any plate at the lowest blowing fraction of 0.001.

Two-dimensionality of a flow can only be determined by elaborate probing of the boundary layer. This was not done, but secondary evidence was obtained by comparing enthalpy thickness derived from plate heat-transfer measurements with values determined from temperature and velocity profiles. Such checks were made possible by thermal data obtained on the apparatus for the same conditions as the hydrodynamic data [15]. Energy balance checks showed agreement within 8 percent for all blowing runs. This is within the uncertainty calculated for the enthalpy-thickness integrals using the method of Kline and McClintock [16].

In view of these results, the observed behavior of the data presented is felt to fairly represent the effects of acceleration and transpiration.

Experimental Determination of Friction Factor

Determination of friction factors to an acceptable degree of accuracy from velocity-profile measurements is extremely difficult at best. When the flow is accelerating, and there is transpiration at the wall, the difficulties are compounded. There is no turbulent "law of the wall" with which to compare profiles; in fact an important objective of the experiments was to attempt to establish a "law of the wall" under these conditions.

There are two physical principles which must hold: (*a*) The momentum integral equation of the boundary layer must be satisfied, and (*b*) in the region very near the wall the turbulent shear stresses should be small relative to viscous shear, i.e., a velocity equation based on viscous shear alone must be satisfied. However, there are considerable experimental uncertainties in using either of these principles to extract friction factors from data. Equation (1) can be solved for $c_f/2$, but uncertainty in the term $d\mathrm{Re}_M/d\mathrm{Re}_x$ (which is never quite zero) coupled with uncertainty as to the degree of two-dimensionality of the flow results in uncertainties in $c_f/2$ of at least ±15 percent for the unblown runs, and as much as ±50 percent for the highly blown runs. On the other hand, the use of a viscous-sublayer equation as suggested in (*b*) above, is subject to uncertainties resulting from the use of a probe which is "large" compared to the boundary layer.

A third principle, which can only really be applied subjectively, is that the final results must be internally consistent. Abrupt changes in $c_f/2$ are not expected when all of the external parameters are held close to constant, and the variation of $c_f/2$ with the external parameters is expected to be continuous. The inner region of the velocity profiles, when plotted on wall coordinates (u^+ vs. y^+), should collapse together when P^+ and $v_w{}^+$ are nearly constant, regardless of whether the profile is obtained very near the asymptotic condition, or considerably before it.

The procedure used here to determine $c_f/2$ was based on the momentum-integral method with the results adjusted inside the uncertainty interval to obtain similarity in the sublayer region ($y^+ < 15$) in u^+, y^+ coordinates.

The first estimates of $c_f/2$ were determined by evaluating the terms of equation (1) at each of four stations inside the constant K region: Note that the most difficult term to evaluate, $d\mathrm{Re}_M/d\mathrm{R}_x$ is nearly zero for the runs reported here (it would be identically zero for a perfectly asymptotic flow). Data from each of the four profiles were then reduced to u^+, y^+ coordinates using the momentum-based values of $c_f/2$ and compared with the laminar-sublayer-equation predictions for the same conditions of blowing and acceleration. A single sublayer prediction was judged appropriate for each run, covering four profiles, since the sublayer equations, equations (3) and (4), are not highly sensitive to the value of $c_f/2$ and the momentum-based values of $c_f/2$ did not vary much along the acceleration region

$$u^+ = \frac{1}{v_w{}^+}\left(1 + \frac{P^+}{v_w{}^+}\right)[\exp(v_w{}^+ y^+) - 1] - P^+ y^+ \qquad (3)$$

$$\text{for} \quad v_w{}^+ \neq 0.0$$

and

$$u^+ = y^+\left[1 + \frac{P^+ y^+}{2}\right] \qquad (4)$$

$$\text{for} \quad v_w{}^+ = 0.0$$

These equations result from integration of the x-momentum equation of the boundary layer, neglecting x-derivatives of velocity and turbulent shear stresses.

In general, the profile data fell close to the sublayer prediction inside y^+ of 15, although not exactly on the curve. Part of the difference was attributed to random uncertainties in the momentum-based friction factor and part to the systematic effect of

Table 1

Run No. 73068

$x = 45.64$ in $U_\infty = 48.7$ ft/sec $Re_M = 775$

$c_f/2 = 0.00248$ $v_w/U_\infty = 0.0$ $K = 1.45 \times 10^{-6}$

$v_w^+ = 0.0$ $P^+ = -0.01172$ $\delta = 0.430$ in

y/δ	u/U_∞	y^+	u^+
0.0163	0.409	8.66	8.22
0.0186	0.440	9.89	8.84
0.0209	0.479	11.1	9.63
0.0233	0.523	12.4	10.5
0.0279	0.566	14.8	11.4
0.0326	0.612	17.3	12.3
0.0419	0.671	22.3	13.5
0.0466	0.691	24.7	13.9
0.0535	0.714	28.4	14.3
0.0675	0.748	35.9	15.0
0.0768	0.765	40.8	15.4
0.0931	0.787	49.5	15.8
0.116	0.809	61.8	16.3
0.144	0.830	76.7	16.7
0.175	0.847	92.7	17.0
0.268	0.890	142.2	17.9
0.326	0.909	173.1	18.3
0.466	0.941	247.3	18.9
0.559	0.954	296.8	19.2
0.640	0.964	340.1	19.4
0.757	0.974	401.9	19.6
0.873	0.981	463.7	19.7
1.11	0.994	587.4	20.0
1.34	0.999	711.0	20.1
1.45	1.000	772.9	20.1

Run No. 51468

$x = 77.79$ in $U_\infty = 78.2$ ft/sec $Re_M = 1674$

$c_f/2 = 0.00219$ $v_w/U_\infty = 0.0$ $K = 0.586 \times 10^{-6}$

$v_w^+ = 0.0$ $P^+ = -0.00571$ $\delta = 0.588$ in

y/δ	u/U_∞	y^+	u^+
0.0102	0.455	11.3	9.7
0.0119	0.505	13.2	10.8
0.0136	0.547	15.0	11.7
0.0187	0.614	20.7	13.1
0.0204	0.628	22.5	13.4
0.0221	0.642	24.4	13.7
0.0255	0.660	28.2	14.1
0.0323	0.687	35.7	14.7
0.0391	0.704	43.2	15.0
0.0459	0.719	50.7	15.4
0.0578	0.738	63.9	15.8
0.0714	0.757	78.9	16.2
0.0799	0.768	88.3	16.4
0.102	0.792	112.7	16.9
0.133	0.818	146.5	17.5
0.170	0.845	187.8	18.0
0.219	0.873	242.3	18.6
0.272	0.894	300.5	19.1
0.335	0.915	370.0	19.5
0.412	0.933	454.5	19.9
0.548	0.959	604.7	20.5
0.718	0.975	792.5	20.8
0.999	0.990	1102.4	21.1
1.34	0.997	1478.0	21.3
1.68	1.000	1853.6	21.3

Run No. 80768

$x = 49.63$ in $U_\infty = 55.4$ ft/sec $Re_M = 353$

$c_f/2 = 0.00310$ $v_w/U_\infty = -0.00205$ $K = 1.51 \times 10^{-6}$

$v_w^+ = -0.0368$ $P^+ = -0.00874$ $\delta = 0.243$

y/δ	u/U_∞	y^+	u^+
0.0268	0.456	10.2	8.19
0.0309	0.499	11.8	8.95
0.0350	0.540	13.4	9.69
0.0391	0.603	15.0	10.8
0.0433	0.637	16.6	11.4
0.0474	0.667	18.1	12.0
0.0515	0.691	19.7	12.4
0.0596	0.716	21.3	12.9
0.0597	0.734	22.9	13.2
0.0680	0.772	26.0	13.9
0.0762	0.800	29.2	14.4
0.0845	0.820	32.3	14.7
0.0968	0.847	37.0	15.2
0.102	0.867	41.8	15.6
0.126	0.888	48.1	15.9
0.146	0.905	55.9	16.3
0.175	0.921	67.0	16.5
0.241	0.941	92.2	16.9
0.344	0.956	131.6	17.2
0.488	0.969	186.7	17.4
0.694	0.981	265.5	17.6
1.00	0.990	383.6	17.8
1.31	0.996	501.8	17.9
1.62	0.999	619.9	17.9
1.93	1.000	738.1	18.0

Run No. 52868

$x = 85.79$ $U_\infty = 91.4$ ft/sec $Re_M = 734$

$c_f/2 = 0.00302$ $v_w/U_\infty = -0.00204$ $K = 0.573 \times 10^{-6}$

$v_w^+ = -0.0370$ $P^+ = -0.00345$ $\delta = 0.257$ in

y/δ	u/U_∞	y^+	u^+
0.0233	0.595	15.3	10.8
0.0272	0.647	17.8	11.8
0.0311	0.687	20.3	12.5
0.0350	0.718	22.9	13.1
0.0389	0.739	25.4	13.4
0.0466	0.766	30.5	13.9
0.0622	0.799	40.7	14.5
0.0894	0.829	58.5	15.1
0.113	0.846	73.7	15.4
0.144	0.863	94.1	15.7
0.183	0.881	119.5	16.0
0.229	0.899	150.0	16.4
0.330	0.929	216.2	16.9
0.389	0.942	254.3	17.1
0.459	0.954	300.1	17.3
0.540	0.965	353.5	17.6
0.637	0.973	417.1	17.7
0.750	0.981	490.8	17.8
0.875	0.987	572.2	18.0
1.01	0.990	661.2	18.0
1.17	0.993	762.9	18.1
1.55	0.997	1017.2	18.2
2.33	1.000	1525.8	18.2

Run No. 41268

$x = 77.79$ in $U_\infty = 77.0$ ft/sec $Re_M = 3720$

$c_f/2 = 0.00107$ $v_w/U_\infty = 0.00403$ $K = 0.586 \times 10^{-6}$

$v_w^+ = 0.1236$ $P^+ = -0.01687$ $\delta = 1.06$ in

y/δ	u/U_∞	y^+	u^+
0.0057	0.293	7.54	8.98
0.0066	0.316	8.79	9.68
0.0075	0.339	10.05	10.39
0.0094	0.389	12.6	11.9
0.0104	0.409	13.8	12.5
0.0170	0.485	22.8	14.9
0.0236	0.523	31.4	16.0
0.0340	0.563	45.2	17.3
0.0528	0.614	70.4	18.8
0.0651	0.639	86.7	19.6
0.0859	0.678	114.3	20.8
0.105	0.706	139.4	21.6
0.129	0.736	172.1	22.6
0.155	0.763	206.0	23.4
0.183	0.790	243.7	24.2
0.216	0.814	287.7	24.9
0.259	0.840	344.2	25.7
0.306	0.863	407.0	26.5
0.372	0.890	495.0	27.3
0.443	0.913	589.2	28.0
0.537	0.934	714.8	28.6
0.678	0.958	903.2	29.4
0.867	0.980	1154.5	30.0
1.06	0.993	1405.7	30.4
1.43	1.000	1908.2	30.6

Run No. 82068

$x = 49.52$ in $U_\infty = 57.0$ ft/sec $Re_M = 1588$

$c_f/2 = 0.00145$ $v_w/U_\infty = 0.00406$ $K = 1.44 \times 10^{-6}$

$v_w^+ = 0.1066$ $P^+ = -0.02597$ $\delta = 0.606$ in

y/δ	u/U_∞	y^+	u^+
0.0099	0.323	6.65	8.48
0.0132	0.395	8.87	10.38
0.0165	0.456	11.1	12.0
0.0215	0.499	14.4	13.1
0.0264	0.535	17.7	14.0
0.0446	0.606	29.9	15.9
0.0611	0.647	41.0	17.0
0.0776	0.676	52.1	17.7
0.102	0.711	68.7	18.6
0.127	0.739	85.4	19.4
0.152	0.764	102.0	20.0
0.185	0.791	124.2	20.7
0.218	0.814	146.3	21.4
0.251	0.833	168.5	21.8
0.292	0.855	196.2	22.4
0.342	0.878	229.5	23.0
0.391	0.897	262.7	23.5
0.457	0.917	307.1	24.1
0.540	0.936	362.5	24.6
0.622	0.951	417.9	25.0
0.746	0.969	501.0	25.4
0.870	0.982	584.2	25.8
1.04	0.992	695.0	26.0
1.20	0.998	805.9	26.2
1.37	1.000	916.7	26.2

the velocity gradient on the apparent location of the pitot probe when near the wall. No attempt was made to evaluate wall-displacement effects on the probe readings. For each run, one or more reference profiles were selected and their $c_f/2$ values fixed exactly at the momentum-based value. Values of $c_f/2$ for the other profiles were then adjusted to force coincidence with these reference profiles in the sublayer region. This is an attempt at removing the random component of the uncertainty in $c_f/2$ by smoothing the momentum-based results through the sublayer equation. It does not constitute a true sublayer method, since no effort was made to eliminate the effects of shear and wall proximity from the data. In all cases the $c_f/2$ values stayed within the calculated uncertainty intervals surrounding the original estimates of skin friction based on the momentum equation.

For the cases of no transpiration, and constant free-stream velocity, a further consideration was that the results should be consistent with the "law of the wall" established by Simpson [9] from measurements on the same apparatus:

$$u^+ = \frac{1}{0.44} \ln y^+ + 5.55 \tag{5}$$

The final skin-friction results for 58 out of 68 profiles fall within ± 10 percent of the results obtained from the momentum-integral method, and all of the profiles presented in this paper are within the ± 10 percent interval. Due to the degree of subjective interpretation involved, the velocity profiles are presented not only in terms of u^+ vs. y^+, but also in their original form, u/U_∞ vs. y/δ. The authors feel that the true values of $c_f/2$ cannot differ from the reported values by more than ± 10 percent if serious internal inconsistencies are not allowable.

Experimental Results

The experimental data consist of mean velocity profiles obtained in near-asymptotic boundary-layer flows where the pressure-gradient parameter K and blowing fraction F are maintained constant. Data are presented for two pressure gradients: $K = 0.57 \times 10^{-6}$ and 1.45×10^{-6}. For each pressure gradient, the conditions investigated cover a range of uniform blowing fractions from $F = -0.002$ to $+0.004$. A complete description of these data is presented by Julien [13] along with other data covering $K = 0.77 \times 10^{-6}$ and data for higher blowing fractions than reported here (up to $F = +0.006$). The data selected for presentation here are believed representative of the processes involved.

Selected data are summarized in Figs. 1–6 and are also presented in Table 1 for the convenience of those wishing quantitative values for comparison with predictions.

The velocity profiles are presented in wall coordinates (u^+ vs. y^+) in Figs. 1–6. For purposes of comparison, the "law of the wall," with constants proposed by Simpson [9], is also presented on each of the graphs. The profile obtained in the constant free-stream velocity approach region is presented along with the profiles obtained in the pressure-gradient region of the duct.

It is shown in Figs. 1 and 2 that, for the impermeable-wall case, $F = 0$, the inner regions of the boundary layer respond rapidly to the imposed pressure gradient and assume a unique distribution corresponding to a given value of K. Similar inner-region profiles

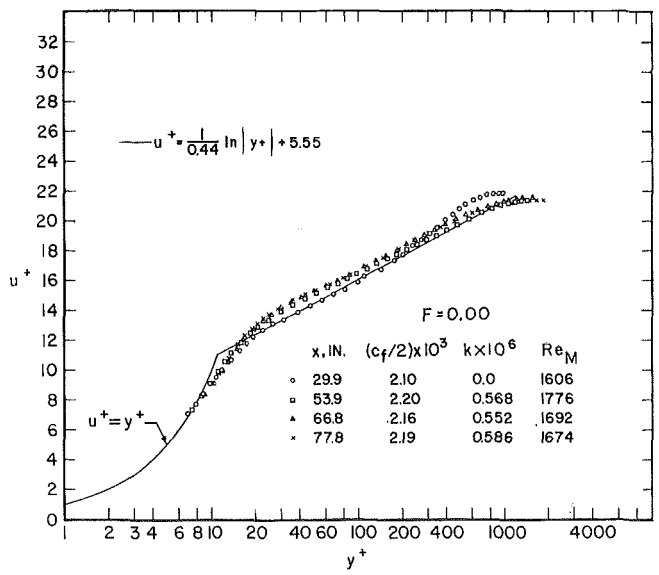

Fig. 1 Mean velocity profiles for $F = 0.000$ with $K = 0.57 \times 10^{-6}$

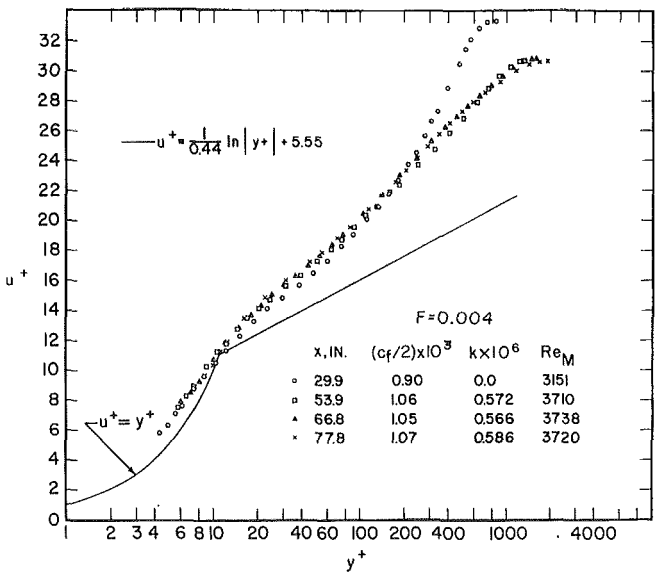

Fig. 3 Mean velocity profiles for $F = 0.004$ with $K = 0.57 \times 10^{-6}$

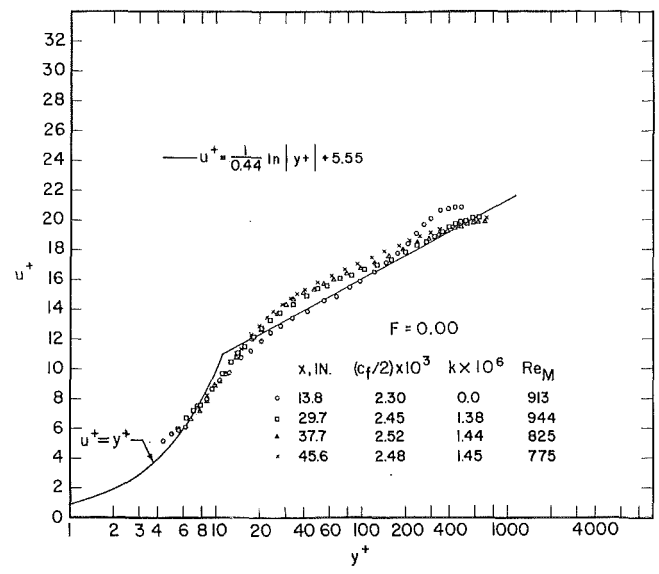

Fig. 2 Mean velocity profiles for $F = 0.000$ with $K = 1.45 \times 10^{-6}$

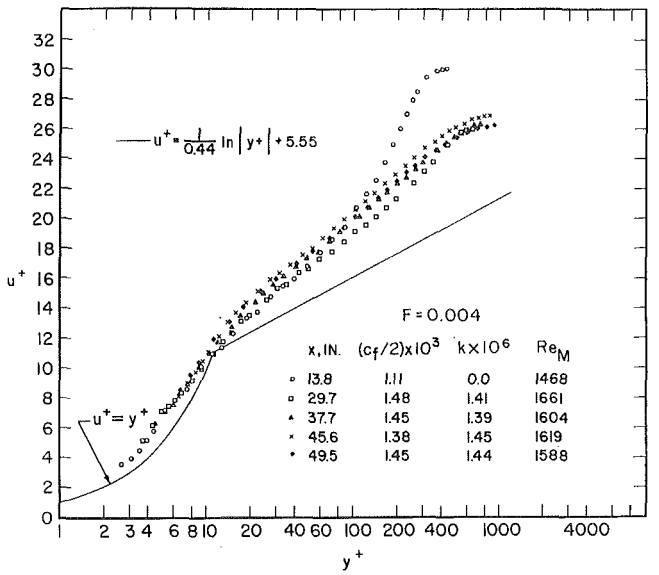

Fig. 4 Mean velocity profiles for $F = 0.004$ with $K = 1.45 \times 10^{-6}$

exist in asymptotic boundary-layer flows, and the shape of the profile is dependent upon the value of the local pressure-gradient parameter K.

Two characteristics of these impermeable-wall boundary-layer flows are shown in inner-region coordinates: (1) The profiles depart from the flat-plate "law of the wall" by an upward displacement in the logarithmic region, and (2) the wake region is substantially diminished. The degree of upward displacement in the logarithmic region increases with K. This behavior can be interpreted as an increase in the thickness of the "viscous-sublayer" region. The diminished wake is a direct result of the low shear stress in the outer regions of the layer, a characteristic associated with favorable pressure gradients.

In Figs. 3 and 4, similar effects of acceleration are shown to exist when there is blowing at the wall ($F = 0.004$). An upward displacement of the "logarithmic" region is noted, together with a reduction of the wake. The wake region shows a more substantial decrease than the unblown layer, indicating a greater increase in friction factor due to acceleration.

The boundary-layer flows in the case of suction at the wall, $F = -0.002$, are shown in Figs. 5 and 6. The upward displacement of the logarithmic region, relative to the sucked but unaccelerated layer, is now much more substantial, and the characteristic shape of a laminar profile (roundness of profile) is approached. It appears that a turbulent boundary layer is still obtained and is approaching an equilibrium state, but for the case in Fig. 6 laminarization is apparently closely approached.

In the outer regions of the boundary layer, similar profile development was attained for all blowing and sucking fractions considered [13]. This similarity is found in "velocity-defect coordinates" $\left(\frac{U_\infty - u}{u_\tau} \text{ vs. } y/\delta\right)$ as well as u/U_∞ vs. y/δ. The outer-region similarity, coupled with the similar conclusion relating to the inner regions, confirms the existence of completely similar profiles in asymptotic turbulent boundary layers.

Empirical Representation of the Data

The primary reason for obtaining and presenting data of the type discussed in this paper is to provide a basis for extending

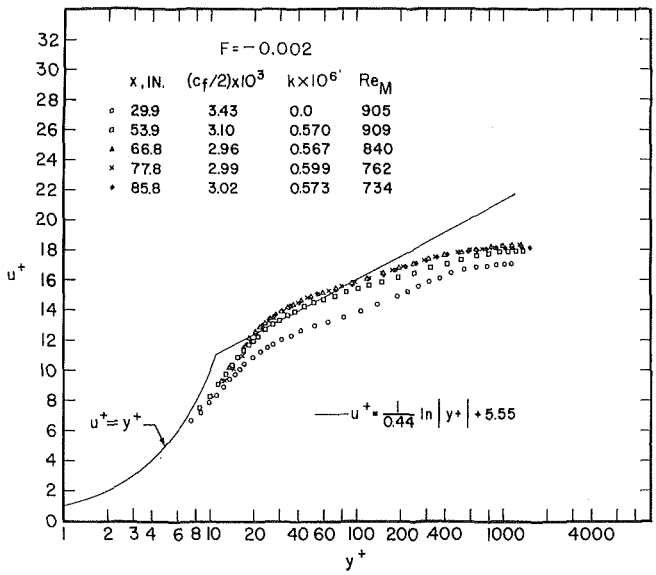

Fig. 5 Mean velocity profiles for $F = -0.002$ with $K = 0.57 \times 10^{-6}$

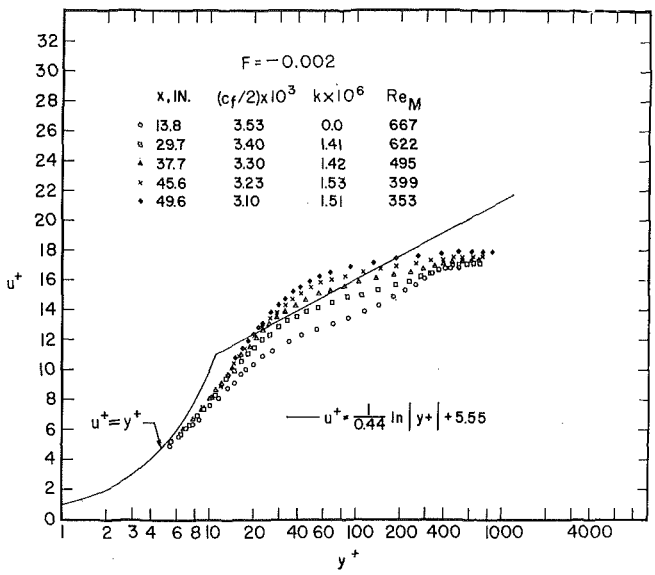

Fig. 6 Mean velocity profiles for $F = -0.002$ with $K = 1.45 \times 10^{-6}$

turbulent-boundary theory and thereby contributing to turbulent boundary-layer prediction methods. The velocity profiles and accompanying estimates of $c_f/2$ are presented in sufficient detail so that, hopefully, other workers can use the data as a proving ground for either existing or new theoretical models of the turbulent momentum-exchange process near a wall.

Although new theoretical models will undoubtedly be developed, the authors have found that all of the results presented here, together with the complete set of data on the transpired turbulent boundary layer with constant U_∞ presented by Simpson [9], can be quite adequately reproduced by a relatively simple mixing-length correlation.

The major influence of both transpiration and acceleration is evidently in the sublayer region. Acceleration apparently increases the effective sublayer thickness (in y^+ coordinates, not necessarily real distance), as does suction. A simple two-layer model of the boundary layer, with the laminar-sublayer thickness treated as a function of $v_w{}^+$ and P^+, and using elementary Prandtl mixing-length theory outside of the laminar sublayer, works remarkably well. However, for computational convenience, and perhaps esthetic reasons as well, the van Driest mixing-length hypothesis is more attractive, and will be used here as a method for correlating the results. No claim will be made regarding a theoretical basis for the van Driest hypothesis: it is merely providing a framework for an empirical correlation of experimental data. The scheme used is as follows.

The total shear stress is considered to consist of the sum of a laminar component and a turbulent component. The latter, τ_t, is calculated from the Prandtl mixing-theory equation,

$$\tau_t = \rho l^2 \left|\frac{\partial u}{\partial y}\right| \frac{\partial u}{\partial y} \tag{6}$$

Equation (6) is used all the way to the wall, and the mixing length, l, is assumed to vary from zero at the wall to ky farther out, according to the following relation.

$$l = ky\left[1 - \exp\left(\frac{-y^+\sqrt{\tau^+}}{A^+}\right)\right] \tag{7}$$

A^+ is an empirical constant to which van Driest [17] originally assigned a value 26. It is essentially an effective laminar-sublayer thickness. The argument of the exponential is frequently expressed as simply $-y^+/A^+$; the product $y^+\sqrt{\tau^+}$ is the *local* value of y^+ rather than the value based on wall shear stress. This alteration has been used by numerous workers because it has the effect of diminishing the sublayer region for blowing, and increasing it for acceleration; in fact, it provides all of the trends of behavior observed. $y^+\sqrt{\tau^+}$ is also approximately proportional to the "local Reynolds number of turbulence" which perhaps provides a further explanation of the significance of A^+. However, despite the fact that evaluation of y^+ at the *local* shear stress (i.e., $y^+\sqrt{\tau^+}$) gives the right trends, the experimental data indicate that a still stronger effect is needed for both transpiration and acceleration. Thus the empirical correlation to which we have been referring is a correlation of A^+ as a function of $v_w{}^+$ and P^+.

It should be further noted that equation (7) is only expected to apply in the region of the boundary layer near the wall, and not in the "wake" region. The latter is quite adequately handled, at least for equilibrium boundary layers, by a method to be described later.

In order to evaluate A^+ from experimental velocity profiles it is first necessary to determine τ^+. For asymptotic accelerating boundary layers the similarity of velocity profiles leads to

$$\tau^+ = 1 + U^+v_w{}^+ + P^+y^+\left[1 - \frac{1}{y}\int_0^y \left(\frac{u}{U_\infty}\right)^2 dy\right] \tag{8}$$

Equations (6)–(8) were used to solve for the values of A^+ necessary to predict the experimental velocity profiles in the region far enough from the wall so that the flow was essentially fully turbulent, but not so far that the wake was included. Essentially this involved matching at about $y^+ = 100$, although this also resulted in a good match over virtually the entire inner region.

The resulting values of A^+ are presented in Table 2 as functions of P^+ and $v_w{}^+$.

A^+ was also extracted from the data of Simpson [9], obtained on the same apparatus for a wide range of transpiration with constant U_∞. Simpson's results can be adequately represented by

$$A^+ = \begin{cases} 26.0 - 88.0v_w{}^+ + 210.0(v_w{}^+)^2 & v_w{}^+ \leq 0 \\ 26.0 - 88.0v_w{}^+ + 110.0(v_w{}^+)^2 & v_w{}^+ \geq 0 \end{cases} \tag{9}$$

A simpler alternative expression which fits Simpson's results nearly as well is

$$A^+ = \frac{4.42}{(v_w{}^+ + 0.17)} \qquad \text{(for all } v_w{}^+\text{)} \tag{9a}$$

Table 2 van Driest damping function A^+

$F \times 10^3$	$K \times 10^6$	$v_w{}^+$	P^+	A^+
0.0	0.552	0.0	−0.00549	33.4
0.0	0.758	0.0	−0.00649	33.5
0.0	1.45	0.0	−0.01137	38.0
1.01	0.613	0.02358	−0.00781	31.0
1.00	0.806	0.02296	−0.00966	32.5
0.99	1.42	0.02071	−0.01293	31.0
1.95	0.557	0.04906	−0.00885	26.5
1.94	0.753	0.04699	−0.01062	27.0
2.04	1.48	0.04571	−0.01658	28.5
3.95	0.566	0.12201	−0.01662	22.0
3.83	0.771	0.11157	−0.01913	23.0
4.06	1.44	0.10661	−0.02597	26.5
6.05	0.793	0.20619	−0.03147	18.0
5.87	1.45	0.17974	−0.04175	22.0
−1.01	0.594	−0.02019	−0.00473	39.5
−2.01	0.599	−0.03690	−0.00367	45.8

An empirical correlation of A^+ as a function of both $v_w{}^+$ and P^+ that will satisfy both equation (9*a*) and the data in Table 2 can obviously also be developed. (Note that for asymptotic accelerating boundary layers P^+ is a unique function of the acceleration parameter K.)

Analysis of the profiles in the wake region for both the present results for asymptotic accelerations, and Simpson's results, indicates that a constant mixing length is an adequate approximation. This scheme has been used extensively in the past; it works particularly well for accelerated flows simply because the shear stress is so low in the wake that high accuracy is not needed.

The wake correlation derived from the present (and Simpson's) results is:

$$\text{for} \quad y/\delta > \lambda/k \qquad l = \lambda\delta \tag{10}$$

where

$$\lambda = 0.25\ \mathrm{Re}_M{}^{-0.125}[1 - 67.5F] \quad \text{for} \quad \lambda > 0.085$$

and

$$\lambda = 0.085 \quad \text{otherwise.}$$

For $y/\delta < \lambda/k$ equation (7) is to be used.

Equations (6)–(11), when used in a finite-difference turbulent boundary-layer prediction program, and employing the A^+ data of Table 2, will reproduce very adequately all of the experimental data presented in this paper, and by Simpson [9].

A solid theoretical basis for the $A^+(v_w{}^+, P^+)$ relationship has yet to be developed, and for this reason the authors have hesitated to suggest complete empirical equations. Furthermore, it is by no means clear that the van Driest exponential damping function using the local shear stress, see equation (7), is the best way of dealing with this problem. More data at higher values of P^+ and $v_w{}^+$ will soon be available and it should then be possible to do a more nearly definitive job. In the meantime it is hoped that other investigators will be encouraged to use the data of this paper for comparison with their theories.

Summary and Conclusions

1 Experimental mean velocity-profile data have been presented for constant K accelerated turbulent boundary layers with and without transpiration. Skin-friction results are included along with shape factors and Reynolds numbers.

2 It is demonstrated that an acceleration at constant K with transpiration leads to an asymptotic boundary layer having inner and outer similarity and constant $c_f/2$, H, and Re_M.

3 Acceleration apparently causes an increase in the thickness of the viscous sublayer. Blowing opposes this effect, while suction enhances it. It seems evident that strong acceleration and/or strong suction will lead to a complete laminarization of the boundary layer, but neither the acceleration nor the suction were carried this far in the present experiments.

4 An empirical correlation of the data is presented in the form of a tabular correlation of the damping constant A^+ in the van Driest mixing-length hypothesis.

Acknowledgment

This work was supported by the National Aeronautics and Space Administration, Grant NGR-05-020-134. The authors would particularly like to thank Mr. Robert W. Graham of Lewis Research Center for his interest.

References

1 Romanenko, P. N., and Kharchenko, V. N., "The Effects of Transverse Mass Flow on Heat Transfer and Friction Drag in a Turbulent Flow of a Compressible Gas Along an Arbitrarily Shaped Surface," *International Journal of Heat and Mass Transfer*, Vol. 6, No. 8, 1963, pp. 727–738.

2 McQuaid, J., "Incompressible Turbulent Boundary Layers with Distributed Injection," PhD thesis, Cambridge University, 1966.

3 Stevenson, T. N., "A Law of the Wall for Turbulent Boundary Layers with Suction or Injection," Cranfield College of Aero. Report 166, 1963.

4 Launder, B. E., and Stinchcombe, H. S., "Non-Normal Similar Turbulent Boundary Layers," TEF/TN21, Mechanical Engineering Department, Imperial College, London, 1967.

5 Launder, B. E., and Jones, W. P., "On the Prediction of Laminarization," Mechanical Engineering Department, Imperial College, London, 1968.

6 Kline, S. J., Reynolds, W. C., Schraub, F. A., and Runstadler, P. W., "The Structure of Turbulent Boundary Layers," *Journal of Fluid Mechanics*, Vol. 30, Part 4, 1967, p. 741.

7 Badri Narayanan, M. A., and Ramjee, V., "On the Criteria for Reverse Transition in a Two-Dimensional Boundary Layer Flow," Report No. AE 68 FM 1, Department of Aeronautical Engineering, Indian Institute of Science, 1968.

8 Patel, V. C., and Head, M. R., "Reversion of Turbulent to Laminar Flow," *Journal of Fluid Mechanics*, Vol. 34, Part 2, 1968, p. 371.

9 Simpson, R. L., "The Turbulent Boundary Layer on a Porous Plate: An Experimental Study of the Fluid Dynamics with Injection and Suction," PhD thesis, Thermosciences Division, Department of Mechanical Engineering, Stanford University, 1967; available from University Microfilms, Ann Arbor, Mich.

10 Moffat, R. J., "The Turbulent Boundary Layer on a Porous Plate: Experimental Heat Transfer with Uniform Blowing and Suction," PhD thesis, Thermosciences Division, Department of Mechanical Engineering, Stanford University, 1967; available from University Microfilms, Ann Arbor, Mich.

11 Moffat, R. J., and Kays, W. M., "The Turbulent Boundary Layer on a Porous Plate: Experimental Heat Transfer with Uniform Blowing and Suction," *International Journal of Heat and Mass Transfer*, Vol. 11, No. 10, 1968, pp. 1547–1566.

12 Simpson, R. L., Moffat, R. J., and Kays, W. M., "The Turbulent Boundary Layer on a Porous Plate: Experimental Skin Friction with Variable Injection and Suction," *International Journal of Heat and Mass Transfer*, Vol. 12, 1969, pp. 771–789.

13 Julien, H. L., "The Turbulent Boundary Layer on a Porous Plate: Experimental Study of the Effects of a Favorable Pressure Gradient," PhD thesis, Thermosciences Division, Department of Mechanical Engineering, Stanford University, 1969; available from University Microfilms, Ann Arbor, Mich.

14 Coles, D. E., "The Turbulent Boundary Layer in a Compressible Fluid," RAND Report R-403-PR, 1962.

15 Thielbahr, W. H., "The Turbulent Boundary Layer: Experimental Heat Transfer with Uniform Blowing, Suction and Favorable Pressure Gradients," PhD thesis, Department of Mechanical Engineering, Stanford University, 1969; available from University Microfilms, Ann Arbor, Mich.

16 Kline, S. J., and McClintock, F. A., "Describing Uncertainties in Single-Sample Experiments," *Mechanical Engineering*, Vol. 75, No. 1, Jan. 1953, pp. 3–8.

17 van Driest, E. R., "On Turbulent Flow Near a Wall," *Journal of Aeronautical Science*, Vol. 23, 1956, p. 1007.

C. A. DEPEW
Associate Professor,
Department of Mechanical Engineering,
University of Washington,
Seattle, Wash.
Mem. ASME

S. E. AUGUST[1]
Humble Pipe Line Co.,
Houston, Texas

Heat Transfer Due to Combined Free and Forced Convection in a Horizontal and Isothermal Tube

The influence of natural convection due to buoyancy has been studied both experimentally and analytically for many cases, but the existing correlations are not accurate for horizontal, isothermal tube flow when the heated length is relatively short. The research reported in this paper was undertaken to alleviate this shortcoming by deriving a correlation to include new experimental data on a tube with $L/D = 28.4$. The experimental data from this and other investigations represents a variety of fluids, heating and cooling, and various apparatus and conditions. The equation which correlates the present and previous data to within ±40 percent is

$$\mathrm{Nu}_a \left(\frac{\mu_w}{\mu_b}\right)^{0.14} = 1.75[\mathrm{Gz} + 0.12(\mathrm{Gz}\ \mathrm{Gr}^{1/3}\mathrm{Pr}^{0.36})^{0.88}]^{1/3}$$

Introduction

The influence of buoyancy forces on convection heat transfer through its effect on fluid motions may be significant for pressure-induced horizontal flows when other forces are not dominant. When the wall is maintained at a uniform temperature, the influence is generally less than when a uniform heat flux is imposed; however, the uniform wall temperature case more closely approximates the majority of industrial applications. At the onset of heating or cooling, the wall to fluid temperature difference is large, but since no fluid thermal profile has developed, there is no net buoyant force. As the flow proceeds down the pipe, a temperature profile develops, and the flow near the wall becomes buoyant producing a secondary circulation. But the process is self-diminishing, since the secondary flow accelerates the approach of the fluid to the wall temperature through enhancement of the convection process. Based on this physical description, it is reasonable to expect that the tube length would have some bearing on the heat transfer performance.

It was during the study of the effect of freezing at the wall [1][2] that the inadequacy of information on short-tube performance first came to the authors' attention. It was shown in this publication that the error in Oliver's correlation [2] was very much dependent on the tube length. Indeed, Oliver warns against placing too much confidence in the L/D dependence of his equation. The research which is being reported herein was initiated to extend the range of application of the existing correlations to include shorter tubes.

Although the heat transfer problem in the vertical orientation is amenable to mathematical treatment due to its inherent symmetry, a measure of success in treating the problem in the horizontal mode has been attained only through the correlation of experimental data. The pertinent modeling laws can be elicited through dimensional analysis or nondimensionalization of the descriptive partial differential equations, and these groups were recognized by the early investigators. The pioneering work of Colburn [3] was modified by the addition of the viscosity ratio factor by Sieder and Tate [4] to read as follows:

$$\mathrm{Nu}_a = 1.75 \left(\frac{\mu_b}{\mu_w}\right)^{0.14} \mathrm{Gz}^{1/3}[1 + 0.01\mathrm{Gr}^{1/3}] \qquad (1)$$

The inclusion of the viscosity ratio rendered the equation more useful since the physical properties were then evaluated at the bulk fluid temperature rather than at the film temperature. A number of years later, Kern and Othmer [5] determined that the function $(\log \mathrm{Re})^{-1}$ as a multiplying factor to the natural convection term produced an improved correlation for their data as well as for others. But it was Eubank and Proctor [6] who first presented the combined Nusselt number correlation in a form that is currently used

$$\mathrm{Nu}_a = 1.75 \left(\frac{\mu_b}{\mu_w}\right)^{0.14} \left[\mathrm{Gz} + 12.6 \left(\frac{\mathrm{Gr\ Pr}\ D}{L}\right)^{0.40}\right]^{1/3} \qquad (2)$$

---

[1] Formerly Research Assistant, College of Engineering, University of Washington, Seattle, Wash.

[2] Numbers in brackets designate References at end of paper.

Contributed by the Heat Transfer Division and presented at the ASME-AIChE Heat Transfer Conference, Tulsa, Okla., August 15–18, 1971. Manuscript received by the Heat Transfer Division October 16, 1970. Paper No. 71-HT-3.

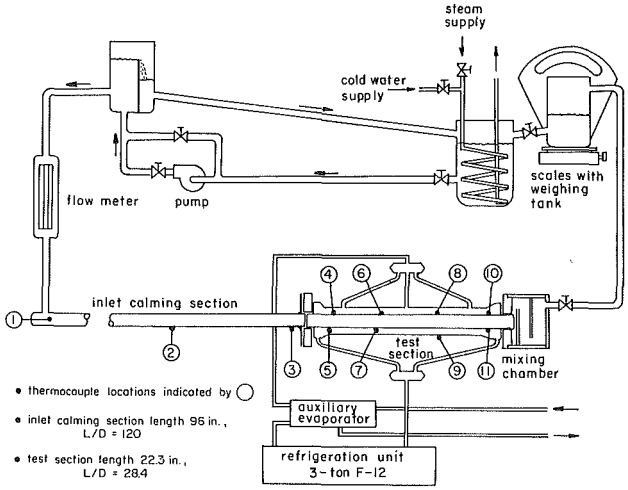

Fig. 1 Experimental apparatus

where Gr is based on the mean bulk to wall temperature difference and all properties are based on the mean bulk fluid temperature with the exception of those in the viscosity ratio term. They took their lead from Martinelli and Boelter's theoretical analysis [7] which was applicable to heating and cooling of flow up or down vertical tubes. The maximum deviation of their data from the values predicted by this equation are +43 percent and −32 percent with the majority of the values lying well within ±25 percent. Jackson, Spurlock, and Purdy [8] reported on their work with air, and they produced an equation which is similar in form to (2), but with more emphasis on the mass flow rate and with D and L absent in explicit form. The work is not directly applicable to the present problem since the heated section was without a flow development section. Oliver [2] presents a lucid account of the combined free and forced convection problem, and he shows the development of an improved correlation based on his own and others' data:

$$\mathrm{Nu}_a = 1.75 \left(\frac{\mu_b}{\mu_w}\right)^{0.14} \left[\mathrm{Gz} + 5.6 \times 10^{-4} \left(\frac{\mathrm{Gr\ Pr}\ L}{D}\right)^{0.70}\right]^{1/3} \tag{3}$$

An interesting feature of this equation is that the free convection component has the D/L term inverted from equation (2). Oliver made an effort to examine this point, but he concluded that the data were too widely scattered when plotted versus L/D to quantitatively define the importance of the term. He cautions that the power of the L/D term must be considered provisional. Experiments were performed with water, ethyl alcohol, and a glycerol–water mixture in a tube with $L/D = 72$. Equation (3) represents the data to −25, + 110 percent.

Brown and Thomas [9] gathered further data with water using tube sizes with $L/D = 36$, 72, and 108. They show convincingly that neither Gr Pr L/D nor Gr Pr D/L adequately represent the data for these sizes, and that the deviation becomes largest with the smallest value of L/D. Brown and Thomas discuss the idea that mass flow rate has a more significant influence on the free convection term than L/D, and it appears reasonable that high mass flow rates may have an effect similar to short tubes. Based on physical arguments they conclude that the basic equation should have the form

$$\mathrm{Nu} \left(\frac{\mu_w}{\mu_b}\right)^{0.14} = 1.75\ [\mathrm{Gz} + \text{function (Gz Gr)}]^{1/3} \tag{4}$$

The final correlation advanced is

$$\mathrm{Nu} = 1.75 \left(\frac{\mu_b}{\mu_w}\right)^{0.14} [\mathrm{Gz} + 0.012(\mathrm{Gz\ Gr}^{1/3})^{4/3}]^{1/3} \tag{5}$$

The equation correlates the water results of the authors to within ±8 percent and the majority of the published data to within ±50 percent.

Experiment

Apparatus. The apparatus, shown diagrammatically in Fig. 1, consisted of a test liquid loop and a Freon-12 loop. Cooling of the test liquid in the test section was accomplished by boiling of the refrigerant in the annular space around the test section. Refrigeration was provided by a 3-ton unit which was controlled by an auxiliary evaporator. Flow of the test fluid was controlled by the elevation of a constant-head tank and its temperature at the test section entrance was controlled by exchanging heat through a coil of copper tubing with a steam–water mixture in the location shown. The flow development section was 96 diameters long and its entire length was wrapped with fiberglass batt insulation. Temperature uniformity and constancy was indicated by three thermocouples attached to the wall along the length of the approach tube. Lucite spacers at the inlet and outlet furnished smooth transition between the calming section and the test section and the mixing chamber, while thermally insulating them and providing for tube alignment.

Nomenclature

c = specific heat of liquid (Btu/lb-deg F)
D = inside diameter of tube (ft)
F_1 = correction factor in equation (8) allows for arithmetic mean rather than logarithmic mean temperature differences
g = acceleration due to gravity (ft/sec²)
h = heat transfer coefficient (Btu/hr-ft²-deg F)
k = thermal conductivity (Btu/hr-ft-deg F)
L = length of tube (ft)
$\dot{m}$ = mass flow rate (lb/min)
T = temperature (deg F)
ΔT = temperature difference, giving rise to free convection, $T_b - T_w$ (deg F)
β = coefficient of expansion of fluid (1/deg F)
ρ = density of fluid (lb/ft³)
μ = dynamic viscosity (lb/ft-sec)

Subscripts

b = refers to average bulk temperature
i = refers to inlet temperature
o = refers to outlet temperature
w = refers to wall temperature

Dimensionless groups (all physical properties evaluated at the average bulk fluid temperature)

Re = Reynolds number $= \dfrac{4\dot{m}}{\pi D \mu}$

Nu_a = Nusselt number $= \dfrac{hD}{k}$ (based on arithmetic mean temperature difference)

Pr = Prandtl number $= \dfrac{c\mu}{k}$

Gz = Graetz number $= \dfrac{\dot{m}c}{kL}$

Gr = Grashof number $= \dfrac{\beta \Delta T D^3 \rho^2 g}{\mu^2}$

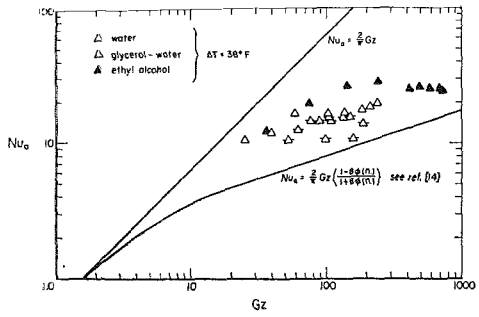

Fig. 2 Experimental results

Table 1 Test results for water

Run No.	T_i	T_o	T_w	$\dot{m}$	Pr	Nu_a	Gz	$Grx10^{-5}$
1	67.0	54.1	48.3	.27	7.96	8.46	25	.702
2	66.3	55.0	48.2	.45	7.95	12.33	42	.718
3	65.9	58.2	48.1	.84	7.74	12.77	79	.910
4	66.1	61.8	48.0	1.55	7.53	12.52	146	1.13
5	65.9	62.0	47.7	1.90	7.53	13.67	178	1.15
6	66.1	63.0	48.6	2.25	7.45	13.09	211	1.17
7	65.7	63.2	47.8	2.89	7.47	12.99	271	1.21
8	65.9	63.6	47.9	3.60	7.43	14.70	338	1.25
9	85.8	55.8	48.0	.27	6.76	10.55	25	2.37
10	86.7	59.6	48.5	.38	6.53	12.15	34	2.88
11	86.7	62.3	47.6	.64	6.40	17.04	59	3.36
12	86.7	70.8	47.9	1.11	6.01	16.70	101	4.70
13	86.7	74.6	48.8	1.51	5.86	16.70	138	5.26
14	86.9	76.8	48.4	2.01	5.76	17.63	183	5.81
15	86.7	77.5	49.1	2.30	5.74	18.62	209	5.80
16	86.7	77.6	49.1	2.67	5.73	21.35	243	5.82

The test section itself, 22.3 in. long of $^3/_4$-in. hard-drawn copper, had an L/D ratio of 28.4. The outer tube which formed the annulus for the Freon-12 was $1^1/_4$-in-dia hard-drawn copper. Freon was admitted at the bottom near the ends, and vapor escaped through three equally spaced tubes on the top.

Primary measurements included the temperatures at 13 points and the test fluid flow rate. Copper–constantan thermocouples were used throughout with a strip-chart recorder having an accuracy of ±0.5 deg F. Flow rate was measured by collecting the outlet flow in a scale tank (the flow meter was used only to indicate steady conditions). Eight of the thermocouples were attached directly to the exterior of the test section; the temperature difference through the tube wall was negligible for all experimental conditions. The maximum variation of tube wall temperature for all test conditions was less than 3 deg F which was about 8 percent of the wall to average bulk fluid temperature difference. This variation in tube wall temperature is tolerable for the purposes of this work. The maximum variation in wall temperature was encountered for the maximum wall to fluid temperature difference which was 40 deg F. Most of the data were taken with the initial temperature difference either at 38 deg F or 18 deg F.

Three different liquids were used in this experiment: water, ethyl alcohol, and a mixture of glycerol and water. These fluids were selected for their availability and their considerable differences in physical properties which gave a broad range of natural convection effects. The ethyl alcohol was 95 percent pure by volume and undenatured, meeting U.S.P. standards for purity. Pure glycerol (glycerin) also meeting U.S.P. standards was thoroughly mixed with water in a proportion of 80 percent glycerol by weight for the glycerol–water solution. References [10–13] were used as sources of physical property data for this work. The apparatus was run with each of the fluids over a range of flow rates and temperatures such that the expected error from measurement was always less than 10 percent.

Results. Calculated Nusselt numbers were based on heat transfer coefficients derived from the bulk inlet and outlet temperatures, average bulk temperature, and the average wall temperature:

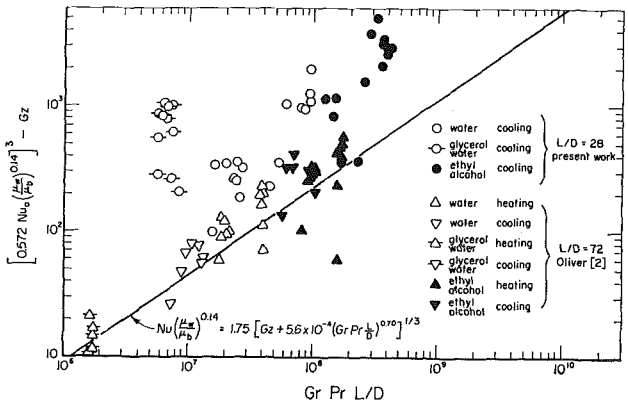

Fig. 3 Present and previous results plotted using Oliver's correlation

Table 2 Test results for ethyl alcohol

Run No.	T_i	T_o	T_w	$\dot{m}$	Pr	Nu_a	Gz	$Grx10^{-5}$
1	67.2	58.2	47.2	.60	16.05	18.21	98	2.68
2	67.2	63.1	47.6	1.39	15.85	17.34	233	3.20
3	67.2	64.2	47.5	1.67	15.79	14.74	280	3.37
4	67.2	64.1	47.3	2.16	15.79	19.53	363	3.39
5	84.5	57.8	46.1	.21	15.30	12.35	36	5.23
6	85.0	62.7	46.7	.43	15.04	19.71	75	6.04
7	84.8	67.5	46.4	.80	14.83	26.27	141	6.97
8	84.3	72.5	46.7	1.35	14.63	28.84	243	7.82
9	84.1	77.5	46.4	2.26	14.41	25.22	412	8.97
10	84.5	78.8	47.1	2.70	14.36	26.06	496	9.18
11	85.0	80.2	47.0	3.17	14.28	25.13	585	9.66
12	84.7	80.6	47.1	3.74	14.27	25.37	691	9.66
13	85.0	81.1	46.9	3.85	14.23	24.48	712	9.91

Table 3 Test results for glycerol–water

Run No.	T_i	T_o	T_w	$\dot{m}$	Pr	Nu_a	Gz	$Grx10^{-2}$
1	86.7	75.9	49.4	.86	350	10.61	98.4	7.32
2	86.7	79.4	48.6	1.35	328	10.47	155.2	8.99
3	86.7	69.8	51.1	.46	388	10.52	53.1	5.10
4	86.7	69.2	50.6	.55	391	12.93	63.5	5.05
5	86.7	70.0	50.7	.68	387	14.91	77.5	5.22
6	86.5	71.5	50.0	.77	380	14.65	89.0	5.68
7	86.7	72.6	49.9	.91	371	15.81	104.8	6.09
8	86.3	73.7	50.0	.95	367	14.61	109.3	6.29
9	86.0	74.6	49.6	1.15	363	15.60	132.0	6.57
10	86.3	76.4	49.4	1.39	350	15.75	159.7	7.36
11	85.0	77.5	48.7	1.64	351	13.81	188.3	7.45

$$Nu_a = \frac{Gz}{\pi} \frac{T_i - T_o}{T_b - T_w} \tag{6}$$

The range of Graetz number was from 25 to 700, and the largest Reynolds number reached was 1800 with ethyl alcohol, although in most cases the value was much lower. The range of Grashof numbers covered for water and ethanol was 7.0×10^4 to 9.9×10^6, while the values for the more viscous glycerol–water mixture were considerably lower, 250 to 960. In all cases the physical properties were evaluated at the average bulk temperature. This scheme is consistent with the majority of the references surveyed, and it yields the most practical and useful correlation.

The results from this investigation for all three fluids with the initial temperature difference equal to 38 deg F are shown in Fig. 2 in comparison to the infinitely long tube value, $Nu = \frac{2}{\pi} Gz$, and the theoretical Graetz–Leveque curve. The effects of natural convection are obvious and it is apparent that the largest increase was incurred by the ethyl alcohol which also has the largest coefficient of expansion. Tabulated results are presented in Tables 1, 2, and 3.

Correlation and Discussion of Results

The objective of the investigation was to originate an improved equation to account for natural convection influence when the tube length is short compared to its diameter. Fig. 3 shows the

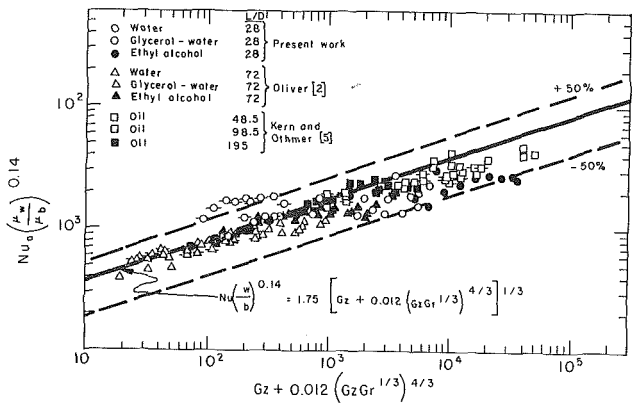

Fig. 4 Present and previous results plotted using Brown and Thomas' correlation

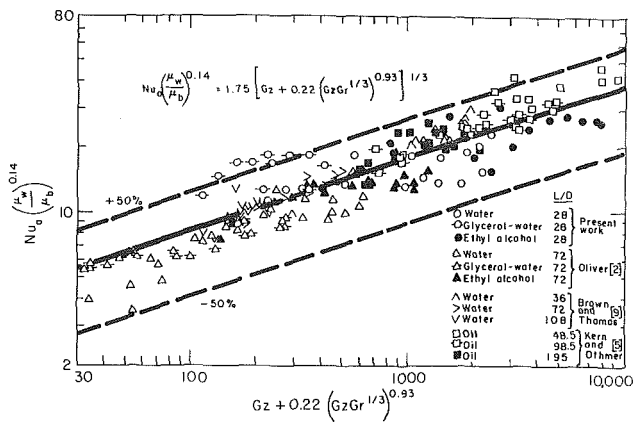

Fig. 5 Present and previous results plotted using equation (7)

Table 4 Data used in natural convection correlations

Workers	Fluid	Run Nos.	Tube Diam. (in.)	$\frac{L}{D}$	Gz	Gr
Oliver (2)	Water	41-64	0.50	72	10-114	1.0×10^4-1.1×10^5
	Ethyl Alcohol	20-40			24-172	4.9×10^4-1.6×10^5
	Glycerol-water	65-74, 83-89			20-176	2.9×10^1-6.4×10^1
Brown and Thomas (9)	Water	38-60	1.00	36	28-112	3.1×10^5-4.9×10^6
		10-19	0.50	72	27-41	7.1×10^4-8.9×10^5
		65-93	0.50	108	19-39	2.9×10^4-7.3×10^5
Kern and Othmer (5)	Oil	26,27,33-35, 73-77,97-101	2.47	48.5	108-440	3.2×10^4-1.9×10^7
		126-30,176-80, 191-95	1.20	99.5	205-428	2.7×10^3-1.8×10^6
		224-32,251-52, 263-65,269-71, 276	0.622	193	137-456	3.7×10^2-3.1×10^5

present results plotted using Oliver's technique, and it is clear that the Nusselt number is larger when L/D is smaller. Obviously, the term Gr Pr L/D has the incorrect geometry relationship. A plausible explanation for this phenomenon is the development of the temperature profile. Since the temperature gradient at the wall must fall with increasing distance along the tube, the gradient for a short tube will remain relatively steep for the entire length. Since the net buoyant force is dependent on the temperature gradient through the density gradient, it is reasonable to presume that a shorter tube will have relatively higher natural convection effects than a longer tube. An attempt to quantitatively assess the influence of L/D was made by plotting

$$\left\{\left[0.572\ \mathrm{Nu}\left(\frac{\mu_w}{\mu_b}\right)^{0.14}\right]^3 - \mathrm{Gz}\right\}\ (\mathrm{Gr\ Pr})^{-0.70}$$

versus L/D using the present data and those listed in Table 4. In spite of the considerable overall range of L/D (28.4 to 193) the scatter in the data was too large to warrant any conclusions except that no tendency existed for natural convection heat transfer to decrease with decreasing tube length, as suggested by equation (3).

Since agreement of the data is poor when compared to Oliver's equation and inconclusive when plotted versus L/D, Brown and Thomas' equation was considered next. These authors have concluded in their publication that the inclusion of neither L/D nor D/L was justified but that their own water data could be correlated to ±8 percent by introducing a mass flow rate influence into the natural convection term. The agreement between Brown and Thomas' equation and data from Table 4 is illustrated in Fig. 4, from which the data of Brown and Thomas have been omitted. An examination of the plot reveals that the Gz $Gr^{1/3}$ term brings the various data points into reasonable agreement but that the curve, though fitting the water data for which it was intended, does not agree well with the other experimental results. The points corresponding to the glycerol–water deviate considerably above the curve for low abscissa values, while most of the data for high abscissa values scatter below the line. In an attempt to improve the relationship equation (5) was used in the form

$$\left\{0.572\ \mathrm{Nu}\left(\frac{\mu_w}{\mu_b}\right)^{0.14}\right\}^3 - \mathrm{Gz} = A(\mathrm{Gz\ Gr}^{1/3})^B \qquad (7)$$

and linear regression analysis was used to determine the constants A and B. The results of this approach are shown in Fig. 5 using the values $A = 0.22$ and $B = 0.93$. This expression does bring many of the data points into better agreement but has a negligible effect on the points corresponding to the glycerol–water data for the present work. The error in $\mathrm{Nu}(\mu_w/\mu_b)^{0.14}$ exceeds +50 percent for several of these points.

Since the major difference in physical properties between glycerol–water and the other liquids is the viscosity, the next effort was to incorporate this influence more directly into the correlation. A correlation was derived using Gr as the independent variable, and this analysis showed that the exponent on Gr should be close to $1/5$ instead of $1/3$. However, the improvement over the previous equations was not profound, and further work was indicated.

Due to the suggested importance of viscosity, the Prandtl number was introduced into the free convection group as Gz $\mathrm{Gr}^{1/3}\mathrm{Pr}^n$. Its influence was evaluated by plotting

$$\left\{\left[0.572\ \mathrm{Nu}\left(\frac{\mu_w}{\mu_b}\right)^{0.14}\right]^3 - \mathrm{Gz}\right\}\ (\mathrm{Gz\ Gr}^{1/3})^{-0.93}$$

against Pr. The exponent n was determined to be 0.33. The remaining coefficients were determined as in equation (5), and the final result is

$$\mathrm{Nu}\left(\frac{\mu_w}{\mu_b}\right)^{0.14} = 1.75F_1[\mathrm{Gz} + 0.12(\mathrm{Gz\ Gr}^{1/3}\mathrm{Pr}^{0.36})^{0.88}]^{1/3} \qquad (8)$$

The correction factor, F_1, has been included in the final correlation to avoid the anomaly caused by the use of the arithmetic mean temperature difference. Without the use of the correction factor, calculated values of Nu_a are greater than the asymptote $\mathrm{Nu}_a = 2\mathrm{Gz}/\pi$ for low Gz. Tables of F_1 versus $\pi\mathrm{Nu}_a/\mathrm{Gz}$ can be found in references [2, 7].

The experimental data of this investigation as well as data produced by Oliver and Brown and Thomas are displayed in Fig. 6 using equation (8). This expression reduces the deviation of the glycerol–water data to approximately 40 percent while the scatter of the oil data points is also decreased. With the exception of 3 points, all of the data are represented to within ±40 percent by equation (8). The two best previous correlations relate the same data to within −100 percent + 45 percent (i.e., Oliver's) and −75 percent + 55 percent (Brown and Thomas').

The results from this investigation definitely show that the

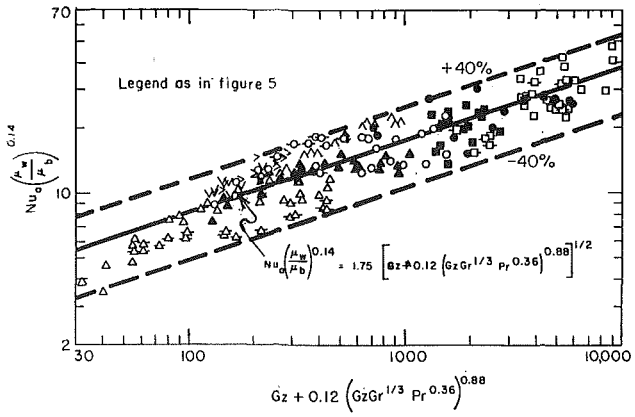

Fig. 6 Present and previous results plotted using equation (8)

presence of the term L/D in the free convection component of the heat transfer equation is inappropriate. Oliver criticized the use of the term D/L on the basis that it produced a fourth-power dependency in the diameter which places too much emphasis on D. The final correlation, equation (8), suggests that the D/L and L/D variables can be omitted from the natural convection function in spite of the fact that the correlation was based on data having a fivefold variation in D.

Conclusions

The present work shows that, when dealing with flows in horizontal tubes, the term Gr Pr L/D does not correctly represent the influence of natural convection for tubes with L/D ratios less than 50. The agreement in the experimental data achieved by equation (8) strongly suggests that the ratio L/D ceases to have significant influence and can be omitted from the natural convection function. Heat transfer data for various liquids can be correlated to within ±40 percent over a wide range of Grashof and Graetz numbers, D, and L by equation (8). The proposed correlation represents a significant improvement over previous equations.

Acknowledgments

Mr. August gratefully wishes to acknowledge the financial support of the College of Engineering, University of Washington, during the performance of the research presented in this paper.

References

1 Depew, C. A., and Zentner, R. C., "Laminar Flow Heat Transfer and Pressure Drop with Freezing at the Wall," *International Journal of Heat and Mass Transfer*, Vol. 12, No. 12, 1969, pp. 1710–1714.

2 Oliver, D. R., "The Effect of Natural Convection on Viscous-Flow Heat Transfer in Horizontal Tubes," *Chemical Engineering Science*, Vol. 17, 1962, pp. 335–350.

3 Colburn, A. P., "A Method of Correlating Forced Convection Heat Transfer Data and a Comparison with Fluid Friction," *Transactions of the American Institute of Chemical Engineers*, Vol. 29, 1933, pp. 174–210.

4 Sieder, E. N., and Tate, G. E., "Heat Transfer and Pressure Drop of Liquids in Tubes," *Industrial and Engineering Chemistry*, Vol. 28, 1936, pp. 1429–1435.

5 Kern, D. Q., and Othmer, D. F., "Effect of Free Convection on Viscous Heat Transfer in Horizontal Tubes," *Transactions of the American Institute of Chemical Engineers*, Vol. 39, 1943, pp. 517–555.

6 Eubank, C. C., and Proctor, W. S., MS thesis in chemical engineering, M.I.T., Cambridge, Mass., 1951.

7 Martinelli, R. C., and Boelter, L. M. K., *University of California Publications in Engineering*, Vol. 5, No. 2, 1942, p. 23.

8 Jackson, T. W., Spurlock, J. M., and Purdy, K. R., "Combined Free and Forced Convection in a Constant Temperature Horizontal Tube," *Journal of the American Institute of Chemical Engineers*, Vol. 7, 1961, pp. 38–45.

9 Brown, A. R., and Thomas, M. A., "Combined Free and Forced Convection Heat Transfer for Laminar Flow in Horizontal Tubes," *Journal of Mechanical Engineering Science*, Vol. 7, No. 4, 1965, pp. 440–448.

10 Dorsey, N. E., *Properties of Ordinary Water Substance*, Reinhold, New York, 1940.

11 Perry, J. H., *Chemical Engineers Handbook*, McGraw-Hill, New York, 1950.

12 Kreith, F., *Principles of Heat Transfer*, International Textbook, Scranton, Pa., 1965.

13 Miner, C. S., and Dalton, N. N., *Glycerol*, Reinhold, New York, 1933.

14 McAdams, W. H., *Heat Transmission*, McGraw-Hill, New York, 1954.

DAVID A. MANDELL
Assistant Professor of Mechanical Engineering, Washington State University, Pullman, Wash.
Assoc. Mem. ASME

Radiative Energy Transfer Within a Nonisothermal Air Plasma[1]

The object of the present work is to study the mechanism of radiative heat transfer within a nonisothermal air plasma. The problem of an air plasma bounded by two parallel black boundaries, and within which there is a uniform heat source, is studied. Local thermodynamic equilibrium and linearized radiation are assumed. Centerline temperature results are presented for boundary temperatures of 5000 deg K, 10,000 deg K, and 15,000 deg K, and for densities from 10 times normal to 0.01 times normal density. The results show that for higher densities, the optically thin, optically thick, and differential approximation results differ significantly from the general solution over a large range of surface spacings.

Introduction

THE OBJECT of the present work is to study the mechanism of radiative heat transfer within a nonisothermal air plasma. In order to study this mechanism, the problem of an air plasma bounded by two parallel black surfaces, and within which there is a uniform heat source, is studied.

For gray gases, that is gases with a constant spectral absorption coefficient, the methods of solution of heat-transfer problems involving radiative heat transfer, as well as other modes of heat transfer, have been reviewed by Sparrow and Cess [1].[2] Infrared gaseous heat transfer has been considered by Cess, Mighdoll, and Tiwari [2]. They considered gases having a single fundamental vibration–rotation band, and found that significant differences exist between results obtained by using the gray-gas approximation and results for real gases. In addition to the above work, results have also been obtained for a hydrogen plasma [3].

Reference [3] shows that the optically thin and optically thick approximations are not of practical importance for a hydrogen plasma, at least for the conditions considered (pressures of 0.43 and 37.5 atm at 10,000 deg K and a pressure of 0.57 atm at 20,000 deg K). These limits are not of practical importance because for optically thin conditions an extremely small surface spacing ($L < 0.003$ cm at 20,000 deg K and 0.57 atm) would be needed for the optically thin solution to approach the general solution. On the other hand, an extremely large surface spacing ($L > 70{,}000$ cm at 20,000 deg K and 0.57 atm) would be needed in the optically thick case [4].

An air plasma is much more complex than a hydrogen plasma due to the large number of species and transitions involved. Wilson and Greif [5] review previous work on air plasmas and calculate the radiation from an isothermal air plasma. In addition they calculate the radiation from a nonisothermal plasma with a known temperature distribution. This is in contrast to the present work in which the temperature distribution is an unknown.

[1] This research was supported by the National Science Foundation through Grant No. GK-5276.

[2] Numbers in brackets designate References at end of paper.

Contributed by the Heat Transfer Division for publication (without presentation) in the JOURNAL OF HEAT TRANSFER. Manuscript received by the Heat Transfer Division September 9, 1970. Paper No. 71-HT-G.

Nomenclature

e_ω = Planck's function
E_2, E_i = exponential integral functions
F_2 = transmission function, equation (1)
F_3 = transmission function, equation (2)
L = surface spacing
m_0, n_0 = parameters in differential approximation, equation (13)
p = air pressure
Q = heat source per unit volume
q_R = radiative heat flux
T = temperature
T_1, T_2 = boundary temperatures
T_c = centerline temperature
y = distance measured from lower boundary
κ_ω = spectral absorption coefficient
κ_{LP} = linear Planck mean absorption coefficient
κ_R = Rosseland mean absorption coefficient
λ = thermal conductivity
ν = frequency
σ = Stefan-Boltzmann constant
ω = wave number

Radiative heat-transfer analyses within absorbing–emitting gases involve integral or integrodifferential equations. If the assumption of a gray gas is made, then the kernel function for the integrals appearing in the radiative flux equation is the second exponential integral function, $E_2(t)$. The kernel function for real gases is an extremely complicated function of the gas and thermodynamic conditions being considered.

For nongray gases the spatial derivative of either the emissivity or the modified emissivity has been used for the kernel function [6, 7]. This formulation requires an exponential to be substituted for $E_2(t)$. Baldwin [8], Wang [9, 10], and Gilles, Cogley, and Vincenti [11] have formulated the radiative flux without approximating $E_2(t)$.

It has been shown both for infrared radiation and for a hydrogen plasma that the results obtained by approximating $E_2(t)$ by an exponential are in close agreement with exact results [12, 13]. In the present work the kernel functions have to be calculated directly from the spectral absorption coefficients and, therefore, there is no advantage in approximating $E_2(t)$. Thus, in the present work the radiative flux will be formulated in terms of the transmission functions defined by Gilles, Cogley, and Vincenti [11].

In order to calculate transmission functions for a particular gas, it is necessary to have the spectral absorption coefficients for the gas as a function of wave number, temperature, and density. The present transmission functions were calculated by using the absorption coefficients reported by Landshoff and Magee [14]. Transmission functions and centerline temperature results are reported for boundary temperatures of 5000 deg K, 10,000 deg K, and 15,000 deg K, and for densities from 10 times normal density to 0.01 times normal. The influence of conduction heat transfer compared to radiative heat transfer is examined. Local thermodynamic equilibrium and linearized radiation are assumed.

Radiative Transfer Analysis

In problems involving radiative heat transfer combined with other modes of heat transfer, the radiative flux or its derivative is needed in the conservation-of-energy equation. For the case of nongray linearized radiation, the radiative flux can be expressed in terms of transmission functions [11].

$$F_2(t) = \frac{1}{4\sigma T_1^3}\int_0^\infty \kappa_\omega \left(\frac{\partial e_\omega}{\partial T}\right)_{T_1} E_2(\kappa_\omega t)d\omega \tag{1}$$

and

$$F_3(t) = \frac{1}{4\sigma T_1^3}\int_0^\infty \left(\frac{\partial e_\omega}{\partial T}\right)_{T_1} E_3(\kappa_\omega t)d\omega \tag{2}$$

where the linearization has been taken about T_1 and κ_ω is thus evaluated at T_1. The linearized radiative flux becomes

$$\begin{aligned} q_R &= 8\sigma T_1^3(T_1 - T_2)F_3(L - y) \\ &+ 8\sigma T_1^3\int_0^y [T(y') - T_1]F_2(y - y')dy' \\ &- 8\sigma T_1^3\int_y^L [T(y') - T_1]F_2(y' - y)dy' \end{aligned} \tag{3}$$

Conduction Neglected. For uniform heat generation, and with conduction neglected, the conservation-of-energy equation becomes $dq_R/dy = Q$. With the two boundaries at the same temperature, the problem is symmetric; that is $q_R = 0$ at $y = L/2$, and thus

$$Q\left(y - \frac{L}{2}\right) = q_R \tag{4}$$

Combining equations (3), with $T_2 = T_1$, and (4) gives

$$\begin{aligned} y - \frac{L}{2} &= \frac{4}{3}\int_0^y \theta(y')F_2(y - y')dy' \\ &- \frac{4}{3}\int_y^L \theta(y')F_2(y' - y)dy' \end{aligned} \tag{5}$$

where

$$\theta = \frac{6\sigma T_1^3(T - T_1)}{Q}$$

The optically thin limit has been discussed previously [3]. In the present case, the optically thin solution is obtained by noting that

$$\lim_{y\to 0} F_2(y) = \kappa_{LP} \tag{6}$$

Substitution of equation (6) into equation (5) and differentiating gives

$$\theta = \frac{3}{8\kappa_{LP}} \tag{7}$$

The optically thick limit has also been discussed in reference [3] and, in the present notation, the optically thick solution is

$$\theta(y) = \frac{9}{16}\kappa_R(yL - y^2) \tag{8}$$

Conduction Included. When conduction is included, the conservation-of-energy equation becomes

$$\lambda\frac{dT}{dy} + Q\left(y - \frac{L}{2}\right) = q_R \tag{9}$$

Combining equations (3), with $T_2 = T_1$, and (9), and letting

$$\phi = \frac{T - T_1}{QL^2/\lambda}$$

gives

$$\begin{aligned} L\frac{d\phi}{dy} + \frac{y}{L} - \frac{1}{2} = \frac{8\sigma T_1^3 L}{\lambda}\Bigg[&\int_0^y \phi(y')F_2(y - y')dy' \\ &- \int_y^L \phi(y')F_2(y' - y)dy'\Bigg] \end{aligned} \tag{10}$$

Since conduction heat transfer is present, temperature continuity exists at the boundaries and the boundary condition for equation (10) is $\phi(0) = 0$.

The optically thin solution in this case can be found by substituting κ_{LP} for F_2 in equation (10) and differentiating. The solution of the resulting ordinary differential equation, with boundary conditions $\phi(0) = 0$ and $\phi(L) = 0$ (or $d\phi/dy = 0$ at $y = L/2$), is

$$\phi(y) = \frac{1}{C_1L^2}\left[1 - \frac{e^{\sqrt{C_1}\,y} + e^{\sqrt{C_1}\,(L-y)}}{1 + e^{\sqrt{C_1}\,L}}\right] \tag{11}$$

where

$$C_1 = \frac{16\sigma T_1^3\kappa_{LP}}{\lambda}$$

The optically thick solution is easily found by substituting the optically thick expression for q_R [1] into equation (9)

$$\phi(y) = \frac{\frac{1}{2}\left(\frac{y}{L} - \frac{y^2}{L^2}\right)}{1 + \frac{16\sigma T_1^3}{3\lambda\kappa_R}} \tag{12}$$

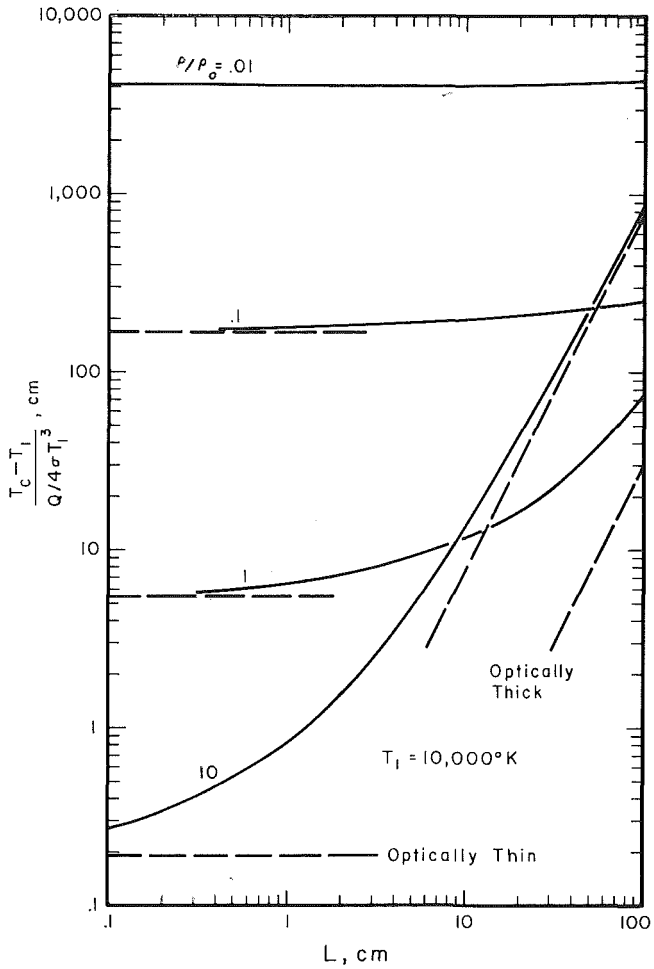

Fig. 1 Centerline temperature results with conduction neglected, T_1 = 10,000 deg K

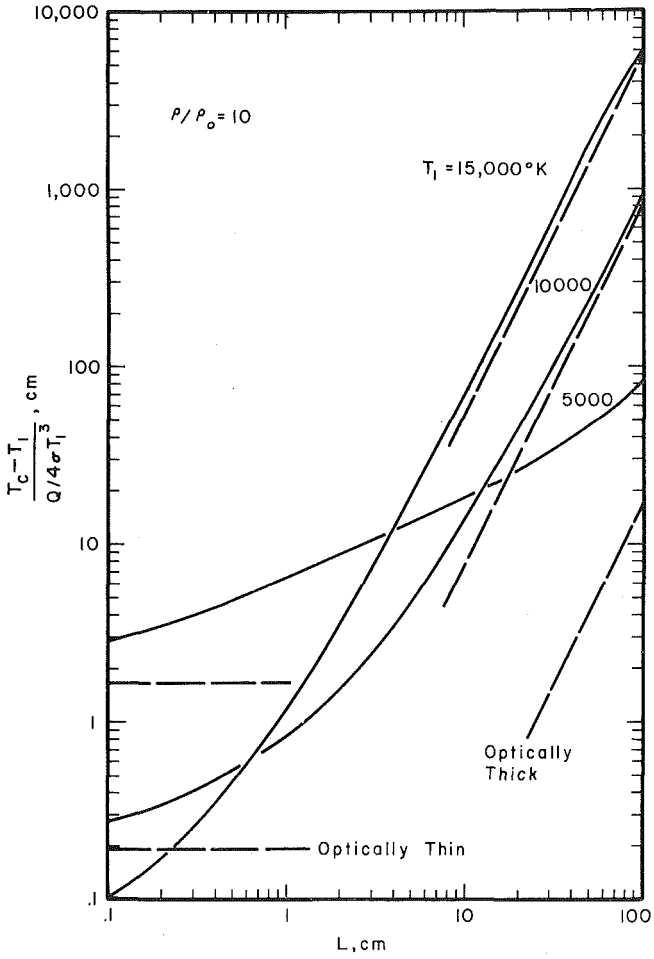

Fig. 2 Centerline temperature results with conduction neglected, ρ/ρ_0 = 10

Equations (5) and (10) were solved by the method of undetermined parameters [1]. Since the problems are symmetric, even-order polynomials were used. With conduction neglected, second- and fourth-order polynomials were used, and when conduction was included, fourth- and sixth-order polynomials were needed. For both problems the agreement between the centerline temperature results for the n and $n + 1$ polynomials was virtually identical.

Differential Approximation

The differential approximation has been used extensively in both gray-gas and nongray-gas analyses [11, 15–17]. In the present work, differential approximation solutions will be obtained by following Gilles, Cogley, and Vincenti [11]. This consists of approximating the transmission functions by an exponential function

$$F_2(y) = m_0 e^{-n_0 y} \tag{13}$$

If equation (13) is substituted into equation (3), then the integrals can be eliminated by differentiation and substitution. The resulting differential equation is

$$\frac{d^2 q_R}{dy^2} - n_0^2 q_R = 16\sigma T_1^3 m_0 \frac{dT}{dy} \tag{14}$$

with the boundary conditions

$$\frac{dq_R(0)}{dy} - n_0 q_R(0) = 16\sigma T_1^3 m_0 [T(0) - T_1] \tag{15}$$

and

$$\frac{dq_R(L)}{dy} + n_0 q_R(L) = 16\sigma T_1^3 m_0 [T(L) - T_1] \tag{16}$$

It should be noted that for the conduction-neglected case, a temperature jump exists at the boundaries, and thus $T(0) \neq T_1$ and $T(L) \neq T_1$.

For conduction neglected, the solution of equations (4) and (14)–(16) is

$$\theta(y) = \frac{3}{8m_0}\left(1 + \frac{n_0 L}{2}\right) - \frac{3n_0^2}{16m_0}(y^2 - Ly) \tag{17}$$

and with conduction included, equations (9) and (14)–(16) give

$$\phi(y) = \frac{\left(\frac{n_0^2}{C_2} - 1\right)\left(1 + \frac{n_0 L}{2}\right)(e^{\sqrt{C_2}(L-y)} + e^{\sqrt{C_2}y} - 1 - e^{\sqrt{C_2}L})}{L^2[C_2(1 + e^{\sqrt{C_2}L}) - n_0\sqrt{C_2}(1 - e^{\sqrt{C_2}L})]} - \frac{C_3}{C_2}(y^2 - Ly) \tag{18}$$

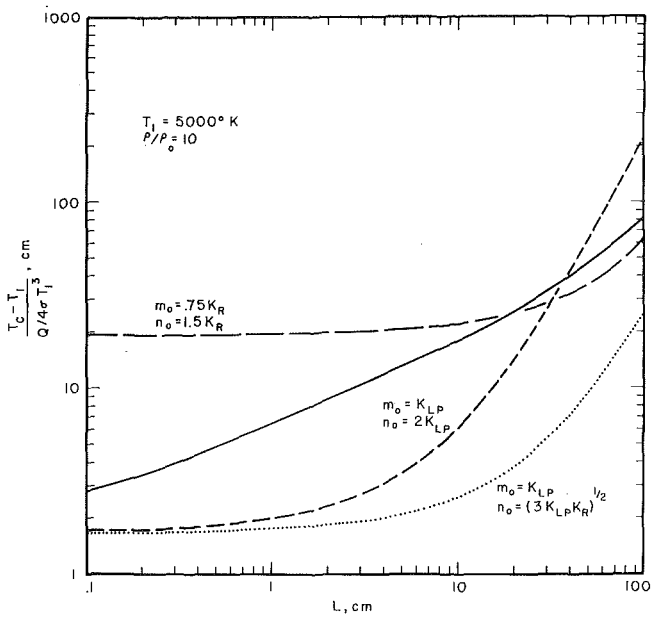

Fig. 3 Comparison of differential approximation results with conduction neglected, T_1 = 5000 deg K and ρ/ρ_0 = 10

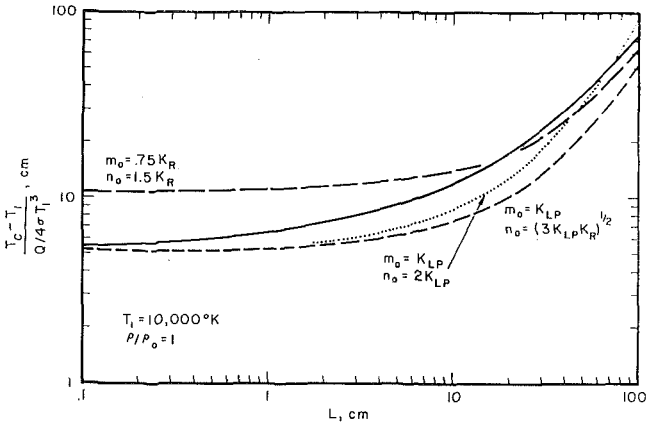

Fig. 4 Comparison of differential approximation results with conduction neglected, T_1 = 10,000 deg K and ρ/ρ_0 = 1

where

$$C_2 = n_0^2 + 16\sigma T_1^3 m_0/\lambda \quad \text{and} \quad C_3 = n_0^2/2L^2$$

Gilles, Cogley, and Vincenti [11] discuss three possible choices for m_0 and n_0. In order to accurately represent the optically thin limit, it is necessary for the zero-intercepts of F_2 and its approximation to agree. This gives $F_2(0) = m_0 = \kappa_{LP}$. If the areas are also matched, then $n_0 = 2\kappa_{LP}$. The optically thick limit will be approximated if the areas and first moments of F_2 and its approximation agree, giving $m_0 = 0.75\kappa_R$ and $n_0 = 1.5\kappa_R$. A compromise between satisfying the optically thin or optically thick limits is achieved if the zero-intercepts and first moments of F_2 and the exponential function, equation (13), are matched. This results in $m_0 = \kappa_{LP}$ and $n_0 = (3\kappa_{LP}\kappa_R)^{1/2}$. A comparison between the solutions obtained by using these choices of m_0 and n_0 with the solutions of equations (5) and (10) will be discussed in the next section.

Results

In order to solve equations (5) and (10) for the temperature distribution between the boundaries it is necessary to have values for the transmission functions for the gas under consideration. For an air plasma, the spectral absorption coefficients are an extremely complex function of the wave number, pressure, and temperature, and thus no analytic expressions exist for $F_2(y)$.

In order to construct tables of $F_2(y)$, the spectral absorption coefficients must be known, and in the present work, the values of κ_ω given by Landshoff and Magee [14] are used. The species and transitions considered in the absorption coefficient values are discussed in detail by Landshoff and Magee and need not be repeated here, but it should be noted that values of the spectral absorption coefficient are not given over the entire spectrum ($h\nu$ from 0.6 to 10.7 ev are given) and the contributions of atomic lines are not included. Contributions from bands and continua are included. Based on previous hydrogen results [3], the influence of atomic lines will be discussed after the present results are discussed. The integrations over wave number were carried out only for the wave number range in which κ_ω values are available.

The absorption coefficient values given by Landshoff and Magee are the most accurate available, and the comparisons between the optically thin, optically thick, differential approximation, and general results are internally consistent since κ_R, κ_{LP}, and $F_2(y)$ are calculated from the same κ_ω values.

Table 1 Transmission functions for T_1 = 5000 deg K

L (cm)	F_2 (cm^{-1})		
	ρ/ρ_0 = 0.1	ρ/ρ_0 = 1	ρ/ρ_0 = 10
0	2.14×10^{-4}	6.97×10^{-3}	0.149
5×10^{-4}	2.14×10^{-4}	6.96×10^{-3}	0.145
1×10^{-3}	2.14×10^{-4}	6.94×10^{-3}	0.142
5×10^{-3}	2.14×10^{-4}	6.87×10^{-3}	0.129
1×10^{-2}	2.14×10^{-4}	6.80×10^{-3}	0.119
5×10^{-2}	2.14×10^{-4}	6.42×10^{-3}	8.89×10^{-2}
1×10^{-1}	2.13×10^{-4}	6.09×10^{-3}	7.20×10^{-2}
5×10^{-1}	2.09×10^{-4}	4.83×10^{-3}	3.60×10^{-2}
1	2.05×10^{-4}	4.07×10^{-3}	2.63×10^{-2}
5	1.84×10^{-4}	2.11×10^{-3}	1.29×10^{-2}
1×10^{1}	1.67×10^{-4}	1.48×10^{-3}	9.10×10^{-3}
5×10^{1}	1.08×10^{-4}	6.74×10^{-4}	2.54×10^{-3}
1×10^{2}	7.97×10^{-5}	4.84×10^{-4}	8.87×10^{-4}

The calculated values of the transmission functions for T_1 = 5000 deg K, 10,000 deg K and 15,000 deg K and for a range of density ratios are given in Tables 1, 2, and 3, respectively.

Conduction Neglected. In order to illustrate the influence of radiative heat transfer within a nonisothermal air plasma, the centerline temperatures as a function of surface spacing will be examined. Fig. 1 shows the centerline temperatures as a function of surface spacing for a boundary temperature of T_1 = 10,000 deg K and for densities from 10 times normal density to 0.01 times normal density. In addition to the solutions of equation (5), the optically thin and optically thick solutions are also shown.

It is seen from Fig. 1 that for low densities, the general solution agrees closely with the optically thin solution over a large range of surface spacings. As the density increases the optically thin solution begins to overestimate the radiative heat transfer, and applies to smaller and smaller surface spacings. For a density ratio, ρ/ρ_0, of 1, the optically thick solution begins to be a good approximation for very large L values, and for ρ/ρ_0 = 10, Fig. 1 shows that the optically thin solution will apply for only extremely small L values (at L = 0.1 cm, the optically thin solution differs by 31 percent from the general solution) while the thick solution applies for moderately large L values (at L = 50 cm, the thick solution overestimates the radiative heat transfer by 19 percent). For the higher densities there is a fairly large range of L values for which neither limiting solution applies.

Fig. 2 shows results for ρ/ρ_0 = 10 and boundary temperatures of 5000 deg K, 10,000 deg K, and 15,000 deg K. The optically thin solutions for these conditions will agree with the general solution only for very small L values. For a given L value, the optically thick results become more applicable as the boundary

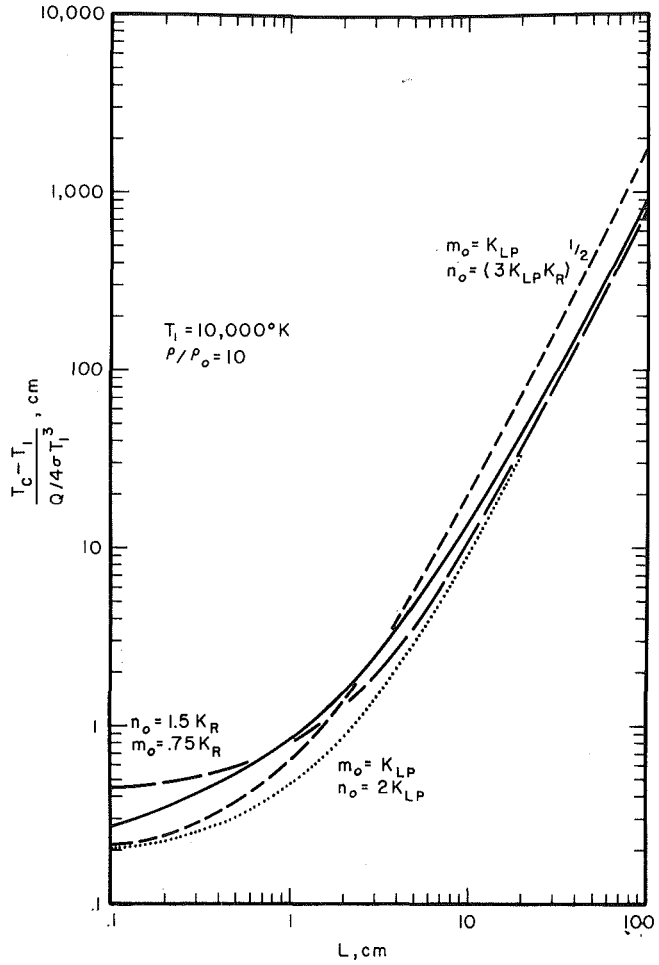

Fig. 5 Comparison of differential approximation results with conduction neglected, $T_1 = 10{,}000$ deg K and $\rho/\rho_0 = 10$

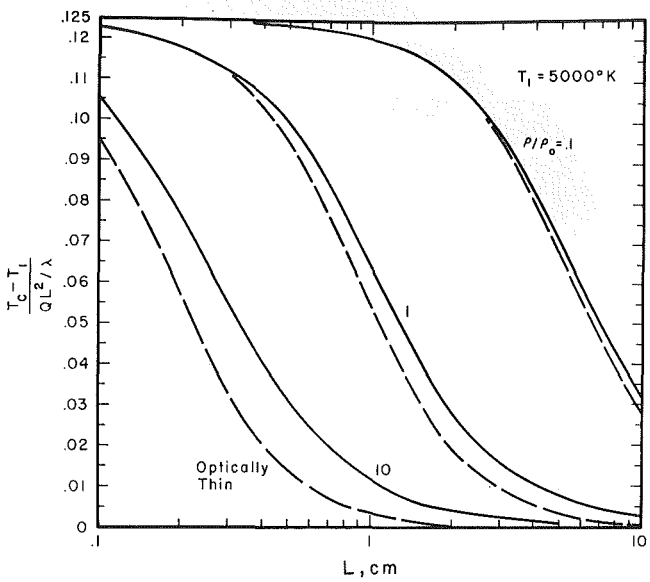

Fig. 6 Centerline temperature results with conduction included, $T_1 = 5000$ deg K

Table 3 Transmission functions for $T_1 = 15{,}000$ deg K

L (cm)	F_2 (cm^{-1})		
	$\rho/\rho_0 = 0.1$	$\rho/\rho_0 = 1$	$\rho/\rho_0 = 10$
0	2.91×10^{-2}	0.424	6.00
5×10^{-4}	2.91×10^{-2}	0.417	5.70
1×10^{-3}	2.90×10^{-2}	0.412	5.51
5×10^{-3}	2.89×10^{-2}	0.388	4.76
1×10^{-2}	2.88×10^{-2}	0.376	4.25
5×10^{-2}	2.81×10^{-2}	0.316	2.41
1×10^{-1}	2.73×10^{-2}	0.285	1.46
5×10^{-1}	2.43×10^{-2}	0.182	8.40×10^{-2}
1	2.21×10^{-2}	0.126	4.64×10^{-3}
5	1.48×10^{-2}	1.89×10^{-2}	0.0
1×10^{1}	1.08×10^{-2}	3.12×10^{-3}	
5×10^{1}	2.41×10^{-3}	4.13×10^{-8}	
1×10^{2}	6.20×10^{-4}	0.0	

temperature increases. As the temperature decreases the range of L values for which neither the thin nor the thick limit applies increases.

The differential approximation results with conduction neglected are shown in Figs. 3–5. For $T_1 = 5000$ deg K and $\rho/\rho_0 = 10$, Fig. 3, none of the choices of m_0 and n_0 produce results in agreement with the general solution. Fig. 4, $T_1 = 10{,}000$ deg K and $\rho/\rho_0 = 1$, shows that for intermediate L values, the differential approximation differs significantly from the general solution, but it does contain the qualitative features of the general solution. For $T_1 = 10{,}000$ deg K and $\rho/\rho_0 = 10$, the general solution and the differential approximation agree for larger L values as would be expected, since the optically thick solution was in good agreement with the general solution for large L values, Fig. 1.

With conduction neglected Figs. 1–5 show that no single approximation agrees adequately with the general solution, for larger densities, over the entire range of surface spacings.

Conduction Included. In order to see the influence of conduction heat transfer compared to radiative heat transfer, the dimensionless centerline temperatures will be divided by the value of the centerline temperature in the absence of radiation [3], 0.125.

Fig. 6 shows the dimensionless centerline temperature as a function of L for $T_1 = 5000$ deg K and ρ/ρ_0 values of 0.1, 1, and 10. The optically thin solutions are also shown, and it can be seen that for $\rho/\rho_0 = 0.1$, the optically thin solution is in close agreement with the general solution. As the density increases, the optically thin solution becomes less applicable.

Table 2 Transmission functions for $T_1 = 10{,}000$ deg K

L (cm)	F_2(cm^{-1})			
	$\rho/\rho_0 = 0.01$	$\rho/\rho_0 = 0.1$	$\rho/\rho_0 = 1$	$\rho/\rho_0 = 10$
0	6.03×10^{-5}	1.49×10^{-3}	4.80×10^{-2}	1.31
5×10^{-4}	6.03×10^{-5}	1.49×10^{-3}	4.76×10^{-2}	1.30
1×10^{-3}	6.03×10^{-5}	1.49×10^{-3}	4.76×10^{-2}	1.29
5×10^{-3}	6.03×10^{-5}	1.48×10^{-3}	4.73×10^{-2}	1.22
1×10^{-2}	6.03×10^{-5}	1.48×10^{-3}	4.70×10^{-2}	1.16
5×10^{-2}	6.03×10^{-5}	1.47×10^{-3}	4.55×10^{-2}	0.904
1×10^{-1}	6.03×10^{-5}	1.46×10^{-3}	4.42×10^{-2}	0.737
5×10^{-1}	6.03×10^{-5}	1.41×10^{-3}	3.82×10^{-2}	0.284
1	6.03×10^{-5}	1.38×10^{-3}	3.40×10^{-2}	0.128
5	6.01×10^{-5}	1.30×10^{-3}	2.07×10^{-2}	4.43×10^{-3}
1×10^{1}	6.00×10^{-5}	1.24×10^{-3}	1.38×10^{-2}	4.35×10^{-4}
5×10^{1}	5.90×10^{-5}	9.94×10^{-4}	1.76×10^{-3}	2.27×10^{-10}
1×10^{2}	5.78×10^{-5}	8.21×10^{-4}	3.22×10^{-4}	0.0

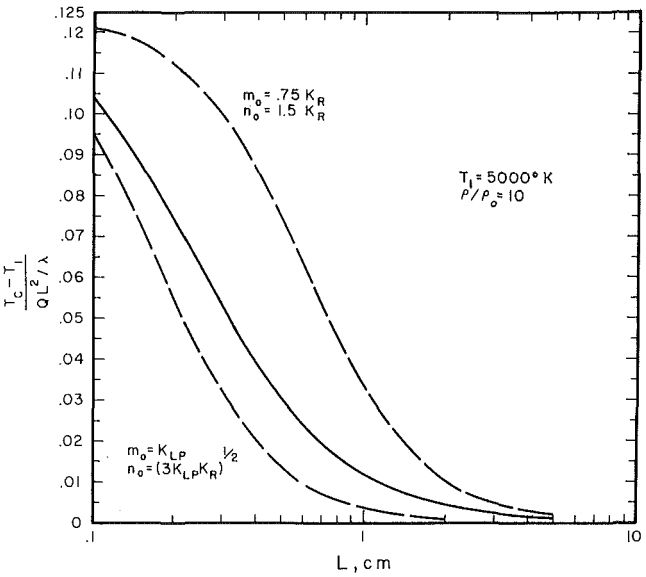

Fig. 7 Comparison of differential approximation results with conduction included, T_i = 5000 deg K and ρ/ρ_0 = 10

Fig. 7 shows the differential approximation for T_i = 5000 deg K and ρ/ρ_0 = 10. The curve for $m_0 = \kappa_{LP}$ and $n_0 = 2\kappa_{LP}$ (not shown) is virtually identical to the curve for $m_0 = \kappa_{LP}$ and $n_0 = (3\kappa_{LP}\kappa_R)^{1/2}$. As can be seen from the figure, the differential approximation differs significantly from the general solution. At lower density ratios and the higher temperatures, the results were identical to the optically thin results.

In order to make calculations for the conduction-included case, thermal conductivity values of air are needed, and the values used for Figs. 6 and 7 were estimated from the calculations reported by Yos [18, 19]. Thermal conductivity values do not appear to be available at ρ/ρ_0 = 10 and temperatures of 10,000 deg K and 15,000 deg K.

As discussed previously, the spectral absorption coefficients used included contributions from bands and continua, but did not include atomic line contributions. In reference [3] it is shown for a hydrogen plasma that at higher pressures the atomic lines have a small influence. For example, at T_i = 10,000 deg K and p = 37.5 atm, the continuum results and continuum plus line results are virtually identical. Reference [3] also shows that the continuum absorption coefficients result in an upper bound on the centerline temperatures.

Air composition results have been given by Gilmore [20], and the pressures corresponding to the present conditions are shown in Table 4. It can be seen from Figs. 1 and 6 that the nongray effects become more important as the density increases. In particular, the general solutions begin to deviate from the optically thin solutions, for practical boundary spacings, for ρ/ρ_0 of one and greater. At these densities, and the temperatures considered, the pressure is very high, Table 4, and thus the atomic line contributions should be negligible, based upon the hydrogen results of reference [3].

Table 4 Gas composition

T_i (deg K)	ρ/ρ_0	p (atm)
5,000	0.1	2.2
5,000	1	21
5,000	10	196
10,000	0.01	0.77[a]
10,000	0.1	7[a]
10,000	1	64[a]
10,000	10	560[a]
15,000	10	1060[b]

[a] average of values at 8000 deg K and 12,000 deg K
[b] average of values at 12,000 deg K and 18,000 deg K

It was shown in references [3, 4] that, for hydrogen, atomic line radiation has its greatest influence for optically thin conditions, and this influence decreases relative to continuum radiation as the boundary spacing increases. Thus for larger L values, the atomic line contributions should again be negligible.

The hydrogen results [3, 4] also show that for small L values, the percentage differences between the general solutions and optically thin solutions are greater when atomic lines are included than for continuum values only. Thus the thin solutions will be less applicable when atomic lines are included than is indicated in the figures.

References

1 Sparrow, E. M., and Cess, R. D., *Radiation Heat Transfer*, Brooks/Cole, Belmont, Calif., 1966.

2 Cess, R. D., Mighdoll, P., and Tiwari, S. N., "Infrared Radiative Heat Transfer in Nongray Gases," *International Journal of Heat and Mass Transfer*, Vol. 10, 1967, pp. 1521–1532.

3 Mandell, D. A., and Cess, R. D., "Radiative Energy Transfer within a Hydrogen Plasma," *International Journal of Heat and Mass Transfer*, Vol. 13, 1970, pp. 1–12.

4 Mandell, D. A., and Cess, R. D., "Radiative Transport Quantities for a Hydrogen Plasma," *Journal of Quantitative Spectroscopy and Radiative Transfer*, Vol. 9, 1969, pp. 981–994.

5 Wilson, K., and Greif, R., "Radiation Transport in Atomic Plasmas," *Journal of Quantitative Specroscopy and Radiative Transfer*, Vol. 8, 1968, p. 1061.

6 Penner, S. S., *Quantitative Molecular Spectroscopy and Gas Emissivities*, Addison-Wesley, Reading, Mass., 1959.

7 Gillie, J., and Goody, R. M., "Convection in a Radiating Gas," *Journal of Fluid Mechanics*, Vol. 20, 1964, pp. 47–79.

8 Baldwin, B. S., Jr., "The Propagation of Plane Acoustic Waves in a Radiating Gas," NASA TR-138, 1962.

9 Wang, L. S., "An Integral Equation of Radiative Equilibrium in Infrared Radiating Gases," *Journal of Quantitative Spectroscopy and Radiative Transfer*, Vol. 8, 1968, pp. 851–853.

10 Wang, L. S., "The Role of Emissivities in Radiative Transport Calculations," *Journal of Quantitative Spectroscopy and Radiative Transfer*, Vol. 8, 1968, pp. 1233–1240.

11 Gilles, S. E., Cogley, A. C., and Vincenti, W. G., "A Substitute-Kernel Approximation for Radiative Transfer in a Nongray Gas Near Equilibrium, with Application to Radiative Acoustics," *International Journal of Heat and Mass Transfer*, Vol. 12, 1969, pp. 445–458.

12 Greif, R., and Habib, I. S., "Infrared Radiation Transport: Exact and Approximate Results," JOURNAL OF HEAT TRANSFER, TRANS. ASME, Series C, Vol. 91, No. 3, May 1969, pp. 282–284.

13 Mandell, D. A., "Exponential Kernal Approximation in Radiative Energy Transfer within a Hydrogen Plasma," *AIAA Journal*, Vol. 8, 1970, pp. 1510–1512.

14 Landshoff, R. K. M., and Magee, J. L., *Thermal Radiation Phenomena, Vol. 1, Radiative Properties of Air*, IFI/Plenum, New York, 1969.

15 Cogley, A. C., Vincenti, W. G., and Gilles, S. E., "On the Differential Approximation for Radiative Transfer in a Nongray Gas," *AIAA Journal*, Vol. 6, 1968, pp. 551–553.

16 Traugott, S. C., "Radiative Heat Flux Potential for a Nongray Gas," *AIAA Journal*, Vol. 4, 1966, pp. 541–542.

17 Traugott, S. C., "On Gray Absorption Coefficients in Radiative Transfer," *Journal of Quantitative Spectroscopy and Radiative Transfer*, Vol. 8, 1968, pp. 971–999.

18 Yos, J. M., "Transport Properties of Nitrogen, Hydrogen, Oxygen, and Air to 30,000°K," Technical Memorandum RAD TM-63-7, 1963, Research and Advanced Development Division, AVCO Corp.

19 Yos, J. M., "Revised Transport Properties for High Temperature Air and Its Components," AVCO Space Systems Division, 1967, unpublished.

20 Gilmore, F. R., "Equilibrium and Thermodynamic Properties of Air to 24,000°K," The Rand Corporation, RM-1543, 1955.

K. R. CHUN
Member Senior Technical Staff,
Northrop Corporate Laboratories,
Hawthorne, Calif.
Assoc. Mem. ASME

R. A. SEBAN
Professor,
University of California,
Berkeley, Calif.
Fellow ASME

Heat Transfer to Evaporating Liquid Films

Results are presented for the heat-transfer coefficient for evaporation from the surface of water films flowing along the outside surface of a vertical tube for the cases of laminar and turbulent flow. Correspondence with results for condensation and liquid heating is shown and the transition from laminar to turbulent flow is indicated to depend on quantities other than Reynolds number.

Introduction

In order to predict the performance of falling film evaporation, it is necessary to know the heat-transfer coefficient for non-nucleating conditions in which all the evaporation takes place from the surface of the film and in consequence essentially all of the heat is conducted through the whole liquid layer. Data on this kind of heat transfer is not extensive and predictions for laminar flow have been based on the Nusselt film or its modification [1][1] for the effect of capillary waves on the surface of the film. For the turbulent regime, initiated at some postulated Reynolds number, theoretical predictions, like those of Dukler [2], have been used to estimate the local heat-transfer coefficient.

To appraise the validity of such estimates, measurements of the heat-transfer coefficient have been made for a water film running down the surface of an electrically heated vertical tube, for saturation temperatures in the range of 83 deg F to 212 deg F, with an overall Reynolds-number range of 320 to 21,000. The apparatus and procedure are described briefly in the Appendix and the results, expressed as the heat-transfer coefficient, are shown as points in Fig. 1. Each point is the appropriate local value for the Reynolds number indicated and because the evaporation was but a small fraction of the flow rate, this coefficient existed over almost the whole tube length. Each point therefore represents the result of one run. Table 1 gives the range of parameters covered experimentally.

Fig. 1 also contains curves showing the prediction values of the heat-transfer coefficient for the Nusselt layer and for turbulent flow according to Dukler, and it is obvious that the results do not correspond well to such predictions. The ensuing consideration deals with the significance and correlation of the heat-transfer co-

[1] Numbers in brackets designate References at end of paper.

Contributed by the Heat Transfer Division for publication (without presentation) in the Journal of Heat Transfer. Manuscript received by the Heat Transfer Division November 6, 1970. Paper No. 71-HT-H.

Nomenclature

A = dimensional constant (Btu/hr·deg F·ft²)
C_f = friction coefficient (dimensionless)
C_p = specific heat (Btu/lb·deg F)
g = gravitational acceleration (ft/hr²)
h = local heat-transfer coefficient (Btu/hr·deg F·ft²)
$\bar{h}$ = average heat-transfer coefficient (Btu/hr·deg F·ft²)
k = thermal conductivity (Btu/hr·deg F·ft)
Ka = Kapitza number, $\frac{\mu^4 g}{\rho\sigma^3}$ (dimensionless)
L = wall length (ft)
n = numerical constant
p = pressure (lbf/ft²)
Pr = Prandtl number, $\frac{C_p\mu}{k}$
q = heat flux (Btu/hr·ft²)
T = temperature (deg F)
$\bar{u}$ = average downward velocity (ft/hr)
x = coordinate down the wall (ft)
We = Weber's number, $\left(\frac{\rho\bar{u}^2\delta}{\sigma}\right)^{1/2}$
α = thermal diffusivity (ft²/hr)
Γ = mass flow rate per unit width of the wall (lb/ft·hr)
δ = film thickness (ft)
λ = latent heat of vaporization (Btu/lb)
μ = absolute viscosity (lb/ft·hr)
ν = kinematic viscosity (ft²/hr)
ρ = density (lb/ft³)
σ = surface tension (lbf/ft)
τ = shear stress at the wall (lbf/ft²)

Subscripts

H = liquid heating without evaporation
i = wave inception
L = at $x = L$
0 = condition at $x = 0$
s = saturation condition
tr = transition
w = at the wall

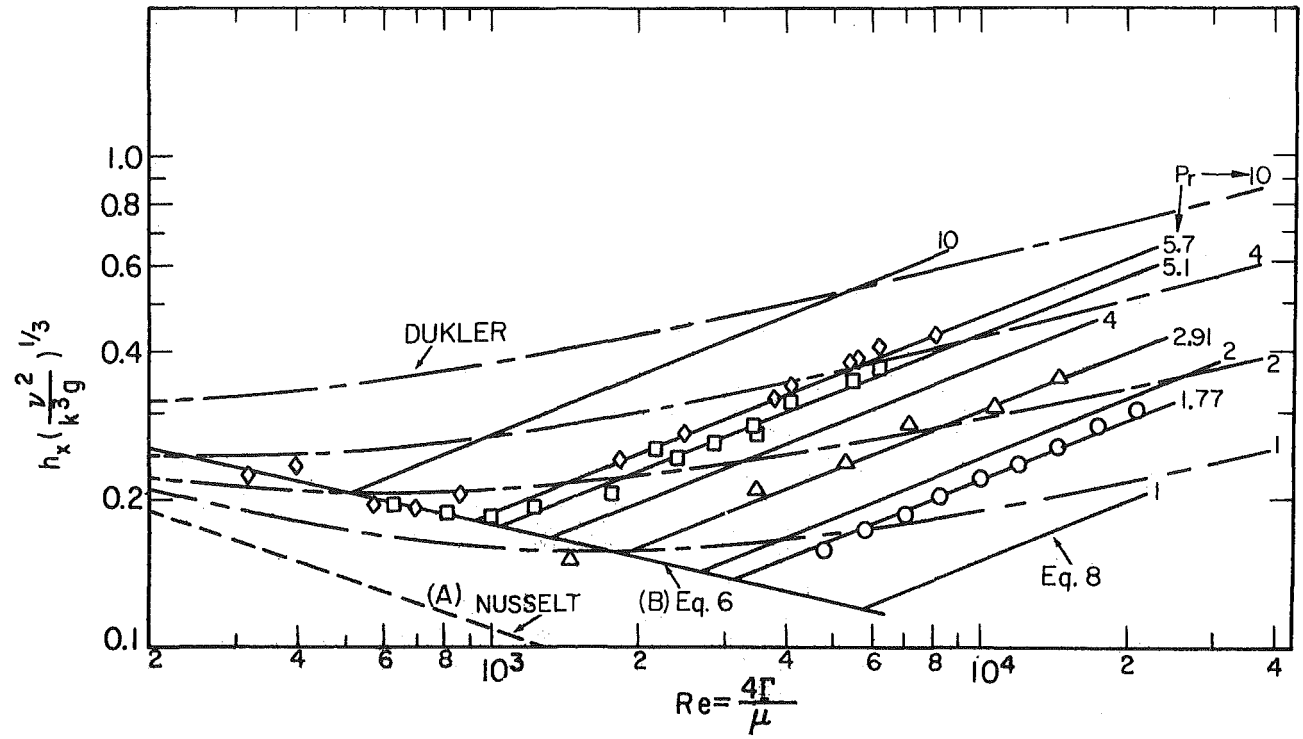

Fig. 1 Local heat-transfer coefficient as function of Reynolds number; curve A is the Nusselt solution, equation (3); curve B is the "wavy laminar" solution, equation (6); for turbulent flow the solid curves are the empirical fit to the data, equation (8), shown for various integral values of the Prandtl number and also for the four particular values for which the indicated data were obtained; the broken curves are the turbulent prediction of Dukler [2]

Table 1 Experimental conditions

Approximate Saturation Pressure (in. Hg)			1.14	1.51	6.52	29.80
Approximate Saturation Temperature (°F)			83	92	144	212
Prandtl Number			5.7	5.1	2.91	1.77
Feed Rate (lbs/hr)		Minimum	47	83	120	240
		Maximum	1190	730	1170	1050
Feed Reynold's Number		Minimum	320	630	1460	4800
		Maximum	8000	5480	14,400	21,000
Film Thickness (mils) (Estimate)		Minimum	10	12	11	15
		Maximum	40	32	35	30
Heat Input	Minimum	Current (amps)	100	133	154	159
		Voltage drop (Volts)	2.1	2.9	3.42	3.66
		BTU/hr	720	1300	1800	2000
	Maximum	Current (amps)	136	147	156	181
		Voltage drop (Volts)	2.94	3.2	3.5	4.2
		BTU/hr	1350	1600	1870	2600

Table 2 Transition values for present experiment

T_{sat}(°F)	212	150	110	83	Equations	
Pr	1.77	2.75	4.05	5.7	Re	δ
Ka	0.0314×10^{-11}	0.107×10^{-11}	0.446×10^{-11}	1.19×10^{-11}		
Re_i	33.3	29.8	26.2	24	4	
Re_{tr}	3160	1980	1320	920	10	
We_{tr}	1.66	1.44	1.35	1.19		1
We_{tr}	2.46	1.97	1.76	1.49		7
Re_{tr}	1700	1280	1000	800	11	
We_{tr}	1.04	1.06	1.06	1.03		1

efficient for the laminar and "turbulent" regimes. The consideration is perforce approximate, since not enough is known about the nature of the flow to permit an analysis based on the dynamics of the fluid motion itself.

Laminar Regime

For the flow of a liquid layer of constant properties down a vertical surface, in the steady region after the flow is developed, the integration of the equation of motion yields a parabolic profile for the velocity distribution and the mass rate of flow is related to the thickness as:

$$\Gamma = \frac{\rho g}{\nu} \frac{\delta^3}{3} \tag{1}$$

If evaporation or condensation takes place at the free surface, then the latent heat must be conducted through the layer, so that

$$\lambda \frac{d\Gamma}{dx} = k \frac{T_s - T_w}{\delta} \tag{2}$$

The combination of equations (1) and (2), with $\Gamma = 0$ at $x = 0$ for $T_s > T_w$ and $\Gamma = \Gamma_0$ at $x = 0$ for $T_w > T_s$, yields the Nusselt solution, which is expressed in terms of the heat-transfer coefficient, $h = k/\delta$. In the evaporation experiments considered here, the evaporation was small compared to the flow $\left(\frac{1}{\Gamma}\frac{d\Gamma}{dx} \rightarrow 0\right)$ and thus the heat-transfer coefficient was essentially constant in the fully developed flow regime.

$$h = \frac{k}{\delta} = \left(\frac{4}{3}\right)^{1/3}\left(\frac{k^3 g}{\nu^2}\right)^{1/3}\left(\frac{4\Gamma}{\mu}\right)^{-1/3} \tag{3}$$

This is curve A of Fig. 1.

Kapitza[2] predicted that capillary waves would form on the laminar-layer surface when the Reynolds number exceeded the value of

$$\left(\frac{4\Gamma}{\mu}\right)_i = 2.43\left(\frac{\mu^4 g}{\rho\sigma^3}\right)^{-1/11} \tag{4}$$

Here $\mu^4 g/\rho\sigma^3$ is the Kapitza number, Ka, and values thereof are shown in Table 2, together with the Reynolds number indicated by equation (4), for the four temperature levels of the experiments; surface ripples are expected to have existed for all operating conditions. The analysis of Kapitza, presuming wavelengths long compared to layer thickness, indicated that the average layer thickness for a given flow rate is reduced by the action of the ripples, so that the heat-transfer coefficient is increased. Zazuli[3] examined condensation data and formulated an empirical correction factor for condensation data in terms of average heat-transfer coefficients

$$(\bar{h})_{\text{ripples}} = 0.8\left(\frac{\Gamma}{\mu}\right)^{0.11}\bar{h}_{\text{Nusselt}} \tag{5}$$

By assuming, for the condensation problem, $h \sim (\Gamma/\mu)^n$, it is found that the local coefficient to be consistent with equation (5) must be

$$h = 0.606\left(\frac{k^3 g}{\nu^2}\right)^{1/3}\left(\frac{\Gamma}{\mu}\right)^{-0.22} \tag{6}$$

or, assuming that the increase in local heat-transfer coefficient arises entirely from a reduction in the average film thickness,

$$\frac{\delta_{\text{ripples}}}{\delta_{\text{Nusselt}}} = 1.33\left(\frac{4\Gamma}{\mu}\right)^{-0.11} \tag{7}$$

Equation (6) is curve B of Fig. 1. It predicts well the experimental results at lower Reynolds numbers as obtained primarily at the two lowest experimental temperatures.

Turbulent Regime

Most of the results shown in Fig. 1 give higher coefficients than those predicted from equation (6) and are considered arbitrarily as being in the turbulent regime, though no hydrodynamic results were obtained to indicate whether or not the flow was really turbulent. These heat-transfer coefficients could be approximately fitted by the relation

$$h\left(\frac{\nu^2}{gk^3}\right)^{1/3} = 3.8 \times 10^{-3}\left(\frac{4\Gamma}{\mu}\right)^{0.4}\left(\frac{\nu}{\alpha}\right)^{0.65} \tag{8}$$

Equation (8) is shown in Fig. 1 by lines for various Prandtl numbers. The fit to the results is good down to the immediate vicinity of the "wavy laminar" line where there is an indication of a more gradual join to the wavy laminar line than is indicated by the intersection of equations (6) and (8). The results for $\nu/\alpha = 5.7$ imply "turbulent" flow at Reynolds numbers down to the order of 1500 and those for the lowest Prandtl number of 1.77 (for which none of the results were near the "laminar" line) imply the possibility of laminar flow up to $4\Gamma/\mu = 3200$, or somewhat less if a more gradual transition is considered.

Wilke [3] presented results for the heating, essentially without evaporation, of falling films of water and mixtures of water and ethylene glycol on the exterior of a vertical tube. He gave a correlation for "turbulent" heat-transfer coefficients as

$$h_H\left(\frac{\nu^2}{gk^3}\right)^{1/3} = 8.7 \times 10^{-3}\left(\frac{4\Gamma}{\mu}\right)^{0.4}\left(\frac{\nu}{\alpha}\right)^{0.344} \tag{9}$$

valid for $4\Gamma/\mu > 3200$, though Wilke implies from the results of Feind that the flow was probably turbulent for $4\Gamma/\mu > 1600$. For "non-laminar" flows for $4\Gamma/\mu < 3200$, Wilke presents separate correlations which, only for water, $\nu/\alpha = 5.4$, depart less than 15 percent from equation (8).

For a Prandtl number of 5, equation (8) gives $h(\nu^2/gk^3)^{1/3} = 10.7 \times 10^{-3}(4\Gamma/\mu)^{0.4}$, while equation (9) gives $15.0 \times 10^{-3}(4\Gamma/\mu)^{0.4}$, the ratio h_H/h thus being 1.40. This ratio is at least in the expected range for the contrast between heating and evaporation though it is greater than can be predicted for films having turbulent characteristics similar to those associated with pipe flows.

It is appropriate to note further the consequences of the usual "analyses" that are based on the conventional hypothesis about turbulent flow that are consistent with pipe flow. In these, since $\tau = \rho g\delta$ and $C_f/2 \sim (4\Gamma/\mu)^{-n}$, there is obtained $\delta \sim \Gamma^{(2-n)/3}$ so that for $n = 0.2$, $\frac{2-n}{3} = 0.60$. Feind gives $\delta \sim \Gamma^{0.53}$ and it is possible that there exists an analog to equation (7) for turbulent flow. If the Colburn analogy is adopted $h = \frac{C_f C_p \Gamma}{2\delta}\left(\frac{\nu}{\alpha}\right)^{2/3}$ and $h \sim \Gamma^m$; $m = \frac{1-2n}{3}$ so that with $n = 0.2$, $m = 0.20$ as given in the limit of high Reynolds numbers by theories such as that of Dukler, shown in Fig. 1, but such values are at variance with the experimental dependence of the heat-transfer coefficient on the Reynolds number. Clearly, there is no conventional friction-factor relationship which will give $m = 0.4$.

Departure From Laminar Regime

The intersection of equations (6) and (8) indicates a departure from the "wavy laminar" regime at the Reynolds number

$$\left(\frac{4\Gamma}{\mu}\right)_{tr} = 5800\left(\frac{\nu}{\alpha}\right)^{-1.06} = 0.215(\text{Ka})^{-1/8} \tag{10}$$

the latter form arising from the fact that the Kapitza number is a power function of the Prandtl number in the temperature range involved, with the viscosity being the controlling element of both Kapitza and Prandtl numbers. Wilke defined a "departure" Reynolds number in his experiments in terms of the first departure of the heat-transfer coefficient from laminar performance. Because the transfer from the laminar to the turbulent line is actually less abrupt than given by the intersection of equations like (6) and (8), his departure Reynolds numbers are relatively lower; they were given by him as:

$$\left(\frac{4\Gamma}{\mu}\right)_{tr} = 2460\left(\frac{\nu}{\alpha}\right)^{-0.65} \tag{11}$$

Table 3 Transition values for Wilke experiment

Mass fraction of glycol (%)	0	16	55.5	77.1	95
Mole fraction of Glycol (%)	0	5	25.7	50	85
Pr	5.4	9.4	43.4	104	210
Ka	1.15×10^{-11}	6.7×10^{-11}	1.29×10^{-8}	3.96×10^{-7}	7.8×10^{-6}
Re_i	24	20.5	12.7	8.5	7.1
Re_{tr}*	830	570	215	122	80
We_{tr}	1.06	1.05	1.11	1.23	1.42

*Eq. (11)

[2] Kutadeladze [1], p. 307.
[3] Kutadeladze [1], p. 307.

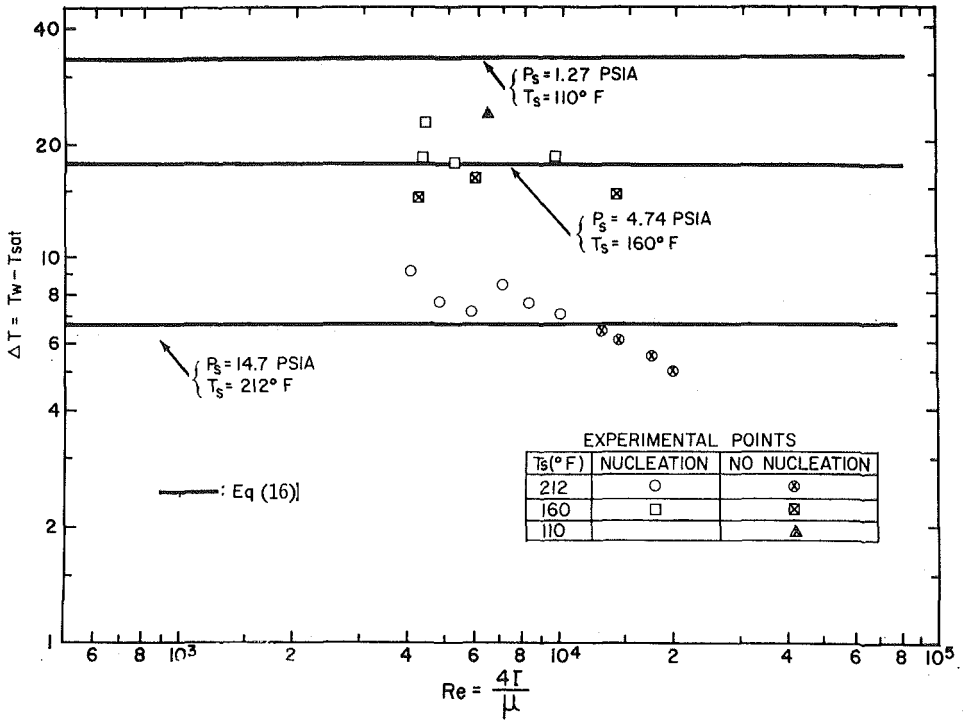

Fig. 2 Wall superheats at incipient boiling as function of Reynolds number at different saturation pressures

The Weber number has been evaluated as a possibly more appropriate departure criterion for this transition. It is

$$\mathrm{We}^2 = \frac{\rho \bar{u}^2 \delta}{\sigma} = \frac{1}{16} \frac{\mu^2}{\rho\sigma} \left(\frac{4\Gamma}{\mu}\right)^2 \frac{1}{\delta} \tag{12}$$

If equation (7) is used to evaluate δ then the values in Table 2 are obtained; slightly lower values of the Weber number proceed from the use of equation (1) to evaluate δ; these too are shown in the table as lower and somewhat less variable values of the Weber number. Table 3 contains a similar appraisal, with δ obtained from equation (1), for the results of Wilke. Again a Weber number of the order of unity is indicated for the point of departure from laminar behavior. The Weber numbers were evaluated using Wilke's tabulated properties [3], except the surface tension which was estimated by taking an average value weighted by mole fractions. These results imply that a Weber number of the order of unity may be a transition criterion in a falling liquid film.

Remarks on Condensation

It is important to note how the "turbulent" results for evaporation, given by equation (8), are related to existing recommendations for the specification of condensation with turbulent flow. With condensation instead of evaporation $d\Gamma/dx$ is always significant and

$$\lambda \frac{d\Gamma}{dx} = h(T'_s - T'_w) \tag{13}$$

Taking $h = A(\Gamma/\mu)^n$, integration yields, for $(\Gamma/\mu) > (\Gamma/\mu)_{tr}$

$$\left(\frac{\Gamma_L}{\mu}\right)^{1-n'} - \left(\frac{\Gamma}{\mu}\right)^{1-n'}_{tr} = \frac{A'(1-n')\Delta TL}{\mu\lambda} - \left(\frac{\Gamma}{\mu}\right)^{1-n}_{tr} \frac{A'(1-n')}{A(1-n)} \tag{14}$$

where the primed quantities are those associated with turbulent flow, equation (8), and the unprimed quantities are those associated with wavy laminar flow, equation (6). Insertion of these quantities and rearrangement gives, for the average heat-transfer coefficient, $\lambda\Gamma/(\Delta TL)$,

$$\bar{h}\left(\frac{\nu^2}{k^3 g}\right)^{1/3} = \frac{4 \times 10^{-3} \left(\frac{\nu}{\alpha}\right)^{0.65} \left(\frac{\Gamma_L}{\mu}\right)^{0.4}}{1 - \left(\frac{\Gamma}{\mu}\right)^{0.6}_{tr} \left(\frac{\mu}{\Gamma_L}\right)^{0.6} - 5.36 \times 10^{-3} \left(\frac{\nu}{\alpha}\right)^{0.65} \left(\frac{\Gamma}{\mu}\right)^{1.22}_{tr} \left(\frac{\mu}{\Gamma_L}\right)^{0.6}} \tag{15}$$

For Reynolds numbers reasonably higher than the transition Reynolds number, the denominator of equation (15) is essentially unity. For a Prandtl number of 5 and a high Reynolds number, equation (15) becomes

$$\bar{h}\left(\frac{\nu^2}{gk^3}\right)^{1/3} = 11.4 \times 10^{-3} \left(\frac{\Gamma}{\mu}\right)^{0.4}$$

Kirkbride's[4] equation, usually taken to represent results for Prandtl numbers like 5, is of this form, with a constant of 13.4×10^{-3}. It is also shown by Chun [5] that there is a reasonable correspondence of equation (15) with other results, such as those of Grigull [6].

For Reynolds numbers near transition, the value of the transition Reynolds number becomes critically important. The inferences of Tables 2 and 3 imply that it should be evaluated on the basis of a Weber number near unity.

Nucleation

Equations (6) and (8) are representative of expectation as long as no nucleate boiling occurs. Boiling could be made to occur in some conditions of operation, usually at a location near the bot-

[4] McAdams [4], p. 335.

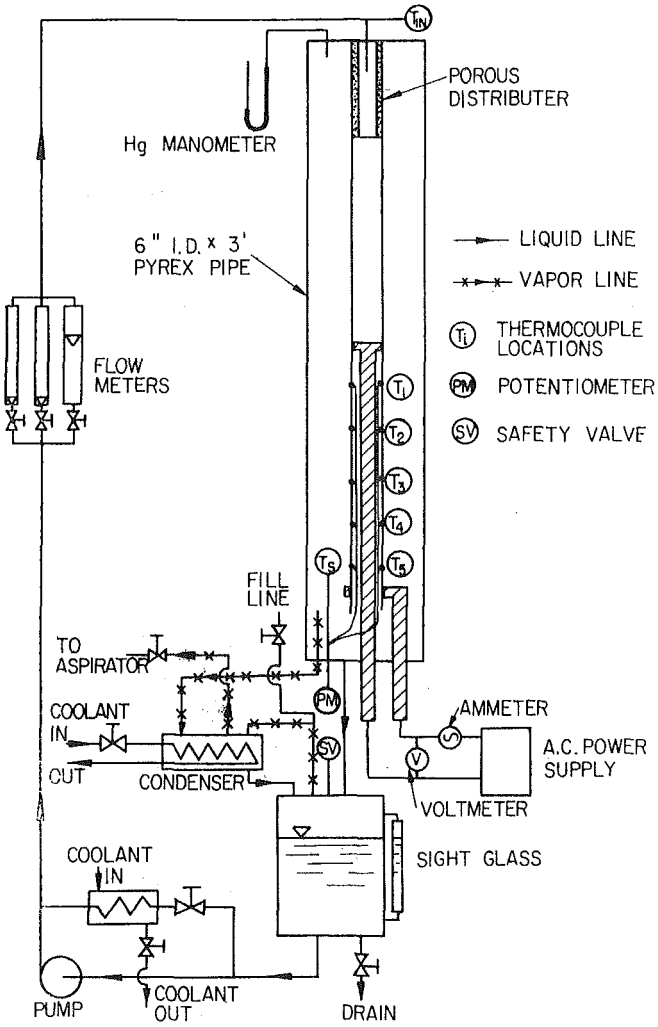

Fig. 3 Schematic drawing of experimental loop

tom of the tube. This could be determined visually and also by a sudden reduction of wall temperature in the region where bubbles were observed. This indicates that once nucleation is initiated it will continue at the lower superheat associated with the higher heat-transfer coefficient for boiling.

Fig. 2 shows wall superheat as a function of Reynolds number for runs with and without boiling, for three saturation temperatures, at two of which boiling was observed. Where the temperature difference exceeds 10 deg F, or boiling is indicated, the runs were made specifically in the search for nucleation, and the results are not shown in Fig. 1. The figure also contains curves indicating the liquid superheat, $T'_g - T_s$, needed for a bubble to grow,

$$T'_g - T_s = \frac{2T'^2_s R\sigma}{\lambda pr} \tag{16}$$

To apply this to the wall heated system, r needs to be visualized as a cavity radius and T_g as the temperature of the wall, T_w.

Equation (16) is then shown in Fig. 2 for a radius of 3.25×10^{-5} ft, the value thereof needed to give a superheat, $T_w - T_s$, of 6.6 deg F for nucleation at atmospheric pressure, to provide correspondence with observation. The results for 4.74 psia correspond to this prediction and, at 1.27 psia, the prediction superheat is 34 deg F and no boiling was observed because the experimental system could not attain heat fluxes which would produce temperature differences as large as this.

Chun [5] has also applied to these results other theories of nucleation and shows that equation (13) is the most appropriate for these results.

Summary

Results have been presented for heat-transfer coefficients for evaporation to surrounding saturated vapor from the surface of a water film running down the exterior of a vertical stainless steel tube. In the laminar regime these results are in accord with inferences made from the behavior of the average heat-transfer coefficient in laminar condensation.

In the regime of apparently turbulent flows there is obtained a correlation of the heat-transfer coefficients of the usual power-law type, which agrees with average heat-transfer coefficients observed for condensation at Prandtl numbers near 5, and with the liquid heating data of Wilke. The influence of Prandtl numbers in the present correlation is larger than expected.

The transition to the "turbulent" flow cannot be characterized by a Reynolds number and there is some indication that the Weber number may have an important influence on transition.

The incidence of nucleate boiling was specified best by the use of the elementary liquid superheat model.

Acknowledgment

This research was supported by the Sea Water Conversion Laboratory of the University of California.

References

1 Kutadeladze, S. S., *Fundamentals of Heat Transfer*, Edward Arnold, London, 1963, p. 307.

2 Dukler, A. E., "Fluid Mechanics and Heat Transfer in Vertical Falling Film Systems," *Chem. Eng. Prog. Symp. Ser.*, Vol. 56, No. 30, 1960, pp. 1–10.

3 Wilke, W., "Wärmeübergang an Reiselfilme," *Ver. Deut. Ingr. Forschungsh.*, Vol. 490, 1962.

4 McAdams, W. H., *Heat Transmission*, 3rd ed., McGraw-Hill, New York, 1954, chap. 13.

5 Chun, K. R., "Evaporation from Thin Liquid Films," PhD dissertation, Univ. of California, Berkeley, 1969.

6 Grigull, U., "Wärmeübergang bei der Kondensation mit Turbulenter Wasserhaut," *Forschung auf dem Gebiete der Ingenieurwesens*, Vol. 13, March 1942, pp. 49–57.

APPENDIX

System and Experiment

The experimental arrangement provided for the flow of distilled water down the exterior of a vertical tube. This tube was 1.125 in. in diameter, with a wall thickness of 0.004 in., and within its $11^1/_2$-in-long heated length contained a cylindrical bakelite insert which supported thermocouples which touched the interior wall of the tube, two at each of the locations shown in Fig. 3. Copper conductors were soldered to the tube, inside at the top of this heated section and outside at its bottom. Electric current was thus passed longitudinally through the tube to provide heating.

About 12 in. of the 24-in-long tube was to permit hydrodynamic development above the heated section, and on top of this was a distributor made of sintered metal to provide for uniform water distribution to the tube. This water supply was provided by the system shown in Fig. 3, incorporating a condenser, pump and flowmeters.

In operation the system was charged with water and this was circulated with vacuum in the tube enclosure to provide deaeration. Electric power was then applied and data were obtained after steady state was attained.

The minimum feedrate was limited by the occurrence of circumferentially nonuniform wetting, with the formation of accompanying rivulets on the surface of the tube. Non-wetting, of course, would lead to serious local overheating. The maximum feedrate was limited by "overshooting" of the feed at the distrib-

utor, so that all the liquid would not attach itself to the tube surface.

The amount of vaporization was deduced from the electrical energy input and the exterior wall temperature from the measured internal temperature, accounting for the heat generation in the wall. The vapor temperature was both measured and deduced from the measured pressure. With this information on heat flux and temperature difference, local heat-transfer coefficients could be evaluated, and the steady values obtained from the lower portion of the heated section constitute the results. The initial region of thermal development was from 3 to 5 in., though in some cases increased liquid subcooling increased this length to 8 in.

All properties involved in the correlation of the heat-transfer coefficient were evaluated at the saturation temperature and since in most cases the overall temperature difference was about 10 deg F or less, this property evaluation is satisfactory.

L. H. BACK
Member Technical Staff.
Mem. ASME

R. F. CUFFEL
Senior Scientist.
Assoc. Mem. ASME

Jet Propulsion Laboratory,
California Institute of Technology,
Pasadena, Calif.

Turbulent Boundary Layer and Heat Transfer Measurements Along a Convergent-Divergent Nozzle[1]

Boundary layer and heat transfer measurements are presented along a cooled, conical nozzle with a convergent and a divergent half-angle of 10 deg. Semi-empirical analyses are considered in conjunction with the measurements. The heat transfer is found to be describable by using the integral form of the energy equation once the relationship between the Stanton number and energy thickness Reynolds number has been established from the measurements. The friction coefficient, however, is not described accurately along the entire nozzle by existing formulations considered.

Introduction

THIS PAPER is concerned with the mean structure and development of a turbulent boundary layer in an accelerating flow through a cooled, supersonic nozzle. The investigation is relevant to rocket engines that operate at thrust levels for which laminarization does not occur. There appears to be an upper bound on the occurrence of laminarization and on the associated reduction in heat transfer below that typical of a turbulent boundary layer. The experimental results in reference [1][2] indicated turbulent boundary layer heat transfer at throat Reynolds numbers Re_{Dth} on the order of one million and higher. The thrust level corresponding to this throat Reynolds number for a hydrogen–oxygen propellant combination for example is F = 10,000 lb if the chamber pressure is 100 psia [2]. At higher chamber pressures and thus thrust levels, throat Reynolds numbers would be higher since $Re_{Dth} \propto (Fp_t)^{1/2}$. Therefore, many rocket engines operate in the turbulent boundary layer regime and consequently there is considerable interest in calculating convective heat transfer from turbulent boundary layers in nozzles. It is realized that such calculations are essentially empirical because of our limited knowledge of the effect of acceleration on the flow and thermal structure of turbulent boundary layers and of the simultaneous effects of wall cooling and compressibility (see the survey by Bartz [3] on the flow of rocket combustion gases and heated air, and recent measurements in heated air flows [4–6]).

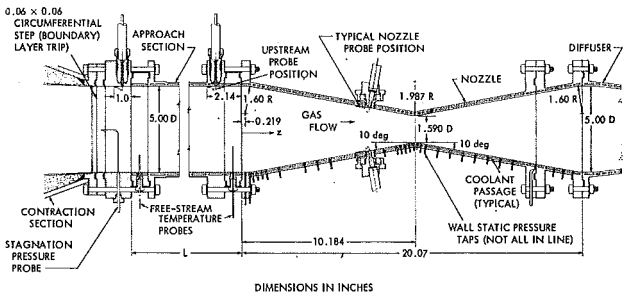

Fig. 1 System investigated

In this investigation boundary layer measurements were made with small pitot tubes and thermocouples along a nozzle (Fig. 1) which had a smooth (32-microinch-finish) wall. Air was compressed and heated to a pressure of 150 psia and a temperature of 1500 deg R at a remote distance upstream of the nozzle. The cooled wall to stagnation temperature ratio was about 0.5. At this operating condition, heat transfer measurements reported in reference [7] over a large range of stagnation pressures (Reynolds numbers) were found to be typical of a turbulent boundary layer. This observation formed the basis for traversing the boundary layer at a number of axial positions in order to study its structure and development.

Misalignment between the flow and the probes in the outer part of the boundary layer was not significant because of the gradual contour of the nozzle. Thus controlled measurements provided information on turbulent boundary layers subjected to

[1] This work presents the results of one phase of research carried out in the Propulsion Research and Advanced Concepts Section of the Jet Propulsion Laboratory, California Institute of Technology, under Contract No. NAS 7-100, sponsored by the National Aeronautics and Space Administration.

[2] Numbers in brackets designate References at end of paper.

Contributed by the Heat Transfer Division and presented at the ASME-AIChE Heat Transfer Conference, Tulsa, Okla., August 15–18, 1971. Manuscript received by the Heat Transfer Division January 16, 1971. Paper No. 71-HT-4.

the kind of flow acceleration found in practice. In this regard the nozzle shape resembles a rocket thrust chamber in which the combustion chamber is an integral part of the nozzle. Of course, combustion and injection effects are not present in this investigation.

At the nozzle inlet, the velocity boundary layer was about 0.40 of the inlet radius and the thermal boundary layer was slightly thicker. The effects of varying the operating conditions and inlet conditions were also investigated, i.e., changing the unit Reynolds number, the inlet boundary layer thicknesses, and the amount of wall cooling. In addition to the heat transfer measurements made along the nozzle, the wall shear stress could also be determined at the probe stations.

Semi-empirical analyses are considered in conjunction with the measurements to obtain information about the flow and to determine the extent to which the flow is predictable. These analyses pertain to the mean structure of turbulent boundary layers as obtained from mixing length and transformation theories, and from solutions of both the integral and differential [8] forms of the boundary layer equations. The integral analyses are based on a solution of the energy equation alone, and on a simultaneous solution of the momentum and energy equations [9].

Measurement Description

Static pressures, semi-local wall heat fluxes, and coolant-side wall temperatures were measured along the nozzle wall. Free-stream conditions upstream of the nozzle were obtained from probe measurements and those along the nozzle were obtained for isentropic expansion of the external flow ($\gamma = 1.4$) to the measured wall static pressures. The heat flux was determined by calorimetric measurements in relatively small circumferential coolant passages. There were 36 such passages along the nozzle. The gas-side wall temperature was calculated from the measured wall heat flux and coolant-side wall temperature. The heat transfer measurements are believed to be accurate to about ± 5 percent when the gas temperature was 1500 deg R. Additional information on the test apparatus and measurement technique as applied to an investigation of a nozzle with a different contour than investigated herein is presented in reference [4].

Boundary layer surveys were made with a small flattened pitot tube 0.005 in. high and with thermocouple probes. Descriptions of the probes used in the convergent section of the nozzle and of the measurement technique are given in reference [7]. There were two rows of probe locations in the streamwise direction

Nomenclature

A = constant
A_{th} = throat cross-sectional area
c = constant
c_D = mass flow coefficient, $\dfrac{\dot{m}}{\dot{m}_{1-D}}$
c_f = friction coefficient, $\dfrac{c_f}{2} = \dfrac{\tau_w}{\rho_e u_e^2}$
c_p = specific heat at constant pressure
D = tube or nozzle diameter
H = enthalpy
K = acceleration parameter, $\dfrac{\nu_e}{u_e^2}\dfrac{du_e}{dx}$
$\bar{K}$ = acceleration parameter, $\dfrac{K}{\left(\dfrac{c_f}{2}\right)^{3/2}}$
L = cooled approach length
$\dot{m}$ = mass flow rate
$\dot{m}_{1-D}$ = one-dimensional value, $\left[\gamma\left(\dfrac{2}{\gamma+1}\right)^{\frac{\gamma+1}{\gamma-1}}\right]^{1/2}\dfrac{p_t A_{th}}{(RT_t)^{1/2}}$
M = Mach number
p = pressure
Pr = Prandtl number
q_w = wall heat flux
r = nozzle radius
r_c = throat radius of curvature
r_{th} = throat radius
R = gas constant
Re_s = Reynolds number, $\dfrac{\rho_e u_e S}{\mu_e}$, where S is $\tilde{\theta}$, $\tilde{\phi}$, or D
St = Stanton number, $\dfrac{q_w}{(H_{aw} - H_w)\rho_e u_e}$
T = temperature
T_t^+ = dimensionless temperature, equation (6)
u = velocity component parallel to wall
u^+ = dimensionless velocity, equation (6)
u_τ = friction velocity, $\left(\dfrac{\tau_w}{\rho_w}\right)^{1/2}$
v = velocity component normal to wall
x = distance along wall
y = distance normal to wall
y^+ = dimensionless normal distance, equation (6)
z = axial distance
α = frictional heating parameter, equation (A-11), or thermal diffusivity
β = cooling parameter, equation (A-10)
γ = specific heat ratio
δ = velocity boundary layer thickness
$\tilde{\delta}^*$ = displacement thickness, $r\tilde{\delta}^* = \delta^*\left(r - \dfrac{\delta^* \cos\sigma}{2}\right) = \displaystyle\int_0^\infty \left(1 - \frac{\rho u}{\rho_e u_e}\right)(r - y\cos\sigma)dy$
ϵ_h = eddy diffusivity for heat transfer
ϵ_m = eddy diffusivity for momentum transfer
$\tilde{\theta}$ = momentum thickness, $r\tilde{\theta} = \theta\left(r - \dfrac{\theta\cos\sigma}{2}\right) = \displaystyle\int_0^\infty \frac{\rho u}{\rho_e u_e}\left(1 - \frac{u}{u_e}\right)(r - y\cos\sigma)dy$
κ = constant
μ = viscosity
ν = kinematic viscosity
ρ = density
σ = angle between wall and axis
τ_w = wall shear stress
$\tilde{\phi}$ = energy thickness, $r\tilde{\phi} = \phi\left(r - \dfrac{\phi\cos\sigma}{2}\right) = \displaystyle\int_0^\infty \frac{\rho u}{\rho_e u_e} \times \left[1 - \left(\frac{H_t - H_w}{H_{t0} - H_w}\right)\right](r - y\cos\sigma)dy$
ω = viscosity–temperature exponent

Subscripts and Superscripts

aw = adiabatic wall condition
e = condition at free-stream edge of boundary layer
i = condition at nozzle inlet
r = reference condition
s = Coles' mean sublayer reference condition
t = stagnation condition
th = throat condition
0 = reservoir condition or value at probe position 0
w = wall condition
$\bar{(\ )}$ = constant property value

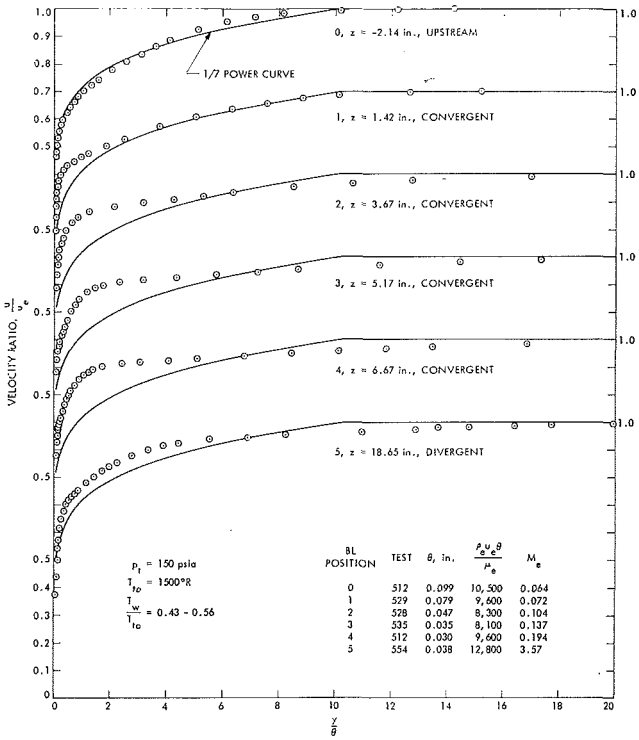

Fig. 2 Velocity profiles

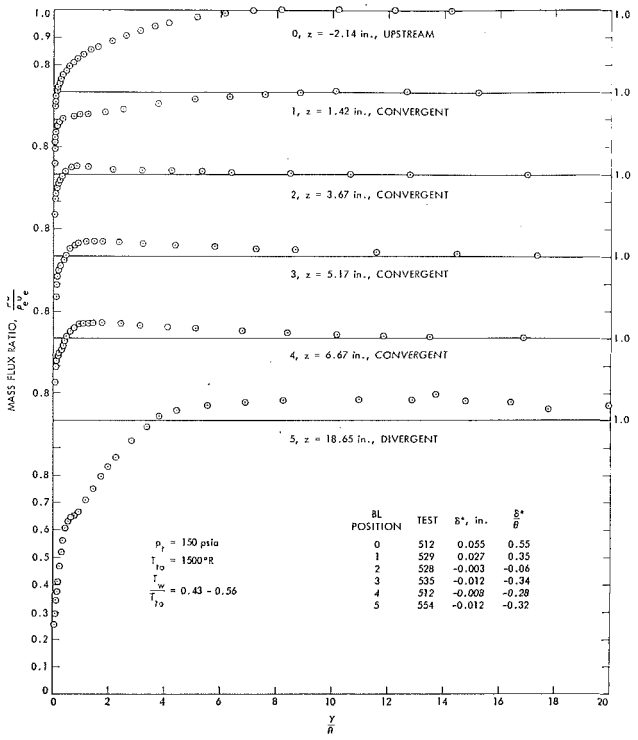

Fig. 3 Mass flux profiles

along the convergent part of the nozzle. To avoid flow interference the probes were moved from one axial location to another from test to test. The pitot tube was always located 90 deg circumferentially from the temperature probe at the same axial location. There were four such pairs of stations. Probe measurements were also made in the supersonic region near the nozzle exit. A shielded, aspirating, thermocouple probe 0.010 in. high was used at the exit station, whereas the thermocouple probe upstream in the convergent section ($M_e < 0.2$) consisted of an exposed thermocouple.

Results

Shape of Boundary Layer Profiles. Velocity profiles are shown upstream and along the nozzle in Fig. 2. The distance across the boundary layer is normalized by using the momentum thickness θ so that the profiles can be compared to each other locally. Along the convergent section acceleration causes a significant departure in the profiles from the $^1/_7$ power curve that is shown as a reference profile, and which is a fair representation of the measured profile upstream of the nozzle. The velocity profiles become steeper near the wall and flatter in the outer part of the layer, although the largest change occurs in going from probe position 1 to 2, with little change then occurring at subsequent stations in the convergent section. Near the nozzle exit where the flow is supersonic and compressibility effects are important, the profile becomes less steep near the wall, presumably as a result of viscous dissipation. The measurement nearest the wall corresponds to a Mach number of 1.03 so that the entire measurable portion of the boundary layer was supersonic. In the outer part of the layer, the profile is the same shape, however, as the profiles obtained in the latter part of the convergent section.

The variation of the boundary layer mass flux profiles upstream and along the nozzle is shown in Fig. 3. Because of the combined effects of acceleration and wall cooling, the mass flux in the outer part of the boundary layer along the convergent section eventually exceeds the free-stream value so that the effective displacement caused by the boundary layer is not into the external flow, but instead into the wall. For this situation the displacement thickness δ^* is negative. Near the nozzle exit the mass flux is appreciably reduced near the wall because of viscous dissipation. However, the mass flux in the outer part of the boundary layer still exceeds the free-stream value by a sufficient amount so that the displacement thickness remains negative.

The velocity and mass flux profiles differ markedly along the nozzle; however, the temperature profiles are remarkably similar as seen in Fig. 4. These profiles are described fairly well by the $^1/_7$ power curve shown. In the representation of Fig. 4, the temperature difference ratio is the local total gas temperature, and the distance normal to the wall is made dimensionless with the energy thickness ϕ.

Heat Transfer. By virtue of the similarity between the temperature profiles along the nozzle on a y/ϕ basis, one suspects that there may also be a relationship between the heat transfer and the energy thickness, which would follow directly for example if the boundary layer were laminar. To test this hypothesis it is first necessary to calculate the energy thickness distribution along the nozzle, and this can be done by using the integral form of the energy equation

$$\frac{d}{dx}[r^j \rho_e u_e \tilde{\phi}(H_{t0} - H_w)] = r^j q_w \qquad (1)$$

This relation applies to axisymmetric flow with $j = 1$ and to flow over a plane surface with $j = 0$. Using the measured energy thickness ϕ upstream of the nozzle as the initial value, the energy equation was integrated along the nozzle by introducing measured wall heat fluxes and the free-stream flow variables to obtain the distribution of $\tilde{\phi}$. The relationship between ϕ and $\tilde{\phi}$ that arises because of the definition of the energy defect in the flow to which ϕ is associated and the integral to which $\tilde{\phi}$ is related in equation (1) is given in the Nomenclature. The difference between ϕ and $\tilde{\phi}$, however, is small.

The result of this calculation is shown in the upper part of Fig. 5 where the Stanton number (actually, St $Pr^{0.6}$) is shown as a function of the energy thickness Reynolds number. Also shown is the relation

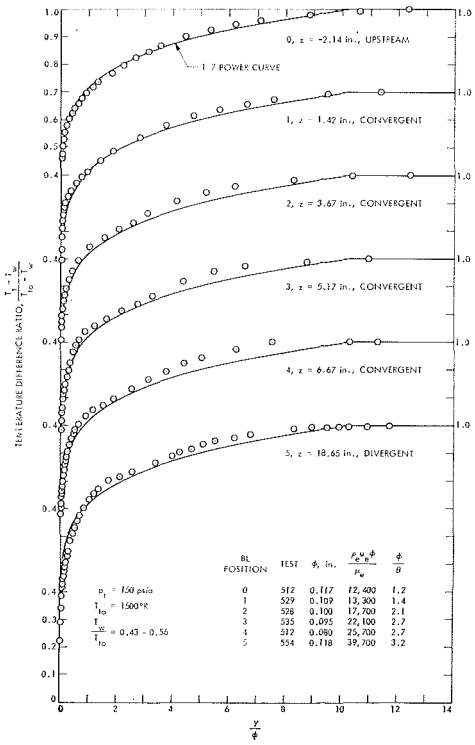

Fig. 4 Temperature profiles

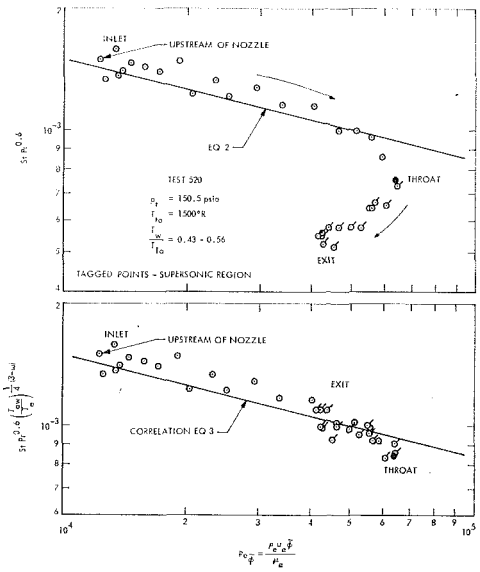

Fig. 5 Heat transfer–energy thickness Reynolds number relation

$$\mathrm{St}\,\mathrm{Pr}^{0.6} = A\left(\frac{\rho_e u_e \tilde{\phi}}{\mu_e}\right)^{-1/4} \tag{2}$$

adopted from the analogous Blasius friction coefficient–momentum thickness Reynolds number relation, and which includes a Prandtl number factor. In this relation A is taken to be 0.015 to fit the data. This value is slightly higher than the Blasius value of 0.0128. In Fig. 5 the experimental results are identified upstream of the nozzle, at the inlet, then along the convergent section to the throat, and then in the divergent section to the exit. Clearly, if a correlation is to be achieved, a correction needs to be made for compressibility effects since the data lie progressively below the curve shown as one proceeds toward the nozzle exit and the Mach number increases (Fig. 6). If instead, the density and viscosity in equation (2) are evaluated at a

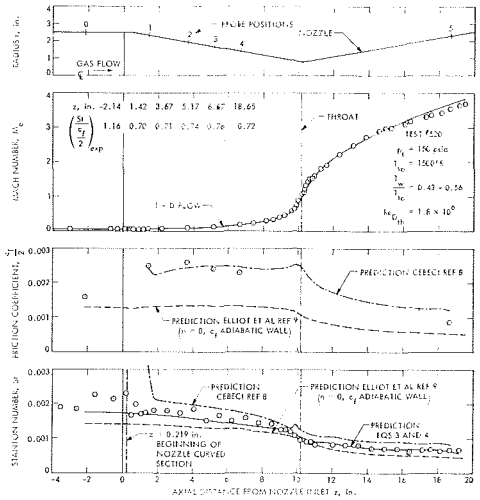

Fig. 6 Mach number, friction coefficient, and Stanton number distributions

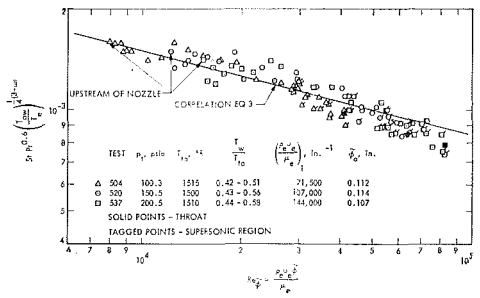

Fig. 7 Effect of unit Reynolds number on the heat transfer–energy thickness Reynolds number relation

reference temperature, the relation becomes

$$\mathrm{St}\,\mathrm{Pr}^{0.6} = A\left(\frac{\rho_r}{\rho_e}\right)^{3/4}\left(\frac{\mu_r}{\mu_e}\right)^{1/4}\left(\frac{\rho_e u_e \tilde{\phi}}{\mu_e}\right)^{-1/4}$$

To establish the magnitude of the compressibility correction that is needed, the reference temperature is taken as the adiabatic wall temperature, and the data are shown in the lower part of Fig. 5 in terms of the heat transfer group

$$\mathrm{St}\,\mathrm{Pr}^{0.6}\left(\frac{T_{aw}}{T_e}\right)^{1/4(3-\omega)}$$

In this relation the viscosity was taken as $\mu\alpha T^{\omega}$, with $\omega = 0.7$ providing a good approximation to the actual variation of viscosity of air with temperature over the temperature range of interest. The adiabatic wall temperature was calculated using a recovery factor of 0.89, a value for air which apparently does not differ much in accelerated turbulent boundary layers [10]. The agreement between the experimental data and the following prediction including the compressibility correction is much improved (lower part of Fig. 5) and indicates the magnitude of the reduction in the Stanton number below the low-speed value.

$$\mathrm{St}\,\mathrm{Pr}^{0.6}\left(\frac{T_{aw}}{T_e}\right)^{1/4(3-\omega)} = A\left(\frac{\rho_e u_e \tilde{\phi}}{\mu_e}\right)^{-1/4} \tag{3}$$

Of note is that the use of the Eckert reference temperature [11] would not correlate the data, e.g., near the end of the nozzle where $M_e = 3.6$, $\frac{T_r}{T_e} = 1.78$, however $\frac{T_{aw}}{T_e} = 3.31$. Consequently, the predicted Stanton number would be about 40 percent higher than given by equation (3).

Some generalizations of the heat transfer results in Figs. 7–9.

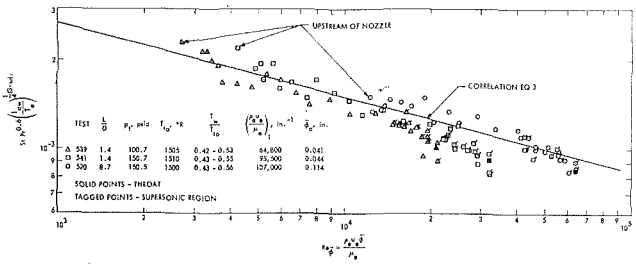

Fig. 8 Effect of inlet layer thermal thickness on the heat transfer–energy thickness Reynolds number relation

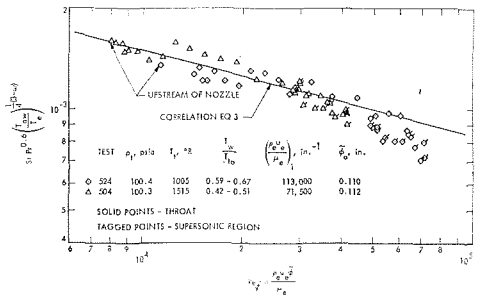

Fig. 9 Effect of wall cooling on the heat transfer–energy thickness Reynolds number relation

In Fig. 7, results are shown at lower and higher stagnation pressures so that the unit Reynolds numbers spanned a twofold range. In Fig. 8, results are shown with a shorter length L of upstream tube so that the energy thickness upstream of the nozzle was less by a factor of about $1/3$. In Fig. 9, results are shown at a lower stagnation temperature so that the amount of wall cooling was less, i.e., larger value of $\frac{T_w}{T_{t0}}$. All of these data are correlated fairly well by equation (3). Unfortunately, it was not possible to obtain reliable heat transfer measurements with a smaller amount of wall cooling or wall heating to ascertain if there is a separate effect of $\frac{T_w}{T_{t0}}$ on the heat transfer correlation. At least for the range of wall cooling investigated, the effect of compressibility appears to predominate in the supersonic region and this is in accordance with the suggestion by Bartz [3]. There may be some effect of wall cooling in the convergent section such as there is upstream of the nozzle in the cooled section [12], but it may be partially obscured by local flow separation that is believed to have occurred in the nozzle inlet section because of a compressive turning of the flow in entering the nozzle (e.g., see reference [13] for flow through a nozzle with a steeper contraction section). The separation region in the nozzle inferred from the measured pressure rise, however, is relatively small, and in this regard, heat transfer measurements are not shown in Figs. 5, 7–9 upstream of the beginning of the curved section of the nozzle (Fig. 6). The values labeled upstream of the nozzle in Figs. 5, 7–9 were obtained near the boundary layer probe station 0 where the heat transfer measurements are of the same magnitude as they are downstream of the beginning of the curved section of the nozzle (Fig. 6).

The fairly good correlation of the heat transfer results suggests a straightforward prediction method involving the energy equation alone, although such a specification is not new, having been suggested earlier by Ambrok [14] and found previously to be in reasonably good agreement for accelerating [3, 4, 15, 16], decelerating [17], and accelerating–decelerating [18] turbulent boundary layers. For completeness the method is given herein. The energy thickness is obtained by integration of equation (1) along the wall to give the following relation once the wall heat flux is specified in terms of the energy thickness by equation (3).

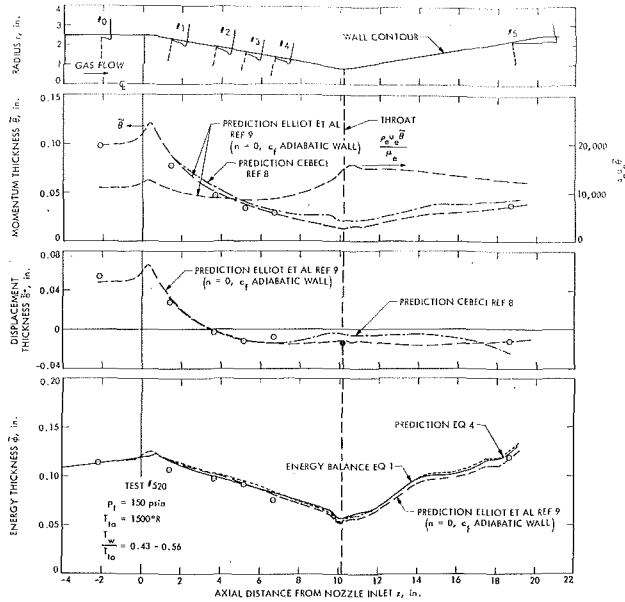

Fig. 10 Boundary layer thickness, $\tilde{\theta}$, $\tilde{\delta}^*$, and $\tilde{\phi}$ distributions

$$\tilde{\phi}^{5/4} = \frac{5}{4} A \frac{1}{\mathrm{Pr}^{0.6}} \frac{1}{\lambda^{5/4}} \int_0^x \left[\frac{\lambda^{5/4}}{(\rho_e u_e/\mu_e)^{1/4}} \xi \right] dx + \left(\frac{\lambda_i \tilde{\phi}_i}{\lambda} \right)^{5/4} \tag{4}$$

where

$$\lambda = r^j \rho_e u_e (H_{t0} - H_w) \qquad \xi = \left(\frac{H_{aw} - H_w}{H_{t0} - H_w} \right) \left(\frac{T_e}{T_{aw}} \right)^{1/4(3-\omega)}$$

Knowing the free-stream flow variables, the thermal condition along the wall, and the initial condition denoted by the subscript i, the energy thickness can be obtained for example as shown in Fig. 10. The Stanton number can then be calculated from equation (3) as shown in particular in Fig. 6, and the heat flux is determined from

$$q_w = \mathrm{St}\, \rho_e u_e (H_{aw} - H_w) \tag{5}$$

Velocity and Temperature Profiles. In addition to observing the shape of the boundary layer profiles as they were shown in the representation of Figs. 2–4, there is also interest in appraising these profiles in terms of existing information on turbulent boundary layers that has been expressed in terms of the dimensionless velocity u^+ and temperature T_t^+ profiles as a function of y^+. These quantities are defined as

$$u^+ = \frac{u}{u_\tau}, \qquad T_t^+ = \frac{T_t - T_w}{(q_w)/(\rho_w u_\tau c_{p_w})}, \qquad y^+ = \frac{\rho_w u_\tau y}{\mu_w} \tag{6}$$

where the friction velocity $u_\tau = \left(\frac{\tau_w}{\rho_w} \right)^{1/2}$. To establish the profiles in this representation it is necessary to determine the wall shear stress τ_w, a quantity that is difficult to measure directly in accelerated flows. Of course, a determination of the wall shear stress is also important in itself to appraise the importance of frictional effects.

Because of the number and relative closeness of the probe stations along the convergent section of the nozzle, the integral form of the momentum equation

$$\frac{d}{dx} (r^j \rho_e u_e^2 \tilde{\theta}) + r^j \rho_e u_e \tilde{\delta}^* \frac{du_e}{dx} = r^j \tau_w \tag{7}$$

could be applied in this region. Integration of equation (7) along the wall gives

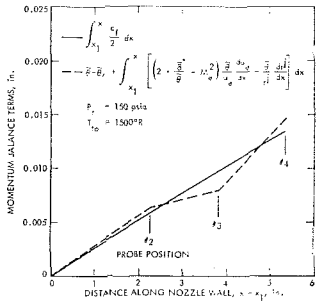

Fig. 11 Momentum balance along the convergent section

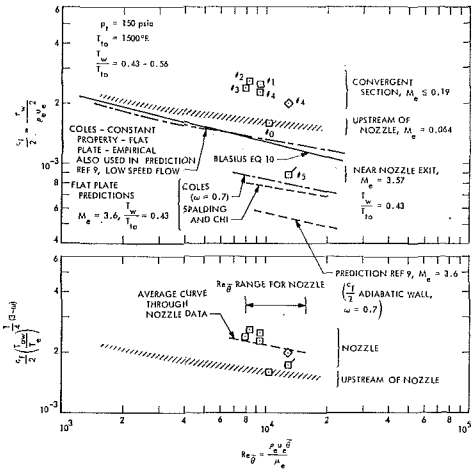

Fig. 12 Friction coefficient–momentum thickness Reynolds number relation. The diamond point (probe position 4) was obtained at a higher stagnation pressure of 200 psia, $T_w/T_{t0} = 0.50$ (reference [7]). The shaded region represents data from reference [21].

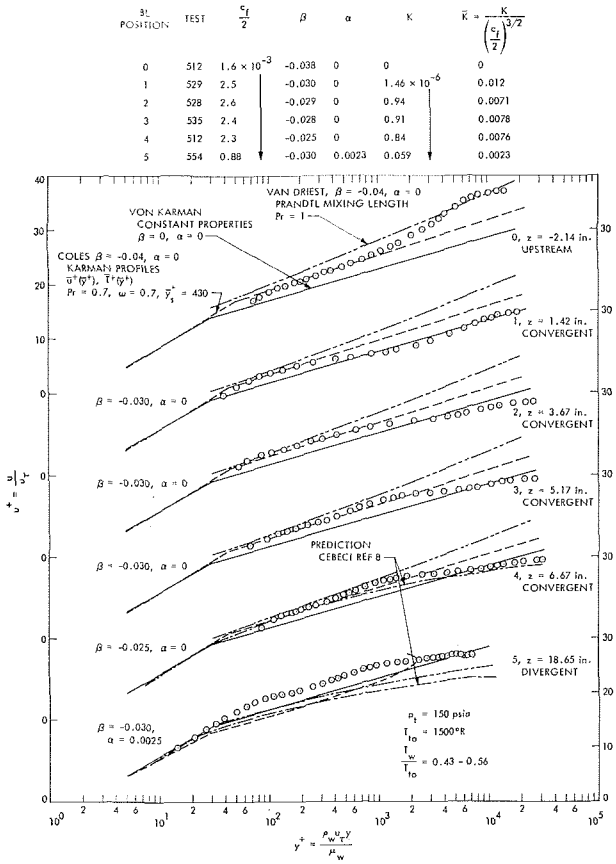

Fig. 13 Velocity profiles in terms of u^+ and y^+

$$\tilde{\theta} - \tilde{\theta}_1 + \int_{x_1}^{x} \left[\left(2 + \frac{\tilde{\delta}^*}{\tilde{\theta}} - \mathrm{M}_e^2 \right) \frac{\tilde{\theta}}{u_e} \frac{du_e}{dx} + \frac{\tilde{\theta}}{r^i} \frac{dr^i}{dx} \right] dx = \int_{x_1}^{x} \frac{c_f}{2} dx \quad (8)$$

The left side of this equation was evaluated from the boundary layer measurements and the known free-stream flow variables beginning from probe position 1. The relationship between θ, δ^* and $\tilde{\theta}$, $\tilde{\delta}^*$ given in the Nomenclature follows directly from the definition of the momentum and mass flow defects to which θ and δ^* are associated and the integrals to which $\tilde{\theta}$ and $\tilde{\delta}^*$ are related in equation (7), similar to the ϕ, $\tilde{\phi}$ relation. This result is shown by the dashed curve in Fig. 11. The friction coefficient is then determined by satisfying the momentum balance as indicated by the solid line shown in Fig. 11.

Upstream of the nozzle at probe position 0, the friction coefficient was inferred from the heat transfer measurements from a form of Reynolds analogy, $\mathrm{St} = 1.16 \frac{c_f}{2}$, for air $\mathrm{Pr} = 0.7$ [19–21], since in this region there was no flow acceleration and conditions were such that a form of Reynolds analogy should apply there [21]. A large momentum thickness Reynolds number range was investigated in reference [21] as indicated by the shaded region in Fig. 12 which represents that data. Near the nozzle exit, the boundary layer measurements extended well into the sublayer, as will be seen subsequently, so that the friction coefficient could be estimated from the velocity profile itself. A discussion of the magnitude of the friction coefficients so deduced at the probe stations is deferred until later. The velocity and temperature profiles are described first.

Velocity profiles are shown in Fig. 13 in terms of u^+ and y^+. Upstream of the nozzle, the effect of wall cooling is to shift the measured velocity profile in the law of the wall region above the von Karman constant property profile.

$$\tilde{u}^+ = c + \frac{1}{\kappa} \ln \tilde{y}^+ \qquad \text{with} \qquad c = 5.5 \quad \text{and} \quad \kappa = 0.4$$

Such departure apparently depends upon a wall cooling parameter β, equation (A-10), and is perhaps better seen in reference [20] where boundary layer measurements were shown at this upstream location over a large range of values of β. Included is the adiabatic wall condition, $\beta = 0$, for which the measured profiles nearly corresponded to the von Karman profile. A brief discussion of how variable property effects due to wall cooling and compressibility might alter a turbulent boundary layer is given in the Appendix. The predicted profiles from either mixing length theory, van Driest [22], or Coles' transformation theory [23] depend upon β and a viscous heating parameter α, equation (A-11). These predicted profiles along with the von Karman profile are shown as reference curves in Fig. 13 at the various probe stations.

Although there is some curvature of the measured profiles near the wall along the convergent section of the nozzle because of the variable shear stress in the wall region accompanying the pressure gradient flow, Fig. 13, there still appears to be a region near the wall where there is fair agreement with the predicted variable property profiles. This correspondence implies that the effect of acceleration on the velocity profiles in the law of the wall region is not appreciable.

A useful acceleration parameter in this regard is given by

$$\bar{K} = \frac{K}{(c_f/2)^{3/2}} = \frac{(\nu_e/u_e^2)(du_e/dx)}{(\tau_w/\rho_e u_e^2)^{3/2}} = \frac{\nu_e \left(-\frac{dp}{dx} \right)}{\rho_e (\tau_w/\rho_e)^{3/2}} \quad (9)$$

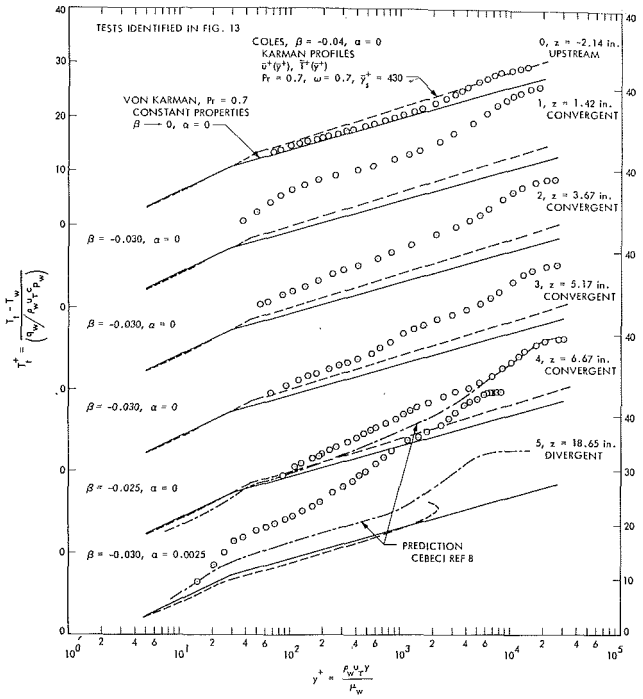

Fig. 14 Temperature profiles in terms of T_t^+ and y^+

which is obtained from a consideration of the effect of acceleration on the shear stress distribution in the wall region or on the production of turbulence near a wall [7]. For the measurements herein the parameter $\bar{K}$ is relatively constant along the central part of the convergent section at a value of about 0.008 (Fig. 13). It is interesting to note in this regard that this value of $\bar{K}$ is also realized in an isothermal, fully developed turbulent flow through a tube where there is pressure drop due to wall friction and the law of the wall relation is known to apply. For a power law variation of the friction coefficient with Reynolds number, $\bar{K} = 20\ \mathrm{Re}_D^{-7/8}$. Thus a value of $\bar{K}$ of 0.008 corresponds to a Reynolds number Re_D of about 8000. Patel and Head [24] in their velocity profile measurements in a constant property, low-speed, accelerated turbulent boundary layer also found a negligible deviation from the law of the wall in the forward part of the acceleration region at a comparable value of the parameter $\bar{K}$. In accelerating flows with larger values of $\bar{K}$, measured velocity profiles deviate from the law of the wall [7, 24] apparently because of a suppression of turbulent transport in the wall vicinity, and eventually become laminar-like in the wall vicinity when $\bar{K}$ is on the order of 0.04 (reference [7], Fig. 7) and larger. In this connection it should be noted that a more intuitive choice perhaps to describe acceleration effects would be the ratio of the pressure force which tends to accelerate the boundary layer to the retardation wall shear force, $\delta\left(-\frac{dp}{dx}\right)\Big/\tau_w$ or $\theta\left(-\frac{dp}{dx}\right)\Big/\tau_w$ since δ is difficult to measure accurately. However, this force ratio is a poor indicator of conditions under which turbulent transport is diminished in the wall vicinity. For example, this force ratio would not change much at probe position 4 as the stagnation pressure or Reynolds number is decreased. Yet laminarization occurred at lower Reynolds numbers or larger values of $\bar{K}$.

Flow acceleration does not appear to significantly influence the velocity profiles in the wall region. It does however affect the outer part of the boundary layer as seen in Fig. 13. The wake-like behavior found upstream of the nozzle disappears along the nozzle, and the profiles become flatter in the outer part of the boundary layer presumably because of the reduced shear stress in this region compared to that for a non-accelerating boundary layer. The slight S shape of the velocity profile at probe position 1 apparently reveals the influence of local separation and reattachment that is believed to have occurred upstream in the vicinity of the beginning of the curved section of the nozzle.

In the supersonic region, near the nozzle exit, the velocity profile is hardly changed in the law of the wall region from the profiles upstream. At this location the measurements extend into the sublayer and reveal a thickening of the sublayer owing to viscous dissipation. The measured profile is similar in shape to that found on a cooled, flat plate in a supersonic flow at about the same values of β and α, except that it does not have a wake component, e.g., see Lobb, Winkler, and Persh's measurements shown in Schlichting [25]. Of note is that the parameter $\bar{K}$ is even smaller near the nozzle exit than in the convergent section of the nozzle. Because of frictional heating, the reference profiles are shifted downward, but they then lie below the measured profile.

The most distinctive feature of the temperature profiles shown in Fig. 14 in terms of T_t^+ and y^+ is that beyond the sublayer, the profiles along the nozzle generally lie considerably above the von Karman constant property profile, especially near the nozzle exit. Correspondingly, the thermal resistance is larger (proportional to T_t^+) and consequently the von Karman form of Reynolds analogy, as well as other forms such as the Colburn relation, would overestimate the heat transfer. Instead, values of $\mathrm{St}/(c_f/2)$ are about 0.7 at the probe positions (Fig. 6). Measured temperature profiles in a constant property, low-speed, accelerated turbulent boundary layer [26] also reveal a similar behavior as observed in Fig. 14. Of note is that the larger thermal resistance implied by the measured profiles is not associated with laminarization for which there is an increase in the thermal resistance across the sublayer [7, 27]. However, there does appear to be some increase in the sublayer thermal resistance (though not a consistent one) for the present measurements, and this trend was also found in reference [26].

Friction Coefficients. Attention is now focused on the friction coefficients that are shown in Fig. 12 as a function of the momentum thickness Reynolds number. The heat transfer–energy thickness Reynolds relation was essentially the same in the convergent section of the nozzle as upstream (Figs. 5, 7–9); however, this is not true for the friction relation. Because of flow acceleration there is an appreciable increase in the friction coefficient along the convergent section of the nozzle that amounts to about 50 percent. The friction coefficient near the nozzle exit is reduced similar to the Stanton number (Fig. 5) presumably because of compressibility. By making a compressibility correction according to the Blasius relation, similar to equation (3),

$$\frac{c_f}{2} = 0.0128\left(\frac{\rho_e u_e \tilde{\theta}}{\mu_e}\right)^{-1/4} \tag{10}$$

Then the data point near the nozzle exit is shifted upward in terms of the friction group

$$\frac{c_f}{2}\left(\frac{T_{aw}}{T_e}\right)^{1/4(3-\omega)}$$

In this representation (lower part of Fig. 12) the data point near the end of the nozzle also lies above the data upstream of the nozzle but by a smaller amount than the data along the convergent section. In view of the rather small range of momentum thickness Reynolds number for the nozzle flow, the friction coefficient might be estimated along the entire nozzle from the average curve drawn through the data.

It should be noted that semi-empirical correlations of friction data for supersonic flows over flat plates by Coles [23] and Spalding and Chi [28] give friction coefficients that are too low near the end of the nozzle as seen in the upper part of Fig. 12. In Coles' formulation the friction coefficients and momentum thickness Reynolds numbers in the variable property flow are

related to the constant property flow by the following relations for a perfect gas

$$\frac{c_f}{2}\frac{T_w}{T_e}\frac{\mu_s}{\mu_w} = \frac{\bar{c}_f}{2}$$
$$\mathrm{Re}_{\tilde{\theta}}\frac{\mu_e}{\mu_s} = \overline{\mathrm{Re}}_{\tilde{\theta}} \tag{11}$$

The mean sublayer temperature T_s defined by Coles as in equation (A-13) can be rewritten as

$$\frac{T_s}{T_w} = 1 - \langle g\rangle\left(\frac{\mathrm{St}}{c_f/2}\right)\left(1 - \frac{T_{aw}}{T_w}\right)\left(\frac{\bar{c}_f}{2}\right)^{1/2} - \langle f^2\rangle\frac{T_e}{T_w}\frac{\gamma-1}{2}\mathbf{M}_e^2\left(\frac{\bar{c}_f}{2}\right) \tag{12}$$

where for abbreviation

$$\langle g\rangle = \frac{1}{\bar{y}_s^+}\int_0^{\bar{y}_s^+}\bar{T}^+ d\bar{y}^+$$
$$\langle f^2\rangle = \frac{1}{\bar{y}_s^+}\int_0^{\bar{y}_s^+}(\bar{u}^+)^2 d\bar{y}^+ \tag{13}$$

Coles has used the Crocco relation (Pr = 1) for which St = $c_f/2$, $T_{aw} = T_{t0}$, and $\langle g\rangle = \langle f\rangle$, and empirically evaluated T_s from wall friction measurements in supersonic air flows over adiabatic flat plates as

$$\frac{T_s}{T_w} = 1 - \langle f\rangle\left(1 - \frac{T_{t0}}{T_w}\right)\left(\frac{\bar{c}_f}{2}\right)^{1/2} - \langle f^2\rangle\frac{T_e}{T_w}\frac{\gamma-1}{2}\mathbf{M}_e^2\left(\frac{\bar{c}_f}{2}\right) \tag{14}$$

The values of $\langle f\rangle = 17.2$ and $\langle f^2\rangle = 305$ imply a relatively thick sublayer extending to $\bar{y}_s^+ = 430$, a location well within the turbulent region of a constant property flow. Using Coles' constant property friction relation $\frac{\bar{c}_f}{2}(\overline{\mathrm{Re}}_{\tilde{\theta}})$ obtained from experimental data on a flat plate (shown in the upper part of Fig. 12), the friction coefficient–momentum thickness Reynolds number relation was calculated from equations (11) and (14) for $\mu \propto T^\omega$ with $\omega = 0.7$. In the empirical method of Spalding and Chi, the friction relations, similar to equation (11), are given by

$$\frac{c_f}{2}F_c = \frac{\bar{c}_f}{2}$$
$$\mathrm{Re}_{\tilde{\theta}}F_{R\theta} = \overline{\mathrm{Re}}_{\tilde{\theta}} \tag{15}$$

F_c and $F_{R\theta}$ depend upon T_w/T_e and $\mathbf{M}_e$ as determined from experimental data including wall cooling. They are tabulated in reference [28].

Furthermore, if one were to apply Coles' formulation or the Spalding and Chi method to the low-speed accelerated flow region along the convergent section of the nozzle, the predicted friction coefficients would lie below the data at about the same level as the measured values upstream of the nozzle since these methods only account for variable property effects, e.g., see reference [21].

Predictions. Predictions from the simultaneous solution of the integral form of the energy and momentum equations (1) and (7), in particular as done by Elliott, Bartz, and Silver [9], are shown in Figs. 6 and 10. The assumptions are that there is similarity in the velocity and total temperature profiles on a 1/7 power basis with respect to their individual thicknesses, which can be different from one another. The friction coefficient is adopted from Coles' formulation, but involves a different interpretation of the sublayer temperature specification in that the wall temperature T_w was replaced by the adiabatic wall temperature T_{aw} in equation (14), which however is then not compatible with equation (12) since the second term on the right side would be zero in this case. Also the wall condition in equation (11) was replaced by the adiabatic wall condition. By doing this the friction coefficient is presumed to be reduced by compressibility effects, but is unchanged by wall cooling, and is based on information obtained for non-accelerating flows. The heat transfer is specified from the von Karman analogy; however, the friction coefficient is not taken to be the actual friction coefficient, but instead the friction coefficient evaluated at the energy thickness Reynolds number ($n = 0$, in their nomenclature). This procedure yields lower predicted Stanton numbers than from the von Karman analogy because the energy thickness is larger than the momentum thickness in an accelerating flow with about equal thicknesses upstream of the nozzle. Alternative friction and heat transfer specifications are included in reference [9], but previous experience has indicated the preference for the preceding relations based on heat transfer measurements. However, no simultaneous information was apparently available heretofore on the friction coefficient for a convergent–divergent nozzle. The prediction was initiated from probe position 0 upstream of the nozzle where $\tilde{\theta}$ and $\tilde{\phi}$ are known.

The predicted momentum and displacement thicknesses shown in Fig. 10 are generally in good agreement with the measured values. This occurs in spite of the much lower predicted friction coefficients compared to the values deduced from the boundary layer measurements (Fig. 6). One would expect the predicted friction coefficients with just a compressibility correction to be too low, as mentioned previously and observed in Fig. 12, and this is indeed the case. They are in fact even lower than those values deduced from Coles, and Spalding and Chi since the predicted effect of wall cooling is to increase the friction coefficient (Fig. 12). The lower predicted shear stresses increase the slope of the predicted momentum thickness along the convergent section relative to that observed experimentally (Fig. 10). This trend can be deduced from the momentum balance equation (7) and is also evident in the predictions made by Cebeci (Fig. 10) (subsequently discussed) wherein better agreement is found between the predicted and measured shear stresses (Fig. 6) along the convergent section. Less detailed information is available along the remainder of the nozzle although it does appear that the predicted momentum thickness near the nozzle exit is not particularly sensitive to the predicted shear stress distribution along the nozzle, although the free-stream velocity gradient term which contains $\tilde{\delta}^*$ also enters into the momentum balance equation (7).

With regard to the displacement thickness it should be mentioned that the flow coefficient c_D for the conditions of test number 520 was greater than unity, being equal to 1.03, as indicated by both a mass flow measurement far upstream of the nozzle with a sharp-edged orifice and by using the probe measurements at the upstream position 0. This implies that the displacement thickness was negative in the throat region, i.e., the mass flux through the boundary layer exceeded that in the free stream. By knowing the flow coefficient, it is possible to infer what the displacement thickness must have been from the following relation that was derived in reference [29] by considering axisymmetric flow in the throat plane

$$c_D \cong c_{D\,\mathrm{inv}} - 2\left(\frac{\delta^*}{r_{th}}\right) \tag{16}$$

Since the inviscid flow coefficient $c_{D\,\mathrm{inv}}$ is essentially unity (0.996) as indicated by the predictions of references [30, 31] ($r_c/r_{th} = 2.5$, $\gamma = 1.4$), the value of the displacement thickness calculated using equation (16) is -0.014 in. This value is shown in Fig. 10 by the shaded symbol; the predicted value agrees quite well with it.

The predicted values of the energy thickness also agree well with those obtained from the energy balance as expected because

of the fairly good agreement in the heat transfer specification (Fig. 6) which, however, is somewhat low. Of particular note is the striking resemblance between the energy thickness distribution and the nozzle wall contour, i.e., the radius r, which undoubtedly has led to the fair correspondence between empirical heat transfer predictions wherein the Stanton number is taken to be related to a Reynolds number based on the nozzle diameter, e.g., see references [3, 4].

As a final view of the experimental data, comparisons are shown from the numerical solution of the differential form of the boundary layer equation which was carried out by Cebeci using the method described in reference [8]. In the calculations the eddy diffusivity for momentum transfer ϵ_m, assumed to be 0.9 of the eddy diffusivity for heat transfer ϵ_h (defined in terms of the turbulent heat transport $\rho\overline{v'H_t'}$), was specified in terms of a mixing length in the inner part of the boundary layer and was reduced near the wall by a damping factor suggested by van Driest [32]

$$\epsilon_{m_i} = \kappa^2 y^2 \left\{1 - \exp\left[-\frac{y(\tau_w/\rho)^{1/2}\rho/\mu}{26(\tau_w/\tau_s)^{1/2}}\right]\right\}^2 \frac{\partial u}{\partial y}$$

The value κ was taken to be 0.4 (reference [8]). In the damping term, ρ and μ were evaluated locally, and the shear stress τ_s refers to a value at $y^+ = 11.8$ (reference [8]). For the calculations herein there is a negligible reduction in the shear stress at $y^+ = 11.8$, so that essentially $\tau_s \cong \tau_w$. In the outer part of the boundary layer a constant value of the eddy diffusivity was used:

$$\epsilon_{m_0} = 0.0168 \int_0^\infty (u_e - u)dy$$

which was reduced by the intermittency factor γ

$$\gamma = \frac{1}{1 + 5.5(y/\delta)^6}$$

The joint between the inner and the outer layer is defined by $\epsilon_{m_i} = \epsilon_{m_0}$, i.e., continuity of ϵ_m. The numerical calculations were initiated at the first probe station in the nozzle (number 1) from the measured velocity and temperature profiles. This location was chosen to avoid trying to integrate the boundary layer equations through the adverse pressure gradient region upstream.

Along the convergent section the predicted friction coefficients (Fig. 6) agree very well with the values deduced from the boundary layer measurements. However, along the divergent section where compressibility effects become important the predicted friction coefficient apparently becomes too large and exceeds the measured value by about $1/3$ near the nozzle exit. At this location the corresponding predicted velocity profile on a u^+, y^+ basis (Fig. 13) lies below the measured profile in the law of the wall region, and this is consistent with the higher friction coefficient predicted. *Note the good agreement with the measured* and predicted velocity profiles at probe position 4 along the convergent section where the friction coefficients also agree well.

The predicted Stanton numbers also lie above the measured values by about $1/4$ along the divergent section (Fig. 6). They are somewhat high along the convergent section too. Inference of the heat flux and therefore Stanton number at the starting location from the measured temperature profile required an interpolation into the sublayer. Apparently this was not done very well in the computer program although the Stanton number quickly recovered. The predicted temperature profile on a $T_t'^+$, y^+ basis (Fig. 14) at probe position 5 near the nozzle exit reflects the smaller thermal resistance predicted and thus higher predicted heat transfer than observed experimentally. At probe position 4 in the convergent section the predicted temperature profile is in better agreement with the measurements and consequently so are the Stanton numbers.

Apparently the eddy diffusivities specified are too large in the divergent part of the nozzle where the combined effects of wall cooling and compressibility become important. Since both the friction coefficient and Stanton number are overestimated by roughly the same amount in this region, it appears that the ratio of the eddy diffusivities ϵ_m/ϵ_h (turbulent Prandtl number) is near unity as presumed in the calculations, and this is consistent with that inferred from observing the relationship between the measured temperature and velocity profiles [33].

The predicted momentum and displacement thicknesses (Fig. 10) are in fair agreement with the measured values. Apparently these thicknesses are rather insensitive to the accuracy with which the friction and heat transfer are predicted. It should be noted that the predicted thicknesses from reference [8] are not consistent with the more general definitions of $\tilde{\theta}$ and $\tilde{\delta}^*$ herein. If they were consistent, the absolute values of the predicted thicknesses would be on the order of 15 percent lower. The predicted thicknesses from reference [9], however, are more nearly consistent with the definitions herein, e.g., see reference [3], Appendix C.

Summary and Conclusions

The effect of acceleration on the mean structure of a turbulent boundary layer was observed experimentally to increase the slope of the velocity profiles near the wall relative to a non-accelerating flow. Correspondingly, the friction coefficient was as much as 50 percent higher along the nozzle convergent section than upstream of the nozzle in the constant velocity region. Compressibility effects then reduced the friction coefficient along the nozzle in the higher flow speed region in a way similar to that found in non-accelerating flows. Because of the combined effects of acceleration and wall cooling, the displacement thickness became negative along the convergent section and remained that way through the nozzle.

The temperature profiles, unlike the velocity profiles, were remarkably similar along the nozzle on a power law basis. Correspondingly, a rather simple relationship between the Stanton number and energy thickness Reynolds number was observed which contains a correlation for compressibility effects similar to that found for the friction coefficient. This finding allowed a rather straightforward application of the integral form of the energy equation to predict heat transfer. The friction coefficient, however, is not specified throughout the nozzle by existing formulations considered. The results should allow improvements to be made in integral analyses as well as establishing a basis on which to judge assumptions that are required in order to solve numerically the differential form of the boundary layer equations.

Acknowledgment

The authors express their gratitude to J. J. Godley for operation of the system and data acquisition, and to others for their contribution to the investigation.

References

1 Back, L. H., Massier, P. F., and Cuffel, R. F., "Some Observations on Reduction of Turbulent Boundary-Layer Heat Transfer in Nozzles," *AIAA Journal*, Vol. 4, 1966, pp. 2226–2229.

2 O'Brien, R. L., "Laminarization of Nozzle Wall Boundary Layers as a Means of Reducing Heat Flux," AFRPL-TR-65-40, United Aircraft Research Laboratories, East Hartford, Conn., Feb. 1965.

3 Bartz, D. R., "Turbulent Boundary-Layer Heat Transfer from Rapidly Accelerating Flow of Rocket Combustion Gases and of Heated Air," in *Advances in Heat Transfer*, Vol. 2, Irvine, T. F., and Hartnett, J. P., eds., Academic Press, New York, 1965.

4 Back, L. H., Massier, P. F., and Cuffel, R. F., "Flow Phenomena and Convective Heat Transfer in a Conical Supersonic Nozzle," *Journal of Spacecraft and Rockets*, Vol. 4, No. 8, Aug. 1967, pp. 1040–1047.

5 Boldman, D. R., Schmidt, J. F., and Ehlers, R. C., "Effect of Uncooled Inlet Length and Nozzle Convergence Angle on the Turbulent Boundary Layer and Heat Transfer in Conical Nozzles Operating

With Air," JOURNAL OF HEAT TRANSFER, TRANS. ASME, Series C, Vol. 89, No. 4, Nov. 1967, pp. 341–350.

6 Back, L. H., Massier, P. F., and Cuffel, R. F., "Effect of Inlet Boundary Layer Thickness and Structure on Heat Transfer in a Supersonic Nozzle," *Journal of Spacecraft and Rockets*, Vol. 5, No. 1, Jan. 1968, pp. 121–123.

7 Back, L. H., Cuffel, R. F., and Massier, P. F., "Laminarization of a Turbulent Boundary Layer in Nozzle Flow—Boundary Layer and Heat Transfer Measurements With Wall Cooling," JOURNAL OF HEAT TRANSFER, TRANS. ASME, Series C, Vol. 92, No. 3, Aug. 1970, pp. 333–344.

8 Cebeci, T., "Calculation of Compressible Turbulent Boundary Layers with Heat Transfer and Mass Transfer," AIAA Paper No. 70-741, July 1970; to be published in *AIAA Journal*.

9 Elliott, D. G., Bartz, D. R., and Silver, S., "Calculation of Turbulent Boundary-Layer Growth and Heat Transfer in Axisymmetric Nozzles," TR 32-387, Jet Propulsion Laboratory, Pasadena, Calif., Feb. 1963.

10 Baron, J. R., and Durgin, F. H., "An Experimental Investigation of Heat Transfer at the Boundaries of Supersonic Nozzles," Naval Supersonic Lab., Massachusetts Institute of Technology, Wright Air Development Center, TR 54-541, 1954.

11 Eckert, E. R. G., "Engineering Relations for Heat Transfer and Friction in High-Velocity Laminar and Turbulent Boundary-Layer Flow Over Surfaces With Constant Pressure and Temperature," TRANS. ASME, Vol. 78, 1956, pp. 1273–1283.

12 Back, L. H., Cuffel, R. F., and Massier, P. F., "Laminar, Transition, and Turbulent Boundary-Layer Heat-Transfer Measurements With Wall Cooling in Turbulent Air Flow Through a Tube," JOURNAL OF HEAT TRANSFER, TRANS. ASME, Vol. 91, No. 4, Nov. 1969, pp. 477–487.

13 Back, L. H., Massier, P. F., and Cuffel, R. F., "Flow and Heat-Transfer Measurements in Subsonic Air Flow Through a Contraction Section," *International Journal of Heat and Mass Transfer*, Vol. 12, No. 1, Jan. 1969, pp. 1–13.

14 Ambrok, G. S., "Approximate Solution of Equations for the Thermal Boundary Layer with Variations in Boundary Layer Structure," *Sovict Physics*, Vol. 2, No. 2, 1957, pp. 1979–1986.

15 Kutateladze, S. S., and Leontev, A. I., "Drag Law in a Turbulent Flow of a Compressible Gas and the Method of Calculating Friction and Heat Exchange," *Akademii Nauk, Belorussk*, SSR, Minsk, 1–23, Jan. 1961, pp. 23–27. Translated and issued by Technical Information and Library Services, Ministry of Aviation, London, England, Dec. 1961.

16 Boldman, D. R., and Graham, R. W., "Heat Transfer and Thermal Boundary Layer in a Conical Nozzle," NASA TM-X-52577, 1969.

17 Romanenko, P. N., Leontev, A. I., and Oblivin, A. N., "Investigation on Resistance and Heat Transfer of Turbulent Air Flow in Axisymmetrical Channels with Longitudinal Pressure Gradient," *International Journal of Heat and Mass Transfer*, Vol. 5, 1962, pp. 541–557.

18 Back, L. H., Cuffel, R. F., and Massier, P. F., "Experimental Convective Heat Transfer and Pressure Distributions and Boundary Layer Thicknesses in Turbulent Flow Through a Variable Cross-Sectional Area Channel," *4th International Heat Transfer Conference*, Paris-Versailles, 1970, Vol. 2, FC 2.1, Elsevier Publishing Co., Amsterdam.

19 Reynolds, W. C., Kays, W. M., and Kline, S. J., "Heat Transfer in the Turbulent Incompressible Boundary Layer with Constant Wall Temperature," Part I, NASA Memo 12-1-58 w, 1958.

20 Chi, S. W., and Spalding, D. B., "Influence of Temperature Ratio on Heat Transfer to a Flat Plate Through a Turbulent Boundary Layer in Air," *Proceedings of the Third International Heat-Transfer Conference, AIChE Journal*, Vol. 2, 1966, pp. 41–49.

21 Back, L. H., Cuffel, R. F., and Massier, P. F., "Effect of Wall Cooling on the Mean Structure of a Turbulent Boundary Layer in Low-Speed Gas Flow," *International Journal of Heat and Mass Transfer*, Vol. 13, No. 6, June 1970, pp. 1029–1047.

22 Van Driest, E. R., "Turbulent Boundary Layer in Compressible Fluids," *Journal of the Aeronautical Sciences*, Vol. 18, No. 3, March 1951, pp. 145–160.

23 Coles, D., "The Turbulent Boundary Layer in a Compressible Fluid," *Physics of Fluids*, Vol. 7, No. 9, Sept. 1964, pp. 1403–1423.

24 Patel, V. C., and Head, M. R., "Reversion of Turbulent to Laminar Flow," *Journal of Fluid Mechanics*, Vol. 34, Part 2, Nov. 1968, pp. 371–392.

25 Schlichting, H., *Boundary Layer Theory*, 6th ed., McGraw-Hill, New York, 1968, pp. 675.

26 Back, L. H., and Seban, R. A., "On Constant Property Turbulent Boundary Layers With Variable Temperature or Heat Flow at the Wall," JOURNAL OF HEAT TRANSFER, TRANS. ASME, Series C, Vol. 87, No. 1, Feb. 1965, pp. 151–156.

27 Back, L. H., and Seban, R. A., "Flow and Heat Transfer in a Turbulent Boundary Layer with Large Acceleration Parameter," *Proceedings of Heat Transfer Fluid Mechanics Institute*, Stanford University Press, Stanford, Calif., 1967, pp. 410–426.

28 Spalding, D. B., and Chi, S. W., "The Drag of a Compressible Turbulent Boundary Layer on a Smooth Flat Plate With and Without Heat Transfer," *Journal of Fluid Mechanics*, Vol. 18, 1964, pp. 117–143.

29 Massier, P. F., Back, L. H., Noel, M. B., and Saheli, F., "Viscous Effects on the Flow Coefficient for a Supersonic Nozzle," *AIAA Journal*, Vol. 8, No. 3, March 1970, pp. 605–607.

30 Sauer, R., "General Characteristics of the Flow Through Nozzles at Near Critical Speeds," NACA TM-1147, June 1947.

31 Oswatitsch, K., and Rothstein, W., "Flow Pattern in a Converging-Diverging Nozzle," NACA TM-1215, March 1949.

32 Van Driest, E. R., "On Turbulent Flow Near a Wall," *Journal of the Aeronautical Sciences*, Vol. 23, No. 11, Nov. 1956, pp. 1007–1011, 1036.

33 Back, L. H., and Cuffel, R. F., "Relationship Between Temperature and Velocity Profiles in a Turbulent Boundary Layer Along a Supersonic Nozzle with Heat Transfer," *AIAA Journal*, Vol. 8, No. 11, Nov. 1970, pp. 2066–2069.

34 Crocco, L., "Transformations of the Compressible Turbulent Boundary Layer with Heat Exchange," *AIAA Journal*, Vol. 1, No. 12, Dec. 1963, pp. 2723–2731.

APPENDIX

Boundary Layer Profiles With Cooling and Compressibility Effects

Coles' Transformation Theory [23]. To gain some idea how cooling and compressibility might affect the sublayer as well as the turbulent region, Coles' ideas are applied to two constant free-stream velocity flows, one a variable property flow and the other a constant property flow with heat transfer, but in which temperature differences are small so that properties are essentially constant. Coles' transformation is applied to the constant property profiles

$$\bar{u}^+ = f\left(\frac{\bar{\rho}\bar{u}_\tau\bar{y}}{\bar{\mu}}\right) \tag{A-1}$$

$$\bar{T}^+ = g\left(\frac{\bar{\rho}\bar{u}_\tau\bar{y}}{\bar{\mu}}, \bar{\mathrm{Pr}}\right) \tag{A-2}$$

where

$$\bar{u}^+ = \frac{\bar{u}}{\bar{u}_\tau}, \quad \bar{T}^+ = \frac{\bar{T}_w - \bar{T}}{\bar{q}_w/\bar{\rho}\bar{u}_\tau\bar{c}_p}, \quad \text{and} \quad \bar{u}_\tau = \left[\frac{\bar{\tau}_w}{\bar{\rho}}\right]^{1/2} \tag{A-3}$$

Using Crocco's specification [34] that the static and total temperature ratios are the same in the two flows, i.e., $\bar{T}/\bar{T}_e = T_t/T_{te}$ (the small variation in specific heat is neglected herein) similar to the velocity ratio $\bar{u}/\bar{u}_e = u/u_e$ from Coles' transformation, and that the Prandtl number is the same in the two flows, the constant property relations take on the following form for a variable property flow

$$\left(\frac{\mu_w}{\mu_s}\right)^{1/2} u^+ = f\left(\left[\frac{\mu_w}{\mu_s}\right]^{1/2}\frac{u_\tau}{\mu_w}\int_0^y \rho dy\right) \tag{A-4}$$

$$\left(\frac{\mu_w}{\mu_s}\right)^{1/2} T_t^+ = g\left(\left[\frac{\mu_w}{\mu_s}\right]^{1/2}\frac{u_\tau}{\mu_w}\int_0^y \rho dy, \mathrm{Pr}\right) \tag{A-5}$$

where u^+, T_t^+, y^+, and u_τ are defined in equation (6). Rather than evaluate the profiles in this form, they are more conveniently expressed in terms of u^+, T_t^+, and y^+, the latter relation being obtained by inverting the $\bar{y}$ to y transformation

$$u^+ = \left[\frac{\mu_s}{\mu_w}\right]^{1/2}\bar{u}^+ \tag{A-6}$$

$$T_t^+ = \left[\frac{\mu_s}{\mu_w}\right]^{1/2}\bar{T}^+ \tag{A-7}$$

$$y^+ = \left[\frac{\mu_s}{\mu_w}\right]^{1/2}\int_0^{\bar{y}^+}\frac{\rho_w}{\rho}\,d\bar{y}^+ \tag{A-8}$$

The density ratio ρ_w/ρ can be expressed in terms of the temperature ratio T/T_w for a perfect gas, and the definition of total temperature $T_t = T + \frac{u^2}{2c_{p_w}}$ used in conjunction with the definition of T_t^+, i.e., $T_t/T_w = 1 - \beta T_t^+$ to give

$$\frac{\rho_w}{\rho} = \frac{T}{T_w} = \frac{T_t}{T_w} - \frac{u^2}{2c_{p_w}T_w} = 1 - \beta T_t^+ - \alpha(u^+)^2 = 1 - \beta\left[\frac{\mu_s}{\mu_w}\right]^{1/2}\bar{T}^+ - \alpha\left[\frac{\mu_s}{\mu_w}\right](\bar{u}^+)^2 \quad \text{(A-9)}$$

where

$$\beta = \frac{q_w}{T_w\rho_w u_\tau c_{p_w}} \quad \text{cooling parameter } (\beta < 0 \text{ cooling}) \quad \text{(A-10)}$$

$$\alpha = \frac{u_\tau^2}{2c_{p_w}T_w} = \frac{c_f}{2}\left[\frac{\gamma - 1}{2}\right]M_e^2$$

frictional heating parameter (A-11)

Substituting this expression for $\frac{\rho_w}{\rho}$ into equation (A-8) gives

$$y^+ = \left[\frac{\mu_s}{\mu_w}\right]^{1/2}\left\{\bar{y}^+ - \beta\left[\frac{\mu_s}{\mu_w}\right]^{1/2}\int_0^{\bar{y}^+}\bar{T}^+ d\bar{y}^+ - \alpha\left[\frac{\mu_s}{\mu_w}\right]\int_0^{\bar{y}^+}(\bar{u}^+)^2 d\bar{y}^+\right\} \quad \text{(A-12)}$$

The mean sublayer temperature T_s defined by Coles can be written as follows by using equation (A-9):

$$\frac{T_s}{T_w} = \frac{1}{\bar{y}_s^+}\int_0^{\bar{y}_s^+}\frac{T}{T_w}\,d\bar{y}^+ = 1 - \frac{1}{\bar{y}_s^+} \times \left\{\beta\left[\frac{\mu_s}{\mu_w}\right]^{1/2}\int_0^{\bar{y}_s^+}\bar{T}^+ d\bar{y}^+ + \alpha\left[\frac{\mu_s}{\mu_w}\right]\int_0^{\bar{y}_s^+}(\bar{u}^+)^2 d\bar{y}^+\right\} \quad \text{(A-13)}$$

The velocity and temperature profiles are of the form

$$\begin{aligned} u^+ &\{y^+, \beta, \alpha, \omega; \quad f(\bar{y}^+), g(\bar{y}^+, \mathrm{Pr}), \bar{y}_s^+\} \\ T_t^+ &\{y^+, \beta, \alpha, \omega; \quad f(\bar{y}^+), g(\bar{y}^+, \mathrm{Pr}), \bar{y}_s^+\} \end{aligned} \quad \text{(A-14)}$$

Mixing Length Theory. Perhaps the simplest appraisal of the effect of cooling and compressibility on the turbulent portion of the boundary layer would be to extend Prandtl's mixing length theory ($l = \kappa y$) to a variable property flow. The predicted velocity profile by van Driest [22], who expressed the density variation in terms of velocity

$$\frac{\rho_w}{\rho} = \frac{T}{T_w} = 1 - \beta u^+ - \alpha(u^+)^2 \quad \text{(A-15)}$$

by assuming a linear variation between total temperature and velocity $T_t^+ = u^+$ thereby implying equal molecular and eddy diffusivities for momentum and heat transfer, i.e., $\nu = \alpha(\mathrm{Pr} = 1)$ and $\epsilon_m = \epsilon_h$ is given by

$$\frac{1}{\alpha^{1/2}}\sin^{-1}\left[\frac{2\alpha u^+ + \beta}{(\beta^2 + 4\alpha)^{1/2}}\right] - \frac{1}{\alpha^{1/2}}\sin^{-1}\left[\frac{\beta}{(\beta^2 + 4\alpha)^{1/2}}\right] = c + \frac{1}{\kappa}\ln y^+ \quad \text{(A-16)}$$

Specification of the values of c and κ, taken as 5.5 and 0.4, respectively, indicates the explicit dependence of the velocity profiles on the parameters β and α. For a low-speed flow, $\alpha \to 0$, the velocity profile is

$$(1 - \beta u^+)^{1/2} - 1 = -\frac{\beta}{2}\left(c + \frac{1}{\kappa}\ln y^+\right) \quad \text{(A-17)}$$

W. C. PETERSON
Associate Professor.

M. G. ZAALOUK[1]
Visiting Assistant Professor.

Electrical Engineering Department,
North Carolina State University,
Raleigh, N. C.

Boiling-Curve Measurements From a Controlled Heat-Transfer Process

Feedback has been introduced around a boiling heat-transfer process in such a way that stable operation of the process has been obtained in all boiling regions including the transition region, in which, as is well known, the process itself is unstable. This system makes it possible to obtain much new information concerning both the steady-state and dynamic characteristics of boiling heat-transfer processes. Pool-boiling data which were obtained by the use of this system are presented. Accurate measurements of heater voltage and current were obtained by a new technique involving the use of digital instruments. These data are presented in the form of plotted experimental points in the nucleate, transition, and film boiling regions. The new measurement technique is described. Values of n in the equation $q/A_s = CT_d^n$ *are determined for all three boiling regions, where* q = Btu/hr, A_s *is heater surface area, and* T_d *is temperature difference between heater surface and ambient liquid. The ambient liquid is distilled water maintained at saturation temperature under atmospheric pressure.*

Introduction

THE PURPOSE of this paper is to report to the heat-transfer community on the development of a system which can be used to obtain much new information concerning the phenomena of boiling heat transfer, and to present some of the information already obtained using this system.

An electrically heated wire or metallic strip (called a heater) immersed in a liquid bath constitutes an elementary boiling heat-transfer process. When enough electrical power is supplied to the heater, boiling takes place around it, and heat is transferred to the liquid. On the basis of the work by Nukiyama [1][2] in 1934, it was found that three different modes of boiling take place, in what are now known as the nucleate, transition, and film boiling regions of the boiling curve. This curve is a plot of heat-transfer rate per unit surface area or heat flux versus the temperature difference between the heater surface and the liquid. It is quite well known that the heat-transfer process is ordinarily unstable in the transition region when power is supplied to the heater by electrical means. Operation at too high a temperature in the nucleate region can lead to a sudden jump into the film boiling region, and heater burnout.

Feedback Control of the Process

It is also known that feedback can be introduced around an unstable process in such a way as to produce stable operation. It was considered that it should be possible to obtain stable operation in the transition region of the heat-transfer process by such means. In particular it was proposed to develop a feedback system which would produce stable operation of the process and control of the heater surface temperature in all boiling regions.

It is generally necessary to gain some understanding of the transfer relations in a process before successful control of the process can be achieved.

The most important transfer relation of the heat-transfer process was considered to be the transfer function $\Delta T(s)/\Delta P_H(s)$ relating the Laplace transforms of incremental heater surface temperature ΔT and incremental heater power input ΔP_H. This transfer function, believed to be valid for operation in all three boiling regions, was developed starting from basic principles, and this became the subject of the paper [2]. Here the concept of the incremental heat-transfer coefficient was introduced for the first time in a published paper and defined as the slope of the boiling curve at any operating point. The transfer function itself took the form

$$\frac{\Delta T(s)}{\Delta P_H(s)} = \frac{K}{1 + \tau s} \tag{1}$$

in which the values of the parameters K and τ were found to depend primarily on the slopes of the boiling curve.

It should be recognized that the typical boiling curve is quite

[1] On leave from UAR Atomic Energy Establishment, Cairo, UAR.

[2] Numbers in brackets designate References at end of paper.

Contributed by the Heat Transfer Division for publication (without presentation) in the JOURNAL OF HEAT TRANSFER. Manuscript received by the Heat Transfer Division November 6, 1970. Paper No. 71-HT-J.

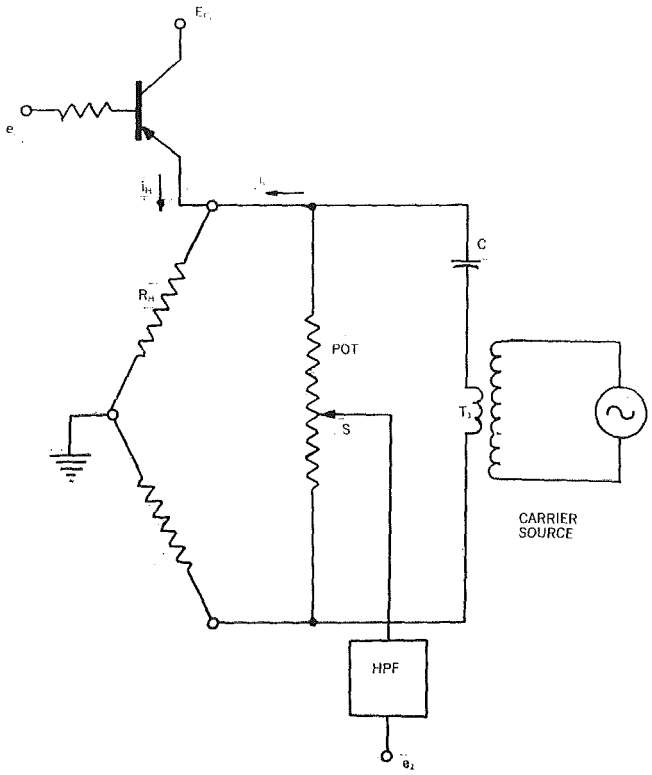

Fig. 1 Comparator bridge circuit

nonlinear. On the other hand it is well known that the transfer-function concept can be applied only to linear situations. These facts would appear to generate difficulties. However, we are concerned here only with operation at specific points on the boiling curve, or with small variations or increments in heater temperature and power in the vicinity of such points. It was found that the relation between small increments was very nearly linear and, therefore, transfer-function concepts could be applied as done in equation (1).

Some knowledge concerning the parameter relations in equation (1) was needed in order to successfully control the process. The parameters K and τ were evaluated for the nucleate and film boiling regions by means of open-loop testing, and ranges of values have been presented [2], but the values in the transition region could only be estimated since the process was unstable in this region when operated open-loop. By "open-loop" operation, we mean operation without feedback control.

In order to sense the heater temperature and its variations, a comparator bridge circuit [3] was designed and constructed. For the convenience of the reader, a diagram of the bridge circuit previously presented is reproduced as Fig. 1 in this paper. The heater (denoted by R_H) became one arm of this bridge. The electrical power input to the heater was obtained from a transistor power amplifier as shown. A high-frequency carrier current I_c was supplied to the bridge. The bridge output, after passing through the high-pass filter HPF, became the modulated signal e_2 whose envelope represented the difference between the temperature set-point value and the actual heater temperature. The set-point value was essentially equivalent to the desired heater temperature. This set point could be adjusted to different values by rotation of the potentiometer forming part of the bridge.

Demodulation of the filtered bridge output developed a signal which could be fed back negatively through a compensation network to produce the power-amplifier input e_1, and in this manner a closed-loop or feedback system resulted. In the final system, the entire boiling curve can be transversed by simply rotating the bridge potentiometer to introduce arbitrary set-point values. In the controlled system, heater surface temperature may be considered an independent variable in the sense that a close correspondence is maintained between this variable and the set-point input, which is certainly independent. The system and circuit details have been presented elsewhere [4].

System and Process Operation

As the set-point value is increased, starting from a very low value, heater temperature and power rise throughout the nucleate region until the peak of the nucleate region is reached. Further increase in the set-point value beyond this point results in a further increase in heater temperature but a reduction in heater power throughout the transition region. Beyond the bottom of the transition region, heater temperature and power both rise again with an increase in the set-point value, in the film boiling region of the boiling curve. It is evident that the system provides means for stable operation at any preselected operating point on the boiling curve. In particular, the "burnout" condition which has been so commonly encountered at the peak of the nucleate region has been eliminated, and experimental data can be obtained in the transition region as well as the other two boiling regions.

The feedback control system has provisions for the introduction of sinusoidal or transient-type electrical signals which can be used to obtain sinusoidal variation of the heater temperature, or any other type of desired and realizable variation. Work is now under way to verify experimentally the theoretical heater transfer function (1). This requires measurements of the responses to sinusoidal driving functions.

Nomenclature

A = heater cross-sectional area, in.^{2}
A_s = heater surface area, ft^2
D = heater wire diameter, in.
e_I = voltage proportional to heater current
e_V = voltage proportional to drop across $R_H + R_x$
I_c = carrier current, amp
$I_{d\text{-}c}$ = d-c current, amp
I_H = d-c heater current, amp
K = transfer-function gain parameter
L = heater length, in.
P_c = power due to carrier current, w
$P_{d\text{-}c}(T)$ = power due to d-c current at temperature T, w
$P_H(T)$ = heater power at temperature T, w
$P_T(T)$ = total power at temperature T, w
$q(T)$ = heat-transfer rate at temperature T, Btu/hr
$R_H(T)$ = heater resistance at temperature T, ohm
$R_T(T)$ = total resistance at temperature T, ohm
R_x = external resistance, ohm
s = Laplace complex variable
T = heater surface temperature, deg C or deg F
T_d = temperature difference between heater surface and ambient liquid, deg C or deg F
$V_{d\text{-}c}$ = d-c voltage
α = temperature coefficient of resistance per deg C
β = temperature coefficient of resistance per (deg C)^2
Δ = notation for increment of a variable
$\rho(T)$ = resistivity at temperature T, μohm·in.
τ = transfer-function time constant, sec

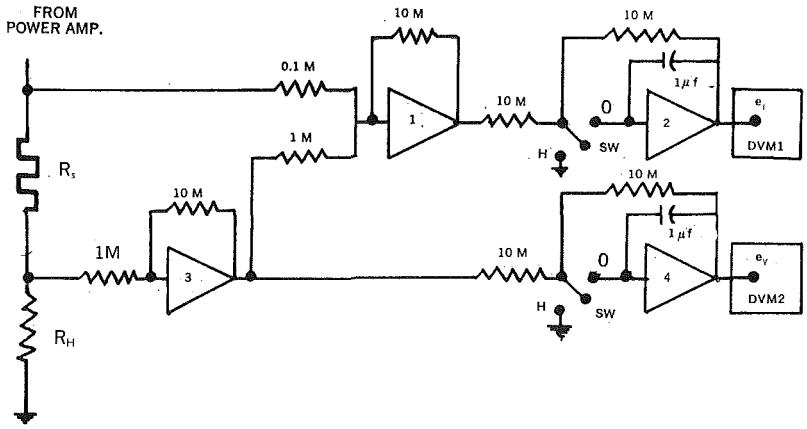

Fig. 2 Analog circuit for use in making measurements

Boiling-Curve Measurements

Steady-state boiling-curve data have been obtained by the use of some analog circuitry and digital instruments to read heater voltage and current during closed-loop operation over the entire boiling curve. In these tests the heater consisted of a 0.005-in-dia platinum wire of approximately 2 in. length. This heater was immersed in a distilled-water bath in a Pyrex baking dish, preheated to saturation temperature by use of a temperature-controlled Sunbeam electric fry pan. The distilled water was passed through a Barnstead standard ion filter before use, producing the effect of a relatively high resistance when tested with an ohmmeter. An anticorrosion electrode was mounted in the bath parallel to the heater to reduce ionization effects, in the manner suggested by McAdams et al. [5], and this electrode was maintained at a potential 9 v negative relative to the negative end of the heater. Number 10 Stakon terminals were crimped onto the heater ends, so that convenient connection could be made to the brass terminal posts extending down through the glass cover on the baking dish and into the bath water.

The circuitry used in making measurements is shown in Fig. 2, in which R_s is a 0.1-ohm instrument shunt, R_H is the heater resistance, and amplifiers 1, 2, 3, and 4 are operational amplifiers in a Model 3400 Donner analog computer. It is evident that the voltage e_I in steady state will be equal to 10 times the current in amperes through the heater, and e_V will be equal to 10 times the heater voltage, or more precisely the voltage across the heater plus whatever cable and terminal resistances are also present.

The system was designed to maintain the heater temperature at any constant set-point value; this is equivalent to maintaining a constant heater resistance. This type of performance is accomplished quite well. But heater resistance is the ratio of heater voltage to heater current, so it is evident that both heater voltage and current can change in such a way that heater resistance remains constant. It was found that the heater voltage and current did not remain constant at any constant set-point value but tended to vary in a random fashion, and this of course made the measurement problem more difficult. It was decided that the most meaningful measure of heater resistance at any set point would be the ratio of average voltage to average current and the heater power should be the product of average voltage and average current. In this connection it should also be noted that the "best value" obtained from a set of random points on the least-square basis is also the average value.

The capacitors shown in the feedback paths of amplifiers 2 and 4 of Fig. 2 produce relatively large time constants which tend to filter out the higher frequency variations so that e_I and e_V become more nearly proportional to the average values of heater current and voltage. The time constants are each 10 sec. The digital voltmeters DVM1 and DVM2 are used to read the voltages e_I and e_V. DVM1 is a Model 202 Wavetek instrument and DVM2 is a Model X-2 Non-linear Systems unit. The procedure used was to obtain 5 readings at each set-point value and then base the heater resistance and power values on the resultant average voltage and current. In this way each plotted point is actually a statistically averaged value.

The switches SW in Fig. 2 are built into the "hold" circuitry of the Donner computer. At the instant when a reading was to be taken, each switch arm was moved from the O (operate) to the H (hold) position. The desired readings were then held constant at the outputs of amplifiers 2 and 4 and the readings could be very conveniently taken with improved accuracy.

The random variations in heater voltage and current are believed to be due primarily to the bubbling action around the heater during nucleate and transition boiling. Essentially no bubbling takes place on the heater surface in film boiling operation where the heater is surrounded by a vapor film. When bubbling occurs, the temperature over the heater surface cannot be uniform. As a consequence, the only meaningful heater resistance we can speak of is the temperature spatially averaged over the heater surface. It is this spatially averaged temperature which is controlled by our system, and the statistical average of the difference between this spatially averaged temperature and the liquid temperature becomes the abscissa variable on the boiling curve.

The voltage e_I is numerically equal to 10 times the heater current in amperes. Also the voltage e_V is equal numerically to 10 times the voltage across the heater resistance plus the inevitable cable and contact-terminal resistance in series with the heater. On this basis we write

$$R_T = R_H + R_x = e_V/e_I \quad \text{ohms} \tag{2}$$

where R_T is total resistance, R_H is heater resistance, and R_x is the external cable and terminal resistance. The heater power component due to the d-c heater current may be expressed as

$$P_{d\text{-}c} = I_{d\text{-}c}^2 R_H \quad \text{watts} \tag{3}$$

where $I_{d\text{-}c}$ in amperes is equal numerically to $e_I/10$. However, a carrier current of 1 amp rms also flows through the heater; therefore, the total heater power becomes

$$\begin{aligned} P_H &= P_{d\text{-}c} + P_c \\ &= P_{d\text{-}c} + I_c^2 R_H \quad \text{watts} \end{aligned} \tag{4}$$

The heater resistance is evidently

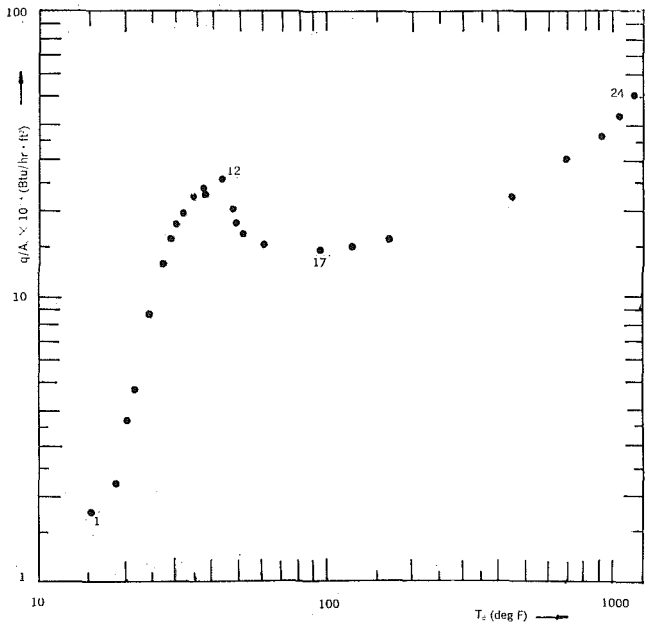

Fig. 3 Temperature difference between heater surface and water versus heat flux—all boiling regions

$$R_H = R_T - R_x \quad \text{ohms} \tag{5}$$

where the value of the external resistance R_x was obtained from readings of the e_V and e_I of Fig. 1 when the heater was replaced by a heavy copper conductor with negligible resistance.

It should be noted that the digital instruments DVM1 and DVM2 respond only to d-c and low-frequency signals; therefore, the carrier current and voltage do not have any influence on the voltages e_V and e_I which are measured. Thus, the carrier power must be accounted for separately.

The heater was annealed by passing enough current through it to operate at a red-heat temperature in air for about 10 min before beginning the boiling-curve measurements, as suggested by McAdams et al. [5]. The formula for resistance

$$R_H(T) = R_H(100)(1 + \alpha T_d + \beta T_d^2) \tag{6}$$

then applies where $R_H(100)$ denotes the resistance at 100 deg C, and the temperature coefficients of resistance are [6]

$$\alpha = 0.00392/\text{deg C}$$

and

$$\beta = -5.5 \times 10^{-7}/(\text{deg C})^2$$

for annealed platinum.

These relations can be used to determine T_d values from the $R_H(T)$ values. If we define

$$\gamma = \frac{R_H(T) - R_H(100)}{R_H(100)} \tag{7}$$

the value of T_d in the nucleate and transition regions where β does not have a significant effect is

$$T_d = \frac{\gamma}{\alpha} \quad \text{deg C} \tag{8}$$

and in the film region where β is significant the value is

$$T_d = \frac{-\alpha}{2\beta} - \sqrt{\left(\frac{\alpha}{2\beta}\right)^2 + \frac{\gamma}{\beta}} \quad \text{deg C} \tag{9}$$

It may be noted that we use the symbol T_d to represent temperature difference rather than the more usual symbol ΔT. This is done because of our use of ΔT to represent a time increment of temperature or $\Delta T(s)$, its transform, as in equation (1). The heat flux becomes

$$\frac{q(T)}{A_s} = \frac{3.415 \times 144}{\pi DL} P_H(T) \quad \text{Btu/hr·ft}^2 \tag{10}$$

The relations given above require that the value of $R_H(100)$ be known for the heater used. This value was determined by measuring the heater resistance and power at several relatively small $I_{d\text{-}c}$ values, and extrapolating these results back to zero power.

On the basis of the known $R_H(100)$ value, an effective length for the heater wire could be found from the relation

$$L = \frac{AR_H(100)}{\rho(100)} \quad \text{in.} \tag{11}$$

It was found that this effective length was somewhat larger than the measured length between terminals because of the end effect due to crimping the Stakon terminals onto the ends of the heater wire. It should be noted that the measured length L was used to compute the surface area A_s used to determine the heat-transfer rate per unit surface area q/A_s. In the present case the measured length was 1.945 in.

The value of R_x for our system was found to be 0.01065 ohm, and the heater resistance at 100 deg C, $R_H(100)$, was 0.60255 ohm.

Boiling-curve measurements were made using the annealed platinum wire heater operating in the distilled-water pool-boiling bath maintained at saturation temperature at atmospheric pressure. Five readings of the voltages e_I and e_V were taken at each of 25 set-point values. From these values the corresponding values of $I_{d\text{-}c}$, the heater current, and $V_{d\text{-}c}$, the voltage across R_H and R_x in series, were determined. Heater resistance values R_H were then determined by use of equations (2) and (5), and heater power values P_H by use of equation (4). Finally, the heat flux values denoted by q/A_s were determined based on equation (10) and T_d values were obtained by use of equations (8) and (9).

In Fig. 3 the values of heat flux q/A_s are plotted versus temperature difference T_d in deg F between heater surface and the ambient water, using log-log coordinate scales. A boiling curve can evidently be obtained by drawing a line essentially through these points, with the exception of one spurious point near the nucleate-region peak. Some difficulty was experienced in obtaining readings in the vicinity of the peak as the random time variations of voltage and current were especially pronounced there, since the nonlinearity of the boiling curve in the vicinity of the peak was especially severe.

Since the boiling data were obtained under atmospheric pressure conditions using filtered distilled water maintained at saturation temperature, the boiling-curve data could be reproduced provided the wire surface conditions did not change. However, it was found that if surface contamination occurred, the nucleate-region boiling curve would shift but would still retain its original shape and original peak flux value, although at a somewhat different temperature. In our investigations, each run was started with a new platinum wire since it was observed that a slight shift in the boiling curve would occur if we used the same wire in a succeeding run.

For convenient reference, the boiling-curve points in Fig. 3 may be numbered from 1 to 24 starting with the lowest temperature point but omitting the spurious point. Four of the data points have been so identified in the figure. Table 1 is presented to show how the $V_{d\text{-}c}$ and $I_{d\text{-}c}$ values for points 8, 10, and 15 of Fig. 3 were obtained. Values for points 8 and 15 are representative of data taken in the more linear regions of the boiling curve while data for point 10 which is near the peak represents a more nonlinear region. Five readings were taken at each set point. The average voltage value is 2.7697 v and the average current

Table 1

	Voltage	Current
For point 8 of Fig. 3 (in nucleate region)		
	2.7947	4.282
	2.7645	4.231
	2.7278	4.176
	2.8238	4.322
	2.7397	4.194
Averages:	2.7697 v	4.2411 amp
For point 15 of Fig. 3 (in transition region)		
	3.0666	4.540
	3.1045	4.593
	3.0437	4.504
	3.0190	4.469
	3.0165	4.463
Averages:	3.0500 v	4.5138 amp
For point 10 of Fig. 3 (nucleate region, near the peak)		
	3.1169	4.746
	3.2049	4.872
	3.1389	4.761
	3.1427	4.768
	3.1515	4.778
Averages:	3.1509 v	4.785 amp

value is 4.2411 amp for point 8, for example, and these are the $V_{d\text{-}c}$ and $I_{d\text{-}c}$ values. Each of the sets of $V_{d\text{-}c}$ and $I_{d\text{-}c}$ values were obtained in the same manner in an effort to cope statistically with the random time variations in voltage and current which occurred at each set-point value. Fig. 3 displays all of the data points obtained from one run, and no data were discarded.

Other investigators have suggested that the heat-transfer rate per unit area should be an exponential function of the temperature difference T_d in each of the boiling regions, so that

$$q/A_s = CT_d^n \tag{12}$$

The question as to the values of n based on our tests was a matter of some interest. It is to be expected that different values of n would be obtained in the three boiling regions, and we may for convenience denote these by n_N, n_T, and n_F for the nucleate, transition, and film boiling regions respectively.

When data points 4 and 9 are used in equation (12) for evaluation purposes, it is found that n_N has the value of 3.7, but when points 4 and 6 are used, the value is 4.5. This range of n_N values from 3.7 to 4.5 checks quite well with values given in the literature [7] for nucleate-region operation.

Applying the same procedure in the transition region, use of points 13 and 16 results in an n_T value of -3.0. Using points 13 and 15, the value is -4.1. The reference literature gives no transition-region values for comparison.

In the film region, this same procedure applied using points 20 and 23 resulted in an n_F value of 0.96. A predicted value from the literature for comparison is 0.75 [8].

It is also of some interest to note that the T_d value was 44 deg F at point 12, where the heat flux had its largest value between the nucleate and transition regions. If this point can be considered to be the peak point, the value compares quite well with values in the literature.

Concluding Comments

A new system in which feedback principles have been applied to control a boiling heat-transfer process has been described.

The boiling-curve data presented should give an indication as to the type of new information which can be obtained using this system. This boiling-curve data includes for the first time easily obtained transition-region points from a heater to which energy is supplied electrically.

No heater burnout can occur in the use of the new system, since operation over the peak point is reliable and consistent. It appears possible that the same principles can be applied in the control of boiling-water nuclear reactors in such a way that fuel-element burnout cannot occur. The authors expect to investigate such possibilities in the course of future work.

Acknowledgment

The support for this work provided by Atomic Energy Commission Research Contract AT-(40-1)-3939 is gratefully acknowledged.

References

1 Nukiyama, S., "Maximum and Minimum Values of Heat Transmitted from Metal to Boiling Water under Atmospheric Pressure," *Jour. Soc. Mech. Engr.*, Japan, Vol. 37, No. 206, 1934, pp. 367–374, 553–554.

2 Peterson, W. C., Zaalouk, M. G., and Goetze, A. J., "Development and Evaluation of Transfer Functions for Nucleate, Transition and Film Boiling," *Journal of the Franklin Institute*, Vol. 285, No. 4, April 1968, pp. 285–296.

3 Peterson, W. C., "A Comparator Bridge Circuit," *Industrial Electronics and Control Instrumentation Transactions of IEEE*, Vol. IECI-16, No. 2, Sept. 1969, pp. 161–164.

4 Peterson, W. C., Thacker, A., and Avery, W. L., "A Feedback System for Control of an Unstable Process," *Industrial Electronics and Control Instrumentation Transactions of IEEE*, Vol. IECI-16, No. 2, Sept. 1969, pp. 165–171.

5 McAdams, W. H., Addoms, J. N., Rinaldo, P. M., and Day, R. S., "Heat Transfer from Single Horizontal Wires to Boiling Water," *Chemical Engineering Progress*, Vol. 44, No. 8, Aug. 1948, pp. 639–646.

6 Vines, R. F., *The Platinum Metals and Their Alloys*, International Nickel Co., New York, 1941.

7 McAdams, W. H., *Heat Transmission*, 3rd ed., McGraw-Hill, New York, 1954.

8 Lottes, P. A., Petrick, M., and Marchaterre, J. F., "Lecture Notes on Heat Extraction from Boiling Water Power Reactors," ANL-6063, Oct. 1959, p. 10.

D. F. D'ARCY
Advance Engineering Branch,
Atomic Energy of Canada Limited,
Chalk River, Ontario, Canada

On Acoustic Propagation and Critical Mass Flux in Two-Phase Flow

Theoretical values for the propagation speed of small pressure disturbances through two-phase fluid have been derived by a method analogous to the well-known method for single-phase fluids and using the well-known separated-flow model of two-phase flow. Since the liquid and vapor phases in general flow at different mean speeds, it is appropriate to compute the propagation speed relative to the laboratory frame of reference, not relative to the fluid as is usually done in single phase. With the extra degree of freedom in two-phase flow, two distinct speeds are found for propagation both upstream and downstream, each representing compatible thermodynamic behavior of both phases. Comparisons between calculations based on the model, and several published sets of experimental values of the speed of sound, tend to confirm the theory at low and at high void fractions. Both propagation speeds have been observed in experiments. Also by analogy with the single-phase case, critical flow is predicted to occur when the upstream propagation speed relative to the laboratory is zero, i.e., when pressure waves cannot travel into the opening from which the flow issues. Flow calculations based on the model under these conditions show agreement with published experimental critical-flow measurements in the regions of low and high void fractions. Thus, a satisfactory explanation of the critical-flow phenomenon in two-phase fluids is obtained in these regions. From the analytical–experimental comparisons it appears that of the two propagation speeds and critical flows, one is observed at low void fraction, and the other at high void fraction. In the intermediate range, the theory and experiment differ and it is probable that the separated-flow model does not adequately represent the flow regimes occurring in this range.

Introduction

Two aspects of two-phase flow which are of importance in the design of process systems, heat-transport systems, etc., are considered in the present paper. These are the speed at which small pressure disturbances travel though the fluid and the critical flow rate or maximum achievable mass flux for given upstream conditions. Neither process is well understood at present. In particular, no completely satisfactory explanation for the existence of choking in two-phase flow has yet been given.

In gas flow, both processes are well understood and are closely related. It would be satisfying to find that two-phase flow behaves in an analogous manner. In the present paper the well-established single-phase method of analysis is extended and applied to two-phase flow in order to test its validity for two-phase flow.

Contributed by the Heat Transfer Division for publication (without presentation) in the Journal of Heat Transfer. Manuscript received by the Heat Transfer Division November 18, 1969; revised manuscript received November 10, 1970. Paper No. 71-HT-K.

Propagation Speed of Small Disturbances

Single-Phase Theory

The speed of propagation of plane pressure disturbances in single-phase flow is computed successfully by considering linearized forms of the one-dimensional continuity and momentum equations, e.g., [1][1]

$$\left.\begin{aligned} \rho\delta c + (c - c_w)\delta\rho &= 0 \\ \rho(c - c_w)\delta c + g\delta p &= 0 \end{aligned}\right\} \tag{1}$$

Use of the energy equation is avoided by assuming that the small pressure and density changes δp, $\delta\rho$ are related by a thermodynamic process and hence

$$\delta p = p'\delta\rho \tag{2}$$

where $p' = dp/d\rho$ is defined by the thermodynamic process. For gases it has been determined experimentally that the process

[1] Numbers in brackets designate References at end of paper.

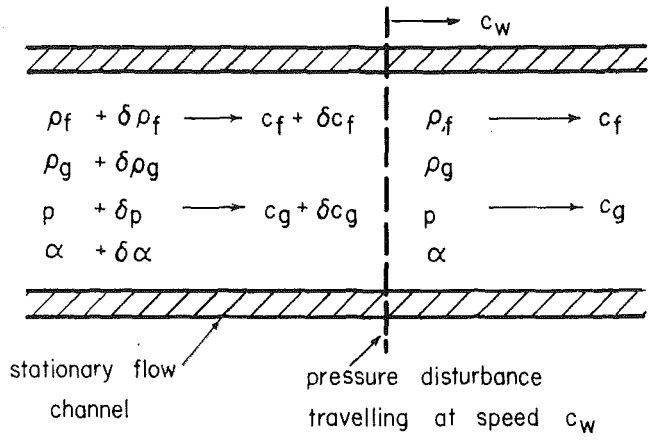

Fig. 1 Conditions in the flow channel before and after passage of the pressure disturbance

is isentropic. Eliminating δp from equations (1) and (2) results in two linear homogeneous equations in δc and $\delta\rho$. The usual expression for the speed of plane wave propagation [1]

$$(c - c_w)^2 = gp' \tag{3}$$

is just the compatibility relation for these two equations. Two propagation speeds are found,

$$c_w = c \pm \sqrt{gp'} \tag{4}$$

and waves can travel upstream or downstream at speed

$$a = \sqrt{gp'} \tag{5}$$

relative to the mean flow c.

Two-Phase Theory

Description of Flow. The same method of analysis has been applied to the propagation of small disturbances in two-phase flow. As in the commonly used separated-flow model it is assumed that a single mean velocity can be used to represent each phase dynamically. The flow is then completely defined by two independent thermodynamic variables, e.g., pressure and quality, and the two phase velocities.

The steady-state continuity equations for the two phases are:

$$\left.\begin{aligned} \rho_f(1 - \alpha)c_f &= (1 - x)G \\ \rho_g\alpha c_g &= xG \end{aligned}\right\} \tag{6}$$

In a typical case, p, x, G would be known. α would either be measured directly or inferred from a void-fraction correlation. c_f and c_g would then be calculated from (6).

Conditions at the Wave Front. As a pressure wave passes an element of the two-phase fluid, there may be some mass transfer between phases. For example, if a small decrease in pressure should occur isentropically, some of the liquid would evaporate and some of the vapor would condense. The result would be a net increase of liquid mass and a decrease of vapor mass, or vice versa, depending on the actual conditions. It is assumed here that a net mass transfer δm from liquid to vapor accompanies a pressure increase δp. δm may be positive, negative, or zero. The flashing liquid would transfer momentum equal to c_f per lb from the liquid to the vapor, and the condensing vapor would transfer momentum c_g per lb to the liquid. The net momentum transfer from liquid to vapor is taken as $\bar{c}\delta m$ where $\bar{c}$ is some unknown mean velocity. Later, the assumption that $\delta m = 0$ will be made and the value of $\bar{c}$ is then immaterial.

Conditions in the flow channel in the neighborhood of the traveling pressure disturbance are illustrated in Fig. 1. The mass and momentum continuity relations for the two phases, including mass transfer, are:

$$\delta[\rho_f(1 - \alpha)(c_f - c_w)] + \delta m = 0 \tag{7}$$

$$\delta[\rho_g\alpha(c_g - c_w)] - \delta m = 0 \tag{8}$$

$$\delta[\rho_f(1 - \alpha)(c_f - c_w)^2] + (\bar{c} - c_w)\delta m = -g\delta[(1 - \alpha)p] \tag{9}$$

$$\delta[\rho_g\alpha(c_g - c_w)^2] - (\bar{c} - c_w)\delta m = -g\delta[\alpha p] \tag{10}$$

Subtracting $(c_f - c_w)$ times (7) from (9) and $(c_g - c_w)$ times (8) from (10) yields

$$\rho_f(1 - \alpha)(c_f - c_w)\delta c_f + (\bar{c} - c_f)\delta m = -g\delta[(1 - \alpha)p] \tag{11}$$

$$\rho_g\alpha(c_g - c_w)\delta c_g - (\bar{c} - c_g)\delta m = -g\delta[\alpha p] \tag{12}$$

We can write $\delta\rho = \rho'\delta p$ where the thermodynamic process has not yet been specified. Some change in α must be allowed for, and we write $\delta\alpha = \alpha'\delta p$. The value of α' will be determined by the compatibility conditions. The four governing equations (7), (8), (11), and (12) can then be written in terms of the four unknowns associated with the disturbance δc_f, δc_g, δm, δp:

$$\rho_f(1 - \alpha)\delta c_f + \delta m + (c_f - c_w)[\rho_f(1 - \alpha)]'\delta p = 0 \tag{13}$$

Nomenclature

a = speed of sound, ft/sec; $a = \sqrt{g/\rho'}$; see note under Q

c = velocity, ft/sec

D = tube diameter, ft

Fr = Froude number = c_{mix}^2/gD, as in reference [10]

G = mass flux, lb/ft²·sec

g = acceleration due to gravity, ft/sec²

M = λ_g/λ_f when $c_w = 0$

m = mass-transfer flux from liquid to vapor based on cross-sectional area, lb/ft²·sec

p = pressure, lb/ft² absolute

Q = $p\rho'/\rho$, i.e., $Q_f = p\rho_f'/\rho_f$ where $\rho_f' = d\rho_f/dp$ is evaluated from water properties along an isentrope at the limiting condition as $p \rightarrow p_{sat}$ for the given isentrope. $a_f^2 = g/\rho_f'$; similar remarks apply for Q_g and a_g, ρ_g' being evaluated from steam properties along an isentrope as $p \rightarrow p_{sat}$

v = specific volume, ft³/lb

x = quality (vapor weight flow/total weight flow)

α = void fraction (time average of the fraction of the flow cross section occupied by vapor)

λ = parameter defined in equations (21)

ρ = density, lb/ft³

δ = symbol for small perturbation

Subscripts

c = refers to critical flow conditions

f = refers to water at saturation pressure

g = refers to steam at saturation pressure

m = mean values, see equation (24)

mix = applies to two-phase mixture; $c_{mix} = G(v_f + xv_{fg})$

w = refers to the propagating disturbance or wave

1, 2, +, − = refer to individual solutions of equations (19) and (20); see Fig. 2

Superscripts

′ = derivative with respect to pressure; see text for description of the thermodynamic process; but, in equations (2)–(5), $p' \equiv dp/d\rho$

¯ = mean value, see discussion of $\bar{c}$ in text

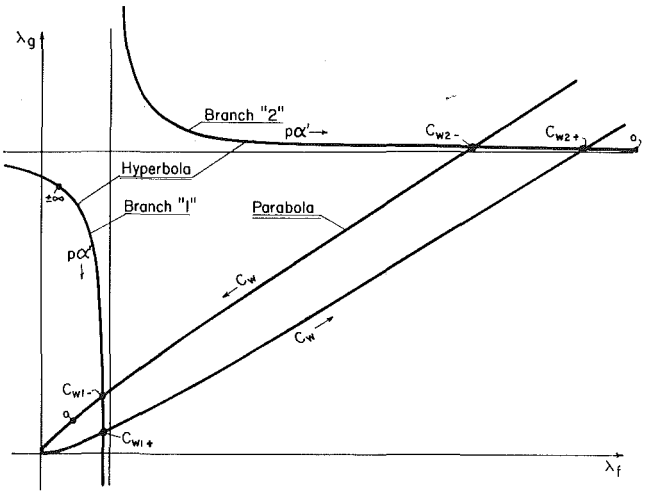

Fig. 2 Designation of roots of equations (19) and (20)

$$\rho_g\alpha\delta c_g - \delta m + (c_g - c_w)[\rho_g\alpha]'\delta p = 0 \quad (14)$$

$$\rho_f(1-\alpha)(c_f - c_w)\delta c_f + (\bar{c} - c_f)\delta m + g[p(1-\alpha)]'\delta p = 0 \quad (15)$$

$$\rho_g\alpha(c_g - c_w)\delta c_g - (\bar{c} - c_g)\delta m + g[p\alpha]'\delta p = 0 \quad (16)$$

These equations for two-phase flow are analogous to equations (1) for single phase. The compatibility condition for these homogeneous linear equations is the vanishing of their determinant. The quantity $\rho_f\rho_g\alpha(1-\alpha)$ which is not zero in two-phase flow can be factored out of the determinant leaving:

$$\{(c_f - c_w)^2[\rho_f(1-\alpha)]' - g[p(1-\alpha)]'\}(\bar{c} - 2c_g + c_w) + \{(c_g - c_w)^2[\rho_g\alpha]' - g[p\alpha]'\}(\bar{c} - 2c_f + c_w) = 0 \quad (17)$$

This is analogous to equation (3) for single-phase flow and bears some resemblance to it.

As in single phase, experimental data are required to determine the thermodynamic and physical processes which occur during the passage of the disturbance. In single-phase flow it was found that the process was isentropic, hence adiabatic, implying that the pressure change δp occurred so rapidly that there was not enough time for local heat transfer. An obvious analogy for two-phase flow is to assume that each phase individually experiences an isentropic change, and further to assume that no flashing or condensation, i.e., no mass transfer, occurs. This implies thermodynamic nonequilibrium during the passage of the disturbance: If $\delta p > 0$, the liquid will become slightly subcooled while the vapor becomes slightly superheated, whereas if $\delta p < 0$ the liquid will become superheated and the vapor subcooled without changing phase. This would be only a temporary condition, but the disturbance would have passed before equilibrium was resumed, hence the method of reaching equilibrium is of no present concern.

It is therefore assumed, and later tested against experiment, that $\delta m = 0$ during the passage of the disturbance. These assumptions imply overall isentropic conditions, in agreement with the single-phase case.

When (17) is satisfied, equations (13)–(16) are not independent and any three of them can be solved, say, for δc_f, δc_g, δm in terms of δp. Solving (13), (14), and (16) for $\delta m/\delta p$,

$$\frac{\delta m}{\delta p} = \frac{(c_g - c_w)^2[\rho_g\alpha]' - g[p\alpha]'}{-(\bar{c} - 2c_g + c_w)} = 0 \quad (18)$$

according to our assumption. By definition, $\bar{c}$ must be of the order of magnitude of c_g, and c_w is usually much larger than c_g; hence $(\bar{c} - 2c_g + c_w) \neq 0$ in general. Therefore, the assumption of zero mass transfer implies that

$$(c_g - c_w)^2 = \frac{g[p\alpha]'}{[\rho_g\alpha]'} \quad (19)$$

Using this in (17), and noting that in general $(\bar{c} - 2c_f + c_w) \neq 0$, implies that

$$(c_f - c_w)^2 = \frac{g[p(1-\alpha)]'}{[\rho_f(1-\alpha)]'} \quad (20)$$

Equations (19) and (20) together form the compatibility condition for equations (13)–(16) and must be satisfied simultaneously. The similar ty of each to equation (3) is striking.

Propagation Speeds. Equations (19) and (20) determine both the wave speed c_w and the physical process $\alpha' = d\alpha/dp$ which occurs during the passage of the disturbance. In order to see the nature of the solutions of these equations, define the parameters

$$\left.\begin{aligned}\lambda_f &= (\rho_f/p)[p(1-\alpha)]'/[\rho_f(1-\alpha)]' \\ &= \frac{(1-\alpha) - p\alpha'}{Q_f(1-\alpha) - p\alpha'} \\ \lambda_g &= (\rho_g/p)[p\alpha]'/[\rho_g\alpha]' = \frac{\alpha + p\alpha'}{Q_g\alpha + p\alpha'}\end{aligned}\right\} \quad (21)$$

Assume that p, α, c_f, c_g are known for a given case. Then, Q_f and Q_g can be calculated directly (see definitions in Nomenclature) and a plot of λ_g versus λ_f according to (21) is a rectangular hyperbola with $p\alpha'$ as parameter. A typical curve is shown in Fig. 2.

According to (19), (20), and (21),

$$\left.\begin{aligned}(c_g - c_w)^2 &= gp\lambda_g/\rho_g \\ (c_f - c_w)^2 &= gp\lambda_f/\rho_f\end{aligned}\right\} \quad (22)$$

Plotting λ_g versus λ_f according to (22) gives a parabola with c_w as parameter. A typical case is also sketched in Fig. 2.

It is seen in Fig. 2 that equations (19) and (20) have four distinct solutions for α' and c_w, representing four possible propagation speeds. There are two solutions on each branch of the hyperbola. For some solutions $c_w < 0$ relating to upstream propagation and for others $c_w > 0$ denoting downstream propagation.

In single-phase flow, the speed of sound relative to the fluid is $a = |c_w - c|$. But in two-phase flow, two different speeds would be obtained depending on whether one took $|c_w - c_f|$ or $|c_w - c_g|$; hence speed of sound cannot be defined in this way. However, if one takes half the difference between the upstream and downstream propagation speeds, an effective speed of sound is obtained. Numbering the roots as in Fig. 2,

$$\left.\begin{aligned}a_1 &= (c_{w1+} - c_{w1-})/2 \\ a_2 &= (c_{w2+} - c_{w2-})/2\end{aligned}\right\} \quad (23)$$

where subscript 1 refers to the left branch and 2 to the right branch of the hyperbola, a_1 and a_2 are plotted against α in Fig. 3 for particular values of p, G, and with x computed from p, α by means of the void-fraction correlation given in [10].

It can easily be shown that

at $\alpha = 0$, $a_1 = a_f$, $a_2 = a_g\sqrt{Q_g}$

and at $\alpha = 1$, $a_1 = a_f\sqrt{Q_f}$, $a_2 = a_g$

Thus, a_1 is continuous with liquid properties at $\alpha = 0$ and a_2 is continuous with vapor properties at $\alpha = 1.0$. One can also define mean effective flow velocities as

$$\left.\begin{aligned}c_{m1} &= (c_{w1+} + c_{w1-})/2 \\ c_{m2} &= (c_{w2+} + c_{w2-})/2\end{aligned}\right\} \quad (24)$$

It is found that at all values of α, $c_{m1} \approx c_f$ and $c_{m2} \approx c_g$. These observations suggest that $c_{w1\pm}$ refer to a propagation mode controlled primarily by the liquid phase and $c_{w2\pm}$ to a mode con-

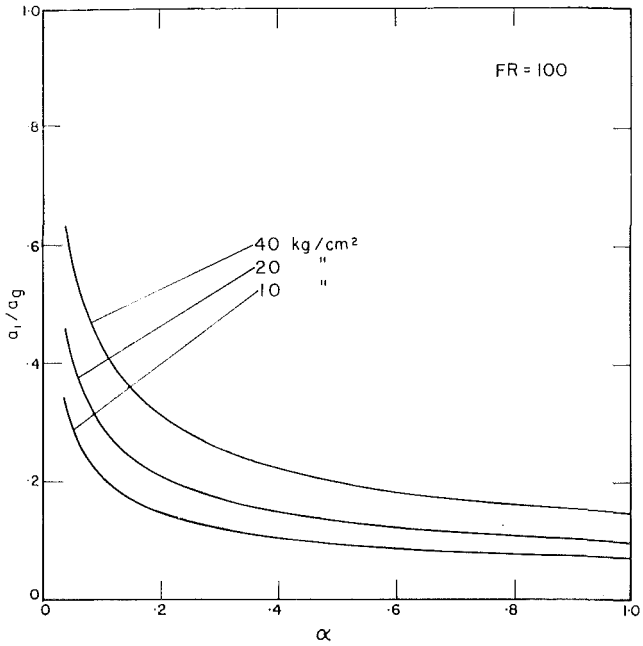

Fig. 3(a) Variation of mean propagation speed with pressure and void fraction (mode 1)

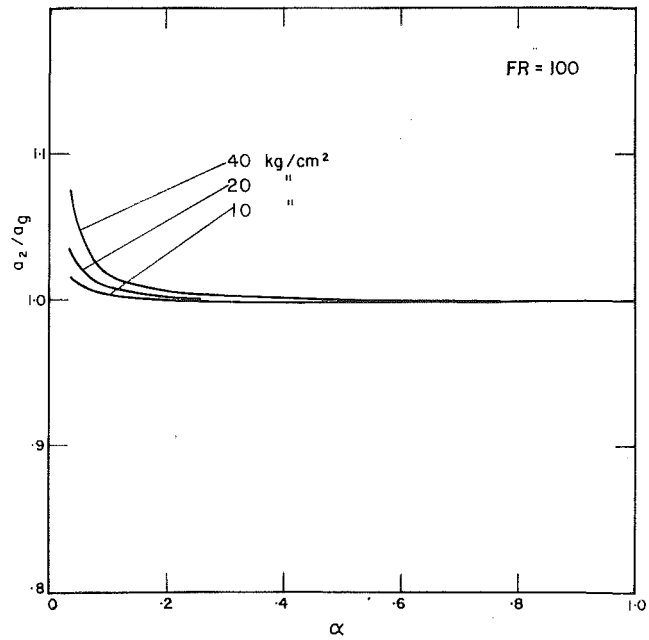

Fig. 3(b) Variation of mean propagation speed with pressure and void fraction (mode 2)

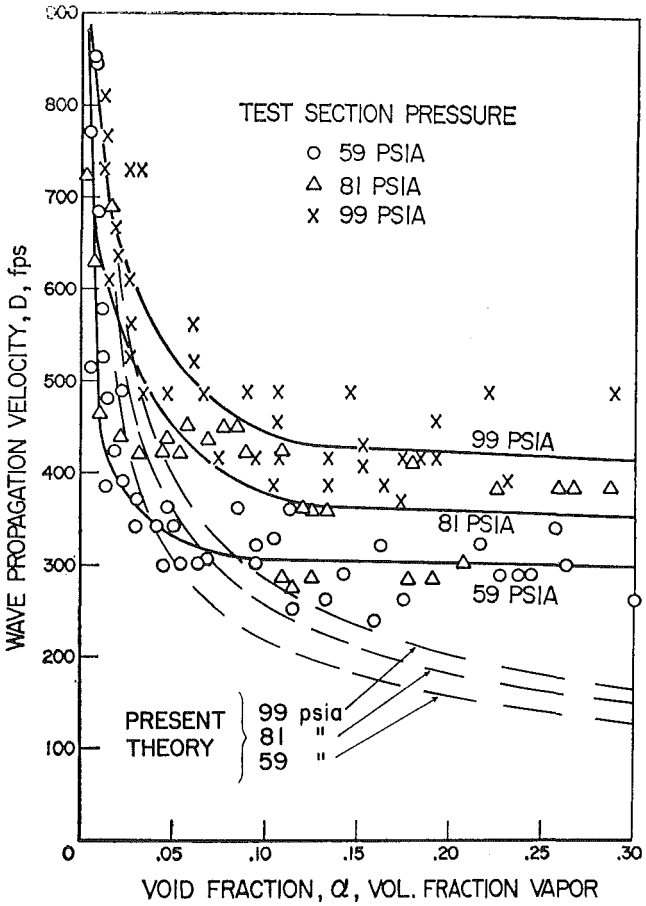

Fig. 4 Results of DeJong and Firey, reference [2]

trolled primarily by the vapor phase. Thus, one would expect $c_{w1\pm}$ to be observed at low void where the liquid phase is continuous and the vapor phase is not, and $c_{w2\pm}$ at high void where the vapor phase is continuous, and the liquid phase, while it may form a continuous film on the tube wall, is not plentiful enough to influence the wave propagation speed. Comparison with experiment is made below on this basis.

In the intermediate void range both phases are plentiful and may be continuous, but the flow regime is very chaotic and the assumption that the flow may be represented simply by two distinct velocities c_f and c_g probably is not valid. Thus, in an experiment at an intermediate void the observed propagation speed may or may not agree with $c_{w1\pm}$ or $c_{w2\pm}$. The published experimental results seem to confirm these observations.

Comparison with Experiment

Measurements of the propagation speed of pressure disturbances in two-phase flow have been published by several experimenters. Usually, however, the published results do not include both the flow quality and void fraction, nor is the mass flux stated. In some cases the flow regime (e.g., whether bubbly, semi-annular or annular) is not known, and in the air–water tests the temperature was usually not given. In most flowing experiments, i.e., $G \neq 0$, some correction c' has been made to the measured propagation speed c_{w-} to obtain the speed of sound, $a = c' - c_{w-}$, but the method of computing the mean flow c' was not specified.

Reasonable assumptions have been made where possible to enable the present theory to be evaluated and compared with the experimental results:

1 DeJong and Firey [2] measured the speed of propagation of both rarefaction and compression waves in flowing steam–water at both high and low void. Either void fraction or quality was measured, but not both. Flow velocity was "less than 1 percent" of the propagation speed. Comparison with theory was made by assuming a value for c_f and a void-quality correlation given by Styrikowich et al. [3]. Both a_1 and a_2, equation (23), were found to be insensitive to c_f in the range $1 \leq c_f \leq 10$ ft/sec.

a_1 is compared to the low-void experimental results in Fig. 4 at pressures of 59, 81, and 99 psia. It is seen that the a_1 values agree reasonably well with the experimental values up to 5 percent void. From 5 to 30 percent void the measured values were

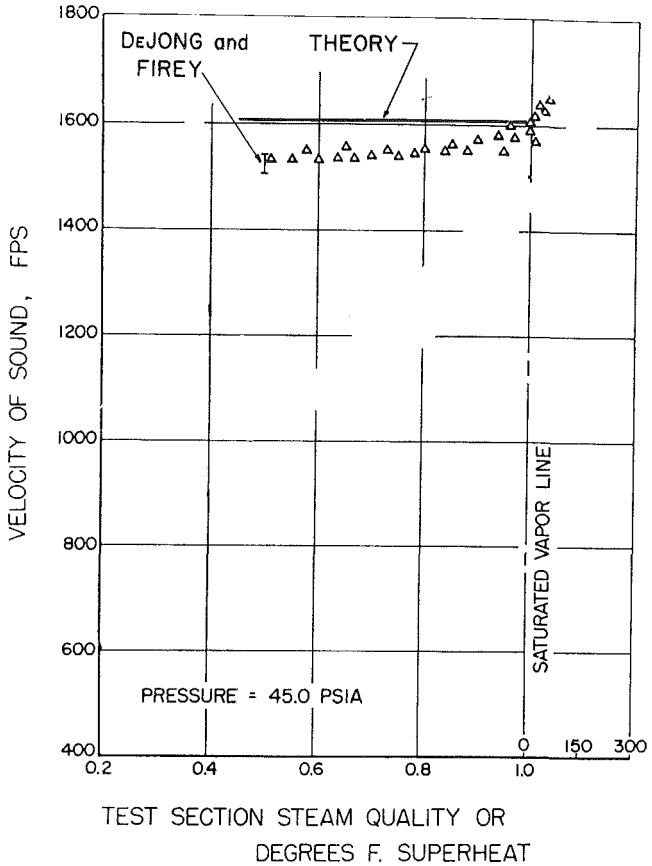

Fig. 5 Experimental results of England et al., reference [4], and DeJong and Firey, reference [2]

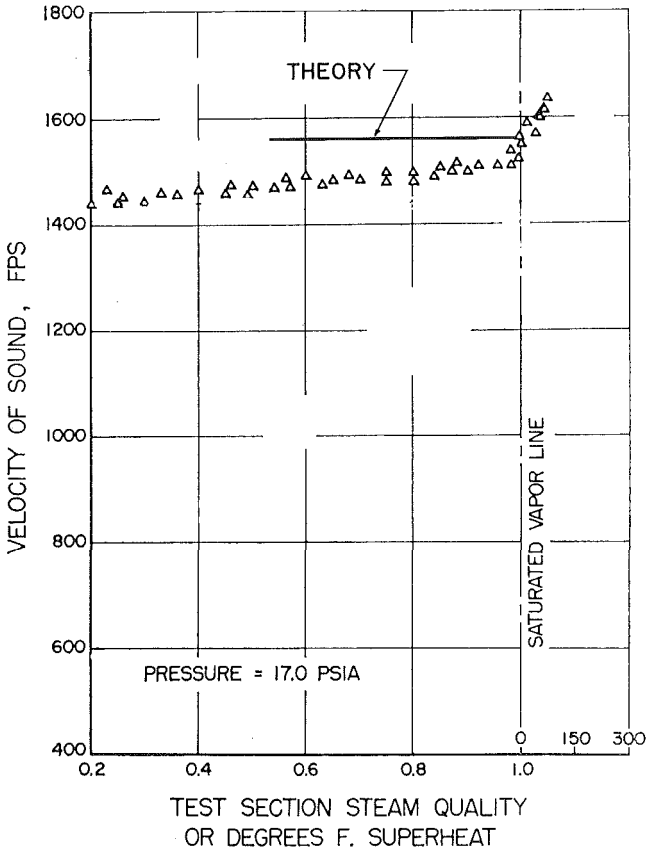

Fig. 6 Experimental results of England et al., reference [4]

appreciably higher than a_1 but much lower than a_2 which was about 1620 ft/sec in this case. The variation of propagation speed with pressure appears to be predicted correctly by the theory.

In Fig. 5, a_2 is compared with the high-void experimental results at 45 psia. The measured point at $x = 0.50$ (Fig. 4 of reference [2]) lies below the a_2 curve by 5 percent.

2 England et al. [4] measured propagation speed in steam–water in mist flow over the range of quality from 0.20 to 1.00 at pressures of 17 and 45 psia. These results and computed values of a_2 are shown in Figs. 5 and 6. Experimental values lie below theoretical values by 1 to 2 percent at $x = 1.0$ and fall to about 8 percent below at $x = 0.20$ ($\alpha \sim 0.995$ at 17 psia according to [3]).

3 Campbell and Pitcher [5] measured the speed of a shock wave traveling downstream through a liquid in which bubbles were rising. In order to achieve a uniform distribution of small bubbles they used a 50:50 solution of water and glycerine as the liquid.

The present theory is equally applicable to two-component systems since no mass transfer is assumed. The only fluid properties used are the density and either Q or the speed of sound in each phase. The values used for comparison with the results in Fig. 8a of reference [5] are:

p = (30 − 20) in. Hg = 4.91 psia
ρ_f = 71.7 lb/ft³ (s.g. = 1.145)
ρ_g = 0.0250 lb/ft³
a_f = 5774 ft/sec (reference [6])
a_g = 1130 ft/sec

It was assumed that the temperature of the fluid was 70 deg F.

Void fraction was measured directly by the authors; c_f was zero in the experiment and c_g, though not zero, was probably small, likely less than 1 ft/sec. The theory was evaluated for both $c_g = 0$ and $c_g = 1$ ft/sec with no noticeable change in c_w.

The computed values of c_{w1-} are compared in Fig. 7 with Campbell and Pitcher's results. The computed values lie considerably below the experimental values. It is thought that the reason for this is in the strong shock waves used in the experiment. Although the authors found no variation in propagation speed as they changed shock strength, they did so by lowering the system pressure with constant (atmospheric) driving pressure. It has been shown by both DeJong and Firey [2] and by Semenov and Kosterin [10] that the speed of sound decreases as pressure decreases in the range of void fraction occurring in Campbell and Pitcher's tests. From single-phase theory one expects the propagation speed to increase with shock strength, and presumably a similar effect in the two-phase mixture cancelled the pressure effect in the experiment. The experimental propagation speeds are 1.8 to 2.1 times as high as the computed values, the ratio at $\alpha = 0.10$ being 1.84. In an attempt to evaluate the effect of the shock strength on the propagation speed, it was observed that the pressure behind the reflected shock at $\alpha = 0.10$ (Fig. 9 of reference [5]) could be fitted by the theoretical expression given by Shapiro [7] if the isentropic constant k is taken as 1.15. Thus, the shock in bubbly two-phase fluid behaved at least partially like a shock in a gas and an equivalent isentropic exponent was found. Using this, the Mach number of the shock relative to the stationary fluid was computed by Shapiro's formula [8]. This value, which is the ratio of the shock speed to the local speed of sound was found to be 1.70 at a diaphragm pressure difference of 20 in. Hg. This is in reasonably close agreement with the figure 1.84 above.

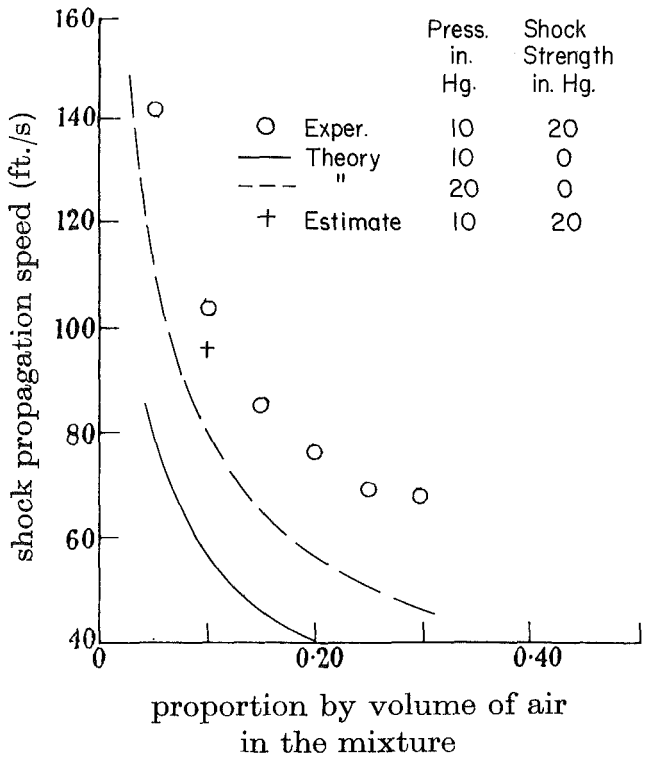

Fig. 7 Experimental results of Campbell and Pitcher, reference [5]

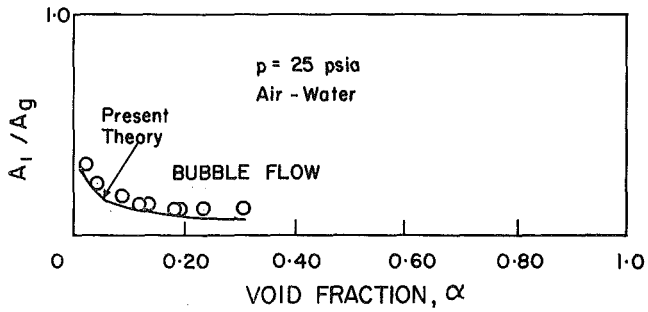

Fig. 8 Results of Henry et al., reference [9]

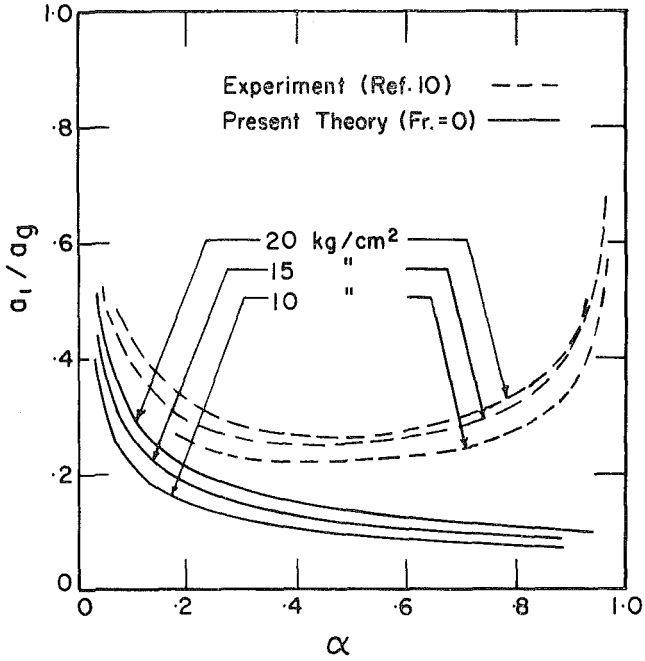

Fig. 9 Results of Semenov and Kosterin, reference [10]

Further evidence of similar behavior of compression waves in bubbly two-phase fluid and in gas is shown by the steepening wave front (Fig. 4 of reference [5]) which is due to higher speed of propagation in the higher pressure, lower void following the compression wave. The present theory predicts $\alpha' < 0$ and Fig. 7 of reference [5] appears to confirm that the void is decreased behind a pressure wave.

4 Henry et al. [9] measured the speed of propagation of both rarefaction and compression waves in air–water in the bubble flow regime at 25 psia. Relatively weak pressure disturbances were used (3 to 5 psi) and no difference in propagation speed was observed (3 percent accuracy) between rarefaction and compression waves.

The effect of shock strength on propagation speed was computed as for Campbell and Pitcher's tests. Using the equivalent isentropic exponent derived from their results it was found that a shock strength of 3 psi would increase the wave speed by 6 percent, i.e., within a ±3 percent scatter band. The tests of Henry et al. were at 25 psia and Campbell and Pitcher's at only 4.9 psia. Also the latter used glycerine–water, not water. Hence some difference in shock strength effect may be expected. However, it seems likely that the effect of shock strength on propagation speed in Henry's experiment might be small enough to lie within the experimental error.

a_1 was computed for $\rho_f = 62.3$, $\rho_g = 0.1277$ lb/ft³, and $a_f = 5100$, $a_g = 1130$ ft/sec, assuming a temperature of 70 deg F. The void correlation of Styrikowich et al. [3] was used. a_1 was insensitive to c_f in the range 1–10 ft/sec which probably covers the velocities used by Henry et al.; a_1/a_g is plotted in Fig. 8 together with their results. The computed values follow the shape of the experimental curve well but lie about 20 percent below it over the range of void from 0.05 to 0.3.

5 Semenov and Kosterin [10] measured the propagation speed in two-phase flow over the wide range of void fraction from 0.1 to 0.95, and at pressures from 10 to 40 kg/cm² absolute. Void fraction was measured directly. The flow velocities were small. It is suggested that Froude number c_{mix}^2/gD did not greatly exceed 100, hence c_g did not greatly exceed 5 m/sec $\ll a_g$ (although in the single-phase steam tests $c_g = 60$ m/sec was used).

The pressure disturbance was generated by closing a valve at the downstream end of the tube. At these low velocities the resulting shock strength was probably weak and the authors reported no effect of shock strength on propagation speed under these conditions.

$\bar{c}_-/a_g$ was computed by the present theory (see below) using the fluid properties given in Table 1 of reference [10], and equation (3) of reference [10] for a_f and a_g. For Froude number = 0 and 100, α was computed from the void correlation given in reference [10]. c_{mix} was obtained from Froude number; hence $G = c_{mix}/(v_f + xv_{fg})$. Finally, $\bar{c}_- = c_{mix} - c_{wl-}$. The results are given in Fig. 9.

The theoretical propagation speeds lie appreciably below the experimental values. The reason for this is not clear, but it may be in the flow pattern. No details of the mixer used are given in [10], and it is not known whether the flow regime was bubbly or whether the bubble distribution was at all uniform. In the range from about 10 to 20 or 30 percent void the theoretical curve follows the shape of the experimental results.

6 White and D'Arcy [11] measured the propagation speed in steam–water at 483 and 1001 psia, mass flux = 159 lb/ft²·sec, and qualities from 0.1 to 0.3. The void range was calculated as

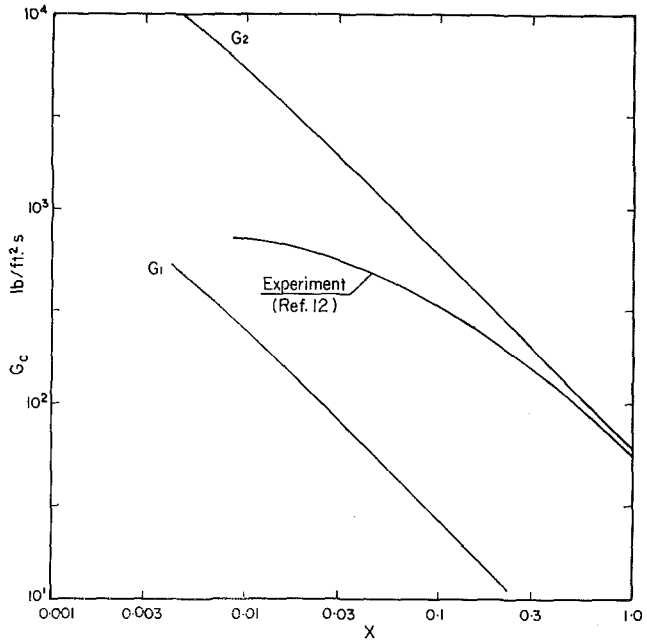

Fig. 10 Critical flow—steam–water at 15 psia, reference [12]

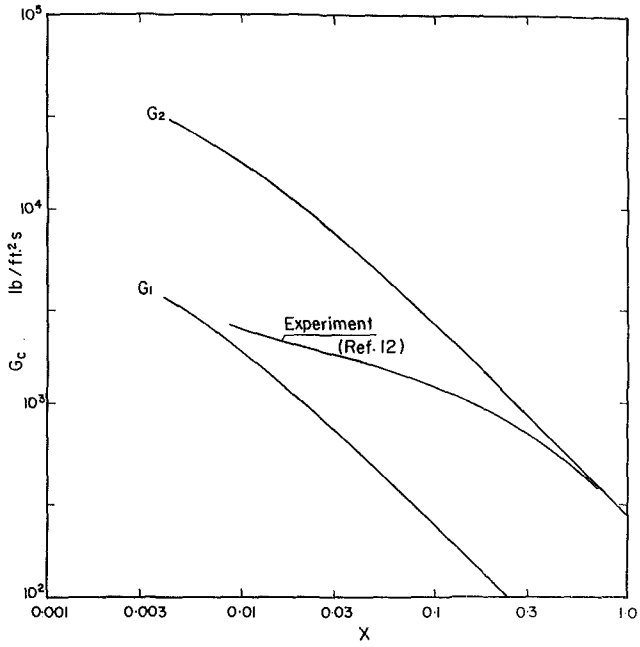

Fig. 11 Critical flow—steam–water at 70 psia, reference [12]

0.68 to 0.87 and the flow regime was stated to be annular. Propagation speed was measured by timing the passage of the head of an expansion wave between two positions about 7 ft apart.

In Fig. 4 of reference [11] the experimental results are compared with calculations of c_{w2-} based on the present theory. Theoretical values exceeded the experimental values by 5 percent or less in all but 2 of 17 cases. The maximum discrepancy was 8.5 percent.

Critical Flow

Theory

In single-phase flow it is found experimentally that when the fluid velocity at some cross section of a duct equals the local speed of sound in the fluid then it is not possible to increase the mass flux by changing only the downstream conditions. This follows because changes in downstream conditions cannot be felt upstream as long as the upstream wave-propagation speed is zero.

Critical flow has also been observed in two-phase flow in the sense that beyond a certain point, lowering the downstream pressure in a duct system does not effect an increase in mass flux. The explanation for critical flow in single phase, if valid, should apply equally to two-phase flow, i.e., maximum mass flux should occur when it is no longer possible for disturbance waves to propagate upstream. Consequently two-phase critical flow is predicted to occur when $c_{w-} = 0$.

Conditions for which $c_w = 0$ can be found by adjusting G until the $c_w = 0$ point of the parabola in Fig. 2 falls on one or other branch of the hyperbola. Thus two critical flows are predicted and are compared with experimental results below.

The calculations were actually made as follows. From (22) and (6) with $c_w = 0$,

$$\frac{\lambda_g}{\lambda_f} = \frac{\rho_g}{\rho_f}\left(\frac{c_g}{c_f}\right)^2 = \frac{\rho_f}{\rho_g}\left(\frac{x}{1-x}\cdot\frac{1-\alpha}{\alpha}\right)^2 = M, \quad \text{say}$$

where p, α, and x, and hence M, are assumed to be known. Then, from (21)

$$A(p\alpha')^2 + Bp\alpha' + C = 0 \tag{25}$$

where $A = M - 1$, $B = (Q_f - M)(1 - \alpha) + (MQ_g - 1)\alpha$, and $C = (Q_f - MQ_g)\alpha(\alpha - 1)$. Equation (25) was solved for two values of $p\alpha'$, hence the two sets of λ_f, λ_g from (21), c_f, c_g from (22), and G from (6). The value of G_c for $c_w = 0$ on the "1" branch of the hyperbola in Fig. 2 is called G_1 and G_2 is on the "2" branch.

Comparison with Experiment

Steady-state critical-flow results for a two-phase mixture issuing from the end of a constant-area duct have been published by several experimenters. Usually the quality just before the end of the duct was computed from measured local pressure and upstream conditions. The void fraction at the duct end was not always measured. Comparison between the present theory and experiment was made using the void-fraction correlation of Styrikowich et al. [3] which is reasonably representative of normal-flow conditions. This is equivalent to assuming that at critical-flow conditions, the upstream propagation speed relative to the upstream flow vanishes.

1 Measurements of critical flow in steam–water by Cruz, Falett, Fauske, and Moy over a wide range of quality and pressure are summarized in [12]. Some of these have been cross-plotted in Figs. 10 and 11 and compared with computed values of G_1 and G_2. The experimental results have been represented by lines faired through them.

2 Fauske [13] published some air–water results which covered the low-quality range 0.0006 to 0.08. Comparison with theory is shown in Fig. 12. In this reference Fauske also measured void fraction and showed that the slip ratio c_g/c_f at critical conditions remained low, between 1 and 3 in his range of quality, in contrast to earlier theories which suggested values of 10 and higher. Fauske's slip values were more consistent with normal flow conditions ($G \ll G_c$). It is of interest to note that Styrikowich's void correlation [3] which is used here implies that slip ratio is ≤ 2.0.

3 Henry [14] measured void fraction and critical flow in steam–water over a range of pressure and quality. His results for 50 psia are compared with the present theory in Fig. 13 using both the void correlation of Styrikowich et al. and a correlation derived from Henry's measurements:

$$\frac{1-\alpha_c}{\alpha_c} = 10^a\left(\frac{1-x_c}{x_c}\right)^{1.942}$$

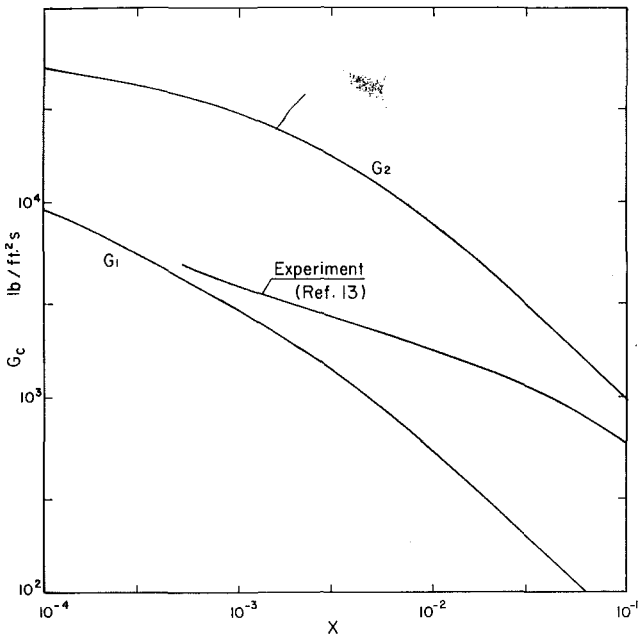

Fig. 12 Critical flow—air-water at 17 psia, reference [13]

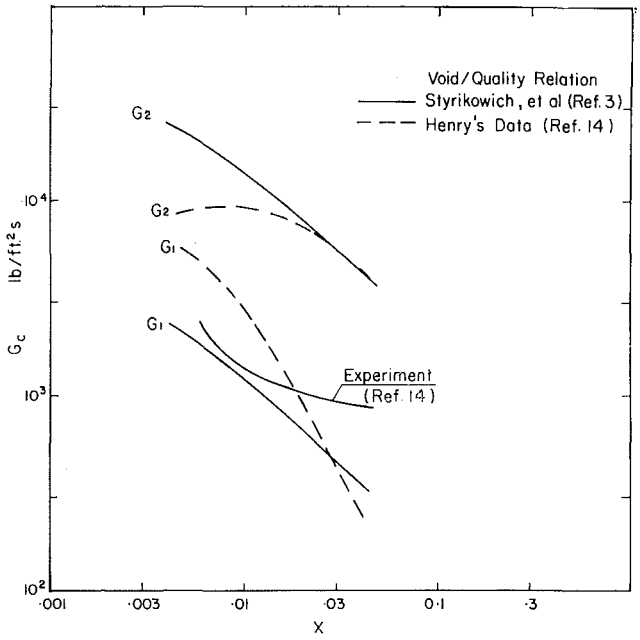

Fig. 13 Critical flow—steam-water at 50 psia, reference [14]

where $a = -4.013 + 0.003398p$. This fits the exit void data in Table 4 of reference [14] fairly well over the range $49.6 \leq p \leq 148.5$ psia.

4 Figs. 10 to 13 all indicate that at low void the experimental results approach the theoretical G_1 curve and at high void they approach G_2. In the mid-range they vary continuously between the two curves. This behavior is very similar to that of the propagation speed.

The computed curves were based on a normal-flow ($G \ll G_c$) void correlation. When a void correlation obtained from critical-flow results is used, the theory and experiment (broken line, Fig. 13) bear no obvious relation.

Discussion and Conclusions

The main point of this study is that a simple theory of both the propagation speed of small disturbances and critical flow has been developed for two-phase fluids in almost exact analogy with well-established single-phase theory. Bearing in mind the experimental difficulties as indicated by the scatter in most of the propagation-speed, critical-flow, and void-fraction [3] measurements, the two-phase theory appears to agree well with experiment in the limits as $\alpha \to 0$ and as $\alpha \to 1$. It is found that there are different modes of propagation of disturbances at low void and at high void. Although both modes are theoretically possible at all voids, in practice only the one mode is observed at any given void.

In the intermediate range of voids the experimental critical-flow results exhibit a continuous variation from one mode to the other. For propagation speed, the results of Semenov and Kosterin [10] suggest similar behavior. The other experimental series do not cover the full void range. In fact, either the flow became unsteady [9] or the bubbles became large and the flow pattern changed [2] as void was increased, so that continuous variation of propagation speed throughout the full void range was not generally observed.

It is apparent that nonuniform flow patterns, e.g., slug flow (flow in which some of the bubbles approach the size of the duct) or spray annular flow (where a considerable portion of the water is entrained in the core) would not satisfy the assumptions made in the theory, either because the character of the flow would vary too much from one cross section to another (e.g., slug flow) or because two mean velocities c_f and c_g would be inadequate to define the flow dynamically (e.g., spray annular flow). These are the conditions which occur in the mid-void range and indeed theory and experiment do not agree there. However, it is interesting to note that in all cases the experimental data lie *between* the two theoretical modes which behave as limiting modes.

The smooth variation of critical flow in the mid-void range, as opposed to the more erratic behavior of the propagation speed, is probably due to the special condition of critical flow (maximum G for given upstream conditions). Most of the propagation-speed measurements were made at very low G and were probably subject to a greater variety of flow patterns.

Critical-flow conditions seem to be governed not by the void conditions at the throat as measured by Henry [14] but by the normal-flow void preceding the critical-flow point.

The importance of flow pattern on propagation speed has been observed by others and must also be concluded from this study. The limitations of the common separated-flow model with a "standard" void-fraction correlation have been shown. In order to analyze the mid-void range, a more sophisticated model such as that of Henry et al. [9] is needed. For critical flow, the situation may not be so complicated because of the maximum G constraint on the flow.

References

1 Shapiro, A. H., "The Dynamics and Thermodynamics of Compressible Fluid Flow," Vol. 2, Ronald Press, New York, 1954, pp. 917–918.

2 DeJong, V. J., and Firey, J. C., "Effect of Slip and Phase Change on Sound Velocity in Steam–Water Mixtures and the Relation to Critical Flow," *I&EC Process Design and Development*, Vol. 7, No. 3, July 1968, pp. 454–463. See also DeJong, V. J., "The Velocity of Sound in Water Containing Steam Bubbles," MS thesis, University of Washington, Seattle, Wash., 1966.

3 Styrikowich, M. A., Nevstrueva, E. I., and Dvorina, G. M., "The Hydrodynamics Phenomena of Cocurrent Steam–Water Flows in Heated and Nonheated Tubes," Paper D2 presented at International Symposium on Research in Cocurrent Gas–Liquid Flow, University of Waterloo, Waterloo, Ontario, Canada, Sept. 18–19, 1968.

4 England, W. G., Firey, J. C., and Trapp, O. E., "Additional Velocity of Sound Measurements in Wet Steam," *I&EC Process Design and Development*, Vol. 5, No. 2, April 1966, pp. 198–202.

5 Campbell, I. J., and Pitcher, A. S., "Shock Waves in a Liquid

Containing Gas Bubbles," *Proceedings of the Royal Society*, London, Ser. A., Vol. 243, No. 1235, Feb. 1958, pp. 534–545.

6 Slie, W. M., Donfor, A. R., Jr., and Litovitz, T. A., "Ultrasonic Shear and Longitudinal Measurements in Aqueous Glycerol," *Journal of Chemical Physics*, Vol. 44, No. 10, 15 May 1966, Table 3.

7 Shapiro, A. H., "The Dynamics and Thermodynamics of Compressible Fluid Flow," Vol. 2, Ronald Press, New York, 1954, p. 1021, equation (25.36).

8 Shapiro, A. H., "The Dynamics and Thermodynamics of Compressible Fluid Flow," Vol. 1, Ronald Press, New York, 1954, p. 118, equation (5.18a).

9 Henry, R. E., Grolmes, M. A., and Fauske, H. K., "Propagation Velocity of Pressure Waves in Gas-Liquid Mixtures," Paper A1 presented at International Symposium on Research in Cocurrent Gas–Liquid Flow, University of Waterloo, Waterloo, Ontario, Canada, Sept. 18–19, 1968.

10 Semenov, N. I., and Kosterin, S. I., "Results of Studying the Speed of Sound in Moving Gas-Liquid Systems," *Thermal Engineering*, Vol. 6, No. 59, 1964.

11 White, R. F., D'Arcy, D. F., "Velocity of Sound and Critical Discharge Pressure in Annular Two Phase Flow," Paper 5 presented at Fluid Mechanics and Measurements in Two-Phase Flow Systems Symposium, The University of Leeds, Leeds, England, Sept. 24–25, 1969.

12 Fauske, H. K., "Contribution to the Theory of Two-Phase, One-Component Critical Flow," ANL-6633, Oct. 1962.

13 Fauske, H. K., "Two-Phase, Two- and One-Component Critical Flow," Paper G1 presented at Symposium on Two Phase Flow, University of Exeter, England, June 21–23, 1965.

14 Henry, R. E., "A Study of One- and Two-Component, Two-Phase Critical Flows at Low Qualities," ANL-7430, March 1968.

E. S. NOWAK
Professor.
Mem. ASME

J. CHAN
Research Assistant.

Faculty of Engineering Science,
The University of Western Ontario,
London, Ontario, Canada

An Experimental Investigation of the Enthalpy of Saturated Heavy-Water Liquid

Measurements on the enthalpy of saturated heavy-water liquid were made for temperatures ranging from 90 to 350 deg F by means of a non-flow, continuous-heating calorimeter. Based on confirmatory tests conducted on light water, it is estimated that the heavy-water enthalpy measurements obtained in this paper are accurate to ±0.5 percent. The experimental data of this research is in reasonable accord with the data obtained by other investigators. It was also found that the difference between the heavy-water enthalpy-change values and the corresponding values for light water is a strong function of temperature varying from about 0.2 percent at 100 deg F to 3.5 percent at 350 deg F.

Introduction

Accurate and detailed knowledge for the enthalpy of heavy water is of significance in the design, power rating, and operation of nuclear power plants moderated and cooled with heavy water. In Canada, heavy-water moderated and cooled nuclear power plants (Candu) are currently being designed to operate at a line pressure of 1300 psia and heavy-water inlet and outlet temperatures of 480 and 560 deg F respectively. In all probability, the next generation of Candu nuclear power plants will be designed to operate at higher pressures and temperatures.

There is a paucity of consistent and detailed information for the thermodynamic properties of heavy water at the higher pressures and temperatures. The senior author therefore initiated a comprehensive experimental program to study the thermal behavior of saturated heavy-water liquid and vapor from the triple point to the critical point. This paper is the third of a series of papers dealing with apparatus development and determinations of various thermodynamic properties of saturated heavy-water liquid and vapor.[1]

The main purpose of this present paper is to assess the validity of previous measurements conducted on saturated heavy-water liquid from 100 to 400 deg F. A description of the non-flow calorimeter and associated instrumentation which was employed in the research of this paper appears elsewhere [13].[2]

Theory of Experiment

The experimental method consisted chiefly of adding electrical energy at a predetermined rate to a non-flow calorimeter containing a known charge of saturated heavy water and its vapor and measuring the magnitude of the temperature rise of the calorimeter and its contents. Two types of experiments were conducted over a given temperature interval. In one experiment the calorimeter contained a mixture of heavy-water liquid and vapor, whereas in the second experiment (tare measurement) the calorimeter was empty.

By utilizing the first law of thermodynamics, the Clausius-Clapeyron equation, and by noting that the thermodynamic heating process occurs at constant total volume and at constant total fluid mass it follows that:

$$h_{f_2} - h_{f_1} = \frac{Q - Q_E}{M} + \frac{V}{M}(P_2 - P_1) + \left[\left(\frac{V}{M} - v_f\right) T \frac{dP}{dT}\right]_1 - \left[\left(\frac{V}{M} - v_f\right) T \frac{dP}{dT}\right]_2 \quad (1)$$

where

Q_E and Q are the quantities of energy that were required to raise the temperatures of the empty and charged calorimeter during the two types of experiments,

h_f is the enthalpy of saturated heavy-water liquid,

M is the mass of the heavy-water sample (mixture of liquid and vapor),

V is the internal volume of the calorimeter,

P is the saturation pressure of the heavy-water sample,

v_f is the specific volume of saturated heavy-water liquid,

T is the absolute temperature of the heavy-water sample,

$\frac{dP}{dT}$ is the change of pressure with respect to temperature at saturation conditions.

Subscripts 1 and 2 refer to initial and final saturation states ($T_2 > T_1$).

The first term on the right-hand side of equation (1) is the net electrical energy added to unit mass of the heavy-water contents.

[1] Details of the first two papers are given in references [11, 13].

[2] Numbers in brackets designate References at end of paper.

Contributed by the Heat Transfer Division for publication (without presentation) in the Journal of Heat Transfer. Manuscript received by the Heat Transfer Division October 23, 1970. Paper No. 71-HT-M.

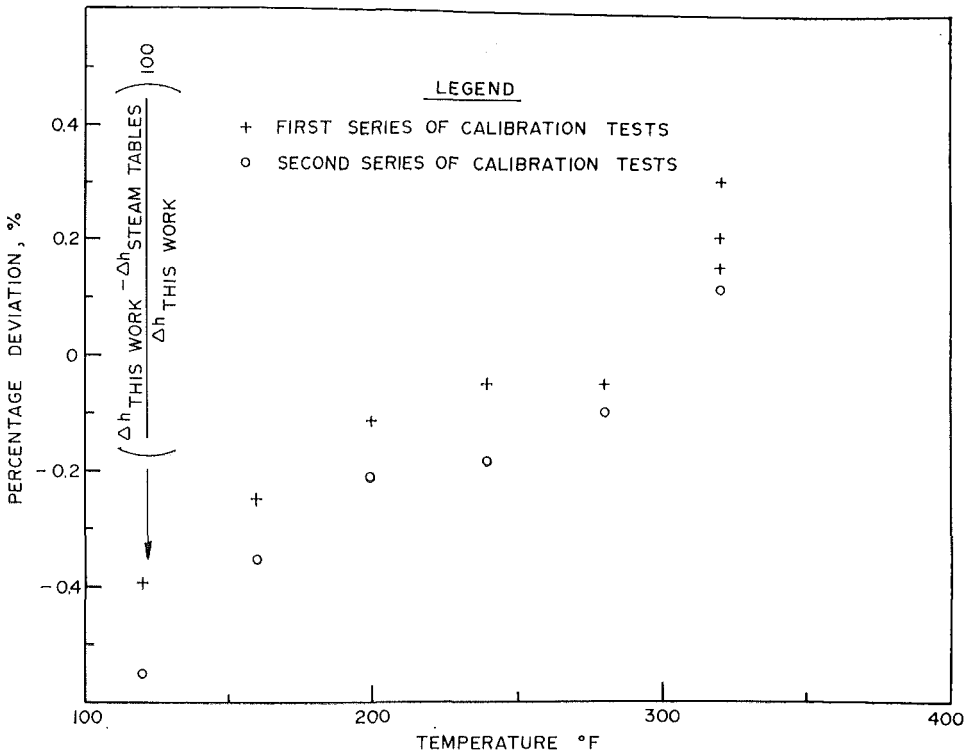

Fig. 1 Deviation between light-water enthalpy measurements and corresponding Keenan and Keyes values

Table 1 Enthalpy-difference measurements on light water (second series)

Details	Run 1	Run 2	Run 3	Run 4	Run 5	Run 6
Initial temp., deg F	100.94	141.27	183.54	223.52	262.92	304.31
Final temp., deg F	141.35	180.50	223.32	262.75	301.63	342.41
Total energy added, Btu	80.19	78.48	80.04	79.57	79.48	79.40
Enthalpy difference for 40 deg F rise, Btu/lb	39.70	39.89	40.10	40.46	40.91	41.59
Keenen and Keyes steam table enthalpy difference for 40 deg F rise[a]	39.92	40.03	40.19	40.53	40.95	41.54

Mass contained in second series of calibration tests = 1.8994 lb.

[a] There is no significant difference between the values for the enthalpy of saturated liquid contained in references [11] and [10].

The magnitude of the last three terms on the right-hand side of equation (1), though small at room temperature, increases with temperature. More specifically, the algebraic sum of the three terms is approximately 0.1, 0.4, 1, and 4 percent of $(Q - Q_E)/M$ at temperatures of 200, 300, 400, and 600 deg F respectively. The property data contained in reference [2] was employed to evaluate the last three terms of equation (1).

Heavy-Water Samples

The heavy-water samples used in this investigation were supplied by Atomic Energy of Canada Limited and certified as possessing a purity of 99.82 percent. During the investigation the calorimeter was charged with an initial mass of heavy water amounting to 2.0446 lb. Upon completion of the investigation the heavy water was discharged from the calorimeter and weighed a final time. The difference between the initial and final mass values was not significant, being less than 0.02 percent.

Experimental Procedure

The experimental procedure followed in the present paper is identical to that described in references [5, 13]. By means of manual control the temperatures of the adiabatic shield and outer guard were made to track the uniformly rising temperature of the calorimeter to within ±0.02 deg F. The equilibrium temperatures of the heavy-water sample at the beginning and at the end of a test run were measured by means of a tiny industrial platinum resistance capsule. Details of the temperature variations on the calorimeter apparatus are given in references [5, 13].

Experimental Results

Tare Measurements. The composite heat capacity of the empty calorimeter may be represented by the following empirical equation:

$$C = 0.98411 \times 10^{-1} + 0.46894 \times 10^{-4} t \qquad (2)$$

where C is the composite heat capacity of the empty calorimeter in Btu/deg F, and t is the temperature in deg F. This empirical equation is valid from 100 to 350 deg F, and it is based on the tare measurements reported in reference [13].

Apparatus Calibration. The reliability of the calorimeter apparatus and its associated instrumentation was evaluated from two series of calibration measurements using light water. The results of the first series of tests which were conducted just prior to the heavy-water experiments of this paper are given in reference [13], whereas the results of the second series of calibration tests which were conducted just after the heavy-water investigations are given in Table 1 of this paper.

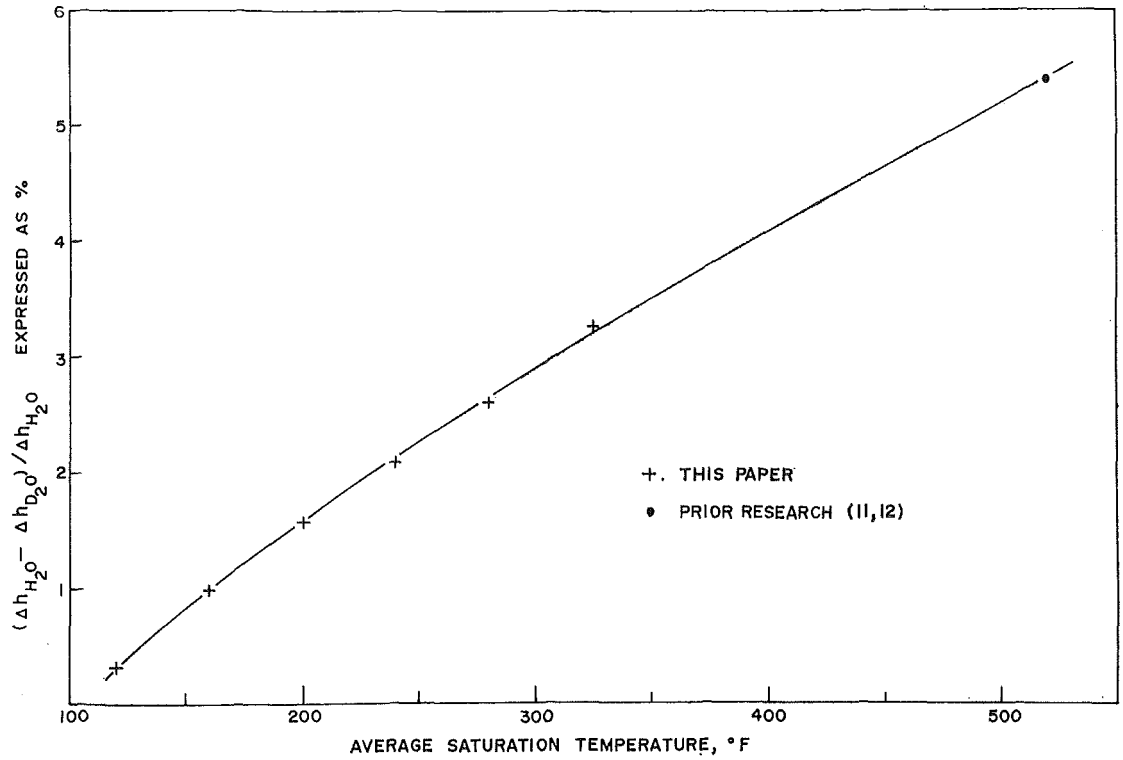

Fig. 2 *Deviations between enthalpy-change values for saturated heavy water and light water*

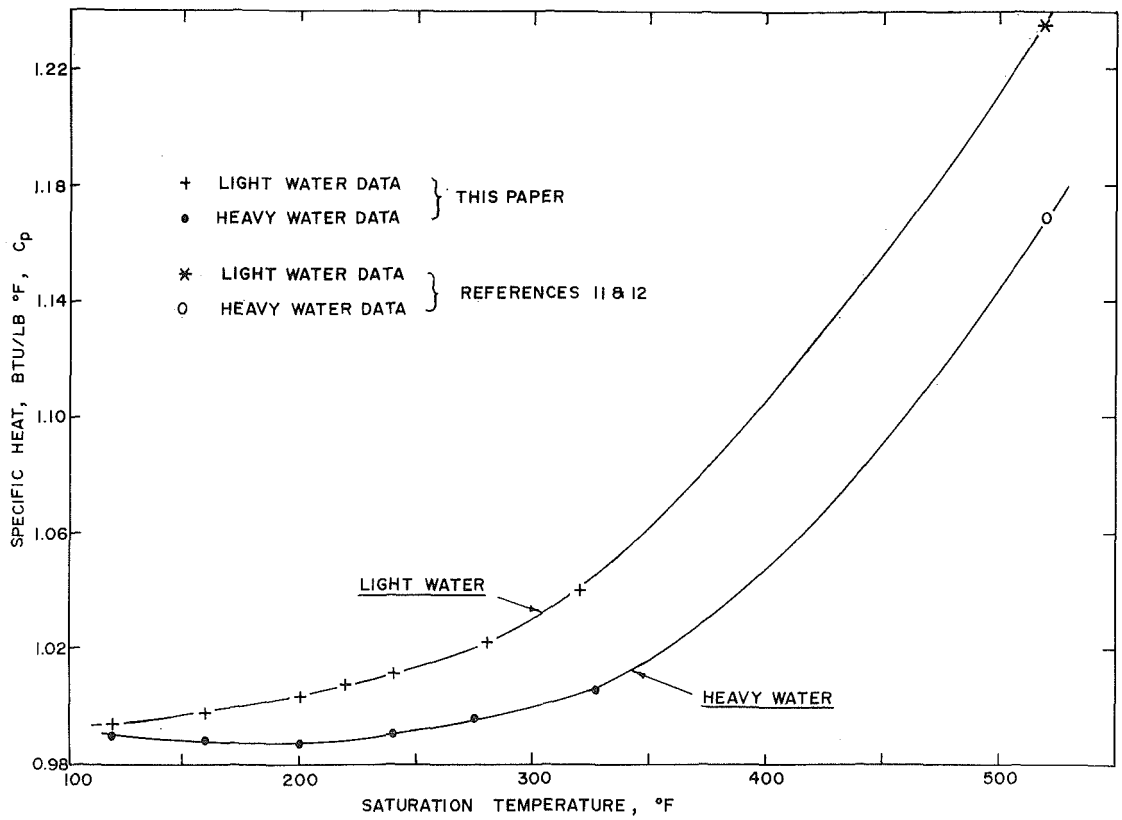

Fig. 3 *Specific heat of saturated light water and heavy water*

Table 2 Measurements on the enthalpy difference of saturated heavy-water liquid

Run	Initial temp. deg F	Final temp. deg F	Heating rate deg F/hr	Total energy Btu	Tare energy Btu	Enthalpy difference for a 40 deg F temperature interval Btu/lb
1	100.58	139.55	18	86.85	4.05	39.63
2	98.42	138.92	13	90.30	4.22	39.64
3	101.48	139.82	23	85.38	4.00	39.59
4	138.39	178.35	18	88.88	4.23	39.51
5	140.18	179.59	13	87.73	4.18	39.54
6	141.61	179.57	23	84.45	4.02	39.52
7	178.89	220.10	18	91.61	4.45	39.46
8	181.31	220.82	13	87.95	4.26	39.51
9	181.40	219.57	23	84.95	4.12	39.50
10	219.11	255.93	18	82.16	4.04	39.59
11	220.17	258.09	23	84.68	4.16	39.63
12	216.32	256.82	13	90.55	4.44	39.66
13	253.67	296.33	18	95.69	4.75	39.81
14	254.21	293.73	13	88.77	4.39	39.88
15	256.80	294.46	23	84.58	4.19	39.87
16	293.81	350.04	18	127.09	6.37	55.27
17	296.79	348.95	13	118.12	5.92	55.38[a]
18	295.85	350.51	23	123.72	6.20	55.36
19	90.15	99.69	13	21.32	0.98	9.9[b]

[a] 55 deg F interval.
[b] 10 deg F interval.

The deviations between the results of these two calibration tests and the corresponding values found in the steam tables of Keenan and Keyes are given in Fig. 1. Fig. 1 indicates that the reproducibility of the present apparatus is ± 0.1 percent whereas the maximum deviation between the experimental enthalpy data of this paper and the corresponding values contained in the Keenan and Keyes steam tables is within approximately 0.5 percent. Assuming no error in the values of the Keenan and Keyes steam tables[3] it may be estimated that the determinations on the enthalpy of saturated heavy-water liquid of this paper are accurate to ± 0.5 percent.

Enthalpy Measurements of Heavy Water. The enthalpy of saturated heavy-water liquid was experimentally determined from 90 to 350 deg F at heating rates ranging from 13 to 23 deg F per hour. Table 2 is a tabulation of the experimental data obtained for each of the individual test runs. A cursory study indicates that the reproducibility of the heavy-water measurements is excellent, being approximately ± 0.1 percent.

Discussion of Results

The percentage deviation between the enthalpy-change values for heavy water and light water of this paper are given in Fig. 2, whereas the specific heats of saturated heavy water and light water are given in Fig. 3 Also included in Figs. 2 and 3 are the data obtained by the senior author of this paper for saturated heavy and light water from 480 to 560 deg F [11, 12].

It is evident from Fig. 2 that the percentage deviation between the enthalpy-change values for light and heavy water is a strong function of temperature. It varies for example from approximately 0.25 percent at 120 deg F to about 3.2 percent at 325 deg F. Fig. 2 also tends to confirm the validity of the prior measurements conducted on light and heavy water from 480 to 560 deg F in references [11, 12].

The experimental specific-heat data for saturated heavy water of this paper along with the experimental data of Baker [2], Brown et al. [4], Cockett et al. [6], Eucken et al. [7], and Rivkin et al. [14, 15] are given in Fig. 4. The maximum deviation between the results of this work and the above-mentioned authors is around 2 percent. This is entirely within the limits of error estimated in references [2, 4, 6, 7, 14, 15].

[3] To this day the pioneer measurements of Osborne et al., conducted at the National Bureau of Standards from 1920 to 1939 essentially form the basis of the various saturation data contained in the different national steam tables. The error in the pioneer experimental enthalpy data of Osborne is in all probability less than ± 0.5 percent at moderate values of temperatures and pressures.

Table 3 Comparisons between observations of this work and others

Temperature interval deg F		Enthalpy difference Btu/lb		
From	To	This work	Baker	Howieson
100	140	39.6	40.0	40.8
140	180	39.5	39.9	40.2
180	220	39.5	39.8	39.4
220	260	39.6	39.8	38.8
260	300	39.9	39.9	38.8
295	350	55.3	55.3	54.4

The measurements of this work along with the smoothed data proposed by Baker [2] and Howieson [9] are shown in Table 3. The maximum deviation between the results of this paper and those proposed by Baker is approximately 1 percent, which is well within his estimated error of measurement, i.e., ± 1.5 percent. The maximum deviation between the measured enthalpy-difference values of this paper and the corresponding values proposed by Howieson is within approximately 3 percent. It should be pointed out that the Howieson enthaly values are based on values deduced by Whalley [16] from the fragmentary saturation data available to him at the time.

Conclusions

1 It is estimated the enthalpy measurements conducted on saturated heavy-water liquid from 90 to 350 deg F are accurate to within ± 0.5 percent.

2 The research of this paper is in reasonable accord with the earlier heavy-water measurements of Baker, Brown, Cockett Eucken, and Rivkin with the maximum deviation being approximately 2 percent.

3 In the region covered by this paper the differences in the enthalpy change of saturated heavy-water liquid and the corresponding enthalpy-change values for saturated light-water liquid were found to be a strong function of temperature.

Acknowledgments

The authors are grateful for the laboratory assistance given to them throughout the summer of 1968 by Mr. M. Emmerson, an engineering undergraduate student. The senior author wishes to acknowledge the financial support received from the National Research Council of Canada and the Faculty of Engineering

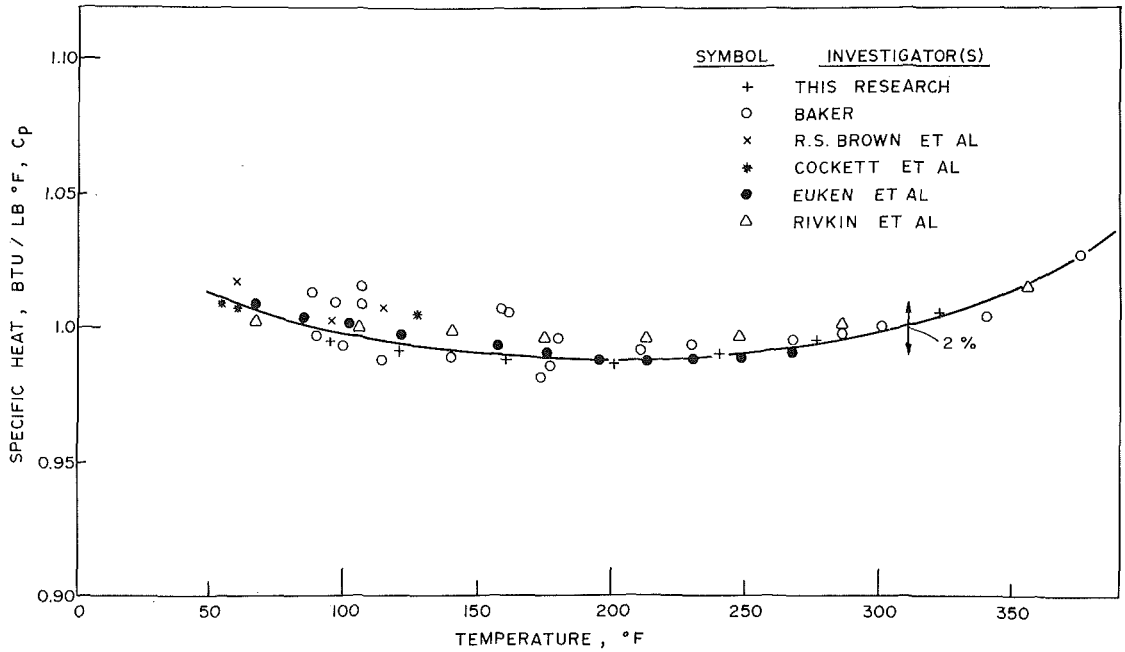

Fig. 4 Specific heat at constant pressure for saturated heavy-water liquid

Science of The University of Western Ontario which made this research possible. He is also grateful to Atomic Energy of Canada Limited for supplying him with several gallons of heavy water and also for the long-term loan of the precision instrumentation employed in this research.

References

1 *Thermodynamic and Transport Properties of Steam*, ASME, New York, 1967.

2 Baker, B. L., "Heat Capacity and Thermodynamic Properties of Saturated Deuterium Oxide," AECU-4738, 1959.

3 Bishop, A. A., and Nelson, P. A., "Transport and Thermodynamic Properties of Saturated and Compressed Heavy Water," Carolina's Virginia Nuclear Power Associates, Inc. 1961.

4 Brown, R. S., Barnes, W. H., and Maass, O., "A Note on the Specific Heats of Liquid Deuterium Oxide," *Canadian Journal of Research*, Vol. 13, 1935, pp. 167–169.

5 Chan, J., "The Design and Construction of an Apparatus to Measure the Enthalpy of Heavy Water," M.E.Sc. thesis, Faculty of Engineering Science, The University of Western Ontario, Canada, 1968.

6 Cockett, A. H., and Ferguson, A., "The Specific Heat of Water and of Heavy Water," *Philosophical Magazine*, Vol. 29, 1940, pp. 185–199.

7 Eucken, A., and Eigen, M., *Zeitschrift Electrochem*, Vol. 55, 1951, pp. 343.

8 Elliott, J. N., "Tables of the Thermodynamic Properties of Heavy Water," AECL-1673, 1963.

9 Howieson, J., "Tables of Properties of Heavy Water at Saturation Temperatures," AECL-1055, 1960.

10 Keenan, J. H., and Keyes, F. G., *Thermodynamic Properties of Steam*, John Wiley & Sons, New York, 1936.

11 Nowak, E. S., "The Enthalpy Change of Saturated Heavy Water," Presented at the Seventh International Conference on the Properties of Steam, Tokyo, Japan, 1968.

12 Nowak, E. S., "A Calorimetric Investigation of the Enthalpy of Heavy Water," University of Western Ontario, Engineering Science Report, HT-1-69, Submitted to Atomic Energy of Canada Limited, Sept. 1969.

13 Nowak, E. S., and Chan, J., "A Calorimeter Apparatus to Measure the Enthalpy Difference of Heavy Water," JOURNAL OF HEAT TRANSFER, TRANS. ASME, Series C, Vol. 91, No. 2, May 1969, pp. 235–240.

14 Rivkin, S. L., and Egorov, B. N., "Experimental Study of Heavy Water Specific Heat," *Atomnaya Energiya*, Vol. 7, No. 5, 1959, pp. 462–465.

15 Rivkin, S. L., and Egorov, B. N., "Specific Heat of Heavy Water at High Temperatures and Pressure," *Atomnaya Energiya*, Vol. 14, No. 4, 1963, pp. 416–418.

16 Whalley, E., "The Thermodynamic and Transport Properties of Heavy Water," *Proceedings and Communications of the Conference on Thermodynamic and Transport Properties of Fluids*, Institution of Mechanical Engineers, London, 1957, pp. 15–26.

DAVID F. DYER
Associate Professor,
Department of Mechanical Engineering,
Auburn University,
Auburn, Ala.
Assoc. Mem. ASME

J. EDWARD SUNDERLAND
Professor,
Department of Mechanical
and Aerospace Engineering,
North Carolina State University,
Raleigh, N. C.
Mem. ASME

Freeze-Drying of Bodies Subject to Radiation Boundary Conditions

A solution is obtained for the transient temperature distribution and the position of the sublimation front for freeze-drying slabs, cylinders, and spheres. The surface is exposed to thermal radiation boundary conditions so that the surface temperature is time dependent. Results, presented in dimensionless form, cover a wide range of variables that should include essentially all food products.

Introduction

THIS PAPER is concerned with the sublimation dehydration of slabs, cylinders, or spheres that are subject to radiant heat sources. The same analysis would also apply for evaporative drying of porous bodies during the falling rate period if the diffusion of water in the liquid state is negligible. The application of most immediate concern is freeze-drying of foods where frozen food is placed in a vacuum chamber. The pressure in the chamber is maintained below the triple point so that the drying process takes place by sublimation. Since the liquid substance is frozen, there is no diffusion of water except for the vapor which moves from the sublimation front to the free surface and subsequently into the vacuum chamber. The physical model considered is essentially that used by the authors in earlier work [1, 2][1] and is shown in Fig. 1. In essence this model assumes that there is a porous outer layer of product which can be idealized as a bundle of straight capillaries. The region of the product farthest from the heater is frozen and heat may or may not be transferred through this region. The transport properties are assumed constant. According to Massey [3], convection to the free surface of the product is very small compared to the rate of heat transfer by thermal radiation. Therefore, the heat input will be assumed to follow the usual fourth-power radiation equations.

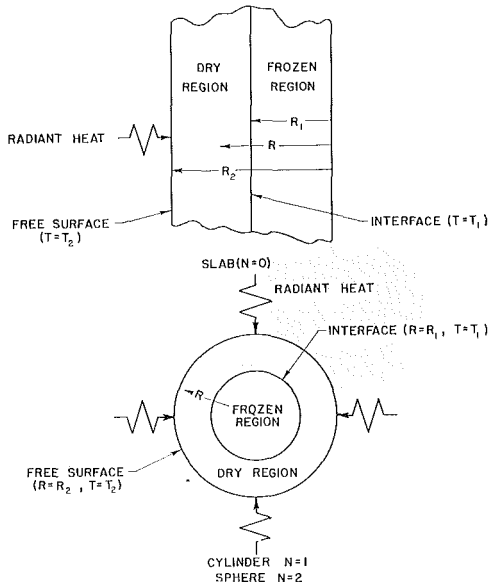

Fig. 1 Physical model

Most analyses of sublimation drying assume that the outer surface to be dried is instantaneously brought to the maximum allowable temperature before scorching. In practice the surface temperature changes slowly from the initial temperature to the scorch temperature. Two recent papers [4, 5] have considered this problem for drying slabs. In these papers the radiant heater was held at a constant temperature until the surface temperature reached scorch conditions. McCulloch and Sunderland [4] solved the problem by integral techniques using an assumed time dependent temperature profile in the dried layer. Later Cho and Sunderland [5] obtained an approximate solution by linearizing the radiation boundary condition. They showed that by assuming a linear temperature profile in the dried region one could obtain good results. This work verifies the quasi-steady assumption, namely, that the sensible heating effects are negligible compared to the latent heat effects. In the present paper it will be assumed that quasi-steady conditions hold, but

[1] Numbers in brackets designate References at end of paper.

Contributed by the Heat Transfer Division and presented at the ASME-AIChE Heat Transfer Conference, Tulsa, Okla., August 15–18, 1971. Manuscript received by the Heat Transfer Division January 11, 1971. Paper No. 71-HT-5.

the radiation boundary condition will not be linearized. The heater will have a constant temperature and the solution will apply until either drying is complete or the surface reaches the scorch temperature, whichever occurs first. If the surface reaches the scorch temperature prior to complete drying, the techniques presented in references [1, 7] can be used to complete the solution.

Analysis

Dried Region. The energy equation for the quasi-steady constant property model [1, 2] is:

$$\frac{d}{dr} r^n \frac{dT}{dr} = 0 \tag{1}$$

where $n = 0, 1, 2$ for a slab, cylinder, and sphere respectively. It should be noted that the convected energy transport is neglected in this equation in accordance with reference [6] and the quasi-steady assumption has eliminated the time dependent term. The boundary conditions are:

$$R_1 = R_2 \quad \text{at} \quad t = 0 \tag{2}$$

$$T = T_1 \quad \text{at} \quad r = R_1 \tag{3}$$

$$q_0 + k \frac{dT}{dr} = -\rho\lambda\Delta H \frac{dR_1}{dt} \quad \text{at} \quad r = R_1 \tag{4}$$

$$k \frac{dT}{dr} = \epsilon\sigma(T_H^4 - T_2^4) \quad \text{at} \quad r = R_2 \tag{5}$$

Equation (2) states that the initial thickness of the dried region is zero while equation (3) is an assumption that the interface temperature is constant. Equation (4) is an energy balance at the frozen–dry interface where it is assumed that the energy input through the frozen region, q_0, is a known weak function of time. Equation (5) is an energy balance at the heated outer surface relating the conduction into the dry layer to the input radiation assuming a black heater surface and a small distance between heater and product compared with typical dimensions of the product.

Equation (1) can be integrated twice to give the following equations:

$$\frac{dT}{dr} = \frac{C_1}{r^n} \tag{6}$$

$$\left.\begin{aligned} T - T_1 &= \frac{C_1}{1-n}(r^{1-n} - R_1^{1-n}); \qquad n \neq 1 \\ T - T_1 &= C_1 \ln (r/R_1); \qquad n = 1 \end{aligned}\right\} \tag{7}$$

where equation (3) has been used to eliminate one integration constant.

The constant C_1 can be determined as a function of the heater surface temperature by substituting equation (6) into equation (5) which gives on rearrangement:

$$C_1 = \frac{\epsilon\sigma R_2^n (T_H^4 - T_2^4)}{k} \tag{8}$$

Equations (7) and (8) give the temperature distribution in the dried layer where T_2 and R_1 are still undetermined functions of time. The interface radius can be related to the surface temperature T_2 by combining equations (8), equation (7), and the definition of T_2. Thus

$$\left.\begin{aligned} R_1 &= \left\{ \frac{T_1 - T_2}{T_H^4 - T_2^4} \frac{k(1-n)}{\epsilon\sigma R_2^n} + R_2^{1-n} \right\}^{\frac{1}{1-n}}; \qquad n \neq 1 \\ R_1 &= R_2 \exp\left\{ \frac{T_1 - T_2}{T_H^4 - T_2^4} \frac{k}{\epsilon\sigma R_2} \right\}; \qquad n = 1 \end{aligned}\right\} \tag{9}$$

The interface radius can be related to time by substituting equation (6) into equation (4) giving

$$-\frac{dt}{\rho\lambda\Delta H} = \frac{R_1^n dR_1}{q_0 R_1^n + kC_1} \tag{10}$$

where kC_1 can be determined from equation (8) and q_0 from the section which follows.

Frozen Region. The term q_0 refers to the heat conducted from the frozen region to the sublimation interface. This heat could be the result of transient effects in the frozen region, distributed heat sources such as microwave or gamma-ray heating, or heat transfer through the frozen region. Furthermore, if the dried region is transparent to thermal radiation at some wavelengths, q_0 could be the energy transmitted through the dried region to the interface. The following discussion applies to heat conducted to the sublimation front from the frozen region.

The energy equation, equation (11), for the dried region also applies to the frozen region because convection is neglected and the transient changes in enthalpy are small compared with the latent heat effects. The boundary condition given by equation (3) is also valid so that if equation (1) is integrated for the frozen region, equation (7) results. The constant C_1 is determined by the condition of the inner surface of the food product. A set of practical conditions for supplying heat through the frozen region is described below with the corresponding boundary condition. For a slab a sheet of material of high electrical resistance could be placed in contact with the frozen surface to maintain the surface at a temperature just below the freezing point. A vapor seal must be placed along this surface to prevent the formation of a low-conductivity dried layer. The boundary condition can be expressed by

$$T = T_0 \quad \text{at} \quad r = 0 \tag{11}$$

For a cylindrical sample a small-diameter wire or pin could be inserted along the centerline of the sample and heated electrically to maintain a temperature just below freezing. This boundary condition is described by

$$T = T_0 \quad \text{at} \quad r = R_0 \tag{12}$$

Nomenclature

C^* = dimensionless quantity defined by equation (18)
ΔH = enthalpy of sublimation, Btu/lb
k = thermal conductivity, Btu/hr-ft-deg F
n = 0, 1, 2, for slab, cylinder, and sphere respectively, dimensionless
q_0 = heat transfer to sublimation front from frozen region, Btu/hr-ft^2
r = distance from centerline, ft
R_0 = radius of heater used for cylinders or spheres, ft
R_1 = position of interface, ft
R_2 = position of free surface, ft
R^* = R_1/R_2, position of interface, dimensionless
t = time, hr
T = temperature, deg F
T_0 = temperature at outerline, deg F
T_1 = interface temperature, deg F
T_2 = temperature of free surface, deg F
T_H = heater temperature, deg F
T^* = dimensionless drying time
ϵ = emittance, dimensionless
θ_1^* = dimensionless interface temperature, T_1/T_H
θ_2^* = dimensionless temperature defined by equation (19)
λ = porosity, ratio of pore volume to total volume, dimensionless
ρ = density, lb/ft^3
σ = Stefan–Boltzmann constant, $0.1713 \cdot 10^{-8}$ Btu/ft^2-hr-deg R^4

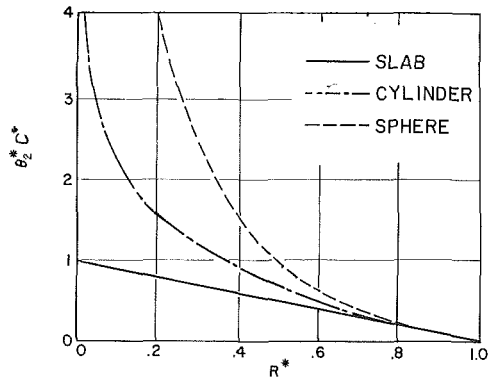

Fig. 2 Free surface temperature times C^* as a function of interface position

where R_0 is the wire radius. An analogous spherical heating element could be used with spherical samples and would give the same boundary condition except that R_0 would be the radius of the spherical heating element. Application of these boundary conditions to the frozen region gives the following temperature distributions in the frozen region:

$$\left.\begin{aligned} \frac{T - T_1}{T_0 - T_1} &= \frac{R_1 - r}{R_1} && \text{slab} \\ \frac{T - T_1}{T_0 - T_1} &= \frac{\ln (r/R_1)}{\ln (R_0/R_1)} && \text{cylinder} \\ \frac{T - T_1}{T_0 - T_1} &= \frac{R_0}{r}\frac{R_1 - r}{R_1 - R_0} && \text{sphere} \end{aligned}\right\} \tag{13}$$

The heat flux is given by

$$q_0 = -k \left.\frac{dT}{dr}\right|_{r=R_1^-} \tag{14}$$

Applying equation (14) to (13) gives

$$\left.\begin{aligned} q_0 &= k\frac{T_0 - T_1}{R_1} && \text{slab} \\ q_0 &= k\frac{T_0 - T_1}{R_1 \ln (R_1/R_0)} && \text{cylinder} \\ q_0 &= k\frac{(T_0 - T_1)R_0}{(R_1 - R_0)R_1} && \text{sphere} \end{aligned}\right\} \tag{15}$$

Solution Procedure. Equation (9) provides a closed-form relationship between R_1 and T_2 both of which depend on time in a complex manner. Since this dependence is implicitly contained in equation (10), it can be numerically integrated by the following procedure:

1 Consider a time period, Δt, in which the free surface temperature changes by the increment ΔT_2 from its initial value, T_{i2}, to a new value,

$$T_2 = T_{i2} + \Delta T_2$$

2 For this value of T_2 calculate R_1 from equation (9).

3 Assume the coefficient of dR_1 in equation (10) to be constant during the time period Δt, so that the equation can be used in finite-difference form to calculate Δt, namely

$$\Delta t = -\rho\lambda\Delta H \frac{R_1^n \Delta R_1}{q_0 R_1^n + kC_1} \tag{16}$$

Note that the quantities R_1, q_0, and kC_1 should be calculated for the average value of R_1 during the time increment which is known from step 2. ΔR_1 is the final interface position minus the initial position.

4 Steps 1–3 can be repeated for subsequent changes in T_2 to generate results for the entire drying process.

Nondimensional Results. Equations (9) and (10) can be nondimensionalized for the case where $q_0 = 0$. For the case where $q_0 \neq 0$ the number of nondimensional parameters required makes the utility of nondimensionalization of little value for presenting general results.

The following nondimensional parameters are required:

$$R^* = R_1/R_2 \tag{17}$$

$$C^* = k/(\epsilon\sigma R_2 T_H^3) \tag{18}$$

$$\theta_2^* = [(T_2/T_H) - (T_1/T_H)]/[1 - (T_2/T_H)^4] \tag{19}$$

$$\theta_1^* = T_1/T_H \tag{20}$$

$$T^* = \frac{\epsilon\sigma T_H^4 t}{\rho\lambda\Delta H R_2} \tag{21}$$

In terms of these parameters equation (9) can be written

$$\left.\begin{aligned} R^* &= 1.0 - \theta_2^* C^* && \text{slab} \\ R^* &= \exp[-\theta_2^* C^*] && \text{cylinder} \\ R^* &= 1.0/[1.0 + \theta_2^* C^*] && \text{sphere} \end{aligned}\right\} \tag{22}$$

Equation (10) can be written

$$-\frac{\epsilon\sigma T_H^4}{\rho\lambda\Delta H R_2}\, dt = \frac{(R_1/R_2)^n\, d(R_1/R_2)}{1 - (T_2/T_H)^4} \tag{23}$$

for the case that $q_0 = 0$. Integrating and substituting the appropriate nondimensional quantities gives

$$T^* = -\int_1^{R^*} \frac{R^* dR^*}{1 - (T_2/T_H)^4} \tag{24}$$

Solution Procedure. The following procedure can be used to solve equations (22)–(24).

1 For a given value of C^* calculate θ_2^* for a small incremental change of R^*(e.g., $\Delta R^* = -0.01$). Notice that R^* varies from 1 to 0 during the process.

2 From equation (19) calculate T_2/T_H for a given value of $\theta_1^* = T_1/T_H$ using the value of θ_2^* calculated in step 1.

3 Integrate equation (24) numerically as follows:

Let

$$\Delta T^* = -\frac{R^*}{1 - (T_2/T_H)^4}\Delta R^*$$

Note that the quantities in the coefficient of ΔR^* have been calculated in steps 1 and 2.

4 Repeat steps 1–3 with small increments of R^* from 1 to 0 to generate results for the entire drying process.

Results

Equations (22) and (24) were programmed on a digital computer as previously discussed. The ranges of variables considered are $0.001 \leq C^* \leq 10$, $0.1 \leq \theta_1^* \leq 0.9$, and $0 \leq R^* \leq 1$. These ranges should cover the conditions likely to be encountered in freeze-drying of foods.

Fig. 2 shows how the nondimensional dry surface temperature varies with the interface position.

The maximum permissible surface temperature will define a θ_2^* for scorch conditions which cannot be exceeded without causing product damage. The present solution is valid for the range of R^* between one and a value which gives θ_2^* at the scorch temperature. The entire range of R^* is given since the value of θ_2^* at scorch conditions depends on the particular applications. The remainder of the problem can be solved by the analyses given in references [1] and [7]. Reference [7] shows that the drying

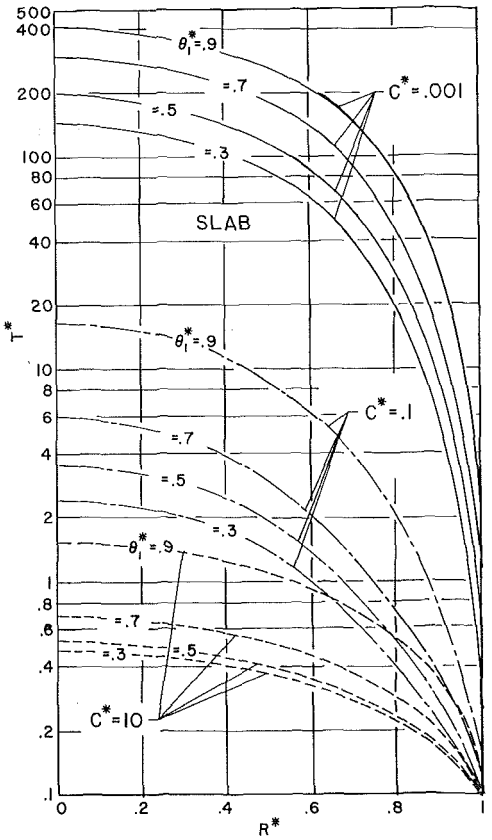

Fig. 3 Time vs. interface position for a slab

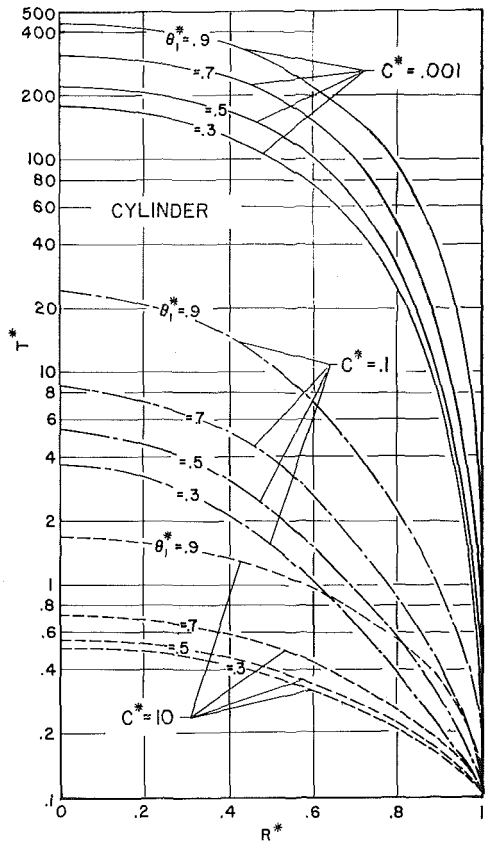

Fig. 4 Time vs. interface position for a cylinder

rate is higher successively for the slab, cylinder, and sphere. Since the drying time is the shortest for the sphere, it was felt that the consideration of the variation of surface temperature during early drying would be most important for the sphere. However, Fig. 2 shows that the sphere reaches a given surface temperature faster than the cylinder and slab so that the relative effect of a varying surface temperature for the three geometries is not as pronounced as was suspected when this work began. Fig. 2 along with Figs. 3–6 will allow one to decide for a given problem whether the effect of variable surface temperature needs consideration.

Figs. 3–5 indicate the time required to reach a given interface position for the range of C^* and θ_1^* considered for the slab, cylinder, and sphere respectively. These curves were generated by numerically integrating the integral in equation (24). Numerical integration for all cases considered was done with finite steps in R^* of 0.01 and 0.005. The results for finite steps in R^* of 0.01 compared within less than 1 percent to the corresponding results with the step in R^* equal to 0.005.

It was noted in the discussion of Fig. 2 that this solution is valid up to an R^* which corresponds to the θ_2^* for scorch conditions. Use of that R^* in Figs. 3–5 gives the nondimensional time required to reach such conditions and defines the time range over which the present solution is valid.

The trends indicated in Figs. 3–5 follow expected behavior. Notice that in each case the figures show that it takes much longer to dry the first 0.2 of the sample thickness than it does to dry the last 0.2 of the sample thickness. This unexpected result is the opposite effect to the solution for a constant surface temperature. The reason for the present results is that during the initial stages of drying the surface temperature is low so that little heat is conducted to the interface. If the surface temperature is allowed to rise until the sample is almost dried the surface temperature will be much hotter so that even with a long conduction path more heat will be transmitted to the interface. The figures also show that the nondimensional time, T^*, decreases roughly in proportion to the increase in C^*. An increasing value of C^* means that for a given energy input the interface velocity increases. Thus one would expect the drying rate to increase and the drying time to decrease which is the trend indicated.

Sample Calculation

Consider the freeze-drying of a sphere of hamburger, with the following properties and boundary conditions:

$$\begin{aligned}
\rho &= 57.4 \text{ lbm/ft}^3 \\
\lambda &= 0.7 \\
\Delta H &= 1488 \text{ Btu/lbm} \\
k &= 0.09 \text{ Btu/hr-ft-deg R} \\
T_H &= 702 \text{ deg R} \\
\epsilon &= 0.74 \\
\sigma &= 0.1713 \times 10^{-8} \text{ Btu/ft}^2\text{-hr-deg R}^4 \\
T_1 &= 492 \text{ deg R} \\
R_2 &= 0.0205 \text{ ft}
\end{aligned}$$

The properties can be obtained in the references cited except for the value of thermal conductivity which has recently been measured by the first author and has not yet been published.

In order to use the figures C^* and θ_1^* are required from their definitions, i.e.

$$C^* \equiv \frac{k}{\epsilon\sigma R_2 T_H^3} =$$

$$\frac{0.09 \text{ Btu/hr-ft-deg R}}{(0.74)(0.1713)10^{-8} \text{ Btu/ft}^2\text{-hr-deg R}^4 \text{ (0.0205) ft (702)}^3 \text{ deg R}^3}$$

$$= 10$$

$$\theta_1^* = \frac{T_1}{T_H} = \frac{492}{702} = 0.7$$

We seek the range of values of R^*(i.e., R_1) for which the present solution is valid. This range is from $R^* = 1$ to a position where T_2 has reached its maximum allowable value. For hamburger, a reasonable value for the scorch temperature is 560 deg R. Thus $T_2 = 560$ deg R and

$$\theta_2^* = \frac{(T_2/T_H) - (T_1/T_H)}{1 - (T_2/T_H)^4} = \frac{(560/702) - (492/702)}{1 - (560/702)^4} = 0.165$$

Therefore $\theta_2^* C^* = 0.165(10) = 1.65$. From Fig. 2, or equation (22), $R^* = 0.377$ at scorch conditions so that $1 \geq R_1/R_2 \geq 0.377$ for this solution. The time required to dry to the radius $R_1 = 0.377\ R_2 = 0.0077$ ft can be determined from Fig. 5 by using the curve for $C^* = 10$, $\theta_1^* = 0.7$, and $R^* = 0.377$. Thus, from Fig. 5,

$$T^* \equiv \frac{\epsilon\sigma T_H^4 t}{\rho\lambda\Delta H R_2} = 0.6$$

Hence

$$t = 0.6\,\frac{57.4\ \text{lbm/ft}^3\ 0.7(1488)\text{Btu/lbm}\ (0.0205)\text{ft}}{(0.74)(0.1713)10^{-8}\ \text{Btu/ft}^2\text{-hr-deg R}^4\ (702)^4\ \text{deg R}^4}$$

$$= 2.4\ \text{hr}$$

The time required for a sphere to dry from an interface position $R_1 = R_{1i}$ to an interface position $R_1 = R_{1f}$ can be determined from reference [7] when T_2 is a constant. The equation for this time is

$$\Delta t = \frac{\lambda\rho C_p}{k \log\{1 - [(T_1 - T_2)/(\Delta H/C_p)]\}} \times \left\{\frac{R_{1f}^3 - R_{1i}^3}{3R_2} - \frac{R_{1f}^2 - R_{1i}^2}{2}\right\}$$

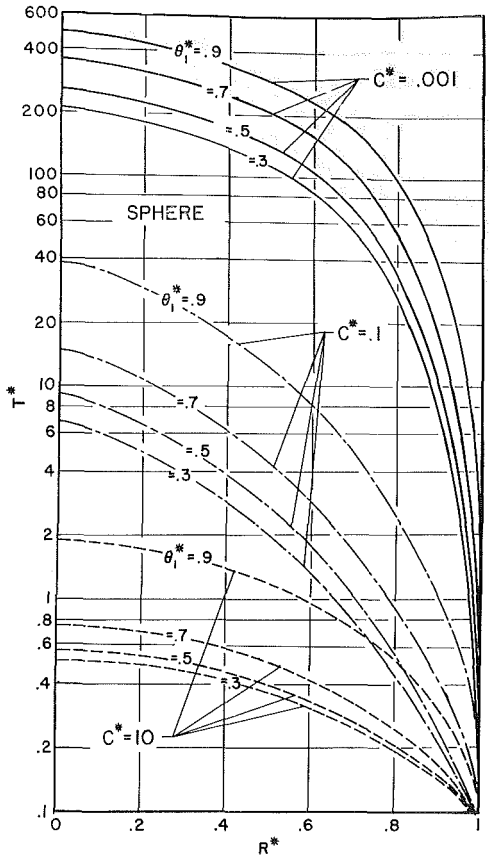

Fig. 5 Time vs. interface position for a sphere

Substituting values[2]

$$\Delta t = \frac{0.7(57.4)\ \text{lbm/ft}^3(0.46)\ \text{Btu/lbm-deg R}}{0.09\ \text{Btu/hr-ft-deg R}\ \log\{1 - [(492 - 560)\ \text{deg R}/(1488)\ \text{Btu/lbm}][0.46\ \text{Btu/lbm-deg R}]\}} \left[\frac{(0.0077)^3\ \text{ft}^3}{3(0.0205)\ \text{ft}} - \frac{(0.0077)^2\ \text{ft}^2}{2}\right]$$

$\Delta t = 0.22$ hr

The total drying time for the sample is

$$(2.4 + 0.22)\text{hr} = 2.62\ \text{hr}$$

Acknowledgment

The authors gratefully acknowledge partial support from the Public Health Service Research Grant FD-00156-03 and from the Food and Drug Administration.

References

1 Dyer, D. F., and Sunderland, J. E., "Heat and Mass Transfer Mechanisms in Sublimation Dehydration," JOURNAL OF HEAT TRANSFER, TRANS. ASME, Series C, Vol. 90, No. 4, Nov. 1968, pp. 379–384.

2 Dyer, D. F., and Sunderland, J. E., "The Transient Temperature Distribution During Sublimation Dehydration," JOURNAL OF HEAT TRANSFER, TRANS. ASME, Series C, Vol. 89, No. 1, Feb. 1967, pp. 109–110.

3 Massey, W. M., Jr., "Heat and Mass Transfer in Semi-Porous Channels," PhD thesis, Georgia Institute of Technology, Atlanta, Ga., 1968.

4 McCulloch, J. W., and Sunderland, J. E., "Integral Techniques Applied to Sublimation Dehydration With Radiation Boundary Conditions," *Journal of Food Science*, Vol. 35, 1970, p. 834.

5 Cho, S. H., and Sunderland, J. E., "An Approximate Solution for the Rate of Sublimation-Dehydration of Foods," *Transactions of ASAE*, Vol. 13, 1970, p. 559.

6 Dyer, D. F., and Sunderland, J. E., "The Role of Convection in Drying," *Chemical Engineering Science*, Vol. 23, 1968, p. 965.

7 Dyer, D. F., and Sunderland, J. E., "Sublimation Dehydration of Particles," *Proceedings of the Sixth Southeastern Seminar on Thermal Sciences*, 1970, p. 33.

[2] C_p is the specific heat of water vapor.

T. B. SWEARINGEN[1]
Assistant Professor,
Mechanical Engineering
Department,
Kansas State University,
Manhattan, Kan.
Mem. ASME

D. M. McELIGOT[2]
Associate Professor,
Energy, Mass and Momentum
Transfer Laboratory,
Aerospace and Mechanical
Engineering Department,
The University of Arizona,
Tucson, Ariz.
Assoc. Mem. ASME

Internal Laminar Heat Transfer With Gas-Property Variation

The results of a numerical investigation of internal laminar heat transfer to a gas with temperature-dependent properties are reported. In this investigation the authors obtained numerical solutions to the coupled partial differential equations of continuity, energy, momentum, and integral continuity describing the two-dimensional flow of perfect gas between heated parallel plates. A sequence of numerical solutions was obtained for the case of constant wall heat flux with a fully developed velocity profile at the start of the heated section and pure forced convection. The results may be summarized by

$$\mathrm{Nu} = \mathrm{Nu}_{const.\ prop.} + 0.024(Q^+)^{0.3}(\mathrm{Gz}_m)^{0.75}$$

$$f \cdot \mathrm{Re}_m = 24(T_{wall}/T_{bulk})$$

where the subscript "m" refers to properties evaluated at the local mixed-mean (or bulk) temperature.

Introduction

THE ANALYSIS of laminar flow between heated parallel plates is of considerable practical importance. In designs where pumping power must be kept low in proportion to heat transfer, as is frequently the case in the design of compact heat exchangers, laminar-flow conditions provide the optimum operation. Other practical examples include nuclear reactors with rectangular flow channels with width–to–spacing ratios which are greater than about 15 and in which the coolant flow rates may be reduced to levels where laminar-flow conditions become established during periods of low-power operation or loss-of-flow incidents. The study of laminar flow between parallel plates is also important for analytical reasons as well, since it represents one geometrical limit for the flow in annuli.

The study of laminar flow between parallel plates had its beginning with the pioneering work of Graetz [1][3] in 1885; however, it was three-quarters of a century later before the digital computer made possible the evaluation of usefully complete sets of eigenvalues and the associated eigenfunctions for the classical problem. A critical review of the problem of laminar flow between heated parallel plates with constant wall heat flux and constant wall temperature as boundary conditions is available in the definitive work of McCuen, Kays, and Reynolds [2].

The effect of fluid-property variation upon heat transfer and fluid flow was first investigated in 1940 by Yamagata [3]. Later, in 1951, Deissler [4] presented an analysis of laminar heat transfer to gases in the downstream region of tubes. He assumed that the density varied inversely with the absolute temperature and that the transport properties varied as the absolute temperature raised to the 0.68 power. Deissler concluded that the effect of the fluid-property variations was to decrease the downstream Nusselt number by 22 percent and to increase the friction factor by 28 percent as the wall–to–bulk temperature increased from 1.0 to 1.8. Deissler's analysis was essentially duplicated six years later by Sze [5] who used experimental property values instead of the power-law approximations. In 1962, Koppel and Smith [6] presented the results of an analytical and experimental investigation of heat transfer to carbon dioxide near its critical point. The extreme variation of the fluid properties in the critical region limits the generality of their results; however, they were the first to point out that the transverse velocity component might have a significant effect upon the heat transfer and fluid friction.

In 1962, Davenport [7, 8], following the lead of Koppel and Smith, published the results of an analytical and experimental investigation of laminar heat transfer in the downstream region

[1] Formerly Research Associate, The University of Arizona.
[2] Presently at Imperial College of Science and Technology, London, England.
[3] Numbers in brackets designate References at end of paper.

Contributed by the Heat Transfer Division for publication (without presentation) in the JOURNAL OF HEAT TRANSFER. Manuscript received by the Heat Transfer Division October 23, 1970. Paper No. 71-HT-N.

of tubes. In this analysis, Davenport postulated several reasonable transverse velocity profiles, relying upon experimental evidence to determine which of the postulated profiles gave the most consistent results. His heat-transfer results were inconclusive due to the data scatter but he could obtain good agreement between his computed and measured friction factors.

In 1965, Worsoe-Schmidt and Leppert [9] published a numerical solution to the problem of variable-property laminar flow in the thermal entrance region of tubes. They employed implicit finite-difference methods to obtain the simultaneous solution to the governing differential equations after these equations had been cast into finite-difference forms. The fluid-property variations were introduced into the analysis by making power-law assumptions. In a note discussing these results, McEligot and Swearingen [10] observed that the effects of property variations are significant only at very short distances from the thermal entrance and that use of local properties in the nondimensional axial distance led to closer correlation with results for constant properties. Subsequently, Worsoe-Schmidt [11] correlated his results for the laminar flow of power-law gases in the thermal entrance region for the case of a fully developed entering-velocity profile and constant wall heat flux by

$$\mathrm{Nu} = \mathrm{Nu}_{cp} + 0.025(Q^+)^{1/2}(\mathrm{Gz}_m - 20)/\mathrm{Gz}_m{}^{3/2}$$

and

$$f\mathrm{Re}_m = 15.5(T_w/T_m)^{1.10}$$

More recently, Deissler and Presler [12] published a numerical analysis of developing laminar flow inside circular tubes. Their results indicated that the effects of property variation on the Nusselt numbers were not significant in the entrance region, but that there was a significant increase in the friction factor due to effects of the axial property variation.

Experimental investigations of laminar flow inside circular tubes have been reported by Kays and Nicoll [13] and Swearingen [14]. The results of Kays and Nicoll agreed, within the limits of experimental uncertainty, with the extended Graetz solutions for wall–to–bulk temperatures up to a maximum of 2.0. Swearingen, by using a vacuum-isolated test section, was able to obtain improved results in the thermal entrance region (x^+ as low as 0.001). His results gave substantial confirmation to the variable-property effects predicted by Worsoe-Schmidt and Leppert [9].

The purpose of the present study was to analyze the diabatic laminar flow of a gas with temperature-dependent properties in the thermal entrance region between heated parallel plates.

Basic Equations

The governing differential equations were essentially developed on the basis of the standard boundary-layer approximations. The justification of the boundary-layer approximations was made primarily on the basis of analytical reasoning since experimental evidence in the immediate thermal entrance region has been plagued with excessively large experimental uncertain-

Nomenclature

a = exponent in the power law for specific heat
b = exponent in the power law for thermal conductivity
c = exponent in the power law for viscosity
c_p = specific heat at constant pressure
$c_p{}^+$ = dimensionless specific heat, c_p/c_{p_0}
f = friction factor, $\tau_w g_c/[{}^1/_2(\rho u)_m u_m]$
g_c = dimensional constant, e.g., 32.174 $\mathrm{ft\cdot lb_f/(lb_m\cdot sec^2)}$
h = enthalpy, heat-transfer coefficient
h^+ = dimensionless enthalpy, $1 + \int_1^{T^+} c_p{}^+ dT^+$
j = designation of arbitrary mesh point in the transverse direction
k = thermal conductivity
k^+ = dimensionless thermal conductivity, k/k_0
n = designation of arbitrary mesh point in the axial direction
p = thermodynamic pressure
p^+ = dimensionless thermodynamic pressure, p/p_0
q_w'' = wall heat flux
u = axial velocity
u^+ = dimensionless axial velocity, u/u_0
u_0 = entering velocity at the midplane
u' = normalized axial velocity, $u^+/u_m{}^+$
$u_m{}^+$ = dimensionless mean (or bulk) velocity, $\frac{1}{A}\int_0^A u^+ dA$
v = transverse velocity
v^+ = dimensionless transverse velocity, $4v\mathrm{Pr}_0\mathrm{Re}_0/u_0$
x = axial coordinate
$x^+, x_0{}^+$ = dimensionless axial coordinate based on inlet conditions, $x/D\mathrm{Pr}_0\mathrm{Re}_0$
$x_m{}^+$ = dimensionless axial coordinate based on local conditions, $x/D\mathrm{Pr}_m\mathrm{Re}_m$
y = transverse coordinate
y^+ = dimensionless transverse coordinate, y/y_0
y_0 = the half-plate spacing, i.e., the distance from the midplane to the wall
A_j, B_j, C_j, D_j, E_j = coefficient vectors used in the finite-difference equations; defined variously
D = hydraulic diameter, $4y_0$
$\mathrm{Gz}, \mathrm{Gz}_0$ = the Graetz number, $1/x^+$ or $1/x_0{}^+$
J = total number of transverse mesh points
$\mathbf{M}_0$ = Mach number based on inlet conditions, $2u_0/3\gamma_0 g_c RT$
Nu = local Nusselt number, $h_x D/k_m$
O = order of
P = pressure defect, $(1 - p^+)/\gamma_0\mathbf{M}_0{}^2$
Pr_0 = Prandtl number based on inlet conditions, $c_{p0}\mu_0/k_0$
Pr_m = Prandtl number based on local conditions, $c_{pm}\mu_m/k_m$
Q^+ = dimensionless heat flux, $q_w{}''y_0/(k_0T_0)$
Re_0 = Reynolds number based on inlet conditions, $2u_0D\rho_0/3\mu_0$
Re_m = Reynolds number based on local conditions, $2u_0D\rho_m/3\mu_m$
T = absolute temperature
T^+ = dimensionless absolute temperature, T/T_0
T' = normalized temperature, $(T_w - T)/(T_w - T_m)$
V = bulk (mean) velocity
V_0 = bulk velocity based on inlet conditions, $2u_0/3$
γ = ratio of specific heats
Δx^+ = dimensionless axial step length
Δy^+ = dimensionless transverse step width
μ = viscosity
ρ = density
τ_w = wall shear stress

Subscripts

cl = centerline
cp = constant (fluid) property
m = mean or bulk value
0 = entrance value
x = local value
w = evaluated at local wall conditions
j = evaluated at the jth transverse mesh point

Superscripts

$^+, '$ = denote dimensionless variables
^{n} = evaluated at the nth axial mesh point

ties. The 1964 paper by Wang and Longwell [15] presented a solution to the momentum equations in the hydrodynamic entrance region between parallel plates. Their results, as well as the earlier results of Schlichting [16] indicated that the transverse-shear term was negligibly small if the Reynolds number, based upon the distance from the entrance, was greater than approximately 200.

It was also assumed that the axial-conduction term in the energy equation was negligible. This assumption was based on the solution to the energy equation obtained by Singh [17] and the approximate solution of Schneider [18], both for conditions for which the Peclet number was above 200.

In the present analysis, the property variations were considered as small perturbing influences in a diabatic problem, with flow predominantly in the axial direction; consequently, an order-of-magnitude analysis led to the usual boundary-layer equations. However, the effect of property variations upon the magnitudes of the neglected terms cannot be estimated a priori. Worsoe-Schmidt and Leppert [9] were able to demonstrate that the boundary-layer approximations were indeed valid as long as the Peclet number, based upon distance from the entrance, was greater than 500.

In summary, the governing differential equations were developed by making the following approximations:

1 The fluid flow and heat transfer are invariant in time; steady state is assumed to exist.

2 The viscous shear associated with the transverse velocity is negligibly small.

3 Heat transfer by conduction occurs in the transverse direction only; axial conduction may be neglected.

4 The flow is two-dimensional; there is no transverse velocity component parallel to the bounding plates.

5 The flow velocity is low; the flow is in the laminar regime and viscous dissipation and compression work can be neglected.

6 There are no free-convection effects; body-force terms can be neglected.

The momentum equations developed on the basis of the above assumptions were combined to eliminate the terms involving the pressure gradient producing, as a result, a single equation containing only the velocity components, and implicitly the temperature, as unknowns. (The technique of developing this combined-momentum equation is detailed by Pai [19] in his discussion of the vorticity equation.)

The resulting differential equations were still too unwieldy to be economically solved so an order-of-magnitude analysis was performed to remove those terms which could be shown to be an order of magnitude (or more) smaller than the remaining terms in the same equation. This analysis, described in detail by Swearingen [14], was based on the fact that the transverse velocity component appears in the governing equations as a small perturbing velocity as a consequence of the fluid-property variations.

The results of this analysis produced the following governing differential equations:

the continuity equation

$$\frac{\partial \rho^+ u^+}{\partial x^+} + \frac{\partial \rho^+ v^+}{\partial y^+} = 0 \tag{1}$$

the combined-momentum equation

$$\frac{\partial}{\partial y^+}\left[\rho^+ u^+ \frac{\partial u^+}{\partial x^+} + \rho^+ v^+ \frac{\partial u^+}{\partial y^+}\right] = \frac{32\mathrm{Pr}_0}{3}\frac{\partial^2}{\partial y^{+2}}\left[\mu^+ \frac{\partial u^+}{\partial y^+}\right] \tag{2}$$

the energy equation

$$\rho^+ u^+ \frac{\partial h^+}{\partial x^+} + \rho^+ v^+ \frac{\partial h^+}{\partial y^+} = \frac{32}{3}\frac{\partial}{\partial y^+}\left[k^+ \frac{\partial T^+}{\partial y^+}\right] \tag{3}$$

and the x-momentum equation

$$\rho^+ u^+ \frac{\partial u^+}{\partial x^+} + \rho^+ v^+ \frac{\partial u^+}{\partial y^+} = \frac{-4}{9\gamma_0 \mathrm{M}_0^2}\frac{\partial p^+}{\partial x^+} + \frac{32\mathrm{Pr}_0}{3}\frac{\partial}{\partial y^+}\left[\mu^+ \frac{\partial u^+}{\partial y^+}\right] \tag{4}$$

The gas was considered to be a perfect gas. Practical considerations led to the choice of power-law approximations to express the property variations. The use of such approximations restricts the range of applicability of the results; however, the use of more-precise formulations or tabular data requires greatly increased computer facilities, both in terms of core storage and processing speed. Power-law property-variation approximations are in wide use and there are several other analyses [4, 7, 9, 11, 12] available for circular tubes to which the present work may be compared. The approximations used in this analysis were:

$c_p{}^+ = (T^+)^a$ where $a = 0.0946$ for air, $a = 0.00$ for helium

$k^+ = (T^+)^b$ where $b = 0.807$ for air, $b = 0.68$ for helium

$\mu^+ = (T^+)^c$ where $c = 0.706$ for air, $c = 0.68$ for helium

The above approximations agree with the tabulated air data of Hilsenrath et al. [20] to within 2 percent over a temperature range from 300 deg R to 3000 deg R at atmospheric pressure.

By substituting the above forms for the fluid properties into equations (2), (3), and (4), the following governing differential equations were obtained:

the combined-momentum equation

$$\frac{\partial^3 u^+}{\partial y^{+3}} = \frac{3}{32\mathrm{Pr}_0 (T^+)^c}\left[\frac{\partial \rho^+ u^+}{\partial y^+}\frac{\partial u^+}{\partial x^+} + \rho^+ u^+ \frac{\partial^2 u^+}{\partial x \partial y} + \frac{\partial \rho^+ v^+}{\partial y}\frac{\partial u^+}{\partial y^+} + \rho^+ v^+ \frac{\partial^2 u^+}{\partial y^{+2}}\right] - \frac{\partial u^+}{\partial y^+}\left[\frac{c(c-1)}{(T^+)^2}\left(\frac{\partial T^+}{\partial y^+}\right)^2 + \frac{c}{T^+}\frac{\partial^2 T^+}{\partial y^{+2}}\right] = \frac{2c}{T^+}\frac{\partial T^+}{\partial y^+}\frac{\partial^2 u^+}{\partial y^{+2}} \tag{5}$$

the energy equation

$$\frac{\partial^2 T^+}{\partial y^{+2}} = \frac{3}{32(T^+)^{b-a}}\left[\rho^+ u^+ \frac{\partial T^+}{\partial y^+}\right] - \frac{b}{T^+}\left(\frac{\partial T^+}{\partial y^+}\right)^2 \tag{6}$$

and the x-momentum equation

$$\frac{\partial p^+}{\partial x^+} = 24\mathrm{Pr}_0 \gamma_0 \mathrm{M}_0^2 (T^+)^c\left[\frac{\partial^2 u^+}{\partial y^{+2}} + \frac{c}{T^+}\frac{\partial u^+}{\partial y^+}\frac{\partial T^+}{\partial y^+}\right] - \frac{9\gamma_0 \mathrm{M}_0^2}{4} + \left[\rho^+ u^+ \frac{\partial u^+}{\partial x^+} + \rho^+ v^+ \frac{\partial u^+}{\partial y^+}\right] \tag{7}$$

These equations were solved using the initial conditions that adiabatic fully developed flow existed at the start of the heated section:

$$\begin{aligned} \text{at}\quad x^+ = 0:\quad & T^+ = 1 \\ & V^+ = 0 \\ & u^+ = 1 - (y^+)^2, \text{ parabolic profile} \\ & p^+ = 1 \end{aligned} \tag{8}$$

The boundary conditions for these differential equations were as follows:

1 The continuity equation (1)

$$\text{at}\quad y^+ = 1,\quad v^+ = 0\quad \text{(wall)} \tag{9}$$

2 The combined-momentum equation (5)

$$\begin{aligned} &\text{at}\quad y^+ = 0,\quad \frac{\partial u^+}{\partial y^+} = 0\quad \text{(center plane)} \\ &\text{at}\quad y^+ = 1,\quad u^+ = 0\quad \text{(wall)} \end{aligned} \tag{10}$$

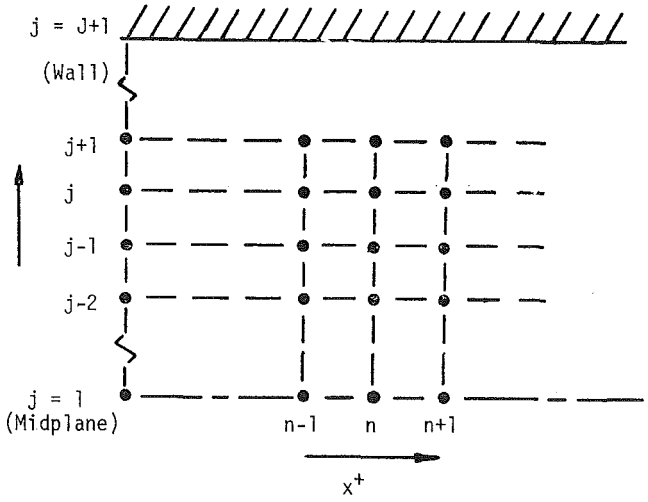

Fig. 1 Mesh network used in the development of the finite-difference equations

A third condition was obtained from the fact that the total mass flow rate was constant axially,

$$2\int_0^1 \rho^+ u^+ dy^+ = 2\int_0^1 (\rho^+ u^+)_{x^+=0}\, dy^+ \qquad (11)$$

For the fully developed parabolic entering velocity profile, the right-hand side of equation (11) equals $^2/_3$.

3 The energy equation (6)

$$\text{at} \quad y^+ = 0, \quad \frac{\partial T^+}{\partial y^+} = 0 \quad \text{(center plane)}$$
$$\text{at} \quad y^+ = 1, \quad Q^+ = \text{a constant} \quad \text{(wall)} \qquad (12)$$

Finite-Difference Approximations

Implicit finite-difference equations were developed by using truncated Taylor's series to approximate the various derivatives. This method of developing finite-difference equations has several important advantages. Two of the more important ones are:

1 This method will insure that the difference equation will reduce to the differential equation as the mesh size is reduced to zero, i.e., this method assures that the two equations are consistent, an important stability criterion, and

2 Finite-difference equations of any desired degree of precision may be obtained merely by including a sufficient number of terms in the approximating series, or, conversely, the precision of a particular approximation may be estimated from the truncated terms.

A detailed discussion of this method and a fairly complete compilation of typical differencing schemes are available in Richtmyer's book [21].

The difference equations employ two points in the marching direction, x^+, except for the continuity equation which requires three. Three nodal points are usually required in the transverse direction, y^+; however, the third-order combined-momentum equation requires four. Fig. 1 shows the most general mesh network used in this analysis for the finite-difference equations. A subscript–superscript notation was used to describe the dependent variables; the subscript, j, denoting the transverse location, and the superscript, n, denoting the axial location. Thus, $T^{+n}{}_j$ is the dimensionless fluid temperature at the point (n, j). The mesh sizes, Δy^+ and Δx^+ were constant across the flow channel. Both Δy^+ and Δx^+ were changed as the solution progressed downstream in order to reduce computing time.

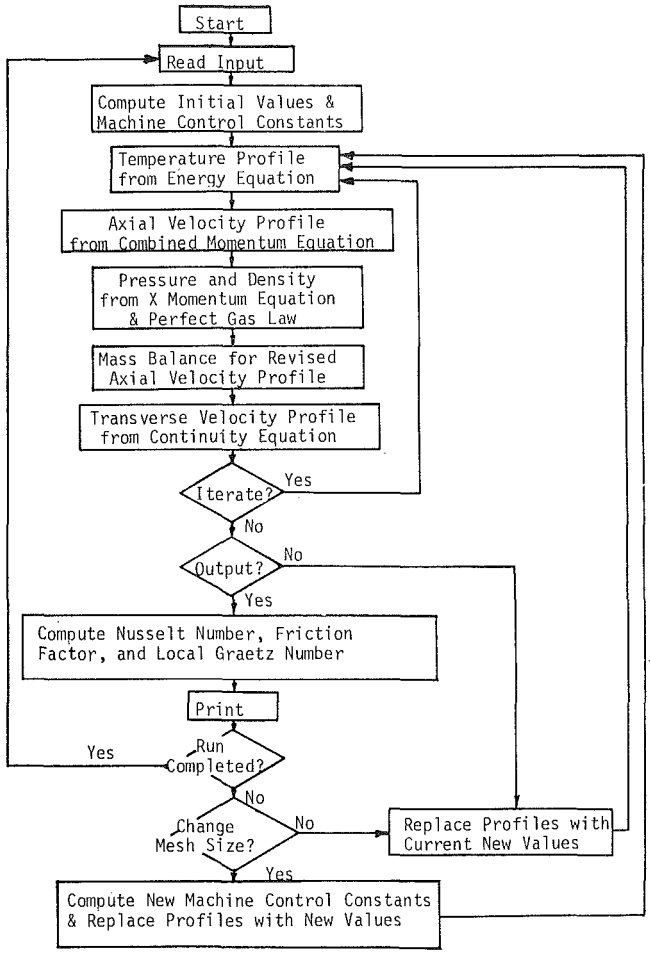

Fig. 2 Flow diagram for the computer program

The finite-difference equations will be described in the same sequence they were solved (see Fig. 2). To accommodate the nonlinearities of the different equations it was necessary to iterate the solution sequence to obtain convergence. This iterative scheme is discussed in detail by Swearingen [14].

The Finite-Difference Energy Equation. The finite-difference approximation to the energy equation and its solution were developed using the general methods described by Richtmyer [21] for second-order parabolic differential equations. The finite-difference equation was similar to the Crank–Nicolson scheme for approximating linear partial differential equations with the following essential difference: The coefficients were functions of the dimensionless temperature, T^{+n+1}, due to the temperature-dependence of the specific heat and thermal conductivity.

The Finite-Difference Combined-Momentum Equation. The finite-difference approximation to the third-order, combined-momentum equation was analogous to the Crank–Nicolson scheme. This third-order analog may be written (after Swearingen [14]):

$$u^{+n+1}{}_{j+1} - 3u^{+n+1}{}_j + 3u^{+n+1}{}_{j-1} - u^{+n+1}{}_{j-2} + u^{+n}{}_{j+1} - 3u^{+n}{}_j + 3u^{+n}{}_{j-1} - u^{+n}{}_{j-2}$$
$$= \frac{\frac{1}{4}\left[\left(\frac{\partial^3 u^+}{\partial y^{+3}}\right)^{n+1/2}_j + 4\left(\frac{\partial^3 u^+}{\partial y^{+3}}\right)^{n+1/2}_{j-1} - \left(\frac{\partial^3 u^+}{\partial y^{+3}}\right)^{n+1/2}_{j-2}\right] + O(\Delta y^{+2})}{2\Delta y^{+3}} \qquad (13)$$

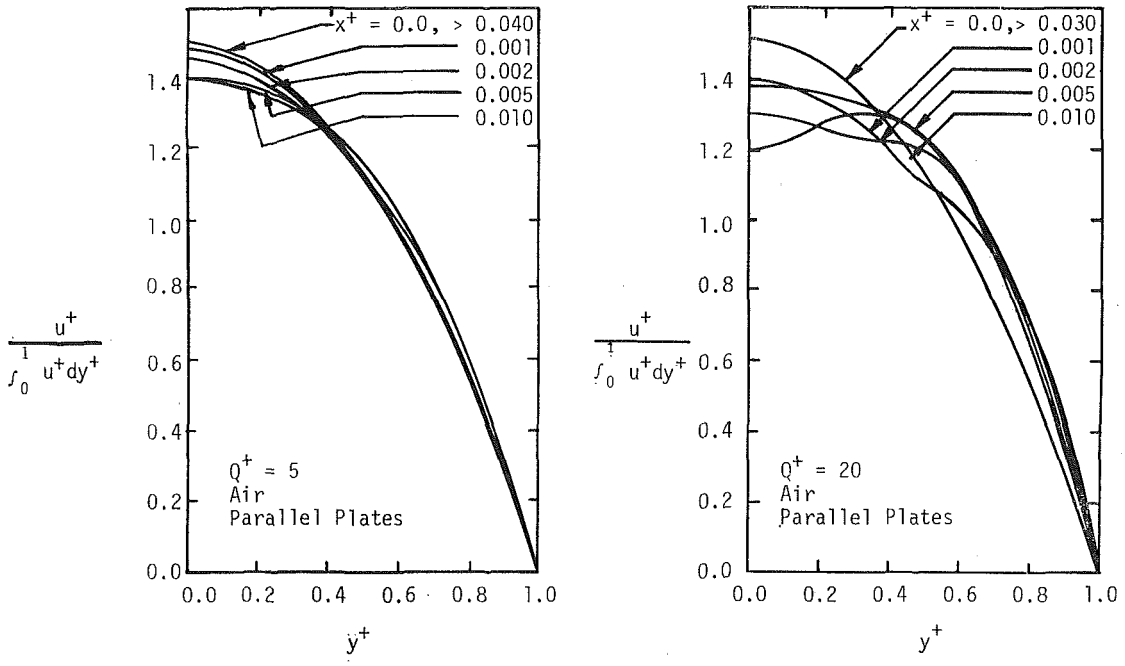

Fig. 3 Axial velocity profiles

These third-order derivatives were available from the combined-momentum equation (5) in terms of the lower-order derivatives. Subsequently, the lower-order derivatives were approximated by finite differences producing, as a final result, a finite-difference equation interrelating the values of the axial velocity at eight discrete locations within the interior of the flow field.

$$A_j u^{+n+1}{}_{j+1} - B_j u^{+n+1}{}_j + C_j u^{+n+1}{}_j = D_j u^{+n+1}{}_{j-2} + E_j = 0 + O(\Delta x^{+2}, \Delta y^{+}) \quad (14)$$

The solution to this equation was obtained on a digital computer using a standard Gaussian reduction technique.

The Finite-Difference x-Momentum Equation. The x-momentum equation was used in this analysis to compute the value of the fluid pressure across the flow channel as it decreased in the axial direction. Since the conditions of this analysis are essentially the usual boundary-layer assumptions, one expects the transverse pressure gradient to be several orders of magnitude smaller than the axial pressure gradient. Therefore, solution of the x-momentum equation across the stream served primarily as a check on the numerical computations.

The Finite-Difference Continuity Equation. The transverse velocity component was computed from the solution to the continuity equation in the form

$$\rho^{+}v^{+n+1}{}_j = \rho^{+}v^{+n+1}{}_{j+1} + \frac{\Delta y^{+}}{4\Delta x^{+}}[3\rho^{+}u^{+n+1}{}_{j+1} - 4\rho^{+}u^{+n}{}_{j+1} + \rho^{+}u^{+n-1}{}_{j+1} + 3\rho^{+}u^{+n+1}{}_j - 4\rho^{+}u^{+n}{}_j + \rho^{+}u^{+n-1}{}_j] + O(\Delta x^{+2}, \Delta y^{+2}) \quad (15)$$

Since equation (15) is explicit in $\rho^{+}v^{+}$, the transverse velocity can be obtained directly; however, the coefficient $\Delta y^{+}/4\Delta x^{+}$ was greater than unity in this study. Consequently, any errors made in the calculation of the axial velocity resulted in even greater errors in the computed transverse velocity. One of the major operational problems of this study was to determine a technique of keeping these errors within acceptable bounds. The technique which was found to give the most rapid convergence was to solve equation (15) after the axial velocities were computed from the combined-momentum equation and after they had been multiplied by a constant to insure that the integral-continuity equation (11) was satisfied.

Parameters. The main heat-transfer and fluid-flow parameters in this analysis were the Nusselt number and the friction factor. Other parameters, such as the bulk velocity, the bulk temperature, and the wall–to–bulk temperature ratio, were evaluated during the numerical solutions.

The Nusselt number is defined as

$$\mathrm{Nu} = \frac{hD}{k_m}$$

where k_m is the fluid thermal conductivity evaluated at the local bulk temperature. In terms of the dimensionless variables, the Nusselt number can be written as

$$\mathrm{Nu} = \frac{4Q^{+}}{(T^{+}{}_{j+1} - T_m{}^{+})(T_m{}^{+})^b} \quad (16)$$

where $T_m{}^{+}$, the bulk temperature, is the dimensionless temperature corresponding to the bulk enthalpy.

The friction factor, defined as

$$f = \frac{\tau_w g_c}{{}^1/_2(\rho u)_m(u_m)}$$

was based on the velocity gradient at the wall. It was evaluated in dimensionless form from the expression

$$f \cdot \mathrm{Re}_m = \frac{16\left(\frac{T_w{}^{+}}{T_m{}^{+}}\right)^c \left(\frac{\partial u^{+}}{\partial y^{+}}\right)_{y^{+}=1}}{\int_0^1 \rho^{+}u^{+}dy \int_0^1 u^{+}dy^{+}} \quad (17)$$

Numerical Results

Once the numerical techniques had been developed to solve each of the above difference equations, a procedure for solving the combination of difference equations was obtained and the number of iterations required at each axial step to give acceptable convergence was determined. For constant fluid properties, convergence requirements could be determined by studying the agreement of the present numerical results with the analytical predictions of McCuen, Kays, and Reynolds [2]. For the present nonlinear problem, no such analytical solutions exist, so

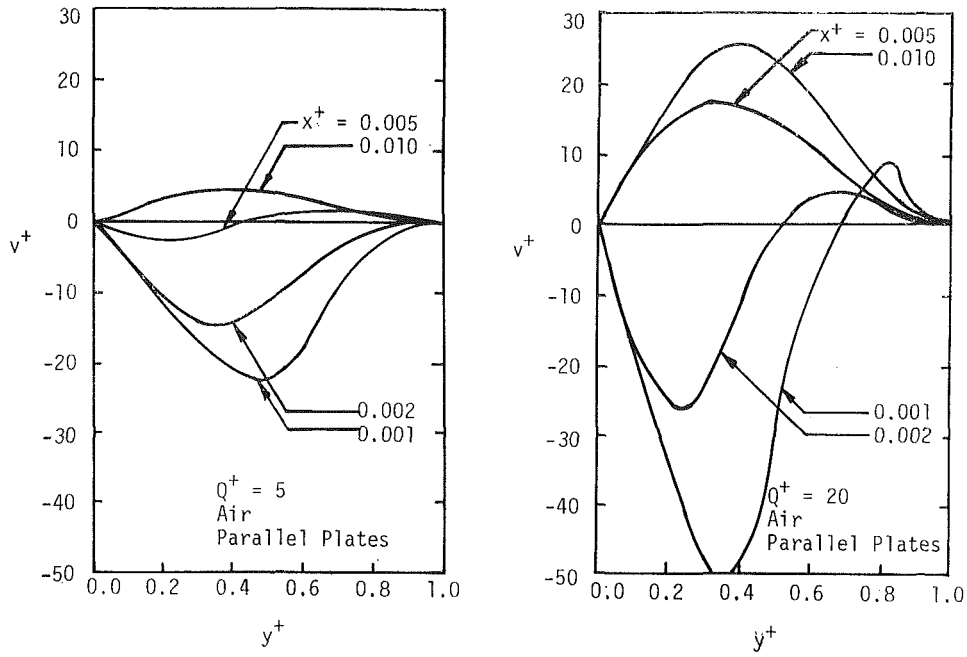

Fig. 4 Transverse velocity profiles

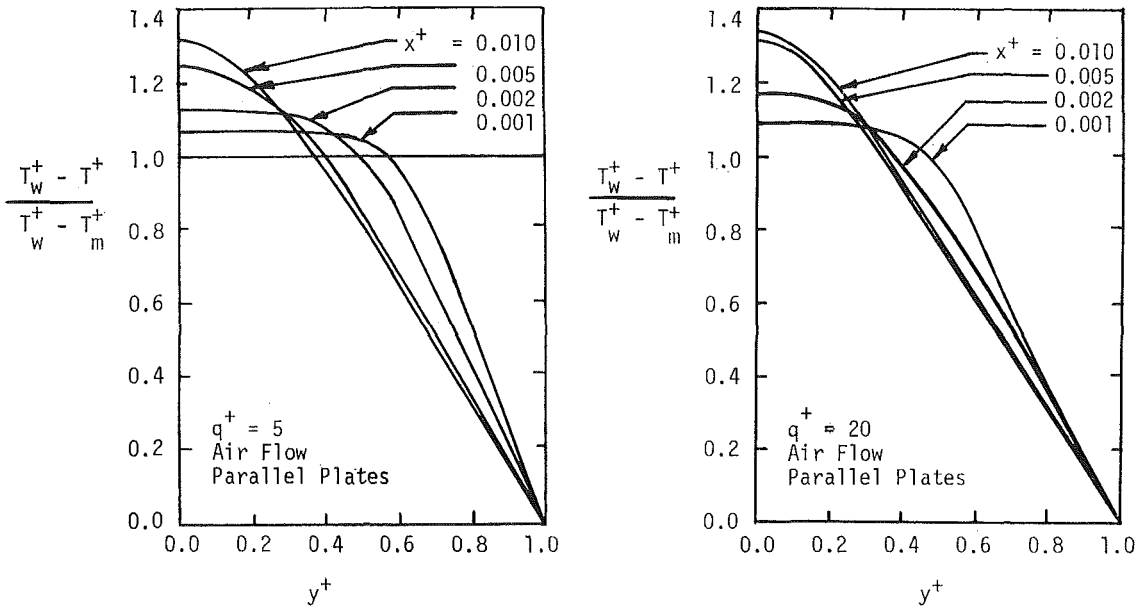

Fig. 5 Temperature profiles

convergence was determined by comparing the fluid bulk enthalpy computed by integrating the temperature profile across the flow channel with the bulk enthalpy computed from the wall heat flux.

Fig. 2 shows the flow diagram of the digital computer program used to solve the set of difference equations. In starting the computer solutions, a fine mesh size was used to reduce truncation errors in the entrance region. In this region, $x^+ < 0.001$, the mesh sizes were $\Delta x^+ = 0.0001$ and $\Delta y^+ = 0.0125$.

During preliminary tests, it was determined that the mesh size could be doubled at two downstream locations to give a considerable reduction in computer time and a reduction in the round-off error. These preliminary tests also showed that three iterations per axial step were sufficient for convergence. The numerical results reported here were obtained with an IBM 360/50 computer.

Air Flow

A sequence of numerical solutions to the governing difference equations was obtained for the case of variable-property flow with constant wall heat flux. Figs. 3–5 show the dimensionless velocity and temperature profiles at several axial locations for two different heating rates, $Q^+ = 5$ and $Q^+ = 20$. The overshoot appearing in the axial velocity profiles for $Q^+ = 20$ is the consequence of the specific volume increase due to heating and not the effect of fluid buoyancy. The effect of gravity forces was neglected for the results reported here. These profiles show substantial agreement with the trends observed in the profiles predicted by Worsoe-Schmidt and Leppert [9] with circular tubes and comparable thermal and hydrodynamic boundary conditions.

The effects of the fluid-property variation upon the heat-

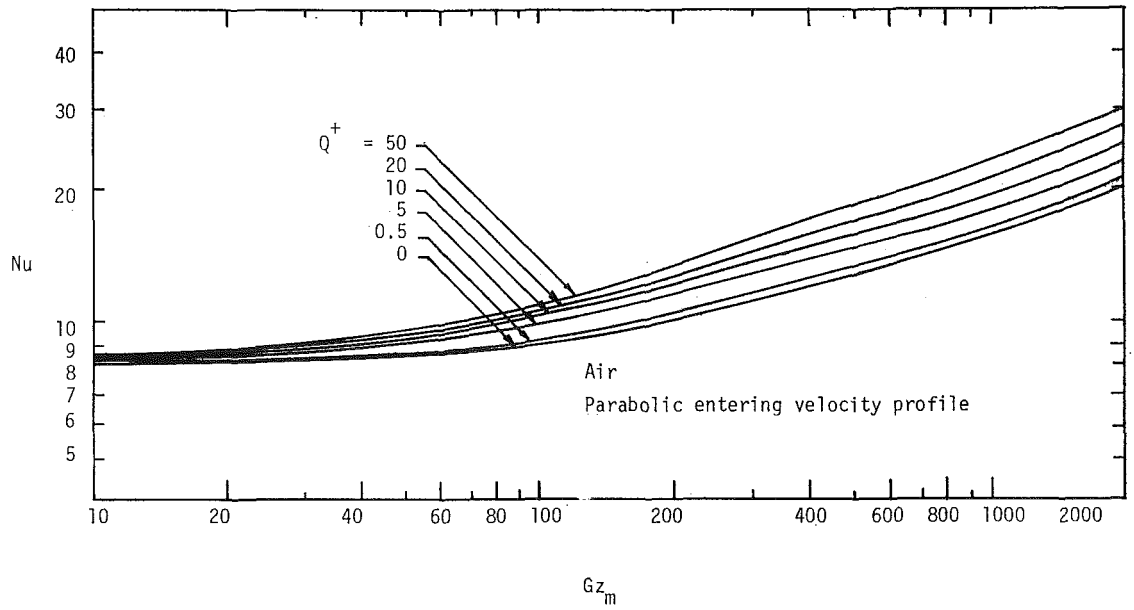

Fig. 6 Local Nusselt numbers

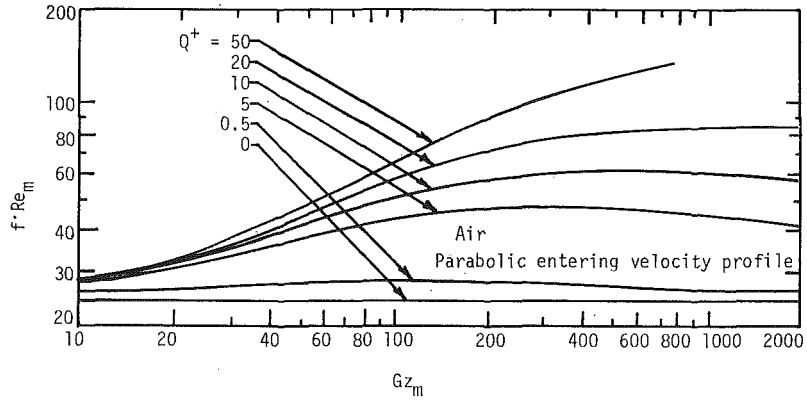

Fig. 7 Axial variation of the friction-factor–Reynolds-number product

transfer and fluid-friction parameters are shown in Figs. 6–8. Fig. 6 shows the variation in the local Nusselt number as a function of the local Graetz number and the heating rate. These results show a substantial increase in the local Nusselt numbers in the near-entrance region (i.e., for Graetz numbers greater than 100) when compared with the constant-fluid-properties solution, plotted as $Q^+ = 0$. For engineering purposes, these results may be correlated by

$$\mathrm{Nu} = \mathrm{Nu}_{cp} + 0.024(Q^+)^{0.3}(\mathrm{Gz}_m)^{0.75} \quad \pm 4 \text{ percent} \qquad (18)$$

The quantity Nu_{cp} represents the constant-property Nusselt number evaluated at Gz_m. This correlation fits the numerical results to within ±4 percent for a range of heat flux from $Q^+ = 0.5$ to $Q^+ = 50$ and for local Graetz numbers ranging from $\mathrm{Gz}_m = 10$ to $\mathrm{Gz}_m \approx 2000$.

The Nusselt numbers plotted in Fig. 6 are shown to approach the constant-property asymptote as the solution progresses downstream toward $\mathrm{Gz}_m = 10$. These Nusselt numbers are above the constant-property prediction whereas for circular tubes an increase in the heating rate decreases the downstream Nusselt numbers [11]. The results reported here are consistent with the downstream analyses of Sze [22].

The selection of an axial-distance parameter based on local properties, Gz_m, rather than inlet properties, Gz_0, leads to a slightly greater separation between the Nusselt numbers, calculated for the different heating rates, than the use of Gz_0. The selection was made so that the effects of property variation would be clearly shown. The correlation for design purposes is also simplified.

The variations in the friction-factor–Reynolds-number product and the variation in the wall-to-bulk temperature ratio with respect to the local Graetz numbers are shown in Figs. 7 and 8. The strong similarity between the two results is consistent with both analytical and experimental results for flow through heated circular tubes [21, 7]. The numerical friction factors are correlated to within 11 percent by

$$f \cdot \mathrm{Re}_m = 24(T_w/T_m) \qquad (19)$$

for $T_w/T_m < 3.59$. These friction-factor results are also consistent with the results reported by Worsoe-Schmidt [11] and equation (19) parallels his recommended correlation for flow inside circular tubes.

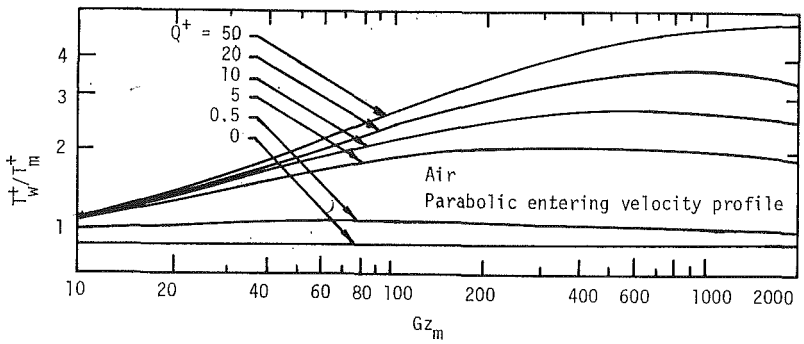

Fig. 8 Axial variation of the wall-to-bulk temperature ratio

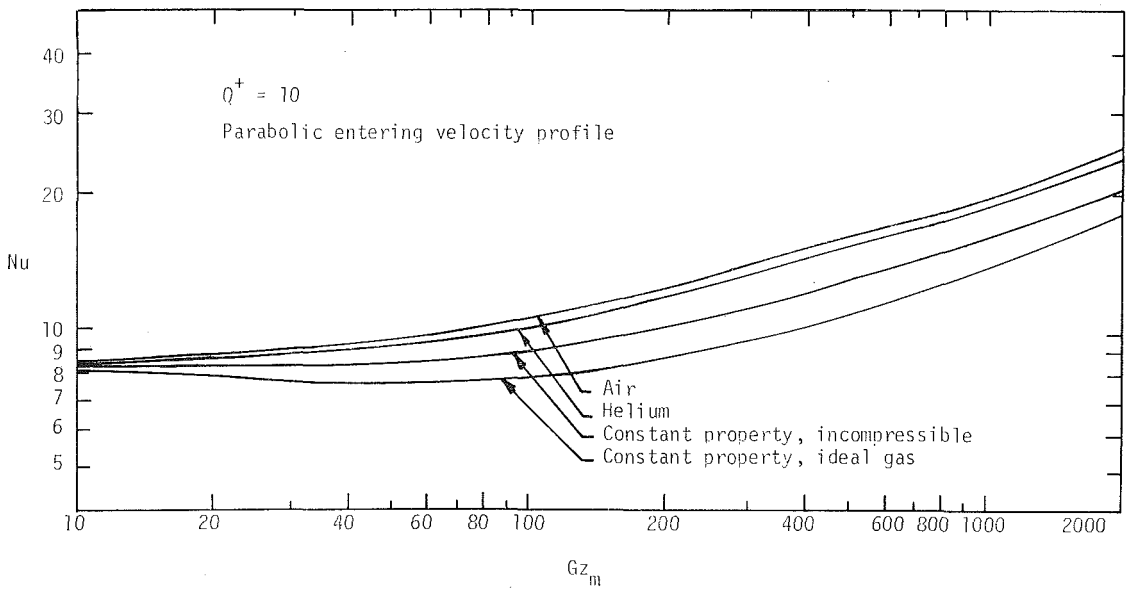

Fig. 9 Local Nusselt numbers for different gases

Gases Other Than Air

Two additional numerical solutions were obtained with the constant-wall-heat-flux boundary condition for the case of pure forced convection and a parabolic entering-velocity profile. These results, shown in Fig. 9, are obtained for:

1 Helium, where the property variation exponents selected were

$$a = 0.0$$

$$b = 0.68$$

$$c = 0.68$$

2 A fictitious, compressible, perfect gas with constant transport properties and specific heat.

The Nusselt-number results for helium are similar to those obtained for air, falling about 5 percent below the corresponding values for air. For the second case the Nusselt-number results were 16 percent below the constant-property, incompressible solution. The trends of these comparisons indicate that the nature of the assumed transport-property variation is significant but that power-law gases having approximately the same exponents follow the same trends.

Acknowledgments

The financial assistance provided by the U.S. Army Research Office–Durham, the National Science Foundation, the Ford Foundation, the Engineering Experiment Station of The University of Arizona, and the U.S. Army Mobility Equipment Research and Development Center, Fort Belvoir, Va., is gratefully acknowledged. Dr. R. W. Shumway provided assistance with the computer programs for the University Computer Center of The University of Arizona. Computing Center personnel at Kansas State University and the NASA Lewis Research Center provided valuable programming assistance and computing time.

References

1 Graetz, L., "Über die Warmeleitungsfähigkeit von Flussigkeiten," *Annalen der Physik*, Vol. 21, 1885, p. 337.

2 McCuen, P. A., Kays, W. M., and Reynolds, W. C., "Heat Transfer with Laminar and Turbulent Flow between Parallel Plates with Constant and Variable Wall Temperature and Heat Flux," Thermoscience Division Report Number AHT-3, Department of Mechanical Engineering, Stanford University, 1963.

3 Yamagata, K., "A Contribution to the Theory of Non-Isothermal Laminar Flow of Fluids Inside a Straight Tube of Circular Cross Section," *Mem. Fac. Engrg.*, Vol. 6, Kyushu Imperial University, Fukuoka, Japan, 1940.

4 Deissler, R. G., "Analytical Investigation of Fully Developed

Laminar Flow in Tubes with Heat Transfer with Fluid Properties Variable Along the Radius," NACA TN 2410, 1951.

5 Sze, B. C., "The Effect of Temperature Dependent Fluid Properties on Heat Transfer In Circular Tubes," PhD thesis, Department of Mechanical Engineering, Stanford University, 1957.

6 Koppel, L. B., and Smith, J. M., "Laminar Flow Heat Transfer for Variable Physical Properties," JOURNAL OF HEAT TRANSFER, TRANS. ASME, Series C, Vol. 84, No. 2, May 1962, pp. 157–163.

7 Davenport, M. E., "The Effect of Transverse Temperature Gradients on the Heat Transfer and Friction for Laminar Flow of Gases," PhD thesis, Department of Mechanical Engineering, Stanford University, 1962.

8 Davenport, M. E., and Leppert, G., "The Effect of Transverse Temperature Gradients on the Heat Transfer and Friction for Laminar Flow of Gases," JOURNAL OF HEAT TRANSFER, TRANS. ASME, Series C, Vol. 87, No. 2, May 1965, pp. 191–196.

9 Worsoe-Schmidt, P. M., and Leppert, G., "Heat Transfer and Friction for Laminar Flow of Gas in a Circular Tube at a High Heating Rate," *International Journal of Heat and Mass Transfer*, Vol. 8, 1965, p. 1301.

10 McEligot, D. M., and Swearingen, T. B., "Prediction of Wall Temperature for Internal Laminar Heat Transfer," *International Journal of Heat and Mass Transfer*, Vol. 9, 1966, p. 1151.

11 Worsoe-Schmidt, P. M., "Heat Transfer and Friction for Laminar Flow of Helium and Carbon Dioxide in a Circular Tube at a High Heating Rate," *International Journal of Heat and Mass Transfer*, Vol. 9, 1966, p. 1291.

12 Deissler, R. C., and Presler, A. F., "Analysis of Developing Laminar Flow and Heat Transfer in a Tube for a Gas with Variable Properties," *Proceedings of the Third International Heat Transfer Conference*, Vol. 1, AIChE, New York, 1966, p. 250.

13 Kays, W. M., and Nicoll, W. B., "Laminar Flow Heat Transfer to a Gas With Large Temperature Differences," JOURNAL OF HEAT TRANSFER, TRANS. ASME, Series C, Vol. 85, No. 4, Nov. 1963, pp. 329–338.

14 Swearingen, T. B., "Internal Laminar Heat Transfer to a Gas with Temperature Dependent Properties, PhD thesis, Department of Aerospace and Mechanical Engineering, University of Arizona, 1969, (DDC AD 69 2317).

15 Wang, Y. L., and Longwell, P. A., "Laminar Flow in the Inlet Section of Parallel Plates," *AIChE Journal*, Vol. 10, 1964, p. 323.

16 Schlichting, H., *Boundary Layer Theory*, 4th ed., McGraw-Hill, New York, 1960.

17 Singh, R., "Heat Transfer by Laminar Flow in a Cylindrical Tube," *Applied Scientific Research*, A10, 1958, p. 325.

18 Schneider, P. J., "Effect of Axial Fluid Conduction on Heat Transfer in the Entrance Regions of Parallel Plates and Tubes," TRANS. ASME, Vol. 79, May 1957, pp. 765–773.

19 Pai, S. I., *Viscous Flow Theory—Laminar Flow*, Vol. 1, Van Nostrand, New York, 1956.

20 Hilsenrath, J., et al., "Tables of Thermal Properties of Gases," National Bureau of Standards, Circular 564, 1955.

21 Richtmyer, R. D., *Difference Methods for Initial Value Problems*, Interscience, New York, 1957.

22 Sze, B. S., "The Effect of Temperature Dependent Fluid Properties on Heat Transfer in Circular Tubes," PhD thesis, Department of Mechanical Engineering, Stanford University 1957.

N. D. JOSHI
Research Scholar.

S. P. SUKHATME
Professor.

Department of Mechanical Engineering,
Indian Institute of Technology,
Powai, Bombay, India

An Analysis of Combined Free and Forced Convection Heat Transfer From a Horizontal Circular Cylinder to a Transverse Flow

Combined free and forced convection heat transfer from a horizontal circular cylinder to a transverse flow is analysed for the case when the forced flow is either in the direction of the free convection flow (parallel flow) or in the direction opposite to it (counter flow). The problem is solved for two cases: (1) a specified surface temperature variation and (2) a specified wall heat flux variation along the circumference. A coordinate perturbation method is used to transform the governing set of partial differential equations into a system of ordinary differential equations, which are solved by numerical methods. The numerical work is done for the boundary conditions of constant surface temperature and constant wall heat flux. The variation of local heat transfer coefficient and wall shear stress along the circumference up to the point of separation and velocity and temperature profiles in the boundary layer are obtained for varying values of the governing parameters $\mathrm{Gr}/\mathrm{Re}^2$ *in the constant temperature case (or* $\overline{\mathrm{Gr}}/\mathrm{Re}^2$ *in the constant heat flux case) and* Pr.

Introduction

In this paper, the problem of heat transfer by combined free and forced convection from a horizontal circular cylinder to a transverse flow is analysed. There are comparatively few such studies in the field of combined free and forced convection heat transfer in external flows. References [1–7][1] list the analytical studies in combined convection from a vertical flat plate. The general practice followed is to use a method of parameter perturbation with the fundamental solution as that for either forced or free convection. The parameter of fundamental importance in this case is found to be $\mathrm{Gr}_x/\mathrm{Re}_x^2$. Acrivos [5] has approached the problem by an integral method, while Sparrow and Lloyd [6], and Tsuruno and Nagai [7] have used a "local similarity" method. Mori [8] and Sparrow and Minkowycz [9] have considered the buoyancy effect on the flow over a horizontal flat plate. Here $\mathrm{Gr}_x/\mathrm{Re}_x^{2.5}$ is found to be the governing parameter.

For body shapes other than a flat plate, the important studies in combined convection are due to Sparrow et al. [10], Gunness and Gebhart [11], Hering and Grosh [12], and Acrivos [13]. Sparrow et al. [10] have analysed a non-isothermal wedge profile and obtained a condition for similarity to exist. They have neglected the effect of body forces in the direction perpendicular to the wedge surface and found $\mathrm{Gr}_x/\mathrm{Re}_x^2$ to be the important parameter. On the other hand, Gunness and Gebhart [11] have also considered the body forces in the direction perpendicular to the surface and shown that as a result, an additional parameter $\mathrm{Gr}_x/\mathrm{Re}_x^{2.5}$ is introduced. The y direction body forces are found to have only secondary effects on the x direction flow and they assume importance only when x direction body forces are completely absent, in which case also their effect is $(1/\sqrt{\mathrm{Re}})$ times smaller than those due to x direction body forces in other cases. Hering and Grosh [12] have reported a theoretical analysis for a laminar combined convection flow over a rotating cone, while Acrivos [13] has presented an approximate method for combined convection from a general body shape.

A few experimental results on combined convection heat transfer from a vertical flat plate [14], a sphere [15, 16], a horizontal circular cylinder in parallel [18] and cross flow [19] are available in the literature. With the exception of the vertical flat plate [14], in all cases overall heat transfer coefficients have been measured and the data correlated.

The present study is for the case in which the forced flow across the cylinder is either in the direction of the free convection flow or in the direction opposite to it. The problem is analysed as a laminar boundary layer flow with the surface temperature or wall heat flux having a specified variation along the circumference. The results of local shear stress, Nusselt number, and velocity and temperature profile are obtained along the circumference up to the point of separation.

[1] Numbers in brackets designate References at end of paper.

Contributed by the Heat Transfer Division for publication (without presentation) in the Journal of Heat Transfer. Manuscript received by the Heat Transfer Division February 2, 1971. Paper No. 71-HT-O.

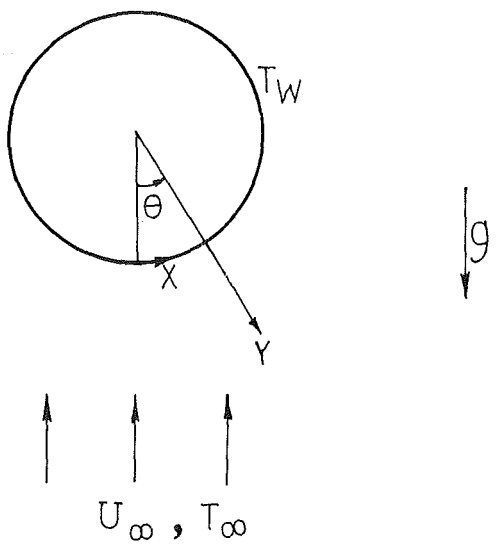

Fig. 1 Configuration under study (parallel flow for $T_w > T_\infty$; counter flow for $T_w < T_\infty$)

Statement of the Problem

Following Schlichting [20], the problem is analysed in orthogonal curvilinear x-y coordinates, since curvature effects are of the order of $(1/\sqrt{\mathrm{Re}})$ and may be neglected (Fig. 1). We have to solve the coupled equations of continuity, momentum, and energy in which the boundary layer approximations have been introduced. Assuming that the flow is steady, two dimensional, and as usual, all properties with the exception of the density variation causing the buoyancy force are constant, we get

$$\frac{\partial u}{\partial x} + \frac{\partial v}{\partial y} = 0 \tag{1}$$

$$u\frac{\partial u}{\partial x} + v\frac{\partial u}{\partial y} = -\frac{1}{\rho}\frac{\partial p}{\partial x} + g\beta\ (T - T_\infty)\sin\frac{x}{R} + \nu\frac{\partial^2 u}{\partial y^2} \tag{2}$$

$$\frac{\partial p}{\partial y} = 0 \tag{3}$$

$$u\frac{\partial T}{\partial x} + v\frac{\partial T}{\partial y} = \alpha\frac{\partial^2 T}{\partial y^2} \tag{4}$$

It will be noted that in equation (3), the buoyancy force term $g\beta(T - T_\infty)\cos(x/R)$ has been omitted. As a result, the analysis simplifies considerably. In doing so, we are following the practice of many previous investigators, e.g., references [5, 10, 22, 23, 24]. However from the work of Gunness and Gebhart [11], it appears that the neglect of the above term in equation (3) may not be appropriate in a small region near the stagnation point where the y direction body force term is large compared to the x direction force and that small errors may result. The extent of the error will depend upon the value of Re, the higher the value, the smaller will be the error. The results presented herein may therefore be considered with this limitation in mind.

The above equations are to be solved subject to the following boundary conditions:

At the wall ($y = 0$), $u = v = 0$, and either the temperature or the gradient of temperature is specified.

Away from the wall ($y \to \infty$), $u \to U$, $T \to T_\infty$.

Outside the boundary layer, it will be assumed that the potential flow distribution is valid. Thus

$$U = 2U_\infty \sin\frac{x}{R} \tag{5}$$

and consequently

$$-\frac{1}{\rho}\frac{\partial p}{\partial x} = \frac{4U_\infty^2}{R}\sin\frac{x}{R}\cos\frac{x}{R} \tag{6}$$

Equation (6) can be assumed to be valid inside the boundary layer also, by virtue of equation (3).

The use of the potential distribution can be subjected to criticism since it is well known from the case of forced convection around a cylinder that the use of the potential distribution results in an overestimate of both the heat transfer coefficient as well as the point of separation. It has also been shown by Hiemenz [21] that by using a measured distribution, the point of separation can be predicted very accurately. However, in a combined convection study, one is handicapped by the fact that there are no available measurements. Consequently there is no alternative but to use the potential flow distribution.

Method of Solution

A coordinate perturbation method is used to transform the partial differential equations into a system of ordinary differential equations. When the combined convection is assumed to be the free convection perturbing the pure forced convection flow, the basic transformations are those for a pure forced convection as used by Schlichting [20]. We consider this approach here. (The other approach is indicated in Appendix 1.) Here x is measured from the direction of forced flow. We define first a new variable

$$\eta = y\sqrt{\frac{2U_\infty}{\nu R}} \tag{7}$$

Nomenclature

D = diameter of the cylinder
$f_1, f_3, f_5, \ldots$ = functions of η, defined by equation (10)
g = acceleration due to gravity
Gr = Grashof number, $g\beta(T_w - T_\infty)D^3/\nu^2$
$\overline{\mathrm{Gr}}$ = modified Grashof number, $g\beta q_{w0}D^4/2k\nu^2$
h = local heat transfer coefficient
k = thermal conductivity of the fluid
Nu = Nusselt number, hD/k
p = pressure
Pr = Prandtl number, ν/α
q_w = wall heat flux
R = radius of the cylinder
Re = Reynolds number, $U_\infty D/\nu$
T = temperature
u = velocity in x direction
U = velocity in x direction just outside the boundary layer
U_∞ = free stream velocity
v = velocity in y direction
x = coordinate measured along surface from front stagnation point
$x^+ = x/R$
y = coordinate normal to surface
α = thermal diffusivity
β = temperature coefficient of volume expansion
μ = viscosity
ρ = density
ν = kinematic viscosity
θ = angle measured from the front stagnation point
η = independent variable, defined by equation (7)
$\Phi_0, \Phi_2, \Phi_4 \ldots$ = functions of η, defined by equation (11)
τ_θ = wall shear stress
ψ = stream function

Subscripts

w = wall
0 = stagnation point
∞ = free stream
x = characteristic dimension x
θ = angle θ

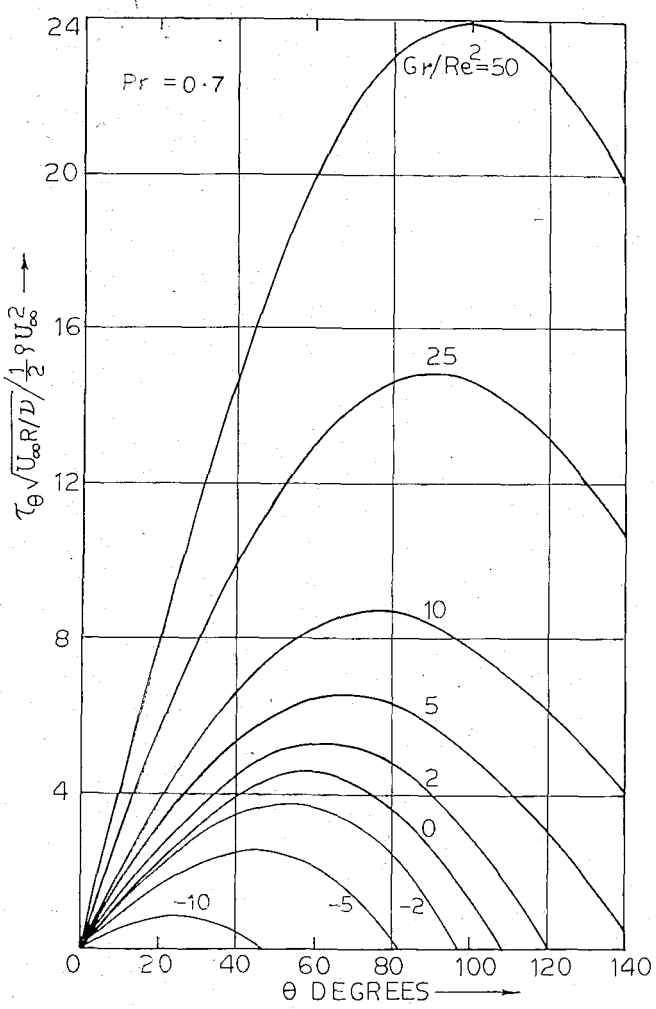

Fig. 2 Variation of wall shear stress along the circumference for Pr = 0.7 (constant surface temperature)

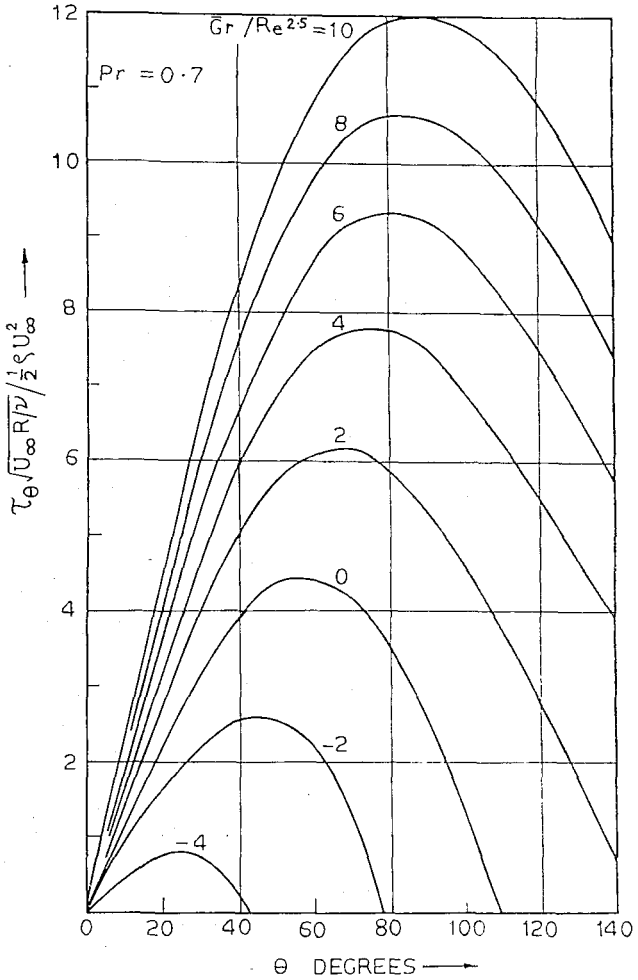

Fig. 3 Variation of wall shear stress along the circumference for Pr = 0.7 (constant wall heat flux)

The situations of specified surface temperature and specified wall heat flux are considered separately.

Case I: Specified Surface Temperature. Let the surface temperature be specified by the equation

$$\frac{T_w - T_\infty}{T_{w0} - T_\infty} = 1 + a_1 \frac{x^{+2}}{2!} + a_2 \frac{x^{+4}}{4!} + a_3 \frac{x^{+6}}{6!} + \dots \quad (8)$$

where $a_1, a_2, a_3, \dots$ are constants.

Defining the stream function ψ by

$$u = \frac{\partial \psi}{\partial y} \quad \text{and} \quad v = -\frac{\partial \psi}{\partial x} \quad (9)$$

the continuity equation (1) is satisfied automatically.

The stream function and the reduced temperature difference are expressed in power series of x^+ as

$$\psi = \sqrt{2U_\infty \nu R}\left(x^+ f_1 - \frac{x^{+3}}{3!} f_3 + \frac{x^{+5}}{5!} f_5 - \dots\right) \quad (10)$$

and

$$\frac{T - T_\infty}{T_w - T_\infty} = \Phi_0 - \frac{x^{+2}}{2!}\Phi_2 + \frac{x^{+4}}{4!}\Phi_4 - \dots \quad (11)$$

where all f's and Φ's are functions of η.

Alternate powers of x^+ are absent in the above series since there is symmetry about $x^+ = 0$. Using the expansions of $\sin x^+$ and $\cos x^+$, we have

$$-\frac{1}{\rho}\frac{\partial p}{\partial x} = \frac{4U_\infty^2}{R}\left[x^+ - x^{+3}\left(\frac{1}{2!} + \frac{1}{3!}\right) + x^{+5}\left(\frac{1}{4!} + \frac{1}{2!3!} + \frac{1}{5!}\right) - \dots\right] \quad (12)$$

and

$$g\beta(T - T_\infty)\sin x^+ = \frac{4U_\infty^2}{R}\frac{\mathrm{Gr}}{8\mathrm{Re}^2}\left[x^+\Phi_0 - x^{+3}\left(\frac{\Phi_2}{2!} + \frac{\Phi_0}{3!}\right) + x^{+5}\left(\frac{\Phi_4}{4!} + \frac{\Phi_2}{2!3!} + \frac{\Phi_0}{5!} - \dots\right)\right] \quad (13)$$

Substituting equations (9) to (13) into equations (2) and (4) and equating the coefficients of like powers of x^+, we get an infinite number of pairs of coupled ordinary differential equations which can be expressed in a general form. The nth pair can be written as

$$\sum_{K=1}^{n} A(2K+1)A(2n-2K+2)[f_{(2n-2K+1)}' f_{(2K-1)}' - f_{(2n-2K+1)} f_{(2K-1)}''] = \sum_{K=1}^{n} A(2K+1)A(2n-2K+2) \times \left[1 + \frac{\mathrm{Gr}}{8\mathrm{Re}^2}\Phi_{(2n-2K)}\right] + A(2n+1) f_{(2n-1)}''' \quad (14)$$

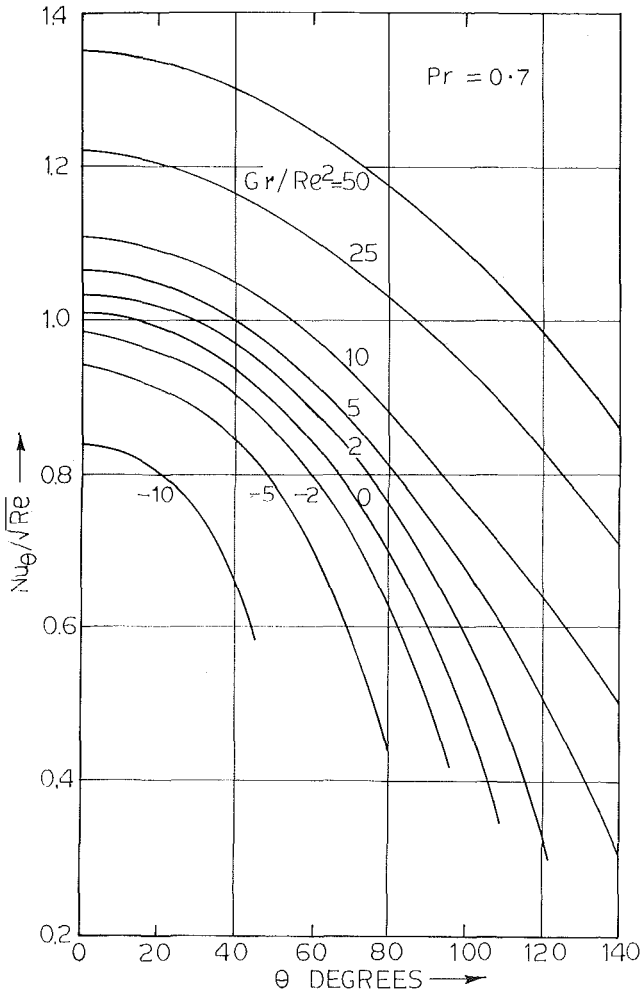

Fig. 4 Variation of $Nu_\theta/\sqrt{Re}$ along the circumference for Pr = 0.7 (constant surface temperature)

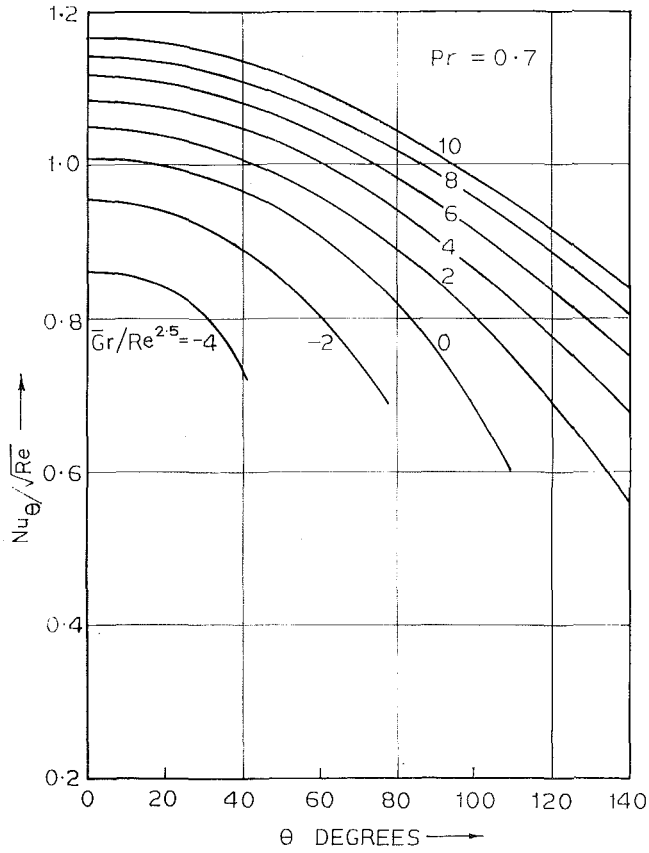

Fig. 5 Variation of $Nu_\theta/\sqrt{Re}$ along the circumference for Pr = 0.7 (constant wall heat flux)

$$\sum_{K=1}^{n} [A(2K+1)A(2n-2K+1)f_{(2K-1)}'\Phi_{(2n-2K)} - A(2n-2K+2)A(2K)f_{(2K-1)}\Phi_{(2n-2K)}'] = \frac{1}{\Pr}A(2n)\Phi_{(2n-2)}'' \quad (15)$$

where the symbol A is defined by $A(1) = 0$, $A(2) = 1$, and $A(K) = 1/(K-2)!$ for $K > 2$.

In equations (14) and (15), all the primes represent differentiation with respect to η. The first pair derived by substituting $n = 1$ in equations (14) and (15) is

$$(f_1')^2 - f_1 f_1'' = 1 + \frac{\mathrm{Gr}}{8\mathrm{Re}^2}\Phi_0 + f_1''' \quad (16)$$

$$-f_1\Phi_0' = \frac{\Phi_0''}{\Pr} \quad (17)$$

The transformed boundary conditions are:
At the surface, $\eta = 0$, $f_1 = f_3 = f_5 = \ldots = 0$

$$f_1' = f_3' = f_5' = \ldots = 0$$

$$\Phi_0 = 1, \quad \Phi_2 = -a_1, \quad \Phi_4 = a_2, \ldots$$

Away from the surface, as

$$\eta \to \infty, \quad f_1' = f_3' = f_5' = \ldots \to 1$$

$$\Phi_0 = \Phi_2 = \Phi_4 = \ldots \to 0$$

It will be noted that the dimensionless parameters appearing in the above equations are $\mathrm{Gr}/\mathrm{Re}^2$ and Pr. For a parallel flow situation $\mathrm{Gr}/\mathrm{Re}^2$ has a positive sign, while for a counter flow, it has a negative sign, since the body force term of equation (2) reverses its sign.

Case II: Specified Wall Heat Flux. Let the wall heat flux be specified by the equation

$$\frac{-k\left(\frac{\partial T}{\partial y}\right)_{y=0}}{q_{w0}} = 1 + b_1\frac{x^{+2}}{2!} + b_2\frac{x^{+4}}{4!} + b_3\frac{x^{+6}}{6!} + \ldots \quad (18)$$

where $b_1, b_2, b_3, \ldots$ are constants.

In this case the transformations, differential equations (14) and (15), and boundary conditions remain the same as in the previous case with the following differences:

1 The basic parameter $(\mathrm{Gr}/\mathrm{Re}^2)$ is replaced by $(\overline{\mathrm{Gr}}/\mathrm{Re}^{2.5})$ where $\overline{\mathrm{Gr}}$ is a modified Grashof number defined as

$$\overline{\mathrm{Gr}} = (g\beta q_{w0}D^4/2k\nu^2) \quad (19)$$

2 Equation (11) is replaced by

$$T - T_\infty = \frac{q_{w0}R}{k}\frac{1}{\sqrt{\mathrm{Re}}}\left(\Phi_0 - \frac{x^{+2}}{2!}\Phi_2 + \frac{x^{+4}}{4!}\Phi_4 - \ldots\right) \quad (20)$$

3 The new boundary conditions on Φ are:

$$\text{At} \quad \eta = 0, \quad \Phi_0' = -1, \quad \Phi_2' = +b_1, \quad \Phi_4' = -b_2, \ldots$$

Thus the problem reduces to solving pairs of coupled ordinary differential equations successively one after the other, the solution of the first pair being fed into the second and so on. To solve any pair numerically, we need the values of corresponding functions f, f', f'', Φ, and Φ' at the starting point ($\eta = 0$). In the present case, however, we have a two point boundary value

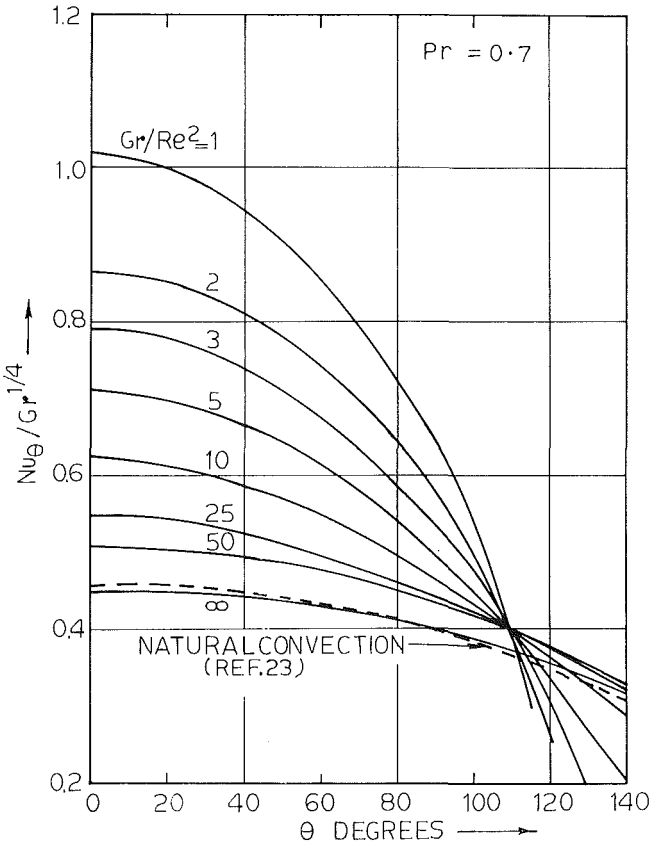

Fig. 6 Variation of $Nu_\theta/Gr^{1/4}$ along the circumference for Pr = 0.7 (constant surface temperature)

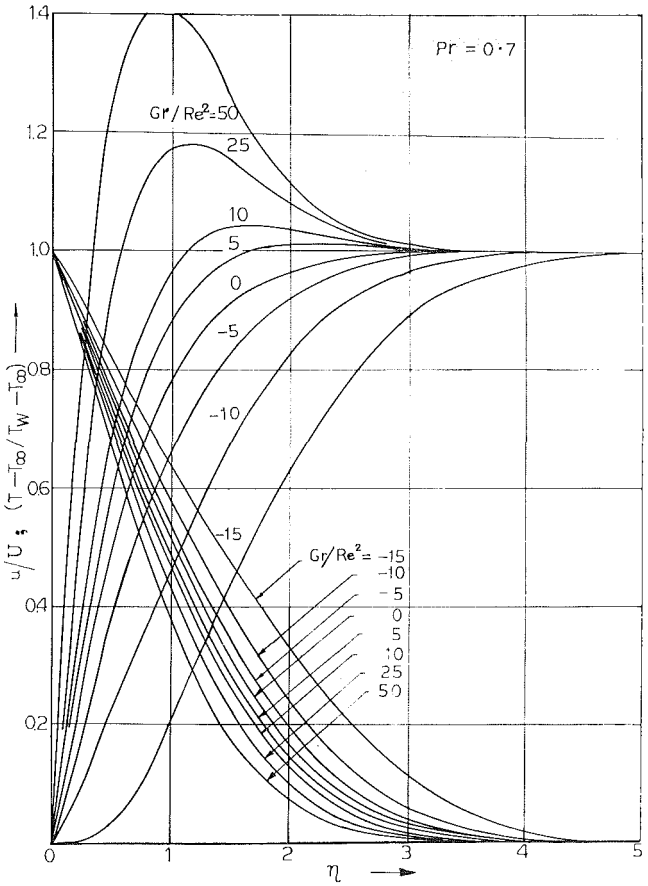

Fig. 7 Velocity and temperature profiles near the front stagnation point for Pr = 0.7 (constant surface temperature)

problem wherein two of the boundary conditions, viz., f'' and Φ' (Φ for case II) are not known at the starting point for each pair of differential equations. Hence, it is necessary to guess these values at $\eta = 0$ and proceed by a numerical method to the other boundary ($\eta \to \infty$) where the numerical solution must merge into the given boundary conditions. To facilitate guessing of correct values, a procedure suggested by Ames [25] has been adopted.

In order that the solution be sufficiently accurate, it is necessary to solve an adequate number of pairs of differential equations. It is observed that the first eight pairs are sufficient for results up to an angle of 140 deg measured from the front stagnation point. For angles greater than 140 deg, slow convergence is obtained and it is seen that the boundary layers become rather thick. Consequently the validity of the differential equations themselves becomes questionable. Hence only the first eight pairs have been solved in each case and the results are presented only up to the angle of 140 deg.

The combined convection parameter Gr/Re^2, which is the principal parameter of interest, is varied from 0 to 50 for the constant surface temperature case ($a_1 = a_2 = \ldots = 0$) in a parallel flow and from 0 to 15 in counter flow for air (Pr = 0.7). The effect of Pr as a parameter has been tested by varying Pr from 0.1 to 100 for $(Gr/Re^2) = 5$ in parallel flow. For the constant heat flux case ($b_1 = b_2 = \ldots = 0$), $\overline{Gr}/Re^{2.5}$, which is the principal parameter of interest, has been varied from 0 to 10 in parallel flow and 0 to 4 in counter flow for air (Pr = 0.7).

Results and Discussion

Wall Shear Stress and Heat Transfer in Combined Convection. The most important results are the variation of the Nusselt number and the wall shear stress along the circumference. These are shown in Figs. 2 to 6 for air (Pr = 0.7) for the constant surface temperature and constant wall heat flux cases.

It can be shown that with a constant surface temperature,

$$Nu_\theta = -2\sqrt{Re}\left[\Phi_0'(0) - \frac{x^{+2}}{2!}\Phi_2'(0) + \frac{x^{+4}}{4!}\Phi_4'(0) - \ldots\right]$$

and that with a constant wall heat flux

$$Nu_\theta = 2\sqrt{Re}\Big/\left[\Phi_0(0) - \frac{x^{+2}}{2!}\Phi_2(0) + \frac{x^{+4}}{4!}\Phi_4(0) - \ldots\right]$$

The local wall shear stress in both the cases is given by

$$\tau_\theta = \frac{4\rho U_\infty^2}{\sqrt{Re}}\left[x^+ f_1''(0) - \frac{x^{+3}}{3!}f_3''(0) + \frac{x^{+5}}{5!}f_5''(0) - \ldots\right]$$

It can be seen from Figs. 2 to 5 that the local Nusselt number, wall shear stress, and angle of separation increase with increasing (Gr/Re^2) or $(\overline{Gr}/Re^{2.5})$. As is to be expected, the results of the present investigation coincide with those for pure forced convection when $(Gr/Re^2) = 0$. The results of shear stress coincide with those presented by Schlichting [20] (Fig. 2), while the results of the Nusselt number coincide with those obtained by using the universal functions given by Fröessling [26] (Fig. 4). It is also to be expected that the results of the present investigation would merge into the known results of natural convection when $(Gr/Re^2) \to \infty$. This is seen to be the case. From Fig. 6, it can be seen that for $(Gr/Re^2) = \infty$, the curve showing the variation of $Nu_\theta/Gr^{1/4}$ with θ agrees closely with the natural convection results of Hermann [23]. From Figs. 4 and 5, it can be approximately stated that with a 10% criterion, buoyancy effects must be considered when $(Gr/Re^2) > 2$ for the constant surface temperature case and when $(\overline{Gr}/Re^{2.5}) > 1$ for the constant wall heat flux case.

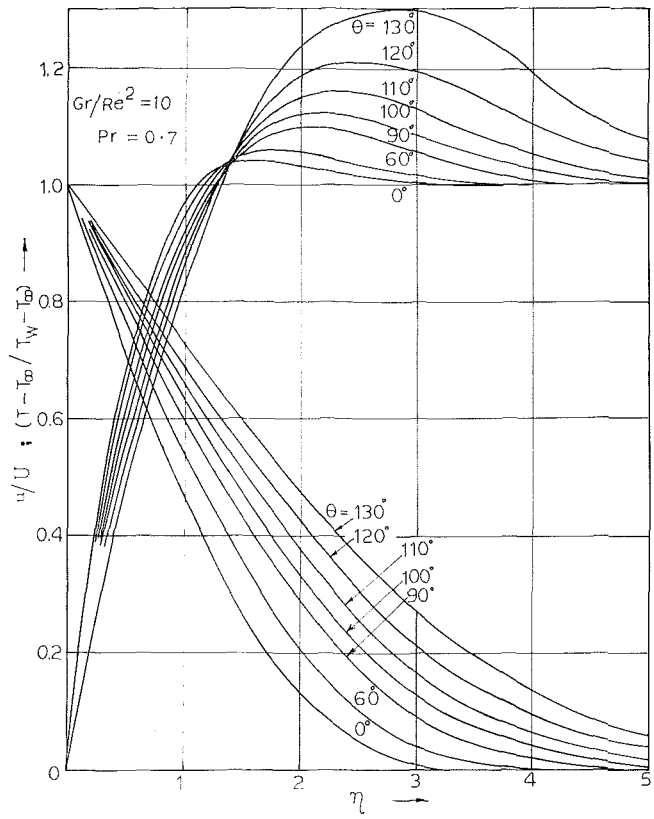

Fig. 8 Velocity and temperature profiles in the boundary layer for Pr = 0.7 and (Gr/Re²) = 10 (constant surface temperature)

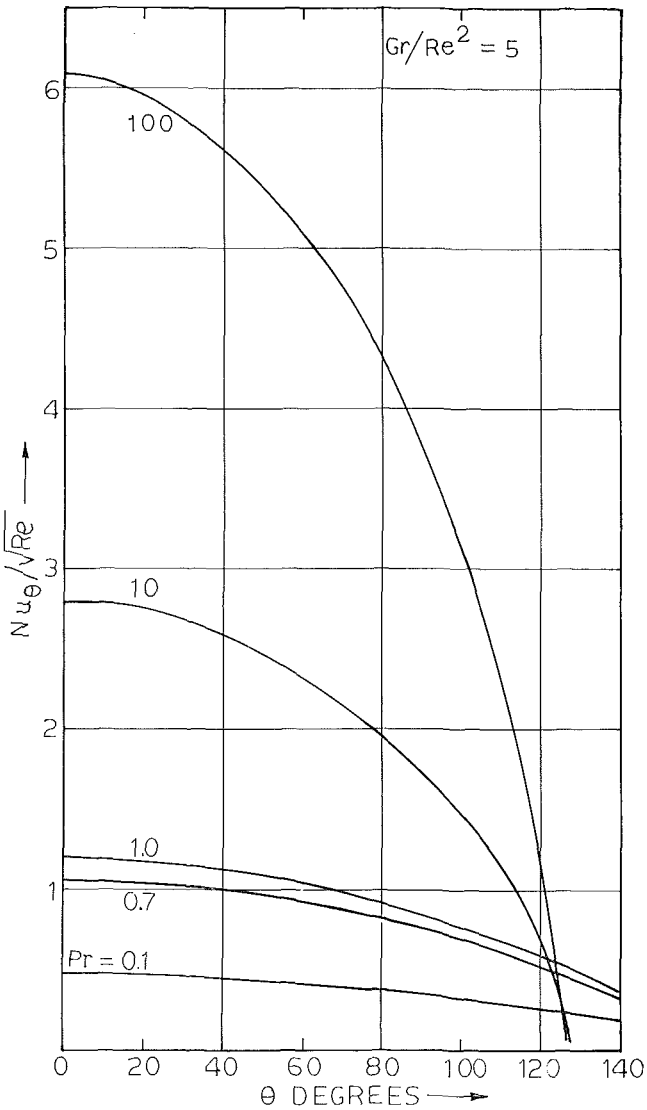

Fig. 9 Variation of $Nu_\theta/\sqrt{Re}$ along the circumference for (Gr/Re²) = 5 with Pr as a parameter (constant surface temperature)

Velocity and Temperature Profiles. Fig. 7 shows the velocity and temperature profiles near the front stagnation point for the constant surface temperature case with Gr/Re² as a parameter, while Fig. 8 shows the velocity and temperature profiles for a fixed value of (Gr/Re²) = 10 for a constant surface temperature parallel flow case, with the angle θ as a parameter. The velocity profile exhibits dual characteristics, as is to be expected in combined convection. The velocity is zero at the wall and merges into the potential flow away from the wall, as happens in pure forced convection. In between it exhibits the characteristic of natural convection and passes through a maximum. The temperature profiles remain more or less unaffected. The velocity and temperature profiles are coupled in a combined convection situation, the strength of the coupling depending on the magnitude of Gr/Re². For a parallel flow, the velocity profile shows a maximum, the magnitude of which increases with the increase of Gr/Re², while the distance at which it occurs decreases. In counter flow the velocity at any point in the boundary layer decreases with the increase of magnitude of Gr/Re². Fig. 8 also shows that in a parallel flow constant surface temperature case, for a fixed value of Gr/Re², the magnitude of the maximum of velocity profile and its distance from the wall increase with angle θ.

Further, it is observed that the velocity and thermal boundary layer thicknesses near the front stagnation point are not affected much by the value of Gr/Re². However, for a fixed value of Gr/Re², both boundary layers increase considerably in thickness along the circumference.

All the above results have been presented for air (Pr = 0.7). The nature of the curves is similar for the constant heat flux case.

Effect of Prandtl Number. Figs. 9 and 10 illustrate the effect of Prandtl number as a parameter in the combined convection region for a parallel flow constant surface temperature case in which (Gr/Re²) = 5. The variation of Nu_θ along the circumference is shown in Fig. 9, while in Fig. 10 are shown the velocity and temperature profiles near the front stagnation point. From Fig. 9, it can be seen that the value of the local Nusselt number is very sensitive to Pr and that the angle of separation decreases with increasing Pr. The interdependence of the velocity and temperature profiles is clearly seen in Fig. 10. These results are presented for Pr = 0.1, 0.7, 1.0, 10, and 100. The maximum value of the velocity as well as the hydrodynamic and thermal boundary layer thicknesses are observed to increase with decreasing Pr.

Acknowledgment

The numerical work has been performed on the CDC 3600 computer of the Tata Institute of Fundamental Research, Bombay, India.

References

1 Sparrow, E. M., and Gregg, J. L., "Buoyancy Effects in Forced-Convection Flow and Heat Transfer," *Journal of Applied Mechanics*, Vol. 26, TRANS. ASME, Series E, Vol. 81, No. 1, March 1959, pp. 133–134.

2 Szewczyk, A. A., "Combined Forced and Free-Convection Laminar Flow," JOURNAL OF HEAT TRANSFER, TRANS. ASME, Series C, Vol. 86, No. 4, Nov. 1964, pp. 501–507.

3 Eshghy, S., "Forced-Flow Effects on Free-Convection Flow

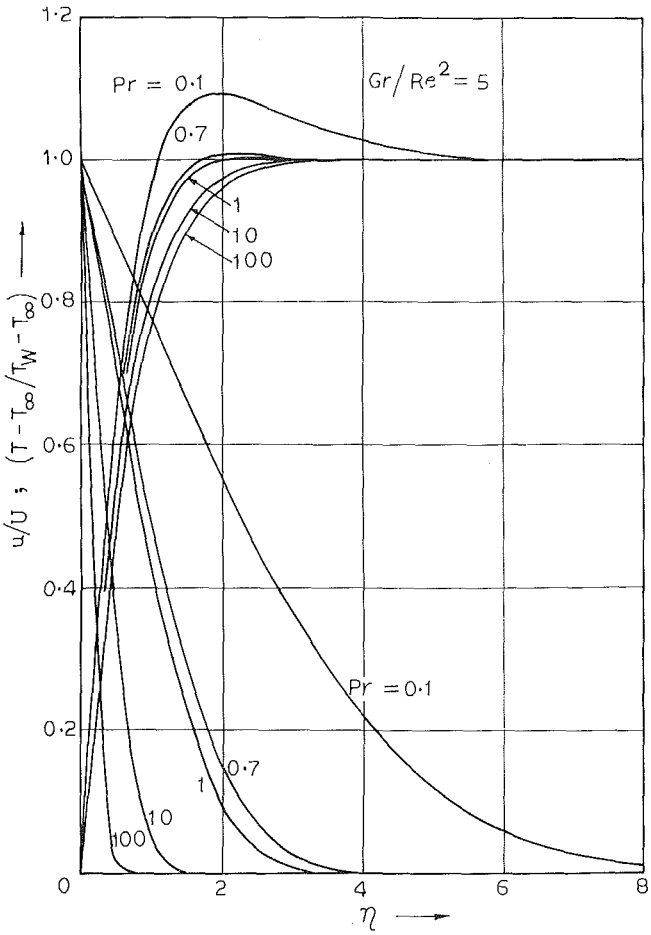

Fig. 10 Velocity and temperature profiles near front stagnation point for (Gr/Re²) = 5 with Pr as a parameter (constant surface temperature)

and Heat Transfer," JOURNAL OF HEAT TRANSFER, TRANS. ASME, Series C, Vol. 86, No. 2, May 1964, pp. 290–291.

4 Merkin, J. H., "The Effect of Buoyancy Forces on the Boundary Layer Flow over a Semi-Infinite Vertical Flat Plate in a Uniform Free Stream," *Journal of Fluid Mechanics*, Vol. 35, 1969, p. 439.

5 Acrivos, A., "Combined Laminar Free and Forced Convection Heat Transfer in External Flows," *AIChE Journal*, Vol. 4, 1958, p. 285.

6 Lloyd, J. R., and Sparrow, E. M., "Combined Forced and Free Convection Flows on Vertical Surfaces," *International Journal of Heat and Mass Transfer*, Vol. 13, 1970, p. 434.

7 Tsuruno, S., and Nagai, S., "Buoyancy Effects in Forced Convection Flow and Heat Transfer," *JSME*, Vol. 12, No. 53, 1969, p. 1129.

8 Mori, Y., "Buoyancy Effects in Forced Laminar Convection Flow Over a Horizontal Flat Plate," JOURNAL OF HEAT TRANSFER, TRANS. ASME, Series C, Vol. 83, No. 4, Nov. 1961, pp. 479–482.

9 Sparrow, E. M., and Minkowycz, W. J., "Buoyancy Effects on Horizontal Boundary Layer Flow and Heat Transfer," *International Journal of Heat and Mass Transfer*, Vol. 5, 1962, p. 505.

10 Sparrow, E. M., Eichhorn, R., and Gregg, J. L., "Combined Forced and Free Convection in a Boundary Layer Flow," *Physics of Fluids*, Vol. 2, 1959, p. 319.

11 Gunness, R. C., and Gebhart, B., "Combined Forced and Natural Convection Flows for a Wedge Geometry," *International Journal of Heat and Mass Transfer*, Vol. 8, 1965, p. 43.

12 Hering, R. G., and Grosh, R. J., "Laminar Combined Convection From a Rotating Cone," JOURNAL OF HEAT TRANSFER, TRANS. ASME, Series C, Vol. 85, No. 1, Feb. 1963, pp. 29–34.

13 Acrivos, A., "On the Combined Effect of Forced and Free Convection Heat Transfer in Laminar Boundary Layer Flows," *Chemical Engineering Science*, Vol. 21, 1966, p. 343.

14 Kliegel, J. R., "Laminar Free and Forced Convection Heat Transfer from a Vertical Flat Plate," PhD thesis, University of California, Berkeley, Calif., 1959.

15 Yuge, T., "Experiments on Heat Transfer From Spheres Including Combined Natural and Forced Convection," JOURNAL OF HEAT TRANSFER, TRANS. ASME, Series C, Vol. 82, No. 3, Aug. 1960, pp. 214–220.

16 Klyachko, L. S., "Heat Transfer Between a Gas and a Spherical Surface With the Combined Action of Free and Forced Convection," JOURNAL OF HEAT TRANSFER, TRANS. ASME, Series C, Vol. 85, No. 4, Nov. 1963, pp. 355–357.

17 Collis, D. C., and Williams, M. J., "Two Dimensional Convection from Heated Wires, at Low Reynolds Numbers," *Journal of Fluid Mechanics*, Vol. 6, 1959, p. 357.

18 Oosthuizen, P. H., and Madan, S., "Combined Convective Heat Transfer From Horizontal Cylinders in Air," JOURNAL OF HEAT TRANSFER, TRANS. ASME, Series C, Vol. 92, No. 1, Feb. 1970, pp. 194–196.

19 Sharma, G. K., and Sukhatme, S. P., "Combined Free and Forced Convection Heat Transfer From a Heated Tube to a Transverse Air Stream," JOURNAL OF HEAT TRANSFER, TRANS. ASME, Series C, Vol. 91, No. 3, Aug. 1969, pp. 457–459.

20 Schlichting, H., *Boundary Layer Theory*, 6th ed., McGraw-Hill, New York, N. Y., 1968, p. 158.

21 Hiemenz, K., "Die Grenzschicht an einem in den gleichförmigen Flüssigkeitsstrom eingetauchten geraden Kreiszylinder," thesis, Göttingen, 1911; *Dingl. Polytechn. J.*, Vol. 326, 1911, p. 32.

22 Chiang, T., and Kaye, J., "On Laminar Free Convection from a Horizontal Cylinder," *Proceedings of the 4th U. S. National Congress of Applied Mechanics*, Vol. 2, 1962, p. 1213.

23 Hermann, R., "Wärmeübertragung bei freier Strömung am waagerechten Zylinder in Zweiatomigen Gasen," *VDI-Forschungsheft*, No. 379, 1936; translated in English in NACA TM 1366.

24 Michiyoshi, I., "Heat Transfer from an Inclined Thin Flat Plate by Natural Convection," *Bulletin of JSME*, Vol. 7, 1964, p. 745.

25 Ames, W. F., *Non-linear Ordinary Differential Equations in Transport Processes*, Academic Press, 1968, p. 232.

26 Fröessling, N., "Verdunstung, Wärmeübertragung und Geschwindigkeits verteilung bei zweidimensionaler und rotationssymmetrischer Grenzschichtströmung," *Lunds Univ. Arssk. N.F. Avd. 2*, Vol. 36, 1940; also NACA TM 1432.

APPENDIX 1

The same problem can be analysed in the reverse manner by considering that the forced flow is perturbing the free convection flow. With this approach, the basic transformations are those for free convection as given by Chiang and Kaye [22].

For a specified surface temperature,

$$\eta = \frac{y}{R}\,\mathrm{Gr}^{1/4}, \qquad \psi = \nu \mathrm{Gr}^{1/4}\left(x^{+}f_1 - \frac{x^{+3}}{3!}f_3 + \ldots\right)$$

and

$$\frac{T - T_\infty}{T_w - T_\infty} = \Phi_0 - \frac{x^{+2}}{2!}\Phi_2 + \frac{x^{+4}}{4!}\Phi_4 - \ldots$$

For a specified wall heat flux,

$$\eta = \frac{y}{R}\,\overline{\mathrm{Gr}}^{1/5}, \qquad \psi = \nu \overline{\mathrm{Gr}}^{1/5}\left(x^{+}f_1 - \frac{x^{+3}}{3!}f_3 + \ldots\right)$$

and

$$(T - T_\infty) = \frac{q_{w0}R}{k}\left(\Phi_0 - \frac{x^{+2}}{2!}\Phi_2 + \frac{x^{+4}}{4!}\Phi_4 - \ldots\right)$$

Here it is observed that $(\mathrm{Re}^2/\mathrm{Gr})$ and $(\mathrm{Re}^2/\overline{\mathrm{Gr}}^{1/5})$ are the governing parameters in the respective cases. With the above transformations the differential equations (14) and (15) and their boundary conditions remain the same, excepting for the following differences:

For the specified surface temperature case,

(*a*) The term $\left[1 + \frac{\mathrm{Gr}}{8\mathrm{Re}^2}\Phi_{(2n-2K)}\right]$ in equation (14) is replaced by $\left[\frac{\mathrm{Re}^2}{\mathrm{Gr}} + \frac{1}{8}\Phi_{(2n-2K)}\right]$

(*b*) The boundary conditions on f are

$$\text{As} \quad \eta \to \infty, \quad f_1' = f_3' = f_5' = \ldots \to \mathrm{Re}/\mathrm{Gr}^{1/2}$$

For the specified wall heat flux case,

(*a*) The term $\left[1 + \frac{\mathrm{Gr}}{8\mathrm{Re}^2}\,\Phi_{(2n-2K)}\right]$ in equation (14) is replaced by $\left[\frac{\mathrm{Re}^2}{\overline{\mathrm{Gr}}^{4/5}} + \frac{1}{8}\,\Phi_{(2n-2K)}\right]$

(*b*) The boundary conditions on f are:

$$\text{As} \quad \eta \to \infty, \quad f_1' = f_3' = f_5' = \ldots \to \mathrm{Re}/\overline{\mathrm{Gr}}^{2/5}$$

Results by this approach have been obtained for various values of $(\mathrm{Re}^2/\mathrm{Gr})$ and $(\mathrm{Re}^2/\overline{\mathrm{Gr}}^{4/5})$ and found to agree very well with the results by the other approach. For high values of $(\mathrm{Gr}/\mathrm{Re}^2)$, it is numerically advantageous to approach the problem from this end. Also the solution for pure free convection can be obtained by putting $(\mathrm{Re}^2/\mathrm{Gr}) = 0$, which is not possible with the other approach as it is not practicable to put $(\mathrm{Gr}/\mathrm{Re}^2) = \infty$ in numerical work. The curve in Fig. 6 corresponding to $(\mathrm{Gr}/\mathrm{Re}^2) = \infty$ has been obtained by putting $(\mathrm{Re}^2/\mathrm{Gr}) = 0$ with this approach.

D. M. FRANCE
Assistant Mechanical Engineer,
Argonne National Laboratory,
Argonne, Ill.

Analytical Solution to Steady-State Heat-Conduction Problems With Irregularly Shaped Boundaries

A method of obtaining an analytical solution to two-dimensional steady-state heat-conduction problems with irregularly shaped boundaries is presented. The technique of obtaining the coefficients to the series solution via a direct least-squares approach is compared to the "point-matching" scheme. The two methods were applied to problems with known solutions involving the three heat-transfer boundary conditions, temperature, heat flux, and convection coefficient specified. Increased accuracy with substantially fewer terms in the series solution was obtained via the least-squares technique.

Introduction

THE TASK of obtaining analytic solutions to engineering problems wherein the system geometry does not lend itself to any one particular coordinate system has been studied by various investigators. One technique presented by Dicker and Friedman [1][1] involves the transformation of the irregularly shaped boundary into a rectangle. This method is applicable to transient problems. A second approach which has been applied predominantly to steady-state problems by many investigators in various engineering disciplines is referred to in general as the "point-matching" technique. For example, Sparrow [2, 3] used this approach to solve for the temperature distribution governed by Laplace's equation inside an irregularly shaped system. Koob and Abbott [4] applied this method to the boundary-layer equations, and Conway [5] applied it to Poisson's equation governing the deflection of clamped plates and the torsion of prismatic bars. The procedure in these cases was to set up a polar coordinate system and to assume the solution

$$T = \sum_{n=0}^{N} A_n X_n \tag{1}$$

where X_n are functions satisfying the particular governing equation. In the case of Laplace's equation, X_n are harmonic functions. For a solution interior to a closed boundary

$$X_n = r^n \cos(n\theta), \qquad r^n \sin(n\theta) \tag{2}$$

and for a solution exterior to a closed boundary

$$X_n = \ln r, \qquad r^{-n} \cos(n\theta), \qquad r^{-n} \sin(n\theta) \tag{3}$$

Various techniques have been proposed to evaluate the coefficients A_n. In the abovementioned cases, the coefficients were determined by evaluation of the solution, equation (1), at $N + 1$ points on the boundary of the system.

This technique was summarized by Ojalvo and Linzer [6] with suggestions for improving the accuracy of the results and will be referred to as the "point-matching" method of solution. The major problem encountered with this approach is the fact that the number of terms, $N + 1$, in the series solution must be exactly equal to the number of boundary points at which the solution is evaluated. In the case of very irregularly shaped boundaries where many boundary points are necessary to obtain an accurate solution, the number of terms in the solution may become excessively large. Dally and Erisman [7] evaluated the coefficients A_n to the solution of Dirichlet's problem by applying the method of least squares to discrete points on the boundary. The least-squares technique allowed the number of terms in the series solution, equation (1), to be independent of the number of boundary points used.

Sparrow and Haji-Sheikh [8, 9] obtained solutions to Laplace's equation in cartesian coordinates using $X_n = \text{Re}\,(x + iy)^n$, $n = 0, 1, 2 \ldots$. The coefficients A_n were determined by the method of orthonormal expansion, essentially a least-squares technique. This method of determining the unknown coefficients of the series solution necessitated the use of library computer codes to obtain a set of orthogonal functions from X_n; the number of boundary points was still a parameter in the solution.

It is the purpose of this investigation to prescribe an alternate general method of obtaining the coefficients A_n to the analytic solution for the temperature distribution governed by Laplace's

[1] Numbers in brackets designate References at end of paper.

Contributed by the Heat Transfer Division for publication (without presentation) in the JOURNAL OF HEAT TRANSFER. Manuscript received by the Heat Transfer Division November 24, 1970. Paper No. 71-HT-P.

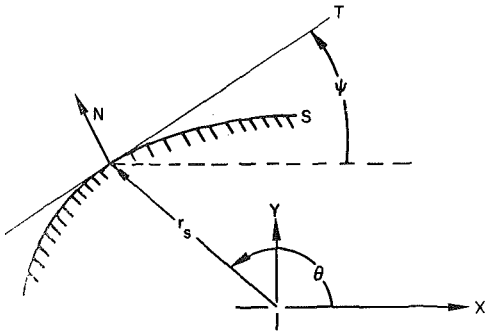

Fig. 1 General boundary diagram

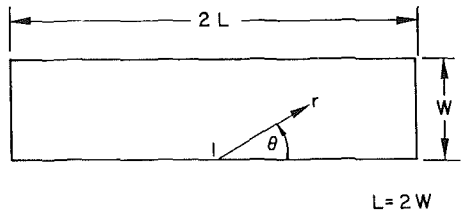

(A) COORDINATE SYSTEM FOR LEAST SQUARE SOLUTIONS

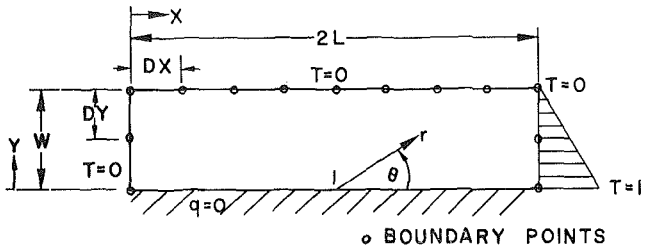

(B) GEOMETRY FOR POINT MATCH SOLUTION

Fig. 2 System geometries

equation in a medium possessing an irregular boundary. (The solution to Poisson's equation may be obtained in a similar manner.) This analysis utilizes the method of least squares directly and has the following advantages:

1 Sophisticated computer codes are not needed as in the case of the orthonormal expansion technique.

2 For a large class of irregular boundaries, the procedure of using a finite number of discrete boundary values may be replaced by an integral along the boundary thus eliminating the number of boundary points as a parameter in obtaining a solution.

A general form for solving problems with temperature, heat flux, and convection specified on various portions of the boundary is described. The solution is obtained in cylindrical coordinates, and the results applied to a sample problem are compared to the point match and exact solutions for various numbers of terms $(N + 1)$ in the series solution.

Theory

Point Matching. Let t_k be given temperatures on the boundary at points k. Then

$$\sum_{n=0}^{N} A_n X_n = t_k \qquad k = 0, 1, \ldots, N \tag{4}$$

Thus, the $N + 1$ coefficients, A_n, are found by the solution of $N + 1$ equations given by (4). Flux, temperature, and convective boundary conditions, and all three together in the same problem, can easily be accommodated since an appropriate equation may be written for each separate boundary point.

Least Squares. For the case of t_l boundary temperatures, the least-squares solution is:

$$\frac{\partial}{\partial A_k} \sum_{l=1}^{M} \left\{ t_l - \sum_{n=0}^{N} A_n X_n \right\}^2 = 0 \qquad k = 0, 1, \ldots, N \tag{5}$$

Note that M does not necessarily equal $N + 1$. Now for a boundary that can be specified in polar coordinates as a function of r and θ, and t specified continuously along the boundary, relation (5) becomes

$$\frac{\partial}{\partial A_k} \oint_s \left\{ t - \sum_{n=0}^{N} A_n X_n \right\}^2 ds = 0 \qquad k = 0, 1, 2, \ldots, N \tag{6}$$

This type of boundary situation occurs frequently and equations (6) are simply the limiting case of relations (5) as the number of boundary points, and thus the index l, approach infinity. The number of terms $(N + 1)$ in the solution is arbitrary. The use of the integral least-squares formulation, equation (6), requires further explanation as to the accommodation of temperature, flux, and convective boundary conditions along a single closed boundary.

The heat flux normal to a surface S, Fig. 1, is

$$-\frac{q}{K} = \nabla T \cdot \underline{N}$$

where $\underline{N}$ is the outward normal. After some manipulation this expression becomes

$$-\frac{q}{K} = \frac{\partial T}{\partial r} \sin(\theta - \psi) + \frac{1}{r} \frac{\partial T}{\partial \theta} \cos(\theta - \psi) \tag{7}$$

in the second quadrant as depicted in Fig. 1. T is given by equation (1), and ψ is the tangent angle, $0 \leq \psi < \pi$. In the case of prescribed heat flux Q at the boundary, the least-squares formulation is

$$\frac{\partial}{\partial A_k} \oint_s \left\{ \frac{Qr_s}{K} - \frac{qr_s}{K} \right\}^2 ds = 0 \qquad k = 0, 1, 2, \ldots, N \tag{8}$$

where the appropriate length r_s has been used such that the units of the quantity in brackets in equations (8) are temperature. This feature allows the use of more than one type of boundary condition in a given problem.

Nomenclature

C = HW/K, dimensionless
H = heat-transfer coefficient, Btu/hr-ft²-deg F
h = H/K, ft^{-1}
K = thermal conductivity, Btu/ft-hr-deg F
L = length of rectangle, ft
q, Q = heat flux, Btu/ft²-hr
r = radial coordinate, ft
s = surface coordinate, ft
T, t = dimensionless temperature
W = width of rectangle, ft
x, y = cartesian coordinates, ft
θ = angular coordinate, rad

Subscripts

s = referring to the boundary surface
∞ = referring to a fluid

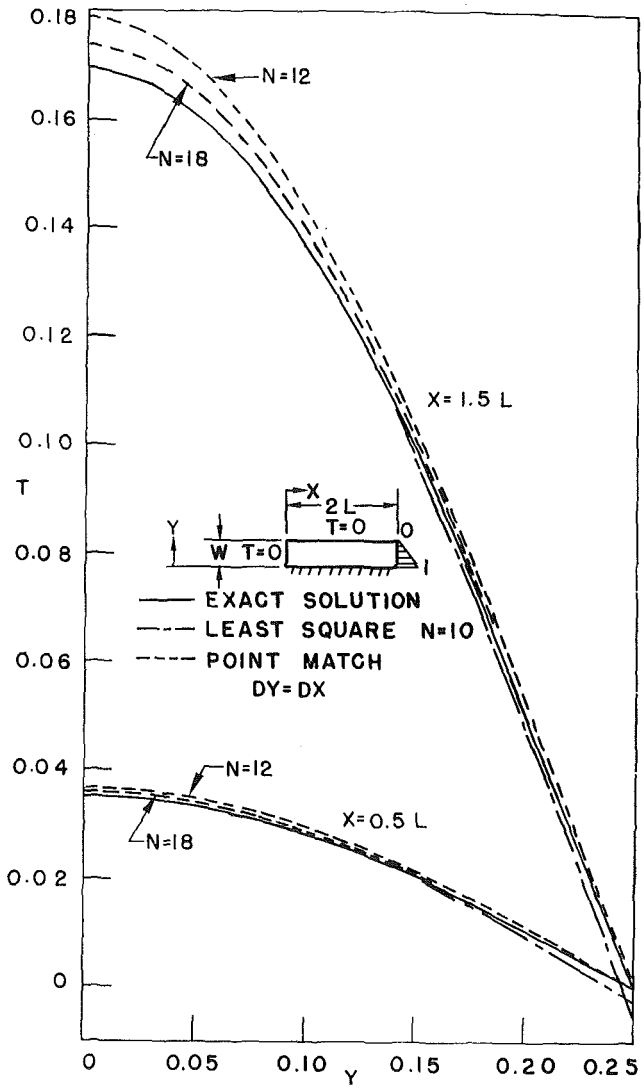

Fig. 3 Comparison of solutions for temperature boundary conditions

In the case of a convective boundary condition to a fluid at t_∞, the appropriate equations are

$$\frac{\partial}{\partial A_k} \oint_s \left\{ t_\infty + \frac{q}{H} - T \right\}^2 ds = 0 \qquad k = 0, 1, 2, \ldots, N \quad (9)$$

where q is found from equation (7) and T from equation (1).

Application

Comparison of Solution Methods. As an example of the application of relations (6), (8), and (9) and their use together, solutions were obtained by the least-squares method for the temperature distribution in the rectangle shown in Fig. 2(A). A closed-form solution to this problem with various boundary conditions is obtainable in cartesian coordinates. However, for demonstration purposes the solution is sought in polar coordinates, i.e., equation (1), since this formulation would be used if the system geometry were irregular, trapezoidal for example. For purposes of comparison, a solution to the problem with boundary conditions as given in Fig. 2(B) was found by the methods of least squares and point matching. The temperature distribution used in connection with both methods is given by equation (1) with X_n given by (2). The coordinate system was placed on the insulated portion of the boundary, and thus from the condition that $q = 0$ at $\theta = n\pi$, equation (1) becomes

$$T = \sum_{n=0}^{N} A_n r^n \cos(n\theta) \quad (10)$$

The insulated boundary condition is thus satisfied identically, and it remains to obtain the coefficients A_n by use of the specified temperatures on the remainder of the boundary. This problem, then, is reduced to the type where the boundary conditions are all in terms of specified temperatures, and the least-squares formulation corresponds to equations (6). Performing the appropriate differentiation yields

$$\int_0^{\theta_m} \left[(1 - 2\tan\phi) - \sum_{n=0}^{N} A_n X_n \right] (-X_k) d\phi + \int_{\theta_m}^{\pi-\theta_m} X_k \sum_{n=0}^{N} A_n X_n d\phi + \int_{\pi-\theta_m}^{\pi} X_k \sum_{n=0}^{N} A_n X_n d\phi = 0$$

and after some rearranging one obtains

$$\sum_{n=0}^{N} [A_n G(k, n)] = B(k) \qquad k = 0, 1, 2, \ldots, N \quad (11)$$

where

$$G(k, n) = [1 + (-1)^{n+k}] L^{n+k} \int_0^{\vartheta_m} F_1(\phi, n, k) d\phi + W^{n+k} \int_{\theta_m}^{\pi-\theta_m} F_5(\phi, n, k) d\phi \quad (12)$$

$$B(k) = L^k \int_0^{\vartheta_m} F_3(\phi, k) d\phi$$

$$F_1(\phi, n, k) = \cos(n\phi) \cos(k\phi)/(\cos\phi)^{n+k} \quad (13)$$

$$F_5(\phi, n, k) = \cos(n\phi) \cos(k\phi)/(\sin\phi)^{n+k}$$

$$F_3(\phi, k) = \cos(k\phi)(1 - 2\tan\phi)/\cos\phi)^k$$

In this case L was chosen as 0.5 and $\theta_m = \tan^{-1}(W/L)$. The solution to equations (11) was obtained by first choosing the number of terms, $N + 1$, in the series solution, then determining the symmetric coefficient matrix, $G(k, n)$, subsequent to the numeric evaluation of the integrals of functions F_1, F_3, and F_5 by means of a 10-point Gauss quadrature formula. The coefficients A_n were found from the solution of $N + 1$ linear equations by the method of triangularization of matrix $G(k, n)$. These computations were performed for various values of N on a CDC 3600 digital computer. A second solution was then obtained to the same problem by the point-matching method. The geometric arrangement of boundary points for evaluation of the coefficients A_n is depicted in Fig. 2(B). The formulation for this method is given by equations (4) where the harmonic functions X_n are the same as used in the least-squares solution to the problem.

The results of the two solutions as well as the exact solution are presented in Fig. 3. The point-matching solution with 18 terms in the series for the case of equally spaced points, $DY = DX$, did not yield as accurate a solution as did the least-squares method with 10 terms in the series. In fact, the point-matching solution is not as accurate as shown in Fig. 3 at all values of X. The point-matching solutions compared in Fig. 4 were obtained for two different point placements, $N = 12$ in both cases. The results at $X = L$ indicate that the solution for equal spacing, $DX = DY$, is somewhat more precise than the results for the situation wherein $DX = 2DY$. Both solutions are identically equal to zero at $Y = 0.25$ because of the presence of a boundary point there in both cases. However, the results at $X = 1.5L$ reveal that the solution for $DX = 2DY$ varies significantly from the exact solution near $Y = 0.25$ while the solution for the case of $DX = DY$ is still equal to zero at $Y = 0.25$. This change in behavior of the solution for $DX = 2DY$ is due to the fact that there

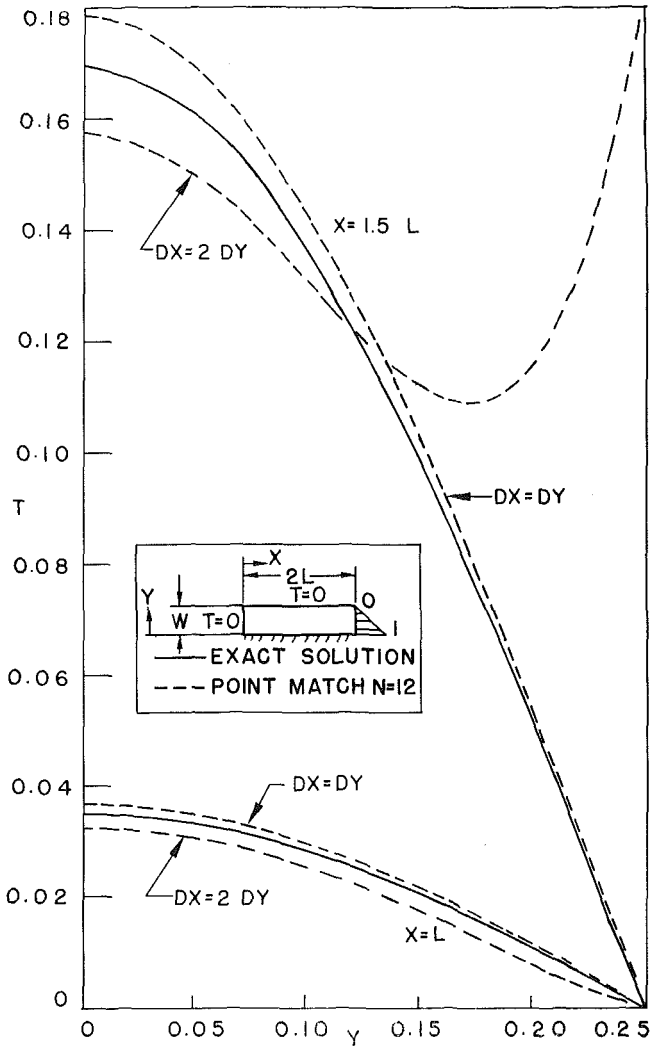

Fig. 4 Variation in point-matching solutions

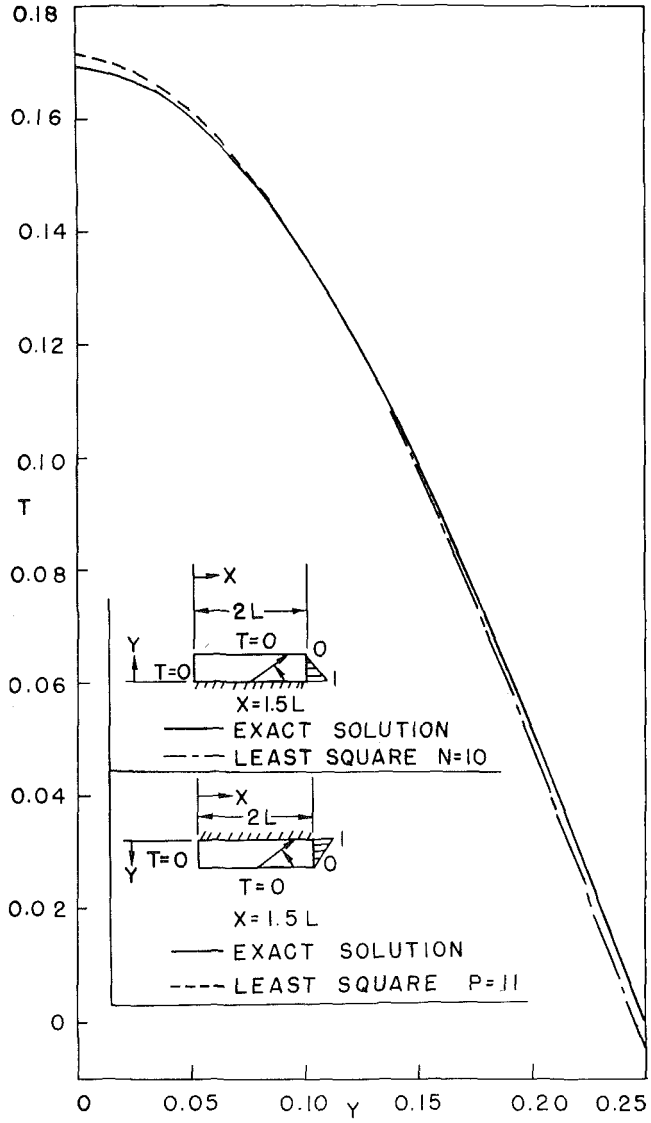

Fig. 5 Solution for temperature and flux boundary conditions

Table 1 Coefficients A_n for temperature distribution in a rectangle

	Boundary Condition						
N	a	b	b	c	d	e	e
0	0.03499	0.03676	0.03582	0.03228	0	0.07206	0.07438
1	0.2219	0.2319	0.2260	0.1776	0.2191	0.4146	0.4004
2	0.6990	0.7277	0.7084	0.6963	0.6811	1.188	1.322
3	1.377	1.542'	1.496	3.038	1.427	2.147	2.855
4	2.047	2.451	2.371	1.565	2.445	2.187	2.752
5	4.401	3.138	3.110	−31.70	2.877	2.971	0.08904
6	6.470	3.963	3.611	−5.918	0.4754	8.290	
7	−5.477	7.197	4.143	281.9	−0.6482	−0.5441	
8	−11.89	7.908	5.886	184.9	11.13	−40.90	
9	31.42	−5.082	12.47	−940.5	8.348	−51.37	
10	52.67	10.17	17.42	−806.7	−35.38	−5.679	
11		96.04	−6.413	1345.	−55.10		
12		104.1	44.69	1449.			
13			404.8				
14			356.3				
15			−1051.				
16			−518.5				
17			4179.				
18			4641.				

$L = 1.0$, $W = 0.25$, $C = 10.0$

a = temperature specified, least-squares solution, Fig. 3.
b = temperature specified, point-matching solution, $DX = DY$, Fig. 3.
c = temperature specified, point-matching solution, $DX = 2DY$, Fig. 4.
d = temperature and flux specified, least-squares olution, Fig. 5.
e = temperature and convection specified, least-squares solution, Fig. 6.

was no boundary point at $X = 1.5L$, $Y = W$. There was a boundary point at $X = 1.5L$, $Y = W$ for the case of $DX = DY$. These comparisons indicate that the accuracy of the solution based on the point-matching method changes significantly at various spatial locations depending on the relative proximity of the boundary points.

It is of interest to note that the addition of more terms to the least-squares solution presented in Fig. 3 did not improve its accuracy. A similar situation was found to exist for the point-matching solution at a larger limiting value of N. These observations are indicative of the inherent accuracy of the computational technique.

Flux Boundary Condition. In order to demonstrate the use of a flux and temperature boundary condition in the same problem a solution was sought to the example discussed above with the coordinate system centered on a zero-temperature section of the boundary, Fig. 5. The assumed solution in this case is

$$T = \sum_{n=1}^{P} A_n r^n \sin(n\theta) \tag{14}$$

and the resulting equations are

$$\sum_{n=1}^{P} [A_n G(k, n)] = B(k) \qquad k = 1, 2, \ldots, P \tag{15}$$

where

$$G(k, n) = [1 + (-1)^{n+k}] L^{n+k} \int_0^{\theta_m} F_4(\phi, n, k) d\phi + nkW^{n+k} \int_{\theta_m}^{\pi - \theta_m} F_2(\phi, n, k) d\phi \tag{16}$$

$$B(k) = L^k \int_0^{\theta_m} F_6(\phi, k) d\phi$$

$$F_4(\phi, n, k) = \sin(n\phi) \sin(k\phi)/(\cos\phi)^{n+k}$$

$$F_2(\phi, n, k) = \cos(n\phi - \phi) \cos(k\phi - \phi)/(\sin\phi)^{n+k}$$

$$F_6(\phi, k) = 2 \sin(k\phi) \tan\phi/(\cos\phi)^k$$

The solution is presented in Fig. 5 for $P = 11$ which corresponds to $N = 10$ in the temperature boundary problem, the results of which are given in Fig. 3. The two solutions to the problem, one employing temperature boundary conditions and the other mixed temperature and flux boundary conditions, are in equally good agreement with the exact solution.

Convective Boundary Condition. As a final example the temperature distribution was found in the rectangle where convection to a medium at temperature t_∞ takes place at one section of the boundary, Fig. 6. The assumed solution is given by equation (10), and the resulting equations by relations (11), where

$$G(k, n) = [1 + (-1)^{n+k}] L^{n+k} \int_0^{\theta_m} F_1(\phi, n, k) d\phi + W^{n+k} \int_{\theta_m}^{\pi - \theta_m} F_7(\phi, n, k) d\phi \tag{17}$$

$$B(k) = L^k \int_0^{\theta_m} F_8(\phi, k) d\phi$$

$$F_7(\phi, n, k) = [\cos(n\phi) - n \sin\phi \sin(n\phi - \phi)/(hW)] \times [\cos(k\phi) - k \sin\phi \sin(k\phi - \phi)/(hW)]/(\sin\phi)^{n+k}$$

$$F_8(\phi, k) = \cos(k\phi)/(\cos\phi)^k$$

and $F_1(\phi, n, k)$ is given by relation (13). The solutions are presented in Fig. 6 for $N = 10$ and $N = 5$. For N greater than 10 the solution did not improve any further. The coefficients A_n for all of the sample solutions are given in Table 1.

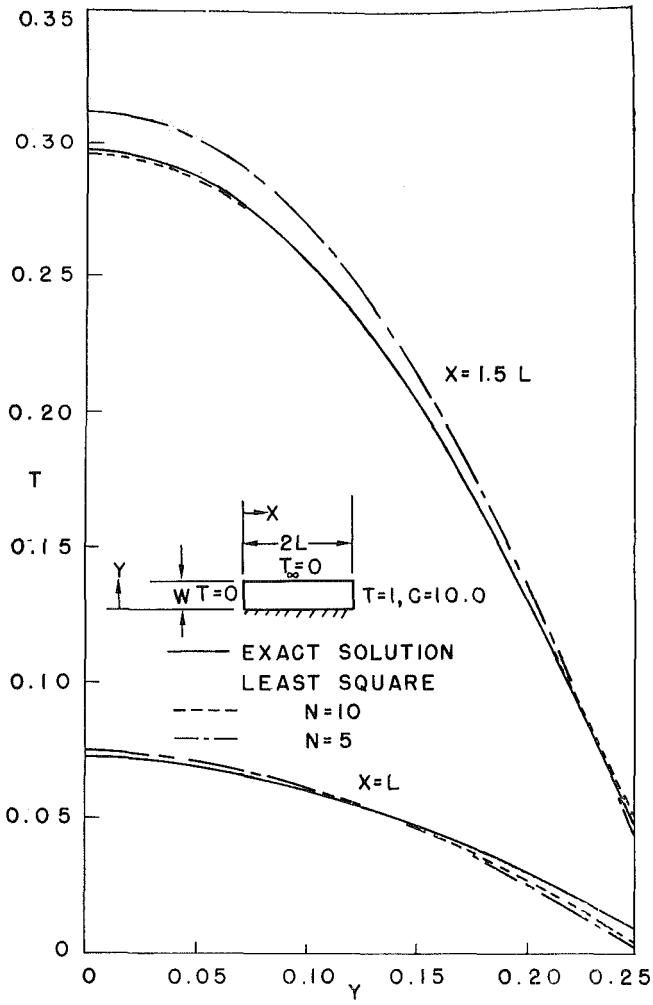

Fig. 6 Solution for temperature and convective boundary conditions

Conclusions

From the presentation of the three sample solutions, the usefulness of the least-squares technique for evaluation of the coefficients in the assumed series solution was confirmed. The accuracy of the solutions was excellent for cases employing the three types of boundary conditions. Further, the least-squares technique was shown to be superior to the point-matching scheme in that fewer terms were required to obtain an accurate solution using the least-squares technique, and the accuracy of the least-squares solution was not dependent upon spatial location in the manner of the point-matching solution. Finally, there was no boundary-point parameter associated with the results of the integral formulation of the least-squares technique.

References

1 Dicker, Daniel, and Friedman, M. B., "Solution of Heat-Conduction Problems With Nonseparable Domains," *Journal of Applied Mechanics*, Vol. 30, TRANS. ASME, Series E, Vol. 85, No. 4, Dec. 1963, pp. 493–499.

2 Sparrow, E. M., and Loeffler, A. L., Jr., "Longitudinal Laminar Flow Between Cylinders Arranged in Regular Array," *AIChE Journal*, Vol. 5, No. 3, Sept. 1959, pp. 325–330.

3 Sparrow, E. M., "Temperature Distribution and Heat-Transfer Results for an Internally Cooled, Heat-Generating Solid," JOURNAL OF HEAT TRANSFER, TRANS. ASME, Series C, Vol. 82, No. 4, Nov. 1960, pp. 389–392.

4 Koob, S. J., and Abbott, D. E., "Investigation of a Method for the General Analysis of Time Dependent Two-Dimensional Laminar Boundary Layer," ASME Paper No. 68-FE-10.

5 Conway, H. D., "The Approximate Analysis of Certain Bound-

ary-Value Problems," *Journal of Applied Mechanics*, Vol. 27, TRANS. ASME, Series E, Vol. 82, No. 2, June 1960, pp. 275–277.
6 Ojalvo, I. U., and Linzer, F. D., "Improved Point-Matching Techniques," *J. Mech. and Appl. Math.*, Vol. 18, 1965, pp. 41–56.
7 Dally, J. W., and Erisman, E. R., "An Analytic Separation Method for Photoelasticity," *Experimental Mechanics*, October 1966.
8 Sparrow, E. M., and Haji-Sheikh, A., "Flow and Heat Transfer in Ducts of Arbitrary Shape With Arbitrary Thermal Boundary Conditions," JOURNAL OF HEAT TRANSFER, TRANS. ASME, Series C, Vol. 88, No. 4, Nov. 1966, pp. 351–358.
9 Sparrow, E. M., and Haji-Sheikh, A., "Transient and Steady Heat Conduction in Arbitrary Bodies With Arbitrary Boundary and Initial Conditions," JOURNAL OF HEAT TRANSFER, TRANS. ASME, Series C, Vol. 90, No. 1, Feb. 1968, pp. 103–108.

J. R. WIEBE[1]
Fuels and Instrument Engineer,
Steel Co. of Canada Ltd.
Hamilton, Ontario, Canada

R. L. JUDD
Assistant Professor of
Mechanical Engineering,
McMaster University,
Hamilton, Ontario, Canada

Superheat Layer Thickness Measurements in Saturated and Subcooled Nucleate Boiling

An experimental study of temperature profiles in water boiling on a horizontal copper surface is reported for incipient boiling conditions and for 20,000, 50,000, and 100,000 Btu/hr-ft^2 *heat flux at various levels of subcooling ranging from 0 to 105* deg F. *The extrapolated superheat layer thickness results for the incipient boiling conditions lend support to Hsu's mathematical model for bubble nucleation. Increasing heat flux and decreasing subcooling were observed to result in a decreasing extrapolated superheat layer thickness. Analysis of some additional results for Freon-113 boiling on a glass surface indicated that the thickness of the extrapolated superheat layer was governed by the bubble flux density which was influenced by both heat flux and subcooling.*

Introduction

It has long been recognized that one of the most important parameters in nucleate boiling is the microstructure of the heating surface, characterized by the size, space, and shape distribution of pits and scratches that constitute nucleation sites. Because of the smallness of these sites and a general lack of understanding as to what constitutes a site, it has been difficult to effectively describe the microstructure in order to incorporate surface condition in relationships of surface superheat and heat flux.

The microstructure of the surface and the energy content of the liquid adjacent to the surface influence but do not uniquely determine the number of bubbles generated per unit area per unit time. At any given heat flux, natural convection and nucleate boiling must combine to transfer the entire heat load. The bubble flux density required to accommodate the nucleate boiling portion is determined by the ability of the bubbles to promote the transfer of heat either by convection currents induced in the liquid by the growth and departure or collapse of the bubbles or by mass transfer through the bubbles resulting from evaporation at the base of the bubble and condensation at the vapor–liquid interface, subject to constraints imposed by the availability of active nucleation sites. The interdependence of natural convection and nucleate boiling has been demonstrated qualitatively in reference [1].[2]

It is interesting to speculate on the relationship between the thickness of the superheat layer adjacent to the heating surface and the bubble flux density. Agitation within the superheat layer induced by the growth and departure or collapse of the bubbles most likely determines the superheat layer thickness so that a positive correlation between superheat layer thickness and bubble flux density is to be expected. As has already been explained, bubble flux density is to a large extent dependent on the microstructure of the heating surface and the energy content of the liquid adjacent to the heating surface which is related to the temperature profile in the superheated layer, so that microstructure, superheat layer thickness, and bubble flux density must also be interrelated in some complicated manner. Hsu [2] related microstructure and superheat layer thickness by formulating a mathematical model to predict bubble nucleation in a nonuniform temperature field. The model was capable of predicting the maximum and minimum sizes of potentially active nucleation cavities but failed to predict active nucleation site density because knowledge of cavity size distribution was lacking. The results of the present investigation will provide additional support for this mathematical model in addition to presenting new data pertaining to the distribution of temperature adjacent to a heating surface for both saturated and subcooled boiling which will enable the interrelationship between superheat layer thickness and bubble flux density to be investigated.

Literature Survey

In 1965, Marcus and Dropkin [3] carried out an extensive investigation of the thermal boundary layer above a nickel-plated copper surface in saturated nucleate pool boiling water which indicated that the value of the thermal boundary layer thickness decreased with increasing heat flux. Furthermore, Marcus and Dropkin demonstrated a functional dependence

[1] Formerly graduate student, Department of Mechanical Engineering, McMaster University, Hamilton, Ontario, Canada.

[2] Numbers in brackets designate References at end of paper.

Contributed by the Heat Transfer Division and presented at the ASME-AIChE Heat Transfer Conference, Tulsa, Okla., August 15–18, 1971. Manuscript received by the Heat Transfer Division November 4, 1970. Paper No. 71-HT-43.

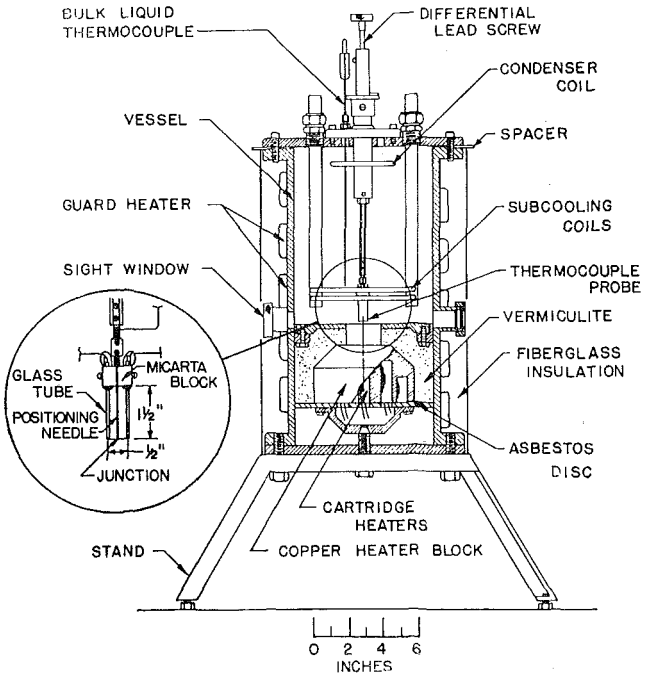

Fig. 1 Sectional view of experimental apparatus

between the extrapolated superheat layer thickness and the heat transfer coefficient.

In 1968, Lippert and Dougall [4] undertook an investigation similar to that of Marcus and Dropkin in which temperature profiles were measured in the thermal boundary layer for Freon-113, methyl alcohol, and water boiling on a copper heating surface. Lippert and Dougall reproduced Marcus and Dropkin's results for water. All tests were done with the bulk liquid at or near the saturation temperature.

In 1968, Bobst and Colver [5] reported temperature measurements in the thermal boundary layer for saturated pool boiling water which substantiated the previous work of Marcus and Dropkin and Lippert and Dougall. In addition, the authors extended the correlation of heat transfer coefficient with extrapolated superheat layer thickness.

Recent work in the measurement of thermal boundary layers was performed by Judd [6] in which Freon-113 was boiled on a glass plate coated with an electrically conducting oxide. Heat flux, subcooling, and acceleration were varied so as to show the individual effects of these parameters. In accordance with previous investigations, Judd found that the thermal boundary layer decreased with increasing heat flux. Furthermore, the superheated boundary layer was found to decrease with acceleration and increase with subcooling. This investigation was accompanied by measurements of active site density and frequency of bubble emission which will be utilized later in this paper.

Experimental Apparatus

A sectional view of the complete boiler assembly is presented in Fig. 1. The vessel and cover plate were fabricated from stainless steel. The heater consisted of a copper cylinder reduced to a diameter of 2 in. at the boiling surface with cartridge heaters installed in the base. A stainless steel skirt was furnace-welded flush with the top of the copper heater block to provide a continuous extension of the boiling surface.

The boiling surface was finished after the skirt was welded in place. Initially a fine slow-speed lathe cut was taken across the surface. In final finishing, number 400 "Diamond Grit" paper was first applied to the surface followed by number 600 "Diamond Grit" paper. The rms roughness of the surface was measured at approximately 5 μin.

The present investigation required that the subcooling in the bulk liquid be variable. A single-pass heat exchanger comprised of eight stainless steel tubes in parallel was located 1 in. above the skirt to provide the bulk subcooling. A vapor condenser comprised of a single stainless steel tube was positioned 1 in. below the cover plate.

Chromel–constantan thermocouples were used in the present investigation. Six thermocouples were installed in the neck of the copper block at various axial and radial positions. Two stainless steel sheathed ceramic-insulated thermocouples measured the bulk temperature 2 in. above the heating surface.

The techniques of Gelb, Marcus, and Dropkin [7] were applied to the design and construction of the thermocouple probe. In the manufacture of the thermocouple itself, bare chromel and constantan wires 0.001 in. in diameter were joined by discharge welding. Experience showed that with care the diameter of the thermocouple bead could be held below 0.003 in. The thermocouple support was constructed of two fine glass capillary tubes mounted in a micarta block. The capillary tubes were slightly sprung inward and while in this condition, the thermocouple was fixed by epoxy applied to the upper end of the capillary tubes.

It was found that deposits which had formed on the copper heating surface prevented the thermocouple head from making electrical contact. A needle was mounted on the probe holder which could penetrate the thin deposits, thus enabling the probe position to be determined with respect to the surface.

Experimental Procedure

The investigation was subdivided into two series of tests: one in which the incipience of boiling was determined for five different levels of subcooling, the other in which the influence of subcooling was explored at three different levels of heat flux. The heat flux levels were selected to explore the three boiling regimes identified by Gaertner [8]: the discrete bubble regime (20,000 Btu/hr-ft²), the bubble transition regime (50,000 Btu/hr-ft²), and the vapor mushroom regime (100,000 Btu/hr-ft²).

At the beginning of each test, a heat flux of 100,000 Btu/hr-ft² was established to insure that the nucleation sites were properly activated. Saturated boiling at this heat flux was allowed

Nomenclature

A = parameter $2\sigma T_{sat}/\rho_v\lambda$
C_1 = constant 2
C_3 = constant 1.6
f = frequency of bubble emission
Gr = Grashof number
h = heat transfer coefficient
k = thermal conductivity of liquid
N/A = active site density
Nu = Nusselt number
Pr = Prandtl number
Q/A = heat flux
r_c = radius of cavity mouth
T = temperature
T_{sat} = saturation temperature
T_w = surface temperature
T_∞ = bulk temperature
$(dT/dZ)_{Z=0}$ = temperature gradient at surface
Z = displacement from surface
δ = extrapolated superheat layer thickness
θ = temperature difference $(T - T_\infty)$
θ_{sat} = temperature difference $(T_{sat} - T_\infty)$
θ_w = temperature difference $(T_w - T_\infty)$
θ_{wo} = temperature difference $(T_w - T_\infty)$ at incipience
λ = latent heat of vaporization
ξ = thermal boundary layer thickness
ρ_v = density of vapor
σ = surface tension of liquid with respect to vapor

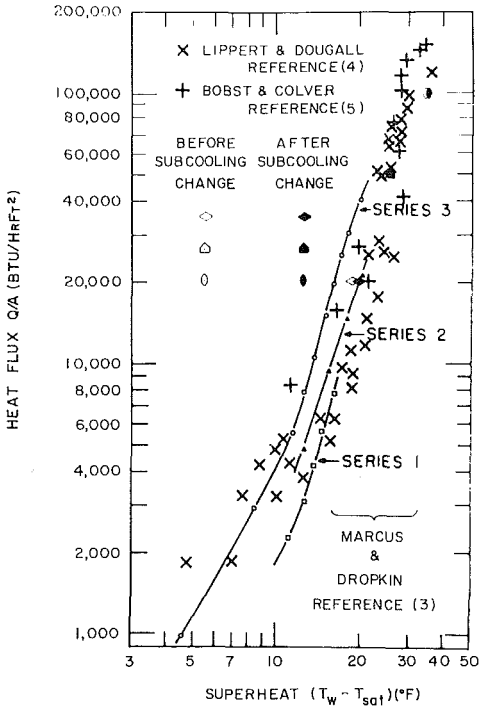

Fig. 2 Heat flux–superheat characteristics

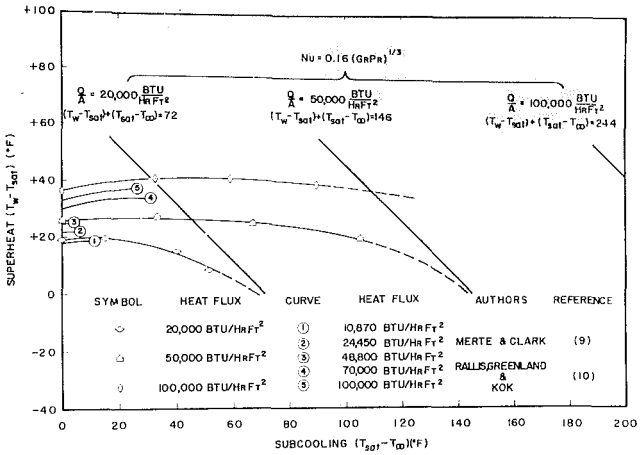

Fig. 3 Variation of wall superheat with bulk subcooling

to continue for 20 min after which the heat flux was reduced to the level desired for the test. For the tests of the incipience of boiling, heat flux was decreased until boiling had ceased. The appearance of the first bubble was sought over a period of time as long as 48 hr while the heat flux was increased incrementally. Then the heat flux and subcooling were noted and a complete traverse was performed. All thermocouples were read on a precision potentiometer immediately before and after the traverse to provide a check on the temperature stability. The probe was lowered from its maximum height in increments of one turn of the lead screw shaft until the probe reached a level of approximately 0.015 in. above the boiling surface where the increments were decreased to half or quarter turns depending on the severity of the temperature gradient in the liquid. At each probe position the temperature fluctuations were recorded on a recording potentiometer for approximately 1 min. For the tests in which probe traverses at different levels of subcooling were required, the first traverse was taken with the water boiling under saturated conditions. Following this, the maximum subcooling condition was established after which two intermediate subcooling conditions were established. The test was ended by allowing the system to regain the saturated boiling condition.

The frequency and amplitude of the probe thermocouple signal made it difficult to determine a mean value for a given probe setting. A planimeter was used to determine the area under a representative length of trace so that an average value could be calculated. In general, a planimeter traverse was taken twice over a given area to assure reproducibility.

Experimental Results

Fig. 2 shows a plot of heat flux Q/A as a function of surface superheat ($T_w - T_{sat}$) for saturated nucleate boiling and compares the results of the present investigation with those of Marcus and Dropkin [3], Lippert and Dougall [4], and Bobst and Colver [5] who have reported measurements of superheat layer thickness for saturated boiling water. The two data points for each heat flux were taken at the beginning and conclusion of each test in which subcooling had been varied. The two data points are nearly coincident, which is indicative that the boiling conditions had not been changed appreciably by a sequence of changes in subcooling. One striking feature of this plot is that the results for all four investigations of water boiling on a copper surface are nearly coincident; more will be made of this observation later on.

Fig. 3 is a plot of wall superheat ($T_w - T_{sat}$) as a function of bulk liquid subcooling ($T_{sat} - T_\infty$) at constant heat flux Q/A in which the results of Merte and Clark [9] for water boiling on a chromium-plated copper surface and Rallis, Greenland, and Kok [10] for water boiling on a horizontal nickel wire are shown for comparison. Observe the initial increase in superheat and the asymptotic approach to the natural convection condition expressed by the relationship

$$\mathrm{Nu} = 0.16(\mathrm{Gr}\ \mathrm{Pr})^{1/3} \tag{1}$$

which under constant heat flux conditions yields the family of straight lines

$$(T_w - T_{sat}) + (T_{sat} - T_\infty) = \text{constant} \tag{2}$$

Although it would appear as if the curve for $Q/A = 20{,}000$ Btu/hr-ft² had nearly attained the natural convection condition, observation of the phenomenon at $(T_{sat} - T_\infty) = 52$ deg F indicated that boiling had not been completely suppressed. The curves in Fig. 3 demonstrate why it has often been claimed that nucleate boiling is insensitive to variation in the level of subcooling, although it is apparent that this is not strictly correct.

Fig. 4 depicts the temperature profiles obtained under incipient boiling conditions. Fig. 5 illustrates the boiling temperature profiles as a function of subcooling at 20,000, 50,000, and 100,000 Btu/hr-ft² nominal heat flux. As explained previously, each of the data points represents the numerical average of the temperature fluctuations measured by the thermocouple probe over the interval during which the probe was held stationary. In both of the figures, the vertical bars associated with each data point indicate the amplitude of the temperature fluctuations. The data points plotted at either edge of the figure and designated T_w and T_∞ are the temperatures obtained by extrapolation of the measurements of the thermocouples in the neck of the copper heater block and the bulk liquid thermocouples located above the heating surface respectively. It can be seen that the temperature profiles based upon the measurements of the thermocouple probe extrapolate to these values quite reasonably, giving confidence in the measuring system and technique for reducing the data.

Discussion

All the measured temperature profiles in the liquid adjacent to the boiling surface appear to be characterized by a linear portion immediately above the boiling surface as seen in Figs. 4 and 5. This feature is most readily seen in the profiles taken at the

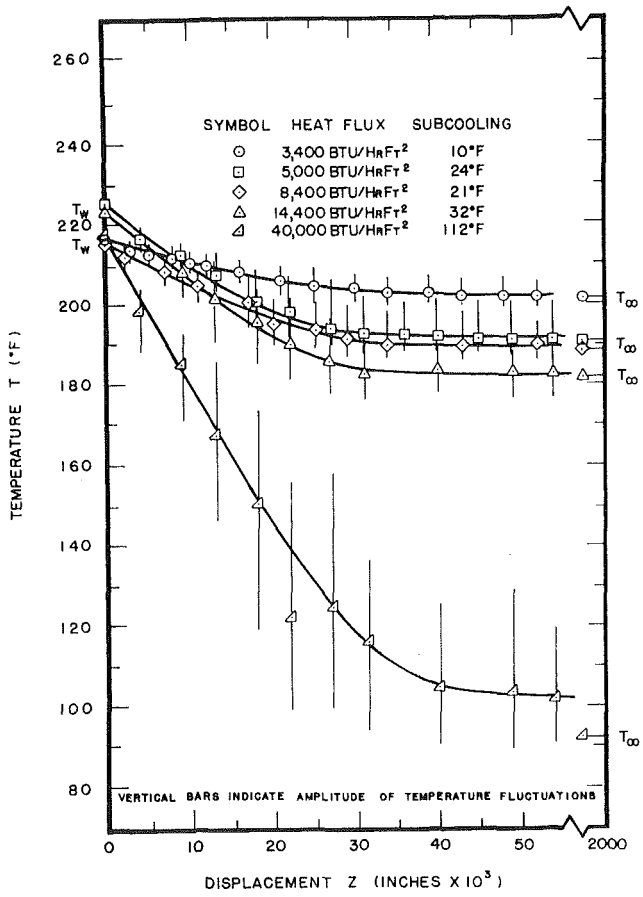

Fig. 4 Temperature profiles at incipient boiling condition

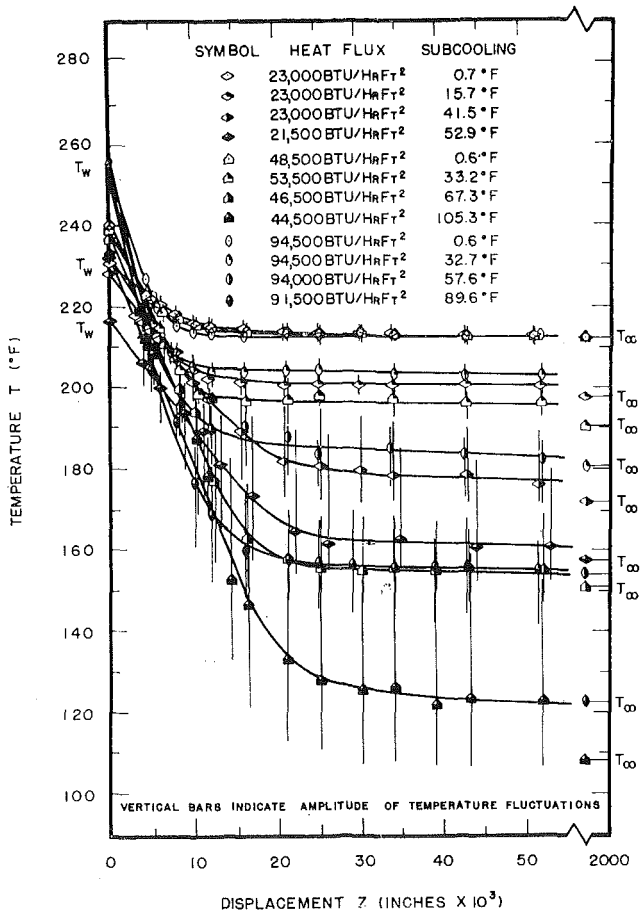

Fig. 5 Temperature profiles at various saturated and subcooled boiling conditions

incipience of boiling where the temperature gradient in the liquid near the surface has the lowest value. Marcus and Dropkin and Lippert and Dougall have indicated that the linear portion of the temperature profile extends to the surface. On this basis, the measured profiles have also been extended to the surface temperature value determined by extrapolating the axial temperature gradient in the neck of the heating block. A significant observation to be made from the temperature profiles is that the amplitudes of the temperature fluctuations appear to reach a maximum at approximately the same distance from the surface that the mean temperature asymptotically approaches the bulk temperature. The temperature fluctuations decrease to a minimum near the surface, supporting Marcus and Dropkin's observation that the surface acts as a "smoothing agent" inhibiting agitation of the liquid.

It is important to define the superheat layer thickness since the present study was undertaken to investigate the variation of this parameter with heat flux and subcooling. Yamagata et al. [11] have defined the "thermal boundary layer thickness" ξ as the height above the surface beyond which the average bulk liquid temperature is uniform. As Marcus and Dropkin have already pointed out, it is difficult to say at exactly what height this condition is attained. However, the region of high liquid superheat extends only a few hundredths of an inch from the surface, considerably less than the thickness ξ as defined by Yamagata. The region of high liquid superheat influences nucleation and bubble dynamics to a large degree and hence it is felt that Yamagata's definition does not sufficiently reflect the importance of the superheat layer.

Marcus and Dropkin [3] have introduced a more representative value for superheat layer thickness. Assuming that the temperature distribution closest to the surface is of greatest importance, a thickness δ can be defined as the height of the intersection between the tangent to the temperature profile at the surface and the constant liquid bulk temperature line. The tangent line which defines δ is actually an extrapolation of the linear portion of the temperature distribution to the bulk liquid temperature. Hence, the parameter δ is called the "extrapolated superheat layer thickness." It is felt that this definition of the superheat layer thickness closely reflects the thickness of the superheat region of the thermal boundary layer and consequently δ was used in the following analysis.

Direct evidence supporting the model for bubble nucleation postulated by Hsu [2] was obtained from the incipient boiling results. Hsu was only able to indicate the validity of the model he proposed indirectly by showing that the data existent at the time did not conflict with the model, because independent measurements of superheat layer thickness were lacking. A short review of the model follows.

Hsu postulated that at the beginning of a cycle of bubble emission, relatively cool bulk liquid at temperature T_∞ surrounded the nucleus at an active site. This cool liquid had replaced the liquid displaced by the previous bubble. As time progressed, the cool liquid was heated by transient conduction and its energy content increased. The thickness of the liquid layer heated in this way increased with time but not without limit, in as much as the ultimate thermal layer thickness was governed by eddy diffusivity and turbulence which tended to hold the temperature constant at the bulk temperature T_∞ beyond a certain distance from the surface. Hsu then postulated the nucleus would not grow until the temperature of the surrounding liquid was such that a heat balance on the nucleus produced a net inflow of heat. When the thermal layer had grown to such an extent that this condition was satisfied, the nucleus would begin to grow.

Using this model Hsu developed an equation to predict the

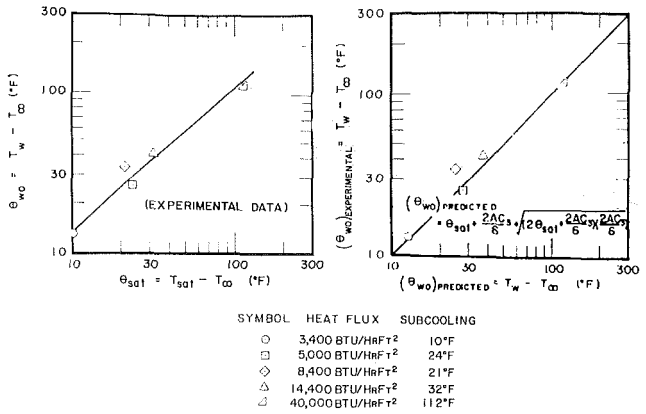

Fig. 6 (a) (left) Incipient boiling heat transfer data; (b) (right) correlation of incipient boiling heat transfer data

maximum and minimum radius for active cavities. For the case of constant surface temperature

$$r_{c_{\max}}^{c_{\min}} = \frac{\delta}{2C_1}\left[1 - \frac{\theta_{sat}}{\theta_w} \pm \sqrt{\left(1 - \frac{\theta_{sat}}{\theta_w}\right)^2 - \frac{4AC_3}{\delta\theta_w}}\right] \quad (3)$$

Hsu explained that although it was necessary that $r_{c_{\min}} < r_c < r_{c_{\max}}$ for a cavity to be active, this condition was not a sufficient condition. In the case of two cavities, both with favorable geometry located close to each other, the one with the shorter bubble emission cycle would be the active site. Hence, equation (3) cannot be used to predict the total number of active sites even if the cavity size distribution for a surface were known, as all the sites within the range $r_{c_{\min}} < r_c < r_{c_{\max}}$ are not necessarily active. From equation (3) Hsu derived a relationship for the incipience of boiling

$$\theta_{wo} = \theta_{sat} + \frac{2AC_3}{\delta} + \sqrt{\left(2\theta_{sat} + \frac{2AC_3}{\delta}\right)\left(\frac{2AC_3}{\delta}\right)} \quad (4)$$

An important parameter in equations (3) and (4) is δ, the limiting thermal layer thickness, defined in the same manner as the extrapolated superheat layer thickness.

One way in which the Hsu model can be tested is to evaluate equation (4) using incipient boiling conditions. At this condition, only one cavity is active and for this reason, cavity size does not appear in equation (4).

Hsu used equation (4) to compute δ from experimental data for incipient boiling, and having obtained a numerical value, proceeded by assuming it did not change with heat flux. Using this assumption, Hsu was able to demonstrate that equation (4) predicts the incipience of boiling for a wide range of bulk liquid subcooling and pressure.

With the incipient boiling results of the present investigation available, it is no longer necessary to proceed in this manner. Fig. 6(*a*) presents the incipient boiling heat transfer data in a plot of the temperature difference at which incipient boiling occurred θ_{wo} as a function of the subcooling θ_{sat}; Fig. 6(*b*) shows that $(\theta_{wo})_{experimental}$ is in excellent agreement with $(\theta_{wo})_{predicted}$, thereby demonstrating the validity of the Hsu model for bubble nucleation.

As reported in references [3–6], the present work confirms that the extrapolated superheat layer thickness is a function of heat flux. The saturated boiling temperature distributions of Fig. 5 indicate that δ decreases with increasing heat flux. For a fourfold increase in heat flux, δ decreases by approximately one-half. The influence of increasing levels of subcooling on δ is noticed to have a reverse effect. Both of these trends are thought to be a direct result of the degree of turbulence in the bulk liquid. In the saturated boiling case, an increase in heat flux results in more vigorous boiling. More bubbles are emitted from the surface

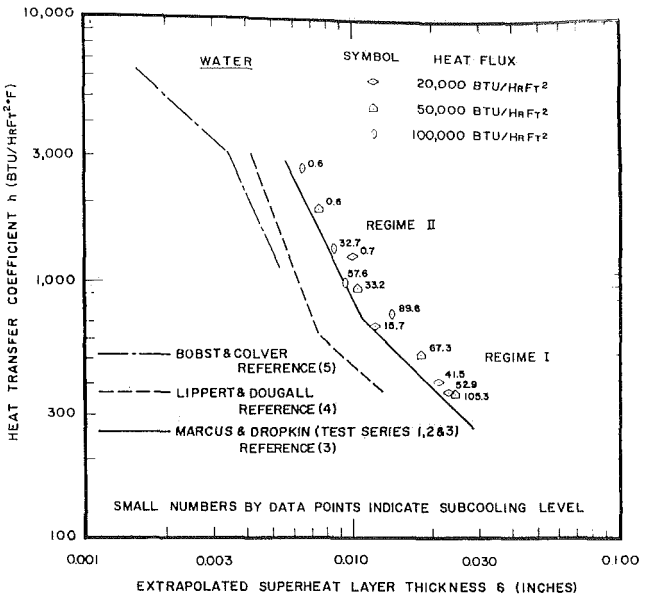

Fig. 7 Superheat layer thickness correlation for water

per unit area per unit time causing greater mixing, resulting in the establishment of a thinner extrapolated superheat layer thickness. The effect of varying the level of subcooling can be explained in a similar manner. It was observed that in the case of boiling with a highly subcooled bulk liquid, fewer smaller bubbles left the boiling surface per unit time per unit area than in the case of saturated boiling. It is reasonable to assume then that by suppressing bubble growth and departure with bulk subcooling, the bulk turbulence and mixing is also suppressed, resulting in the establishment of a thicker extrapolated superheat layer thickness.

Marcus and Dropkin [3] have reported a relationship between heat transfer coefficient h and extrapolated superheat layer thickness δ. In Fig. 7 all the experimental data for the present work have been plotted in a similar manner. In as much as the present work presents both saturated and subcooled boiling data, the heat transfer coefficient was computed by

$$h = \frac{Q/A}{(T_w - T_\infty)} \quad (5)$$

and the extrapolated superheat layer thickness was calculated by

$$\delta = \frac{(T_w - T_\infty)}{(dT/dZ)_{Z=0}} \quad (6)$$

to accommodate both types of data. It can be seen that Marcus and Dropkin's correlations for the discrete bubble regime (Regime I) in which δ varied with h^{-1} and the bubble transition regime (Regime II) in which δ varied with $h^{-1/2}$ also correlate the results of the present investigation satisfactorily.

When comparing the data of Marcus and Dropkin with the present work, it is important to recall that the heater surfaces were different. Nevertheless, it has been shown in Fig. 2 that the two investigations yielded nearly identical heat flux–superheat characteristics and Fig. 7 shows excellent agreement of the results. It would seem that the two investigations resulted in nearly identical heat transfer processes and that the levels of agitation within the thermal boundary layer were much the same. The experimental investigations of Lippert and Dougall and Bobst and Colver were seen to have produced the same heat flux–superheat characteristics as well, but the correlations of heat transfer coefficient with extrapolated superheat layer thickness do not agree, as seen in Fig. 7. These investigations have resulted in significantly thinner thermal layers, presumably as

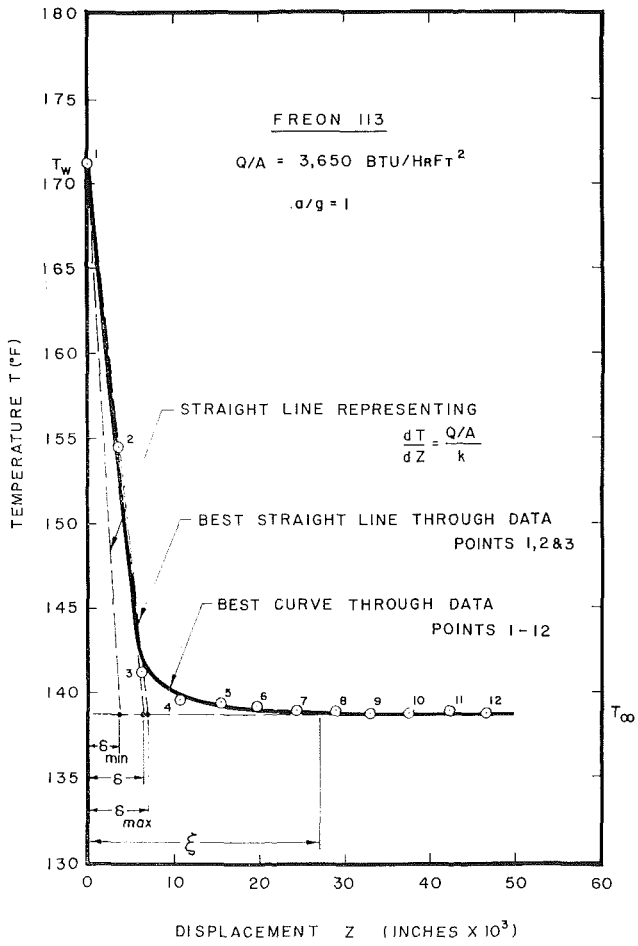

Fig. 8 Representative saturated boiling temperature profile

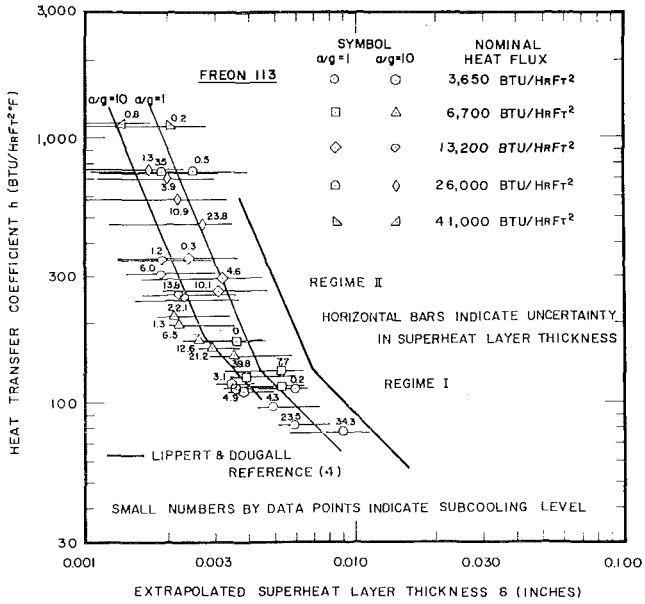

Fig. 9 Superheat layer thickness correlation for Freon-113

the result of greater agitation resulting from the generation of greater numbers of bubbles per unit area per unit time. This explanation is admittedly conjectural in as much as its proof requires information concerning the active site density, frequency of bubble emission, and bubble growth characteristics which is lacking for water boiling on a solid surface.

The fact that plotting heat transfer coefficient h against extrapolated superheat layer thickness δ seems to draw all the data together irrespective of the level of heat flux or subcooling, would indicate that the mechanism of nucleate boiling heat transfer responds to an increase in subcooling at constant heat flux in the same manner that it responds to a decrease in heat flux under saturated conditions. In other words, the variation of these parameters independently must bring about similar boiling conditions (similar bubble flux densities). This hypothesis is investigated by an analysis of saturated and subcooled boiling Freon-113 data reported in reference [6] for which temperature profiles, active site density data, and bubble frequency measurements were reported as a function of heat flux Q/A and two levels of acceleration a/g.[3]

An example of the temperature profiles presented in reference [6] is shown in Fig. 8 in order to explain the origin of the rather large uncertainty which accompanies the extrapolated superheat layer thickness data derived from them. Because of the extremely thin superheat layer, it was only possible to obtain one or two data points within the region of high superheat, since the microthermocouple junction in the 0.001-in-dia thermocouple was of the order of 0.003 in. in diameter. As a consequence, the value of the extrapolated superheat layer thickness δ is somewhat in doubt although there is considerably less uncertainty concerning the value of the thermal boundary layer thickness ξ. In the analysis which follows, bars have been placed on the data points to indicate the magnitude of this uncertainty; the lowest estimate δ_{min} is determined from the intersection with the straight line expressing the Fourier conduction law, whereas the highest estimate δ_{max} is determined from the intersection with the best straight line through the data points in the region of high superheat.

The heat transfer coefficient–extrapolated superheat layer thickness correlation is shown in Fig. 9 in which Lippert and Dougall's plot has been included for comparison. Similar to the water data, it can be seen that this treatment of the data draws saturated and subcooled boiling results together at constant acceleration, although the influence of increasing acceleration is seen to decrease the extrapolated superheat layer thickness and to increase the heat transfer coefficient at which the transition from Regime I to Regime II occurs.

A positive correlation of extrapolated superheat layer thickness δ and thermal boundary layer thickness ξ with bubble flux density $(N/A)f$ is demonstrated in Fig. 10. The variation of extrapolated superheat layer thickness with bubble flux density seems to parallel that of thermal boundary layer thickness, although it is not possible to state this observation conclusively because of the relatively large uncertainty in the extrapolated superheat layer thickness data. However, if it is assumed that extrapolated superheat layer thickness and thermal boundary layer thickness vary similarly with bubble flux density, then

$$\delta \alpha [(N/A)f]^{-1/2} \qquad \text{(Regime I)} \tag{7}$$

for values of $(N/A)f$ less than 55×10^3 bubbles/in.^{2}-sec and

$$\delta \alpha [(N/A)f]^{-1/3} \qquad \text{(Regime II)} \tag{8}$$

for values of $(N/A)f$ greater than 55×10^3 bubbles/in.^{2}-sec. Given that

$$\frac{Q}{A} = k_{eff} \left[\frac{dT}{dZ}\right]_{Z=0} \tag{9}$$

where k_{eff} has been used to denote that the rate of heat transfer is greater than that due to the mechanism of conduction, then making use of equation (6)

$$\frac{Q}{A} \alpha [(N/A)f]^{1/2}(T_w - T_\infty) \qquad \text{(Regime I)} \tag{10}$$

[3] Some additional temperature profiles not reported in reference [6] were included in this analysis.

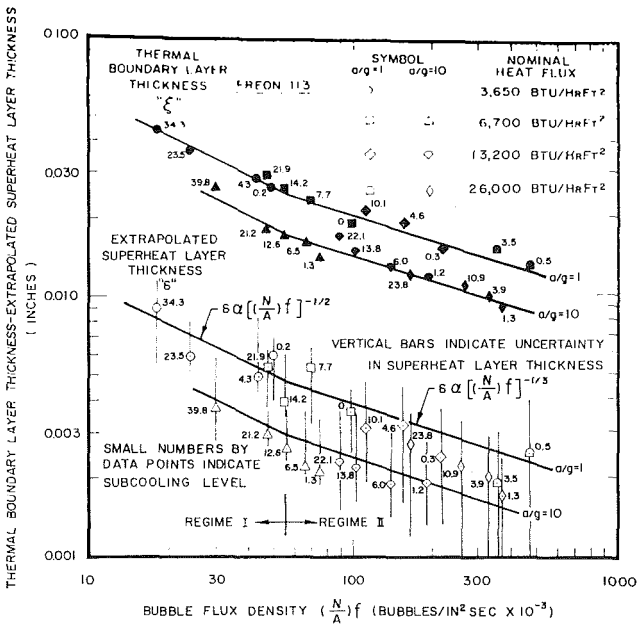

Fig. 10 Correlation of boundary layer thickness and superheat layer thickness with bubble flux density

$$\frac{Q}{A} \alpha [(N/A)f]^{1/3}(T_w - T_\infty) \qquad \text{(Regime II)} \qquad (11)$$

Under saturated boiling conditions, it is shown in reference [6] that the frequency of bubble emission f is nearly insensitive to variation in $(T_w - T_\infty)$ and (N/A) so that equation (10) and equation (11) reduce to the form

$$\frac{Q}{A} = a(N/A)^b(T_w - T_{sat})^c \qquad (12)$$

which has been advocated by a number of investigators as an appropriate form of correlation for saturated nucleate boiling results.

Conclusions

This study presents a comprehensive set of measurements for water boiling on a copper heating surface resulting in temperature profiles in the liquid adjacent to the heating surface for incipient boiling conditions and for various combinations of heat flux and subcooling. To the authors' knowledge, little of the information has been reported in the literature previously. The temperature profiles obtained enabled the extrapolated superheat layer thickness to be evaluated.

The values obtained for the incipient boiling condition lend support to Hsu's mathematical model for bubble nucleation. Increasing heat flux and decreasing subcooling has the effect of reducing the extrapolated superheat layer thickness. The results of the present investigation indicate that saturated and subcooled boiling results can be drawn together in a correlation of heat transfer coefficient with extrapolated superheat layer thickness. The fact that such a correlation is possible suggests that similar boiling conditions can be brought about by independent changes in heat flux or subcooling.

Analysis of some data for Freon-113 boiling on a glass surface indicated that the extrapolated superheat layer thickness is governed by the bubble flux density for the particular test condition, irrespective of whether the result was achieved by varying heat flux or subcooling.

Acknowledgment

The support of the National Research Council of Canada through Grant A4362 is gratefully acknowledged.

References

1 Judd, R. L., and Merte, H., Jr., "Influence of Acceleration on Subcooled Nucleate Pool Boiling," *Fourth International Heat Transfer Conference*, Paris-Versailles, 1970.

2 Hsu, Y. Y., "On the Size Range of Active Nucleation Cavities on a Heating Surface," JOURNAL OF HEAT TRANSFER, TRANS. ASME, Series C, Vol. 84, No. 3, Aug. 1962, pp. 207–216.

3 Marcus, B. D., and Dropkin, D., "Measured Temperature Profiles Within the Superheated Boundary Layer Above a Horizontal Surface in Saturated Nucleate Pool Boiling of Water," JOURNAL OF HEAT TRANSFER, TRANS. ASME, Series C, Vol. 87, No. 3, Aug. 1965, pp. 333–341.

4 Lippert, T. E., and Dougall, R. S., "A Study of the Temperature Profiles Measured in the Thermal Sublayer of Water, Freon-113, and Methyl Alcohol During Pool Boiling," JOURNAL OF HEAT TRANSFER, TRANS. ASME, Series C, Vol. 90, No. 3, Aug. 1968, pp. 347–352.

5 Bobst, R. W., and Colver, C. P., "Temperature Profiles up to Burnout Adjacent to a Horizontal Heating Surface in Nucleate Pool Boiling Water," *Chem. Eng. Prog. Sym. Series*, Vol. 64, No. 82, 1968.

6 Judd, R. L., "Influence of Acceleration on Subcooled Nucleate Boiling." PhD thesis, University of Michigan, University Microfilms Inc. #69-12148.

7 Gelb, G. H., Marcus, B. D., and Dropkin, D., "On the Manufacture of Fine Wire Thermocouple Probes," *Review of Scientific Instruments*, Vol. 35, No. 1, 1964.

8 Gaertner, R. F., "Photographic Study of Nucleate Pool Boiling on a Horizontal Surface," JOURNAL OF HEAT TRANSFER, TRANS. ASME, Series C, Vol. 87, No. 1, Feb. 1965, pp. 17–29.

9 Merte, H., Jr., and Clark, J. A., "Pool Boiling in an Accelerating System," JOURNAL OF HEAT TRANSFER, TRANS. ASME, Series C, Vol. 83, No. 3, Aug. 1961, pp. 233–242.

10 Rallis, C. J., Greenland, R. V., and Kok, A., "Stagnant Pool Nucleate Boiling from Horizontal Wires under Saturated and Subcooled Conditions," *South African Mechanical Engineer*, Vol. 10, No. 1, 1961.

11 Yamagata, K., Hirono, R., Nishikawa, R., and Matsuoka, H., "Nucleate Boiling of Water on the Horizontal Heating Surface," *Mem. Faculty of Engineering Kyushu*, Vol. 15, No. 1, 1955.

journal of heat transfer

technical briefs

This section consists of contributions of 1500 words or less (about 2½ double-spaced typewritten papes, including figures). Technical Briefs will be reviewed and approved by the specific Division's reviewing committee prior to publication. After approval such contributions will be published as soon as possible, normally in the next issue of the Journal.

Optimum Spacing of Fins Cooled by Free Convection

NANCY D. FITZROY[1]

Nomenclature

$c_{p,f}$ = specific heat of fluid, Btu/lb-deg F, evaluated at film temperature, t_f

g = acceleration due to gravity, 4.17×10^8 ft/hr²

h_d = average heat-transfer coefficient for inner surfaces at surface spacing d, Btu/(hr-ft²-deg F)

h_∞ = average heat-transfer coefficient for a single vertical plate remote from any other surface, Btu/(hr-ft²-deg F)

k_f = thermal conductivity, Btu/(hr-ft²-deg F), evaluated at film temperature, t_f

t = temperature, deg F

Δt = temperature difference between surface and ambient $(t_s - t_a)$, deg F

β_a = volumetric expansion coefficient, $(1/T$ for perfect gases), 1/deg R, evaluated at ambient temperature, $T_a = t_a + 460$

ρ_f = density of fluid, lb/ft³, evaluated at film temperature, t_f

μ_f = viscosity of fluid, lb/(ft-hr), evaluated at film temperature, t_f

Subscripts

m = at point of maximum heat transfer

Results for determining the optimum spacing of a set of parallel vertical fins dissipating heat by free convection in the laminar flow regime are presented. These are based on combining the correlation of Elenbaas [1][2] for spaced fins and that of McAdams [2] for a single vertical plate. Details of the analysis are given in reference [3].

By evaluating properties at a mean film temperature, Elenbaas' results (converted to the above notation) can be correlated by:

$$\frac{h_d H}{k} = \frac{1}{24}\,\frac{F^4}{(d/H)}\,[1 - e^{-24/(1.68F^3)}] \qquad (1a)$$

where

$$F = (d/H)(N_{\mathrm{Gr,H}} N_{\mathrm{Pr}})^{1/4} \qquad (1b)$$

and d/H and $N_{\mathrm{Gr,H}} N_{\mathrm{Pr}}$ are as defined in Fig. 1.

McAdams, for a single vertical fin, gives

$$\frac{h_\infty H}{k_f} = 0.59(N_{\mathrm{Gr,H}} N_{\mathrm{Pr}})_f^{1/4} \qquad (2)$$

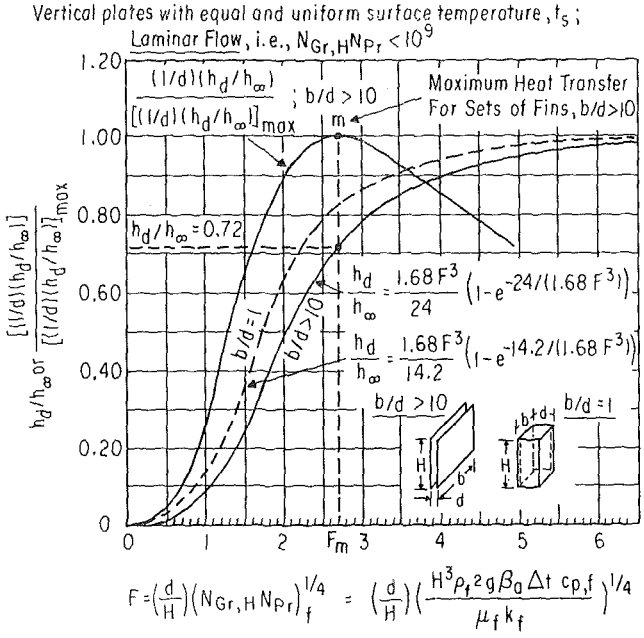

Fig. 1 Free-convection heat transfer from finned surfaces—proximity effect and maximum heat transfer

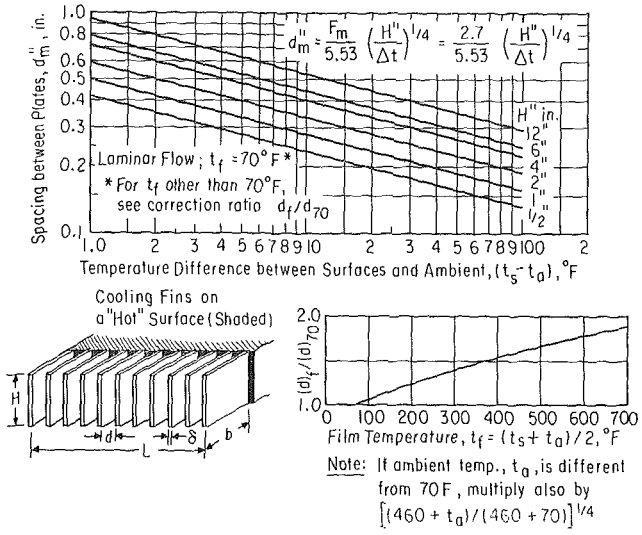

Fig. 2 Spacing for vertical fins in air for maximum total heat transfer

The ratio of h_d/h_∞ then becomes

$$\frac{h_d}{h_\infty} = \frac{1.68}{24} F^3[1 - e^{-24/(1.68F^3)}] \qquad (3)$$

where F is given above.

[1] Heat Transfer Engineer, Corporate Research and Development, General Electric Co., Schenectady, N. Y. Mem. ASME.

[2] Numbers in brackets designate References at end of technical brief.

Contributed by the Heat Transfer Division of The American Society of Mechanical Engineers. Manuscript received by the Heat Transfer Division February 17, 1971.

The ratio h_d/h_∞ is plotted in Fig. 1 (along with a similar ratio for square vertical ducts).

Since the number of fins, and hence the total finned area, which can be placed on a surface is inversely proportional to the fin spacing d, the optimum spacing (neglecting the fin-thickness effects on fin spacing and on fin effectiveness) can be determined by the ratio

$$\frac{(1/d)(h_d/h_\infty)}{(1/d)(h_d/h_\infty)_{\max}} \tag{4}$$

which is also shown in Fig. 1. The optimum spacing for infinite vertical plates of height H occurs at $F_m = 2.7$ where $h_d/h_\infty = 0.72$.

Fig. 2 gives the same results in dimensional form for air. The best spacing for maximum heat transfer (d_m'', in.) can be read as a function of fin height (H'', in.) and temperature rise of the fin over air temperature in degrees Fahrenheit, ($t_s - t_a$, deg F).

References

1 Elenbaas, W., "The Dissipation of Heat By Free Convection from the Inner Surfaces of Vertical Tubes of Different Shapes of Cross Section," *Physica*, Vol. 9, No. 8, Sept. 1942, pp. 865–874.

2 McAdams, W. H., *Heat Transmission*, 3rd ed., McGraw-Hill, New York N. Y., 1954.

3 Fitzroy, N. D., "A Simplified Design Procedure for Optimizing Fin Spacing of Extended Surfaces in Free Convection," ASHRAE Bulletin "Design and Optimization of Extended Surface Heat Exchangers," ASHRAE, New York, N. Y., July 1970, pp. 5–10.

Optimum Plate Spacings for Laminar Natural Convection Heat Transfer From Parallel Vertical Isothermal Flat Plates

E. K. LEVY[1]

The problem of determining the optimum spacings between parallel vertical isothermal flat plates which are dissipating heat by natural convection to the environment is discussed. One optimum, first suggested by experimental data of Elenbaas with air and later derived theoretically by Bodoia, corresponds to the spacing between parallel vertical plates attached to a surface which will permit the maximum rate of heat transfer from that surface. A different optimum is derived in this paper which for a given heat flux gives the minimum plate spacing required to minimize the temperature difference between the plates and the fluid. The minimum temperature difference is shown to occur when the plate spacing is made sufficiently large that the wall boundary layers do not merge. It is shown that Elenbaas' optimum, although requiring a plate spacing only 54 percent of that for minimum ΔT, produces a temperature difference which is 38 percent higher than the minimum.

Nomenclature

- a = one-half the plate spacing
- b = plate spacing
- C_p = constant pressure specific heat
- g = acceleration due to gravity
- Gr = Grashof number $\left[\mathrm{Gr} = \frac{g\beta\Delta T b^3}{\nu^2}\right]$
- $\bar{h}$ = average heat transfer coefficient
- k = thermal conductivity

[1] Assistant Professor, Department of Mechanical Engineering and Mechanics, Lehigh University, Bethlehem, Pa., Assoc. Mem. ASME.

Contributed by the Heat Transfer Division of THE AMERICAN SOCIETY OF MECHANICAL ENGINEERS. Manuscript received by the Heat Transfer Division October 26, 1970.

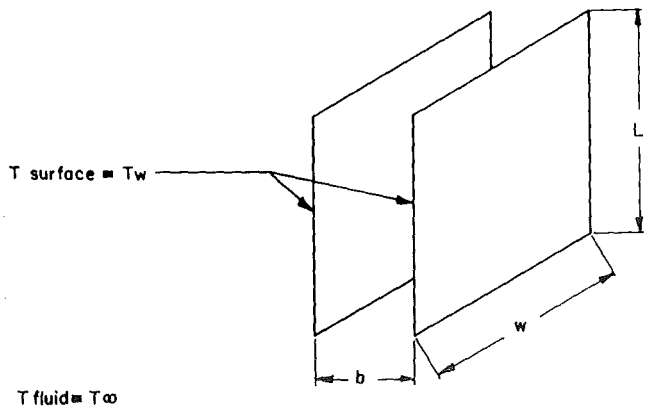

Fig. 1 A pair of vertical parallel plates

- L = height of plate
- $\overline{\mathrm{Nu}}$ = average Nusselt number $\left[\overline{\mathrm{Nu}} = \frac{\bar{h}b}{k}\right]$
- Pr = Prandtl number $\left[\mathrm{Pr} = \frac{\mu C_p}{k}\right]$
- Q = heat transfer rate
- T_w = wall temperature
- T_∞ = temperature of fluid before it enters the channel
- ΔT = $T_W - T_\infty$
- ΔT_T = minimum temperature difference
- w = width of plate
- β = coefficient of thermal expansion
- η = $\mathrm{Gr}\ \mathrm{Pr}\ \frac{b}{L}$
- μ = absolute viscosity
- ν = kinematic viscosity

Introduction

ALTHOUGH the information available in the literature on laminar natural convection heat transfer from parallel vertical flat plates is somewhat limited and incomplete, it is still useful for indicating the directions which one should follow in designing a natural convection system. The purpose of this paper is to review that portion of the existing literature which is concerned with optimizing the spacing between the plates and to derive a criterion for the minimum plate spacing which for a given rate of heat transfer will give a minimum difference in temperature between the plates and the fluid.

Survey of the Literature

The earliest and most widely referenced study is an experimental investigation by Elenbaas [1, 2][2] of the natural convection heat transfer from isothermal parallel vertical flat plates. These experiments were performed with pairs of square plates in air (Fig. 1) and the data shown in Fig. 2 are correlated by the functional relation

$$\overline{\mathrm{Nu}} = f(\eta) \tag{1}$$

with $\eta = \frac{b}{L}\ \mathrm{Gr}\ \mathrm{Pr}$.

Elenbaas recommended that for the dissipation of the maximum amount of heat from the plate surfaces, the plate spacing be determined from the expression

$$\eta = \left[\frac{b}{L}\ \mathrm{Gr}\ \mathrm{Pr}\right] \approx 50 \tag{2}$$

Bodoia and Osterle [3, 4] obtained an analytical solution to the isothermal wall parallel vertical flat plate problem (their results

[2] Numbers in brackets designate References at end of technical brief.

The ratio h_d/h_∞ is plotted in Fig. 1 (along with a similar ratio for square vertical ducts).

Since the number of fins, and hence the total finned area, which can be placed on a surface is inversely proportional to the fin spacing d, the optimum spacing (neglecting the fin-thickness effects on fin spacing and on fin effectiveness) can be determined by the ratio

$$\frac{(1/d)(h_d/h_\infty)}{(1/d)(h_d/h_\infty)_{\max}} \tag{4}$$

which is also shown in Fig. 1. The optimum spacing for infinite vertical plates of height H occurs at $F_m = 2.7$ where $h_d/h_\infty = 0.72$.

Fig. 2 gives the same results in dimensional form for air. The best spacing for maximum heat transfer (d_m'', in.) can be read as a function of fin height (H'', in.) and temperature rise of the fin over air temperature in degrees Fahrenheit, ($t_s - t_a$, deg F).

References

1 Elenbaas, W., "The Dissipation of Heat By Free Convection from the Inner Surfaces of Vertical Tubes of Different Shapes of Cross Section," *Physica*, Vol. 9, No. 8, Sept. 1942, pp. 865–874.

2 McAdams, W. H., *Heat Transmission*, 3rd ed., McGraw-Hill, New York N. Y., 1954.

3 Fitzroy, N. D., "A Simplified Design Procedure for Optimizing Fin Spacing of Extended Surfaces in Free Convection," ASHRAE Bulletin "Design and Optimization of Extended Surface Heat Exchangers," ASHRAE, New York, N. Y., July 1970, pp. 5–10.

Optimum Plate Spacings for Laminar Natural Convection Heat Transfer From Parallel Vertical Isothermal Flat Plates

E. K. LEVY[1]

The problem of determining the optimum spacings between parallel vertical isothermal flat plates which are dissipating heat by natural convection to the environment is discussed. One optimum, first suggested by experimental data of Elenbaas with air and later derived theoretically by Bodoia, corresponds to the spacing between parallel vertical plates attached to a surface which will permit the maximum rate of heat transfer from that surface. A different optimum is derived in this paper which for a given heat flux gives the minimum plate spacing required to minimize the temperature difference between the plates and the fluid. The minimum temperature difference is shown to occur when the plate spacing is made sufficiently large that the wall boundary layers do not merge. It is shown that Elenbaas' optimum, although requiring a plate spacing only 54 percent of that for minimum ΔT, produces a temperature difference which is 38 percent higher than the minimum.

Nomenclature

a = one-half the plate spacing
b = plate spacing
C_p = constant pressure specific heat
g = acceleration due to gravity
Gr = Grashof number $\left[\mathrm{Gr} = \dfrac{g\beta\Delta T b^3}{\nu^2}\right]$
$\bar{h}$ = average heat transfer coefficient
k = thermal conductivity

[1] Assistant Professor, Department of Mechanical Engineering and Mechanics, Lehigh University, Bethlehem, Pa., Assoc. Mem. ASME.

Contributed by the Heat Transfer Division of THE AMERICAN SOCIETY OF MECHANICAL ENGINEERS. Manuscript received by the Heat Transfer Division October 26, 1970.

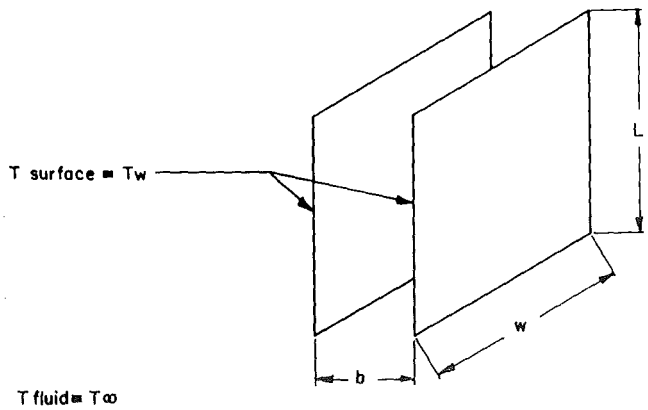

Fig. 1 A pair of vertical parallel plates

L = height of plate
$\overline{\mathrm{Nu}}$ = average Nusselt number $\left[\overline{\mathrm{Nu}} = \dfrac{\bar{h}b}{k}\right]$
Pr = Prandtl number $\left[\mathrm{Pr} = \dfrac{\mu C_p}{k}\right]$
Q = heat transfer rate
T_w = wall temperature
T_∞ = temperature of fluid before it enters the channel
ΔT = $T_W - T_\infty$
ΔT_T = minimum temperature difference
w = width of plate
β = coefficient of thermal expansion
η = $\mathrm{Gr}\ \mathrm{Pr}\ \dfrac{b}{L}$
μ = absolute viscosity
ν = kinematic viscosity

Introduction

ALTHOUGH the information available in the literature on laminar natural convection heat transfer from parallel vertical flat plates is somewhat limited and incomplete, it is still useful for indicating the directions which one should follow in designing a natural convection system. The purpose of this paper is to review that portion of the existing literature which is concerned with optimizing the spacing between the plates and to derive a criterion for the minimum plate spacing which for a given rate of heat transfer will give a minimum difference in temperature between the plates and the fluid.

Survey of the Literature

The earliest and most widely referenced study is an experimental investigation by Elenbaas [1, 2][2] of the natural convection heat transfer from isothermal parallel vertical flat plates. These experiments were performed with pairs of square plates in air (Fig. 1) and the data shown in Fig. 2 are correlated by the functional relation

$$\overline{\mathrm{Nu}} = f(\eta) \tag{1}$$

with $\eta = \dfrac{b}{L}\ \mathrm{Gr}\ \mathrm{Pr}$.

Elenbaas recommended that for the dissipation of the maximum amount of heat from the plate surfaces, the plate spacing be determined from the expression

$$\eta = \left[\frac{b}{L}\ \mathrm{Gr}\ \mathrm{Pr}\right] \approx 50 \tag{2}$$

Bodoia and Osterle [3, 4] obtained an analytical solution to the isothermal wall parallel vertical flat plate problem (their results

[2] Numbers in brackets designate References at end of technical brief.

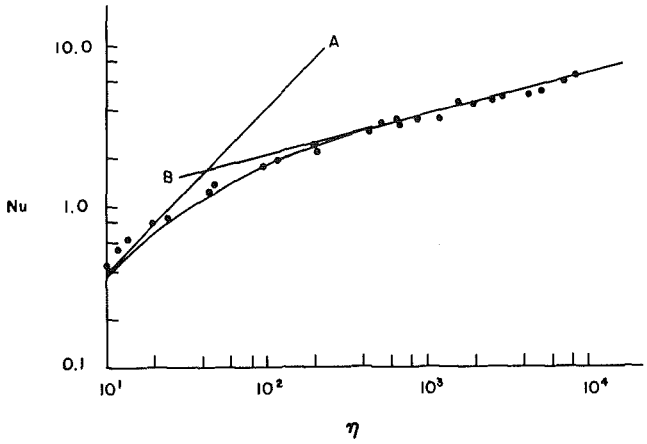

Fig. 2 Comparison of solution of Bodoia with data of Elenbaas; from [3]

are summarized for air in Fig. 2) and found that the solution approached two limits.

For small values of η (that is for small b/L), the flow will become fully developed before it reaches the top of the channel and the solution is of the form

$$\overline{\mathrm{Nu}} = \frac{\eta}{24} \tag{3}$$

(See curve A, Fig. 2.)

For large η (large plate spacings) the boundary layers do not meet and the solution tends to the form

$$\overline{\mathrm{Nu}} = f(\mathrm{Pr}) \times \eta^{1/4} \tag{4}$$

(curve B, Fig. 2).

This of course is the solution for a single isothermal vertical plate in an infinite fluid. From Fig. 2 the single plate limit is seen to be valid for values of η greater than approximately 600.

Starting from their numerical results Bodoia and Osterle were able to derive a criterion for the plate spacing (b) which offers the maximum heat dissipation for a heat exchanger of a fixed volume. They found that for this optimum case $\overline{\mathrm{Nu}} \sim \eta^{1/2}$, which for air corresponds to the point $\eta = 70$. This is close to the value of $\eta = 50$ obtained experimentally by Elenbaas. This particular criterion proposed by both Bodoia and Elenbaas corresponds to the physical problem of determining how many isothermal vertical fins should be attached to a surface of a given size in order to maximize the heat dissipation from that surface. However, in practice this is not the only design objective which one might encounter. For example, when designing a heat exchanger to cool electronic integrated circuit elements mounted on the surfaces of parallel vertical plates, one has not only the problem of dissipating the heat generated by the integrated circuit components but also of maintaining the integrated circuits below a certain critical temperature. In this case, the minimum plate spacing which for a given heat flux will minimize the ΔT between the plates and the fluid will be of interest.

In the present paper, the minimum plate spacing required for the minimum temperature difference is derived from the basic governing equations. As pointed out above, this is a fundamentally different optimum than the one determined by Elenbaas and Bodoia. A comparison of the resultant plate spacings and temperature differences is then made with those obtained from the criterion of Bodoia and Elenbaas.

Analysis

Consider two isothermal vertical parallel flat plates of width w, height L, and spacing b. The heat transfer from the two inside surfaces is

$$Q = 2Lw\bar{h}\Delta T \tag{5}$$

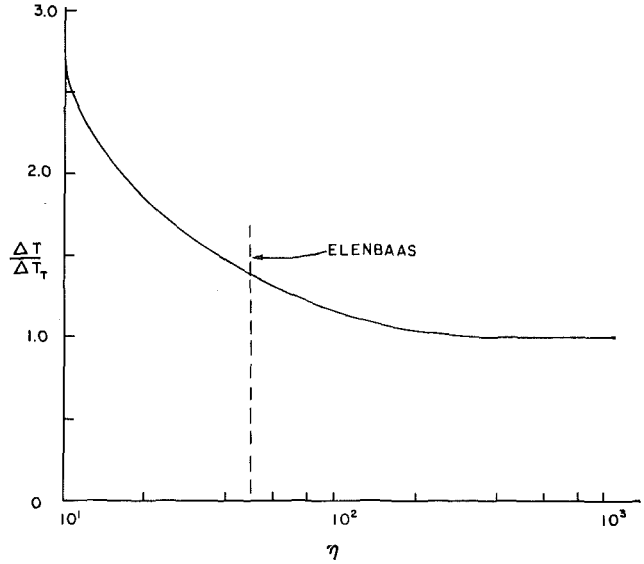

Fig. 3 Comparison of ΔT with ΔT_T for air

where the average film coefficient $\bar{h}$ is

$$\bar{h} = \frac{k}{b}\overline{\mathrm{Nu}}(\eta) \tag{6}$$

and

$$\Delta T = T_w - T_\infty$$

Eliminating $\bar{h}$ and rearranging one obtains

$$\Delta T = \gamma \frac{b}{\overline{\mathrm{Nu}}} \tag{7}$$

where $\gamma = Q/2Lwk$ is a constant.

Differentiating with respect to plate spacing b

$$\frac{\partial(\Delta T)}{\partial b} = \gamma\left\{\frac{1}{\overline{\mathrm{Nu}}} - \frac{b}{\overline{\mathrm{Nu}}^2}\frac{\partial\overline{\mathrm{Nu}}}{\partial b}\right\} \tag{8}$$

Now

$$\frac{\partial\overline{\mathrm{Nu}}}{\partial b} = \frac{\partial\overline{\mathrm{Nu}}}{\partial\eta}\frac{\partial\eta}{\partial b} \tag{9}$$

But

$$\eta = \frac{b}{L}\,\mathrm{Gr}\,\mathrm{Pr} = C\Delta T b^4 \tag{10}$$

where

$$C = \frac{g\beta\mathrm{Pr}}{\nu^2 L} = \text{constant}$$

Hence one can finally write

$$\frac{\partial\Delta T}{\partial b} = \gamma\left\{\frac{1}{\overline{\mathrm{Nu}}} - \frac{Cb}{\overline{\mathrm{Nu}}^2}\left(\frac{\partial\overline{\mathrm{Nu}}}{\partial\eta}\right)\left[\left(\frac{\partial\Delta T}{\partial b}\right)b^4 + 4b^3\Delta T\right]\right\} \tag{11}$$

To minimize ΔT set $\partial\Delta T/\partial b = 0$. Hence

$$0 = \overline{\mathrm{Nu}} - 4Cb^4\Delta T\frac{\partial\overline{\mathrm{Nu}}}{\partial\eta} \tag{12}$$

which leads to

$$\frac{d\overline{\mathrm{Nu}}}{\overline{\mathrm{Nu}}} = \frac{1}{4}\frac{d\eta}{\eta}$$

Integrating this, the criterion for minimum ΔT is obtained

$$\overline{\mathrm{Nu}} = C_1\eta^{1/4} \tag{13}$$

where C_1 is the constant of integration. Equation (13) is the same as the expression for a single vertical plate in an infinite fluid. This suggests that for minimum ΔT, the plate boundary layers must not merge. From Bodoia's analysis and from Fig. 2 this is the case for values of η approximately greater than 600. Therefore the minimum plate spacing for minimum plate temperature is obtained from the relation

$$\frac{b}{L}\,\mathrm{Gr}\,\mathrm{Pr} = 600 \tag{14}$$

For a given value of heat transfer Q, to determine how the temperature difference for an arbitrary plate spacing compares to that for minimum ΔT, one can write the expression for temperature difference in the following form

$$\Delta T = \frac{Q}{2Lwk}\frac{b}{\overline{\mathrm{Nu}}} \tag{15}$$

But

$$b = \left\{\frac{\eta}{\frac{g\beta\mathrm{Pr}}{\nu^2 L}\Delta T}\right\}^{1/4} \tag{16}$$

Eliminating b and solving for ΔT

$$\Delta T = \left\{\frac{Q}{2Lwk\left(\frac{g\beta\mathrm{Pr}}{\nu^2 L}\right)^{1/4}}\right\}^{4/5}\left\{\frac{\eta^{1/5}}{\overline{\mathrm{Nu}}^{4/5}}\right\} \tag{17}$$

If Q is treated as constant the ratio of the temperature difference for arbitrary b to that for minimum ΔT is

$$\frac{\Delta T}{\Delta T_T} = \left\{\frac{\eta}{\eta_T}\right\}^{1/5}\left\{\frac{\overline{\mathrm{Nu}}_T}{\overline{\mathrm{Nu}}}\right\}^{4/5} \tag{18}$$

where the subscript T denotes the minimum ΔT case.

Using the solution for $\overline{\mathrm{Nu}} = f(\eta)$ from Fig. 2 along with the condition that $\mathrm{Nu}_T = 3.35$ and $\eta_T = 600$, the parameter $\Delta T/\Delta T_T$ is plotted as a function of η in Fig. 3. It is seen that Elenbaas' optimum, the ΔT for the maximum Q case, yields a temperature difference which is 1.38 times ΔT_T.

The ratio of the plate spacings for the two optimums can be determined from the expression

$$\frac{b_Q}{b_T} = \left\{\frac{\eta_Q}{\eta_T}\right\}^{0.25} \tag{19}$$

where the subscript Q denotes the maximum Q case. Thus the minimum spacing required for minimum ΔT is 85 percent greater than that for maximum Q. In practice, due to the asymptotic nature of the solution in Fig. 3, it may be possible to reduce the spacing somewhat below the optimum (b_T) value without suffering a large increase in ΔT.

It should be noted that the aforementioned analysis assumes plates of large width w and thus does not account for fluid entrainment or leakage at the sides. Furthermore Bodoia assumed that uniform temperature and velocity profiles occur at the leading edge of the vertical channel. The uniform velocity profile boundary condition has been a source of some controversy in the literature [4]. This should not affect the conclusion that the minimum ΔT is obtained when the boundary layers do not merge; however, if the velocity boundary condition is greatly in error it may introduce some error in the numerical values shown in Fig. 3. The excellent agreement obtained between theory and experiment (Fig. 2) suggests that such an error might not be too serious.

Concluding Remarks

A criterion has been obtained which can be used to determine the minimum spacing between vertical isothermal parallel flat plates required for a minimum difference in temperature between the plates and the fluid. The differences between this particular optimum spacing and the plate spacing derived previously by Bodoia and Elenbaas for the maximum rate of heat dissipation from a surface are pointed out. It is shown that plate spacings smaller than the optimum value derived here produce temperature differences larger than the minimum. In particular the criterion first proposed by Elenbaas for optimum plate spacing produces a temperature difference which is 38 percent higher than the minimum.

Acknowledgment

The author is grateful to Dr. F. Howland, Dr. V. Holt, and Dr. B. Nevis of the Bell Telephone Laboratories for their suggestions and to the Bell Telephone Laboratories for supporting this study.

References

1 Elenbaas, W., "Heat Dissipation of Parallel Plates by Free Convection," *Physica*, Vol. 9, No. 1, Holland, 1942.

2 Kreith, F., *Principles of Heat Transfer*, International Textbook Co., 1965.

3 Bodoia, J. R., PhD thesis, Carnegie Institute of Technology.

4 Bodoia, J. R., and Osterle, J. F., "The Development of Free Convection Between Heated Vertical Plates," JOURNAL OF HEAT TRANSFER, TRANS. ASME, Series C, Vol. 84, No. 1, Feb. 1962, pp. 40–44.

High Sc Limit of Free Convection at a Vertical Plate With Uniform Flux Condition

JAN ROBERT SELMAN[1,2] and JOHN NEWMAN[1]

IN THE course of an investigation of mass transfer by free convection in electrolytic solutions [1, 2],[3] numerical solutions were obtained for the problem of laminar free convection heat (or mass) transfer to a vertical plate in the limit of very high Prandtl (or Schmidt) number. Free convection at a vertical plate under conditions of uniform temperature (or concentration) at the plate is treated extensively in standard textbooks [3]. The condition of uniform flux has been dealt with by Sparrow and Gregg [4] with the Prandtl number as a parameter. No solution is available in the literature for the case of infinitely high Prandtl (or Schmidt) number.

In the limit of high Prandtl numbers the equation of motion[4]

$$u\frac{\partial u}{\partial x} + v\frac{\partial u}{\partial y} = \nu\frac{\partial^2 u}{\partial y^2} + g\beta(t - t_\infty) \tag{1}$$

after being brought in the form

$$F''' + 4FF'' - 3F'F' + \theta = 0 \tag{2}$$

by the transformation [4]

[1] Inorganic Materials Research Division, Lawrence Radiation Laboratory, and Department of Chemical Engineering, University of California, Berkeley, Calif.

[2] Present address: Chemical Engineering Division, Argonne National Laboratory, Argonne, Ill.

[3] Numbers in brackets designate References at end of technical brief.

Contributed by the Heat Transfer Division of THE AMERICAN SOCIETY OF MECHANICAL ENGINEERS. Manuscript received by the Heat Transfer Division February 1, 1971.

[4] Notation is that of reference [4]. Note also that the transformed momentum equation (2*a*) given in reference [4] is in error (should be $+\theta$, not $-\theta$).

where C_1 is the constant of integration. Equation (13) is the same as the expression for a single vertical plate in an infinite fluid. This suggests that for minimum ΔT, the plate boundary layers must not merge. From Bodoia's analysis and from Fig. 2 this is the case for values of η approximately greater than 600. Therefore the minimum plate spacing for minimum plate temperature is obtained from the relation

$$\frac{b}{L}\,\mathrm{Gr}\,\mathrm{Pr} = 600 \tag{14}$$

For a given value of heat transfer Q, to determine how the temperature difference for an arbitrary plate spacing compares to that for minimum ΔT, one can write the expression for temperature difference in the following form

$$\Delta T = \frac{Q}{2Lwk}\frac{b}{\overline{\mathrm{Nu}}} \tag{15}$$

But

$$b = \left\{\frac{\eta}{\frac{g\beta\mathrm{Pr}}{\nu^2 L}\,\Delta T}\right\}^{1/4} \tag{16}$$

Eliminating b and solving for ΔT

$$\Delta T = \left\{\frac{Q}{2Lwk\left(\frac{g\beta\mathrm{Pr}}{\nu^2 L}\right)^{1/4}}\right\}^{4/5}\left\{\frac{\eta^{1/5}}{\overline{\mathrm{Nu}}^{4/5}}\right\} \tag{17}$$

If Q is treated as constant the ratio of the temperature difference for arbitrary b to that for minimum ΔT is

$$\frac{\Delta T}{\Delta T_T} = \left\{\frac{\eta}{\eta_T}\right\}^{1/5}\left\{\frac{\overline{\mathrm{Nu}}_T}{\overline{\mathrm{Nu}}}\right\}^{4/5} \tag{18}$$

where the subscript T denotes the minimum ΔT case.

Using the solution for $\overline{\mathrm{Nu}} = f(\eta)$ from Fig. 2 along with the condition that $\mathrm{Nu}_T = 3.35$ and $\eta_T = 600$, the parameter $\Delta T/\Delta T_T$ is plotted as a function of η in Fig. 3. It is seen that Elenbaas' optimum, the ΔT for the maximum Q case, yields a temperature difference which is 1.38 times ΔT_T.

The ratio of the plate spacings for the two optimums can be determined from the expression

$$\frac{b_Q}{b_T} = \left\{\frac{\eta_Q}{\eta_T}\right\}^{0.25} \tag{19}$$

where the subscript Q denotes the maximum Q case. Thus the minimum spacing required for minimum ΔT is 85 percent greater than that for maximum Q. In practice, due to the asymptotic nature of the solution in Fig. 3, it may be possible to reduce the spacing somewhat below the optimum (b_T) value without suffering a large increase in ΔT.

It should be noted that the aforementioned analysis assumes plates of large width w and thus does not account for fluid entrainment or leakage at the sides. Furthermore Bodoia assumed that uniform temperature and velocity profiles occur at the leading edge of the vertical channel. The uniform velocity profile boundary condition has been a source of some controversy in the literature [4]. This should not affect the conclusion that the minimum ΔT is obtained when the boundary layers do not merge; however, if the velocity boundary condition is greatly in error it may introduce some error in the numerical values shown in Fig. 3. The excellent agreement obtained between theory and experiment (Fig. 2) suggests that such an error might not be too serious.

Concluding Remarks

A criterion has been obtained which can be used to determine the minimum spacing between vertical isothermal parallel flat plates required for a minimum difference in temperature between the plates and the fluid. The differences between this particular optimum spacing and the plate spacing derived previously by Bodoia and Elenbaas for the maximum rate of heat dissipation from a surface are pointed out. It is shown that plate spacings smaller than the optimum value derived here produce temperature differences larger than the minimum. In particular the criterion first proposed by Elenbaas for optimum plate spacing produces a temperature difference which is 38 percent higher than the minimum.

Acknowledgment

The author is grateful to Dr. F. Howland, Dr. V. Holt, and Dr. B. Nevis of the Bell Telephone Laboratories for their suggestions and to the Bell Telephone Laboratories for supporting this study.

References

1 Elenbaas, W., "Heat Dissipation of Parallel Plates by Free Convection," *Physica*, Vol. 9, No. 1, Holland, 1942.

2 Kreith, F., *Principles of Heat Transfer*, International Textbook Co., 1965.

3 Bodoia, J. R., PhD thesis, Carnegie Institute of Technology.

4 Bodoia, J. R., and Osterle, J. F., "The Development of Free Convection Between Heated Vertical Plates," JOURNAL OF HEAT TRANSFER, TRANS. ASME, Series C, Vol. 84, No. 1, Feb. 1962, pp. 40–44.

High Sc Limit of Free Convection at a Vertical Plate With Uniform Flux Condition

JAN ROBERT SELMAN[1,2] and JOHN NEWMAN[1]

IN THE course of an investigation of mass transfer by free convection in electrolytic solutions [1, 2],[3] numerical solutions were obtained for the problem of laminar free convection heat (or mass) transfer to a vertical plate in the limit of very high Prandtl (or Schmidt) number. Free convection at a vertical plate under conditions of uniform temperature (or concentration) at the plate is treated extensively in standard textbooks [3]. The condition of uniform flux has been dealt with by Sparrow and Gregg [4] with the Prandtl number as a parameter. No solution is available in the literature for the case of infinitely high Prandtl (or Schmidt) number.

In the limit of high Prandtl numbers the equation of motion[4]

$$u\frac{\partial u}{\partial x} + v\frac{\partial u}{\partial y} = \nu\frac{\partial^2 u}{\partial y^2} + g\beta(t - t_\infty) \tag{1}$$

after being brought in the form

$$F''' + 4FF'' - 3F'F' + \theta = 0 \tag{2}$$

by the transformation [4]

[1] Inorganic Materials Research Division, Lawrence Radiation Laboratory, and Department of Chemical Engineering, University of California, Berkeley, Calif.

[2] Present address: Chemical Engineering Division, Argonne National Laboratory, Argonne, Ill.

[3] Numbers in brackets designate References at end of technical brief.

Contributed by the Heat Transfer Division of THE AMERICAN SOCIETY OF MECHANICAL ENGINEERS. Manuscript received by the Heat Transfer Division February 1, 1971.

[4] Notation is that of reference [4]. Note also that the transformed momentum equation (2*a*) given in reference [4] is in error (should be $+\theta$, not $-\theta$).

$$\eta = y\left(\frac{g\beta q}{5k\nu^2 x}\right)^{1/5}$$

$$F = \frac{\psi}{5x\nu}\left(\frac{5k\nu^2 x}{g\beta q}\right)^{1/5} \tag{3}$$

$$\theta = \frac{k(t_\infty - t)}{q}\left(\frac{g\beta q}{5k\nu^2 x}\right)^{1/5}$$

can be further simplified by stretching the variables

$$\zeta = \eta\,\mathrm{Pr}^{1/5}, \qquad f = F\,\mathrm{Pr}^{4/5}, \qquad \Theta = \theta\,\mathrm{Pr}^{1/5} \tag{4}$$

In the limit $\mathrm{Pr} \to \infty$ the inertial terms in

$$f''' + \frac{1}{\mathrm{Pr}}(4ff'' - 3f'f') + \Theta = 0 \tag{5}$$

become negligible, i.e., viscous friction alone balances the buoyancy force in the thin region where density variations occur. (In this and subsequent equations, primes denote differentiation with respect to ζ.)

The set of coupled equations

$$f''' + \Theta = 0 \tag{6}$$

i.e., the equation of motion, and

$$\Theta'' + 4f\Theta' - f'\Theta = 0 \tag{7}$$

i.e., the transformed thermal energy equation, have been solved with the boundary conditions:

$$\eta = 0, \qquad f = f' = 0, \qquad \Theta' = 1 \tag{8}$$

$$\eta = \infty, \qquad f'' = 0, \qquad \Theta = 0 \tag{9}$$

The boundary condition at $\eta = \infty$ corresponds to the matching condition for the inner region (the diffusion layer) in the first term of a singular perturbation expansion for large Schmidt numbers [5]. The inner region can be solved without treating the outer region. The equivalent problem in free convection to an isothermal plate has been solved by Le Fevre [6], Kuiken [7], and Roy [8].

The results of interest are the local temperature difference $t_\infty - t_0$ and the local shear stress τ_0 at the plate:

$$t_\infty - t_0 = \frac{q}{k}\left(\frac{5k^2\nu x}{g\beta q\rho C_p}\right)^{1/5}\Theta(0) \tag{10}$$

$$\tau_0 = -\frac{5\mu k x}{\rho C_p}\left(\frac{g\beta q\rho C_p}{5k^2\nu x}\right)^{3/5} f''(0) \tag{11}$$

The values of $\Theta(0)$ and $f''(0)$ are

$$\Theta(0) = -1.14747$$

$$f''(0) = 0.83789$$

Table 1 shows that these results are in good agreement with the trend of the values $\Theta(0)$ and $F''(0)$ reported by Sparrow and Gregg [4].

Table 1 Dimensionless temperature difference and shear stress as reported by Sparrow and Gregg [4] and in this work

Pr	$\theta(0)$	$\Theta(0)$	$F''(0)$	$f''(0)$	Ref.
0.1	−2.7507	−1.7356	1.6434	0.65425	4
1	−1.3574	−1.3574	0.72196	0.72196	4
10	−0.76746	−1.2163	0.30639	0.76962	4
100	−0.46566	−1.1697	0.12620	0.79628	4
∞		−1.14747		0.83789	1

References

1 Selman, Jan Robert, and Newman, John, "Migration in Supported Electrolyte Solutions with Free Convection," UCRL-20322, Oct. 1970.

2 Selman, Jan Robert, and Newman, John, "Free-Convection Mass Transfer with a Supporting Electrolyte," *Journal of the Electrochemical Society*, Vol. 118, 1971, pp. 1070–1078.

3 Schlichting, Hermann, *Boundary-Layer Theory*, 6th ed., McGraw-Hill, New York, N. Y., 1968, chap. 12, sec. h, "Thermal Boundary Layers in Natural Flow."

4 Sparrow, E. M., and Gregg, J. L., "Laminar Free Convection From a Vertical Plate With Uniform Surface Heat Flux," TRANS. ASME, Vol. 78, 1956, pp. 435–440.

5 Morgan, George W., and Warner, W. H., "On Heat Transfer in Laminar Boundary Layers at High Prandtl Number," *Journal of the Aeronautical Sciences*, Vol. 23, 1956, pp. 937–948.

6 Le Fevre, E. J., "Laminar Free Convection from a Vertical Plane Surface." *Actes, IX Congrès International de Mécanique Appliquée*, Vol. 4, Brussels, 1957, pp. 168–174.

7 Kuiken, H. K., "An Asymptotic Solution for Large Prandtl Number Free Convection," *Journal of Engineering Mathematics*, Vol. 2, 1968, pp. 355–371.

8 Roy, Sreedhan, "A Note on Natural Convection at High Prandtl Numbers," *International Journal of Heat and Mass Transfer*, Vol. 12, 1969, pp. 239–241.

Effect of Inhomogeneous Thin Films on the Emittance of a Metal Substrate

R. P. CAREN[1] and C. K. LIU[2]

Introduction

Cravalho and Coburn [1][3] have recently investigated the effect of thin surface films on the total hemispherical radiative properties of metal surfaces by assuming the film to be a homogeneous, nonabsorbing and nondispersive layer. Two of the film-substrate systems considered were metals with oxide films. In practice, the oxides appear in nucleate forms and the oxide surface has a microscopically rough characteristic. The purposes of this discussion are to determine the effect of this fine-scale oxide film roughness on the hemispherical emittance of the metal-oxide film system and to compare the results with the corresponding results obtained by Cravalho and Coburn.

Analysis

In a previous paper [2], the emission of thermal radiation from a microscopically roughened dielectric surface into a vacuum was treated by using a laminar-inhomogeneous layered model for a representation of the roughened surface. A similar model is used in this paper.

As shown in Fig. 1, the metal is separated from the vacuum by a laminar-inhomogeneous dielectric layer of thickness d, in which the index of refraction $n(z)$ is assumed to be an arbitrary function of z. The metal substrate has a complex index of refraction $\tilde{n} = n_m + ik_m$. The optical constants of the metal at room temperature at an angular frequency ω can be computed from a modified free-electron theory [3]:

$$n_m^2 = \frac{\nu_p^2}{2(\omega^2 + \nu_r^2)}\left\{\left[1 + \left(\frac{\nu_r}{\omega}\right)^2\right]^{1/2} - 1\right\} \tag{1a}$$

$$k_m^2 = \frac{\nu_p^2}{2(\omega^2 + \nu_r^2)}\left\{\left[1 + \left(\frac{\nu_r}{\omega}\right)^2\right]^{1/2} + 1\right\} \tag{1b}$$

[1] Director, Research Staff, Engineering Sciences Directorate, Lockheed Palo Alto Research Laboratory, Palo Alto, Calif.

[2] Member, Research Staff, Engineering Sciences Directorate, Lockheed Palo Alto Research Laboratory, Palo Alto, Calif.

[3] Numbers in brackets designate References at end of technical brief.

Contributed by the Heat Transfer Division of THE AMERICAN SOCIETY OF MECHANICAL ENGINEERS. Manuscript received by the Heat Transfer Division December 14, 1970.

$$\eta = y\left(\frac{g\beta q}{5k\nu^2 x}\right)^{1/5}$$

$$F = \frac{\psi}{5x\nu}\left(\frac{5k\nu^2 x}{g\beta q}\right)^{1/5} \tag{3}$$

$$\theta = \frac{k(t_\infty - t)}{q}\left(\frac{g\beta q}{5k\nu^2 x}\right)^{1/5}$$

can be further simplified by stretching the variables

$$\zeta = \eta\,\mathrm{Pr}^{1/5}, \qquad f = F\,\mathrm{Pr}^{4/5}, \qquad \Theta = \theta\,\mathrm{Pr}^{1/5} \tag{4}$$

In the limit $\mathrm{Pr} \to \infty$ the inertial terms in

$$f''' + \frac{1}{\mathrm{Pr}}(4ff'' - 3f'f') + \Theta = 0 \tag{5}$$

become negligible, i.e., viscous friction alone balances the buoyancy force in the thin region where density variations occur. (In this and subsequent equations, primes denote differentiation with respect to ζ.)

The set of coupled equations

$$f''' + \Theta = 0 \tag{6}$$

i.e., the equation of motion, and

$$\Theta'' + 4f\Theta' - f'\Theta = 0 \tag{7}$$

i.e., the transformed thermal energy equation, have been solved with the boundary conditions:

$$\eta = 0, \qquad f = f' = 0, \qquad \Theta' = 1 \tag{8}$$

$$\eta = \infty, \qquad f'' = 0, \qquad \Theta = 0 \tag{9}$$

The boundary condition at $\eta = \infty$ corresponds to the matching condition for the inner region (the diffusion layer) in the first term of a singular perturbation expansion for large Schmidt numbers [5]. The inner region can be solved without treating the outer region. The equivalent problem in free convection to an isothermal plate has been solved by Le Fevre [6], Kuiken [7], and Roy [8].

The results of interest are the local temperature difference $t_\infty - t_0$ and the local shear stress τ_0 at the plate:

$$t_\infty - t_0 = \frac{q}{k}\left(\frac{5k^2\nu x}{g\beta q\rho C_p}\right)^{1/5}\Theta(0) \tag{10}$$

$$\tau_0 = -\frac{5\mu k x}{\rho C_p}\left(\frac{g\beta q\rho C_p}{5k^2\nu x}\right)^{3/5} f''(0) \tag{11}$$

The values of $\Theta(0)$ and $f''(0)$ are

$$\Theta(0) = -1.14747$$

$$f''(0) = 0.83789$$

Table 1 shows that these results are in good agreement with the trend of the values $\Theta(0)$ and $F''(0)$ reported by Sparrow and Gregg [4].

Table 1 Dimensionless temperature difference and shear stress as reported by Sparrow and Gregg [4] and in this work

Pr	$\theta(0)$	$\Theta(0)$	$F''(0)$	$f''(0)$	Ref.
0.1	−2.7507	−1.7356	1.6434	0.65425	4
1	−1.3574	−1.3574	0.72196	0.72196	4
10	−0.76746	−1.2163	0.30639	0.76962	4
100	−0.46566	−1.1697	0.12620	0.79628	4
∞		−1.14747		0.83789	1

References

1 Selman, Jan Robert, and Newman, John, "Migration in Supported Electrolyte Solutions with Free Convection," UCRL-20322, Oct. 1970.

2 Selman, Jan Robert, and Newman, John, "Free-Convection Mass Transfer with a Supporting Electrolyte," *Journal of the Electrochemical Society*, Vol. 118, 1971, pp. 1070–1078.

3 Schlichting, Hermann, *Boundary-Layer Theory*, 6th ed., McGraw-Hill, New York, N. Y., 1968, chap. 12, sec. h, "Thermal Boundary Layers in Natural Flow."

4 Sparrow, E. M., and Gregg, J. L., "Laminar Free Convection From a Vertical Plate With Uniform Surface Heat Flux," TRANS. ASME, Vol. 78, 1956, pp. 435–440.

5 Morgan, George W., and Warner, W. H., "On Heat Transfer in Laminar Boundary Layers at High Prandtl Number," *Journal of the Aeronautical Sciences*, Vol. 23, 1956, pp. 937–948.

6 Le Fevre, E. J., "Laminar Free Convection from a Vertical Plane Surface." *Actes, IX Congrès International de Mécanique Appliquée*, Vol. 4, Brussels, 1957, pp. 168–174.

7 Kuiken, H. K., "An Asymptotic Solution for Large Prandtl Number Free Convection," *Journal of Engineering Mathematics*, Vol. 2, 1968, pp. 355–371.

8 Roy, Sreedhan, "A Note on Natural Convection at High Prandtl Numbers," *International Journal of Heat and Mass Transfer*, Vol. 12, 1969, pp. 239–241.

Effect of Inhomogeneous Thin Films on the Emittance of a Metal Substrate

R. P. CAREN[1] and C. K. LIU[2]

Introduction

Cravalho and Coburn [1][3] have recently investigated the effect of thin surface films on the total hemispherical radiative properties of metal surfaces by assuming the film to be a homogeneous, nonabsorbing and nondispersive layer. Two of the film-substrate systems considered were metals with oxide films. In practice, the oxides appear in nucleate forms and the oxide surface has a microscopically rough characteristic. The purposes of this discussion are to determine the effect of this fine-scale oxide film roughness on the hemispherical emittance of the metal-oxide film system and to compare the results with the corresponding results obtained by Cravalho and Coburn.

Analysis

In a previous paper [2], the emission of thermal radiation from a microscopically roughened dielectric surface into a vacuum was treated by using a laminar-inhomogeneous layered model for a representation of the roughened surface. A similar model is used in this paper.

As shown in Fig. 1, the metal is separated from the vacuum by a laminar-inhomogeneous dielectric layer of thickness d, in which the index of refraction $n(z)$ is assumed to be an arbitrary function of z. The metal substrate has a complex index of refraction $\tilde{n} = n_m + ik_m$. The optical constants of the metal at room temperature at an angular frequency ω can be computed from a modified free-electron theory [3]:

$$n_m^2 = \frac{\nu_p^2}{2(\omega^2 + \nu_r^2)}\left\{\left[1 + \left(\frac{\nu_r}{\omega}\right)^2\right]^{1/2} - 1\right\} \tag{1a}$$

$$k_m^2 = \frac{\nu_p^2}{2(\omega^2 + \nu_r^2)}\left\{\left[1 + \left(\frac{\nu_r}{\omega}\right)^2\right]^{1/2} + 1\right\} \tag{1b}$$

[1] Director, Research Staff, Engineering Sciences Directorate, Lockheed Palo Alto Research Laboratory, Palo Alto, Calif.

[2] Member, Research Staff, Engineering Sciences Directorate, Lockheed Palo Alto Research Laboratory, Palo Alto, Calif.

[3] Numbers in brackets designate References at end of technical brief.

Contributed by the Heat Transfer Division of THE AMERICAN SOCIETY OF MECHANICAL ENGINEERS. Manuscript received by the Heat Transfer Division December 14, 1970.

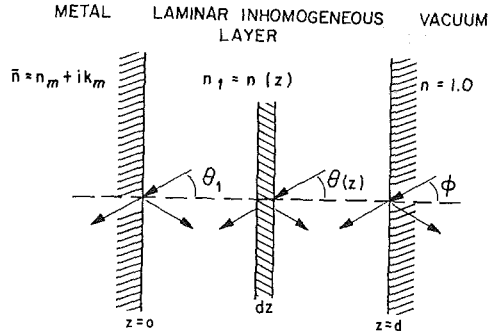

Fig. 1 Reflection geometry for thin, inhomogeneous dielectric film on a metal substrate

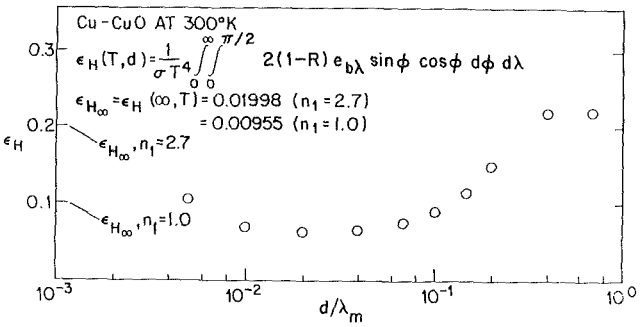

Fig. 2 Total hemispherical emittance of copper oxide on copper at 300 deg K

where $\nu_p = (4\pi Ne^2/m)^{1/2}$ is the plasma frequency in the metal and $\nu_r = Ne^2/m\sigma$ is the electron collision frequency where

N = conduction electron density in the metal (e/cm^3)
e = electronic charge (C)
m = effective electron mass (kg)
$\sigma = Ne^2\tau/m$, direct current conductivity (mho $\cdot m^{-1}$)

The amplitude reflection coefficient $V(z)$ at the position z in an inhomogeneous film for a plane electromagnetic wave of wavelength λ incident at the angle $\theta(z)$, taking into account the multiple reflections in the layer, is given by the Ricatti equation [2],

$$\frac{dV}{dz} = -2imV + \gamma(1 - V^2) \tag{2}$$

where

$$m(z) = \frac{2\pi}{\lambda} n(z) \cos\theta(z) \tag{3}$$

The value of $\gamma(z)$ depends on the polarization state of the incident electromagnetic wave. For the case in which the electric vector is polarized parallel to the plane of incidence (p wave),

$$\gamma_p(z) = \frac{m'}{2m} - \frac{n'}{n} = \frac{n'(z)}{n(z)}\left[\frac{1}{2\cos^2\theta(z)} - 1\right] \tag{4a}$$

and for polarization in the plane of incidence (s wave),

$$\gamma_s(z) = \frac{m'}{2m} = \frac{n'(z)}{2n(z)\cos^2\theta} \tag{4b}$$

where m' and n' are, respectively, the derivatives of m and n with respect to z. Snell's law has been used to obtain the relationship between θ' and n'.

Letting $V = X + iY$, the real and imaginary parts of equation (2) become

$$\frac{dX}{dz} = 2mY + \gamma(1 + Y^2 - X^2) \tag{5a}$$

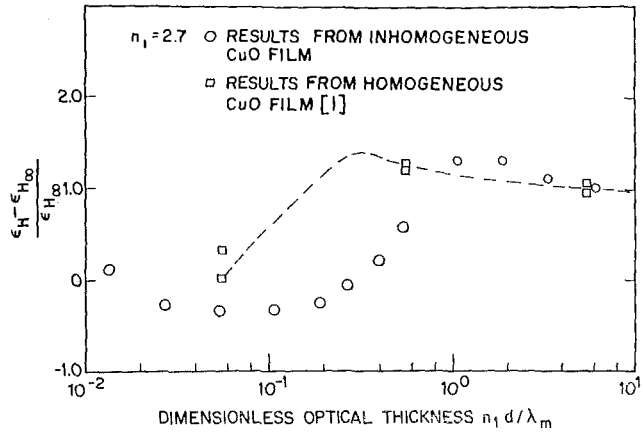

Fig. 3 Comparison of effects of homogeneous and inhomogeneous copper oxide films on the total hemispherical emittance of copper

$$\frac{dY}{dz} = 2X(m + \gamma Y) \tag{5b}$$

To solve equations (5), the value of V at $z = 0$ is assumed to be that of a bare metal facing a homogeneous medium of refractive index $n_1 = n(0)$. Solutions of these equations for the p-wave and s-wave cases are determined separately. In each case, the value of the spectral complex amplitude reflectance at $z = 0$ is determined by substituting the spectral values of the optical constants given in equations (1) into the expressions for the complex reflectances (p wave and s wave) of a metal surface facing a homogeneous dielectric given by Born and Wolf [4]. This provides the values of X_s, Y_s, X_p, and Y_p at $z = 0$. Starting with these initial conditions, the components X_s, Y_s, X_p, and Y_p are determined at $z = d$ by numerical integration of equations (5) with a modified Runge–Kutta approximation [5].

For unpolarized thermal radiation, the energy reflectance R at $z = d$ is given by

$$R(T, d, \lambda, \varphi) = \tfrac{1}{2}(V_s^2 + V_p^2) \tag{6}$$

where

$$V_s^2 = X_s^2 + Y_s^2 \quad \text{and} \quad V_p^2 = X_p^2 + Y_p^2$$

Since the layer is assumed to be nonabsorbing, Kirchhoff's law yields the total hemispherical emittance at $z = d$:

$$\epsilon_H(T, d) = \frac{1}{\sigma T^4}\int_0^\infty\int_0^{\pi/2} 2(1 - R)e_{b\lambda} \sin\varphi \cos\varphi d\varphi d\lambda \tag{7}$$

where $e_{b\lambda}$ is the spectral blackbody emissive power and $\varphi = \theta(z)$ at $z = d$.

For purposes of comparison, the total hemispherical emittance of a bare metal facing vacuum through a thick homogeneous medium of refractive index n_1 is also calculated from equation (7) where the values of R are based simply on the previous values of X_s, Y_s, X_p, and Y_p at $z = 0$.

Results

To illustrate the method described, the film substrate system of copper oxide on copper was investigated. Since the variation of $n(z)$ in a dielectric laminar-inhomogeneous layer does not significantly affect the energy reflectance for a given $n(0)$ and layer thickness [2], the following simple distribution of $n(z)$ was used in the calculations:

$$n(z) = 1 + [n(0) - 1]\left(1 - \frac{z}{d}\right) \tag{8}$$

The physical properties used to calculate the optical constants of copper at 300 deg K are $N = 5.2 \times 10^{28}$ m^{-3} and $\nu_r^{-1} = 1.93$

$\times 10^{-14}$ sec^{-1}. The total hemispherical emittance was calculated from equation (7) for $d/\lambda_m = 0.005$ to 0.7, where λ_m is the wavelength at which $e_{b\lambda}$ is maximum, yielding a film thickness of 0.048 to 6.72 μ. The index of refraction of bulk copper oxide, i.e., $n(0)$, is taken to be 2.7 [1].

Fig. 2 shows the total hemispherical emittance of copper oxide on copper. As the inhomogeneous copper oxide layer thickness increases, the emittance first decreases to a minimum, as expected [6], and then increases to that of a pure copper facing vacuum through a thick homogeneous medium of copper oxide. The latter occurs because the metal substrate "sees" a thin film with the refractive index of copper oxide when the inhomogeneous layer is sufficiently thick. On the other hand, it is apparent from Fig. 3 that the copper oxide layer has no significant effect on the emittance of the copper at an $n_1 d/\lambda_m$ of less than 0.3. The value is higher than that of 0.11, based on an analysis of a homogeneous copper oxide layer [1], indicating that a thicker layer of inhomogeneous copper oxide film can be tolerated without significant changes in the thermal radiation properties of the pure copper.

At first glance, this result is surprising, since the inhomogeneous film represents a smoother transition in terms of impedance than the abrupt change at the dielectric–vacuum interface for a homogeneous film, and higher emittance values would therefore be expected for the former case. However, as has previously been demonstrated [2], although this logic applies for the normal direction, it does not apply for larger angles of emission, where, instead, the emittance is significantly lower for the inhomogeneous film.

These results lead to the general conclusion that fine-scale roughness in the oxide layers on metal surfaces cause a reduction in emittance relative to that of a homogeneous oxide layer of equivalent thickness.

References

1 Cravalho, E. G., and Coburn, E. L., "The Effect of Thin Surface Films on the Radiative Properties of Metal Surfaces," *Progress in Astronautics and Aeronautics*, Vol. 23, Academic Press, New York, N. Y., 1970, p. 363.

2 Caren, R. P., and Liu, C. K., "Thermal Radiation from a Microscopically Roughened Dielectric Surface," ASME Paper No. 71-HT-U, to be published in JOURNAL OF HEAT TRANSFER.

3 Caren, R. P., and Liu, C. K., "Emission, Total Internal Reflection and Tunneling of Thermal Radiation in Metals," *Progress in Astronautics and Aeronautics*, Vol. 21, Academic Press, New York, N. Y., 1969, pp. 509–530.

4 Born, M., and Wolf, E., *Principles of Optics*, Pergamon Press, New York, N. Y., 1965, p. 627.

5 Boche, R. E., and Moore, R. E., "Some Efficient Machine Programs for Solving Ordinary Differential Equations," Report 6-90-64-3, Lockheed Missiles & Space Company, Feb. 1964.

6 Born and Wolf, loc. cit., pp. 62–63.

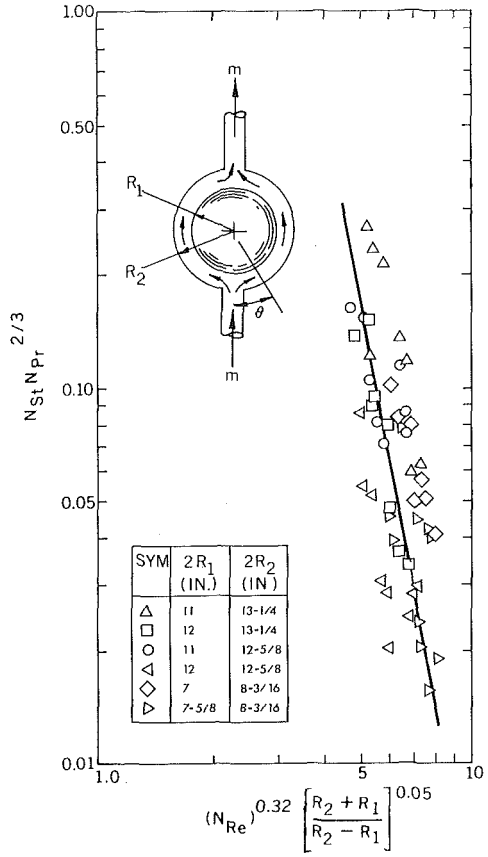

Fig. 1 Correlation of concentric-sphere heat exchanger data

The Concentric-Sphere Heat Exchanger

J. E. COX[1] and B. K. SAHNI[2]

THE dissipation of energy from a spherical heat source to a fluid in a surrounding annulus has received limited attention due to the specialized geometry. Bishop [1][3] experimentally studied free convection where the working fluid is sealed in the annulus. Rundell [2] performed a preliminary experimental study of forced convection where the cooling fluid enters and leaves the annulus through diametrically opposed openings in the outer sphere. The geometrical configuration is shown schematically in the insert of Fig. 1. The inner sphere is copper into which saturated steam is supplied for a constant-temperature heat source. As the fluid travels through the annulus, the coolant (water) absorbs energy from the inner sphere. The outer sphere is fiberglass; the outer surface of the fiberglass was found to be within 1 deg of the surrounding temperature so that losses to the environment could be neglected.

This presentation extends the work of Rundell (a) by verifying and extending the range of variables (generally lower mass flow rates) on two of his sphere-size combinations ($R_2 = 13\frac{1}{4}$-in.; $R_1 = 11$ in. and 12 in.), and (b) by investigating an additional four sphere-size combinations. The new combinations provide a reduced gap distance in the annulus. The overall heat transfer characteristics of the spherical heat exchanger involve the determination of: (a) the change in the bulk fluid temperature of the coolant ($T_0 - T_i$) passing through the spherical annulus; (b) the average surface temperature of the inner sphere T_w; and (c) the mass flow rate of the coolant water $\dot{m}$. The experimental data shown in Fig. 1 are correlated by the relation

$$N_{St} N_{Pr}^{2/3} = 1230 N_{Re}^{-1.76} \left(\frac{R_2 - R_1}{R_2 + R_1}\right)^{0.275} \quad (1)$$

The properties of water are evaluated at the average bulk fluid temperature, $\frac{1}{2}(T_0 + T_i)$. Since the coolant velocity V varies with angular position, the velocity in the Reynolds number N_{Re} and the Stanton number N_{St} is evaluated at $\theta = 90$ deg such that

$$V = \frac{\dot{m}}{\pi\rho(R_2^2 - R_1^2)} \quad (2)$$

[1] Associate Professor of Mechanical Engineering, University of Houston, Houston, Texas. Mem. ASME.

[2] Currently with HEATRAN Equipment Division, Houston, Texas.

[3] Numbers in brackets designate References at end of technical brief.

Contributed by the Heat Transfer Division of THE AMERICAN SOCIETY OF MECHANICAL ENGINEERS. Manuscript received by the Heat Transfer Division May 6, 1971.

$\times 10^{-14}$ sec^{-1}. The total hemispherical emittance was calculated from equation (7) for $d/\lambda_m = 0.005$ to 0.7, where λ_m is the wavelength at which $e_{b\lambda}$ is maximum, yielding a film thickness of 0.048 to 6.72 μ. The index of refraction of bulk copper oxide, i.e., $n(0)$, is taken to be 2.7 [1].

Fig. 2 shows the total hemispherical emittance of copper oxide on copper. As the inhomogeneous copper oxide layer thickness increases, the emittance first decreases to a minimum, as expected [6], and then increases to that of a pure copper facing vacuum through a thick homogeneous medium of copper oxide. The latter occurs because the metal substrate "sees" a thin film with the refractive index of copper oxide when the inhomogeneous layer is sufficiently thick. On the other hand, it is apparent from Fig. 3 that the copper oxide layer has no significant effect on the emittance of the copper at an $n_1 d/\lambda_m$ of less than 0.3. The value is higher than that of 0.11, based on an analysis of a homogeneous copper oxide layer [1], indicating that a thicker layer of inhomogeneous copper oxide film can be tolerated without significant changes in the thermal radiation properties of the pure copper.

At first glance, this result is surprising, since the inhomogeneous film represents a smoother transition in terms of impedance than the abrupt change at the dielectric–vacuum interface for a homogeneous film, and higher emittance values would therefore be expected for the former case. However, as has previously been demonstrated [2], although this logic applies for the normal direction, it does not apply for larger angles of emission, where, instead, the emittance is significantly lower for the inhomogeneous film.

These results lead to the general conclusion that fine-scale roughness in the oxide layers on metal surfaces cause a reduction in emittance relative to that of a homogeneous oxide layer of equivalent thickness.

References

1 Cravalho, E. G., and Coburn, E. L., "The Effect of Thin Surface Films on the Radiative Properties of Metal Surfaces," *Progress in Astronautics and Aeronautics*, Vol. 23, Academic Press, New York, N. Y., 1970, p. 363.

2 Caren, R. P., and Liu, C. K., "Thermal Radiation from a Microscopically Roughened Dielectric Surface," ASME Paper No. 71-HT-U, to be published in JOURNAL OF HEAT TRANSFER.

3 Caren, R. P., and Liu, C. K., "Emission, Total Internal Reflection and Tunneling of Thermal Radiation in Metals," *Progress in Astronautics and Aeronautics*, Vol. 21, Academic Press, New York, N. Y., 1969, pp. 509–530.

4 Born, M., and Wolf, E., *Principles of Optics*, Pergamon Press, New York, N. Y., 1965, p. 627.

5 Boche, R. E., and Moore, R. E., "Some Efficient Machine Programs for Solving Ordinary Differential Equations," Report 6-90-64-3, Lockheed Missiles & Space Company, Feb. 1964.

6 Born and Wolf, loc. cit., pp. 62–63.

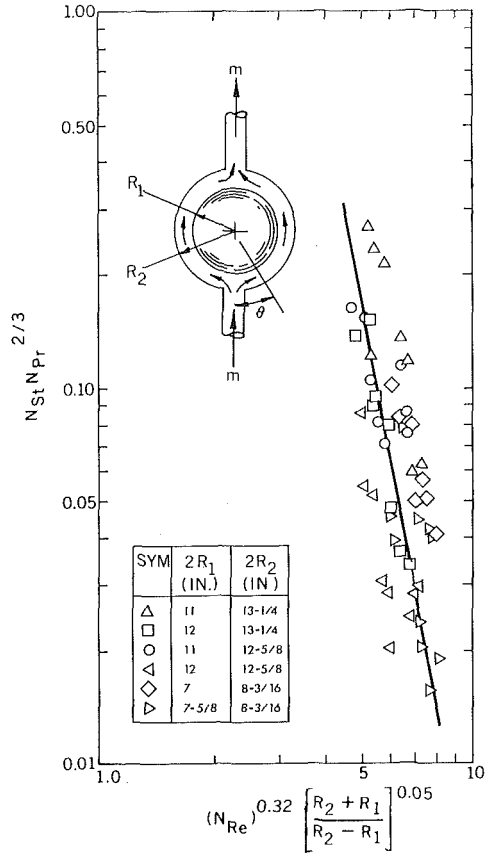

Fig. 1 Correlation of concentric-sphere heat exchanger data

The Concentric-Sphere Heat Exchanger

J. E. COX[1] and B. K. SAHNI[2]

THE dissipation of energy from a spherical heat source to a fluid in a surrounding annulus has received limited attention due to the specialized geometry. Bishop [1][3] experimentally studied free convection where the working fluid is sealed in the annulus. Rundell [2] performed a preliminary experimental study of forced convection where the cooling fluid enters and leaves the annulus through diametrically opposed openings in the outer sphere. The geometrical configuration is shown schematically in the insert of Fig. 1. The inner sphere is copper into which saturated steam is supplied for a constant-temperature heat source. As the fluid travels through the annulus, the coolant (water) absorbs energy from the inner sphere. The outer sphere is fiberglass; the outer surface of the fiberglass was found to be within 1 deg of the surrounding temperature so that losses to the environment could be neglected.

This presentation extends the work of Rundell (a) by verifying and extending the range of variables (generally lower mass flow rates) on two of his sphere-size combinations ($R_2 = 13\frac{1}{4}$-in.; $R_1 = 11$ in. and 12 in.), and (b) by investigating an additional four sphere-size combinations. The new combinations provide a reduced gap distance in the annulus. The overall heat transfer characteristics of the spherical heat exchanger involve the determination of: (a) the change in the bulk fluid temperature of the coolant ($T_0 - T_i$) passing through the spherical annulus; (b) the average surface temperature of the inner sphere T_w; and (c) the mass flow rate of the coolant water $\dot{m}$. The experimental data shown in Fig. 1 are correlated by the relation

$$N_{St} N_{Pr}^{2/3} = 1230 N_{Re}^{-1.76} \left(\frac{R_2 - R_1}{R_2 + R_1}\right)^{0.275} \quad (1)$$

The properties of water are evaluated at the average bulk fluid temperature, $\frac{1}{2}(T_0 + T_i)$. Since the coolant velocity V varies with angular position, the velocity in the Reynolds number N_{Re} and the Stanton number N_{St} is evaluated at $\theta = 90$ deg such that

$$V = \frac{\dot{m}}{\pi\rho(R_2^2 - R_1^2)} \quad (2)$$

[1] Associate Professor of Mechanical Engineering, University of Houston, Houston, Texas. Mem. ASME.

[2] Currently with HEATRAN Equipment Division, Houston, Texas.

[3] Numbers in brackets designate References at end of technical brief.

Contributed by the Heat Transfer Division of THE AMERICAN SOCIETY OF MECHANICAL ENGINEERS. Manuscript received by the Heat Transfer Division May 6, 1971.

The equivalent diameter D_e employed in the Reynolds number is given by

$$D_e = (R_2^2 - R_1^2)\left(\frac{\sqrt{R_2^2 - R_1^2 + R_2R_1}}{R_2^2 + R_1^2 + R_1R_2}\right) \quad (3)$$

Since the heat transfer coefficient is dependent on the motion of the fluid near the heat transfer surface, the flow characteristics in the annulus govern the performance of the spherical heat exchanger. The inner surface of the outer sphere turns the fluid in the annulus in a rolling motion toward the heat transfer surface. This turbulent motion assists the heat transfer mechanism so that significant heat transfer rates can be secured at relatively low coolant flow rates. To achieve the same turbulent effect in a conventional heat exchanger, much larger flow rates would be required. An interesting characteristic of the concentric-sphere heat exchanger is the significant decrease in the heat transfer coefficient with an increase in the coolant flow rate.

References

1 Bishop, E. H., Kolflat, R. S., Mack, L. R., and Scanlan, J. A., "Convective Heat Transfer Between Concentric Spheres," *Proceedings of the 1964 Heat Transfer and Fluid Mechanics Institute*, Stanford University Press, 1964, p. 69.

2 Rundell, H. A., Ward, E. G., and Cox, J. E., "Forced Convection in Concentric-Sphere Heat Exchangers," JOURNAL OF HEAT TRANSFER, TRANS. ASME, Series C, Vol. 90, No. 1, Feb. 1968, pp. 125–129.

Laminar Gas Flow and Heat Transfer in a Parallel-Plate Channel With Large Temperature Differences

J. W. CHRISTIAN[1] and J. E. HITCHCOCK[2]

Nomenclature

c_p = constant-pressure specific heat
G = mass flux, $\rho_0 u_0$
h = convection heat transfer coefficient
i = enthalpy
k = thermal conductivity
Nu_M = mean Nusselt number, $hs/k_{\ln}$
p = pressure
ΔP = dimensionless pressure drop, $(p - p_0)\rho_{\ln}/G^2$
ΔP_{1D} = ΔP due to density change, from one-dimensional analysis, $(1 - T_B/T_0)\cdot(T_0/T_{\ln})$
Pr = Prandtl number, $\mu c_p/k$
s = distance between plates
t = temperature
T = absolute temperature
$t_{\ln}$ = log mean temperature, $t_w - \Delta t_{\ln}$
$\Delta t_{\ln}$ = log mean temperature difference, $[(t_w - t_0) - (t_w - t_B)]/\ln[(t_w - t_0)/(t_w - t_B)]$
u_0 = inlet velocity
x = axial distance from entrance
μ = dynamic viscosity
ξ = dimensionless axial distance, $(x/s)/(Gs/\mu_{\ln})$
ρ = density

Subscripts

B = bulk mean
0 = inlet
w = plate
$\ln$ = log mean

[1] Captain, USAF, Aerospace Research Laboratories, Wright-Patterson AFB, Ohio. Assoc. Mem. ASME.

[2] Professor of Mechanical Engineering, Air Force Institute of Technology, Wright-Patterson AFB, Ohio. Assoc. Mem. ASME.

Contributed by the Heat Transfer Division of THE AMERICAN SOCIETY OF MECHANICAL ENGINEERS. Manuscript received by the Heat Transfer Division March 30, 1971.

Introduction

IN A paper by Mercer, Pearce, and Hitchcock [1],[3] numerical and experimental results were presented for laminar forced convection in the entrance region between parallel flat plates. Simultaneously developing momentum and thermal boundary layers were considered. Previously, the corresponding flow characteristics, including pressure drop, were reported by Bodoia and Osterle [2]. These numerical solutions apply to flows in which fluid properties remain essentially constant, i.e., small temperature differences.

In this brief, numerical results are presented which include the effects of variable gas properties on flow and heat transfer in the entrance region between parallel, flat isothermal plates. Specifically, mean Nusselt numbers and dimensionless pressure gradients are given for cooling and heating air in the temperature range 500 deg R to 3000 deg R. The data are presented in a form which at most represents an approximate correlation or at least facilitates interpolation. A summary of previous work on the influence of temperature-dependent fluid properties can be found in reference [3].

Analysis

The assumptions employed in the analysis were:

1 The flow is laminar.
2 The flow and heat transfer are steady and two-dimensional.
3 Gas density is inversely proportional to absolute temperature, i.e., the ideal gas law applies and percentage changes in pressure are small (low-speed flow).
4 Viscous dissipation and work of compression are negligible compared with heat conduction.
5 Buoyant forces are negligible compared with viscous and pressure forces.
6 The usual boundary layer assumptions apply, e.g., axial conduction is negligible compared with transverse conduction.
7 Gas velocity and temperature are uniform across the entrance.
8 Both plates have the same uniform temperature.

The governing partial differential equations and a description of the numerical method used to solve them are contained in reference [4]. The method of solution is basically the same as that in reference [1]. Real gas properties were used in the form of third-degree polynomial functions of temperature obtained by least-squares curve fits of tabulated data. Mean Nusselt numbers, based on log mean temperature difference, $\Delta t_{\ln}$, were determined from local values of bulk mean enthalpy, i_B.

$$\mathrm{Nu}_M = {}^1/_2(\mathrm{Pr}_{\ln}/\xi)(i_B - i_0)/(c_{p\ln}\Delta t_{\ln}) \quad (1)$$

where the dimensionless axial distance $\xi = (x/s)/(Gs/\mu_{\ln})$. Mean dimensionless pressure gradients were determined by integrating local pressure gradients along the channel:

$$\Delta P/\xi = (\rho_{\ln}/G^2\xi)\int_{p_0}^{p}(dp/dx)dx \quad (2)$$

Results and Discussion

The flow and heat transfer results presented herein are specifically for air. However, because of the similar dependence of the properties of different gases on absolute temperature, they can reasonably be expected to apply to other gases. In particular, the corresponding results for hydrogen in reference [4] are essentially the same as those for air.

In Fig. 1, mean Nusselt numbers are plotted as a function of

[3] Numbers in brackets designate References at end of technical brief.

The equivalent diameter D_e employed in the Reynolds number is given by

$$D_e = (R_2^2 - R_1^2)\left(\frac{\sqrt{R_2^2 - R_1^2 + R_2R_1}}{R_2^2 + R_1^2 + R_1R_2}\right) \quad (3)$$

Since the heat transfer coefficient is dependent on the motion of the fluid near the heat transfer surface, the flow characteristics in the annulus govern the performance of the spherical heat exchanger. The inner surface of the outer sphere turns the fluid in the annulus in a rolling motion toward the heat transfer surface. This turbulent motion assists the heat transfer mechanism so that significant heat transfer rates can be secured at relatively low coolant flow rates. To achieve the same turbulent effect in a conventional heat exchanger, much larger flow rates would be required. An interesting characteristic of the concentric-sphere heat exchanger is the significant decrease in the heat transfer coefficient with an increase in the coolant flow rate.

References

1 Bishop, E. H., Kolflat, R. S., Mack, L. R., and Scanlan, J. A., "Convective Heat Transfer Between Concentric Spheres," *Proceedings of the 1964 Heat Transfer and Fluid Mechanics Institute*, Stanford University Press, 1964, p. 69.

2 Rundell, H. A., Ward, E. G., and Cox, J. E., "Forced Convection in Concentric-Sphere Heat Exchangers," JOURNAL OF HEAT TRANSFER, TRANS. ASME, Series C, Vol. 90, No. 1, Feb. 1968, pp. 125–129.

Laminar Gas Flow and Heat Transfer in a Parallel-Plate Channel With Large Temperature Differences

J. W. CHRISTIAN[1] and J. E. HITCHCOCK[2]

Nomenclature

c_p = constant-pressure specific heat
G = mass flux, $\rho_0 u_0$
h = convection heat transfer coefficient
i = enthalpy
k = thermal conductivity
Nu_M = mean Nusselt number, $hs/k_{\ln}$
p = pressure
ΔP = dimensionless pressure drop, $(p - p_0)\rho_{\ln}/G^2$
ΔP_{1D} = ΔP due to density change, from one-dimensional analysis, $(1 - T_B/T_0)\cdot(T_0/T_{\ln})$
Pr = Prandtl number, $\mu c_p/k$
s = distance between plates
t = temperature
T = absolute temperature
$t_{\ln}$ = log mean temperature, $t_w - \Delta t_{\ln}$
$\Delta t_{\ln}$ = log mean temperature difference, $[(t_w - t_0) - (t_w - t_B)]/\ln[(t_w - t_0)/(t_w - t_B)]$
u_0 = inlet velocity
x = axial distance from entrance
μ = dynamic viscosity
ξ = dimensionless axial distance, $(x/s)/(Gs/\mu_{\ln})$
ρ = density

Subscripts

B = bulk mean
0 = inlet
w = plate
ln = log mean

Introduction

IN A paper by Mercer, Pearce, and Hitchcock [1],[3] numerical and experimental results were presented for laminar forced convection in the entrance region between parallel flat plates. Simultaneously developing momentum and thermal boundary layers were considered. Previously, the corresponding flow characteristics, including pressure drop, were reported by Bodoia and Osterle [2]. These numerical solutions apply to flows in which fluid properties remain essentially constant, i.e., small temperature differences.

In this brief, numerical results are presented which include the effects of variable gas properties on flow and heat transfer in the entrance region between parallel, flat isothermal plates. Specifically, mean Nusselt numbers and dimensionless pressure gradients are given for cooling and heating air in the temperature range 500 deg R to 3000 deg R. The data are presented in a form which at most represents an approximate correlation or at least facilitates interpolation. A summary of previous work on the influence of temperature-dependent fluid properties can be found in reference [3].

Analysis

The assumptions employed in the analysis were:

1 The flow is laminar.
2 The flow and heat transfer are steady and two-dimensional.
3 Gas density is inversely proportional to absolute temperature, i.e., the ideal gas law applies and percentage changes in pressure are small (low-speed flow).
4 Viscous dissipation and work of compression are negligible compared with heat conduction.
5 Buoyant forces are negligible compared with viscous and pressure forces.
6 The usual boundary layer assumptions apply, e.g., axial conduction is negligible compared with transverse conduction.
7 Gas velocity and temperature are uniform across the entrance.
8 Both plates have the same uniform temperature.

The governing partial differential equations and a description of the numerical method used to solve them are contained in reference [4]. The method of solution is basically the same as that in reference [1]. Real gas properties were used in the form of third-degree polynomial functions of temperature obtained by least-squares curve fits of tabulated data. Mean Nusselt numbers, based on log mean temperature difference, $\Delta t_{\ln}$, were determined from local values of bulk mean enthalpy, i_B.

$$\mathrm{Nu}_M = {}^1/_2(\mathrm{Pr}_{\ln}/\xi)(i_B - i_0)/(c_{p\ln}\Delta t_{\ln}) \quad (1)$$

where the dimensionless axial distance $\xi = (x/s)/(Gs/\mu_{\ln})$. Mean dimensionless pressure gradients were determined by integrating local pressure gradients along the channel:

$$\Delta P/\xi = (\rho_{\ln}/G^2\xi)\int_{p_0}^{p}(dp/dx)dx \quad (2)$$

Results and Discussion

The flow and heat transfer results presented herein are specifically for air. However, because of the similar dependence of the properties of different gases on absolute temperature, they can reasonably be expected to apply to other gases. In particular, the corresponding results for hydrogen in reference [4] are essentially the same as those for air.

In Fig. 1, mean Nusselt numbers are plotted as a function of

[1] Captain, USAF, Aerospace Research Laboratories, Wright-Patterson AFB, Ohio. Assoc. Mem. ASME.
[2] Professor of Mechanical Engineering, Air Force Institute of Technology, Wright-Patterson AFB, Ohio. Assoc. Mem. ASME.

Contributed by the Heat Transfer Division of THE AMERICAN SOCIETY OF MECHANICAL ENGINEERS. Manuscript received by the Heat Transfer Division March 30, 1971.

[3] Numbers in brackets designate References at end of technical brief.

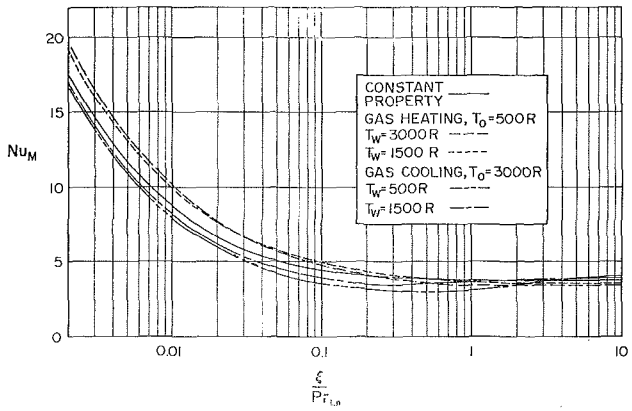

Fig. 1 Heat transfer correlation

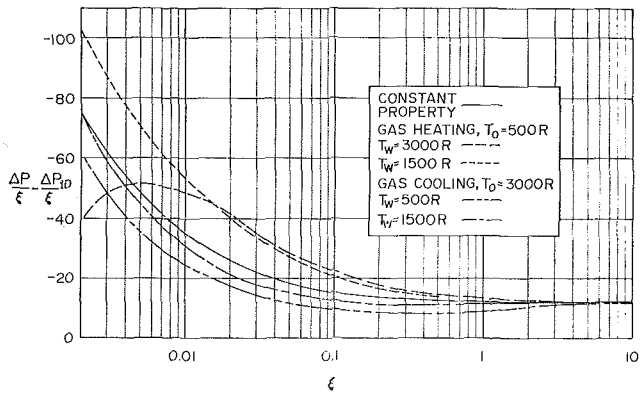

Fig. 2 Pressure drop correlation

the dimensionless distance from the channel entrance divided by the Prandtl number. Note that all fluid properties have been evaluated at the log mean temperature, t_{ln}, where $t_{ln} = t_w - \Delta t_{ln}$. The use of t_{ln} as the reference temperature for properties effectively correlates the results throughout the entrance region. Furthermore, it is a convenient reference temperature since Nu_M is based on Δt_{ln}. Because the correlation is effective, only two heating and two cooling solutions, and the constant-property solution, are shown in Fig. 1. The maximum deviation from the constant-property solution is less than 25 percent. For greater accuracy, one can interpolate. An empirical equation for the constant-property solution was presented in reference [1].

$$Nu_M = 3.77 + \frac{0.066(Pr_{ln}/\xi)^{1.2}}{1 + 0.1Pr_{ln}^{0.87}(1/\xi)^{0.7}} \quad (3)$$

For the variable-property solutions, the limiting value of Nu_M as $\xi \rightarrow \infty$ is given by

$$Nu_M = \frac{3.77(i_w - i_0)}{c_{p_w}(t_w - t_0)} \quad (4)$$

Total pressure changes along the channel are related to the rate of change of momentum of the gas and wall friction. In gas heating, as compared with the constant-property case, a decreasing gas density requires an increased pressure drop to accelerate the flow in order to maintain a constant mass flow rate. Furthermore, increased velocity gradients together with increased gas viscosity near the plates require additional pressure drop to overcome wall friction. The opposite effects are observed for gas cooling. As a consequence, the pressure drops for the maximum heating and cooling cases considered differ by two orders of magnitude.

An estimate of the pressure change required to accelerate or decelerate the flow due to density change can be obtained from a one-dimensional analysis. In the form of a mean dimensionless pressure gradient, the result is

$$\Delta P_{1D}/\xi = (1 - T_B/T_0) \cdot (T_0/T_{ln})/\xi \quad (5)$$

In Fig. 2, mean pressure gradients, equation (2), minus one-dimensional mean pressure gradients, equation (5), have been plotted versus dimensionless distance from the channel entrance. All fluid properties have again been evaluated at the log mean temperature, t_{ln}. The constant-property solution, shown as a solid line in Fig. 2, is represented by the following empirical equation to within 2 percent:

$$\Delta P/\xi = -12.0 - \frac{0.32(1/\xi)^{1.2}}{1 + 0.1(1/\xi)^{0.7}} \quad (6)$$

For gas heating, an approximate correlation of the data has been achieved. Only very near the channel entrance does the maximum heating solution appear to deviate substantially. It is reasonable that in the near entrance region the simple one-dimensional estimate of the effect of density change would be inadequate. However, it should be noted that in this region relatively large values of $\Delta P_{1D}/\xi$ are to be added to ordinate values in Fig. 2 to arrive at $\Delta P/\xi$. Consequently, the percent errors in $\Delta P/\xi$ are considerably less than the apparent percent differences between curves. The maximum error in $\Delta P/\xi$ which results from using the constant-property curve in Fig. 2 is less than 25 percent. For gas cooling, much larger percent errors result; therefore, interpolation is recommended.

Application of Results

The correlations presented in Figs. 1 and 2 enable one to include entrance-region effects in the design or analysis of a parallel-plate heat exchanger with low-speed laminar gas flow and large temperature differences.

The design problem consists of determining the length of channel necessary to heat or cool a gas to a given exit temperature with specified inlet and wall temperatures. Either an iterative or a graphic solution can be used. For example: given the exit temperature, the log mean temperature and fluid properties are determined first. Then a curve of Nu_M versus ξ/Pr_{ln}, from equation (1), is plotted on the graph in Fig. 1. The intersection of this curve with the appropriate pre-existing curve yields ξ/Pr_{ln} at the channel exit. From this, the channel length is determined directly.

To analyze the extent to which a gas will be heated or cooled by a given channel with specified inlet and wall temperatures requires more effort. Given the channel length, one assumes a value of exit temperature and computes corresponding values of ξ/Pr_{ln} and Nu_M, again using equation (1). By iteration, the exit temperature is determined when the calculated values of Nu_M and ξ/Pr_{ln} plot as a point on the appropriate curve in Fig. 1.

With both exit temperature and channel length known, from one or the other of the foregoing heat transfer solutions, the total pressure drop can be determined without iteration. The value of $\Delta P_{1D}/\xi$, from equation (5), is added to the ordinate value in Fig. 2 corresponding to the known ξ. Then the pressure drop, Δp, is computed from the resulting value of the mean dimensionless pressure gradient, $\Delta P/\xi$.

Acknowledgment

The authors wish to acknowledge the Computer Science Center of the Aeronautical Systems Division, Wright-Patterson Air Force Base, Ohio, for the use of its IBM 7094 computer.

References

1 Mercer, W. E., Pearce, W. M., and Hitchcock, J. E., "Laminar Forced Convection in the Entrance Region Between Parallel Flat Plates," JOURNAL OF HEAT TRANSFER, TRANS. ASME, Series C, Vol. 89, No. 3, Aug. 1967, pp. 251–257.

2 Bodoia, J. R., and Osterle, J. F. "Finite Difference Analysis of Plane Poiseuille and Couette Flow Developments," *Applied Scientific Research*, Vol. 10, Sec. A, 1961, pp. 265–276.

3 Kays, W. M., *Convective Heat and Mass Transfer*, McGraw-Hill, New York, N. Y., 1966, chapter 12.
4 Christian, J. W., "Real Gas Property Effects on Flow and Heat Transfer in the Entrance Region of a Parallel-Plate Channel," MS thesis, Department of Mechanical Engineering, Air Force Institute of Technology, Wright-Patterson Air Force Base, Ohio, 1967.

Temperature Effectiveness of Multiple Sandwich Rectangular Plate-Fin Surfaces

RAMESH K. SHAH[1]

Nomenclature

A = total convective heat transfer area, inclusive of the extended and direct surface
A_f = total fin convective heat transfer area
E_i = dimensionless parameter = $(\tanh m_i l_i)/m_i l_i$
h = convective heat transfer coefficient for the fin surface
k = thermal conductivity of the fin material
l = fin length for the conduction heat transfer
m = fin parameter = $\sqrt{\frac{2h}{k\delta}\left(1+\frac{\delta}{\xi}\right)}$
q_e = heat leakage rate at the fin end
q_0 = heat transfer rate from primary surface to the fin
t_a = ambient fluid temperature
t_0 = fin temperature at the base, at the primary surface
δ = fin thickness
η_f = temperature effectiveness of the fin defined as the ratio of the actual q_0 to that which would be obtained if the thermal conductivity of the fin material were infinite
η_0 = overall fin surface temperature effectiveness = $1-\frac{A_f}{A}(1-\eta_f)$
ξ = fin length in air or gas flow direction

Introduction

HEAT exchangers with highly compact surfaces usually have a large frontal area and a small flow length. To achieve high frontal area with plate–fin type surfaces, one or more layers of the compact surface are used between two passages of the other heat transfer fluid. Fig. 1 is a sketch of the single–triple sandwich construction of a rectangular plate–fin surface.

The determination of temperature effectiveness η_f, also referred to as fin effectiveness, of multiple sandwich surfaces is essential for the evaluation of surface basic heat transfer characteristics. It is also needed to account for a decrease in the overall heat transfer coefficient used in the design of such a heat exchanger.

The analysis for the determination of temperature effectiveness of multiple sandwich fins is somewhat complicated. Attempts were made to derive closed-form solutions for triple sandwich fins [1],[2] and double sandwich fins [2]. The procedure for the reduction of triple sandwich η_f to the double sandwich η_f in [1] was in doubt, because of some ambiguities in the boundary conditions. The η_f in [2] was evaluated for the symmetric geometries. The objectives of this note are twofold: to present the η_f of multiple sandwich and other related fins, and to show the effect on the η_f of aligned and nonaligned fin passages of double and triple sandwich construction. In multiple sandwich surfaces, the fin passages among different layers are generally not aligned. The extreme cases, perfect alignment and nonalignment of fin passages, will be considered in the analysis.

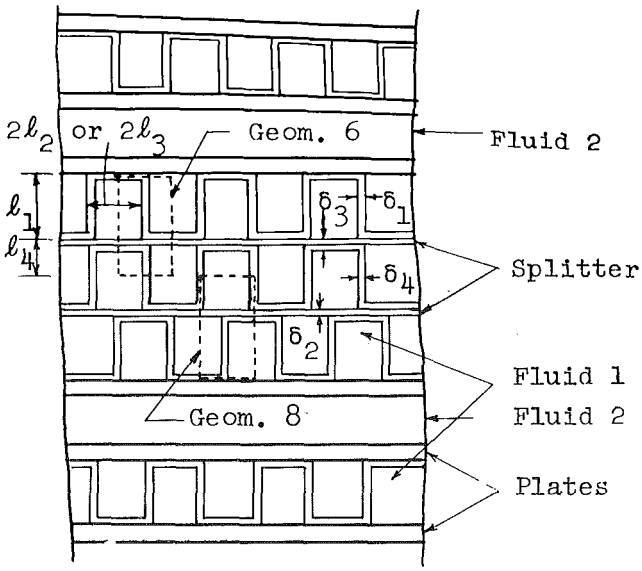

Fig. 1 Single–triple sandwich rectangular plate–fin surface, as it is shown in the figure, $\delta_1 = \delta_2 = \delta_4$

Analysis and Discussion

The temperature effectiveness of a single sandwich fin (one-half of the fin represented by Geometry 1 in Table 1) is determined from a one-dimensional analysis of heat transfer through the fin. The analysis employs uniform and constant thermal conductivity, heat transfer coefficient, and ambient fluid temperature. The radiation heat transfer, contact thermal resistance, and thermal energy sources are neglected. The fin effectiveness of the single sandwich surface is obtained as follows [3]:

$$\eta_f = \frac{\tanh m_1 l_1}{m_1 l_1}$$

The analysis for the multiple sandwich fins follows exactly under the same idealizations and method used for single sandwich fins. Ordinary linear differential equations are obtained for each branch and are coupled at the junction by the energy balance. The temperature effectiveness of various multiple sandwich fins thus determined is presented in Table 1. The details of the analysis for each of the geometries are presented in [3].

For triple sandwich fins, Geometry 6 is used as an approximation to determine the η_f, if the passages are aligned, as are the first two layers of the triple sandwich fin in Fig. 1. For nonaligned fin passages, however, such as the second and third layer of the triple sandwich fin in Fig. 1, the fins are approximated using Geometry 8.

The fin effectiveness of a particular triple sandwich surface [1] was determined using the η_f formulae for the aligned and nonaligned passages. The results are tabulated in [3] as a function of heat transfer coefficient. The overall fin effectiveness η_0 for the nonaligned passages was found to be only a maximum of 0.33 percent higher than that for the aligned passages. Considering the complexity of the problem and the many idealizations made for arriving at η_0, the use of the more simple aligned passage case is therefore recommended for the determination of η_0. For the case of double sandwich fins, the η_0 calculated for the aligned passages is approximately the mean value of the two extreme cases (within ± 0.19 percent) of the nonaligned passages [3], and is therefore recommended for the fin effectiveness evaluation.

[1] Graduate Student, Department of Mechanical Engineering, Stanford University, Stanford, Calif. Assoc. Mem. ASME.
[2] Numbers in brackets designate References at end of technical brief.
Contributed by the Heat Transfer Division of THE AMERICAN SOCIETY OF MECHANICAL ENGINEERS. Manuscript received by the Heat Transfer Division February 18, 1971.

3 Kays, W. M., *Convective Heat and Mass Transfer*, McGraw-Hill, New York, N. Y., 1966, chapter 12.
4 Christian, J. W., "Real Gas Property Effects on Flow and Heat Transfer in the Entrance Region of a Parallel-Plate Channel," MS thesis, Department of Mechanical Engineering, Air Force Institute of Technology, Wright-Patterson Air Force Base, Ohio, 1967.

Temperature Effectiveness of Multiple Sandwich Rectangular Plate-Fin Surfaces

RAMESH K. SHAH[1]

Nomenclature

A = total convective heat transfer area, inclusive of the extended and direct surface
A_f = total fin convective heat transfer area
E_i = dimensionless parameter = $(\tanh m_i l_i)/m_i l_i$
h = convective heat transfer coefficient for the fin surface
k = thermal conductivity of the fin material
l = fin length for the conduction heat transfer
m = fin parameter = $\sqrt{\frac{2h}{k\delta}\left(1+\frac{\delta}{\xi}\right)}$
q_e = heat leakage rate at the fin end
q_0 = heat transfer rate from primary surface to the fin
t_a = ambient fluid temperature
t_0 = fin temperature at the base, at the primary surface
δ = fin thickness
η_f = temperature effectiveness of the fin defined as the ratio of the actual q_0 to that which would be obtained if the thermal conductivity of the fin material were infinite
η_0 = overall fin surface temperature effectiveness = $1-\frac{A_f}{A}(1-\eta_f)$
ξ = fin length in air or gas flow direction

Introduction

HEAT exchangers with highly compact surfaces usually have a large frontal area and a small flow length. To achieve high frontal area with plate–fin type surfaces, one or more layers of the compact surface are used between two passages of the other heat transfer fluid. Fig. 1 is a sketch of the single–triple sandwich construction of a rectangular plate–fin surface.

The determination of temperature effectiveness η_f, also referred to as fin effectiveness, of multiple sandwich surfaces is essential for the evaluation of surface basic heat transfer characteristics. It is also needed to account for a decrease in the overall heat transfer coefficient used in the design of such a heat exchanger.

The analysis for the determination of temperature effectiveness of multiple sandwich fins is somewhat complicated. Attempts were made to derive closed-form solutions for triple sandwich fins [1],[2] and double sandwich fins [2]. The procedure for the reduction of triple sandwich η_f to the double sandwich η_f in [1] was in doubt, because of some ambiguities in the boundary conditions. The η_f in [2] was evaluated for the symmetric geometries. The objectives of this note are twofold: to present the η_f of multiple sandwich and other related fins, and to show the effect on the η_f of aligned and nonaligned fin passages of double and triple sandwich construction. In multiple sandwich surfaces, the fin passages among different layers are generally not aligned. The extreme cases, perfect alignment and nonalignment of fin passages, will be considered in the analysis.

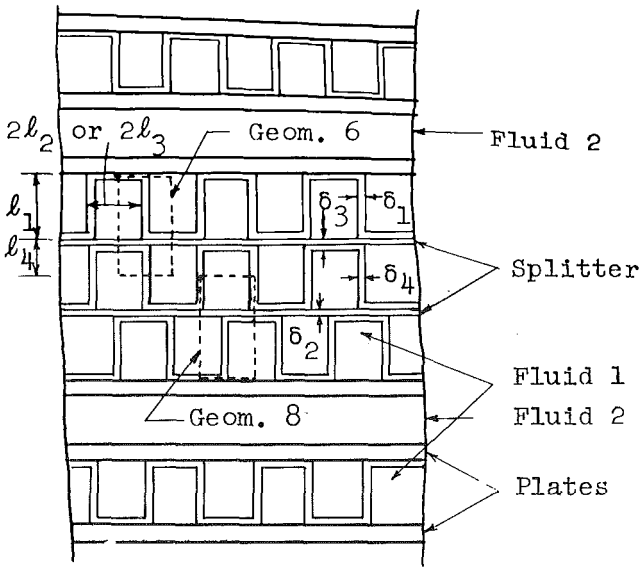

Fig. 1 Single–triple sandwich rectangular plate–fin surface, as it is shown in the figure, $\delta_1 = \delta_2 = \delta_4$

Analysis and Discussion

The temperature effectiveness of a single sandwich fin (one-half of the fin represented by Geometry 1 in Table 1) is determined from a one-dimensional analysis of heat transfer through the fin. The analysis employs uniform and constant thermal conductivity, heat transfer coefficient, and ambient fluid temperature. The radiation heat transfer, contact thermal resistance, and thermal energy sources are neglected. The fin effectiveness of the single sandwich surface is obtained as follows [3]:

$$\eta_f = \frac{\tanh m_1 l_1}{m_1 l_1}$$

The analysis for the multiple sandwich fins follows exactly under the same idealizations and method used for single sandwich fins. Ordinary linear differential equations are obtained for each branch and are coupled at the junction by the energy balance. The temperature effectiveness of various multiple sandwich fins thus determined is presented in Table 1. The details of the analysis for each of the geometries are presented in [3].

For triple sandwich fins, Geometry 6 is used as an approximation to determine the η_f, if the passages are aligned, as are the first two layers of the triple sandwich fin in Fig. 1. For nonaligned fin passages, however, such as the second and third layer of the triple sandwich fin in Fig. 1, the fins are approximated using Geometry 8.

The fin effectiveness of a particular triple sandwich surface [1] was determined using the η_f formulae for the aligned and nonaligned passages. The results are tabulated in [3] as a function of heat transfer coefficient. The overall fin effectiveness η_0 for the nonaligned passages was found to be only a maximum of 0.33 percent higher than that for the aligned passages. Considering the complexity of the problem and the many idealizations made for arriving at η_0, the use of the more simple aligned passage case is therefore recommended for the determination of η_0. For the case of double sandwich fins, the η_0 calculated for the aligned passages is approximately the mean value of the two extreme cases (within ± 0.19 percent) of the nonaligned passages [3], and is therefore recommended for the fin effectiveness evaluation.

[1] Graduate Student, Department of Mechanical Engineering, Stanford University, Stanford, Calif. Assoc. Mem. ASME.
[2] Numbers in brackets designate References at end of technical brief.
Contributed by the Heat Transfer Division of THE AMERICAN SOCIETY OF MECHANICAL ENGINEERS. Manuscript received by the Heat Transfer Division February 18, 1971.

Table 1 A catalog of temperature effectiveness of straight rectangular plate–fin surfaces

Geometry No.	q_o - Heat transfer rate from primary surface to the fin All the figures below show the fin or extended surface only	$m_i = \sqrt{\frac{2h}{k\delta_i}\left(1 + \frac{\delta_i}{\ell_i}\right)}$, $E_i = \frac{\tanh m_i \ell_i}{m_i \ell_i}$, $i = 1,2,3,4,5,6$ ‖ means no heat transfer through the surface
1		$\eta_f = E_1$
2	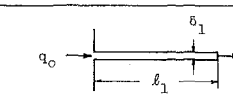	$\eta_f = \dfrac{hA_1(t_o - t_a)\dfrac{\sinh m_1\ell_1}{m_1\ell_1} + q_e}{\cosh m_1\ell_1\left[hA_1(t_o - t_a) + q_e\dfrac{t_o - t_a}{t_\ell - t_a}\right]}$
3	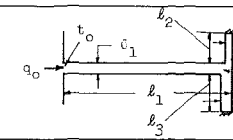	$\eta_f = \dfrac{2E_1\ell_1 + E_2\ell_2 + E_3\ell_3}{2\ell_1 + \ell_2 + \ell_3}\left[\dfrac{1}{1 + \frac{m_1^2}{2}\ell_1E_1(E_2\ell_2 + E_3\ell_3)}\right] = \eta_{f123}$
4	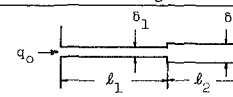	$\eta_f = \dfrac{E_1\ell_1 + E_2\ell_2}{\ell_1 + \ell_2}\left[\dfrac{1}{1 + m_1^2\ell_1\ell_2E_1E_2}\right] = \eta_{f12}$
5	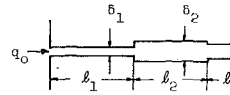	$\eta_f = \dfrac{E_3\ell_3 + \eta_{f12}(\ell_1 + \ell_2)/(\ell_1 + \ell_2 + \ell_3)}{1 + m_3^2\ell_3E_3\eta_{f12}(\ell_1 + \ell_2)}$ For η_{f12}, see Geometry 4 above.
6	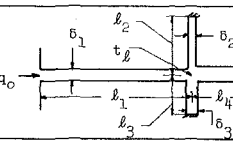	$\eta_f = \dfrac{(E_1\ell_1 + E_2\ell_2 + E_3\ell_3 + E_4\ell_4)/(\ell_1 + \ell_2 + \ell_3 + \ell_4)}{1 + m_1^2\ell_1E_1(E_2\ell_2 + E_3\ell_3 + E_4\ell_4)}$
7	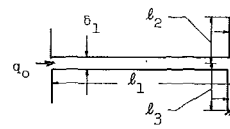	$\eta_f = \dfrac{(E_1\ell_1 + E_2\ell_2 + E_3\ell_3)/(\ell_1 + \ell_2 + \ell_3)}{1 + m_1^2\ell_1E_1(E_2\ell_2 + E_3\ell_3)}$
8	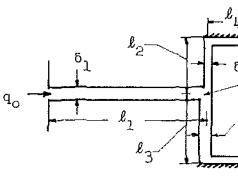	$\eta_f = \dfrac{(E_1\ell_1 + \eta_{f24}\ell_{24} + \eta_{f34}\ell_{34})/(\ell_1 + \ell_2 + \ell_3 + \ell_4)}{1 + m_1^2\ell_1E_1(\eta_{f24}\ell_{24} + \eta_{f34}\ell_{34})}$ $\eta_{f24} = \dfrac{(2E_2\ell_2 + E_4\ell_4)/(2\ell_2 + \ell_4)}{1 + \frac{1}{2}m_2^2\ell_2\ell_4E_2E_4}$ $\quad \ell_{24} = 2\ell_2 + \ell_4$ $\eta_{f34} = \dfrac{(2E_3\ell_3 + E_4\ell_4)/(2\ell_3 + \ell_4)}{1 + \frac{1}{2}m_3^2\ell_3\ell_4E_3E_4}$ $\quad \ell_{34} = 2\ell_3 + \ell_4$
9	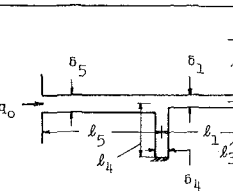	$\eta_f = \left[\dfrac{2E_5\ell_5 + 2E_4\ell_4 + \eta_{f123}(2\ell_1 + \ell_2 + \ell_3)}{2\ell_5 + 2\ell_4 + 2\ell_1 + \ell_2 + \ell_3} \cdot \dfrac{1}{1 + \frac{m_5^2}{2}\ell_5E_5[2E_4\ell_4 + \eta_{f123}(2\ell_1 + \ell_2 + \ell_3)]}\right]$ For η_{f123}, see Geometry 3 above.
10	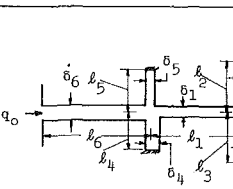	$\eta_f = \left[\dfrac{2E_6\ell_6 + 2E_5\ell_5 + 2E_4\ell_4 + \eta_{f123}(2\ell_1 + \ell_2 + \ell_3)}{2\ell_6 + 2\ell_5 + 2\ell_4 + 2\ell_1 + \ell_2 + \ell_3} \cdot \dfrac{1}{1 + \frac{m_6^2}{2}\ell_6E_6[2E_5\ell_5 + 2E_4\ell_4 + \eta_{f123}(2\ell_1 + \ell_2 + \ell_3)]}\right]$ For η_{f123}, see Geometry 3 above.

A refinement in the determination of triple sandwich η_f may be needed in special cases. In the analysis summarized in Table 1, it was assumed that the temperature of the fluid in all three passages at a given flow cross section of the heat exchanger remains the same. However, if there is no cross-mixing of the fluid between the center and two outer flow passages along the flow length of the heat exchanger, the temperature of the fluid in the outer passages will be higher than that in the center passage. An approximate method was devised to account for this effect of no cross-mixing of the fluid [3]. For the particular triple sandwich plate–fin surface [1], it was shown that the error introduced in η_f due to different temperatures in three passages was negligible.

As a final remark, the fin effectiveness formulae presented in this brief are useful and directly applicable when the heating on the plate–fin surface occurs symmetrically, e.g., in a two-fluid heat exchanger. For nonsymmetric heating, as in the case of a multi-fluid cryogenic heat exchanger, the η_f formulae are still valid, but the plane of zero heat flux may be difficult to locate. Using the appropriate η_f expression, an iterative method may be employed to determine the zero heat flux plane and the correct η_f for the nonsymmetric heating case.

Acknowledgment

The work was performed under the Office of Naval Research Contract Nonr 225(91), NR-090-342.

References

1 Kays, W. M., "The Basic Heat Transfer and Flow Friction Characteristics of Six Compact High-Performance Heat Transfer Surfaces," *Journal of Engineering for Power*, TRANS. ASME, Series A, Vol. 82, No. 1, Jan. 1960, pp. 27–34; also, "The Heat Transfer and Flow Friction Characteristics of Three Double and Triple Sandwich High Performance Heat Transfer Surfaces," TR No. 37, Department of Mechanical Engineering, Stanford University, Stanford, Calif., 1958.

2 Theoclitus, G., and Eckrich, T. L., "An Experimental Technique for Determining the Effectiveness of Extended Surfaces," *Symposium on Air-Cooled Heat Exchanger*, ASME, New York, N. Y., 1964.

3 Shah, R. K., "Temperature Effectiveness of Multiple Sandwich Rectangular Plate-Fin Surfaces," TR No. 71, Department of Mechanical Engineering, Stanford University, Stanford, Calif., 1969.

Influence of Optically Thin Radiation on Heat Transfer in the Thermal Entrance Region of a Narrow Duct[1]

R. GREIF[2] and D. M. McELIGOT[3]

ACCOUNTING for the influence of radiation on the local heat transfer in the entrance region of ducts is a difficult problem. As a result, studies have been limited to specific heating conditions [1, 2][4] or based on simplifying assumptions [3, 4, 5]. The complexity of non-gray radiating flows suggests that the optically thin condition be studied first. Investigations of this simple but relevant regime for flow in tubes resulted in greater insight and ultimately increased understanding of more general and more complex phenomena [6, 7, 8]. For this reason an analysis of the local heat transfer in the entrance region of a narrow duct, assuming optically thin conditions, was undertaken. The walls were considered to be black and maintained at a uniform temperature, T_w, with the gas entering at a uniform temperature, T_0.

In the optically thin limit, the divergence of the radiative flux is given by

$$\text{div } q_R = 4K_p\sigma T^4 - 4K_m\sigma T_w^4 \tag{1}$$

where K_p is the Planck mean coefficient for emission, and K_m, the modified Planck mean coefficient for absorption. The latter is accurately given by $K_{p,w}T_w/T$ (Cess, Mighdoll, and Tiwari [9]). The Planck mean coefficient will be taken to vary inversely with the temperature, cf. Tien [10], p. 313. The energy equation is then given by

$$u^+\frac{\partial T^+}{\partial x^+} = \frac{1}{4}\frac{\partial^2 T^+}{\partial y^{+2}} + J\left[\frac{T_w{}^+}{T^+} - \left(\frac{T^+}{T_w{}^+}\right)^3\right] \tag{2a}$$

with

$$T^+ = T/T_0, \quad u^+ = u/V_b, \quad y^+ = y/D_h,$$

$$x^+ = 4x/D_h \text{ Re Pr}, \quad J = \frac{K_{p,w}\sigma T_w{}^4 D_h}{(kT_0/D_h)}$$

The hydraulic diameter, D_h, is equal to twice the channel spacing, $2b$, and the parameter J is a measure of the importance of the optically thin radiation transport relative to the conduction transport, cf. Sparrow and Cess [11], p. 258. The initial and boundary conditions are given by:

$$T^+(0, y^+) = 1;$$

$$T^+(x^+, 0) = T^+(x^+, \tfrac{1}{2}) = T_w{}^+ = T_w/T_0 \tag{2b}$$

Two velocity profiles are studied: namely, uniform slug flow and the fully developed hydrodynamic condition in laminar flow, the parabolic profile. It should be noted that the slug-flow problem is equivalent to the problem of unsteady one-dimensional energy transport (Chang [12]).

We note that two parameters are necessary to specify the Graetz problem for the idealized gas in the optically thin regime: J and T_w/T_0. For the non-radiating Graetz problem there are no free parameters and a single universal solution may be obtained.

We first consider the case when the temperature differences are small and linearize the radiation term. The resulting partial differential equation is readily solved by use of the Laplace transformation to yield:

$$\phi = \frac{T - T_w}{T_0 - T_w} = e^{-Mx^+}\left(\frac{-4}{\pi}\right)\sum_{n=1}^{\infty}\frac{(-1)^n}{(2n-1)}e^{-4(n-\frac{1}{2})^2\pi^2 x^+} \times \cos\left[(2n-1)2\pi\eta^+\right] \tag{3}$$

with $\eta^+ = y^+ - \frac{1}{4}$ and $M = 4JT_0/T_w$. Note that in the absence of radiation, $M = 0$, so that

$$\frac{\phi_{\text{with rad}}}{\phi_{\text{non-rad}}} = e^{-Mx^+} = \frac{(q_{\text{cond}})_{\text{with rad}}}{(q_{\text{cond}})_{\text{non-rad}}} \tag{4}$$

Thus, the temperature profiles may be obtained simply by solving the non-radiating problem and then multiplying the result by e^{-Mx^+}.

The magnitude of the radiative flux at the wall, $q_{R,w}$, is given by:

$$q_{R,w} = 2\sigma T_w{}^4 K_{p,w} D_h \int_{-1/4}^{1/4} 4\left(\frac{T_w - T}{T_w}\right) d\eta^+ = \frac{4JkT_0}{D_h T_w}(T_w - T_b) \tag{5}$$

The total Nusselt number, defined by $q_{\text{tot},w}D_h/k(T_w - T_b)$, is then given by:

$$\text{Nu}_{\text{tot}} = \frac{4J}{(T_w/T_0)} + \pi^2\frac{\sum_{n=1}^{\infty}\exp\left[-4(n-\frac{1}{2})^2\pi^2 x^+\right]}{\sum_{n=1}^{\infty}\frac{\exp\left[-4(n-\frac{1}{2})^2\pi^2 x^+\right]}{(2n-1)^2}} \tag{6}$$

$$\text{Nu}_{\text{tot}} = \text{Nu}_{\text{rad}} + \text{Nu}_{\text{cond}} \tag{7}$$

Note that the conduction contribution is independent of radiation, cf. equation (4). We also see that Nu_{rad} is invariant with respect to axial distance. It should be emphasized that the above results have only been obtained for the linearized slug-flow problem. For the more general non-linear problem we now refer to our numerical calculations.

The numerical method is described by Bankston and McEligot [13] and Schade [14]. The radiation term has been added to the program and solutions are obtained by successive substitution.

Typical results for the temperature distribution are presented

[1] This work was supported by the National Science Foundation, by the U. S. Army Research Office–Durham, and by the U. S. Army Mobility Equipment Research and Development Center, Fort Belvoir, Va. The use of the Computer Center at the University of London is appreciated.

[2] Associate Professor, Imperial College of Science and Technology, London, England; on leave from the University of California, Berkeley, Calif. Mem. ASME.

[3] Professor, Imperial College of Science and Technology, London, England; on leave from the University of Arizona, Tucson, Ariz. Assoc. Mem. ASME.

[4] Numbers in brackets designate References at end of technical brief

Contributed by the Heat Transfer Division of THE AMERICAN SOCIETY OF MECHANICAL ENGINEERS. Manuscript received by the Heat Transfer Division January 22, 1971.

Acknowledgment

The work was performed under the Office of Naval Research Contract Nonr 225(91), NR-090-342.

References

1 Kays, W. M., "The Basic Heat Transfer and Flow Friction Characteristics of Six Compact High-Performance Heat Transfer Surfaces," *Journal of Engineering for Power*, TRANS. ASME, Series A, Vol. 82, No. 1, Jan. 1960, pp. 27–34; also, "The Heat Transfer and Flow Friction Characteristics of Three Double and Triple Sandwich High Performance Heat Transfer Surfaces," TR No. 37, Department of Mechanical Engineering, Stanford University, Stanford, Calif., 1958.

2 Theoclitus, G., and Eckrich, T. L., "An Experimental Technique for Determining the Effectiveness of Extended Surfaces," *Symposium on Air-Cooled Heat Exchanger*, ASME, New York, N. Y., 1964.

3 Shah, R. K., "Temperature Effectiveness of Multiple Sandwich Rectangular Plate-Fin Surfaces," TR No. 71, Department of Mechanical Engineering, Stanford University, Stanford, Calif., 1969.

Influence of Optically Thin Radiation on Heat Transfer in the Thermal Entrance Region of a Narrow Duct[1]

R. GREIF[2] and D. M. McELIGOT[3]

ACCOUNTING for the influence of radiation on the local heat transfer in the entrance region of ducts is a difficult problem. As a result, studies have been limited to specific heating conditions [1, 2][4] or based on simplifying assumptions [3, 4, 5]. The complexity of non-gray radiating flows suggests that the optically thin condition be studied first. Investigations of this simple but relevant regime for flow in tubes resulted in greater insight and ultimately increased understanding of more general and more complex phenomena [6, 7, 8]. For this reason an analysis of the local heat transfer in the entrance region of a narrow duct, assuming optically thin conditions, was undertaken. The walls were considered to be black and maintained at a uniform temperature, T_w, with the gas entering at a uniform temperature, T_0.

In the optically thin limit, the divergence of the radiative flux is given by

$$\text{div } q_R = 4K_p\sigma T^4 - 4K_m\sigma T_w^4 \tag{1}$$

where K_p is the Planck mean coefficient for emission, and K_m, the modified Planck mean coefficient for absorption. The latter is accurately given by $K_{p,w}T_w/T$ (Cess, Mighdoll, and Tiwari [9]). The Planck mean coefficient will be taken to vary inversely with the temperature, cf. Tien [10], p. 313. The energy equation is then given by

$$u^+\frac{\partial T^+}{\partial x^+} = \frac{1}{4}\frac{\partial^2 T^+}{\partial y^{+2}} + J\left[\frac{T_w{}^+}{T^+} - \left(\frac{T^+}{T_w{}^+}\right)^3\right] \tag{2a}$$

with

$$T^+ = T/T_0, \quad u^+ = u/V_b, \quad y^+ = y/D_h,$$

$$x^+ = 4x/D_h \text{ Re Pr}, \quad J = \frac{K_{p,w}\sigma T_w{}^4 D_h}{(kT_0/D_h)}$$

The hydraulic diameter, D_h, is equal to twice the channel spacing, $2b$, and the parameter J is a measure of the importance of the optically thin radiation transport relative to the conduction transport, cf. Sparrow and Cess [11], p. 258. The initial and boundary conditions are given by:

$$T^+(0, y^+) = 1;$$

$$T^+(x^+, 0) = T^+(x^+, \tfrac{1}{2}) = T_w{}^+ = T_w/T_0 \tag{2b}$$

Two velocity profiles are studied: namely, uniform slug flow and the fully developed hydrodynamic condition in laminar flow, the parabolic profile. It should be noted that the slug-flow problem is equivalent to the problem of unsteady one-dimensional energy transport (Chang [12]).

We note that two parameters are necessary to specify the Graetz problem for the idealized gas in the optically thin regime: J and T_w/T_0. For the non-radiating Graetz problem there are no free parameters and a single universal solution may be obtained.

We first consider the case when the temperature differences are small and linearize the radiation term. The resulting partial differential equation is readily solved by use of the Laplace transformation to yield:

$$\phi = \frac{T - T_w}{T_0 - T_w} = e^{-Mx^+}\left(\frac{-4}{\pi}\right)\sum_{n=1}^{\infty}\frac{(-1)^n}{(2n-1)}e^{-4(n-\frac{1}{2})^2\pi^2 x^+} \times \cos\left[(2n-1)2\pi\eta^+\right] \tag{3}$$

with $\eta^+ = y^+ - \frac{1}{4}$ and $M = 4JT_0/T_w$. Note that in the absence of radiation, $M = 0$, so that

$$\frac{\phi_{\text{with rad}}}{\phi_{\text{non-rad}}} = e^{-Mx^+} = \frac{(q_{\text{cond}})_{\text{with rad}}}{(q_{\text{cond}})_{\text{non-rad}}} \tag{4}$$

Thus, the temperature profiles may be obtained simply by solving the non-radiating problem and then multiplying the result by e^{-Mx^+}.

The magnitude of the radiative flux at the wall, $q_{R,w}$, is given by:

$$q_{R,w} = 2\sigma T_w{}^4 K_{p,w} D_h \int_{-1/4}^{1/4} 4\left(\frac{T_w - T}{T_w}\right) d\eta^+ = \frac{4JkT_0}{D_h T_w}(T_w - T_b) \tag{5}$$

The total Nusselt number, defined by $q_{\text{tot},w}D_h/k(T_w - T_b)$, is then given by:

$$\text{Nu}_{\text{tot}} = \frac{4J}{(T_w/T_0)} + \pi^2\frac{\sum_{n=1}^{\infty}\exp\left[-4(n-\frac{1}{2})^2\pi^2 x^+\right]}{\sum_{n=1}^{\infty}\frac{\exp\left[-4(n-\frac{1}{2})^2\pi^2 x^+\right]}{(2n-1)^2}} \tag{6}$$

$$\text{Nu}_{\text{tot}} = \text{Nu}_{\text{rad}} + \text{Nu}_{\text{cond}} \tag{7}$$

Note that the conduction contribution is independent of radiation, cf. equation (4). We also see that Nu_{rad} is invariant with respect to axial distance. It should be emphasized that the above results have only been obtained for the linearized slug-flow problem. For the more general non-linear problem we now refer to our numerical calculations.

The numerical method is described by Bankston and McEligot [13] and Schade [14]. The radiation term has been added to the program and solutions are obtained by successive substitution.

Typical results for the temperature distribution are presented

[1] This work was supported by the National Science Foundation, by the U. S. Army Research Office–Durham, and by the U. S. Army Mobility Equipment Research and Development Center, Fort Belvoir, Va. The use of the Computer Center at the University of London is appreciated.

[2] Associate Professor, Imperial College of Science and Technology, London, England; on leave from the University of California, Berkeley, Calif. Mem. ASME.

[3] Professor, Imperial College of Science and Technology, London, England; on leave from the University of Arizona, Tucson, Ariz. Assoc. Mem. ASME.

[4] Numbers in brackets designate References at end of technical brief

Contributed by the Heat Transfer Division of THE AMERICAN SOCIETY OF MECHANICAL ENGINEERS. Manuscript received by the Heat Transfer Division January 22, 1971.

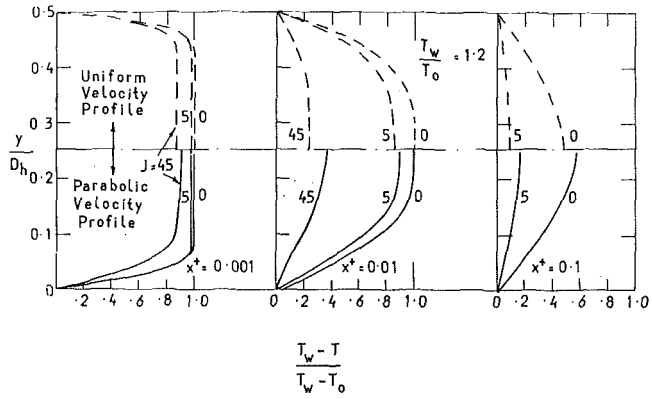

Fig. 1 Dimensionless temperature profiles for the uniform and the parabolic velocity profiles

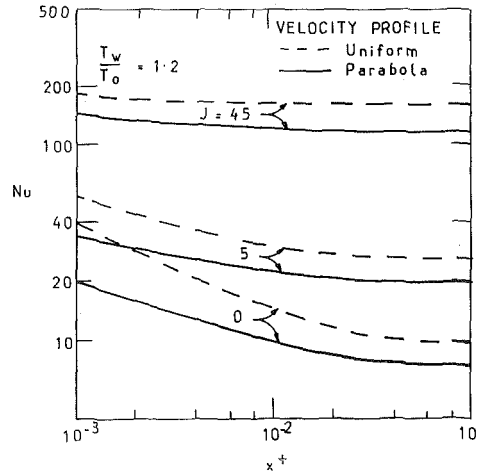

Fig. 2 Nusselt-number variations for the uniform and the parabolic velocity profiles

in Fig. 1. All the curves shown correspond to the temperature ratio, $T_w/T_0 = 1.2$, although the non-radiating curves, $J = 0$, are independent of T_w/T_0.

For linearized radiation in slug flow we showed that the effect of radiation is to reduce the temperature difference below that resulting from conduction alone without altering the form of the temperature difference. This result also appears to hold approximately for the non-linear slug-flow problem. However, with a parabolic velocity distribution, at large values of the parameter J there is a distinct change in the shape of the temperature profile. The result is a significant decrease in the temperature difference in a region near the wall where the smaller velocities or, correspondingly, the longer exposure, allow a strong interaction to take place. On the other hand, in the region away from the wall the velocities are larger than the bulk value, which is also equal to the slug-flow velocity, so that the heating (or cooling) is less effective in the large outer or core region. The overall result is that the heating (or cooling) is more effective for slug flow giving rise to the higher Nusselt numbers, cf. Fig. 2, and smaller dimensionless bulk-temperature differences.

To discuss further the situation when radiation dominates consider the limiting case when conduction can be neglected. Then, for small temperature differences the non-conducting profile is given by

$$\phi = e^{-Mx^+/u^+} \tag{8}$$

This linearized (radiating only) solution has been plotted in Fig. 3 along with the profiles which include conduction and radiation. With the parabolic velocity profile, it is clear that as u^+ approaches zero the local temperature rapidly approaches the wall

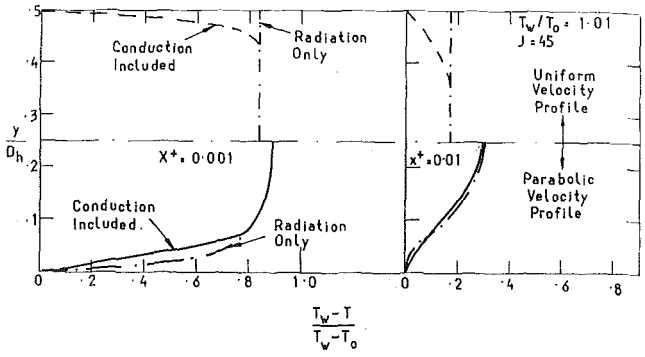

Fig. 3 Dimensionless temperature profiles with radiation dominant

Table 1 Results for the Nusselt number with the uniform velocity profile; $T_w/T_0 = 1.4$

J→ x⁺	0 Nu_{cond}	1 ←(Nu_{cond}) with rad present→	5	10	45	1 ←Nu_{rad}→	5	10	45
.001	38.8	38.8	38.8	38.8	38.7	2.59	13.0	25.9	117.
.002	28.4	28.4	28.4	28.4	28.3	2.59	13.0	26.0	118.
.005	19.2	19.2	19.1	19.1	19.0	2.60	13.0	26.1	121.
.010	14.7	14.7	14.7	14.6	14.6	2.61	13.1	26.4	124.
.020	11.8	11.8	11.8	11.8	11.8	2.62	13.3	26.9	127.
.050	10.1	10.1	10.0	10.0	10.1	2.67	13.7	27.9	133.
.100	9.86	9.85	9.84	9.84	-	2.74	14.1	28.4	-

temperature, cf. equation (8) and Fig. 3. Indeed, in this region for the non-conducting condition, the heating (or cooling) is more effective than for the conducting case. Recall that in the optically thin limit the gas does not absorb any of its own emitted radiation, so exchange is directly from the wall to the gas or vice versa. Thus, when there is a strong radiation interaction in the region close to the wall (large values of J with the parabolic velocity profile) the energy which has been absorbed in the wall region cannot be transferred to the core if the mechanism of conduction is absent. The results are smaller temperature differences close to the wall and larger temperature differences in the core. Note that with conduction present the temperature profile is smoother, cf. Fig. 3, because the energy absorbed is then *conducted* to the core which is at a lower temperature.

Calculations have been carried out over the range $0.7 \leq T_w/T_0 \leq 1.4$ and $0 \leq J \leq 45$ and tabulations of results are available from the authors. Some results are presented in Tables 1 and 2.[5] Over the range studied the maximum deviation of (Nu_{cond}) with radiation present from Nu_{cond} is about 3 percent for slug flow. This is a real, albeit small, variation since numerical errors are about 1 percent or less. Unfortunately, for the parabolic velocity profile the conduction contribution to the Nusselt number is much more sensitive to radiation, cf. Table 2, and therefore must be obtained from the solution to the complete problem which includes the radiation contribution.

References

1 Nichols, L. D., "Temperature Profile in the Entrance Region of an Annular Passage Considering the Effects of Turbulent Convection and Radiation," *International Journal of Heat and Mass Transfer*, Vol. 8, 1965, p. 589.

2 DeSoto, S., "Coupled Radiation, Conduction, and Convection in Entrance Region Flow," *International Journal of Heat and Mass Transfer*, Vol. 11, 1968, pp. 39–54.

3 Pearce, B. E., and Emery, A. F., "Heat Transfer by Thermal Radiation and Laminar Forced Convection to an Absorbing Fluid in the Entry Region of a Pipe," JOURNAL OF HEAT TRANSFER, TRANS. ASME, Series C, Vol. 92, No. 2, May 1970, pp. 221–230.

4 Timofeyev, V. N., Shklyar, F. R., Malkin, V. M., and Berland, A. Kh., "Combined Heat Transfer in an Absorbing Stream Moving

[5] Detailed results for both the Nusselt number and the bulk temperature are available from the authors.

Table 2 Results for the Nusselt number with the parabolic velocity profile; $T_w/T_0 = 1.4$

$J \rightarrow$ / x^+	0	1	5	10	45	1	5	10	45
	Nu_{cond}	← $(Nu_{cond})_{with\ rad\ present}$ →				← Nu_{rad} →			
.001	19.9	19.8	19.4	18.9	15.9	2.36	11.8	23.5	105.
.002	16.0	15.8	15.4	14.9	11.6	2.31	11.6	23.1	103.
.005	12.1	12.0	11.4	10.8	7.31	2.25	11.2	22.4	99.8
.010	10.0	9.86	9.30	8.63	5.10	2.21	11.0	22.0	98.7
.020	8.57	8.42	7.82	7.12	3.69	2.18	10.9	21.9	98.6
.050	7.66	7.50	6.88	6.18	2.92	2.18	11.0	22.3	98.7
.100	7.55	7.38	6.76	6.05	-	2.22	11.3	22.7	-

in a Flat Channel, Part II," *Heat Transfer, Soviet Research*, Vol. 1, No. 6, 1969, pp. 84–93.

5 Kurosaki, Y., "Heat Transfer by Simultaneous Radiation and Convection in an Absorbing and Emitting Medium in a Flow between Parallel Plates," *Fourth International Heat Transfer Conference*, Paris, Vol. 3, R 2.5, 1970.

6 Landram, C. S., Greif, R., and Habib, I. S., "Heat Transfer in Turbulent Pipe Flow With Optically Thin Radiation," JOURNAL OF HEAT TRANSFER, TRANS. ASME, Series C, Vol. 91, No. 3, Aug. 1969, pp. 330–336.

7 Habib, I. S., and Greif, R., "Heat Transfer to a Flowing Non-gray Radiating Gas: An Experimental and Theoretical Study," *International Journal of Heat and Mass Transfer*, Vol. 13, 1970.

8 Emmons, H. W., "Recent Developments in Plasma Heat Transfer," *Modern Developments in Heat Transfer*, edited by W. E. Ibele, Academic Press, New York, 1963, p. 419.

9 Cess, R. D., Mighdoll, P., and Tiwari, S. N., "Infrared Radiative Heat Transfer in Non-Gray Gases," *International Journal of Heat and Mass Transfer*, Vol. 10, 1967, pp. 1521–1532.

10 Tien, C. L., "Thermal Radiation Properties of Gases," *Advances in Heat Transfer*, Vol. 4, Academic Press, New York, 1968.

11 Sparrow, E. M., and Cess, R. D., *Radiation Heat Transfer*, Brooks/Cole, Belmont, Calif., 1966.

12 Chang, Y. P., and Kang, C. S., "Transient and Steady Heat Transfer in a Conducting and Radiating Medium," *American Institute of Aeronautics Journal*, Vol. 8, 1970, pp. 609–613.

13 Bankston, C. A., and McEligot, D. M., "Turbulent and Laminar Heat Transfer to Gases with Varying Properties in the Entry Region of Circular Ducts," *International Journal of Heat and Mass Transfer*, Vol. 13, 1970, pp. 319–344.

14 Schade, K. W., "A Numerical Solution for the Turbulent Flow of a Gas with Strong Property Variation between Parallel Plates," M.S.E. Reports, Aerospace and Mech. Eng. Dept., University of Arizona, 1969.

A Table of *P-v-T* Properties for Superheated Heavy Water Vapor (570 to 700 deg F and 910 to 2030 psia)

C. M. IVEY[1] and J. D. TARASUK[2]

IN THE steam tables of Vukalovitch [1][3] an equation of state is presented together with details of its development and application for an imperfect polyatomic gas based on the theory of "association." In this study the experimental data of Kirillin and Ulibin [2] together with the critical-point data of Whalley [3] were employed to determine constants C_1 and C_2 for this equation of state for the case of superheated heavy water. The equation in the following form with constants C_1 and C_2 accounts for association of heavy water molecules into groups or assemblies of not greater than three molecules. The equation for pressure follows:

$$P = \frac{1}{144v^2}\left\{\left[\frac{v^2RT}{v-b}\left(1 - \frac{A_1(T)}{v-b} - \frac{A_2(T)}{(v-b)^2}\right)\right] - a\right\} \quad (1)$$

where

$$A_1(T) = \frac{C_1 N}{T^{7/2}} \cdot e^{T_c/T}; \qquad A_2 = \frac{N^2}{T^7}(C_2T - 4C_1^2) \cdot e^{2T_c/T}$$

$$a = \frac{27}{8} RT_c b; \quad b = \frac{RT}{8P_c}$$

P = pressure, psia
v = specific volume, ft^3-mole^{-1}
T = temperature, deg R
T_c = critical temperature
N = Avogadro's number
R = gas constant
$C_1 = 0.1874879 \times 10^{-17}$
$C_2 = 0.3117819 \times 10^{-35}$

Tables 1 and 2 display the data of references [2] and [3] respectively which were employed in evaluating constants C_1 and C_2.

The computed values for pressure in Table 3 were calculated by equation (1). Since the experimental data of Kirillin and Ulibin in Table 2 are limited, the equation of state was also determined for superheated light water vapor. The experimental data of Keyes, Smith, and Gerry [4] and the critical-point data of Whalley [3] produced the following values for C_1 and C_2 for light water:

$$C_1 = 0.1801301 \times 10^{-17}; \qquad C_2 = 0.1987865 \times 10^{-35}$$

A total of 21 data points for specific volume ranging from 7.5 to 20.0 cm^3/g and corresponding temperatures ranging from 310 to 370 deg C were applied in determining the constants. The equation of state satisfied all data points greater than 10.0 cm^3/g to within 4.5 percent. For the higher specific volumes and temperatures, within the above range, agreement to within 1 percent was achieved.

The values for the pressure of superheated heavy water vapor shown in Table 3 indicate a similar trend to that for light water.

Table 1 Critical properties of heavy water [2]

T_c, deg C	v_c, cm^3-mole^{-1}	P_c, bar
371.1 ± 0.2	55.0 ± 0.5	218.8 ± 0.5

Table 2 Experimental values for the specific volume of heavy water [3]

	T, deg C					
	300	350	360	369	371	372
P, kg-cm^{-2}	86.64	89.38	74.29	77.87	120.84	93.94
		147.61	135.68	126.25	171.85	152.19
v, cm^3-g^{-1}	19.21	24.02	31.11	30.14	17.42	24.24
		11.12	13.88	16.21	9.912	12.40

[1] Graduate Assistant, Faculty of Engineering Science, The University of Western Ontario, London, Ontario, Canada.

[2] Assistant Professor, Faculty of Engineering Science, The University of Western Ontario, London, Ontario, Canada.

[3] Numbers in brackets designate References at end of technical brief.

Contributed by the Heat Transfer Division of THE AMERICAN SOCIETY OF MECHANICAL ENGINEERS. Manuscript received by the Heat Transfer Division September 9, 1970.

Table 2 Results for the Nusselt number with the parabolic velocity profile; $T_w/T_0 = 1.4$

$J \rightarrow$ / x^+	0	1	5	10	45	1	5	10	45
	Nu_{cond}	← $(Nu_{cond})_{with\ rad\ present}$ →				← Nu_{rad} →			
.001	19.9	19.8	19.4	18.9	15.9	2.36	11.8	23.5	105.
.002	16.0	15.8	15.4	14.9	11.6	2.31	11.6	23.1	103.
.005	12.1	12.0	11.4	10.8	7.31	2.25	11.2	22.4	99.8
.010	10.0	9.86	9.30	8.63	5.10	2.21	11.0	22.0	98.7
.020	8.57	8.42	7.82	7.12	3.69	2.18	10.9	21.9	98.6
.050	7.66	7.50	6.88	6.18	2.92	2.18	11.0	22.3	98.7
.100	7.55	7.38	6.76	6.05	-	2.22	11.3	22.7	-

in a Flat Channel, Part II," *Heat Transfer, Soviet Research*, Vol. 1, No. 6, 1969, pp. 84–93.

5 Kurosaki, Y., "Heat Transfer by Simultaneous Radiation and Convection in an Absorbing and Emitting Medium in a Flow between Parallel Plates," *Fourth International Heat Transfer Conference*, Paris, Vol. 3, R 2.5, 1970.

6 Landram, C. S., Greif, R., and Habib, I. S., "Heat Transfer in Turbulent Pipe Flow With Optically Thin Radiation," JOURNAL OF HEAT TRANSFER, TRANS. ASME, Series C, Vol. 91, No. 3, Aug. 1969, pp. 330–336.

7 Habib, I. S., and Greif, R., "Heat Transfer to a Flowing Non-gray Radiating Gas: An Experimental and Theoretical Study," *International Journal of Heat and Mass Transfer*, Vol. 13, 1970.

8 Emmons, H. W., "Recent Developments in Plasma Heat Transfer," *Modern Developments in Heat Transfer*, edited by W. E. Ibele, Academic Press, New York, 1963, p. 419.

9 Cess, R. D., Mighdoll, P., and Tiwari, S. N., "Infrared Radiative Heat Transfer in Non-Gray Gases," *International Journal of Heat and Mass Transfer*, Vol. 10, 1967, pp. 1521–1532.

10 Tien, C. L., "Thermal Radiation Properties of Gases," *Advances in Heat Transfer*, Vol. 4, Academic Press, New York, 1968.

11 Sparrow, E. M., and Cess, R. D., *Radiation Heat Transfer*, Brooks/Cole, Belmont, Calif., 1966.

12 Chang, Y. P., and Kang, C. S., "Transient and Steady Heat Transfer in a Conducting and Radiating Medium," *American Institute of Aeronautics Journal*, Vol. 8, 1970, pp. 609–613.

13 Bankston, C. A., and McEligot, D. M., "Turbulent and Laminar Heat Transfer to Gases with Varying Properties in the Entry Region of Circular Ducts," *International Journal of Heat and Mass Transfer*, Vol. 13, 1970, pp. 319–344.

14 Schade, K. W., "A Numerical Solution for the Turbulent Flow of a Gas with Strong Property Variation between Parallel Plates," M.S.E. Reports, Aerospace and Mech. Eng. Dept., University of Arizona, 1969.

A Table of *P-v-T* Properties for Superheated Heavy Water Vapor (570 to 700 deg F and 910 to 2030 psia)

C. M. IVEY[1] and J. D. TARASUK[2]

IN THE steam tables of Vukalovitch [1][3] an equation of state is presented together with details of its development and application for an imperfect polyatomic gas based on the theory of "association." In this study the experimental data of Kirillin and Ulibin [2] together with the critical-point data of Whalley [3] were employed to determine constants C_1 and C_2 for this equation of state for the case of superheated heavy water. The equation in the following form with constants C_1 and C_2 accounts for association of heavy water molecules into groups or assemblies of not greater than three molecules. The equation for pressure follows:

$$P = \frac{1}{144v^2}\left\{\left[\frac{v^2RT}{v-b}\left(1 - \frac{A_1(T)}{v-b} - \frac{A_2(T)}{(v-b)^2}\right)\right] - a\right\} \quad (1)$$

where

$$A_1(T) = \frac{C_1 N}{T^{7/2}} \cdot e^{T_c/T}; \qquad A_2 = \frac{N^2}{T^7}(C_2T - 4C_1^2) \cdot e^{2T_c/T}$$

$$a = \frac{27}{8} RT_c b; \quad b = \frac{RT}{8P_c}$$

P = pressure, psia
v = specific volume, ft^3-mole^{-1}
T = temperature, deg R
T_c = critical temperature
N = Avogadro's number
R = gas constant
$C_1 = 0.1874879 \times 10^{-17}$
$C_2 = 0.3117819 \times 10^{-35}$

Tables 1 and 2 display the data of references [2] and [3] respectively which were employed in evaluating constants C_1 and C_2.

The computed values for pressure in Table 3 were calculated by equation (1). Since the experimental data of Kirillin and Ulibin in Table 2 are limited, the equation of state was also determined for superheated light water vapor. The experimental data of Keyes, Smith, and Gerry [4] and the critical-point data of Whalley [3] produced the following values for C_1 and C_2 for light water:

$$C_1 = 0.1801301 \times 10^{-17}; \qquad C_2 = 0.1987865 \times 10^{-35}$$

A total of 21 data points for specific volume ranging from 7.5 to 20.0 cm^3/g and corresponding temperatures ranging from 310 to 370 deg C were applied in determining the constants. The equation of state satisfied all data points greater than 10.0 cm^3/g to within 4.5 percent. For the higher specific volumes and temperatures, within the above range, agreement to within 1 percent was achieved.

The values for the pressure of superheated heavy water vapor shown in Table 3 indicate a similar trend to that for light water.

Table 1 Critical properties of heavy water [2]

T_c, deg C	v_c, cm^3-mole^{-1}	P_c, bar
371.1 ± 0.2	55.0 ± 0.5	218.8 ± 0.5

Table 2 Experimental values for the specific volume of heavy water [3]

	T, deg C					
	300	350	360	369	371	372
P, kg-cm^{-2}	86.64	89.38	74.29	77.87	120.84	93.94
		147.61	135.68	126.25	171.85	152.19
v, cm^3-g^{-1}	19.21	24.02	31.11	30.14	17.42	24.24
		11.12	13.88	16.21	9.912	12.40

[1] Graduate Assistant, Faculty of Engineering Science, The University of Western Ontario, London, Ontario, Canada.

[2] Assistant Professor, Faculty of Engineering Science, The University of Western Ontario, London, Ontario, Canada.

[3] Numbers in brackets designate References at end of technical brief.

Contributed by the Heat Transfer Division of THE AMERICAN SOCIETY OF MECHANICAL ENGINEERS. Manuscript received by the Heat Transfer Division September 9, 1970.

Table 3 Pressures of superheated heavy water vapor, psia

v, ft³/lbm	T, deg F													
	570	580	590	600	610	620	630	640	650	660	670	680	690	700
.510	911	924	937	949	962	974	986	998	1010	1022	1034	1046	1058	1069
.500	926	939	952	964	977	990	1002	1015	1027	1039	1051	1064	1076	1088
.490	940	954	967	980	993	1006	1019	1032	1044	1057	1069	1082	1094	1106
.480	955	969	983	996	1010	1023	1036	1049	1062	1075	1088	1101	1113	1126
.470	971	985	999	1013	1027	1040	1054	1067	1081	1094	1107	1120	1133	1146
.460	987	1001	1016	1030	1044	1058	1072	1086	1100	1113	1127	1140	1153	1167
.450	1003	1018	1033	1048	1062	1077	1091	1105	1119	1133	1147	1161	1174	1188
.440	1020	1035	1051	1066	1081	1096	1110	1125	1139	1154	1168	1182	1196	1210
.430	1037	1053	1069	1085	1100	1115	1130	1146	1160	1175	1190	1204	1219	1233
.420	1055	1071	1088	1104	1120	1136	1151	1167	1182	1197	1212	1227	1242	1257
.410	1073	1090	1107	1124	1140	1156	1173	1189	1204	1220	1236	1251	1267	1282
.400	1091	1109	1127	1144	1161	1178	1195	1211	1228	1244	1260	1276	1292	1307
.390	1110	1129	1147	1165	1183	1200	1217	1234	1251	1268	1285	1301	1318	1334
.380	1130	1149	1168	1186	1205	1223	1241	1259	1276	1293	1311	1328	1345	1361
.370	1149	1169	1189	1208	1228	1246	1265	1283	1301	1320	1337	1355	1373	1390
.360	1169	1190	1211	1231	1251	1271	1290	1309	1328	1347	1365	1383	1402	1420
.350	1190	1212	1233	1254	1275	1295	1316	1336	1355	1375	1394	1413	1432	1450
.340	1210	1233	1256	1278	1300	1321	1342	1363	1383	1403	1423	1443	1463	1482
.330	1231	1255	1279	1302	1325	1347	1369	1391	1412	1433	1454	1475	1495	1515
.320		1277	1302	1327	1350	1374	1397	1419	1442	1464	1486	1507	1528	1550
.310		1300	1326	1351	1376	1401	1425	1449	1472	1495	1518	1541	1563	1585
.300			1349	1376	1403	1428	1454	1479	1504	1528	1552	1575	1599	1622
.290				1401	1429	1456	1483	1509	1535	1561	1586	1611	1635	1660
.280				1425	1455	1484	1513	1540	1568	1595	1621	1647	1673	1699
.270					1481	1512	1542	1571	1601	1629	1657	1685	1712	1739
.260						1539	1571	1602	1633	1664	1694	1723	1752	1780
.250						1564	1599	1633	1666	1698	1730	1761	1792	1822
.240							1626	1662	1697	1732	1766	1800	1832	1865
.230								1689	1728	1765	1802	1837	1873	1907
.220								1713	1755	1796	1835	1874	1912	1949
.210									1779	1823	1866	1908	1949	1990
.200										1845	1892	1938	1983	2027

Above 650 deg F and for specific volumes greater than 0.250 ft³/lbm as shown to the right and above the heavy line, agreement with data points was approximately 1 percent. In this same region the difference between the pressures of light and heavy water vapor may differ by more than 9 percent. For states below 0.250 ft³/lbm and temperatures above 650 deg F the maximum variation from the data of Table 2 does not exceed 3.5 percent.

Equation (1) satisfies the one data point at 300 deg C (572 deg F) of Table 2 to approximately 4 percent. Based on the previous trend indicated for light water it would be reasonable to expect that better agreement would be obtained for high specific volumes and temperatures between 570 and 650 deg F. For specific volumes below those indicated in Table 3, the conditions of saturated vapor are approached. These conditions are approximated in reference [3]. It appears that the application of this equation of state to the available data near the saturated vapor line does not result in the same order of accuracy as found in the results of Table 3.

References

1 Vukalovitch, M. P., *Thermodynamic Properties of Water and Steam*, 6th ed., State Scientific Technical Publication, Moscow, U.S.S.R., 1958.

2 Kirillin, V. A., and Ulibin, S. A., "Experimental Determination of the Specific Volume of Heavy Water over a Wide Range of Temperatures and Pressures," *Proceedings of the Second United Nations International Conference on Peaceful Uses of Atomic Energy*, Geneva, Switzerland, Vol. 28, 1958, p. 159.

3 Whalley, E., "The Thermodynamic and Transport Properties of Heavy Water," *Proceedings of Conference on Thermodynamic and Transport Properties of Fluids*, London, England, 1958, p. 15.

4 Keyes, F. G., Smith, L. B., and Gerry, H. T., "The Specific Volume of Steam in the Saturated and Superheated Condition together with Derived Values of the Enthalpy, Entropy, Heat Capacity and Joule-Thomson Coefficients," *Proceedings American Academy of Arts and Sciences*, Vol. 70, 1936, p. 319.

The Thermal Entry Problem for Laminar Flow Between Parallel Porous Plates

JOHN R. DOUGHTY[1] and HENRY C. PERKINS, JR.[2]

Nomenclature

c_p = specific heat at constant pressure
D = hydraulic diameter, twice the plate spacing
k = thermal conductivity
Nu = Nusselt number, hD/k
Pr = Prandtl number

[1] Major, USAF, Air Force Weapons Laboratory, Kirtland AFB, New Mexico. Mem. ASME.

[2] Professor, Energy, Mass and Momentum Transfer Laboratory, Aerospace and Mechanical Engineering Department, University of Arizona, Tucson, Ariz. Mem. ASME.

Contributed by the Heat Transfer Division of THE AMERICAN SOCIETY OF MECHANICAL ENGINEERS. Manuscript received by the Heat Transfer Division March 9, 1970; revised manuscript received June 8, 1970.

Table 3 Pressures of superheated heavy water vapor, psia

v, ft³/lbm	T, deg F													
	570	580	590	600	610	620	630	640	650	660	670	680	690	700
.510	911	924	937	949	962	974	986	998	1010	1022	1034	1046	1058	1069
.500	926	939	952	964	977	990	1002	1015	1027	1039	1051	1064	1076	1088
.490	940	954	967	980	993	1006	1019	1032	1044	1057	1069	1082	1094	1106
.480	955	969	983	996	1010	1023	1036	1049	1062	1075	1088	1101	1113	1126
.470	971	985	999	1013	1027	1040	1054	1067	1081	1094	1107	1120	1133	1146
.460	987	1001	1016	1030	1044	1058	1072	1086	1100	1113	1127	1140	1153	1167
.450	1003	1018	1033	1048	1062	1077	1091	1105	1119	1133	1147	1161	1174	1188
.440	1020	1035	1051	1066	1081	1096	1110	1125	1139	1154	1168	1182	1196	1210
.430	1037	1053	1069	1085	1100	1115	1130	1146	1160	1175	1190	1204	1219	1233
.420	1055	1071	1088	1104	1120	1136	1151	1167	1182	1197	1212	1227	1242	1257
.410	1073	1090	1107	1124	1140	1156	1173	1189	1204	1220	1236	1251	1267	1282
.400	1091	1109	1127	1144	1161	1178	1195	1211	1228	1244	1260	1276	1292	1307
.390	1110	1129	1147	1165	1183	1200	1217	1234	1251	1268	1285	1301	1318	1334
.380	1130	1149	1168	1186	1205	1223	1241	1259	1276	1293	1311	1328	1345	1361
.370	1149	1169	1189	1208	1228	1246	1265	1283	1301	1320	1337	1355	1373	1390
.360	1169	1190	1211	1231	1251	1271	1290	1309	1328	1347	1365	1383	1402	1420
.350	1190	1212	1233	1254	1275	1295	1316	1336	1355	1375	1394	1413	1432	1450
.340	1210	1233	1256	1278	1300	1321	1342	1363	1383	1403	1423	1443	1463	1482
.330	1231	1255	1279	1302	1325	1347	1369	1391	1412	1433	1454	1475	1495	1515
.320		1277	1302	1327	1350	1374	1397	1419	1442	1464	1486	1507	1528	1550
.310		1300	1326	1351	1376	1401	1425	1449	1472	1495	1518	1541	1563	1585
.300			1349	1376	1403	1428	1454	1479	1504	1528	1552	1575	1599	1622
.290				1401	1429	1456	1483	1509	1535	1561	1586	1611	1635	1660
.280				1425	1455	1484	1513	1540	1568	1595	1621	1647	1673	1699
.270					1481	1512	1542	1571	1601	1629	1657	1685	1712	1739
.260						1539	1571	1602	1633	1664	1694	1723	1752	1780
.250						1564	1599	1633	1666	1698	1730	1761	1792	1822
.240							1626	1662	1697	1732	1766	1800	1832	1865
.230								1689	1728	1765	1802	1837	1873	1907
.220								1713	1755	1796	1835	1874	1912	1949
.210									1779	1823	1866	1908	1949	1990
.200										1845	1892	1938	1983	2027

Above 650 deg F and for specific volumes greater than 0.250 ft³/lbm as shown to the right and above the heavy line, agreement with data points was approximately 1 percent. In this same region the difference between the pressures of light and heavy water vapor may differ by more than 9 percent. For states below 0.250 ft³/lbm and temperatures above 650 deg F the maximum variation from the data of Table 2 does not exceed 3.5 percent.

Equation (1) satisfies the one data point at 300 deg C (572 deg F) of Table 2 to approximately 4 percent. Based on the previous trend indicated for light water it would be reasonable to expect that better agreement would be obtained for high specific volumes and temperatures between 570 and 650 deg F. For specific volumes below those indicated in Table 3, the conditions of saturated vapor are approached. These conditions are approximated in reference [3]. It appears that the application of this equation of state to the available data near the saturated vapor line does not result in the same order of accuracy as found in the results of Table 3.

References

1 Vukalovitch, M. P., *Thermodynamic Properties of Water and Steam*, 6th ed., State Scientific Technical Publication, Moscow, U.S.S.R., 1958.

2 Kirillin, V. A., and Ulibin, S. A., "Experimental Determination of the Specific Volume of Heavy Water over a Wide Range of Temperatures and Pressures," *Proceedings of the Second United Nations International Conference on Peaceful Uses of Atomic Energy*, Geneva, Switzerland, Vol. 28, 1958, p. 159.

3 Whalley, E., "The Thermodynamic and Transport Properties of Heavy Water," *Proceedings of Conference on Thermodynamic and Transport Properties of Fluids*, London, England, 1958, p. 15.

4 Keyes, F. G., Smith, L. B., and Gerry, H. T., "The Specific Volume of Steam in the Saturated and Superheated Condition together with Derived Values of the Enthalpy, Entropy, Heat Capacity and Joule-Thomson Coefficients," *Proceedings American Academy of Arts and Sciences*, Vol. 70, 1936, p. 319.

The Thermal Entry Problem for Laminar Flow Between Parallel Porous Plates

JOHN R. DOUGHTY[1] and HENRY C. PERKINS, JR.[2]

Nomenclature

c_p = specific heat at constant pressure
D = hydraulic diameter, twice the plate spacing
k = thermal conductivity
Nu = Nusselt number, hD/k
Pr = Prandtl number

[1] Major, USAF, Air Force Weapons Laboratory, Kirtland AFB, New Mexico. Mem. ASME.

[2] Professor, Energy, Mass and Momentum Transfer Laboratory, Aerospace and Mechanical Engineering Department, University of Arizona, Tucson, Ariz. Mem. ASME.

Contributed by the Heat Transfer Division of THE AMERICAN SOCIETY OF MECHANICAL ENGINEERS. Manuscript received by the Heat Transfer Division March 9, 1970; revised manuscript received June 8, 1970.

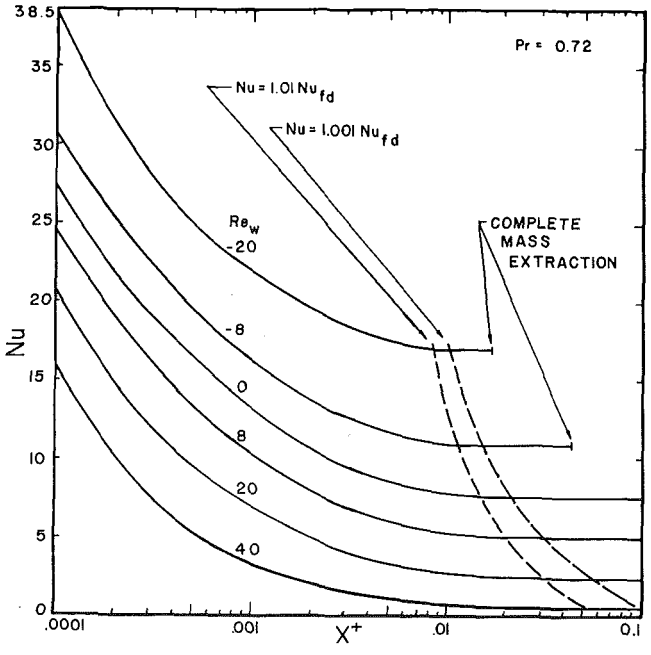

Fig. 1 Constant-property Nusselt numbers for the entrance region of a porous parallel-plate channel

Re_0 = main-channel Reynolds number at the entrance to thermal section, $\rho U_0 D/\mu$
Re_w = wall Reynolds number, positive for injection, $\rho V_w D/\mu$
T = fluid temperature
T_b = local bulk fluid temperature
T_w = wall temperature
u = axial velocity
U_b = bulk axial velocity
U_0 = axial velocity at thermal entrance
v = transverse velocity
V_w = transverse velocity at the wall
x = axial cartesian coordinate
x^+ = inverse Graetz number, $x/D\mathrm{Re}_0\mathrm{Pr}$
y = transverse cartesian coordinate
η = $1-4y/D$, dimensionless transverse coordinate
μ = dynamic viscosity
ρ = density

Introduction

Laminar-flow porous-wall *entrance* problems are being investigated by the authors for constant- and variable-property flows. The results for the hydrodynamic entry problem, that is the length required for flow development with injection or extraction, have been presented in [1].[3] This note presents constant-property solutions for the thermal entry problem for uniform injection and suction through constant-temperature, parallel porous plates. The velocity profiles employed are completely fully developed including the effects of injection or extraction, i.e., the dimensionless velocity profile u/U_b has become invariant with regard to axial position. The problem is of interest for nuclear applications such as the gas-core nuclear rocket where the channel walls may be protected by transpiration cooling and for chemical process applications such as the study of film condensation in vertical ducts where the vapor–liquid interface may be treated as a stationary permeable boundary, i.e., a porous wall.

There are two known previous investigations concerning heat transfer in a laminar flow between parallel porous plates. The first was accomplished by Terrill [2] who obtained solutions for hydrodynamically and thermally fully developed laminar flow for the case of small injection or suction at the wall. He used completely fully developed velocity profiles that result from a third-order perturbation solution of the axial-momentum equation. His solution employs a perturbation method to the Sturm-Liouville problem which results from analysis of the following form of the energy equation

$$\rho c_p\left(u\frac{\partial T}{\partial x}+v\frac{\partial T}{\partial y}\right)=k\frac{\partial^2 T}{\partial y^2} \tag{1}$$

This form is for steady, incompressible, constant-property flow in which viscous dissipation, axial heat conduction, and pressure work terms are neglected. The entry temperature profile of the flow is uniform and at the wall temperature. The flow subsequently encounters a step increase in the wall temperature and solutions are sought for this boundary condition. Terrill indicated his results to be valid over the range $|\mathrm{Re}_w\mathrm{Pr}| < 12$ where $\mathrm{Re}_w\mathrm{Pr}$ is the perturbation parameter. He found there was analogous behavior between heat and momentum transfer in that the friction coefficient and Nusselt number for fully developed conditions decrease with increasing injection. Other parameters of interest such as the temperature profile were not presented in his paper. Terrill and Walker [3] refined the above work and extended it to include the cases of very large suction and injection. They gave fully developed Nusselt-number results for $|\mathrm{Re}_w\mathrm{Pr}| > 80$. The Nusselt number for large injection was found to approach zero asymptotically. For large suction, Nu approaches $-\mathrm{Re}_w\mathrm{Pr}$ which agrees with Kinney's results [4] for the same problem in a porous tube.

Table 1 Fully developed Nusselt numbers, Pr = 0.72

Re_w	Terrill and Walker, equation (30)	Present results
−20	17.12	16.95
−12	12.74	12.71
−8	10.83	10.82
−4	9.09	9.09
−2	8.29	8.29
0	7.54	7.54
2	6.83	6.83
4	6.17	6.16
8	4.99	4.97
12	3.98	3.96
20	2.52	2.40
32	1.70	1.02
40	2.06	0.54

Solution Approach

Predictions for the behavior of the Nusselt number in the thermal entry region were obtained in the present work by using the numerical method of Patankar and Spalding [5] as amended by Bankston and McEligot [6] for internal flow. The method consists of a simultaneous solution of the continuity, energy, and axial-momentum equations at each axial station and is a marching integration routine which depends upon the values obtained at the previous station. The method is treated in complete detail in reference [6] and for the sake of brevity is not repeated here. The computer program used in this work is based upon one developed by Schade [7] for the study of variable-property turbulent flow between parallel non-porous plates. The assumptions relative to equation (1) were the same for this work as those used by Terrill as described above. Consequently, since the properties are held constant and the velocity profiles used are for completely fully developed flow, only the energy-equation solution is required at each axial location. The injected or extracted fluid is assumed to be identical with that of the main-channel flow and to be at the wall temperature when it enters or leaves the wall.

The criterion for thermal development is taken to be when the local Nusselt number is within a certain percentage of the fully developed Nusselt number. The thermal entry lengths for cases where the Nusselt number is within 1 percent and 0.1 percent of the fully developed value are shown in Fig. 1.

[3] Numbers in brackets designate References at end of technical brief.

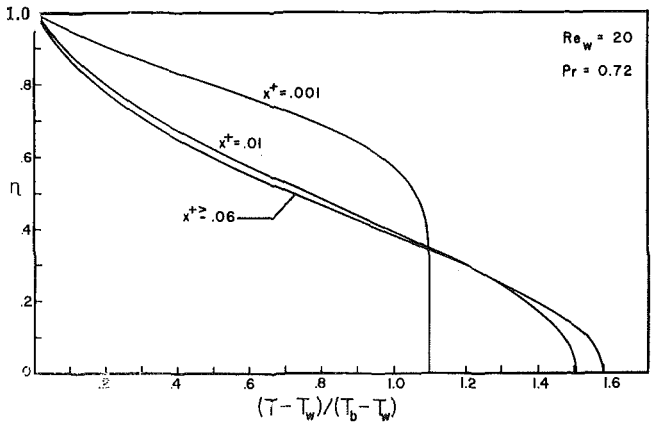

Fig. 2 Development of the dimensionless temperature profile between constant-temperature, parallel porous plates—moderate injection

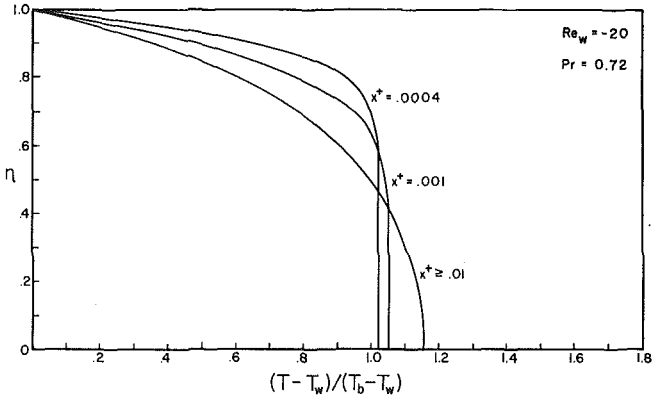

Fig. 3 Development of the dimensionless temperature profile between constant-temperature, parallel porous plates—moderate suction

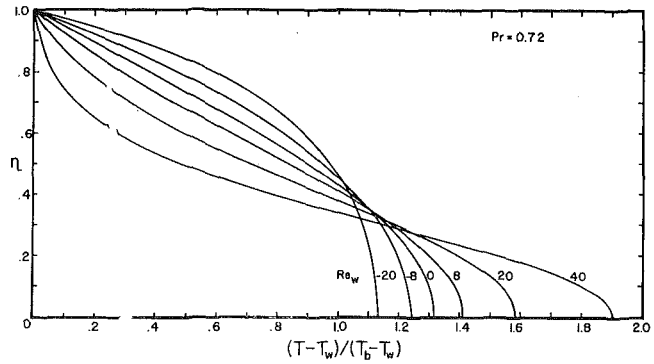

Fig. 4 Fully developed temperature profiles for constant-property laminar flow between parallel porous plates

Results

One of the means used to check the plausibility of the computer-program results was a comparison with solutions obtained by the authors using equation (30) of Terrill and Walker [3]. The comparison in Table 1 is very good in the range for which Terrill held his results to be valid. At moderate wall Reynolds numbers the perturbation solutions lose their validity and the present results are considered to be more accurate, especially for the case of injection. The behavior of the Nusselt number in the thermal entrance region is given in Fig. 1 and is analogous to that of the fraction factor in the hydrodynamic entry region [1], in that the effect of injection is to reduce friction and heat transfer. However, the effect of the injection is to increase the thermal entry length, whereas it was found that injection decreased the hydrodynamic entry length. This observation is in keeping with the solutions given by Pederson [8] for the porous tube where a similar behavior was noted. The present results are in good agreement with known results for $Re_w = 0$.

The behavior of temperature profile after the flow encounters a step increase in the wall temperature is shown for an injection and suction case in Figs. 2 and 3. Fully developed dimensionless temperature profiles for air (Pr = 0.72) at various wall Reynolds numbers are presented in Fig. 4. They exhibit the same behavior and general form as those obtained by Kinney [4] for the porous tube. The decreasing nature of the Nusselt number for moderate injection as shown in Fig. 1 is indicated by the decreasing temperature gradient at the wall for increasing injection. Thus, if one desires to protect walls of a channel or a surface from a hot gas or liquid, one solution, as is presently being used in advanced rocket engines, is to inject a relatively cool fluid at a moderate wall Reynolds number. For sufficiently long channels, the flow will eventually undergo transition to turbulent flow due to the mass addition; however, Huesmann and Eckert [9] found for flow in a porous tube that transition was delayed until the local Reynolds number was 10,000 for an injection wall Reynolds number of 140.

The case of heat transfer with a plane Poiseuille velocity profile at the entry to the porous section and the start of heating (injection and heating start at the same point) was also examined. It was found that there was a negligible difference in the Nusselt-number prediction over that case where the flow is hydrodynamically fully developed (including the effects of injection or suction) prior to heating.

Acknowledgments

Maj. Doughty's work was supported by the Air Force Institute of Technology, Wright-Patterson AFB, Ohio, and the Air Force Weapons Laboratory, Kirtland AFB, New Mexico. The authors wish to acknowledge the computer time furnished by the latter organization and the University of Arizona Computer Center. Partial financial support was also provided by NASA Grant NGR-03-002-213.

References

1 Doughty, J. R., and Perkins, H. C., Jr., "Hydrodynamic Entry Length for Laminar Flow Between Parallel Porous Plates," *Journal of Applied Mechanics*, Vol. 37, TRANS. ASME, Series E, Vol. 92, No. 2, June 1970, pp. 548–550,

2 Terrill, R. M., "Heat Transfer in Laminar Flow between Parallel Porous Plates," *International Journal of Heat and Mass Transfer*, Vol. 8, 1965, pp. 1491–1497.

3 Terrill, R. M., and Walker, G., "Heat and Mass Transfer in Laminar Flow between Parallel Porous Plates," *Applied Scientific Research*, Vol. 18, 1967, pp. 193–220.

4 Kinney, Robert B., "Fully Developed Frictional and Heat-Transfer Characteristics of Laminar Flow in Porous Tubes," *International Journal of Heat and Mass Transfer*, Vol. 11, 1968, pp. 1393–1401.

5 Patankar, S. V., and Spalding, D. B., "A Finite-Difference Procedure for Solving the Equations of the Two-Dimensional Boundary Layer," *International Journal of Heat and Mass Transfer*, Vol. 10, 1967, pp. 1389–1411.

6 Bankston, C. A., and McEligot, D. M., "Numerical Solutions for Turbulent and Laminar Thermal Entries with Gas Property Variations," *International Journal of Heat and Mass Transfer*, Vol. 13, No. 2, 1970, pp. 319–343.

7 Schade, Karl W., "A Numerical Solution for the Turbulent Flow of a Gas with Strong Property Variation between Parallel Plates," MS project, Aerospace and Mechanical Engineering Department, University of Arizona, Tucson, Ariz., 1969.

8 Pederson, Ronald J., "Entry Region Heat Transfer Characteristics for Laminar Flow in Porous Tubes," MS project, Aerospace and Mechanical Engineering Department, University of Arizona, Tucson, Ariz., 1969.

9 Huesmann, K., and Eckert, E. R. G., "Untersuchungen über die laminare Strömung und den Umschlag zur Turbulenz in porösen Rohren mit gleichmässiger Einblasung durch die Rohrwand," *Wärme- und Stoffübertragung*, Vol. 1, 1968, pp. 2–9.

Recommendations for Data Compilations and for the Reporting of Measurements of the Thermal Conductivity of Gases[1]

Introductory Remarks

Since the importance of thermal conductivity data for gases is well established, a program for the evaluation of such data was among the early efforts of the Office of Standard Reference Data to develop a National Standard Reference Data System. This program called for evaluators with various interests and backgrounds to match the needs of the various users. Coordination was necessary to provide basic standards of quality and content, and uniformity of presentation. Accordingly, a panel of experts, interested in the program of the Office of Standard Reference Data, was asked what criteria should be established for critical evalutations in this field.

How well data can be evaluated depends in large measure on the method of measurement and of presentation of the original results. Where positive information is lacking on a particular point, a data evaluator must adopt a very cautious attitude to the results in question; therefore, if an author fails to describe his method adequately, his results may not receive the proper attention or weight. To help avoid such an occurrence, the panel has emphasized the experimental features which are most important to the evaluator.

The primary purpose of the panel meeting, coordination of efforts among evaluators of the Office of Standard Reference Data, has already been served. However, it was felt that the results of the meeting might be of interest to other evaluators of data, and indeed to authors of experimental papers in the field, and editors and reviewers concerned with such papers. No claim can be made that the thoughts contained in these considerations are original or particularly subtle, but it is the experience of the panel members involved that at least one of the important features is missing from a large number of potentially important papers. Systematic attention to these considerations in the designing of experiments and the presentation of results would assure the experimenter of the maximum utilization of his results.

These are the reasons for the present communication.

Recommendations for Compilation of Critically Evaluated Data

Presentation of Evaluated Data. The "recommended" or "best" or "definitive" data should be presented in tabular form even if equations have been developed which are thought to fit all or part of the data within their reliability. If graphical representation is desirable, it should be given in addition to the tabular material. If at all feasible, the interval of presentation in the tables should be such as to allow linear interpolation between points.

Units. The International System of Units (SI units) or units approved for use with the SI units should be used. Where desirable to improve communication or to enhance the usefulness to primary recipients, other units can be expressed by indication of conversion factors, inclusion of parallel columns of converted values, or in other suitable supplementary ways. For further information on SI units see "Policy for NBS Usage of SI Units," *NBS Technical News Bulletin*, Vol. 55, No. 1, Jan. 1971 and "ASTM Metric Practice Guide" *NBS Handbook 102* available from the Superintendent of Documents, U. S. Government Printing Office, Washington, D. C. 20402.

Reliability. Explicit quantitative estimates of the reliability of recommended values should be given. These estimates should take account of the precision of experimental measurements and the estimated magnitudes of systematic errors. A good discussion of methods of treating various degrees of imprecision and systematic error is presented by C. Eisenhart in "Expression of the Uncertainties of Final Results," *Science*, Vol. 160, June 14, 1968, p. 1201. Limits of reliability should also be given for any polynomial or graphical representation that is recommended. Consideration or errors necessarily includes those which might be introduced by manipulative procedures such as extrapolation to an axis or by theoretical approximations in addition to those inherent in the experimental measurements.

Discoursive Material. As a general rule, the various decisions which have been made and the reasons for them should be discussed. There are several types. The field covered by the monograph should be explicitly defined. If closely related material, which is usually considered simultaneously with the material at hand, is omitted, it may be advisable to point out the omission and its reason. The theoretical basis for analysis, for conversion of primary measurements of one type to data of another, for extrapolation, approximation, or other manipulative procedures should be dealt with fully. Auxiliary data used should be considered as well as primary data. As far as is feasible, the reasons for selecting specific data should be detailed.

Whether original data need to be tabulated or not is a matter for discretion. If there are relatively few, tablulation is probably desirable. Selected individual results should be tabulated, especially in cases where some of them have been difficult to obtain, or, if the evaluator has had to make unit conversions or other transformations, to put the original results on a comparable basis. In any event, it is usually desirable to compare the recommended values with the individual measurements, at least in cases where there are several sets of measurements. This can often be done very effectively by graphical methods. A preferred graphical method, where the grouping of the results allows it, is the "deviation plot," in which deviations of individual results from the recommended values are plotted against some experimental parameter. All pertinent experimental results should be included in a deviation plot, and the limits of reliability of the recommended values should be shown.

Bibliography. As a general rule the bibliography should be as comprehensive as possible. If certain types of results are being omitted, for example those obtained using a certain method or those made using a certain instrument before it was developed to a given sensitivity, the omissions should be mentioned explicitly in the text along with reasons. Otherwise it is desirable to include reference to pertinent measurements even if they are not weighted heavily in determining recommended values. One of the evaluator's tasks is to make it unnecessary for others to search the literature prior to his work. He distills the essence of the literature into his recommended value; but others, approaching with other backgrounds, with other purposes, or in the light of subsequent developments, may wish to rework the data to obtain other numbers or to apply new weighting factors. The evaluator's bibliography and his comments then provide the raw material for their efforts.

Recommendations for the Reporting of Experimental Measurements

It is obvious that experimental papers are not written for the exclusive use of data compilers or evaluators. However, when the experimenter intends to provide definitive data on a given system, he must perforce consider certain factors. If he reports fully on these factors, he eases the evaluator's job and assures maximum utilization of his efforts.

---

[1] Considerations of an ad hoc group of specialists assembled by the Office of Standard Reference Data, National Bureau of Standards, consisting of the following members: H. Hanley, NBS Boulder; M. Klein, NBS Washington; P. E. Liley, TPRC Purdue University; S. C. Saxena, TPRC Purdue University (current address, Dept. of Energy Engineering, University of Illinois at Chicago Circle); J. V. Sengers, NBS Washington (current address, Institute for Molecular Physics, University of Maryland); G. Thodos, Northwestern University; and H. J. White, Jr., Office of Standard Reference Data, National Bureau of Standards, U. S. Department of Commerce, Washington, D. C. 20234, to whom inquiries should be directed.

Communicated through S. P. Kezios, Past Senior Technical Editor, Journal of Heat Transfer. Manuscript received April 1, 1970.

If at all possible, tables of original measurements should be given. When the number of measurements, or the editorial policy of the journal in which the paper is published, precludes publication in tabluar form, the results should be made available either through the American Documentation Institute, directly from the author, or in some other way, and this availability declared in the paper.

The results should be subjected to a detailed error analysis. This analysis should include not only the usual precision measures, but also an analysis of possible systematic errors and of correction factors used.

A full description of experimental details should be given, including specifically the following points:

1 A direct experimental assessment of radiative losses.

2 Experimental proof of the absence of convection.

3 A discussion of parasitic conduction and of the efforts made to estimate its magnitude and correct for it.

4 A discussion of the temperature-gradient measurement including specification of the size of the temperature difference and a discussion of the relation of the measured temperature difference and the gradient in the fluid.

5 A discussion of the method of measuring heat flow and its accuracy.

6 Experimental confirmation that the measured thermal conductivity is independent of the magnitude of the temperature gradient (Fourier's law).

7 The determination of the geometrical constants of the system.

8 The geometry of the temperature field.

9 Accommodation coefficients.

10 If the experimental method is a relative method, the calibration and proof of validity of the method.

11 The purity and composition of the sample.

12 Specification of the state variables, including the temperature, at the position in the cell at which the thermal conductivity is measured.

In addition C_p and the equation of state are desirable although not strictly necessary.